

# Les Rencontres de Physique de la Vallée d'Aoste

Results and Perspectives in Particle Physics

Edited by M. Greco

*La Thuile, Aosta Valley*

*February 24<sup>th</sup> - March 1<sup>st</sup>, 2008*



**ISTITUTO NAZIONALE DI FISICA NUCLEARE**  
**Laboratori Nazionali di Frascati**

# **Les Rencontres de Physique de la Vallée d'Aoste**

**Results and Perspectives in Particle Physics**

FRASCATI PHYSICS SERIES

Series Editor

*Danilo Babusci*

Technical Editor

*Luigina Invidia*

---

Volume XLVII — Special Issue

---

*Istituto Nazionale di Fisica Nucleare – Laboratori Nazionali di Frascati  
Divisione Ricerca – SIS – Ufficio Pubblicazioni  
P.O. Box 13, I-00044 Frascati (Roma) Italy  
email: sis.publications@lnf.infn.it*



## FRASCATI PHYSICS SERIES

Les Rencontres de Physique de la Vallée d'Aoste

### **RESULTS AND PERSPECTIVES IN PARTICLE PHYSICS**

Copyright © 2008, by INFN Laboratori Nazionali di Frascati  
SIS – Ufficio Pubblicazioni

*All rights reserved. No part of this publication may be reproduced, stored in retrieval system or transmitted, in any form or by any means, electronic, mechanical, photocopying, recording or otherwise, without the prior permission of the copyright owner.*

ISBN—978—88—86409—56—8

*Printed in Italy by Poligrafica Laziale  
P.le Sandro Pertini 4-6  
00044 Frascati*

FRASCATI PHYSICS SERIES

Volume XLVII

**Les Rencontres de Physique  
de la Vallée d'Aoste**

**Results and Perspectives in Particle Physics**

Editor  
Mario Greco

La Thuile, Aosta Valley, February 24<sup>th</sup> – March 1<sup>st</sup>, 2008

*Conference Organizers*

Giorgio Bellettini	<i>Pisa</i>
Giorgio Chiarelli	<i>Pisa</i>
Mario Greco	<i>Roma III</i>

*List of Chairpersons*

Arnon Dar	<i>Israel</i>
Alvaro De Rujula	<i>CERN</i>
Douglas Bryman	<i>University of British Columbia</i>
Henry Lubatti	<i>University of Washington</i>
Rino Castald	<i>Pisa</i>
Giorgio Chiarelli	<i>Pisa</i>
Victor Novikov	<i>ITEP</i>
Eduard Masso'	<i>University of Barcelona</i>
Mario Greco	<i>Roma III</i>
Peter Minkowski	<i>University of Bern</i>
Giorgio Bellettini	<i>Pisa</i>

## FOREWORD

The 2008 Rencontres de Physique de la Vallée d'Aoste were held at the Planibel Hotel of La Thuile, Aosta Valley, on February 24<sup>th</sup> – March 1<sup>st</sup>, with the twenty–second edition of "Results and Perspectives in Particle Physics".

The physics programme included various topics in particle physics, also in connection with present and future experimental facilities, as cosmology, astrophysics and neutrino physics, CP violation and rare decays, electroweak and hadron physics with  $e^+e^-$  and hadron colliders, heavy flavours and prospects at future facilities.

The Session on "Physics and Society" included special colloquia on New nuclear reactors, and Physics methods in Information Theory.

We are very grateful to Jacopo Buongiorno and Hans Grassmann for their participation.

Giorgio Bellettini, Giorgio Chiarelli and I should like to warmly thank the session chairpersons and the speakers for their contribution to the success of the meeting.

The regional government of the Aosta Valley, in particular through the Minister of Public Education and Culture Laurent Vierin, has been very pleased to offer its financial support and hospitality to the Rencontres of La Thuile. Also on behalf of the participants, representatives of some major Laboratories and Institutes in the world, we would like to thank all the Regional Authorities. Special thanks are also due to Bruno Baschiera, local coordinator of the Rencontres.

We are grateful to the President of INFN Roberto Petronzio, the Directors of INFN Laboratori Nazionali di Frascati, Mario Calvetti and INFN Sezione di Pisa, Rino Castaldi, for the support in the organization of the Rencontres. We would like to thank also Lucia Lilli, Claudia Tofani and Paolo Villani for their help in both planning and running the meeting. We are also grateful to Alessandra Miletto for her valuable

contribution to the local organization of the meeting. The excellent assistance provided by Giovanni Nicoletti and Mauro Giannini made it possible to set up the computer link to the international network. Special thanks are due to Luigina Invidia for valuable help in the technical editing of the Proceedings.

Finally we would like to thank the Mayor Gilberto Roullet and the local authorities of La Thuile and the “Azienda di Promozione Turistica del Monte Bianco” for their warm hospitality, and the Planibel Hotel staff for providing us an enjoyable atmosphere.

September 2008

Mario Greco

## CONTENTS

<b>Foreword</b>	.....	<b>VII</b>
<b>SESSION I – COSMOLOGY AND ASTROPHYSICS</b>	.....	<b>1</b>
Kampert Karl-Heinz	Cosmic Rays at the Highest Energies: Results from the Pierre Auger Observatory.....	3
Ogburn Walter	Results from CDMS .....	17
Marco Casolino	The Pamela Cosmic Ray Space Observatory: Detector, Objectives and First Results .....	19
Dell’Agnello Simone	Probing Gravity in the Solar System with Satellite Laser Ranging .....	49
Colafrancesco Sergio	What an Astrophysicist can tell about the Nature of Dark Matter? .....	57
Dolgov Alexander	Cosmic AntiMatter: Models and Observational Bound .....	69
<b>SESSION II – ASTROPARTICLE AND NEUTRINO PHYSICS</b>	.....	<b>89</b>
Ferroni Fernando	$0\nu\beta\beta$ Present and Future .....	91
Papaevangelou Thomas	Result from CAST .....	101
Ianni Aldo	Detection of Solar Neutrinos with the Borexino Experiment.....	103
Aguilar-Arevalo A.A.	Results from Miniboone .....	109
Garfagnini Alberto	Observation of Neutrino Interactions in the OPERA Detector .....	121
Weber Alfons	Recent results from the MINOS Experiment..	133
Fritzscht Harald	Flavor symmetry and neutrino mixing ..	141
Falk Harris Elizabeth	Double Chooz .....	147
Yeongduk Kim	The Current Status of the RENO Experiment.....	149

Spurio Maurizio	Antares: Towards a Large Underwater Neutrino Experiment ..... 159
Caravaglios Francesco	Neutrinos, Grand Unified Theories and the Hierarchy problem .....175
Kayser Boris	Neutrinos: What We Know, and What We Would Like To Find Out .....191

**SESSION III – QCD AND HADRONIC INTERACTIONS ..... 193**

R. Craig Group	Recent QCD Studies at the Tevatron .... 195
Stanco Luca	From HERA to LHC: Implications and Constraints .....211
Magnea Lorenzo	Analytical Studies for Non-Perturbative QCD of Jets at Hadron Colliders ..... 221
Pakhlov Pasha	Charmonium and New States at B Factories..229
Mizuk Roman	New Resonances at BELLE .....231
Polosa Antonello	Spectrum and Decays of Diquark Antidiquark States .....233
Franco Buccella	Spectrum of Positive and Negative Parity Pentaquarks, Including $SU(3)_F$ Breaking . 235

**SESSION IV – ELECTROWEAK AND TOP PHYSICS ..... 243**

Andrew Askew	Electroweak Measurements (Including Dibosons) at the Tevatron ..... 245
Tassi Enrico	Electroweak Physics Measurements at HERA .....257
Adelman Jahred	Top Quark Mass Measurements at the Tevatron .....259
Pleier Marc-André	Top Quark Pair Production and Properties Measurements at the Tevatron ..... 267
Dong Peter	Measurement of the Electroweak Single Top Production Cross Section at the Tevatron ..281

Bellomo Massimiliano	Standard Model Physics in ATLAS at the Start of the LHC .....	295
Wardrope David	W and Z Measurements with the Initial CMS Data .....	307
Piccinini Fulvio	Drell-Yan Processes at LHC .....	317
<b>SESSION V – HEAVY FLAVOUR PHYSICS .....</b>		<b>327</b>
Matthew Jones	B States at the Tevatron .....	329
Neri Nicola	Charm Decays, Mixing and CP Vilation at the B Factories .....	349
Pedlar Todd	Results from CLEO-C .....	359
Du ShuXian	Recent Results from BESII .....	361
Yuan Ye	BESIII: A Status Report .....	363
Chiang -C.Mark	Measurement of $B^0 \rightarrow \pi^+ \pi^- \pi^+ \pi^-$ Decays and Search for $B^0 \rightarrow \rho^0 \rho^0$ .....	365
Playfer Steve	Radiative and Electroweak Penguins ...	379
Gardi Einan	On the Determination of $ V_{ub} $ from Inclusive Semileptonic B Decays .....	381
<b>SESSION VI – CP VIOLATION AND RARE DECAYS .....</b>		<b>407</b>
Gatti Claudio	K decays Measurements with the KLOE Detector .....	409
Voena Cecilia	Measurements of CKM at the B-Factories ..	417
Castilla Heriberto	CPV and B_s Physics at the Tevatron ...	429
Goudzovski Evgueni	New Results from the NA48/2 experiment at CERN SPS: Radiative Nonleptonic KAON Decays .....	431
Blucher Ed	$e'/e$ with KTEV .....	447
Barberio Elisabetta	Semileptonic B Decays and Measurements of CKM Elements at B Factories .....	449

<b>SESSION VII – SEARCHING THE HIGGS .....</b>		<b>465</b>
Sanders Michiel P.	Search For Low Mass SM Higgs at The Tevatron .....	467
Whiteson Daniel	Search for the Standard Model Higgs with $m_h > 130 - 200$ GeV at the Tevatron.....	475
Nikolopoulos Konstantinos	Search for the Standard Model <i>Higgs</i> $\rightarrow ZZ^{(*)} \rightarrow 4$ leptons Searches in ATLAS .	481
Ronga Frederic	Prediction for the Lightest Neutral Higgs Boson in MSSM .....	495
Gentile Simonetta	Detect MSSM Neutral Higgs Bosons at LHC.	497
St. Denis Rick	Searching for the Higgs at the Tevatron and the LHC. A Critical Assessment .....	519
Khoze Valery	Testing Predictions for Central Exclusive Processes in the Early LHC Runs .....	535
<b>SESSION VIII – SEARCHES FOR NEW PHYSICS .....</b>		<b>545</b>
Sasha Pronko	Non-SUSY Exotics Searches at the Tevatron..	547
Verdier Patrice	Search for SuperSymmetry at the Tevatron..	563
List Jenny	Searches for New Physics at HERA .....	565
Manoni Elisa	Lepton Flavor Violation in $\tau$ and $B$ Decays at BaBar.....	573
Norbert Neumeister	Physics Beyond the Standard Model in CMS at the Startup of the LHC .....	585
Mateev Matey	A Maximal Mass Model .....	595
Sannino Francesco	(Near) Conformal Technicolor: What is Really New? .....	617
<b>SESSION IX – PERSPECTIVES .....</b>		<b>629</b>
Latino Giuseppe	The TOTEM Experiment at LHC .....	631
Kaysner Boris	Project X and the Future Fermilab Program .....	647

---

Mangano Michelangelo	Physics with High Intensity Facilities (Project X, SLHC) .....	649
<b>SESSION X – PHYSICS AND SOCIETY .....</b>		<b>651</b>
Grassmann Hans	Applying Physics Methods to Information Theory .....	653
Buongiorno Jacopo	New Safer Nuclear Reactors .....	667
<b>Participants</b>	.....	<b>669</b>



## ***SESSION I – COSMOLOGY AND ASTROPHYSICS***

- Kampert Karl-Heinz* Cosmic Rays at the Highest Energies: Results from the Pierre Auger Observatory
- Ogburn Walter* Results from CDMS
- Marco Casolino* The Pamela Cosmic Ray Space Observatory: Detector, Objectives and First Results
- Dell'Agnello Simone* Probing Gravity in the Solar System with Satellite Laser Ranging
- Colafrancesco Sergio* What an Astrophysicist can tell about the Nature of Dark Matter?
- Dolgov Alexander* Cosmic AntiMatter: Models and Observational Bound



# COSMIC RAYS AT THE HIGHEST ENERGIES: RESULTS FROM THE PIERRE AUGER OBSERVATORY

Karl-Heinz Kampert for the Pierre Auger Collaboration  
*Bergische Universität Wuppertal*  
*Fachbereich C - Physik, Gaußstr. 20, D-42119 Wuppertal*  
email: [kampert@uni-wuppertal.de](mailto:kampert@uni-wuppertal.de)

## Abstract

The Pierre Auger Observatory has been designed to measure the most energetic particles in nature. It is located on a plateau in the Province of Mendoza, Argentina, and covers an area of 3000 km<sup>2</sup>. The construction is nearing completion and almost 1600 water Cherenkov detectors positioned on a 1.5 km hexagonal grid combined with 24 large area fluorescence telescopes erected at the perimeter of the array continuously take data. After briefly sketching the design of the observatory, we shall discuss selected first results covering (i) the energy spectrum of cosmic rays with the observation of a flux suppression starting at the GZK energy-threshold, (ii) upper limits of the photon and neutrino flux, and (iii) studies of anisotropies in the arrival direction of cosmic rays including the observation of directional correlations to nearby AGNs.

## 1 Introduction

Understanding the origin of the highest energy cosmic rays is one of the most pressing questions of astroparticle physics. Cosmic rays (CR) with energies exceeding  $10^{20}$  eV have been observed for more than 40 years (see e.g. <sup>1)</sup>) but due to their low flux only some ten events of such high energies could be detected up to recently. There are no generally accepted source candidates known to be able to produce particles of such extreme energies. An excellent review, published by Michael Hillas more than 20 years ago, presented the basic requirements for particle acceleration to energies  $\geq 10^{19}$  eV by astrophysical objects <sup>3)</sup>. The requirements are not easily met, which has stimulated the production of a large number of creative papers. Moreover, there should be a steeping in the energy spectrum near  $10^{20}$  eV due to the interaction of cosmic rays with the microwave background radiation (CMB). This Greisen-Zatsepin-Kuzmin (GZK) effect <sup>2)</sup> severely limits the horizon from which particles in excess of  $\sim 6 \cdot 10^{19}$  eV can be observed. For example, the sources of protons observed with  $E \geq 10^{20}$  eV need to be within a distance of less than 50 Mpc <sup>4)</sup>. The non-observation of the GZK-effect in the data of the AGASA experiment <sup>5)</sup> has motivated an enormous number of theoretical and phenomenological models trying to explain the absence of the GZK-effect and has stimulated the field as a whole.

Besides astrophysics, there is also a particle physics interest in studying this energy regime. This is because CRs give access to elementary interactions at energies much higher than man-made accelerators can reach in foreseeable future. This opens opportunities to both measuring particle interactions (e.g. proton-nucleus, nucleus-nucleus,  $\gamma$ -nucleus, and  $\nu$ -nucleus interactions) at extreme energies as well as to probe fundamental physics, such as the smoothness of space or the validity of Lorentz invariance in yet unexplored domains.

After decades of very slow progress because of lack of high statistics and high quality data, the situation has changed considerably during the last year. This is mostly due to the advent of the hybrid data from the Pierre Auger Observatory (PAO). Both, the HiRes and the Pierre Auger experiments have reported a flux suppression as expected from the GZK-effect <sup>6, 7)</sup>. The very recent breaking news about the observation of directional correlations of the most energetic Pierre Auger events with the positions of nearby AGN <sup>8)</sup> complements the observation of the GZK effect very nicely and provides evidence

for an astrophysical origin of the most energetic cosmic rays. Another key observable allowing one to discriminate different models about the origin of high-energy cosmic rays is given by the mass composition of CRs. Unfortunately, the interpretation of such data is much more difficult due to the strong dependence on hadronic interaction models. Only primary photons and neutrinos can be discriminated safely from protons and nuclei and recent upper limits to their fluxes largely rule out top-down models, originally invented to explain the apparent absence of the GZK-effect in AGASA data.

## 2 The Pierre Auger Observatory

The two most important design criteria for the Pierre Auger Observatory were to achieve a sufficiently large aperture at  $E \gtrsim 10^{19}$  eV so that the answer about the existence of the GZK-effect could already be given within the first years of operation, and to measure CR induced air showers simultaneously by two independent observation techniques in order to better control systematic uncertainties in the event reconstruction. This is called the *hybrid* approach. Another important objective was to achieve a uniform full sky-coverage to allow studying global anisotropies of CRs and correlations with matter concentrations in the nearby Universe. This is planned to be realized by one observatory each on the southern and northern hemisphere. Because of funding constraints, the Pierre Auger Collaboration decided to start constructing the southern site first with the northern one to follow as soon as possible.

The first of the two design criteria asked for a detector area of  $\gtrsim 3000$  km<sup>2</sup> in order to collect about one event per week and site above  $10^{20}$  eV, depending on the extrapolation of the flux above the GZK threshold. The most cost-effective hybrid approach was found to be a combination of an array of surface detectors (SD) of water Cherenkov tanks, operating 24 hours a day and a set of air fluorescence detectors (FD) observing the light emission of extensive air showers above the array in clear moonless nights.

The ground array at the southern site comprises 1600 cylindrical water Cherenkov tanks of 10 m<sup>2</sup> surface area and 1.2 m height working autonomously by solar power and communicating the fully digitized data by radio links. The tanks are arranged on a hexagonal grid with a spacing of 1.5 km yielding full efficiency for extensive air shower (EAS) detection above  $\sim 5 \cdot 10^{18}$  eV. Presently (May 2008), about 1580 tanks are in operation and taking data.

Charged particles propagating through the atmosphere excite nitrogen molecules causing the emission of (mostly) ultraviolet light. The fluorescence yield is very low, approx. four photons per meter of electron track (see e.g. <sup>9</sup>), but can be measured with large area imaging telescopes during clear new- to half-moon nights (duty cycle of  $\approx 10\text{-}15\%$ ). The fluorescence detector of the southern site comprises 24 telescopes arranged into four ‘eyes’ located at the perimeter of the ground array. Each eye houses six Schmidt telescopes with a  $30^\circ \times 30^\circ$  field of view (f.o.v.). Thus, the 6 telescopes of an eye provide a  $180^\circ$  view towards the array center and they look upwards from  $1^\circ$  to  $31^\circ$  above the horizon. All 24 telescopes are in operation and taking data.

The layout of the southern site and its current status is depicted in Fig. 1. It shows the locations of the four eyes and of the water tanks already in operation. Further details about the experiment and its performance can be found in Refs. <sup>10, 11</sup>). Nearing completion of the southern site, the collaboration has selected southeast Colorado to site the northern detector and started to perform related R&D work.

### 3 The Energy Spectrum

A very important step towards unveiling the origin of the sources of UHECR is provided by measurements of the CR energy spectrum. The *ankle* observed at  $E \simeq 4 \cdot 10^{18}$  eV is believed to be either due to the onset of an extragalactic CR component or due to energy losses of extragalactic protons by  $e^+e^-$  pair production in the CMB <sup>12</sup>). At energies  $E \simeq 6 \cdot 10^{19}$  eV the the GZK-effect <sup>2</sup>) is expected due to photo-pion production of extragalactic protons in the CMB.

Recent measurements of the CR energy spectrum by AGASA and HiRes have yielded results which differ in their shape and overall flux <sup>13</sup>). This may be explained by the fact that the energy determination of CR particles by ground arrays like AGASA relies entirely on EAS simulations with their uncertainties originating from the limiting knowledge of hadronic interactions at the highest energies (total inelastic cross sections, particle multiplicities, inelasticities, etc.). SENECA simulations <sup>14</sup>) have shown that the muon density at ground predicted by different hadronic interaction models differ by up to 30%. Fluorescence telescopes, such as operated by HiRes and the PAO, observe the (almost) full longitudinal shower development in the atmosphere. In this way, the atmosphere is employed as a homogenous calorimeter with an absorber thickness of

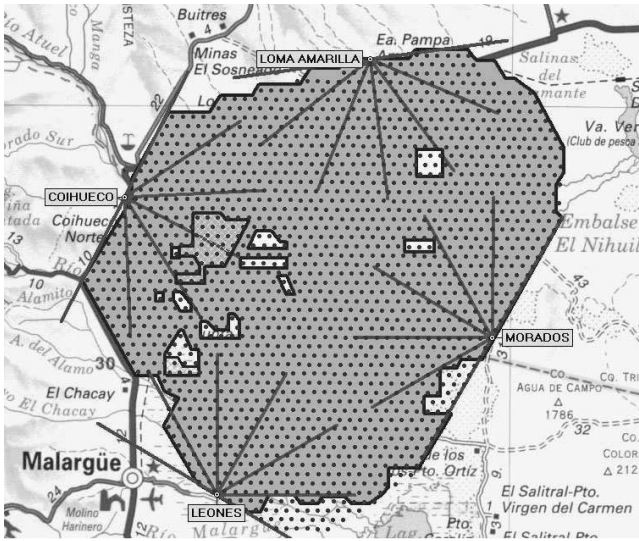


Figure 1: *Layout of the southern site with the locations of the surface detector tanks indicated. Also shown are the locations of the fluorescence eyes with the f.o.v. of their telescopes. The blue region indicates the part of the ground array currently in operation (May 2008). Furthermore, all 24 telescopes distributed over the four sites Los Leones, Coihueco, and Loma Amarilla and Los Morados are in operation.*

30 radiation lengths or 11 hadronic interaction lengths. Corrections for (model dependent) energy ‘leakage’ into ground - mostly by muons and neutrinos - are below 10% and their uncertainties are only a few percent. As a consequence, fluorescence detectors provide an energy measurement which is basically independent from hadronic interaction models. Uncertainties in the energy scale arise most dominantly from the fluorescence yield in the atmosphere. Several measurements have been performed in the past, e.g. the Auger Collaboration uses the fluorescence yield by Nagano et al. <sup>15)</sup> and HiRes by Kakimoto et al. <sup>9)</sup>. Major efforts have been started to remeasure the fluorescence yield as a function of temperature, pressure and humidity with high precision <sup>16)</sup> in order to reduce this source of uncertainty.

Taking benefit of the Auger hybrid detector, the Auger Collaboration has used a clean set of hybrid data, in which EAS have been detected simultaneously by at least one fluorescence eye and the ground array, to calibrate the

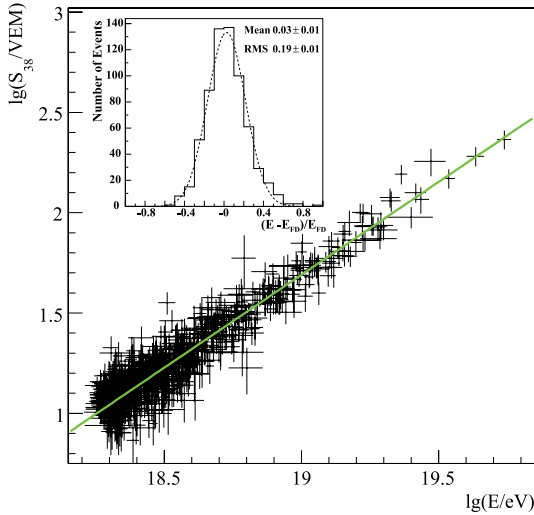


Figure 2: Correlation between  $\lg S_{38^\circ}$  and  $\lg E_{FD}$  for hybrid events. The full line is the best fit to the data. The fractional difference between the FD and SD energies is shown in the inset <sup>7)</sup>.

observatory. This is shown in Fig. 2, where the shower size parameter  $S(1000)$  extracted from lateral particle density distribution of EAS at a distance of 1000 m (and normalized to zenith angles of  $38^\circ$ ) is plotted versus the CR energy determined from the fluorescence telescopes. The straight line represents the fitted calibration relation which is applied to the much larger data set of the ground array. The 19% rms value shown in the inset of the figure is found to be in good agreement to the quadratic sum of the  $S_{38^\circ}$  and  $E_{FD}$  uncertainties.

The resulting energy spectrum based on  $\sim 20\,000$  events is displayed in Fig. 3. To enhance the visibility of the spectral shape, the fractional difference of the measured flux with respect to an assumed flux  $\propto E^{-2.69}$  is shown. The suppression of the flux above  $\sim 5 \cdot 10^{19}$  eV and the ankle at  $E \simeq 4 \cdot 10^{18}$  eV are evident. Data from HiRes-I <sup>6)</sup> are also shown. In the region where our index is measured as -2.69, the HiRes data indicate a softer spectrum.

Using different statistical approaches, a significance for flux suppression at a level of more than 6 standard deviations can be derived from the Auger data <sup>7)</sup>. The observation of the GZK-effect 40 years after its prediction provides for the first time evidence for an extragalactic origin of EHECRs. Of course,

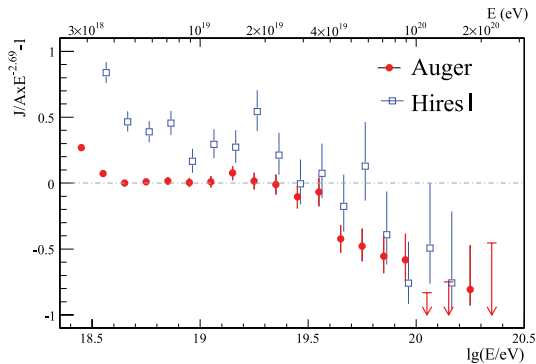


Figure 3: *Fractional difference between the derived energy spectrum and an assumed flux  $\propto E^{-2.69}$  as a function of energy  $\gamma$ .*

this interpretation is challenged if the sources would happen to run out of acceleration power just at the value of the GZK threshold. However, this would be a strange coincidence and in fact is not supported by Pierre Auger data (see Sect. 5).

#### 4 Photon and Neutrino Limits

Primary photons can experimentally be well separated from primary hadrons as they penetrate deeper into the atmosphere, particularly at energies above  $10^{18}$  eV. Their EAS development is also much less affected by uncertainties of hadronic interaction models due to the dominant electromagnetic shower component. They are of interest for several reasons: top-down models, invented to explain the apparent absence of the GZK-effect in AGASA data, predict a substantial photon flux at high energies<sup>19)</sup>. In the presence of a GZK effect, UHE photons can also act as tracers of the GZK process and provide relevant information about the sources and propagation. Moreover, they can be used to obtain input to fundamental physics and UHE photons could be used to perform EHE astronomy.

Experimentally, photon showers can be identified by their longitudinal shower profile, most importantly by their deep  $X_{\max}$  position and low muon numbers. Up to now, only upper limits could be derived from various experiments, either expressed in terms of the photon fraction or the photon flux.

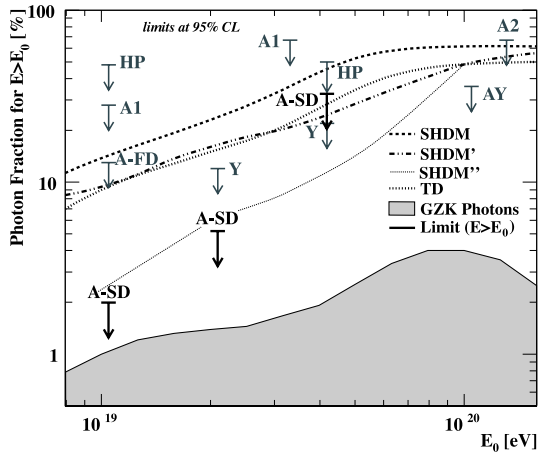


Figure 4: Upper limits on the fraction of photons in the integral CR flux compared to predictions. The lower curve is for a subdominant SHDM contribution <sup>17)</sup>. For other references see <sup>18)</sup>.

Figure 4 presents a compilation of present results on the photon fraction. The most stringent limits are provided by the Auger surface detector <sup>18)</sup>. Current top-down models appear to be ruled out by the current bounds. This result can be considered an independent confirmation of the GZK-effect seen in the energy spectrum. The lowest model curve in figure 4 represents most recent SHDM calculations <sup>17)</sup> which are still compatible with the Auger energy spectrum and current photon limits. However, the contribution would have to be subdominant and the decaying mass  $M_X > 10^{23}$  eV. In future measurements and after several years of data taking it will be very exciting to possibly touch the flux levels expected for GZK-photons ( $p + \gamma_{CMB} \rightarrow p + \pi^0 \rightarrow p + \gamma\gamma$ ).

The detection of UHE cosmic neutrinos is another long standing experimental challenge. All models of UHECR origin predict neutrinos from the decay of pions and kaons produced in hadronic interactions either at the sources or during propagation in background fields. Similarly to GZK-photons one also expects GZK-neutrinos, generally called ‘cosmogenic neutrinos’. Moreover, top-down models predict dominantly neutrinos at UHE energies. Even though neutrino flavors are produced at different abundances, e.g. a 1:2 ratio of  $\nu_e:\nu_\mu$  results from pion decay, neutrino oscillations during propagation will lead

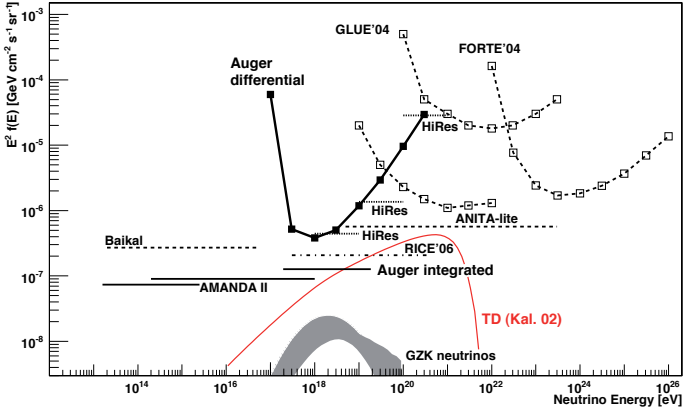


Figure 5: Limits at the 90 % C.L. for a diffuse flux of  $\nu_\tau$  assuming a 1:1:1 ratio of the 3 neutrino flavors ( <sup>20</sup> and references therein) and predictions for a top-down model <sup>21</sup>) (Taken from <sup>13</sup>).

to equal numbers of  $\nu_e$ ,  $\nu_\mu$ , and  $\nu_\tau$  at Earth. At energies above  $10^{15}$  eV, neutrinos are absorbed within the Earth so that upgoing neutrino induced showers cannot be detected anymore. Only tau neutrinos entering the Earth just below the horizon (Earth-skimming) can undergo charged-current interactions to produce  $\tau$  leptons which then can travel several tens of kilometers in the Earth and emerge into the atmosphere to eventually decay in flight producing a nearly horizontal air shower above the detector. Such showers can be searched for in ground arrays and fluorescence detectors. The absence of any candidates observed in the detectors has been used to place upper limits on diffuse neutrino fluxes. As can be seen from Fig. 5, AMANDA and the PAO provide at present the best upper limits up to energies of about  $10^{19}$  eV and, similarly to the photons discussed above, they already constrain top-down models and are expected to reach the level of cosmogenic neutrinos after several years of data taking.

## 5 Arrival Directions and Correlations with AGN

Recently, the Pierre Auger Collaboration reported the observation of a correlation between the arrival directions of the highest energy CRs and the positions of nearby AGN from the Véron-Cetty - Véron catalogue at a confidence level

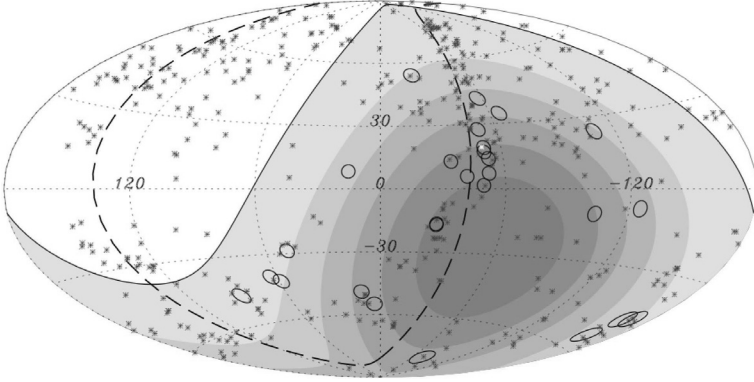


Figure 6: Aitoff projection of the celestial sphere in galactic coordinates. The positions of the AGN within  $D < 71$  Mpc (stars) and of the events with  $E > 57$  EeV (circles) are marked. The colors indicate equal exposure <sup>8, 22</sup>).

of more than 99% <sup>8, 22</sup>). Since several claims about seeing clustering of EHE-CRs were already made in the past with none of them being confirmed by independent data sets, the Auger group has performed an ‘exploratory’ scan of parameters using an initial data-set and applied these parameters to a new independent data-set for confirmation. With the parameters specified *a priori* the analysis avoids the application of penalty factors which otherwise would need to be applied for in *a posteriori* searches. The correlation has maximum significance for CRs with energies greater than  $5.7 \cdot 10^{19}$  eV and AGN at a distance less than  $\sim 71$  Mpc. At this energy threshold, 20 of the 27 events in the full data set correlate within  $3.2^\circ$  with positions of nearby AGNs.

Observing such kind of anisotropy can be considered the first evidence for an extragalactic origin of the most energetic CRs because none of any models of galactic origin even when including a very large halo would result in an anisotropy such as observed in the data. Besides this, the correlation parameters itself are highly interesting as the energy threshold at which the correlation becomes maximized matches the energy at which the energy spectrum shows the GZK feature ( $\sim 50\%$  flux suppression), i.e. CRs observed above this threshold - irrespective of their masses - need to originate from within the GZK-horizon of  $\sim 100$ - $200$  Mpc. This number again matches (within a factor of two) the maximum distance for which the correlation is observed. Thus, the

set of the two parameters suggests that the suppression in the energy spectrum is indeed due to the GZK-effect, rather than to a limited energy of the accelerators. Thereby, the GZK-effect acts as an effective filter to nearby sources and minimizes effects from extragalactic magnetic field deflections. On top of this, it is also the large magnetic rigidity which helps to open up the window for performing charged particle astronomy.

The correlation may tell us also about the strength of galactic and extragalactic magnetic fields. The galactic fields are reasonably well known and one expects strong deflections for particles arriving from nearby the galactic plane even at energies of 60 EeV. And in fact, 5 of the 7 events that do not correlate with positions of nearby AGN arrive with galactic latitudes  $|b| < 12^\circ$ . The angular scale of the observed correlation also implies that the intergalactic magnetic fields do not deflect the CRs by more than a few degrees and one can constrain models of turbulent magnetic fields to  $B_{\text{rms}}\sqrt{L_c} \leq 10^{-9} \text{ G}\sqrt{\text{Mpc}}$  within the GZK horizon assuming protons as primary particles <sup>22)</sup>.

The results have stimulated a large number of papers discussing the correlation results and their interpretation and/or applying the Auger correlation parameters to other data-sets, part of which will be discussed below.

## 6 Discussion and Concluding Remarks

Remarkable progress has been made in cosmic ray physics at the highest energies, particularly by the start-up of the (still incomplete) Pierre Auger Observatory. The event statistics above  $10^{19}$  eV available by now allows detailed comparisons between experiments and indicates relative shifts of their energy scales by  $\pm 25\%$ . Given the experimental and theoretical difficulties in measuring and simulating extensive air showers at these extreme energies, this may be considered a great success. On the other hand, knowing about overall mismatches of the energy scales between experiments may tell us something. Clearly, in case of fluorescence detectors better measurements of the spectral and absolute fluorescence yields and their dependence on atmospheric parameters are needed and will hopefully become available in the very near future <sup>16)</sup>. This should furnish all fluorescence experiments with a common set of data. Differences in the calibration between surface detectors and fluorescence telescopes, best probed by hybrid experiments like Auger and the Telescope Array <sup>23)</sup>, may then be used to test the modelling of EAS. The muon component at ground,

known to be very sensitive to hadronic interactions at high energies <sup>14)</sup>, could in this way serve to improve hadronic interaction models in an energy range not accessible at man-made accelerators. In fact, several studies (e.g. <sup>24)</sup>) indicate a deficit of muons by 30% or more in interaction models like QGSJET.

The energy scale is of great importance also for the AGN correlation discussed in the previous section. As shown in <sup>22)</sup>, the correlation sets in abruptly at an threshold energy of about 57 EeV. The distance parameter of the correlation of 71 Mpc may indicate a mismatch of the energy scale: For protons above 57 EeV the GZK horizon would be 200 Mpc <sup>4)</sup> but already for 20% higher energy it would shrink by more than a factor of two to become consistent to the correlation parameter. Another puzzling feature is the observed small deflection of particles which suggests dominantly protons as primaries. Note that 90% of the events (20/22) off the galactic plane are correlated to within  $\sim 3^\circ$  which AGN positions which is very unlikely for heavy nuclei. On the other hand, the elongation curves seen by Auger <sup>25)</sup> suggests an admixture of heavy nuclei by more than 10%. This may be related again to imperfections of the hadronic interaction models used for comparison in the elongation curves.

Irrespective from the details in the energy calibration, the observation of the highest energy events from different directions in the sky and from distances larger than the scale of the solar system has been used to derive the best present limits about the smoothness of classical spacetime <sup>26)</sup>. This conclusion is based on the apparent absence of vacuum Cherenkov radiation which would degrade the CR energy already on very short distance scales. Another conjecture is that the fundamental length scale of quantum spacetime may be different from the Planck length <sup>26)</sup>.

Another test of fundamental physics based on the upper limits of photons is discussed in Ref. <sup>27)</sup>. In presence of the GZK effect, one expects high energy photons from the  $\pi^0$ -decay resulting from  $p + \gamma_{CMB} \rightarrow p + \pi^0$  interactions. The photons then rapidly cascade down to low energies by pair production. However, in many models of Lorentz-Invariance Violation (LIV), the dispersion relation is modified to  $\omega^2 = k^2 + m^2 + \xi_n k^2 (k/M_{Pl})^n$  so that the cascading of photons would be suppressed dependent on the LIV parameters  $\xi_n$  resulting in high  $\gamma$ /hadron-ratios. Again, the limits on LIV based on the Auger photon data are better by orders of magnitude compared to previous limits. All of these results come for free, just making use of the enormous energies of CRs.

All of this tells us that the near future will be highly exciting: The question of the energy scales will soon be settled and more detailed comparisons between experiments will become possible. The shape of the energy spectrum in the GZK region will tell us about the source evolution, the composition in the ankle region will answer the question about the galactic-extragalactic transition, observations of cosmogenic photons and neutrinos are in reach and in case of neutrinos will probe the GZK effect over larger volumes, the correlations will be done with better statistics, with improved search techniques and with more appropriate source catalogues and source selection parameters to tell us about source densities, and finally about the true sources of EHE-CRs. Very important to note is that different pieces of information start to mesh and are being accessed from different observational techniques and can be cross-checked.

Given the scientific importance of this, it would be a mistake to have only one observatory taking data - even when operated as a hybrid detector. Auger-North will be imperative and needs immediate vigorous support. The next generation experiment JEM EUSO to be mounted at the Exposed Facility of Japanese Experiment Module JEM EF will potentially reach much larger exposures but still faces many experimental challenges to be addressed.

### Acknowledgement

I would like to thank the organizers of the La Thuile conference for arranging an interesting meeting at the interface of particle and astrophysics. Also, it's a pleasure to thank many of my colleagues for stimulating discussions. The German Ministry for Research and Education (BMBF) is gratefully acknowledged for financial support.

### References

1. M. Nagano and A.A. Watson, *Rev. Mod. Phys.* **72** (2000) 689.
2. K. Greisen, *Phys. Rev. Lett.* **16** (1966) 748, and G.T. Zatsepin and V.A. Kuz'min, *Sov. Phys. JETP Lett.* (Engl. Transl.), **4** (1966) 78.
3. M. Hillas, *Ann. Rev. Astron. Astrophys.* **22** (1984) 425.
4. D. Harari, S. Mollerach, E. Roulet, *JCAP* **012** (2006) 611.
5. M. Takeda et al. [AGASA Collaboration] *Astropart. Phys.* **19** (2003) 447.

6. R. Abbasi et al. [HiRes Collaboration], *Phys. Rev. Lett.* **100** (2008) 101101.
7. J. Abraham et al. [Pierre Auger Coll.], *Phys. Rev. Lett.* (2008) in press.
8. J. Abraham et al. [Pierre Auger Coll.], *Science* **318** (2007) 938.
9. F. Kakimoto et al., *Nucl. Instr. Meth.* **A372** (1996) 527.
10. J. Abraham et al. [Pierre Auger Coll.], *Nucl. Instr. Meth.* **A523** (2004) 50.
11. K.-H. Kampert et al. [Pierre Auger Collaboration], *Nucl. Phys. B (Proc. Suppl.)* **151** (2006) 393-400
12. V. Berezhinsky, A.Z. Gazizov, S.I. Grigorieva, *Phys. Rev.* **D74** (2006) 043005.
13. K.-H. Kampert, to appear in *J. of Phys.* **G** (2008); astro-ph/0801.1986
14. H.J. Drescher et al., *Astropart. Phys.* **21** (2004) 87.
15. M. Nagano et al., *Astropart. Phys.* **22** (2004) 235.
16. see 5<sup>th</sup> Fluorescence Workshop, El Escorial, Spain, 16.-20.9. 2007, to appear in *Nucl. Instr. Meth.* **A**
17. R. Aloisio, F. Tortorici, *Astropart. Phys.* **29** (2008) 307
18. J. Abraham et al. [Pierre Auger Collabor.], *Astropart. Phys.* **29** (2008) 243
19. M. Risse, P. Homola, *Mod. Phys. Lett.* **A22** (2007) 749 - 766
20. J. Abraham et al. [Pierre Auger Coll.], *Phys. Rev. Lett.* **100** (2008) 211101.
21. O.E. Kalashev et al., *Phys. Rev.* **D66** (2002) 063004
22. J. Abraham et al. [Pierre Auger Coll.], *Astropart. Phys.* **29** (2008) 188
23. M. Fukushima et al. [Telescope Array Collaboration], *Proc. 30th ICRC, Mérida* (2007) p.955
24. R. Engel et al. [Pierre Auger Collaboration], *Proc. 30th ICRC, Mérida* (2007) p.605
25. M. Unger et al. [Pierre Auger Collaboration], *Proc. 30th ICRC, Mérida* (2007) p.594
26. F.R. Klinkhamer, M. Risse, *Phys. Rev.* **D77** (2007) 016002; F.R. Klinkhamer, arXiv:0710.3075
27. M. Galaverni, G. Sigl, *Phys. Rev. Lett.* **100** (2008) 021102
28. T. Ebisuzaki et al. [JEM-EUSO Collaboration], *Proc. 30th ICRC, Mérida* (2007) p.831

**RESULTS FROM CDMS**

Walter Ogburn  
*Caltech, USA*

Written contribution not received



# THE PAMELA COSMIC RAY SPACE OBSERVATORY: DETECTOR, OBJECTIVES and FIRST RESULTS

Marco Casolino, Nicola De Simone

*INFN and Physics Department of University of Rome "Tor Vergata"*  
on behalf of the PAMELA collaboration <sup>1</sup>

## Abstract

PAMELA is a satellite borne experiment designed to study with great accuracy cosmic rays of galactic, solar, and trapped nature in a wide energy range (protons: 80 MeV-700 GeV, electrons 50 MeV-400 GeV). Main objective is the study of the antimatter component: antiprotons (80 MeV-190 GeV), positrons (50 MeV-270 GeV) and search for antimatter with a precision of the order of  $10^{-8}$ . The experiment, housed on board the Russian Resurs-DK1 satellite, was launched on June, 15 2006 in a  $350 \times 600$  km orbit with an inclination of 70 degrees. The detector is composed of a series of scintillator counters arranged at the extremities of a permanent magnet spectrometer to provide charge, Time-of-Flight and rigidity information. Lepton/hadron identification is performed by a Silicon-Tungsten calorimeter and a Neutron detector placed at the bottom of the device. An Anticounter system is used offline to reject false triggers coming from the satellite. In self-trigger mode the Calorimeter, the neutron detector and a shower tail catcher are capable of an independent measure of the lepton component up to 2 TeV. In this work we describe the experiment, its scientific objectives and the performance in its first two years of operation. Data on protons of trapped, secondary and galactic nature - as well as measurements of the December 13 2006 Solar Particle Event - are provided.

---

<sup>1</sup>Daniel Bongue<sup>1</sup>, Maria Pia De Pascale<sup>1</sup>, Valeria Di Felice<sup>1</sup>, Laura Marcelli<sup>1</sup>, Mauro Minori<sup>1</sup>, Piergiorgio Picozza<sup>1</sup>, Roberta Sparvoli<sup>1</sup>, Guido Castellini<sup>2</sup>, Oscar Adriani<sup>3</sup>, Lorenzo Bonechi<sup>3</sup>, Massimo Bongi<sup>3</sup>, Sergio Bottai<sup>3</sup>, Paolo Papini<sup>3</sup>, Sergio Ricciarini<sup>3</sup>, Piero Spillantini<sup>3</sup>, Elena Taddei<sup>3</sup>, Elena Vannuccini<sup>3</sup>, Giancarlo Barbarino<sup>4</sup>, Donatella Campana<sup>4</sup>, Rita Carbone<sup>4</sup>, Gianfranca De Rosa<sup>4</sup>, Giuseppe Osteria<sup>4</sup>, Mirko Boezio<sup>5</sup>, Valter Bonvicini<sup>5</sup>, Emiliano Mocchiutti<sup>5</sup>, Andrea Vacchi<sup>5</sup>, Gianluigi Zampa<sup>5</sup>, Nicola Zampa<sup>5</sup>, Alessandro Bruno<sup>6</sup>, Francesco Saverio Cafagna<sup>6</sup>, Marco Ricci<sup>7</sup>, Petter Hofverberg<sup>8</sup>, Mark Pearce<sup>8</sup>, Per Carlson<sup>8</sup>, Edward Bogomolov<sup>9</sup>, S.Yu. Krutkov<sup>9</sup>, N.N. Nikonov<sup>9</sup>, G.I.Vasilyev<sup>9</sup>, Wolfgang Menn<sup>10</sup>, Manfred Simon<sup>10</sup>, Arkady Galper<sup>11</sup>, Lubov Grishantseva<sup>11</sup>, Sergey Koldashov<sup>11</sup>, Alexey Leonov<sup>11</sup>, Vladimir V. Mikhailov<sup>11</sup>, Sergey A. Voronov<sup>11</sup>, Yuri T. Yurkin<sup>11</sup>, Valeri G. Zverev<sup>11</sup>, Galina A. Bazilevskaya<sup>12</sup>, Alexander N. Kvashnin<sup>12</sup>, Osman Maksumov<sup>12</sup>, Yuri Stozhkov<sup>12</sup>

<sup>1</sup> INFN and Physics Department of University of Rome "Tor Vergata" , <sup>2</sup> IFAC, Florence, Italy , <sup>3</sup> INFN, and Physics Department of University of Florence , <sup>4</sup> INFN, and Physics Department of University of Naples "Federico II" , <sup>5</sup> INFN, and Physics Department of University of Trieste, <sup>6</sup> INFN, and Physics Department of University of Bari, <sup>7</sup> INFN, Laboratori Nazionali di Frascati, Italy, <sup>8</sup> KTH, Stockholm, Sweden, <sup>9</sup> Ioffe Physical Technical Institute, St. Petersburg, Russia, <sup>10</sup> Universität Siegen, Germany , <sup>11</sup> Moscow Engineering and Physics Institute, Moscow, Russia, <sup>12</sup> Lebedev Physical Institute, Moscow, Russia

## 1 Introduction

The Wizard collaboration is a scientific program devoted to the study of cosmic rays through balloon and satellite-borne devices. Aims involve the precise determination of the antiproton<sup>1)</sup> and positron<sup>2)</sup> spectrum, search of antimatter, measurement of low energy trapped and solar cosmic rays with the NINA-1<sup>3)</sup> and NINA-2<sup>4)</sup> satellite experiments. Other research on board Mir and International Space Station has involved the measurement of the radiation environment, the nuclear abundances and the investigation of the Light Flash<sup>5)</sup> phenomenon with the Siley experiments<sup>6)7)</sup>. PAMELA is the largest and most complex device built insofar by the collaboration, with the broadest scientific goals. In this work we describe the detector, and its launch and commissioning phase. Scientific objectives are presented together with the report of the first observations of protons of solar, trapped and galactic nature.

## 2 Instrument Description

In this section we describe the main characteristics of PAMELA detector; a more detailed description of the device and the data handling can be found in<sup>8-10)</sup>. The device (Figure 1) is constituted by a number of highly redundant detectors capable of identifying particles providing charge, mass, rigidity and beta over a very wide energy range. The instrument is built around a permanent magnet with a silicon microstrip tracker with a scintillator system to provide trigger, charge and time of flight information. A silicon-tungsten calorimeter is used to perform hadron/lepton separation. A shower tail catcher and a neutron detector at the bottom of the apparatus increase this separation. An anticounter system is used to reject spurious events in the off-line phase. Around the detectors are housed the readout electronics, the interfaces with the CPU and all primary and secondary power supplies. All systems (power supply, readout boards etc.) are redundant with the exception of the CPU which is more tolerant to failures. The system is enclosed in a pressurized container (Figure 2,3) located on one side of the Resurs-DK satellite. In a twin pressurized container is housed the Arina experiment, devoted to the study of the low energy trapped electron and proton component. Total weight of PAMELA is 470 kg; power consumption is 355 W, geometrical factor is  $21.5\text{cm}^2\text{sr}$ .

### 2.1 Resurs-DK1 Satellite

The Resurs-DK1 satellite (Figure 2) is the evolution of previous military reconnaissance satellites flown during in the years 1980 - 1990. It was developed by TsSKB Progress plant<sup>11)</sup> in the city of Samara (Russia), in cooperation with NPP OPTEKS, OAO Krasnogorskiy Zavod, NIITP and NTsOMZ (Russia's Science Center for Remote Sensing of Earth)<sup>12)</sup>. The spacecraft is three-axis

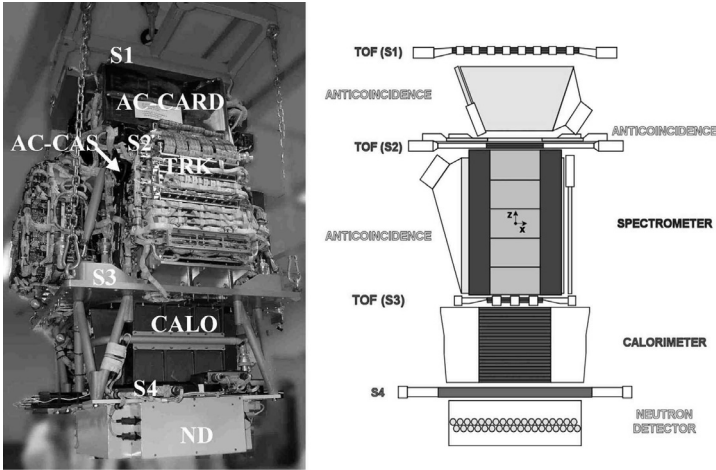


Figure 1: Left: Photo of the PAMELA detector during the final integration phase in Tor Vergata clean room facilities, Rome. It is possible to discern, from top to bottom, the topmost scintillator system, S1, the electronic crates around the magnet spectrometer, the baseplate (to which PAMELA is suspended by chains), the black structure housing the Si-W calorimeter, S4 tail scintillator and the neutron detector. Right: scheme - approximately to scale with the picture - of the detectors composing PAMELA .

stabilized, with axis orientation accuracy 0.2 arcmin and angular velocity stabilization accuracy of  $0.005^\circ/\text{s}$ . The spacecraft has a mass of about 6650 kg, height of 7.4 m and a solar array span of about 14 m. It is designed to provide imagery of the Earth surface for civilian use and is the first Russian non-military satellite with resolution capability of  $\simeq 0.8$  m in composite color mode<sup>1</sup>. The imaging system has a coverage area at 350 km of 28.3 448 km, obtained with oscillation of the satellite by  $30^\circ$  in the cross-track direction. Onboard memory capacity is 769 Gbit. The RF communications for the payload data are in X-band at 8.2-8.4 GHz with a downlink data rate of 75, 150 and 300 Mbit/s. PAMELA data amounts to about 16 Gbyte/day, sent to ground and processed in NTsOMZ station in Moscow, where also the data analysis and quicklook procedures for PAMELA are performed.

<sup>1</sup>Observations are performed in three bands (  $0.50 - 0.60\mu\text{m}$  ,  $0.60 - 0.70\mu\text{m}$  ,  $0.70 - 0.80\mu\text{m}$  ) each with 2.5-3.5 m resolution to produce a composite color image.

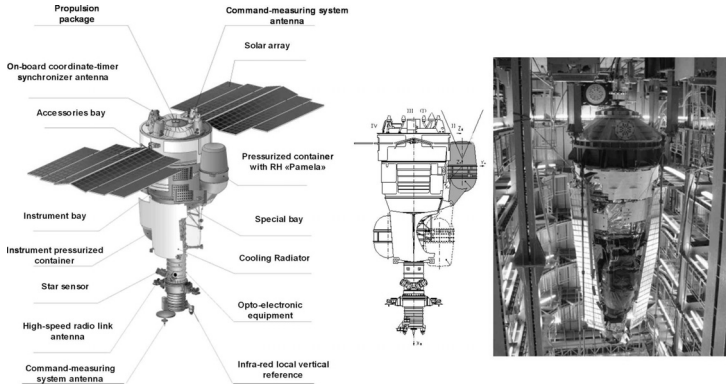


Figure 2: Left: Scheme of the Resurs-DK1 satellite. PAMELA is located in the pressurized container on the right of the picture. In the center panel it is possible to see the container in the launch position and in the extended (cosmic ray acquisition) configuration. In the right panel it is possible to see a picture of the satellite in the assembly facility in Samara. The picture is rotated 180 degrees to compare the photo with the scheme. The dashed circle shows the location of PAMELA pressurized container in the launch position.



Figure 3: Left: Photo of Resurs in the final integration phase in Baikonur. It is possible to discern the the optical sensor on top, the two pressurized containers on the sides, and the white heat cooling panel in the forefront. Right: close up picture of the integration phase of PAMELA in the pressurized container (right in picture).

## 2.2 Scintillator / Time of Flight system

The scintillator system<sup>13)</sup> provides trigger for the particles and time of flight information for incoming particles. There are three scintillator layers, each composed by two orthogonal planes divided in various bars (8 for S11, 6 for S12, 2 for S21 and S12 and 3 for S32 and S33) for a total of 6 planes and 48 phototubes (each bar is read by two phototubes). S1 and S3 bars are 7 mm thick and S2 bars are 5 mm. Interplanar distance between S1-S3 of 77.3 cm results in a TOF determination of 250 ps precision for protons and 70 ps for C nuclei (determined with beam tests in GSI), allowing separation of electrons from antiprotons up to  $\simeq 1$  GeV and albedo rejection. The scintillator system is also capable of providing charge information up to  $Z = 8$ .

## 2.3 Magnetic Spectrometer

The permanent magnet<sup>14)</sup> is composed of 5 blocks, each divided in 12 segments of Nd-Fe-B alloy with a residual magnetization of 1.3 T arranged to provide an almost uniform magnetic field along the  $y$  direction. The size of the cavity is  $13.116.144.5 \text{ cm}^3$ , with a mean magnetic field of 0.43 T. Six layers of  $300 \mu\text{m}$  thick double-sided microstrip silicon detectors are used to measure particle deflection with  $3.00.1 \mu\text{m}$  and  $11.50.6 \mu\text{m}$  precision in the bending and non-bending views. Each layer is made by three ladders, each composed by two  $5.337.00 \text{ cm}^2$  sensors coupled to a VA1 front-end hybrid circuit. Maximum Detectable Rigidity (MDR) was measured on CERN proton beam to be  $\simeq 1TV$ .

## 2.4 Silicon Tungsten Calorimeter

Lepton/Hadron discrimination is performed by the Silicon Tungsten sampling calorimeter<sup>15)</sup> located on the bottom of PAMELA. It is composed of 44 silicon layers interleaved by 22 0.26 cm thick Tungsten plates. Each silicon layer is composed arranging 33 wafers, each of  $80 \times 80 \times .380 \text{ mm}^3$  and segmented in 32 strips, for a total of 96 strips/plane. 22 planes are used for the X view and 22 for the Y view in order to provide topological and energetic information of the shower development in the calorimeter. Tungsten was chosen in order to maximize electromagnetic radiation lengths ( $16.3 X_0$ ) minimizing hadronic interaction length ( $0.6 \lambda_{int}$ ). The CR1.4P ASIC chip is used for front end electronics, providing a dynamic range of 1400 mips (minimum ionizing particles) and allowing nuclear identification up to Iron.

## 2.5 Shower tail scintillator

This scintillator ( $48 \times 48 \times 1 \text{ cm}^3$ ) is located below the calorimeter and is used to improve hadron/lepton discrimination by measuring the energy not contained

in the shower of the calorimeter. It can also function as a standalone trigger for the neutron detector.

## 2.6 Neutron Detector

The  $60 \times 55 \times 15 \text{ cm}^3$  neutron detector is composed by 36  $^3\text{He}$  tubes arranged in two layers and surrounded by polyethylene shielding and a 'U' shaped cadmium layer to remove thermal neutrons not coming from the calorimeter. It is used to improve lepton/hadron identification by detecting the number of neutrons produced in the hadronic and electromagnetic cascades. Since the former have a much higher neutron cross section than the latter, where neutron production comes essentially through nuclear photofission, it is estimated that PAMELA overall identification capability is improved by a factor 10. As already mentioned, the neutron detector is used to measure neutron field in Low Earth Orbit and in case of solar particle events as well as in the high energy lepton measurement.

## 2.7 Anticoincidence System

To reject spurious triggers due to interaction with the main body of the satellite, PAMELA is shielded by a number of scintillators used with anticoincidence functions<sup>16) 17)</sup>. CARD anticoincidence system is composed of four 8 mm thick scintillators located in the area between S1 and S2. CAT scintillator is placed on top of the magnet: it is composed by a single piece with a central hole where the magnet cavity is located and read out by 8 phototubes. Four scintillators, arranged on the sides of the magnet, make the CAS lateral anticoincidence system.

## 3 Integration, Launch and Commissioning

Pamela was integrated in INFN - Rome Tor Vergata clean room facilities; tests involved first each subsystem separately and subsequently the whole apparatus simulating all interactions with the satellite using an Electronic Ground Support Equipment. Final tests involved cosmic ray acquisitions with muons for a total of about 480 hours. The device was then shipped to TsKB Progress plant, in Samara (Russia), for installation in a pressurized container on board the Resurs-DK satellite for final tests. Also in this case acquisitions with cosmic muons (140 hours) have been performed and have shown the correct functioning of the apparatus, which was then integrated with the pressurized container and the satellite. The detector was then dismounted from the satellite and shipped by air to Baikonur cosmodrome (Kazakstan) where the the final integration phase took place in 2006.

The Soyuz-U rocket was launched from Baikonur Cosmodrome Pad 5 at Site

1, the same used for manned Soyuz and Progress cargoes to the International Space Station. Launch occurred on June 15<sup>th</sup> 2006, 08:00:00.193 UTC with the payload reaching orbit after 8 minutes. Parking orbit had a semimajor axis of 6642 km. Final boost occurred on June 18<sup>th</sup> 2006 when the orbit was raised with two engine firings to a semimajor axis of 6828 km. The maneuver was completed before 17:00 Moscow time. The transfer orbit resulted in a height increase from  $198 \times 360$  km to  $360 \times 604$  km, with the apogee of the lower orbit becoming perigee of the final orbit. Also inclination of the satellite (Figure 5) was increased from  $69.93^\circ$  to  $\simeq 69.96^\circ$ . In the same Figure it is also possible to see long term variations of  $0.1^\circ$  in a period of 5 months due to the oblateness of the Earth. In Figure 4 it is possible to see the altitude of the satellite after launch, showing the final boost and the secular variation due to atmospheric drag, resulting in a decrease of the apogee of 10 km in 5 months and a corresponding increase of the number of revolutions/day (spacecraft velocity is inversely proportional to square root of height). To compensate for atmospheric drag, the altitude of the satellite is periodically reboosted by vernier engines. To perform this maneuver the pressurized container housing PAMELA is folded back in the launch position, the satellite is rotated  $180^\circ$  on its longitudinal axis and then engines are started. Reboost frequency depends from orbital decay, due to atmospheric drag. Up to December 2006 the activity has been low with two small Solar Particle Events in summer and three larger events generated by sunspot 930 in December, so there has not been the need to perform this maneuver so far. In Figure 6 is shown the value of the angle (Beta angle) between the orbital plane and the Earth-Sun vector. This value should vary with a one-year periodicity but the oblateness of the Earth causes to precess with a higher frequency. The position of the orbital plane affects the irradiation and temperature of the satellite, which is - for instance - always under the Sun for high values of the absolute value of beta. These thermal excursions are greatly reduced in the pressurized container of PAMELA thanks to the cooling loop with a fluid at a temperature of  $28 - 33^\circ$  which maintains the temperature of the detector relatively low and reduces fluctuations within some degrees.

As already mentioned Resurs-DK1 oscillates on its longitudinal axis when performing Earth observations: a detailed information of the attitude of the satellite is provided to the CPU of PAMELA in order to know the orientation of the detector with precision of  $\simeq 1$  degree. Position and attitude information of the satellite are provided to PAMELA CPU via a 1553 interface (used also for Command and Control) and are based on the GLONASS (GLOBAL Navigation Satellite System), similar to the GPS positioning system.

On June 22, ground control successfully tested the Geoton-1 optical-electronic system and the Sangur-1 data receiving and processing system, according to Roskosmos. On June 23, 2006, NTsOMZ received first images from the satellite: the satellite conducted two photographic sessions, lasting five seconds each. On

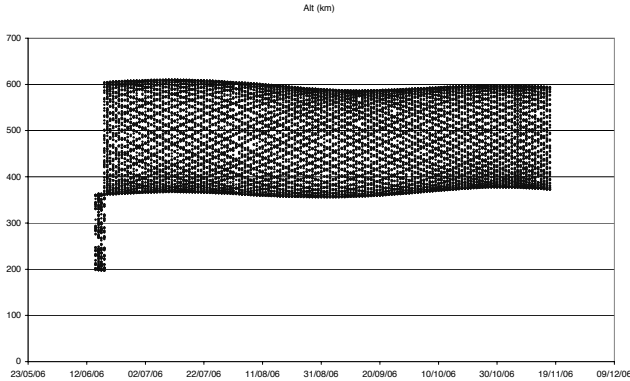


Figure 4: Height of Resurs as a function of time. After four days in a parking orbit with  $198 \times 360$  km the orbit was boosted to  $360 \times 604$  km. As of 17/11/2006 height has passed to  $372 \times 594$  km.

September 15, 2006, Roskosmos announced that testing of the spacecraft was successfully completed on that day and State Commission planned to convene on September 21, 2006, to declare the satellite operational. On September 22, 2006, Roskosmos confirmed that the spacecraft was declared operational as scheduled. Commissioning of the experiment proceeded in parallel with Resurs-DK1 and mostly consisted in a fine tuning of the observational parameters of PAMELA and the on board software, optimizing time and schedule of downlinks to maximize live time of the instrument.

#### 4 In flight data and instrument performance in Low Earth Orbit

PAMELA was first switched on June, 26<sup>th</sup> 2006. Typical events are shown in Figure 7 where an electron and a positron crossing the detector and being bent in different directions by the magnetic field are shown. In the third panel a proton interacting hadronically in the calorimeter is visible. Note that the two leptons have energies too low to give appreciable electromagnetic showers.

In Figure 8 are shown PAMELA world particle rate for S11\*S12 at various altitudes (integral fluxes of  $E > 35$  MeV p;  $E > 3.5$  MeV  $e^-$ ), showing the high latitude electron radiation belts and the proton belt in the South Atlantic Anomaly. Outside the SAA it is possible to see the increase of particle rate at

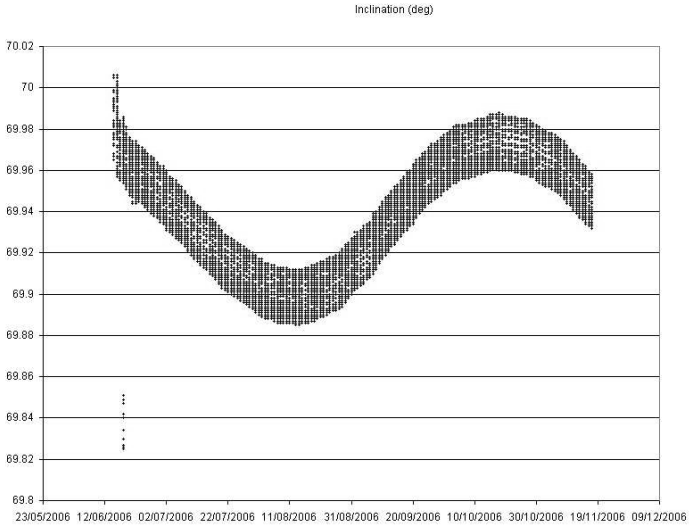


Figure 5: Inclination of Resurs satellite as a function of time. The final boost after launch increased inclination of the satellite. It is possible to see secular oscillation of  $\approx 0.1^\circ$  and short term (daily) variation of  $0.03^\circ$ .

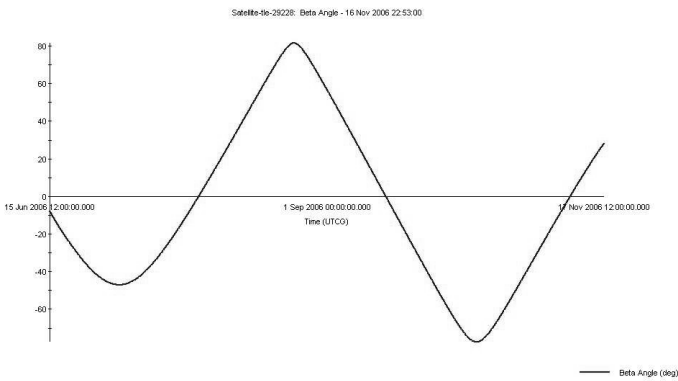


Figure 6: Beta angle of satellite vs time. The inclined orbit of the satellite and the oblateness of the Earth result in the precession of the node line resulting in a faster oscillation of the angle.

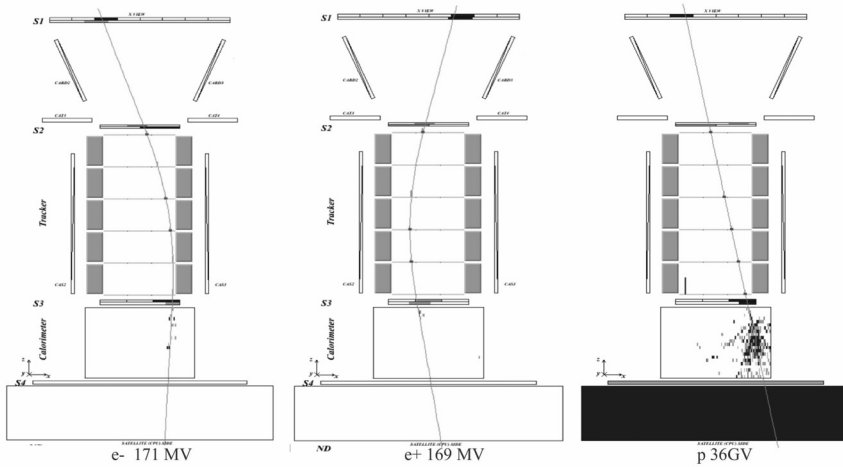


Figure 7: Some cosmic ray events observed with PAMELA . Left: 0.171 GV  $e^-$ . The particle enters the detector from the top hitting the two layers of S1 and the two layers of S2, located just above the magnet cavity. The trajectory is bent by the magnetic field and its rigidity is revealed by the microstrip detector of the tracker. The particle interacts with the bottom scintillator (S3) before absorption by the Si-W tracking calorimeter. Centre: 0.169 GV positron. Aside from the opposite curvature, the particle interacts as in the preceding case. Right: 36 GV proton. Its high rigidity reduces the magnet curvature. The calorimeter shows the shower from an hadronic interaction, with secondary particles hitting the shower tail scintillator (S4) and the neutron detector.

the geomagnetic poles due to the lower geomagnetic cutoff. The highest rates are found when the satellite crosses the trapped components of the Van Allen Belts in agreement with AP-8 and AE-8 models for trapped radiation<sup>18)</sup>.

In Figure 9 is shown the  $\beta = v/c$  of particles measured with the Time of Flight (TOF) system as function of the geographical latitude observed. It is possible to see the effect of geomagnetic cutoff on low energy particles, present only closer to the poles. Also the South Atlantic region, composed mostly of low energy ( $E < 200 MeV$ ), low  $\beta$  trapped protons is clearly seen at the latitudes between  $40^\circ$  and  $20^\circ$  S. Also albedo ( $\beta < 0$ ) particles crossing the detector from the bottom to the top are shown in the plot. Note the absence of high energy albedo particles.

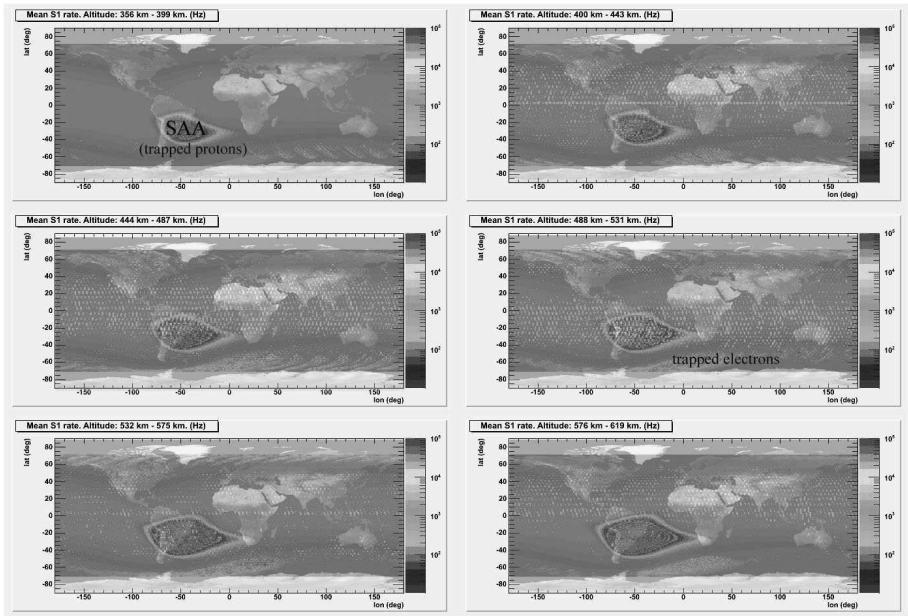


Figure 8: All particle map ( $E > 35$  MeV p;  $E > 3.5$  MeV  $e^-$ ) measured at various altitudes with PAMELA. In it are visible the proton (equatorial) and electron (high latitude) radiation belts, regions of trapped particles where the flux can increase several orders of magnitude. The size of the belts increases with altitude where the weaker magnetic field is capable of trapping lower energy particles.

## 5 Scientific Objectives and first observations

PAMELA can perform a detailed measurement of the composition and energy spectra of cosmic rays of galactic, trapped and secondary nature in Low Earth Orbit. Its  $70^\circ$ ,  $350 \times 600$  km orbit makes it particularly suited to study items of galactic, heliospheric and trapped nature. Furthermore, the long duration of the mission and the orbit configuration should allow for studies of spatial and temporal dependence in solar quiet and active conditions<sup>19–21</sup>). Indeed for its versatility and detector redundancy PAMELA is capable to address at the same time a number of different cosmic ray issues ranging over a very wide energy range, from the trapped particles in the Van Allen Belts, to electrons of Jovian origin, to the study of the antimatter component. Figure 11 shows the different components of the cosmic ray particle and antiparticle fluxes with some of the

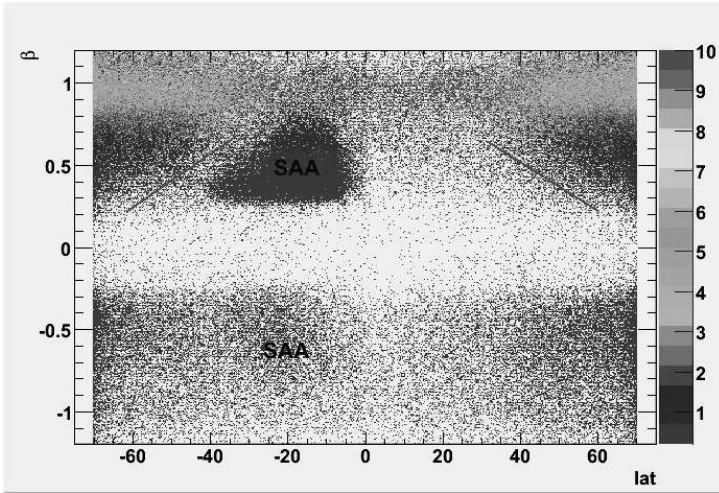


Figure 9:  $\beta$  vs geographical latitude of particles measured with PAMELA . Color code represents rigidity measured with the tracker. The red lines are to guide the eye and show the cutoff on galactic particles. High rigidity particles are present at all latitudes, whereas lower  $\beta$  events (mostly due to protons) are observed only at high latitudes and in the SAA.

PAMELA measurements. Galactic protons are dominant, with Solar Energetic and trapped particles being the only components more abundant, albeit in an interval of time and in a specific region of the orbit respectively. Here we briefly describe the main scientific objectives of the experiment and some of the preliminary results obtained up to now.

### 5.1 Antimatter research.

The study of the antiparticle component ( $\bar{p}$ ,  $e^+$ ) of cosmic rays is the main scientific goal of PAMELA . A long term and detailed study of the antiparticle spectrum over a very wide energy spectrum will allow to shed light over several questions of cosmic ray physics, from particle production and propagation in the galaxy to charge dependent modulation in the heliosphere to dark matter detection. In Figure 12 and 13 are shown the current status of the antiproton and positron measurements compared with PAMELA expected measurements in three years. In each case the two curves refer to a secondary only hypothesis with an additional contribution of a neutralino annihilation. Also cosmological issues related to detection of a dark matter signature and search for antimatter

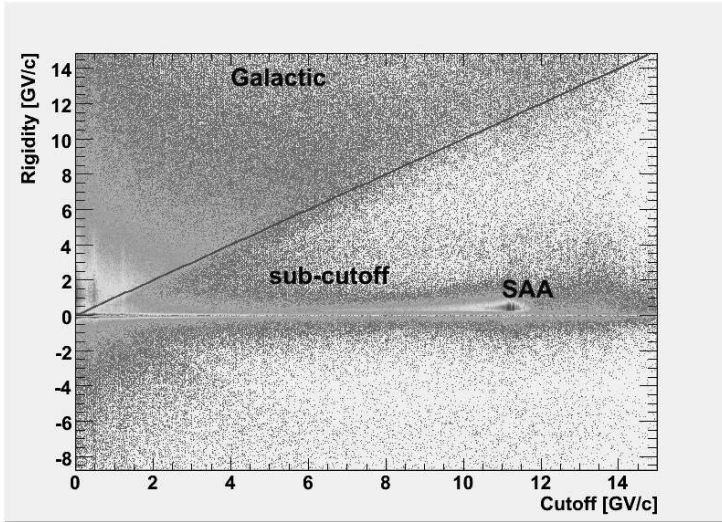


Figure 10: Rigidity vs Stormer Cutoff observed with PAMELA . Colour bar represents  $\beta$  of particles measured from the TOF. The effect of the geomagnetic field on galactic particles is clearly visible. Primary particles have an energy above the cutoff and are well separated from reentrant albedo events produced in the interaction of particles with the Earth's atmosphere.

(PAMELA will search for  $\overline{He}$  with a sensitivity of  $\approx 10^{-8}$ ) will therefore be addressed with this device.

### 5.1.1 Antiprotons

PAMELA detectable energy spectrum of  $\overline{p}$  ranges from 80 MeV to 190 GeV. Although the quality of  $\overline{p}$  data has been improving in the recent years, a measurement of the energy spectrum of  $\overline{p}$  will allow to greatly reduce the systematic error between the different balloon measurements, to study the phenomenon of charge dependent solar modulation, and will for the first time explore the energy range beyond  $\simeq 40$  GeV. Possible excesses over the expected secondary spectrum could be attributed to neutralino annihilation;<sup>43-45)</sup> show that PAMELA is capable of detecting an excess of antiprotons due to neutralino annihilation in models compatible with the WMAP measurements. Also<sup>46)</sup> estimate that PAMELA will be able to detect a supersymmetric signal in many minimal supergravity (mSUGRA) models. The possibility to extract a neutralino annihilation signal from the background depends on the parameters used, the boost

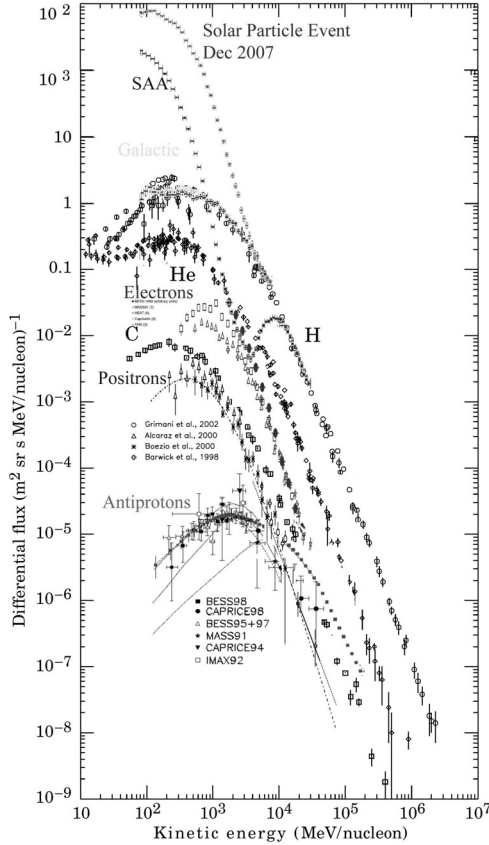


Figure 11: Differential energy spectra of the different particles detectable by PAMELA . Protons and Helium nuclei dominate the positive charge spectrum and electrons the negative charge spectrum. Antiparticles are extremely rare in cosmic rays, with positrons as abundant as Carbon nuclei. PAMELA acceptance energy range is 80 MeV - 190 GeV for antiprotons and 50 MeV - 270 GeV for positrons. On the experimental data for antiproton spectra is shown an expected contribution in case of a 964 GeV neutralino. Most intense fluxes refer to the trapped protons in the South Atlantic Anomaly and those coming from the December 13, 2006 Solar Particle event.

factor (BF) and the galactic proton spectrum. Other scenarios<sup>47) 48)</sup> suppose the existence of heavy neutrinos or stable heavy particles as DM constituents.

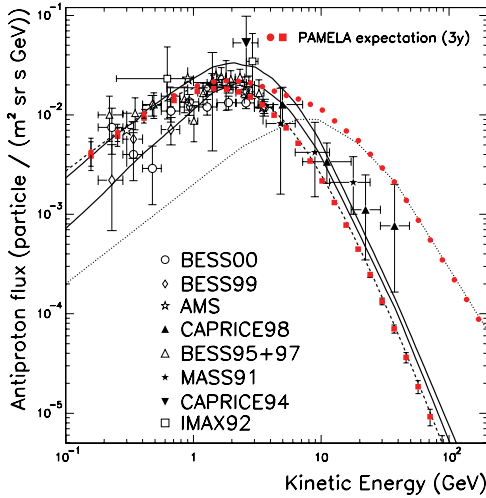


Figure 12: Recent experimental  $\bar{p}$  spectra (BESS00 and BESS99 <sup>22)</sup>, AMS<sup>23)</sup>, CAPRICE98<sup>24)</sup>, BESS95+97<sup>25)</sup>, MASS91<sup>26)</sup>, CAPRICE94<sup>1)</sup>, IMAX92<sup>27)</sup>) along with theoretical calculations for pure  $\bar{p}$  secondary production (solid lines:<sup>28)</sup> dashed line:<sup>29)</sup>) and for pure  $\bar{p}$  primary production (dotted line:<sup>30)</sup>), assuming the annihilation of neutralinos of mass  $964 \text{ GeV}/c^2$ ). (Taken from<sup>8)</sup>)

In<sup>49)</sup> the preliminary results of PAMELA on  $\bar{p}$  are compared with other measurements to explore the possibility of DM signature in fermion 3-plet or 5-plet scenarios and conclude the possibility to extract a signal in case of  $\text{BF}=10$ .

Charge dependent solar modulation, observed with the BESS balloon flights at Sun field reversal<sup>22)</sup> and more recently on a long duration balloon flight<sup>50)</sup> will be monitored during the period of recovery going from the 23<sup>rd</sup> solar minimum going to the 24<sup>th</sup> solar maximum. Also the existence, intensity and stability of secondary antiproton belts<sup>51)</sup>, produced by the interaction of cosmic rays with the atmosphere will be measured.

### 5.1.2 Positrons

A precise measurement of the positron energy spectrum is needed to distinguish dark matter annihilation from other galactic sources such as hadronic production in giant molecular clouds,  $e^+/e^-$  production in nearby pulsars or decay from radioactive nuclei produced in supernova explosions. An interesting

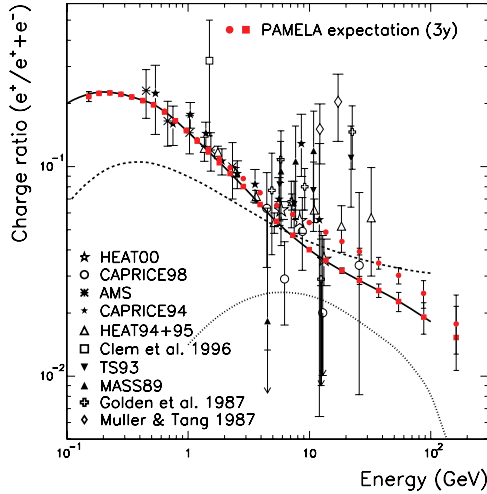


Figure 13: The positron fraction as a function of energy measured by several experiments (<sup>31–33</sup>) and MASS89<sup>34</sup>), TS93<sup>35</sup>), HEAT94+95<sup>36</sup>), CAPRICE94<sup>2</sup>), AMS<sup>37</sup>), CAPRICE98<sup>38</sup>), HEAT00<sup>39</sup>)). The dashed<sup>40</sup>) and the solid<sup>41</sup>) lines are calculations of the secondary positron fraction. The dotted line is a possible contribution from annihilation of neutralinos of mass 336 GeV/c<sup>2</sup><sup>42</sup>). The expected PAMELA performance, in case of a pure secondary component (full boxes) and of an additional primary component (full circles), are indicated in both panels. Only statistical errors are included in the expected PAMELA data. Taken from<sup>8</sup>).

feature of  $e^+$  is that - as electrons - they lose most of length scales of a few kiloparsecs ( $\approx 50$ ). The cosmic positron spectrum is therefore a samples of only the local dark matter distribution<sup>52</sup>). PAMELA is capable to detect  $e^+$  in the energy range 50 MeV to 270 GeV. Possibilities for dark matter detection in the positron channel depend strongly on the nature of dark matter, its cross section and the local inhomogeneity of the distribution. Hooper and Silk<sup>53</sup>) perform different estimation of PAMELA sensitivity according to different hypothesis of the dark matter component: detection is possible in case of an higgsino of mass up to 220 GeV (with BF=1) and to 380 GeV (with BF=5). Kaluza Klein models<sup>54</sup>) would give a positron flux above secondary production increasing above 20 GeV and thus clearly compatible with PAMELA observational parameters. In case of a bino-like particle, as supposed by Minimal Supersymmetric Stan-

Standard Model, PAMELA is sensible to cross sections of the order of  $2 - 3 \times 10^{-26}$  (again, depending of BF). In case of Kaluza Klein excitations of the Standard Model the sensitivity of PAMELA is for particles up to 350 and 550 GeV. In the hypothesis of the lightest Higgs model with T parity, the dark matter candidate is a heavy photon which annihilates mainly into weak gauge bosons in turn producing positrons. In<sup>55)</sup> is shown that PAMELA will be able to identify this signal if the mass of the particle is below 120 GeV and the BF is 5. Hisano et al.,<sup>56)</sup> assume a heavy wino-like dark matter component, detectable with PAMELA in the positron spectrum (and with much more difficulty in the antiproton channel) for mass of the wino above 300 GeV. This model predicts that if the neutralino has a mass of 2 TeV the positron flux increases by several orders of magnitude due to resonance of the annihilation cross section in  $W^+W^-$  and  $ZZ$ : in this scenario not only such a signal would be visible by PAMELA but also be consistent with the increase of positrons measured by HEAT<sup>57)</sup>. In conclusion a detailed measurement of the positron spectrum, its spectral features and its dependence from solar modulation will either provide evidence for a dark matter signature or strongly constrain and discard many existing models.

## 5.2 Galactic Cosmic Rays

Proton and electron spectra will be measured in detail with PAMELA. Also light nuclei (up to O) are detectable with the scintillator system. In this way it is possible to study with high statistics the secondary/primary cosmic ray nuclear and isotopic abundances such as B/C, Be/C, Li/C and  $^3\text{He}/^4\text{He}$ . These measurements will constrain existing production and propagation models in the galaxy, providing detailed information on the galactic structure and the various mechanisms involved.

## 5.3 Solar modulation of GCR

Launch of PAMELA occurred in the recovery phase of solar minimum with negative polarity ( $qA_j0$ ) toward solar maximum of cycle 24. We are currently in an unusually long solar minimum with disagreement over prediction on the behavior of the intensity and peaking time of next maximum. In this period PAMELA has been observing solar modulation of galactic cosmic rays during decreasing solar activity. A long term measurement of the proton, electron and nuclear flux at 1 AU can provide information on propagation phenomena occurring in the heliosphere. As already mentioned, the possibility to identify the antiparticle spectra will allow to study also charge dependent solar modulation effects. In Figure 14 are shown the proton fluxes measured in various periods of the solar minimum. It is possible to see how the effect of decreasing solar activity on the flux of cosmic rays is visible even during this solar quiet

period, in agreement with the increase of neutron monitor fluxes. Future work will involve correlation of the particle flux and solar modulation with variation with time of tilt angle.

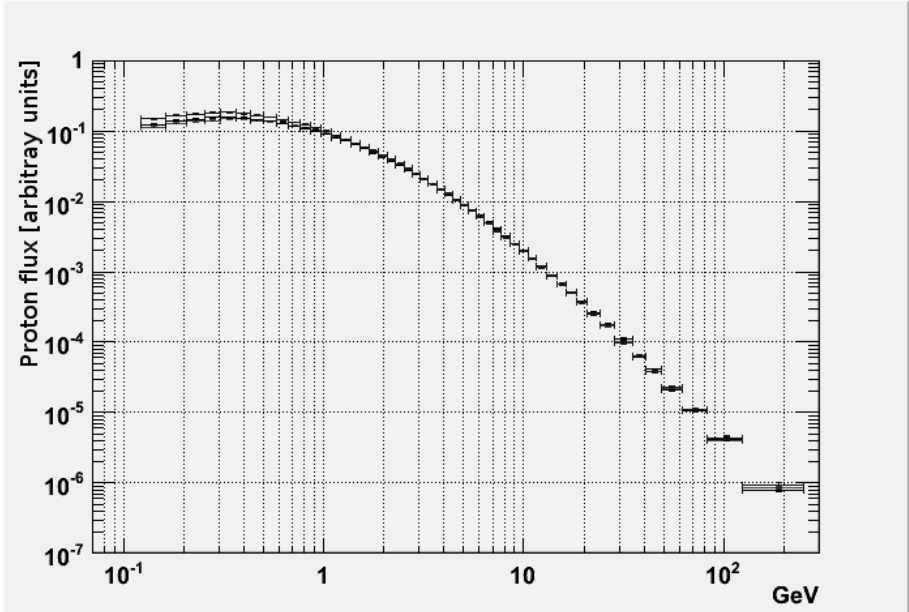


Figure 14: Differential spectrum of protons measured in July 2006 (red), January 2007 (black), August 2008 (blue). Below 1 GeV it is possible to see the flux variation due to solar modulation.

#### 5.4 Trapped particles in the Van Allen Belts

The 70° orbit of the Resurs-DK1 satellite allows for continuous monitoring of the electron and proton belts. The high energy ( $> 80\text{MeV}$ ) component of the proton belt, crossed in the South Atlantic region will be monitored in detail with the magnetic spectrometer. Using the scintillator counting rates it will be possible to extend measurements of the particle spectra to lower energies using the range method. Montecarlo simulations have shown that the coincidence of the two layers of the topmost scintillator (S1) allows PAMELA to detect  $e^-$  from 3.5 MeV and  $p$  from 36 MeV. Coincidence between S1 and the central scintillator (S2) allows us to measure integral spectra of 9.5  $e^-$  and 63 MeV  $p$ . In this way it will be possible to perform a detailed mapping

of the Van Allen Belts showing spectral and geometrical features. Also the neutron component will be measured, although some care needs to be taken to estimate the background coming from proton interaction with the main body of the satellite. In Figure 15 is shown the differential energy spectrum measured in different regions of the South Atlantic Anomaly. It is possible to see flux increase toward the centre of the anomaly. Particle flux exceeds several orders of magnitude the flux of secondary (reentrant albedo) particles measured in the same cutoff region outside the anomaly and is maximum where the magnetic field is lowest. However this is not the location of the flux at lowest energies according to scintillator counting rate. The reason for this difference is currently under investigation with comparison with existing models<sup>18) 58) 59)</sup>.

### 5.5 Secondary particles production in the Earth's atmosphere

To clearly separate primary component from the reentrant albedo (particles produced in interactions of cosmic rays with the atmosphere below the cutoff and propagating on Earth's magnetic field line) component it is necessary to evaluate the local geomagnetic cutoff. This is estimated using IGRF magnetic field model along the orbit; from this the McIlwain  $L$  shell is calculated<sup>60)</sup>. In this work we have used the vertical Stormer (defined as  $G = 14.9/L^2$ ) approximation<sup>61)</sup>. Figure 10 shows the rigidity of particles as function of the evaluated cutoff  $G$ . The primary (galactic) component, with rigidities above the cutoff is clearly separated from the reentrant albedo (below cutoff) component, containing also trapped protons in the SAA. Note that color code shows the absolute value of  $\beta$  so that negative rigidity particles in the SAA region are albedo ( $\beta < 0$  protons) with negative curvature in the tracker due to the opposite velocity vector. In Figure 16 is shown the particle flux measured at different cutoff regions. It is possible to see the primary (above cutoff) and the secondary (reentrant albedo - below cutoff) component. At the poles, where cutoff is below the detection threshold of PAMELA the secondary component is not present. Moving toward lower latitude regions the cutoff increases and it is possible to see the two components, with the position of the gap increasing with the increase of the cutoff. An accurate measurement of the secondary component is of relevance both in the calculation of the atmospheric neutrino<sup>62) 63)</sup> flux and in the estimation of hadronic cross sections (protons on O or N) at high energies, not otherwise determinable on ground.

### 5.6 Solar energetic particles

PAMELA observations are taking place at solar minimum, where about 10 significant solar events are expected during the three years experiment's lifetime<sup>61)</sup>. The observation of solar energetic particle (SEP) events with a mag-

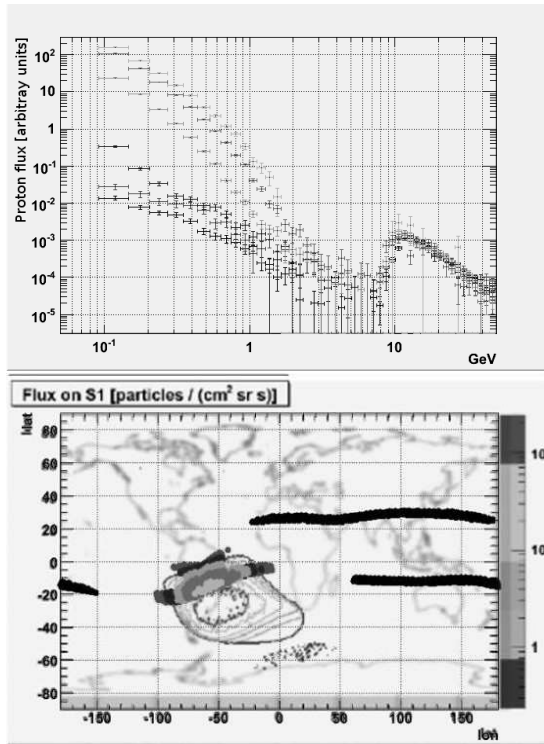


Figure 15: Top: Plot of the differential energy spectrum of PAMELA in different regions of the South Atlantic Anomaly. Regions are selected according to different intensity of the magnetic field (Black  $B > 0.3G$  - outside the SAA, Red  $0.22G < B < 0.23G$  Blue  $0.21G < B < 0.22G$  Green  $0.20G < B < 0.21G$  Pink  $0.19G < B < 0.20G$  Turquoise  $0.19G > B$ ) in the cutoff region  $10.8GV < Cutoff < 11.5GV$ . Trapped particles over the secondary particle flux measured in the same cutoff region outside the anomaly (black curve) are evident up to and above 1 GeV. Bottom: geographical regions corresponding to the above selection. The color bar corresponds to counting rate of the S1 (topmost) scintillator. Note the geographical shift between the peak of the SAA spectrum at high energy and the peak of the scintillator counting rate.

netic spectrometer will allow several aspects of solar and heliospheric cosmic ray physics to be addressed for the first time.

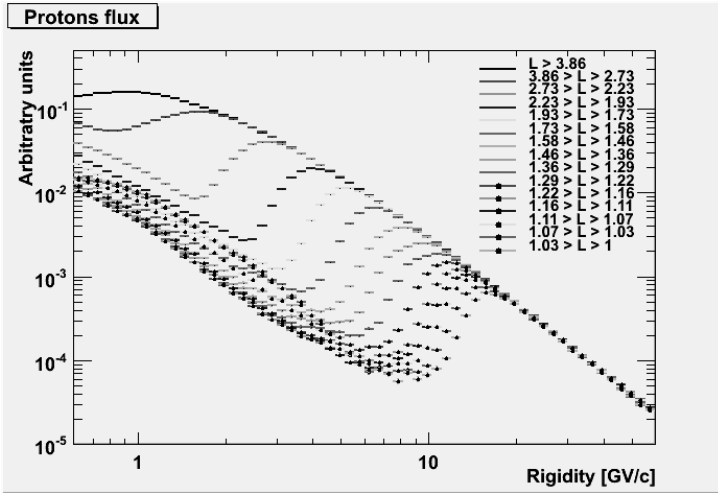


Figure 16: Plot of the differential energy spectrum of PAMELA at different L shells (according to McIlwain parameter). It is possible to see the primary spectrum at high rigidities and the reentrant albedo (secondary) flux at low rigidities. The transition between primary and secondary spectra is lower at lower cutoffs.

### 5.6.1 Electrons and Positrons

Positrons are produced mainly in the decay of  $\pi^+$  coming from nuclear reactions occurring at the flare site. Up to now, they have only been measured indirectly by remote sensing of the gamma ray annihilation line at 511 keV. Using the magnetic spectrometer of PAMELA it will be possible to separately analyze the high energy tail of the electron and positron spectra at 1 Astronomical Unit (AU) obtaining information both on particle production and charge dependent propagation in the heliosphere in perturbed conditions of Solar Particle Events.

### 5.6.2 Protons

PAMELA is capable to measure the spectrum of cosmic-ray protons from 80 MeV up to almost 1 TeV and therefore will be able to measure the solar component over a very wide energy range (where the upper limit will be limited by size and spectral shape of the event). These measurements will be correlated with other instruments placed in different points of the Earth's magnetosphere to give information on the acceleration and propagation mechanisms of SEP events. Up to now there has been no direct measurement<sup>64</sup> of the high energy (>1 GeV) proton component of SEPs. The importance

of a direct measurement of this spectrum is related to the fact<sup>65)</sup> that there are many solar events where the energy of protons is above the highest ( $\simeq 100$  MeV) detectable energy range of current spacecrafts, but is below the detection threshold of ground Neutron Monitors<sup>66)</sup>. However, over the PAMELA energy range, it will be possible to examine the turnover of the spectrum, where we find the limit of acceleration processes at the Sun.

### 5.6.3 Nuclei

PAMELA can identify light nuclei up to Carbon and isotopes of Hydrogen and Helium. Thus we can investigate the light nuclear component related to SEP events over a wide energy range. This should contribute to establish whether there are differences in the composition of the high energy (1 GeV) ions to the low energy component ( $\simeq 20$  MeV) producing  $\gamma$  rays or the quiescent solar corona<sup>67)</sup>. These measurements will help us to better understand the selective acceleration processes in the higher energy impulsive<sup>68)</sup> events.

### 5.6.4 Lowering of the geomagnetic cutoff

The high inclination of the orbit of the Resurs-DK1 satellite will allow PAMELA to study<sup>69) 70)</sup> the variations of cosmic ray geomagnetic cutoff due to the interaction of the SEP events with the geomagnetic field.

### 5.6.5 13 December 2006 Solar Particle event

At the time of writing the most significant events detected by PAMELA occurred between December 6<sup>th</sup> and 17<sup>th</sup> 2006 and were originated from region 930. Dec 6<sup>th</sup> event was originated in the East, resulting in a gradual proton event reaching Earth on Dec 7<sup>th</sup> and lasting until the events of Dec 13 and 14<sup>71)</sup>. On 13 December 2006, 02:38 UT an X3.4/4B solar flare occurred in active region NOAA 10930 ( $S06^{\circ}W23^{\circ}$ ). The interaction between the fast rotating sunspot and the ephemeral regions triggers continual brightening and finally produces the major flare<sup>72)</sup>. The intensity of the event (the second largest GLE of cycle 23) is quite unusual for a solar minimum condition. Starting at 2:50 UT on December 13, 2006, various neutron monitors, with cutoff rigidities below about 4.5 GV, recorded a Ground Level Enhancement (GLE70) with relative increases ranging from 20% up to more than 80% (Apaty, Oulu)<sup>73) 74)</sup>. Apaty and Oulu also registered the peak of the event between 02:40 UT and 03:10 UT, while most of the neutron monitors had it between 03:10 UT and 03:40 UT. The spectrum and its dynamic was investigated at higher energies using ground measurements by neutron monitors at different cutoff rigidities<sup>75)</sup> resulting in a spectral estimation of  $\gamma = 6$ . The onset time was later for the proton channels on-board of GOES-11 satellite: 03:00 UT for greater than 100

MeV protons and 03:10 for greater than 10 MeV protons<sup>74</sup>). PAMELA was in an high cutoff region at the flare occurrence and reached the South Polar region at about 03:10 UT. Muon monitors were also able to detect the GLE event and its spatial-angular anisotropy has been measured<sup>76</sup>). Differential proton spectra were directly measured by GOES, ACE, Stereo, SAMPEX at energies below 400 MeV. With these instruments it was also possible to measure the elemental composition of the various events<sup>77) 78</sup>).

The event produced also a full-halo Coronal Mass Ejection (CME) with a projected speed in the sky of 1774 km/s<sup>79</sup>). The forward shock of the CME reached Earth at 14:38 UT on December 14, causing a Forbush decrease of galactic cosmic rays which lasted for several days. A second SPE of lower intensity and energy occurred in conjunction with a X1.5 flare from the same active region (NOAA 10930, S06°W46°). A fourth event was observed at 17:23 UT on December 16 by ACE with the downstream passage of the CME. In Figure 17 is shown the differential energy spectrum measured with PAMELA in different periods of the event of the 13 December. It is possible to see that the event produced accelerated particles up to 3-4 GeV. A second smaller event occurred on Dec 14, superimposing on the Forbush decrease caused by the Coronal Mass Ejection of the previous event reaching Earth. Galactic particle flux thus decreased in the energy range up to 3 GeV, whereas solar particles were accelerated up to 1 GeV for this event. The decrease was also observed by Wind, Stereo and Polar but not by the GOES satellites, with the exception of some variation in the 15-40 MeV channel of GOES-12<sup>80</sup>). The relative decrease record by PAMELA was up to 20%, depending on the energy.

## 5.7 High energy lepton component

The calorimeter can provide an independent trigger to PAMELA for high energy releases due to showers occurring in it: a signal is generated with the release of energy above 150 mip in all the 24 views of planes from 7 to 18. With this requirement the geometrical factor of the calorimeter self-trigger is  $400 \text{ cm}^2 \text{ sr}$  if events coming from the satellite are rejected. In this way it is possible to study the electron and positron flux in the energy range between 300 GeV and 2 TeV, where measurements are currently scarce<sup>81</sup>). At this energy discrimination with hadrons is performed with topological and energetic discrimination of the shower development in the calorimeter coupled with neutron information coming from the neutron detector. This is because neutron production cross-section in an e.m. cascade is lower than in a hadronic cascade<sup>82</sup>).

## 6 Conclusions

PAMELA was successfully launched on June 2006 and is currently operational in Low Earth Orbit. The satellite and the detectors are functioning correctly.

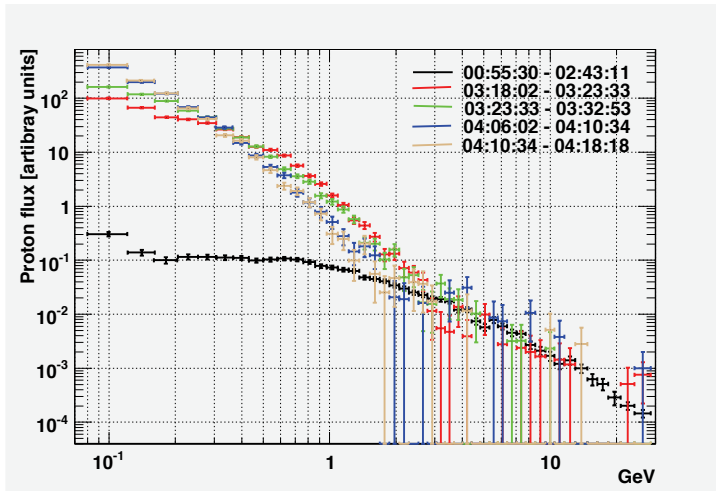


Figure 17: Proton differential energy spectra in different time intervals during the event of the 13th December 2006. The black line is the spectrum before the arrival of the charged particles with a small peak at low energy due to the presence of solar protons from previous events. It can be observed that the maximum flux of the high energy component of the solar protons arrives at the beginning of the event while only one hour later the maximum flux at low energy is detected. On the other hand, the flux at high energy decreases faster than at low energy.

It is expected that data from PAMELA will provide information on several items of cosmic ray physics, from antimatter to solar and trapped particles.

## References

- 1 . M. Boezio, et al., The Cosmic-Ray Antiproton Flux between 0.62 and 3.19 GeV Measured Near Solar Minimum Activity, *ApJ* 487 (1997) 415–+.
- 2 . M. Boezio, et al., The Cosmic-Ray Electron and Positron Spectra Measured at 1 AU during Solar Minimum Activity, *ApJ* 532 (2000) 653–669.
- 3 . V. Bidoli, et al., In-Orbit Performance of the Space Telescope NINA and Galactic Cosmic-Ray Flux Measurements, *ApJS* 132 (2001) 365–375.
- 4 . V. Bidoli, et al., Isotope composition of secondary hydrogen and helium

- above the atmosphere measured by the instruments NINA and NINA-2, *Journal of Geophysical Research (Space Physics)* 108 (2003) 1211–+.
- 5 . M. Casolino, et al., Space travel: Dual origins of light flashes seen in space, *Nature* 422 (2003) 680–+.
  - 6 . V. Bidoli, et al., In-flight performance of SilEye-2 experiment and cosmic ray abundances inside the Mir space station, *Journal of Physics G Nuclear Physics* 27 (2001) 2051–2064.
  - 7 . M. Casolino, et al., Detector response and calibration of the cosmic-ray detector of the Sileye-3/Alteino experiment, *Advances in Space Research* 37 (2006) 1691–1696.
  - 8 . P. Picozza, et al., PAMELA - A payload for antimatter matter exploration and light-nuclei astrophysics, *Astroparticle Physics* 27 (2007) 296–315.
  - 9 . M. Casolino, et al., The PAMELA Storage and Control Unit, *Advances in Space Research* 37 (2006) 1857–1861.
  - 10 . M. Casolino, et al., YODA++: A proposal for a semi-automatic space mission control, *Advances in Space Research* 37 (2006) 1884–1888.
  - 11 . <http://www.samspace.ru/eng>.
  - 12 . <http://eng.ntsomz.ru>.
  - 13 . G. Barbarino, et al., The PAMELA time-of-flight system: status report, *Nuclear Physics B Proceedings Supplements* 125 (2003) 298–302.
  - 14 . O. Adriani, et al., The magnetic spectrometer of the PAMELA satellite experiment, *Nuclear Instruments and Methods in Physics Research A* 511 (2003) 72–75.
  - 15 . M. Boezio, et al., A high granularity imaging calorimeter for cosmic-ray physics, *Nuclear Instruments and Methods in Physics Research A* 487 (2002) 407–422.
  - 16 . S. Orsi, et al., The anticoincidence shield of the PAMELA space experiment, *Advances in Space Research* 37 (2006) 1853–1856.
  - 17 . M. Pearce, et al., The Anticounter System of the PAMELA Space Experiment, in: *International Cosmic Ray Conference*, Vol. 4 of *International Cosmic Ray Conference*, 2003, pp. 2125–+.

- 18 . J. D. Gaffey, Jr., et al., NASA/National Space Science Data Center trapped radiation models, *Journal of Spacecraft and Rockets* 31 (1994) 172–176.
- 19 . On Behalf Of The Pamela Collaboration, M. Casolino, P. Picozza, On behalf of the PAMELA collaboration, Launch and commissioning of the PAMELA experiment on board the Resurs-DK1 satellite, *Advances in Space Research* 41 (2008) 2064–2070.
- 20 . V. di Felice, M. Casolino, N. de Simone, P. Picozza, PAMELA observational capabilities of Jovian electrons, *Advances in Space Research* 41 (2008) 2037–2042.
- 21 . On Behalf Of The Pamela Collaboration, M. Casolino, P. Picozza, On Behalf of the PAMELA collaboration, The PAMELA experiment: A space-borne observatory for heliospheric phenomena, *Advances in Space Research* 41 (2008) 2043–2049.
- 22 . Y. Asaoka, et al., Measurements of Cosmic-Ray Low-Energy Antiproton and Proton Spectra in a Transient Period of Solar Field Reversal, *Physical Review Letters* 88 (5) (2002) 051101–+.
- 23 . M. Aguilar, et al., The alpha magnetic spectrometer (ams)on the international space station : Part i - results from the test flight on the space shuttle.  
URL <http://democrite.in2p3.fr/democrite-00011810/en/>
- 24 . M. Boezio, et al., The Cosmic-Ray Antiproton Flux between 3 and 49 GeV, *ApJ* 561 (2001) 787–799.
- 25 . S. Orito, et al., Precision Measurement of Cosmic-Ray Antiproton Spectrum, *Physical Review Letters* 84 (2000) 1078–1081.
- 26 . M. Hof, et al., Measurement of Cosmic-Ray Antiprotons from 3.7 to 19 GeV, *ApJ* 467 (1996) L33+.
- 27 . J. W. Mitchell, et al., Measurement of 0.25-3.2 GeV Antiprotons in the Cosmic Radiation, *Physical Review Letters* 76 (1996) 3057–3060.
- 28 . M. Simon, et al., A New Calculation of the Interstellar Secondary Cosmic-Ray Antiprotons, *ApJ* 499 (1998) 250–+.
- 29 . L. Bergström, P. Ullio, private communication (1999).

- 30 . L. Bergström, et al., Cosmic Antiprotons as a Probe for Supersymmetric Dark Matter?, *ApJ* 526 (1999) 215–235.
- 31 . R. L. Golden, et al., Observation of cosmic ray positrons in the region from 5 to 50 GeV, *A&A*188 (1987) 145–154.
- 32 . D. Mueller, et al., Cosmic-ray positrons from 10 to 20 GeV - A balloon-borne measurement using the geomagnetic east-west asymmetry, *ApJ* 312 (1987) 183–194.
- 33 . J. M. Clem, et al., Solar Modulation of Cosmic Electrons, *ApJ*464 (1996) 507–+.
- 34 . R. L. Golden, et al., Observations of cosmic-ray electrons and positrons using an imaging calorimeter, *ApJ* 436 (1994) 769–775.
- 35 . R. L. Golden, et al., Measurement of the Positron to Electron Ratio in Cosmic Rays above 5 GeV, *ApJ*457 (1996) L103+.
- 36 . S. W. Barwick, et al., The Energy Spectra and Relative Abundances of Electrons and Positrons in the Galactic Cosmic Radiation, *ApJ* 498 (1998) 779–+.
- 37 . J. Alcaraz, et al., Leptons in near earth orbit, *Physics Letters B* 484 (2000) 10–22.
- 38 . M. Boezio, et al., Measurements of cosmic-ray electrons and positrons by the Wizard/CAPRICE collaboration, *Advances in Space Research* 27 (2001) 669–674.
- 39 . J. J. Beatty, et al., New Measurement of the Cosmic-Ray Positron Fraction from 5 to 15GeV, *Physical Review Letters* 93 (24) (2004) 241102–+.
- 40 . R. J. Protheroe, On the nature of the cosmic ray positron spectrum, *ApJ* 254 (1982) 391–397.
- 41 . I. V. Moskalenko, et al., Production and Propagation of Cosmic-Ray Positrons and Electrons, *ApJ* 493 (1998) 694–+.
- 42 . E. A. Baltz, et al., Positron propagation and fluxes from neutralino annihilation in the halo, *Physical Review D*59 (2) (1999) 023511–+.
- 43 . S. Profumo, et al., The role of antimatter searches in the hunt for supersymmetric dark matter, *Journal of Cosmology and Astro-Particle Physics* 7 (2004) 6–+.

- 44 . P. Ullio, Signatures of exotic physics in antiproton cosmic ray measurements, ArXiv Astrophysics e-prints.
- 45 . F. Donato, et al., Antiprotons in cosmic rays from neutralino annihilation, Phys.Rev.D 69 (6) (2004) 063501–+.
- 46 . A. M. Lionetto, et al., Uncertainties of cosmic ray spectra and detectability of antiproton mSUGRA contributions with PAMELA, Journal of Cosmology and Astro-Particle Physics 9 (2005) 10–+.
- 47 . K. M. Belotsky, et al., Composite dark matter and its charged constituents, Gravitation and Cosmology 12 (2006) 93–99.
- 48 . K. M. Belotsky, et al., May heavy neutrinos solve underground and cosmic-ray puzzles?, Physics of Atomic Nuclei 71 (2008) 147–161.
- 49 . M. Cirelli, et al., Minimal Dark Matter predictions for galactic positrons, anti-protons, photons, ArXiv e-prints 802.
- 50 . K. Abe, et al., Measurement of cosmic-ray low-energy antiproton spectrum with the first BESS-Polar Antarctic flight, ArXiv e-prints 805.
- 51 . H. Miyasaka, et al., Cosmic Ray Produced Antiprotons Confined in the Innermost Magnetosphere, in: International Cosmic Ray Conference, Vol. 7 of International Cosmic Ray Conference, 2003, pp. 4265–4268.
- 52 . D. Hooper, E. A. Baltz, Strategies for Determining the Nature of Dark Matter, ArXiv e-prints 802.
- 53 . D. Hooper, et al., Searching for dark matter with future cosmic positron experiments, Physical Review D71 (8) (2005) 083503–+.
- 54 . D. Hooper, et al., Kaluza-Klein dark matter and the positron excess, Phys.Rev.D 70 (11) (2004) 115004–+.
- 55 . M. Asano, et al., Cosmic positron signature from dark matter in the littlest Higgs model with T parity, Physical Review D75 (6) (2007) 063506–+.
- 56 . J. Hisano, et al., Heavy wino-like neutralino dark matter annihilation into antiparticles, Physical Review D73 (5) (2006) 055004–+.
- 57 . S. W. Barwick, et al., Measurements of the Cosmic-Ray Positron Fraction from 1 to 50 GeV, ApJ 482 (1997) L191+.

- 58 . R. S. Selesnick, et al., A theoretical model of the inner proton radiation belt, *Space Weather* 5 (2007) S04003.
- 59 . R. S. Selesnick, et al., Geomagnetically trapped antiprotons, *Geophysical Research Letters* 34 (2007) 20104–+.
- 60 . Igrf-10 coefficients, Tech. rep., IAGA (2005).
- 61 . M. A. Shea, et al., Estimating cosmic ray vertical cutoff rigidities as a function of the McIlwain L-parameter for different epochs of the geomagnetic field, *Physics of the Earth and Planetary Interiors* 48 (1987) 200–205.
- 62 . M. Honda, et al., New calculation of the atmospheric neutrino flux in a three-dimensional scheme, *Physical Review D* 70 (4) (2004) 043008–+.
- 63 . T. Sanuki, et al., Study of cosmic ray interaction model based on atmospheric muons for the neutrino flux calculation, *Physical Review D* 75 (4) (2007) 043005–+.
- 64 . L. I. Miroshnichenko (Ed.), *Solar Cosmic Rays*, Vol. 260 of *Astrophysics and Space Science Library*, 2001.
- 65 . J. M. Ryan, Long-Duration Solar Gamma-Ray Flares, *Space Science Reviews* 93 (2000) 581–610.
- 66 . G. A. Bazilevskaya, et al., On The Stratospheric Measurements of Cosmic Rays, *Space Science Reviews* 85 (1998) 431–521.
- 67 . J. M. Ryan, Solar emissions (SH-1), in: *International Cosmic Ray Conference*, Vol. 10 of *International Cosmic Ray Conference*, 2005, pp. 357–+.
- 68 . D. V. Reames, Particle acceleration at the Sun and in the heliosphere, *Space Science Reviews* 90 (1999) 413–491.
- 69 . R. C. Ogliore, et al., A direct measurement of the geomagnetic cutoff for cosmic rays at space station latitudes, in: *International Cosmic Ray Conference*, Vol. 10 of *International Cosmic Ray Conference*, 2001, pp. 4112–4115.
- 70 . R. A. Leske, et al., Observations of geomagnetic cutoff variations during solar energetic particle events and implications for the radiation environment at the Space Station, *Journal of Geophysical Research* 106 (2001) 30011–30022.

- 71 . D. Wilkinson, Goes sem data summary 2006, Tech. rep., NOAA's National Geophysical Data Center (2006).
- 72 . J. Zhang, et al., Interaction between a Fast Rotating Sunspot and Ephemeral Regions as the Origin of the Major Solar Event on 2006 December 13, *ApJl* 662 (2007) L35–L38.
- 73 . J. W. Bieber, et al., A Maverick GLE: The Relativistic Solar Particle Event of December 13, 2006, in: *ICRC 2007 Proceedings*.
- 74 . Y. Q. Tang, Study of the ground level enhancement of 13 December 2006, in: *ICRC 2007 Proceedings*.
- 75 . E. Vashenyuk, et al., The GLE of December 13, 2006 according to the ground level and balloon observations, in: *ICRC 2007 Proceedings*.
- 76 . D. A. Timashkov, et al., Ground-Level Enhancement of December 13, 2006 in muon hodoscopes data, in: *ICRC 2007 Proceedings*.
- 77 . R. A. Mewaldt, et al., Observations of the December 2006 solar energetic particle events with the Low Energy Telescope (LET) on STEREO, in: *ICRC 2007 Proceedings*.
- 78 . C. M. S. Cohen, et al., Comparing observations and expectations of SEP composition in the two December 2006 events, in: *ICRC 2007 Proceedings*.
- 79 . Y. Liu, et al., A Comprehensive View of the 13 December 2006 CME: From the Sun to Interplanetary Space, *ArXiv e-prints* 802.
- 80 . T. Mulligan, et al., Unusual solar energetic proton fluxes at 1 AU within an interplanetary CME, in: *ICRC 2007 Proceedings*.
- 81 . T. Kobayashi, et al., in: *26<sup>th</sup> Int. Cosm. Ray Conf.*, Salt Lake City, Vol. 3 61, 1999.
- 82 . A. Galper, Measurement of primary protons and electrons in the energy range of  $10^{11} - 10^{13}$  ev in the pamela experiment, in: *Proceedings ICRC*, 2001.

# PROBING GRAVITY WITH SATELLITE AND LUNAR LASER RANGING IN THE SOLAR SYSTEM

A. Boni, C. Cantone, S. Dell'Agnello, G. O. Delle Monache, M. Garattini,  
N. Intaglietta, C. Lops, M. Maiello, M. Martini, C. Prosperi  
*Laboratori Nazionali di Frascati dell'INFN, Frascati, ITALY*

D. G. Currie,

*University of Maryland at College Park, MD, USA*

R. Vittori

*ESA Astronaut Corps and Italian Air Force, ITALY*

G. Bellettini, R. Tauraso

*University of Rome Tor Vergata, ITALY*

R. March

*CNR-IAC, Rome, ITALY*

## Abstract

We describe the experimental tests of gravity carried out with the techniques of satellite and lunar laser ranging in the solar system, the prospects for new measurements and for the development of new laser retro-reflector payloads. We also report the technological application of SLR to the satellite navigation<sup>1</sup>.

---

<sup>1</sup>Presented by S. Dell'Agnello

## 1 Introduction

Satellite laser ranging (SLR) and lunar laser ranging (LLR) are two consolidated time-of-flight techniques which provide the most precise AND, at the same time, the most cost-effective method to track in space the position of satellites or test-masses equipped with cube corner laser retro-reflectors (CCRs). The first and most important experiments were Apollo on the Moon surface (missions 11, 14, 15) and LAGEOS-I (1976) at 6000 Km Earth altitude. These are still operational and actively analyzed today. SLR and LLR missions produced a host of precise tests of General Relativity (GR) and unique measurements in Space Geodesy and Geo-dynamics.

A new “Satellite/lunar laser ranging Characterization Facility (SCF)”, has been built in the context of the ETRUSCO experiment (see section 6) and is operational at INFN-LNF to perform the detailed calibration of the thermal properties and the laser-ranging performance of CCRs in a realistic space environment. Such a qualification has never been performed before and this INFN facility is defining the standard for SLR and LLR space characterization <sup>1)</sup>.

## 2 Physics with Second Generation Lunar Laser Ranging

The Apollo Lunar Laser Langing gives the most accurate measurement of the De Sitter effect in GR (PPN parameter  $\beta$ ) and of Yukawa-like deviations from the  $1/r^2$  law. Together with laboratory tests at very small distances, LLR gives the most accurate test of the Weak Equivalence Principle. It also allows for a unique,  $10^{-4}$ -level test of the Strong Equivalence Principle which is at the heart of GR. Current limits are shown in Table 1, together with the tighter constraints that can be done with a 2<sup>nd</sup> generation CCR array like the one that we are developing for NASA and ASI.

In 2006 An R&D for a 2<sup>nd</sup> generation LLR experiment (MoonLIGHT<sup>2</sup>) has been proposed to NASA by a US-ITALY team led by the University of Maryland (UMCP) and co-led by INFN-LNF. At the same time a robotic deployment version of this project was the subject of an ASI study. MoonLIGHT was approved by NASA in the context of the Lunar Sortie Scientific Opportunity (LSSO) program, which is targeted to the manned landings of the late next decade. We have developed an LLR payload capable of improving the space segment contribution to positioning on the Moon by a factor 100 or more. This will be achieved by replacing the small (38mm diameter), tightly spaced Apollo CCRs with a sparse array of single, large (100 mm diameter) CCRs separated by few tens of meters in order that their laser returns yeald separate return signals on the Earth detectors. Such an array will not suffer from the time

---

<sup>2</sup>Moon Laser Instrumentation for General reletivity High-accuracy Tests.

Table 1: *Limits on gravity tests based on LLR data and expected physics reach for second generation LLR.*

Phenomenon	Current LLR	1mm LRR	0.1mm LLR	Measurment. timescale
Weak Equivalence Principle ( $\Delta a/a$ )	$10^{-13}$	$\sim 10^{-14}$	$\sim 10^{-15}$	2 yr
Strong Equivalence (Nordtvedt param.)	$4 \times 10^{-4}$	$\sim 10^{-5}$	$\sim 10^{-6}$	2 yr
Gdot/G	$10^{-12}/yr$	$\sim 10^{-13}/yr$	$\sim 10^{-14}/yr$	4 yr
Geodetic Precession (PPN parameter $\beta$ )	$3 \times 10^{-3}$	$\sim 10^{-4}$	$\sim 10^{-5}$	6-10 yr
Deviations from $1/r^2$ (Yukawa)	$10^{-10}$ $\times$ gravity	$\sim 10^{-11}$ $\times$ gravity	$\sim 10^{-12}$ $\times$ gravity	6-10 yr

broadening of the return pulse from the Apollo arrays due to the Moon geometric librations. These librations currently limits the LLR accuracy to 1-2 cm. Testing of the new 100-mm CCR at the SCF has started in September 2008 with the measurement of the solar absorptivity of the CCR, which is an important engineering number driving the thermal distortions of the CCR far field diffraction pattern back to the Earth.

Note that the replacement of the CCR must be followed by a similar improvement of the ground segment of LLR, that is, of the atmospheric corrections, hydrogeological loading of the Earth crust, laser pulse length, laser readout electronics, etc. In the decades following the Apollo missions, the wide geodesy, planetology and laser-user communities made very significant progress in their fields, which allowed for the major success of the 1<sup>st</sup> generation LLR shown in Fig. 2.

An example of new theory that can be tested with 2<sup>st</sup> generation LLR is the brane-world theory of ref. 3). This is a new quantum theory in a weaker gravity at horizon scales explains the apparent acceleration of the universe without Dark Energy and, at the same time, predicts a correction to the Moon geodetic precession by about 1mm/orbit. This is not detectable with 1<sup>st</sup> generation LLR (as opposed to the GR geodetic precession of about 3m/orbit, which is measured with the accuracy of 1-2 cm), but it will be well in the domain of a MoonLIGHT array.

### 3 The International Lunar Network (ILN)

On July 24, 2008, space agencies (including ASI), met at NASA-AMES and signed a Statement of Intent (SoI) to establish a network of standardized pay-

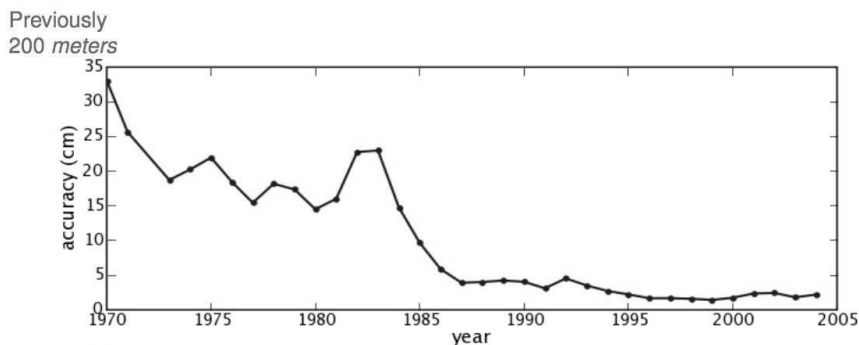


Figure 1: Historical accuracy of the 1<sup>st</sup> generation LLR.

loads composed by a set of common core instruments to be deployed with robotic missions. In order to advise the agencies, two working groups were formed: 1) the Core Instrument Working Group (CIWG), in which INFN-LNF participates; 2) the Communications Working Group. A third group on Enabling Technologies, particularly dedicated to the generation of power on the surface is being formed, while a fourth one on the choice of the landing sites will be created in 2009. The text of the SoI is reported in the Appendix.

NASA is preparing two lunar missions to establish initial anchor nodes in 2013-14 and 2015-16. Their science definition team (SDT) has foreseen a core payload of four basic instruments: 1) seismometer, 2) EM sounding, 3) heat flow probe, 4) CCR. The SDT specs for the CCR are: 10 cm diameter, weight of 1Kg for the payload, plus additional weight for the CCR deployment hinge. The MoonLIGHT CCR meets these specs and it was proposed as a natural candidate for the anchor nodes at the July ILN meeting.

#### 4 Physys with the LAsER GEODynamics Satellites (LAGEOS)

LAGEOS I and II are laser-ranged test masses used to define the position of the Earth center of mass (Geocenter), the Earth global scale of length and observation of the Lense-Thirring effect (LT, or “frame-dragging”), a truly rotational, non-static effect predicted with GR in 1918. Current LT measurement with LAGEOS agrees with GR with a relative accuracy of 10% <sup>2)</sup>.

Using this LAGEOS measurement of the LT effect, we present the preliminary limit on an the parameters of an extention of GR with the addition of Torsion that was developed by Mao, Tegmark, Guth and Cabi <sup>4)</sup> to con-

strain torsion with the data of the Gravity Probe B mission (GP-B). This work on the limit on torsion with LAGEOS data was suggested by I. Ciufolini, the theoretical calculations have been performed by March, Belletini and Tauraso.

This GR with torsion model is determined by a set  $t_1, t_2, w_1, \dots, w_5$  of seven parameters describing torsion and three further parameters describing the metric <sup>4)</sup>. Using the average LAGES nodal rate of <sup>2)</sup> we can only constrain a linear combination of a function  $f(t_1, t_2)$  of  $t_1, t_2$ , and of  $w_2, w_4$ . The function  $f$  depends linearly on  $t_1$  and  $t_2$ . Similarly to <sup>4)</sup> we report this preliminary limit graphically in fig. 4, together with the other current constraints on the PPN parameters  $\gamma$  and  $\alpha_1$ .

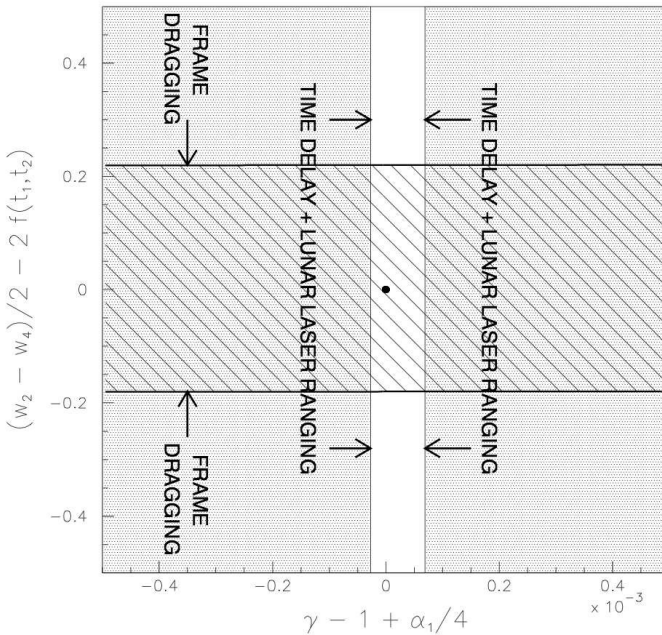


Figure 2: constraints on PPN parameters ( $\gamma, \alpha_1$ ) and on torsion parameters ( $t_1, t_2, w_2, w_4$ ) from solar system tests. The grey area is the region excluded by lunar laser ranging, Cassini tracking and VLBI. The LAGEOS measurement of the Lense-Thirring effect excludes values of  $(w_2 - w_4)/2 - 2f(t_1, t_2)$  outside the hatched region. General Relativity corresponds to  $\gamma = 1, \alpha_1 = 0$  and all torsion parameters = 0 (black dot).

It is not known whether torsion is an intrinsic feature of the ultimate, quantum theory of gravity. If torsion exists, it is also not known what its nature is: whether it is spacetime torsion (as considered in this case) or whether it is related to the spin of elementary particles yet to be discovered, hopefully finding hints of new physics at the Large Hadron Collider of CERN. If torsion does exist, however, the combined constraints from gyroscope (GP-B) and orbital Lense-Thirring experiments (LAGEOS) are effective probes to search for its experimental signatures, even if the analyses reported in <sup>4)</sup> and here fall within the framework of classic (i.e., non-quantum), non-standard torsion theories which extend General Relativity. In this sense, LAGEOS and GPB are to be considered complementary frame-dragging and, at the same time, torsion experiments.

## 5 Satellite Laser Ranging in Deep Space

INFN-LNF is also developing a prototype laser-ranged test mass for the Deep Space Gravity Probe (DSGP) mission, led by JPL (PI is S. Turyshev), proposed to the ESA "Cosmic Visions" Program. DSGP is conceived to study the Pioneer 10/11 effect in the outer reaches of the Solar System. This R&D work is being financed by ASI in the context of the three-year study on "Cosmology and Fundamental Physics (COFIS)", led by P. de Bernardis. DSGP is a satellite formation made by a main, active spacecraft, which will release a few CCR-equipped test-masses in deep space and laser-range them. The ultimate test of the PA will be performed by using the active spacecraft (tracked with microwaves from the Earth) as bridge to determine the motion of the laser-ranged test masses in the field of the Sun.

The magnitude of the "so-called" Pioneer Anomaly (PA) is  $\sim 10^{-9}$  m/sec<sup>2</sup>, which is a factor 10 larger than the highest non-gravitational perturbations (NGPs) that act on LAGEOS. These NGPs, in turn, can be characterized with the SCF at the 10% level <sup>1)</sup>. This implies that the SCF can characterize NGPs which are 1/100th of the PA. Therefore, we can reach the goal of designing and calibrating a laser-ranged test mass for DSGP.

## 6 Applications to Satellite Navigation

SLR will play another very important role for the Global Navigation Satellite System (GNSS) with the mission-critical large-scale deployment of LRR arrays on all 30 satellites of the European GNSS constellation, GALILEO. SLR will provide 'absolute' positioning, as well as long-term stability to the orbits of GALILEO satellites with respect to the Geocenter, which is uniquely defined by the LAGEOS. The addition of SLR to the standard microwave ranging will improve the absolute positioning accuracy of GNSS by one order of magnitude,

down to cm level. SLR, coupled to the precise time measurement with H-maser clocks aboard GALILEO, will allow for the improvement of the measurement of the gravitational redshift with the first satellites of the constellation. An approved multidisciplinary INFN experiment, ETRUSCO<sup>3</sup>, is dedicated to the SCF calibration of the laser retro-reflector payloads of the GNSS. With ETRUSCO we performed the thermal and optical qualification of a flight model CCR array used for the American GPS-2 (whose basic CCR is also used on the Russian GLONASS constellation) on loan from UMCP and due to fly on the next satellites of the GPS-3 constellation (see Fig. 6).

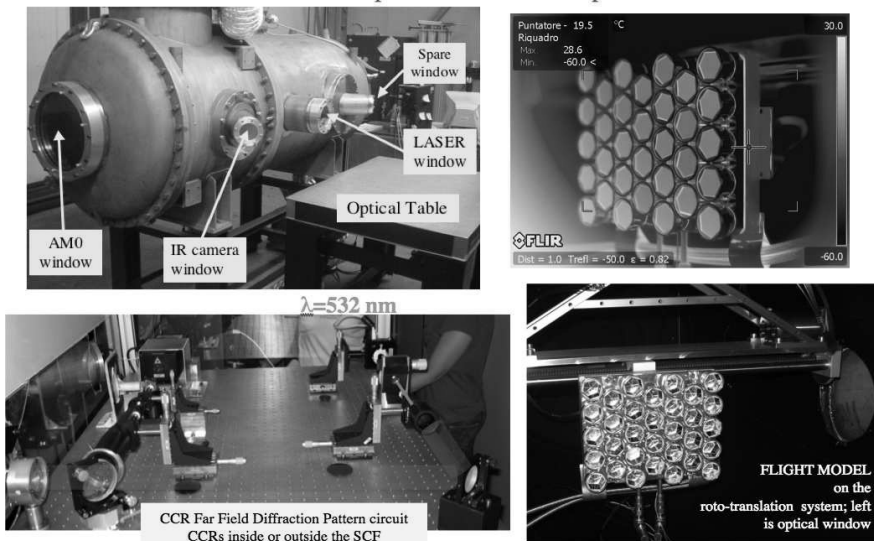


Figure 3: SCF-Test of the GPS-2 CCR array flight model.

## 7 Conclusions

In summary, the Frascati SCF is performing for the first time ever the integrated thermal and optical calibration of laser-ranged payloads in a realistic space environment for applications of GR, new gravitational theories, Space Geodesy and Satellite Navigation in Earth Orbits, on the Moon and in the outer solar system. So far we have tested CCR prototypes of LAGEOS, of

<sup>3</sup>Extra Terrestrial Ranging to Unified Satellite Constellations

the 1<sup>st</sup> generation Apollo cubes, of Glonass and GPS-2. In the near future we will SCF-Test an innovative hollow retro-reflector in collaboration with NASA-GSFC, which is proposing the hollows for the GPS-3 constellation (first satellite launched ny 2014). Hollow cubes are lighter than the standard, solid, fused-silica CCRs and can be made more compact thus saving weight and space onboard the satellites. However, since they are usually made of three separate pieaces glued and bolted together, a thorough check of the their structural stability and of their optical performace in space must be performed with the SCF prior to their deployment on any expensive and critical mission.

## References

1. A. Bosco, C. Cantone, S. Dell'Agnello, G. O. Delle Monache *et al*, Probing Gravity in NEO's with High-accuracy Laser-ranged Test Masses, *Int. Jou. Mod. Phys. D***16-12a**, 2271-2285 (2007).
2. I. Ciufolini, E.C. Pavlis, A confirmation of the general relativistic prediction of the Lense-Thirring effect, *Nature* **431** (2004), 958.
3. The Accelerated Universe and the Moon, G. Dvali, A. Gruzinov, M. Zaldarriaga, *Phys. Rev. D* **68** 024012 (2003).
4. Constraining Torsion with Gravity Probe B, Y. Mao, M. Tegmark, A.H. Guth, S. Cabi, *Phys. Rev. D* **76**, 1550 (2007).

# WHAT AN ASTROPHYSICIST CAN TELL ABOUT THE NATURE OF DARK MATTER ?

Sergio Colafrancesco

*ASI-ASDC, c/o ESA-ESRIN, Via G. Galilei, 00040 Frascati, Italy*

## **Abstract**

The nature of Dark Matter is still elusive to the ongoing experimental search. We discuss some astrophysical techniques to search for the nature of DM through a multi-frequency analysis of cosmic structures on large scales, from dwarf galaxies to galaxy clusters.

## 1 Signals from the dark universe

There is overwhelming evidence that we live in a flat ( $\Omega_0 \approx 1$ ), dark universe dominated by a dark form of matter (Dark Matter, DM) and an obscure form of energy (Dark Energy, DE). DM provides a fraction  $\Omega_m \approx 0.23$  of the overall matter-energy content, the rest being provided by DE with  $\Omega_{DE} \approx 0.73$  with the baryonic contribution limited to  $\Omega_b \approx 0.04$  <sup>23)</sup>. Given the basic properties that DM is observed to have it has been not difficult to think of possible candidates <sup>3)</sup>, but despite the large experimental efforts for their studies, the nature of the DM basic constituents is still unknown. Direct detection is the cleanest and most decisive discriminant. However, it would be interesting if astronomical techniques were to reveal some of the fundamental properties of DM particles. The dark side of the universe sends us, in fact, signals of the presence and of the nature of DM that can be recorded using different astrophysical probes. These probes are of *inference* and *physical* character.

*Inference probes* (i.e., the CMB anisotropy spectrum <sup>23)</sup>, the dynamics of galaxies <sup>28)</sup>, the hydrodynamics of the hot intra-cluster gas <sup>2)</sup> and the gravitational lensing distortion of background galaxies by the intervening potential wells of galaxy clusters <sup>4)</sup> tell us about the presence, the total amount and the spatial distribution of DM in the large scale structures but cannot provide detailed information on the nature of DM. *Physical probes* tell us about the nature and the physical properties of the DM particles and can be obtained by studying the astrophysical signals of their interaction/annihilation in the atmospheres of DM-dominated structures (like galaxy cluster and galaxies). These probes can be recorded over a wide range of frequencies from radio to  $\gamma$ -rays and prelude to a full multi-frequency search for the nature of DM in cosmic structures.

The most viable candidates proposed so far for a cosmologically relevant DM – i.e., neutralinos with a mass  $M_\chi$  in the range between a few GeV to a few hundreds of GeV; sterile neutrinos with masses larger than a few keV; and more generally light DM particles with masses in the range from keV to MeV – yield emission properties in DM halos that are markedly different and, therefore, allow a clear distinction of the relative DM nature. We will discuss in the following the two extreme DM halo cases available: galaxy clusters, i.e. the largest gravitationally bound DM containers in the universe, and dwarf spheroidal galaxies, i.e. the darkest galactic structures in the universe.

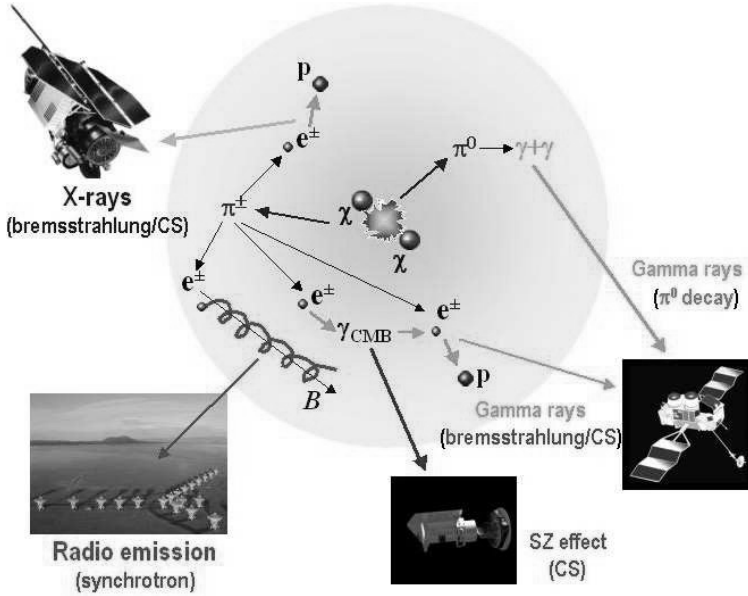


Figure 1: *The basic astrophysical mechanisms underlying the multi-frequency search for the nature of ( $\chi$ ) DM particles in large-scale structures (e.g., galaxy clusters and galaxies). These mechanisms are, among others:  $\gamma$ -ray emission from  $\pi^0 \rightarrow \gamma + \gamma$ , relativistic bremsstrahlung of secondary  $e^\pm$  and ICS of CMB photons by secondary  $e^\pm$ ; X-ray/UV emission due to bremsstrahlung and ICS of background photons by secondary  $e^\pm$ ; synchrotron emission by secondary  $e^\pm$  diffusing in the ambient magnetic field;  $SZ_{\text{DM}}$  (ICS of CMB photons by secondary  $e^\pm$ ) effect.*

## 2 A test case: neutralino DM

The  $\chi$  annihilation rate  $R = n_\chi(r)\langle\sigma v\rangle$ , depends on the  $\chi$  number density  $n_\chi(r) = n_{\chi,*}g(r)$ , with a spatial profile given by the general formula  $g(r) = (r/r_s)^{-\eta}(1+r/r_s)^{\eta-\xi}$  with  $\eta = 1$  and  $\xi = 3$  reproducing the NFW <sup>21</sup> profile, and from the  $\chi\chi$  annihilation cross section  $\langle\sigma v\rangle$  averaged over a thermal velocity distribution at freeze-out temperature <sup>20</sup>. The range of  $M_\chi$  and  $\langle\sigma v\rangle$  in the most general supersymmetric DM setup is extremely wide <sup>12, 13</sup>. In the following discussion, we will consider two representative SUSY models: a soft  $b\bar{b}$  model with  $M_\chi = 40$  GeV and a hard  $W^+W^-$  model with  $M_\chi = 81$  GeV, with their appropriate annihilation cross-sections (see <sup>12</sup>) for details).

Neutralinos which annihilate inside a DM halo produce quarks, leptons, vector bosons and Higgs bosons, depending on their mass and physical composition.

Electrons are then produced from the decay of the final heavy fermions and bosons. The different composition of the  $\chi\chi$  annihilation final state will in general affect the form of the electron spectrum (11)–(12).

Secondary  $e^\pm$  are produced through various prompt generation mechanisms and by the decay of charged pions  $\pi^\pm \rightarrow \mu^\pm \nu_\mu(\bar{\nu}_\mu)$ , with  $\mu^\pm \rightarrow e^\pm + \bar{\nu}_\mu(\nu_\mu) + \nu_e(\bar{\nu}_e)$  and are subject to spatial diffusion and energy losses. Both spatial diffusion and energy losses contribute to determine the evolution of the  $e^\pm$  source spectrum into their equilibrium spectrum. The time evolution of the  $e^\pm$  spectrum is described by the transport equation:

$$\frac{\partial n_e}{\partial t} = \nabla [D\nabla n_e] + \frac{\partial}{\partial E} [b_e(E)n_e] + Q_e(E, r), \quad (1)$$

where  $Q_e(E, r)$  is the  $e^\pm$  source spectrum,  $n_e(E, r)$  is the equilibrium spectrum and  $b_e$  (given here in units of GeV/s) is the  $e^\pm$  energy loss per unit time,  $b_e = b_{ICS} + b_{synch} + b_{brem} + b_{Coul}$ , with  $b_{ICS} \approx 2.5 \cdot 10^{-17} (E/GeV)^2$ ,  $b_{synch} \approx 2.54 \cdot 10^{-18} B_\mu^2 (E/GeV)^2$ ,  $b_{brem} \approx 1.51 \cdot 10^{-16} (n_{th}/cm^{-3}) (\log(\Gamma/n_{th}) + 0.36)$ ,  $b_{Coul} \approx 7 \cdot 10^{-16} (n_{th}/cm^{-3}) (1 + \log(\Gamma/n_{th})/75)$ . Here  $n_{th}$  is the ambient gas density and  $\Gamma \equiv E/m_e c^2$ . The DM source spectrum,  $Q_e(E, r)$ , is constant over time and the  $e^\pm$  population can be described by a quasi-stationary ( $\partial n_e/\partial t \approx 0$ ) transport equation from which  $n_e(E, r)$  reaches its equilibrium configuration mainly due to synchrotron and IC losses at  $E \gtrsim 150$  MeV and to Coulomb losses at smaller energies. Spatial diffusion can be neglected in galaxy clusters while it is relevant on galactic and sub-galactic scales (12, 13).

## 2.1 Spectral Energy Distribution from neutralino DM annihilation

The astrophysical signals of DM annihilation cover the entire e.m. spectrum, from radio to  $\gamma$ -ray frequencies (see Figs.1 and 2).

**Gamma rays.** Gamma-ray emission is predominantly due to the hadronization of the decay products of  $\chi\chi$  annihilation with a continuum spectrum due to the decay  $\pi^0 \rightarrow \gamma + \gamma$  (11, 12), even though the direct  $\chi\chi$  annihilation results in a line emission feature at an energy  $\sim M_\chi$ . Gamma-ray emission is also expected from secondary  $e^\pm$  through bremsstrahlung and ICS of CMB photons. Gamma-ray emission from DM annihilation could be revealed provided that i) sufficient spectral and spatial resolution can be achieved by the  $\gamma$ -ray experiments and ii) a clear understanding of other competing emission mechanisms expected to work in cosmic structures (9) will be obtained.

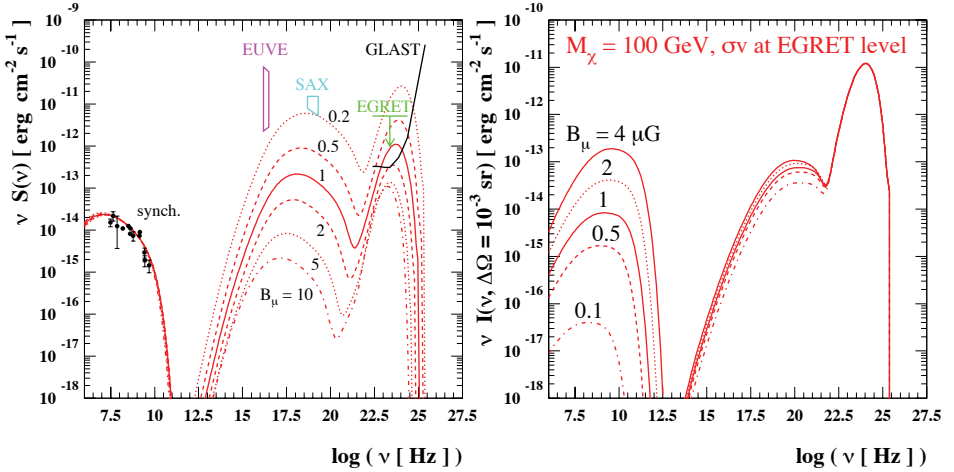


Figure 2: *Left.* Multi-frequency spectrum of the best fit models of the radio halo flux of Coma:  $M_\chi = 40$  GeV ( $b\bar{b}$ ). The halo profile is the best fit NFW (21) profile with  $M_{\text{vir}} = 0.9 \cdot 10^{15} M_\odot h^{-1}$  and  $c_{\text{vir}} = 10$ , with subhalo setup as given in (12). The scaling of the multi-frequency spectrum with the value for the mean magnetic field  $B_\mu$  in Coma is shown. *Right.* The multi-frequency spectrum of Draco dwarf galaxy for  $M_\chi = 100$  GeV ( $b\bar{b}$ ), and the effect of varying the magnetic field strength. The  $\chi\chi$  annihilation rate has been tuned to give a  $\gamma$ -ray signal at the level of the EGRET upper limit.

For the Coma cluster, the  $\gamma$ -ray flux produced by the  $\chi$  model here considered is dominated by the continuum  $\pi^0 \rightarrow \gamma\gamma$  component and it is a factor  $\sim 5$  lower than the EGRET upper limit. For Draco, the dominant  $\gamma$ -ray emission is still given by the continuum  $\pi^0 \rightarrow \gamma\gamma$  component while the dominant IC emission (i.e. that of the IC on CMB photons) peaks at much lower frequencies and is a factor  $\sim 10^2$  less intense.

**Radio emission.** Secondary  $e^\pm$  produced by  $\chi\chi$  annihilation can produce synchrotron emission in the magnetized atmosphere of galaxy clusters (as well as galaxies) and can be observed as a diffuse radio emission centered on the DM halo. Observations of cluster radio-halos are, in principle, very effective in constraining the neutralino mass and composition (11, 12, 13) under the hypothesis that DM annihilation provides a major contribution to the radio-

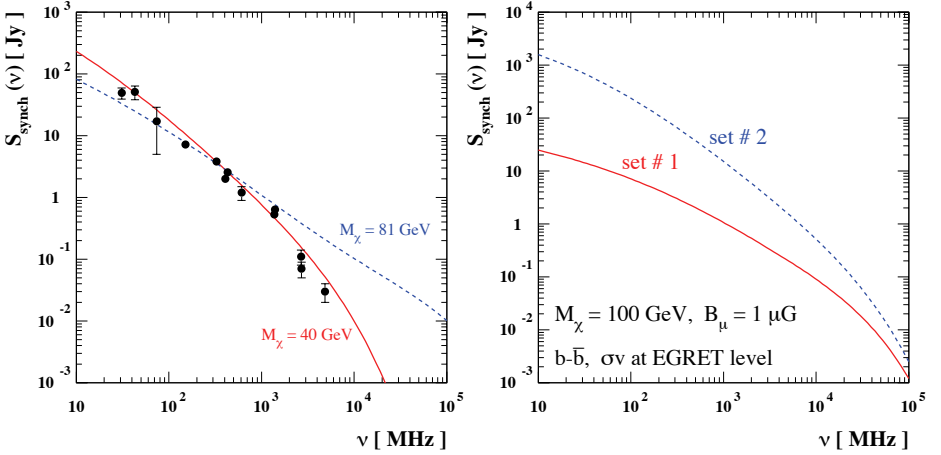


Figure 3: *Left.* The radio flux density spectrum for Coma for a soft spectrum due to a  $b\bar{b}$  annihilation final state (solid line) with  $M_\chi = 40$  GeV, and a hard spectrum due to a  $W^+W^-$  channel (dashed line) with  $M_\chi = 81$  GeV. *Right.* Radio flux density spectrum of Draco for a  $\chi b\bar{b}$  model with  $M_\chi = 100$  GeV with  $\langle\sigma v\rangle$  tuned to give 2 events in EGRET. Results are given for two choices of propagation parameters: a conservative choice ("set # 1") or a more extreme choice ("set # 2") (see <sup>13</sup>) for details).

halo flux. Under this hypothesis, a soft DM model ( $b\bar{b}$  with  $M_\chi = 40$  GeV) is able to reproduce both the overall radio-halo spectrum of Coma and the spatial distribution of its surface brightness <sup>12)</sup> (see Fig.3).

For the case of Draco, radio emission is strongly affected by propagation effects. Kolmogorov-type diffusion,  $D(E) = D_0/B_\mu^{1/3} (E/1 \text{ GeV})^{1/3}$ , with  $D_0 = 3 \cdot 10^{28} \text{ cm}^2 \text{ s}^{-1}$  (set up #1) induce a depletion of the  $e^\pm$  populations with a significant fraction leaving the diffusion region, while for  $D(E) = D_0 (E/1 \text{ GeV})^{-0.6}$  with  $D_0 = 3 \cdot 10^{26} \text{ cm}^2 \text{ s}^{-1}$  (set up #2) they are more efficiently confined within the diffusion region, but still significantly misplaced with respect to the emission region. Diffusion effects produce also a steeper spectral slope when the  $e^\pm$  are more efficiently confined within the diffusion region (set up #2) w.r.t. the case (set #1) where there is a larger depletion of the  $e^\pm$  populations <sup>13)</sup>.

**ICS of CMB: from infrared to  $\gamma$ -rays.** Secondary  $e^\pm$  up-scatter CMB

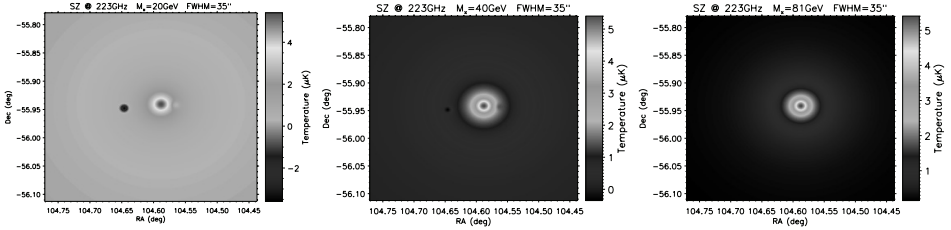


Figure 4: *Simulated SZ maps of the cluster 1ES0657-556a observable with the SPT at  $\nu = 223$  GHz for three different  $\chi$  masses:  $M_\chi = 20$  GeV (left panel), 40 GeV (mid panel) and 81 GeV (right panel) (see <sup>16</sup>) for details.*

(and other background) photons that redistribute on a wide frequency range up to  $\gamma$ -ray frequencies (see Fig.2). The soft  $\chi$  model with  $M_\chi = 40$  GeV and  $\langle\sigma v\rangle = 4.7 \cdot 10^{-25} \text{cm}^3 \text{s}^{-1}$ , with  $B_\mu = 1.2$  that fits the Coma radio halo data <sup>12)</sup> yields UV and hard X-ray fluxes which are much fainter than the data in order to be consistent with the EGRET upper limit (see Fig.2). It is, therefore, impossible to fit all the non-thermal emission features of Coma for a consistent choice of the DM model and of the cluster magnetic field <sup>12)</sup>. For Draco the dominant IC on CMB component produces an X-ray flux of  $\sim 10^{-15} - 10^{-14}$  erg  $\text{cm}^{-2} \text{s}^{-1}$  when the  $\gamma$ -ray flux is normalized to the EGRET upper limit. The constraints obtainable by the coming GLAST observation will set much more realistic expectations for the diffuse X-ray emission produced from DM annihilation in Draco which could eventually be tested with high sensitivity X-ray experiments.

**SZ effect from DM annihilation.** Secondary  $e^\pm$  produced by DM annihilation interact with the CMB photons and up-scatter them to higher frequencies producing a SZ effect with specific spectral and spatial features <sup>10)</sup>. The  $\chi$  model with  $M_\chi = 40$  GeV produces a temperature decrement in Coma of  $\sim 40$  to  $15 \mu\text{K}$  in the range  $\sim 30$  to  $150$  GHz <sup>12)</sup> The presence of a substantial  $\text{SZ}_{\text{DM}}$  effect is likely to dominate the overall SZ signal at  $\nu \sim 220 - 250$  GHz providing a negative total SZ effect. This specific spectral property allows to

perform a very clear separation of thermal and DM-induced SZE in clusters (like 1ES0657-556) for which there is a clear spatial offset of DM and baryons (see Fig.4).

The  $SZ_{DM}$  effect in Draco, even though could be a definite probe of the DM annihilation in such DM-dominated systems <sup>10, 15, 13)</sup>, is quite low due to the effects of secondary  $e^\pm$  spatial diffusion.

## 2.2 Other test cases: light DM particles

As for *sterile neutrinos*, their radiative decay  $\nu_s \rightarrow \nu_i + \gamma$  (where  $\nu_i$  indicate the standard low-mass neutrinos) produces a narrow line emission whose energy provides information on the sterile neutrino mass  $m_s$ . X-ray emission spectra from galaxy clusters are a powerful tool to set constraints on sterile neutrinos in the plane  $m_s - \sin^2(2\theta)$ . The available constraints on sterile neutrinos from X-ray spectra of clusters, combined with those obtained from the CXB, Ly $\alpha$  limits and gamma-ray line limits from the MW are shown in Fig.5. The constraints from Coma observations in the 20-80 keV band obtained here are shown by the cyan dashed area. Models with lower mixing angles  $\theta$  and neutrino masses  $m_s$  up to a few hundreds keV or  $\gtrsim$  MeV are still available. In this case, next generation high-sensitivity hard X-ray detectors like SimbolX <sup>18)</sup> or next coming soft gamma-ray experiments will be able to set relevant constraints to this DM model.

Other light DM candidates have been proposed so far (e.g., the MeV DM model claimed to be responsible for the 511 keV annihilation line observed by INTEGRAL at the galactic center <sup>6)</sup> or Bose-Einstein condensates with  $\gtrsim$  keV mass <sup>8)</sup>) and they could have visible e.m. features in galaxies and galaxy clusters.

## 3 Optimal astrophysical laboratories for DM search

The analysis of the spatial and spectral intensity of the astrophysical signals coming from DM annihilation and/or decay could be a powerful tool to unveil the elusive nature of Dark Matter. However, such DM-induced signals are expected to be confused or even overcome by other astrophysical signals originating from the ambient plasmas (thermal and/or non-thermal), especially when all these components are co-spatially distributed with the DM component. An ideal system to detect DM annihilation signals would be, therefore,

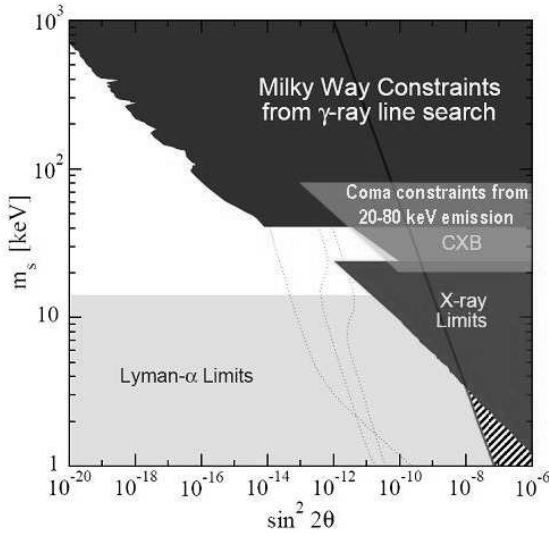


Figure 5: The sterile neutrino mass  $m_s$  and mixing  $\sin^2(2\theta)$  parameter space, with shaded regions excluded. The strongest direct bounds are shown, labeled as Milky Way <sup>26)</sup>, CXB <sup>7)</sup>, and X-ray limits <sup>27)</sup>. The strongest indirect bounds <sup>22, 25)</sup> are shown by the grey horizontal band. The excluded Dodelson-Widrow model <sup>17)</sup> is shown by the solid line; rightward, the DM density is too high (stripes). The dotted lines indicate example models <sup>1)</sup>, now truncated by the available constraints. The cyan shaded area indicates our constraints from the HXR (soft gamma-ray) limit on Coma. Figure adapted from <sup>26)</sup>.

a system which is either devoid of diffuse emitting material (this is the case of dark galaxies) or a system with a clear spatial separation between the various matter components (this is the case of the cluster 1ES0657-556).

Dwarf (dark) galaxies are among the best sites for the astrophysical search for DM but their multi-frequency SED is usually quite dim. The combination of radio and  $\gamma$ -ray observations of dwarf galaxies with the coming high-sensitivity instruments (SKA, LOFAR, EVLA, GLAST) could, nevertheless, set strong constraints on the nature of the DM particles <sup>13)</sup>.

The cluster 1ES0657-556 (where the spatial distribution of DM is clearly offset w.r.t. that of the intra-cluster gas) is an optimal laboratory for astrophysical DM search because one expects that the DM signals are clearly spatially sepa-

rated from the other astrophysical signals originating in the atmosphere of this cluster <sup>14</sup>). However, the expected  $\gamma$ -ray emission associated to the  $\chi$  DM clumps of this cluster is too low ( $\lesssim 1$  count vs.  $\sim 10$  background counts at  $E > 1$  GeV) and cannot be resolved by GLAST from other possible sources of  $\gamma$ -ray emission, both from the cluster 1ES0657-556 and from AGNs in the field. Radio telescopes have, in principle, excellent resolution and sensitivity to probe the different spectra and brightness distribution of the DM-induced synchrotron emission (the DM induced radio emission from the largest DM clump is  $\sim 3 - 10$  mJy at  $\nu = 100$  MHz (for a smooth or smooth plus 50% mass clumpiness NFW DM profile, soft  $b\bar{b}$  model with  $M_\chi = 40$ , with a  $B = 1 \mu\text{G}$ ), still marginally detectable by LOFAR <sup>14</sup>), but the uncertainties associated to the radio emission of the DM clumps of 1ES0657-556 render the prediction of these signals quite uncertain. In such a context, the possible observation of the  $SZ_{DM}$  effect for this system <sup>14</sup>) (see Fig.4) will provide an important complementary, and maybe unique, probe of the nature of DM.

#### 4 Epilogue

Viable DM models which are consistent with WMAP and with the viable structure formation scenario are able to produce observable astrophysical signals especially detectable at radio, microwave and gamma-ray frequencies. The constraints that the multi-frequency astrophysical observations can set on the  $\langle\sigma v\rangle$ - $M_\chi$  plane, are able to efficiently restrict the available neutralino models <sup>12, 13</sup>). Additional restrictions of this plane may be obtained by comparing the astrophysical constraints to those coming from both accelerator physics and from other astrophysical probes (e.g., the study of IMBHs <sup>5</sup>); the study of the galactic center region, see <sup>19</sup>) for recent review). Direct DM detection experiments have already explored large regions of the most optimistic SUSY models, and the planned next-generation experiments will probably be able to explore also the core of the SUSY models. In this context, the astrophysical study of DM annihilation proves to be complementary, but hardly competitive, especially when a full multi-frequency approach is chosen. When combined with future accelerator results, such multi-frequency astrophysical search might greatly help us to unveil the elusive nature of DM.

**References**

1. Abazajian & Fuller, Phys. Rev. D 66, 023526
2. Arnaud, M. 2005, astro-ph/0508159
3. Baltz, E. 2004, astro-ph/0412170
4. Bartelmann, M. & Schneider, P. 1999, Phys.Rep., 340, 291
5. Bertone, G., Zentner, A: and Silk, J. 2005, PRD, 72, 103517
6. Boehm, C. et al. 2004, Phys.Rev.Lett. 92 101301
7. Boyarsky et al. 2006, MNRAS, 370, 213
8. D. Boyanovsky, H. J. de Vega, N. Sanchez 2007, (arXiv:0710.5180)
9. Colafrancesco, S. 2004a, in Frontiers of Cosmology, A. Blanchard & M. Signore Eds., p.75 and p.85
10. Colafrancesco, S. 2004b, A&A, 422, L23
11. Colafrancesco, S. & Mele, B. 2001, ApJ, 562, 24
12. Colafrancesco, S., Profumo, S. & Ullio, P. 2006, A&A, 455, 21
13. Colafrancesco, S., Profumo, S. & Ullio, P. 2007, PRD, 75, 3513
14. Colafrancesco, S. et al. 2007, A&A, in press
15. Culverhouse, T., Ewans, W. and Colafrancesco, S. 2006, MNRAS, 368, 659
16. Colafrancesco, S. et al. 2007, A&A, 467, L1
17. Dodelson, S. & Widrow, A. 1994, Phys. Rev. Lett. 72, 17
18. Ferrando, P. et al. arXiv:astro-ph/0508674
19. Fornengo, N. 2006, astro-ph/0612786
20. Jungman, G., Kamionkowski, M. & Griest, K. 1996, PhR, 267, 195
21. Navarro, J., Frenk, C. & White, S.D.M. 1997, ApJ, 490, 493; Navarro, J.F. et al. 2004, MNRAS, 349, 1039

22. Seljak, U. et al. 2006, Phys. Rev. Lett. 97, 191303,
23. Spergel, D. et al. 2003, ApJS, 148, 175
24. Shaposhnikov, M. 2007, arXiv:astro-ph/0703673
25. Viel, M. et al., Phys. Rev. Lett. 97, 071301
26. Yuksel et al. 2007 (arXiv:0706.4084v1)
27. Watson et al. 2006, Phys. Rev. D 74, 033009
28. Zwicky, F. 1933, Helv.Phys.Acta, 6, 110

# COSMIC ANTIMATTER: MODELS AND OBSERVATIONAL BOUNDS

A.D. Dolgov

*ITEP, 117218, Moscow, Russia*

*INFN, Ferrara 40100, Italy*

*University of Ferrara, Ferrara 40100, Italy*

## Abstract

A model which leads to abundant antimatter objects in the Galaxy (anti-clouds, anti-stars, etc) is presented. Observational manifestations are analyzed. In particular, the model allows for all cosmological dark matter to be made out of compact baryonic and antibaryonic objects.

## 1 Introduction

The origin of the observed excess of matter over antimatter in the universe is believed to be pretty well understood now. As formulated by Sakharov <sup>1)</sup>:

- 1) nonconservation of baryonic number,
- 2) breaking of C and CP, and
- 3) deviation from thermal equilibrium

lead to different cosmological abundances of baryons and antibaryons. The cosmological baryon asymmetry is characterized by the dimensionless ratio of the difference between the number densities of baryons and antibaryons to the number density of photons in the cosmic microwave background radiation:

$$\beta = \frac{n_B - n_{\bar{B}}}{n_\gamma} \approx 6 \cdot 10^{-10} \quad (1)$$

There are many theoretical scenarios which allow to “explain” this value of the baryon asymmetry, for the review see <sup>2)</sup>. Unfortunately “many” means that we do not know the single one (or several?) of the suggested mechanisms which was indeed realized. Usually in such cases experiment is the judge which says what is right or wrong. However, it is impossible to distinguish between competing mechanisms having in one’s disposal only one number, the same for all the scenarios. We would be in much better situation if  $\beta$  is not a constant over all the universe but is a function of space point,  $\beta = \beta(x)$ . So it is interesting to study the mechanisms which might lead to space varying  $\beta$  and especially, in some regions of space, to  $\beta < 0$ , i.e. to possible generation of cosmological antimatter.

There is an increasing experimental activity in search for cosmic antimatter. In addition to the already existing detectors, BESS, Pamela, and AMS, a few more sensitive ones shall be launched in the nearest years, AMS-02 (2009), PEBS (2010), and GAPS (2013), see the review talk <sup>3)</sup> at TAUP 2007. To the present time no positive results indicating an astronomically significant cosmic antimatter have been found but still the bounds are rather loose and as we see in what follows, it is not excluded that the amount of antimatter in the universe may be comparable to that of matter and astronomically large antimatter objects can be in our Galaxy quite close to us.

If this is the case, one should search and may hope to observe cosmic antinuclei starting from  ${}^4He$  to much heavier ones, excessive antiprotons and

positrons, flux of energetic gamma rays with energies about 100 MeV from  $p\bar{p}$ -annihilation and 0.511 MeV from  $e^-e^+$ -annihilation, violent phenomena from antistars and anticlouds, and some other more subtle ones.

We cannot say, of course, if there is any reasonable chance to find all that, but at least there is a simple theoretical model according to which galaxies, including the Galaxy, though possibly dominated by matter, may include astronomically significant clumps of antimatter on the verge of possible detection.

This talk consists of the following two main parts:

- I. The mechanism of the antimatter creation leading to considerable amount of antimatter in the Galaxy in the form of compact objects or clouds.
- II. Antimatter phenomenology, observational signatures, and bounds.

The talk is based on several papers written in collaboration with C. Bambi, M. Kawasaki, N. Kevlishvili, and J. Silk <sup>4, 5, 6</sup>), where a detailed discussion and more complete list of references can be found.

## 2 Standard homogeneous baryogenesis and bounds on antimatter

Up to now we have observed only matter and no antimatter, except for a little antiprotons and positrons most probably of secondary origin. However, the observed intensive 0.511 MeV line from the galactic center <sup>7</sup>), which surely originated from the electron-positron annihilation,  $e^+e^- \rightarrow 2\gamma$ , may be a signature of cosmic antimatter. Still astronomical data rather disfavor cosmologically significant amount of antimatter. In our neighborhood the nearest anti-galaxy may be at least at the distance of 10 Mpc <sup>8</sup>). This result can be obtained as follows. At such distance the antigalaxy should be in the same cloud of intergalactic gas as e.g. our Galaxy. The number of annihilation per second of the intergalactic gas inside such antigalaxy can be estimated as:

$$\dot{N} = \sigma_{ann} v N_{gal} \langle n_p \rangle = 10^{47} / \text{sec} \quad (2)$$

where  $\sigma_{ann} v = 10^{-15} \text{ cm}^3/\text{s}$ ,  $N_{gal} \sim 10^{67}$  is the total number of antiprotons in the gas which is contained in the antigalaxy,  $\langle n_p \rangle \sim 10^{-5}/\text{cm}^3$  is the number density of protons in the intergalactic gas. The gamma ray luminosity produced by the annihilation is  $L = 10^{43} \text{ erg/s}$ . It would create the constant in time energy flux on the Earth,  $F = 10^{-3} \text{ MeV/cm}^2/\text{s}$ , which is excluded by

observations. For comparison, the typical (short-time) flux from the gamma-bursts is about  $10^2$  MeV/cm<sup>2</sup>/s.

There are observed colliding galaxies at larger distances. They should consist of the same kind of matter (or antimatter?). If galaxy and antigalaxy collide the gamma-ray luminosity would be 5 orders of magnitude higher (proportional to the number density of gas inside galaxies) than the luminosity in the case of antigalaxy washed by the intergalactic gas. This allows to conclude that colliding galaxy and antigalaxy should be at 300 times larger distance, i.e. at or outside the present day cosmological horizon.

Esthetically attractive is the charge symmetric cosmology, with equal weight of cosmologically large domains of matter and antimatter. Such situation is almost inevitable if CP is spontaneously broken <sup>9)</sup>. It was shown, however, that in charge symmetric universe the nearest antimatter domain should be at the distance larger than a Gpc <sup>10)</sup>, because the matter-antimatter annihilation at the domain boundaries would produce too intensive gamma ray background.

So we have to conclude that an asymmetric production of matter and antimatter is necessary. In the model considered below it is almost symmetric but the bulk of baryonic and/or antibaryonic matter can escape observations if antimatter “lives” in compact high density objects. Observational restrictions on astronomically large but subdominant antimatter objects/domains, anti-stars, anti-clouds, etc, are rather loose and strongly depend upon the type of the objects.

### **3 Anti-creation mechanism**

The model which leads to creation of an almost baryosymmetric universe with the bulk of matter in the form of relatively compact objects consisting of baryons and antibaryons was put forward in ref. <sup>4)</sup> and recently further developed in <sup>6)</sup>. The model is based on the slightly modified version of the Affleck-Dine (AD) baryogenesis scenario <sup>11)</sup>. According to AD scenario a very large baryon asymmetry of the universe might be generated due to accumulation of baryonic charge along flat directions of the potential of a scalar field  $\chi$  with nonzero baryonic number. Normally very high  $\beta \sim 1$  is predicted and theoretical efforts are needed to diminish the result. However, if the window to the flat directions is open only during a short period, cosmologically small

but possibly astronomically large bubbles with high  $\beta$  could be created, while the rest of the universe would have the normal  $\beta \approx 6 \cdot 10^{-10}$ . Such high  $B$  bubbles would occupy a small fraction of the universe volume, but may make a dominant contribution to the total mass of the baryonic matter. They can even make all cosmological dark matter in the form of compact already dead (anti)stars or primordial black holes (PBH).

To achieve this goal one should add a general renormalizable coupling of the scalar baryon  $\chi$  to the inflaton  $\Phi$ :

$$U_\chi(\chi, \Phi) = \lambda_1(\Phi - \Phi_1)^2 |\chi|^2 + \lambda_2 |\chi|^4 \ln \frac{|\chi|^2}{\sigma^2} + m_0^2 |\chi|^2 + m_1^2 \chi^2 + m_1^{*2} \chi^{*2}. \quad (3)$$

where  $\Phi_1$  is some value of the inflaton field which it passes closer to the end of inflation. Its value is chosen so that after passing  $\Phi_1$  inflation is still significant to make large B-bubbles. The second term in the potential is Coleman-Weinberg potential <sup>12)</sup> which is obtained by summation of one loop corrections to the quartic potential,  $\lambda_2 |\chi|^4$ . The last two mass terms are not invariant with respect to the phase rotation:

$$\chi \rightarrow e^{i\theta} \chi \quad (4)$$

and thus break baryonic current conservation. It can be seen from the following mechanical analogy. The equation of motion of homogeneous field  $\chi(t)$ :

$$\ddot{\chi} + 3H\dot{\chi} + \frac{\partial U(\chi, \Phi)}{\partial \chi^*} = 0 \quad (5)$$

is just the equation of motion of point-like particle in potential  $U$  with the liquid friction term proportional to the Hubble parameter  $H$ . In this language the baryonic number, which is the time component of the current

$$J_\mu^{(B)} = i\chi^\dagger \partial_\mu \chi + h.c., \quad (6)$$

is the angular momentum of this motion. If the potential is spherically symmetric i.e. it depends upon  $|\chi|$ , angular momentum is conserved. The last two terms break spherical symmetry and give rise to B-nonconservation.

Depending upon the value of  $\Phi$ , potential  $U(\chi, \Phi)$  has either one minimum at  $\chi = 0$ , or two minima: at  $\chi = 0$  and some  $\chi_2(\Phi) \neq 0$ , or again one minimum at  $\chi_2(\Phi)$ , see fig. 1.

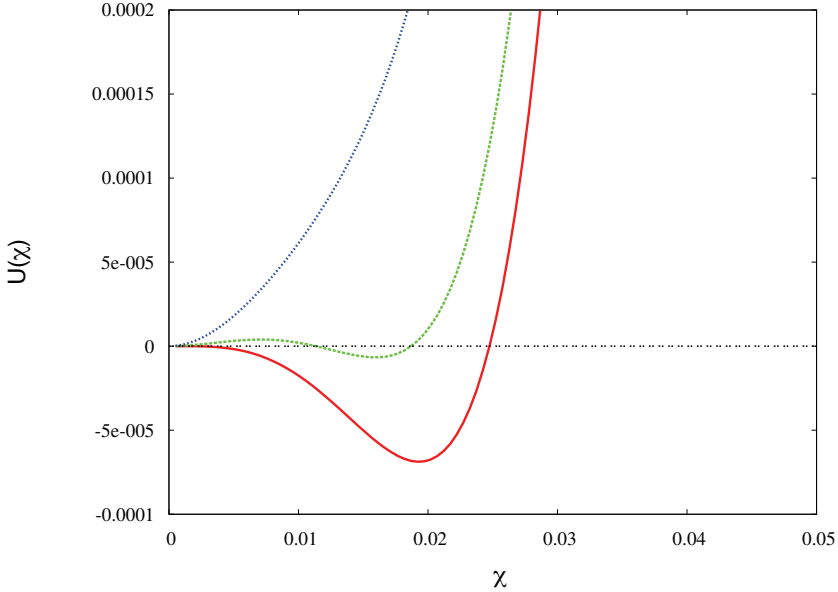


Figure 1: *The evolution of potential  $U(\chi, \Phi)$  for different values of the inflaton field  $\Phi$ .*

The behavior of  $\chi$  in this potential is more or less evident. When the potential well near the minimum at  $\chi = 0$  becomes low, the field can quantum fluctuate away from zero and if  $\chi$  reaches sufficiently large magnitude during period when the second deeper minimum at  $\chi_2$  exists, it would live there till this second minimum disappears. Otherwise  $\chi$  would remain at  $\chi = 0$ . Choosing the parameters of the potential we can make the probability to fluctuate to the second minimum sufficiently small. When the minimum at  $\chi_2$  disappears  $\chi$  would move down to zero oscillating around it with decreasing amplitude. The decrease is due to the cosmological expansion and to particle production by the oscillating field  $\chi$ . The evolution of  $\chi$  is presented in fig. 2, according to numerical calculations of ref. 6).

An important feature of the solution is the rotation of  $\chi$  around the point  $\chi = 0$ , induced by the non-sphericity of the potential at low  $\chi$ . As is argued above, this rotation is just non-zero baryonic charge density of  $\chi$ . Baryonic number stored in this rotation is transformed into excess of quarks over antiquarks or vice versa by B-conserving  $\chi$  decays.

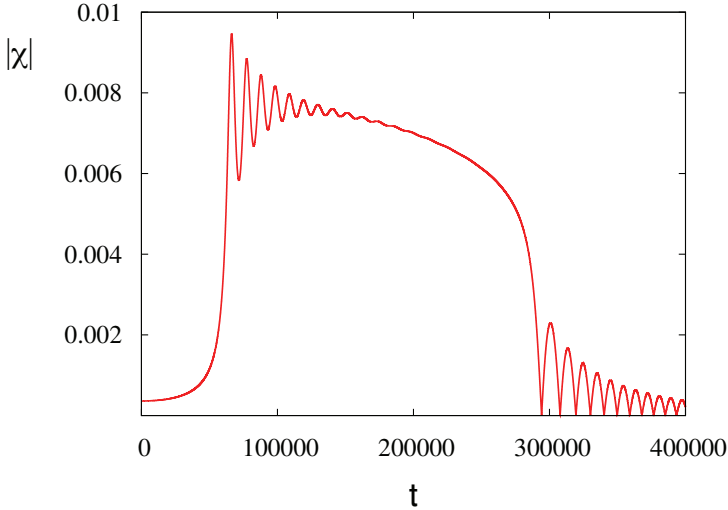


Figure 2: *Evolution of  $|\chi|$  because of the shift of the position of the second minimum in  $U(\chi, \Phi)$ .*

The magnitude of the baryon asymmetry,  $\beta$ , inside the bubbles which were filled with large  $\chi$  (B-balls) and the bubble size are stochastic quantities. The initial phase,  $\theta$ , is uniform in the interval  $[0, 2\pi]$  since due to the large Hubble term,  $H \gg m_1$ , quantum fluctuations equally populate the circle of the second minimum of  $U(\chi, \Phi)$  (3) where  $\chi = \chi_2$ . The generated baryonic number (angular momentum) is proportional to the displacement of the phase with respect to the valley where  $m_1^2 \chi^2 + m_1^{*2} \chi^{*2}$  has minimal value. Evidently the bubbles with negative and positive  $\beta$  are equally probable. The magnitude of the asymmetry inside B-bubbles is also uniformly distributed in the interval  $[-\beta_m, \beta_m]$ , where  $\beta_m$  is the maximum of the asymmetry which may be of the order of unity. The baryon asymmetry inside the bubbles can be especially large if  $\chi$  decayed much after the inflaton decay. In this case the cosmological energy density would be dominated by non-relativistic  $\chi$  prior to its decay and all the baryonic number would be normalized to photons produced by  $\chi$  decay products only.

A simple modification of the potential  $U(\chi, \Phi)$  (3) can shift the matter-

antimatter symmetry of B-bubble population in either way and magnitude, see e.g. <sup>13)</sup>. In this way the universe with the homogeneous background baryon asymmetry  $\beta = 6 \cdot 10^{-10}$  and small regions with  $\beta \sim 1$  of both signs can be created. Despite a small fraction of the volume, B-bubbles may dominate in the cosmological energy density.

The size of B-ball is determined by the remaining inflationary time after inflaton field passed  $\Phi_1$  and can be as large as the solar mass or even much larger, or as small as  $10^{15} - 10^{20}$  g or even smaller.

According to the calculations of refs. <sup>4, 6)</sup> the initial mass spectrum has a very simple log-normal form:

$$\frac{dN}{dM} = C \exp \left[ -\gamma \ln^2 \left( \frac{M}{M_1} \right) \right], \quad (7)$$

where  $C$ ,  $\gamma$ , and  $M_1$  are unknown constant parameters. If  $M_1 \sim M_\odot$  some of these high  $\beta$  bubbles might form stellar type objects and primordial black holes (PBH). With much smaller  $M_1$  light PBHs, but still with sufficiently large masses to save them from the Hawking evaporation during the universe life-time, could be created. Relatively light PBH with  $M \approx 10^{17}$  g and mass spectrum (7) may be the source of 0.511 line from  $e^+e^-$ -annihilation <sup>14)</sup>, observed in the galactic center. In all the cases of heavy or light PBH and/or evolved, now dead or low luminosity, stars, they could make (all) cosmological dark matter.

Due to subsequent accretion of matter the initial spectrum (7) would be somewhat distorted. The calculations are in progress but here in phenomenological application we assume that the spectrum is not modified.

#### 4 Inhomogeneities

In this scenario there two mechanisms of creation of density perturbations at small scales:

1. After formation of domains with large  $\chi$  the equation of state inside and outside of the domains would be different. Inside the domains  $\langle \chi \rangle \neq 0$  and the equation of state approaches the nonrelativistic one, while outside the domains the equation of state remains relativistic for a long time. As is known, in this case isocurvature perturbations are generated which in the course of evolution are transformed into real density perturbations with  $\delta\rho \neq 0$ .

2. After the QCD phase transition at  $T \sim 100$  MeV, when quarks made non-relativistic protons, the matter inside B-balls would quickly become nonrelativistic and a large density contrast could be created.

As we just have mentioned the initially inhomogeneous  $\chi$  and/or  $\beta$  lead to isocurvature perturbations. The amplitude of such perturbations is restricted by CMBR at about 10% level, but the bounds from CMBR are valid at quite large wave lengths, larger than  $\sim 10$  Mpc.

If  $\delta\rho/\rho = 1$  at horizon crossing, PBHs could be formed. The mass inside the horizon as a function of the cosmological time is:

$$M_{hor} = 10^{38} \text{g (t/sec)} \quad (8)$$

For relativistic expansion regime time is related to temperature as  $t(\text{sec}) \approx 1/T^2(\text{MeV})$ . Thus for  $T = 10^8$  GeV at the horizon crossing the PBH mass would be  $10^{16}$  g. At the QCD phase transition and below the mass inside the horizon can be from the solar mass up to  $10^{6-7} M_{\odot}$  on the tail of the distribution. This presents a new mechanism of an early quasar formation which naturally explains their large masses already at high red-shifts and their evolved chemistry.

Anti-BH may be surrounded by anti-atmosphere if  $\beta$  slowly decreases. There is no observational difference between black holes and anti black holes but the atmosphere may betray them

The masses may be even larger than millions solar masses, but we assume that  $M_0$  in eq. (7) does not exceed a few solar masses, so the formation of BHs much more massive than indicated above is strongly suppressed. Compact objects (not BH) with smaller masses might be formed too depending upon the relation between their mass and the Jeans mass (see below).

The density contrast created by an almost instant transformation of relativistic quarks into nonrelativistic baryons is equal to:

$$r_B = \frac{\delta\rho}{\rho} = \frac{\beta n_{\gamma} m_p}{(\pi^2/30) g_* T^4} \approx 0.07 \beta \frac{m_p}{T}. \quad (9)$$

The nonrelativistic baryonic matter started to dominate inside the bubble at the temperature:

$$T = T_{in} \approx 65 \beta \text{ MeV} \quad (10)$$

The mass inside a baryon-rich bubble at the radiation dominated stage is

$$M_B \approx 2 \cdot 10^5 M_\odot (1 + r_B) \left( \frac{R_B}{2t} \right)^3 \left( \frac{t}{\text{sec}} \right) \quad (11)$$

The mass density in such a bubble at the onset of matter domination is

$$\rho_B \approx 10^{13} \beta^4 \text{ g/cm}^3. \quad (12)$$

When a B-bubble entered under horizon its evolution in the early universe is determined by the relation between its radius,  $R_B$  and the Jeans wave length,  $\lambda_J$ . The latter at the onset of MD-dominance is

$$\lambda_J = c_s \left( \frac{\pi M_{Pl}^2}{\rho} \right)^{1/2} \approx 10t \left( \frac{T}{m_N} \right)^{1/2} \quad (13)$$

where the speed of sound is taken as  $c_s \approx (T/m_N)^{1/2}$ .

The bubbles with  $\delta\rho/\rho < 1$  but with  $R_B > \lambda_J$  and correspondingly  $M_B > M_{Jeans}$  at horizon would decouple from cosmological expansion and form compact stellar type objects or “low” density clouds. For further implication it is important to know what anti-objects could survive against an early annihilation?

The initial value of the Jeans mass is equal to:

$$M_J \approx 135 \left( \frac{T}{m_N} \right)^{3/2} M_{Pl}^2 t \approx 100 \frac{M_\odot}{\beta^{1/2}} \quad (14)$$

Taken literally this expression leads to a slow, as  $1/\sqrt{T}$ , increase of  $M_J$  and  $\lambda_J$ . However, this is not so because in a matter dominated object with a high baryon-to-photon ratio the temperature drops as  $T \sim 1/a^2$  and  $M_J$  decreases too:  $M_J \sim 1/a^{3/2}$ . For example, for B-balls with approximately solar mass  $M_B \sim M_\odot$  and the radius  $R_B \approx 10^9$  cm at horizon crossing the mass density behaves as:

$$\rho_B = \rho_B^{(in)} (a_{in}/a)^3 \approx 6 \cdot 10^5 \text{ g/cm}^3. \quad (15)$$

The temperature inside such a B-ball at the moment when  $M_J = M_\odot$  is equal to:

$$T \approx T_{in} (a_{in}/a)^2 \approx 0.025 \text{ MeV}. \quad (16)$$

Such an object is similar to the red giant core.

## 5 Universe heating by B-balls

There are three processes of energy release which are potentially important for B-ball survival and for the physics of the early universe (BBN, CMBR, reionization, etc):

1. Cooling down of B-balls because of their high internal temperature.
2. Annihilation of the surrounding matter on the surface.
3. Nuclear reactions inside.

We will briefly discuss them in what follows.

1. Initially the temperature inside B-balls was smaller than the outside temperature because of faster cooling of nonrelativistic matter. So such stellar-like object were formed in the background plasma with higher temperature and higher external pressure. It is in a drastic contrast with normal stars where the situation is the opposite.

After the B-bubble mass became larger than the Jeans mass, the ball expansion stopped and the internal temperature gradually became larger than the external one and B-balls started to radiate into external space. The cooling time is determined by the photon diffusion:

$$t_{diff} \approx 2 \cdot 10^{11} \text{ sec} \left( \frac{M_B}{M_\odot} \right) \left( \frac{\text{sec}}{R_B} \right) \left( \frac{\sigma_{e\gamma}}{\sigma_{Th}} \right) \quad (17)$$

The thermal energy stored inside B-ball is

$$E_{therm}^{(tot)} = 3TM_B/m_N \approx 1.5 \cdot 10^{50} \text{ erg} \quad (18)$$

and the luminosity determined by the diffusion time (17) would be  $L \approx 10^{39}$  erg/sec.

If B-balls make all cosmological dark matter, their fraction cannot exceed  $\Omega_{DM} = 0.25$ . Hence the thermal keV photons would make  $(10^{-4} - 10^{-5})\Delta$  of CMBR, red-shifted today to the background light. Here  $\Delta$  is the fraction of B-balls with solar mass and  $\sim$ keV internal temperature.

2. If B-ball is similar to the red giant core the nuclear helium burning inside would proceed through the reaction  $3He^4 \rightarrow C^{12}$ , however with larger T by the factor  $\sim 2.5$ . Since the luminosity with respect to this process strongly depends upon the temperature,  $L \sim T^{40}$ , the life-time of such B-ball would be very short. The total energy influx from such B-ball would be below  $10^{-4}$  of

CMBR if  $\tau < 10^9$  s. The efficient nuclear reactions inside B-balls could lead to B-ball explosion and creation of solar mass anti-cloud which might quickly disappear due to matter-antimatter annihilation inside the whole volume of the cloud. It is difficult to make a qualitative conclusion without detailed calculations.

3. For compact objects, in contrast to clouds, the annihilation could proceed only on the surface and they would have much longer life-time. The (anti)proton mean free path before recombination is small:

$$l_p = \frac{1}{(\sigma n)} \sim \frac{m_p^2}{\alpha^2 T^3} = 0.1 \text{ cm} \left( \frac{\text{MeV}}{T} \right)^3 \quad (19)$$

and the annihilation can be neglected. After recombination the number of annihilation on one B-ball per unit time would be:

$$\dot{N} = 10^{31} V_p \left( \frac{T}{0.1 \text{ eV}} \right)^3 \left( \frac{R_B}{10^9 \text{ cm}} \right)^2, \quad (20)$$

The energy release from this process would give about  $10^{-15}$  of the CMBR energy density.

## 6 Early summary

1. Compact anti-objects mostly survived in the early universe.
2. A kind of early dense stars might be formed with initial pressure outside larger than that inside.
3. Such “stars” may evolve quickly and, in particular, make early SNs, enrich the universe with heavy (anti)nuclei and re-ionize the universe.
4. The energy release from stellar like objects in the early universe is small compared to CMBR.
5. B-balls are not dangerous for BBN since the volume of B-bubbles is small. Moreover, one can always hide any undesirable objects into black holes.

For more rigorous conclusion detailed calculations are necessary.

## 7 Antimatter in contemporary universe

Here we will discuss phenomenological manifestations of possible astronomical anti-objects which may be in the Galaxy. We will use the theory discussed

above which may lead to their creation as a guiding line but will not heavily rely on any theory for the conclusions. We assume that anything which is not forbidden is allowed and consider observational consequences of such practically unrestricted assumption.

Astronomical objects which may live in our neighborhood include:

1. Gas clouds of antimatter.
2. Isolated antistars.
3. Anti stellar clusters.
4. Anti black holes.
5. Anything else not included into the list above.

Such objects may be: inside galaxies or outside galaxies, inside galactic halos or in intergalactic space. We will consider all the options.

### 7.1 Photons from annihilation

The observational signatures of these (anti)objects would be a 100 MeV gamma background, excessive antiprotons and positrons in cosmic rays, antinuclei, compact sources of gamma radiation, and probably more difficult, a measurement of photon polarization from synchrotron radiation and fluxes of neutrino versus antineutrino in neutrino telescopes.

Astronomically large antimatter objects is convenient to separate into two different classes: clouds of gas and compact star-like or smaller but dense clumps of antimatter. The boundary line between this two classes is determined by the comparison of the mean free path of protons inside them,  $l_p$ , and their size,  $R_B$ . If  $l_p > R_B$  the annihilation of antimatter in the cloud proceeds in all the volume of such B-bubble. In the opposite case the annihilation takes place only on the surface. The proton mean free path can be estimated as:

$$l_p = \frac{1}{\sigma_{tot} n_{\bar{p}}} = 10^{24} \text{ cm} \left( \frac{\text{cm}^{-3}}{n_{\bar{p}}} \right) \left( \frac{\text{barn}}{\sigma_{tot}} \right) \quad (21)$$

If the number density of antiprotons inside the bubble,  $\bar{n}$ , is much larger (which is typically the case) than the number density of protons in the background, i.e.  $n_{\bar{p}} \gg n_p$ , then it is possible that for B-ball smaller than  $l_{gal} = 3 - 10 \text{ kpc}$  both limiting cases can be realized: volume annihilation  $l_{free} > R_B$ , i.e. clouds, and surface annihilation,  $l_{free} < R_B$ , i.e. compact (stellar-like) objects.

One should expect that typically an anti-cloud could not survive in a

galaxy. It would disappear during

$$\tau = 10^{15} \text{ sec} \left( \frac{10^{-15} \text{ cm}^3/\text{s}}{\sigma_{ann} v} \right) \left( \frac{\text{cm}^{-3}}{n_p} \right), \quad (22)$$

if the supply of protons from the galactic gas is sufficient. The proton flux into an anti-cloud is equal to:

$$F = 4\pi l_c^2 n_p v = 10^{35} \text{ sec}^{-1} \left( \frac{n_p}{\text{cm}^3} \right) \left( \frac{l_c}{\text{pc}} \right)^2, \quad (23)$$

where  $l_c$  is the cloud size, previously denoted as  $R_B$ . The total number of  $\bar{p}$  in the cloud is  $N_{\bar{p}} = 4\pi l_c^3 n_{\bar{p}}/3$ . The flux of protons from the galactic gas is sufficient to destroy the anti-cloud in less than the universe age, i.e.  $3 \cdot 10^{17}$  seconds, if:

$$\left( \frac{n_{\bar{p}}}{\text{cm}^3} \right) \left( \frac{l_c}{\text{pc}} \right) < 3 \cdot 10^4 \quad (24)$$

Thus very large clouds might survive even in a galaxy. Almost surely they would survive in the halo.

In the case of volume annihilation, i.e. for  $l_{free}^p > l_c$  the number of annihilation per unit time and volume is

$$\dot{n}_p = v \sigma_{ann} n_p n_{\bar{p}} \quad (25)$$

The total number of annihilation per unit time is:  $\dot{N}_p = 4\pi l_c^3 \dot{n}_p/3$ . The total number of  $\bar{p}$  in the cloud is equal to:  $N_{\bar{p}} = 4\pi l_c^3 n_{\bar{p}}/3$ . Comparing these two expressions we find the life-time (22) of the cloud.

The luminosity for volume annihilation is equal to:

$$L_{\gamma}^{(vol)} \approx 10^{35} \frac{\text{erg}}{\text{s}} \left( \frac{R_B}{0.1 \text{ pc}} \right)^3 \left( \frac{n_p}{10^{-4} \text{ cm}^{-3}} \right) \left( \frac{n_{\bar{p}}}{10^4 \text{ cm}^{-3}} \right). \quad (26)$$

and the flux of gamma rays on the Earth from anti-cloud at the distance of  $d=10$  kpc would be:  $10^{-7} \gamma/\text{s}/\text{cm}^2$  or  $10^{-5} \text{ MeV}/\text{s}/\text{cm}^2$ , to be compared with cosmic background  $10^{-3}/\text{MeV}/\text{s}/\text{cm}^2$ . Still such annihilating cloud can be observed with a sufficiently good angular resolution of the detector.

The compact stellar type objects for which  $l_s \gg l_{free}$  experience only the surface annihilation - all that hits the surface annihilate. There should be different sources of photons with quite different energies. The gamma-radiation

from  $\bar{p}p \rightarrow \text{pions}$  and  $\pi^0 \rightarrow 2\gamma$  ( $E_\pi \sim 300$  MeV) would have typical energies of hundreds MeV. The photons from  $e^+e^-$ -annihilation originating from  $\pi^\pm$ -decays  $\pi \rightarrow \mu\nu$ ,  $\mu \rightarrow e\nu\bar{\nu}$ , would be mostly below 100 MeV, while those from the "original" positrons in the B-ball would create a pronounced 0.511 MeV line.

The total luminosity with respect to surface annihilation is proportional to the number density of protons in the Galaxy and to their velocity,  $L_{tot} = 8\pi m_p l_s^2 \dot{M}$ . From this we obtain:

$$L_{tot} \approx 10^{27} \frac{\text{erg}}{\text{sec}} \left( \frac{n_p}{\text{cm}^3} \right) \left( \frac{l_s}{l_\odot} \right)^2, \quad (27)$$

from which the fraction into gamma-rays is about 20-30%.

## 7.2 Antimatter from stellar wind

Surprisingly the luminosity created by the annihilation of antiprotons from the stellar wind may be larger than that from the surface annihilation. The flux of particles emitted by an antistar per unit time can be written as:

$$\dot{M} = 10^{12} W \text{ g/sec} \quad (28)$$

where parameter  $W$  describes the difference of matter emission by solar type star and the anti-star under consideration:  $W = \dot{M}/\dot{M}_\odot$ . For solar type anti-star  $W \approx 1$ , while for already evolved antistar  $W \ll 1$ . If all "windy" particles (antiprotons and heavier antinuclei) annihilate, the luminosity per antistar would be  $L = 10^{33} W \text{ erg/sec}$ .

One sees that the luminosity of compact antimatter objects in the Galaxy is not large and it is not an easy task to discover them. However such objects may have an anomalous chemical content which would be an indication for possible antimatter. According to the discussed above scenario of generation of cosmic antimatter objects they should have anomalously large baryon-to-photon ratio. This leads to anomalous abundances of light elements in this regions, for example such domains should contain much less anti-deuterium and more anti-helium than in the standard case with  $\beta = 6 \cdot 10^{-10}$ . Moreover, some heavier primordial elements in the regions with high  $\beta$  can be formed<sup>15)</sup>. So the search for antimatter should start from a search of cosmic clouds with anomalous chemistry. If such a cloud or compact object is found, one should

search for a strong annihilation there. With 50% probability this may be, however, the normal matter with anomalous  $n_B/n_\gamma$  ratio, i.e. B-bubble with positive baryonic number.

Stellar wind and explosions of antistars would lead to enrichment of the Galaxy with low energy antiprotons. The life-time of  $\bar{p}$  with respect to annihilation in the Galaxy can be estimated as:

$$\tau = 3 \cdot 10^{13} \text{ sec} (barn/\sigma_{ann} v). \quad (29)$$

The total number of antiparticles in a galaxy is determined by the equation:

$$\dot{N} = -\sigma_{ann} v n_p n_{\bar{p}} V_{gal} + S \quad (30)$$

where  $S$  is the source, i.e.  $S = W\epsilon(N_s/10^{12}) 10^{48}/\text{sec}$ ,  $N_s$  is the number of stars in the galaxy,  $\epsilon$  is the fraction of antistars. The stationary solution of the above equation is

$$n_{\bar{p}} = \left( \frac{3 \cdot 10^{-5}}{\text{cm}^3} \right) \epsilon W \left( \frac{N_s}{10^{12}} \right) \left( \frac{barn}{\sigma_{ann} v} \right). \quad (31)$$

The number density of antinuclei is bounded by the density of “unexplained”  $\bar{p}$  and the fraction of antinuclei in stellar wind with respect to antiprotons. It may be the same as in the Sun but if antistars are old and evolved, this number may be much smaller. Heavy antinuclei from anti-supernovae may be abundant but their ratio to  $\bar{p}$  cannot exceed the same for normal SN. Explosion of anti-SN would create a large cloud of antimatter, which should quickly annihilate producing vast energy - a spectacular event. However, most probably such stars are already dead and SN might explode only in very early galaxies or even before them.

### 7.3 Cosmic positrons

Antistars can be powerful sources of low energy positrons. The gravitational proton capture by an antistar is more efficient than capture of electrons because of a larger mobility of protons in the interstellar medium. A positive charge accumulated by the proton capture should be neutralized by a forced positron ejection. It would be most efficient in galactic center where  $n_p$  is large. The observed 0.511 MeV annihilation line must be accompanied by wide spectrum  $\sim 100$  MeV radiation.

#### 7.4 Violent phenomena

A collision of a star with an anti-star of comparable mass would lead to a spectacular event of powerful gamma radiation similar to  $\gamma$ -bursters. The estimated energy release would be of the order of:

$$\Delta E \sim 10^{48} \text{ erg} \left( \frac{M}{M_{\odot}} \right) \left( \frac{v}{10^{-3}} \right)^2 \quad (32)$$

Since the annihilation pressure pushes the stars apart, the collision time would be quite short,  $\sim 1$  sec. The radiation would be most probably emitted in a narrow disk but not in jets.

Another interesting phenomenon, though less energetic, is a collision of an anti-star with a red giant. In this case the compact anti-star would travel inside the red giant creating an additional energy source. It could lead to a change of color and luminosity. The expected energy release is  $\Delta E_{tot} \sim 10^{38}$  erg during the characteristic time  $\Delta t \sim$  month.

The transfer of material in a binary star-antistar system would lead to a very energetic burst of radiation similar to a hypernova explosion.

More difficult for observation and less spectacular effects include the photon polarization. Since positrons are predominantly “right handed”, the same helicity is transferred to bremsstrahlung photons. Indeed, neutron decay creates left-handed  $e^-$  and antineutron creates right-handed positrons. The first burst from SN explosion consists predominantly of antineutrinos while that from anti-SN consists of neutrinos.

#### 7.5 Baryonic and antibaryonic dark matter

The model considered above opens a possibility that all cosmological dark matter is made out of normal baryonic and antibaryonic stuff in the form of compact stellar-like objects as early formed and now dead stars or primordial black holes, either with mass near solar mass or much smaller, e.g. near  $10^{20}$ g.

Such objects could make all cold dark matter (CDM) in the universe but in contrast to the usually considered CDM they are much heavier and have a dispersed (log-normal) mass spectrum. Very heavy ones with  $M > 10^6 M_{\odot}$  which might exist on the high mass tail of the distribution could be the seeds of large galaxy formation. Lighter stellar type objects would populate galactic halos as usual CDM.

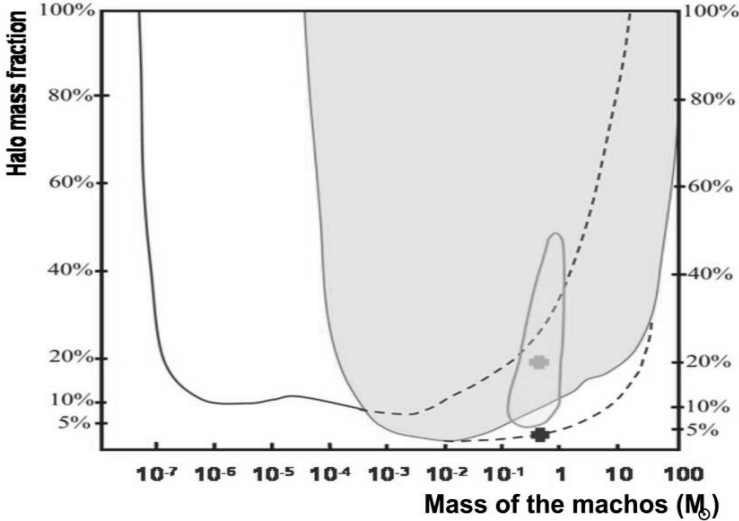


Figure 3: *Micro-lensing bounds on compact objects in the galactic halo as a function of their mass*

The bounds on stellar mass object in the halo of the Galaxy is presented in Fig. 3, taken from ref. <sup>16)</sup>. No luminous stars are observed in the halo. It means that all high B compact objects are mostly already dead stars or PBH. So the stellar wind must be absent. However, annihilation of background protons on the surface should exist and lead to gamma ray emission.

## 7.6 Observational bounds

The total galactic luminosity of the 100 MeV photons,  $L_\gamma = 10^{39}$  erg/s, and the flux of the  $e^+e^-$ -annihilation line,  $F \sim 3 \cdot 10^{-3}$  cm<sup>2</sup>/s, allow to put the following bound on the number of antistars in the Galaxy from the consideration of the stellar wind:

$$N_{\bar{S}}/N_S \leq 10^{-6} W^{-1}. \quad (33)$$

It is natural to expect that  $W \ll 1$  because the primordial antistars should be already evolved.

From the bound on the antihelium-helium ratio (see e.g. review <sup>3)</sup>) follows:

$$N_{\bar{S}}/N_S = (\bar{H}e/He) \leq 10^{-6}, \quad (34)$$

if the antistars are similar to the usual stars, though they are most probably not.

The only existing now signature in favor of cosmic antimatter is the observed 0.511 MeV photon line from galactic center and probably even from the galactic halo. However, other explanations are also possible (for the list of references see <sup>14)</sup>).

## 8 Conclusion

1. The Galaxy may possess a noticeable amount of antimatter. Both theory and observations allow for that.
2. Theoretical predictions are vague and strongly model dependent.
3. Not only  ${}^4\bar{H}e$  is worth to look for but also heavier anti-elements. Their abundances should be similar to those observed in SN explosions.
4. The regions with anomalous abundances of light elements suggest that they consist of antimatter.
5. A search of cosmic antimatter has non-vanishing chance to be successful.
6. Dark matter made of BH, anti-BH, and dead stars is a promising candidate. There is a chance to understand why  $\Omega_B = 0.05$  is similar by magnitude to  $\Omega_{DM} = 0.25$ .

## References

1. A.D. Sakharov, Pisma Zh. Eksp. Teor. Fiz. **5**, 32 (1967).
2. A.D. Dolgov, Phys. Repts. **222**, 309 (1992);  
V.A. Rubakov and M.E. Shaposhnikov, Phys. Usp. **39**, 461 (1996); Usp. Fiz. Nauk **166**, 493 (1996), hep-ph/9603208.  
A.D. Dolgov, hep-ph/9707419, lectures at 25th ITEP Winter School of Physics, Moscow, Russia, 27 February, 1997;  
A. Riotto and M. Trodden, Ann. Rev. Nucl. Part. Sci. **49**, 35 (1999), hep-ph/9901362.

3. P. Picozza, presented at TAUP, September, 2007, Sendai, Japan.
4. A. Dolgov and J. Silk, *Phys. Rev.* **D47**, 4244 (1993).
5. C. Bambi and A.D. Dolgov, *Nucl. Phys.* **B784**, 132 (2007), [astro-ph/0702350](#).
6. A.D. Dolgov, M. Kawasaki, and N. Kevlishvili, [arXiv:0806.2986](#).
7. W.N. Johnson, F.R. Harnden and R.C. Haymes, *Astrophys. J.* **172**, L1 (1972);  
M. Leventhal, C.J. MacCallum and P.D. Stang, *Astrophys. J.* **225**, L11 (1978);  
W.R. Purcell et al., *Astrophys. J.* **491**, 725 (1997);  
P.A. Milne, J.D. Kurfess, R.L. Kinzer and M.D. Leising, *New Astron. Rev.* **46**, 553 (2002) [[arXiv:astro-ph/0110442](#)];  
J. Knodlseder et al., *Astron. Astrophys.* **441**, 513 (2005) [[arXiv:astro-ph/0506026](#)];  
P. Jean et al., *Astron. Astrophys.* **445**, 579 (2006) [[arXiv:astro-ph/0509298](#)];  
G. Weidenspointner et al., *Astron. Astrophys.* **450**, 1013 (2006) [[arXiv:astro-ph/0601673](#)].
8. G. Steigman, *Ann. Rev. Astron. Astrophys.* **14**, 339 (1976).
9. T.D. Lee, *Phys. Rev.*, **D8**, 1226 (1973).
10. A.G. Cohen, A. De Rujula, and S.L. Glashow, *Astrophys. J.* **495**, 539 (1998).
11. I. Affleck and M. Dine, *Nucl. Phys.*, **B249**, 361 (1985).
12. S. R. Coleman and E. Weinberg, *Phys. Rev.* **D7**, 1888 (1973).
13. A.D. Dolgov, *Nucl. Phys. Proc. Suppl.* **113** 40 (2002).
14. C. Bambi, A.D. Dolgov, A.A. Petrov, [arXiv:0801.2786](#).
15. S. Matsuura, A.D. Dolgov, S. Nagataki, K. Sato, *Prog. Theor. Phys.* **112** (2004) 971;  
S. Matsuura, S.-I. Fujimoto, S. Nishimura, M.-A. Hashimoto, K. Sato, *Phys. Rev.* **D72** (2005) 123505;  
S. Matsuura, S-i. Fujimoto, M.-a. Hashimoto, K. Sato, *Phys. Rev.* **D75** (2007) 068302.
16. P. Tisserand, A. Milsztajn, [arXiv:astro-ph/0501584v3](#).

## ***SESSION II – ASTROPARTICLE AND NEUTRINO PHYSICS***

<i>Ferroni Fernando</i>	<i><math>0\nu\beta\beta</math></i> Present and Future
<i>Papaevangelou Thomas</i>	Result from CAST
<i>Ianni Aldo</i>	Detection of Solar Neutrinos with the Borexino Experiment
<i>Aguilar-Arevalo A.A.</i>	Results from Miniboone
<i>Garfagnini Alberto</i>	Observation of Neutrino Interactions in the OPERA Detector
<i>Weber Alfons</i>	Recent results from the MINOS Experiment
<i>Fritzscht Harald</i>	Flavor symmetry and neutrino mixing
<i>Falk Harris Elizabeth</i>	Double Chooz
<i>Yeongduk Kim</i>	The Current Status of the RENO Experiment
<i>Spurio Maurizio</i>	Antares: Towards a Large Underwater Neutrino Experiment
<i>Caravaglios Francesco</i>	Neutrinos, Grand Unified Theories and the Hierarchy problem
<i>Kayser Boris</i>	Neutrinos: What We Know, and What We Would Like To Find Out



## $0\nu\beta\beta$ : PRESENT AND FUTURE

Fernando Ferroni

*Sapienza Università di Roma & INFN Roma  
Piazza A. Moro 2, 00185 Roma, Italy*

### **Abstract**

We examine the status of the research in neutrino-less double beta decay with particular attention on the technique that have passed the test of first generation experiment and are now being considered for the next generation. The goal of the experiments to come is to be able to deal with the inverted hierarchy of the, yet unknown, neutrino mass spectrum. CUORE, to be carried on at LNGS and under construction now is the most promising project and will be described in some detail.

## 1 Introduction

Mysteries about neutrinos are several and of different nature. We know that they are neutral particles with an extraordinary little mass compared to the one of all the other particles. Although they are massive we have not succeeded yet in measuring their mass. We do not know if the neutrino is a particle different from its antiparticle or rather as hypothesized <sup>1)</sup> by Majorana in 1937 they are the same particle. Majorana observed that the minimal description of spin 1/2 particles involves only two degrees of freedom and that such a particle, absolutely neutral, coincides with its antiparticle. If the Majorana conjecture holds then it will be possible to observe an extremely fascinating and rare process that takes the name of Neutrinoless Double Beta Decay ( $0\nu$  DBD). The net effect of this ultra rare process will be to transform two neutrons in a nucleus into two protons and simultaneously to emit two electrons. Since no neutrinos will be present in the final state the sum of the energy of the two electrons will be a line. The rate of this yet unobserved phenomenon will also allow a determination, although not precise, of the neutrino mass. A set of pioneering experiments <sup>2)</sup> has been performed for this search. With the exception of one, all of them resulted into a negative observation. The one claiming a positive evidence <sup>3)</sup> (about  $4\sigma$ ) has not fully convinced the community and it is waiting for a possible confirmation. A new generation of experiments is in preparation for challenging this difficult problem. They shall meet the requirement of having a sensitivity such to be able to probe the inverted hierarchy region of the neutrino mass spectrum as described by the most recent analyses <sup>4)</sup> of the global neutrino data.

## 2 Majorana Neutrinos and Double Beta Decay

Neutrinoless double-beta decay is an old subject. What is new is the fact that, recently, neutrino oscillation experiments have unequivocally demonstrated that neutrinos do have a non zero mass and that the neutrino mass eigenstates do mix. Indeed the massive nature of neutrinos is a key element in resurrecting the interest for the Majorana conjecture. The difference between Dirac neutrinos and Majorana ones is shown in Fig. 1.

The practical possibility to test the Majorana nature of neutrinos is indeed in detecting the process shown in Fig. 2, the Double Beta Decay (DBD) without

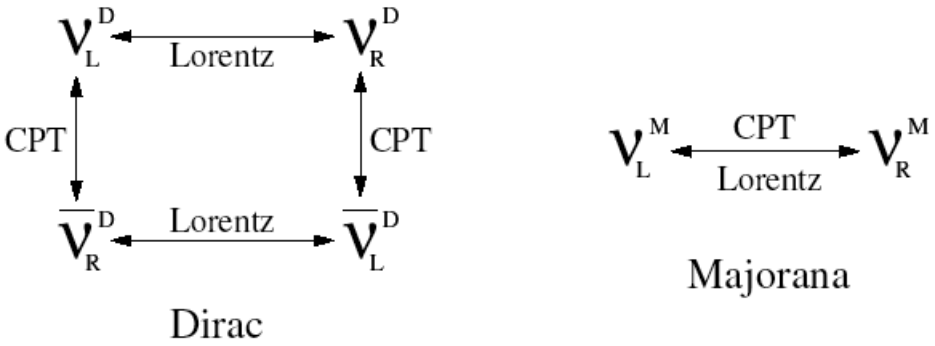


Figure 1: Dirac and Majorana neutrinos.

emission of neutrinos.

Although the possibility for this process was pointed out by W. Furry <sup>5)</sup> far in the past the experimental search looked just impossible. The key element for the process to occur is in fact in the helicity flip needed. As long as the neutrino was thought to be massless this could just not happen. Nowadays we know that this is indeed possible. The discriminant between Dirac and Majorana neutrinos is in the lepton flavour conservation, required by Dirac and violated by Majorana. So that the observation of neutrinoless DBD would be the proof of the Majorana conjecture. The oscillation experiments have yielded valuable information on the mixing angles and on the mass differences of the three eigenstates. They cannot, however, determine the scale of the neutrino mass, which is fixed by the lightest neutrino mass eigenvalue. This can only be directly determined by beta decay end point spectral shape measurements, or in the case of Majorana neutrinos, by the observation and measurement of the neutrinoless double-beta decay half-life. The oscillation experiments yield values for the mixing angles and mass differences accurate enough to allow the prediction of a range of values of the effective mass of the Majorana electron neutrino. As a function of the oscillation parameters indeed we find that

$$m_{\beta\beta} = \sum m_{\nu_k} U_{ek}^2 = \cos^2\theta_{13}(m_1 \cos^2\theta_{12} + m_2 e^{2i\alpha} \sin^2\theta_{12}) + m_3 e^{2i\beta} \sin^2\theta_{13}$$

According to most theoretical analyses of present neutrino experiment results, next-generation DBD experiments with mass sensitivities of the order

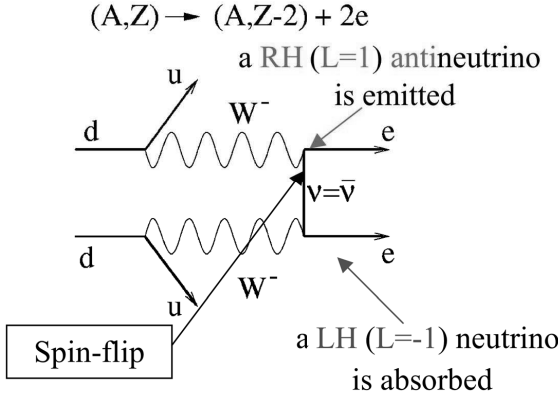


Figure 2: *Neutrinoless Double Beta Decay diagram.*

of 10 meV may find the Majorana neutrino if its mass spectrum is of the quasi-degenerate type or it exhibits inverted hierarchy.

### 3 Experimental techniques

The DBD are extremely rare processes. In the two neutrino decay mode their half-lives range from  $T_{1/2} \simeq 10^{18}y$  to  $10^{25}y$ . The rate for this process will go as

$$1/\tau = G(Q, Z) |M_{nucl}|^2 m_{\beta\beta}^2$$

The first factor (phase space) that goes like  $Q^5$  is easily calculated. The second (nuclear matrix element) is hard to compute. Several calculations made under different approaches<sup>6)</sup> exist and although the agreement is getting better with time still they worryingly differ.

The experimental investigation of these phenomena requires a large amount of DBD emitter, in low-background detectors with the capability for selecting reliably the signal from the background. The sensitivity of an experiment will go as

$$S^{0\nu} \propto a \left( \frac{MT}{b\Delta E} \right)^{1/2} \epsilon$$

Isotopic abundance ( $a$ ) and efficiency ( $\epsilon$ ) will end up in a linear gain, while mass ( $M$ ) and time ( $T$ ) only as the square root. Also background level ( $b$ ) and energy resolution ( $\Delta E$ ) behaves as a square root. In the case of the neutrinoless decay searches, the detectors should have a sharp energy resolution, or good tracking of particles, or other discriminating mechanisms. There are several natural and enriched isotopes that have been used in experiments with tens of kilograms. Some of them could be produced in amounts large enough to be good candidates for next generation experiments. The choice of the emitters should be made also according to its two-neutrino half-life (which could limit the ultimate sensitivity of the neutrinoless decay), according also to its nuclear factor-of-merit and according to the experimental sensitivity that the detector can achieve. The element has to be chosen amongst the one in the following figure 3.

Isotope	$Q_{\beta\beta}$ (MeV)	Isotopic abundance (%)
$^{48}\text{Ca}$	4.271	0.0035
$^{76}\text{Ge}$	2.039	7.8
$^{82}\text{Se}$	2.995	9.2
$^{96}\text{Zr}$	3.350	2.8
$^{100}\text{Mo}$	3.034	9.6
$^{116}\text{Cd}$	2.802	7.5
$^{128}\text{Te}$	0.868	31.7
$^{130}\text{Te}$	2.533	34.5
$^{136}\text{Xe}$	2.479	8.9
$^{150}\text{Nd}$	3.367	5.6

Figure 3: *Candidate elements for  $0\nu$  DBD.*

Double beta decay experiments can be divided into two main categories (see Fig. 4): measurement with source being separate from the detector and measurement with a detector that also acts as the source.

When the source is the same as the detector (calorimetric type), source mass is maximized while materials that could potentially contribute to the background is minimized. Also energy resolution can be optimized. However

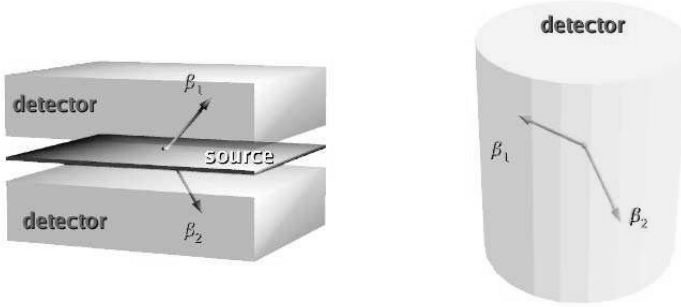


Figure 4: *Schematics of main DBD detector types.*

the absence of topological signature does not allow to reject on the event-by-event basis the background coming from photons. Conversely the other type of detectors (spectrometer type) can optimize the background rejection although at the cost of a reduced mass, a complicate geometry and a definitely worse energy resolution.

#### 4 The present: CUORICINO

Cryogenic bolometers, with their excellent energy resolution, flexibility in material, and availability in high purity of material of interest, are excellent detectors for search for neutrinoless double beta decay. Kilogram-size single crystals (cubic crystals of 5cm side) of  $TeO_2$  are now available and utilized in CUORICINO in an array for a total detector mass of 40 kg. CUORICINO results from a total exposure of 8.38 kg-yr of  $^{130}Te$  (Fig. 5) show no evidence for a peak at 2530 keV, the expected Q-value for for  $^{130}Te$ . The absence of any excess events above backgrounds in the region of interest gives a limit of  $T_{1/2} \geq 2.4 \times 10^{24}y$  (90%) C.L. on the  $0\nu$  decay rate of  $^{130}Te$ . This corresponds to an effective neutrino mass of  $m_{\beta\beta} \leq 0.18 - 0.94$  eV, the range reflecting the spread in nuclear matrix element calculations. The background measured in the region of interest is  $0.18 \pm 0.01$  counts/keV/kg/y.

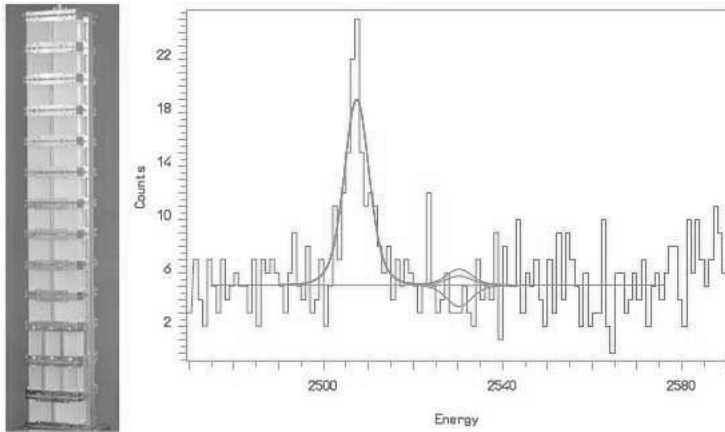


Figure 5: *CUORICINO* sketch (left) and results (right).

## 5 An almost realistic future

A few experiments on  $0\nu\text{DBD}$  are in preparation around the world. To my personal taste the most promising and justified are: GERDA at LNGS, SuperNemo whose location is at present undecided, EXO at WIPP and CUORE at LNGS. They are representative of the different options and technologies. All of them push the present technology further in a more or less credible way. They are reasonably costly, in the range that the community is ready to accept. They will get close or even bite into the inverted hierarchy mass range. They have a chance to discover the process or at worse to indicate the road for yet another step. In brief, let's examine the strong points of each of them.

### *GERDA*

The experiment GERDA <sup>7)</sup>, actually in preparation at LNGS with the goal of starting data taking in 2009 is a 3-phased project. It is a ionization calorimeter utilizing at the beginning the enriched- $^{76}\text{Ge}$  diodes recuperated from Heidelberg-Moscow <sup>8)</sup> and IGEX <sup>9)</sup>. The technology differs from the former two experiments in having bare diodes operating in a tank filled by LAr with the function of shield. Its goal on phase 1 is to scrutinize, in about one year running time, the claim of the only positive evidence so far obtained. It will

do so by having higher mass and less background. Germanium for additional diodes has been already purchased and enriched and it will be transformed into detectors in the future for phase 2 (40 kg in total). An important improvement in phase 2 will be the segmentation of the detectors for a better background rejection. The reach of phase 2 will be between 100 and 200 meV of effective neutrino mass depending on the uncertainty in background and matrix elements. An eventual phase 3 is under discussion and might involve a merging with the Majorana collaboration <sup>10</sup>).

### *SuperNemo*

NEMO, actually running at Modane laboratory in the Frejus tunnel, is a beautiful exemplification of the power of a tracking device for background rejection. In fig. 6 there is an event of double beta decay with two neutrinos perfectly reconstructed.

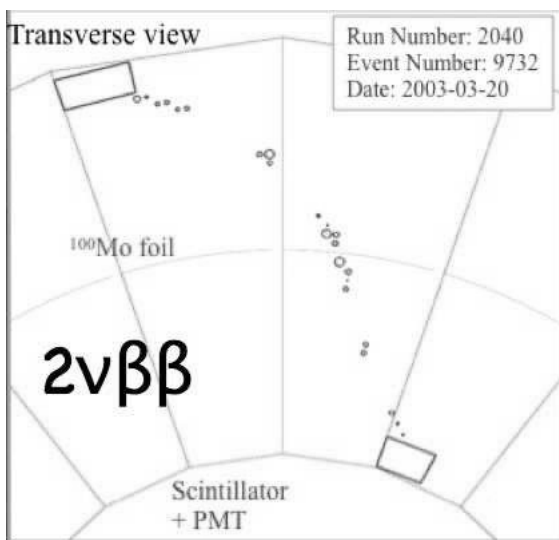


Figure 6: A DBD with emission of two neutrinos reconstructed in the NEMO detector.

The problem of a future expansion (SUPERNEMO <sup>11</sup>) of this experiment is mainly in the scale. To get a sufficient mass a very, very big detector has to be build. Whether this is compatible with the stringent requirements

imposed by this kind of experimentation it has to be seen. Still the potential of this specific technique is high, also because many different isotopes could be tested. The final sensitivity is expected in the range of 50 meV.

### *EXO*

EXO experiment <sup>12)</sup>, in preparation at WIPP <sup>13)</sup> facility is a two-stage experiment. The first data taking will happen with a 200 kg LXe detector (80% enriched in <sup>136</sup>Xe). The strong point of the detector will be the extremely good energy resolution ( $\sigma_E/E = 1.6\%$ ). The reach will be in the few hundredths of meV in a run of two years. The dramatic jump in sensitivity should come later by exploiting a concept that in principle should bring the experiment to run with much reduced background. The transition producing the process shall be  $^{136}\text{Xe} \rightarrow ^{136}\text{Ba}^{++} + 2e^-$ . The idea is to grab the Ba ion, bring it outside the calorimeter and identify it. The last part would make use of a laser exciting an optical transition and it has already been proven to be effective. How to practically trap the Ba ion is still matter of an intense R&D. The success of it, might bring the EXO phase 2 (1 ton Xe complemented by the Ba identification) to a level of 50 meV sensitivity range.

### *CUORE*

CUORE <sup>14)</sup> is the natural extrapolation of CUORICINO. 19 towers CUORICINO-like in a large cryostat. The main changes are in a better surface treatment of both the crystals and the copper mechanical structure, a better shielding made by Roman lead and a liquid-free refrigerator. The hope is to get the background reduced by no less than one order of magnitude with respect to CUORICINO. The experiment is in preparation at LNGS and its data-taking is expected in 2011. The sensitivity, scaled from what is now measured in CUORICINO, will be in the dozens of meV. At least a part of the mass region allowed by the inverted hierarchy will be attained.

## **6 Conclusion**

Neutrino physics is one of the leading field of the high energy research today. One of the top question that has to be answered is about the Dirac or Majorana nature of neutrino mass. The neutrino-less double beta decay search is the only experimental line that can answer this fundamental question and it might also be the sole chance to provide a measure of neutrino mass. Many experiments

are in preparation in several underground laboratories in the world. GERDA at LNGS will definitely check the only existing claim on the matter. SuperNEMO will try to extrapolate to a very large scale the concept of a tracking detector. EXO has the ambition of opening a complete new frontier for going to an almost zero background experiment. CUORE, solidly backed up by the CUORICINO experience and results, looks ready to challenge, at least partially, the mass region predicted by the inverted hierarchy. Exciting times are in front of us.

## References

1. E. Majorana, *Il Nuovo Cimento*, **14**, 171 (1937).
2. See for example presentations at Neutrino06 by M. Hirsch, F. Simkovic, S. Elliott, and A. Barabash.
3. H. V. Klapdor-Kleingrothaus et al., *Nucl. Instrum. Meth.*, **A522**, 371 (2004).
4. A. Strumia and F. Vissani, *Nucl. Phys.* **B276**, 294 (2005); G. L. Fogli et al., *Prog. Part. Nucl. Phys.*, **57**, 742 (2006).
5. W. H. Furry, *Phys. Rev.*, **56**, 1184 (1939).
6. F. Simkovic et al., arXiv:0710.2055v3, 2007 and references therein.
7. I. Abt et al., GERDA Technical Proposal, 2005.
8. H.V. Klapdor-Kleingrothaus, Proposal MPI-1987-V17, 1987.
9. C. Aalseth et al., *Phys. Rev.*, **C59**, 2108, 1999.
10. C.E. Alseth et al., The proposed Majorana  $^{76}\text{Ge}$  double beta decay experiment, *Nucl. Phys. Proc. Suppl.*, **138**, 217 (2005).
11. Ph. Adamson et al., EoI in the SuperNemo double beta decay program, 2004.
12. M. Danilov et al., *Phys. Lett.*, **B 480**, 12, 2000; M. Breidenbach et al., Letter of intent to SLAC EPAC, LOI2001.1, 2001.
13. E.I. Esch et al., *Nucl. Instr. Meth.* **A 538**, 516, 2005.
14. R. Ardito et al., hep-ex/0501010.

**RESULT FROM CAST**

Thomas Papaevangelou  
*CEA Saclay, France*

Written contribution not received



# **DETECTION OF SOLAR NEUTRINOS WITH THE BOREXINO EXPERIMENT**

Aldo Ianni on behalf of the Borexino collaboration  
*I.N.F.N. Gran Sasso Laboratory, Italy*

## Abstract

Borexino at the Gran Sasso Underground Laboratory has started taking data in May 2007. Borexino is a real-time solar neutrino detector with a threshold at about 200 keV. First detection of solar neutrinos from  ${}^7\text{Be}$  with Borexino are presented. The no oscillation hypothesis is rejected at  $4\sigma$  level with the present measurement. Perspectives and implications are discussed.

## 1 Introduction

The Sun is a huge source of electron neutrinos, so-called solar neutrinos, produced by a number of reactions in the pp and CNO chains. Solar neutrinos are mainly low energy neutrinos with a mean energy of about 250 keV. These are the most important pp neutrinos. With a smaller probability (15%) neutrinos up to 15 MeV can be produced. Among these high energy neutrinos of particular interest are the so-called  ${}^7\text{Be}$  neutrinos produced by electron capture on Be. These  ${}^7\text{Be}$  neutrinos are monoenergetic (862 keV, 90%) and a factor of 10 less in flux with respect to the pp neutrinos. The main goal of Borexino is the detection of  ${}^7\text{Be}$  neutrinos. In order to achieve this goal Borexino makes use of 100 tons Fiducial Mass (FM) of liquid scintillator based on pseudocumene ( $C_9H_{12}$ ) and 1.5 g/l of PPO.  ${}^7\text{Be}$  neutrinos are detected via the neutrino-electron elastic scattering. The main signature in the scattered electron spectrum is the Compton-like edge at 665 keV due to the fact that the incoming neutrinos are monoenergetic. Another smaller signature is due to the Earth's eccentricity which implies a seasonal change of the detected rate. The background is a fundamental issue in Borexino. As a matter of fact electron-like events induced by solar neutrino interactions cannot be distinguished on an event-by-event basis from electrons or gammas due to radioactive decays. Therefore, the background in the FM must be such to give a signal-to-noise ratio of the order of 1 or more. The detector has been built following a self shielding design in order to reduce the external background by increasing the radiopurity while moving closer to the FM. In order to reach a signal-to-noise ratio of 1 an intrinsic radiopurity of  $\sim 4 \times 10^{-4} \mu\text{Bq/kg}$  is required both for  ${}^{238}\text{U}$  and  ${}^{232}\text{Th}$ . The strategy of Borexino <sup>1)</sup> to reach this extraordinary level is: precision cleaning of the as-built experimental plant to reduce particulate, filtration at the level of  $0.05 \mu\text{m}$ , multi-stage distillation and high purity nitrogen sparging. In Borexino the liquid scintillator is contained in a stainless steel sphere <sup>2)</sup> 13.7 m in diameter. Inside this sphere a 125  $\mu\text{m}$  nylon vessels contains 278 tons of scintillator. By a software cut based on the vertex position a FM of 100 tons is selected. The scintillator light is viewed by 2212 8" photomultipliers attached to the inner surface of the stainless steel sphere. The sphere is inside a stainless steel water tank which works as shielding against neutrons and gammas from the surrounding rocks and as Cherenkov light detector serving as a muon veto.

A real-time measurement of  ${}^7\text{Be}$  solar neutrinos could probe the MSW LMA oscillation scenario <sup>3)</sup> below 1 MeV, that is below the matter-vacuum transition region predicted by the global fits to solar and reactor neutrino data. Moreover, a  ${}^7\text{Be}$  neutrino measurement can shed light on the Solar Standard Model (SSM) proving how the Sun produces energy at the level of a few %. At present, new determinations of the heavy elements abundances in the Sun

4) have caused a controversy between predictions of the most up-to-date SSM and helioseismology measurements 5). It turns out that a measurement of the  ${}^7\text{Be}$  neutrinos and in particular of the CNO neutrinos from the Sun could help solving the controversy and could serve as a fundamental test of the SSM assumptions.

## 2 Borexino results

After an exhausting work of purification and filling Borexino was eventually ready to start taking data in May 2007. The Borexino program started in 1993 with the construction of the prototype, the Counting test Facility (CTF) and continued later in 1998 with the construction of the Borexino external water tank. The construction of the Borexino apparatus started after important results on the scintillator radiopurity were achieved with the CTF. The strategy adopted for the filling of the detector has been defined by performing tests with the CTF. The CTF is a 4-ton liquid scintillator detector equipped with 100 8" photomultipliers. First results on the internal background using correlated events from the  ${}^{238}\text{U}$  and  ${}^{232}\text{Th}$  chains have shown that the background achieved is much better than the designed level. In particular, the equivalent  ${}^{238}\text{U}$  contamination is measured to be  $(1.6 \pm 0.1) \times 10^{-17}$  g/g and for  ${}^{232}\text{Th}$  to be  $(6.5 \pm 1.5) \times 10^{-18}$  g/g. The designed level was  $10^{-16}$  g/g. This high level of radiopurity opens new opportunity 6) for detection of CNO neutrinos. As underlined above a measurement of these neutrinos is crucial for resolving the metallicity controversy. In Fig. 1 the measured spectrum in 192 days is shown. It can be noticed that an important  $\alpha$  peak is present in the data after the fiducial volume cut. This peak is due to a  ${}^{210}\text{Po}$  contamination still present in the liquid scintillator after purification and filling. The possibility to have such a contamination was known from CTF tests. However, constraints on the pseudocumene procurements did not allow to have enough time to understand the source of this contamination.  ${}^{210}\text{Po}$  decays with a mean life of about 200 days. After quenching its peak is expected at about 400 keV, which is below the 665 keV Compton-like edge from solar neutrino scattering. At the beginning of the data taking in May 2007 the  ${}^{210}\text{Po}$  activity was on the order of 60 cpd/ton.  ${}^{210}\text{Po}$  comes from  ${}^{210}\text{Pb}$ .  ${}^{210}\text{Pb}$  decays to  ${}^{210}\text{Bi}$  which has an end-point energy at about 1 MeV. The measured activity of  ${}^{210}\text{Po}$  is clearly not in equilibrium with a  ${}^{210}\text{Pb}$  source. Therefore, the  ${}^{210}\text{Po}$  will decay away with his mean life. As a matter of fact this decay trend has been measured. From the spectrum in Fig. 1 one can clearly see the expected Compton-like edge due to  ${}^7\text{Be}$  solar neutrinos. Moreover, it can be seen that at high energy the spectrum is dominated by a cosmogenic component well known, the  ${}^{11}\text{C}$ .  ${}^{11}\text{C}$  is produced underground by muons interacting with  ${}^{12}\text{C}$  in the liquid scintillator. This background depend on the depth of the underground laboratory.



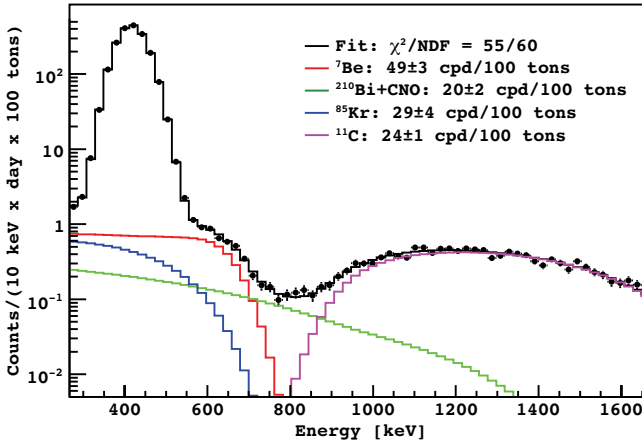


Figure 2: *Spectral fit in the energy region 260-1670 keV. See text for details.*

and low metallicity scenario. Under the assumption of the SSM constraint the solar neutrino survival probability is measured to be  $P_{ee} = 0.56 \pm 0.10$ . This value allows to reject the no oscillation hypothesis at the level of  $4\sigma$ . The present result allow to study solar neutrino fluxes under the neutrino oscillation hypothesis and using other solar neutrino measurements. As it has been reported in <sup>9)</sup> the ratio between the "true" and the SSM predicted value for pp solar neutrinos is found to be  $f_{pp} = 1.005^{+0.008}_{-0.020}$  under the luminosity constraint. The same  ${}^7\text{Be}$  measurement allows to set an upper bound on the CNO contribution to the solar luminosity at 5.4% (90% C.L.). These values are the best at present.

### 3 Perspectives

The first Borexino results have shown for the first time the feasibility to measure solar neutrinos in the sub-MeV range in real-time. Moreover, the high level of radiopurity achieved allows to perform new measurements. Of particular interest is the CNO neutrino detection provided the possibility to tag and remove  ${}^{11}\text{C}$  background. This goal is at present under investigation and it is based on the idea of a three-fold coincidence between the muon, the captured neutron and the  $\beta$  decay of  ${}^{11}\text{C}$ . Other measurements are of interest as well: neutrino magnetic moment,  ${}^8\text{B}$  solar neutrinos above 3 MeV via charged current on  ${}^{13}\text{C}$  and elastic scattering and geoneutrinos. Borexino is also a supernova

neutrino detector with the possibility to detect events through the neutral current neutrino-proton elastic scattering, which is of particular interest to measure the temperature of muon and tau neutrinos. The technology developed in Borexino offers the opportunity to plan future projects which makes use of massive liquid scintillator target.

## References

1. J. Benziger et al., "The Scintillator Purification System for the Borexino Solar Neutrino Experiment", paper in preparation.
2. G. Alimonti et al., Borexino collaboration, *Astrop. Phys.* 16, 205 (2002).  
G. Alimonti et al., Borexino collaboration, submitted to NIM A.
3. G.L. Folgi, E. Lisi, A. Marrone, A. Palazzo and A.M. Rotunno, *Prog. Part. Nucl. Phys.* 57, 71 (2006). J.N. Bahcall, M.C. Gonzalez-Garcia and C. Pena-Garay, *JHEP* 0408, 016 (2004).
4. M. Asplund, N. Grevesse and A.J. Sauval, in ASPConf. Ser. 336, *Cosmic Abundances as Records of Stellar Evolution and Nucleosynthesis*, ed. T.G. Barnes III and F.N. Bash, San Francisco (2004).
5. J.N. Bahcall and A. Serenelli, *The Astrophys. J.* 621: L85-L88, 2005. S. Basu and H.M. Antia, *The Astrophys. J.*, 606: L85-L88, 2004.
6. H. Back et al., Borexino collaboration, *Phys. Rev. C* 71, 045805 (2006).
7. C. Pena-Garay and A.M. Serenelli, 2008 in preparation.
8. S. Abe et al., KamLAND collaboration, arXiv:0801.4589v2, submitted to *Phys. Rev. Lett.* (2008).
9. C. Arpesella et al., Borexino collaboration, arXiv:0805.3843.

## RESULTS FROM MINIBOOONE

Alexis A. Aguilar-Arevalo, for the MiniBooNE Collaboration  
*TRIUMF, 4004 Wesbrook Mall, V6T-2A3, Vancouver, B.C., Canada*  
*(Previously at Department of Physics, Columbia University, New York)*

### Abstract

We present the results from the MiniBooNE neutrino oscillations search at the  $\Delta m^2 \sim 1\text{eV}^2$  scale. No significant excess of events is observed above background for reconstructed neutrino energies greater than 475 MeV, as expected for no oscillations within a two-neutrino appearance only model. An excess of  $186 \pm 27$  (stat)  $\pm 33$  (syst) events that cannot be explained by such model is observed below this threshold. We also present a recent analysis that combines two largely independent  $\nu_e$  samples with a high statistics  $\nu_\mu$  sample used to reduce the effect of systematic uncertainties (all MiniBooNE data) in the oscillations fit. Recent advances on the understanding of the excess of low energy events are discussed, including a study of  $\nu_\mu$  and  $\nu_e$  events from the nearby NuMI neutrino source.

## 1 Introduction

MiniBooNE was motivated by the result of the LSND experiment <sup>1)</sup> which observed a  $\sim 3.8 \sigma$  excess of  $\bar{\nu}_e$  events over its expectation for a pure  $\bar{\nu}_\mu$  beam. When interpreted as  $\bar{\nu}_\mu \rightarrow \bar{\nu}_e$  oscillations in the  $\Delta m^2 \sim 1 \text{ eV}^2$  scale (determined by the experiment's neutrino energy and baseline) this excess corresponds to a  $\bar{\nu}_\mu \rightarrow \bar{\nu}_e$  oscillation probability of  $0.26 \pm 0.08\%$ . When the positive observations of solar and atmospheric neutrinos are taken into account, the LSND result requires the existence of at least one non-interacting (*sterile*) neutrino <sup>2)</sup> to give a consistent picture. MiniBooNE probed the same region of the oscillations parameter space as LSND by having the same  $L/E$  ratio but a higher neutrino energy and baseline distance. The oscillation analyses presented here are performed within a two neutrino appearance-only  $\nu_\mu \rightarrow \nu_e$  oscillation model where  $\nu_\mu$  events are used to constrain the predicted  $\nu_e$  rate.

## 2 The MiniBooNE Experiment

The experiment uses neutrinos from the Fermilab Booster neutrino beam (BNB) produced when  $8.89 \text{ GeV}/c$  momentum protons hit a  $71 \text{ cm}$  long beryllium target located inside a magnetic focusing horn. Typically, pulses of  $4 \times 10^{12}$  protons hit the target within a  $\sim 1.6 \mu\text{s}$  spill at a rate of  $4 \text{ Hz}$ . Positive mesons are focused by the toroidal magnetic field of the horn and are allowed to decay along a  $50 \text{ m}$  long cylindrical decay region. The neutrino beam comes predominantly from the decay of  $\pi^+$  and  $K^+$  into  $\nu_\mu$ , having an intrinsic component of  $\nu_e$  from  $K^+$  and  $\mu^+$  decay with a flux ratio of  $\nu_e/\nu_\mu = 0.5\%$ . The detector, located  $541 \text{ m}$  downstream of the beryllium target is a spherical steel tank with inner radius  $610 \text{ cm}$  and is filled with  $800$  tons of pure mineral oil. Charged particles moving through the oil medium produce prompt directional Cherenkov light and delayed isotropic scintillation light. The detector is divided into an inner spherical region  $575 \text{ cm}$  in radius and an optically isolated outer shell  $35 \text{ cm}$  thick used as veto. The inner region is viewed by  $1280$  8-inch photomultiplier tubes (PMTs) providing a  $\sim 10\%$  photocathode coverage, while the veto region is viewed by  $240$  8-inch PMTs. The apparatus can detect  $\nu$  events with energies ranging from  $\sim 100 \text{ MeV}$  to a few  $\text{GeV}$ , and can reconstruct event vertices, particle tracks, measure the incident  $\nu$  energy, and is able to separate events induced by  $\nu_e$  from those induced by  $\nu_\mu$ . Integrated over the entire flux,

the dominant  $\nu$  interactions are charged-current quasi-elastic (CCQE) scattering (39%), neutral-current (NC) elastic scattering (16%), charged current (CC) single pion production (29%), and NC single pion production (12%).

### 3 Data analysis and event reconstruction

The PMT time and charge information in a 19.2  $\mu\text{s}$  data acquisition (DAQ) window containing the beam spill is used to reconstruct  $\nu$  interactions by forming charge and time likelihoods maximized to fit the observed hit patterns. Clusters of PMT hits within 100 ns are used to define “subevents” within the DAQ window. Candidate  $\nu_e$  events are required to have only one subevent (as expected for  $\nu_e$  CCQE events), with fewer than 6 hits in the veto and more than 200 in the main tank (above the endpoint of the spectrum from muon-decay electrons); fully contained  $\nu_\mu$  CCQE events have 2 subevents. Particle types can be identified by their time structure and hit patterns: muons have a sharp outer Cherenkov ring that is filled in by the muon travel distance, NC  $\pi^0$  events have two Cherenkov rings from the two photons of  $\pi^0$  decays, and signal-like electrons have a single ring that appears diffused due to multiple scattering and the electromagnetic shower process.

Two particle identification (PID) algorithms were used to isolate a rich sample of  $\nu_e$ -induced CCQE events. One is based on likelihood ratios extracted from fits to the PMT hit patterns using a detailed light emission model from extended tracks, which we refer to as the track-based likelihood (TBL) analysis. The other is based on a boosted decision tree (BDT) machine learning technique<sup>4</sup>) and was used as a complementary analysis. For the TBL analysis, the PMT hit patterns in the events are reconstructed under four hypotheses: *i*) a single electron-like Cherenkov ring, *ii*) a single muon-like ring, *iii*) two photon-like rings with unconstrained kinematics, and *iv*) two photon-like rings with  $M_{\gamma\gamma} = m_{\pi^0}$ . To identify  $\nu_e$ -induced events and reject events with  $\mu$  and  $\pi^0$  in the final state, visible energy ( $E_{\text{vis}}$ ) dependent cuts are applied on  $\log(L_e/L_\mu)$ ,  $\log(L_e/L_{\pi^0})$ , and  $M_{\gamma\gamma}$ , where  $L_e$ ,  $L_\mu$ , and  $L_{\pi^0}$  are the likelihoods for each event maximized under hypotheses *i*, *ii*, and *iv*, respectively, and  $M_{\gamma\gamma}$  is obtained from the fit to hypothesis *iii*. The reconstruction used in the BDT analysis uses a simpler model of light emission and propagation. A single PID classifier variable is derived from 172 quantities such as charge and time likelihoods in angular bins,  $M_{\gamma\gamma}$ , and likelihood ratios ( $e/\pi^0$  and  $e/\mu$ ) which are inputs to

a BDT algorithm trained on sets of simulated signal events and background events with a cascade-training technique <sup>5)</sup>.

#### 4 Neutrino Oscillation Analyses

In April of 2007 <sup>3)</sup> MiniBooNE reported the agreement of the observed number of  $\nu_e$ -induced events with background expectations in the absence of  $\nu_\mu \rightarrow \nu_e$  appearance-only oscillations of the LSND <sup>1)</sup> type in the range of 475 MeV to 3000 MeV of reconstructed  $\nu$  energy,  $E_\nu^{QE}$ , using the TBL analysis cuts. The analysis used a high statistics sample of  $\nu_\mu$  CCQE events to correct the number of expected background events to the  $\nu_\mu \rightarrow \nu_e$  oscillations search, and to reduce the magnitude of the systematic uncertainties associated with these predictions. The corrected predictions and reduced errors were then used in a fit of the  $E_\nu^{QE}$  distribution to a two- $\nu$  appearance-only oscillations model. Backgrounds are separated into  $\nu_e$ -induced and  $\nu_\mu$ -induced. The intrinsic  $\nu_e$  from  $\mu$ ,  $\pi$ , and  $K$  that survive the analysis cuts can be distinguished from the expected signal by their energy spectrum. The dominant  $\nu_\mu$ -induced backgrounds are from NC  $\pi^0$  production events in which one of the photons from the  $\pi^0$  decay is missed mimicking a single electron event from a  $\nu_e$  CCQE interaction. A dedicated measurement of the NC  $\pi^0$  events in  $\pi^0$  momentum bins was used to constrain the Monte Carlo prediction of these events <sup>6)</sup>. Interactions in the dirt surrounding the detector are also constrained with a dedicated sample of high radius inward-going events. Systematic uncertainties from the flux predictions, cross section models, and optical modeling of the oil are included in a fully correlated matrix in  $E_\nu^{QE}$  bins. The predicted number of background events with  $475 \text{ MeV} < E_\nu^{QE} < 1250 \text{ MeV}$  after the complete TBL selection is applied is  $358 \pm 35(\text{syst})$ . For comparison, the estimated number of  $\nu_e$  CCQE signal events is  $126 \pm 21(\text{syst})$  for the LSND central expectation of 0.26%  $\nu_\mu \rightarrow \nu_e$  transmutation. The data showed  $380 \pm 19(\text{stat})$  events in this energy range. This agreement implies that there is no indication of an oscillation signal in the MiniBooNE data. The best fit parameters are  $(\Delta m^2, \sin^2 2\theta) = (4.0\text{eV}^2, 0.001)$ , with at probability of 99% as compared to a 93% probability for the null hypothesis.

Fig.1 shows the  $E_\nu^{QE}$  distribution of  $\nu_e$  candidate events in the TBL analysis. The vertical dashed line indicates the minimum  $E_\nu^{QE}$  used in the oscillation analysis. There is no significant excess of events ( $22 \pm 19 \text{ stat} \pm$

35 syst) in the analysis region, however, an excess ( $186 \pm 27$  stat  $\pm 33$  syst) is observed below 475 MeV that cannot be explained by a two- $\nu$  oscillations model. A single-sided raster scan of the parameter space is performed with events in the energy range  $475 \text{ MeV} < E_\nu^{QE} < 3000 \text{ MeV}$  to find the 90% C.L. limit corresponding to  $\Delta\chi^2 = \chi_{\text{limit}}^2 - \chi_{\text{best fit}}^2 = 1.64$  shown in fig.2. The complementary analysis based on the BDT algorithm yielded a consistent result (dashed curve in fig.2) using the technique of introducing its own  $\nu_\mu$  CCQE sample<sup>1</sup> into the  $\chi^2$  minimization of the oscillations fit to constrain the systematic uncertainties and achieve the desired sensitivity.

#### 4.1 Combining the $\nu_e$ -BDT $\nu_e$ -TBL and $\nu_\mu$ -CCQE samples

The TBL and BDT analyses make use of distinct but complementary  $\nu_e$  candidate samples. An error matrix in bins of  $E_\nu^{QE}$  is calculated containing the correlations between the three samples ( $\nu_e$ -TBL,  $\nu_e$ -BDT, and  $\nu_\mu$ -CCQE) that are due to systematic effects. Inclusion of the shared events in the two  $\nu_e$  samples requires knowledge of the statistical correlations that are induced in their  $E_\nu^{QE}$  distributions by the event overlap ( $> 22\%$ ). These correlations produce off-diagonal elements in the statistical component of the error matrix, which in the absence of overlap would be diagonal<sup>2</sup>. The total error matrix is the sum in quadrature of the systematic and statistical components. With this matrix a  $\chi^2$  statistic is calculated comparing the observed energy distributions for the  $\nu_e$  and  $\nu_\mu$  samples with the predictions for a given point in the oscillations parameter space. The use of both  $\nu_e$  candidate samples yields a significantly higher sensitivity to oscillations ( $\sim 20\%$  more coverage) than that obtained when only one of the  $\nu_e$  samples is used in combination with the  $\nu_\mu$  sample, which was the case of the BDT analysis put forward in our first publication. Fig.3 (left) shows the  $E_\nu^{QE}$  distributions of the  $\nu_\mu$ -CCQE sample (top) and the two  $\nu_e$  candidate samples (BDT -middle- and TBL -bottom-) after the fit. The smooth dashed curves represent the systematic uncertainties constrained by the use of the observed  $\nu_\mu$ -CCQE data in the fit. For the  $\nu_\mu$ -CCQE sample the systematic errors are forced to be of the size of the negligibly small statistical uncertainty. On the right hand side plot in fig.3 we compare the result in

<sup>1</sup>Different from that used for the first TBL analysis; it is discussed in Ref. 7).

<sup>2</sup>For a more detailed discussion see Ref. 9).

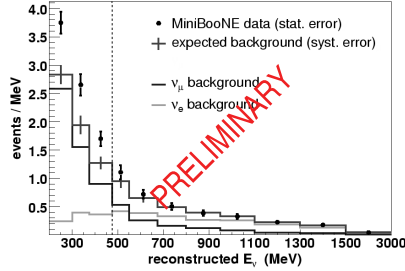


Figure 1:  $E_{\nu}^{QE}$  distribution for  $\nu_e$  candidate events in the TBL analysis. The points represent the data with statistical errors. The top-most histogram is the expected background with total systematic errors. The vertical dashed line indicates the oscillation analysis threshold.

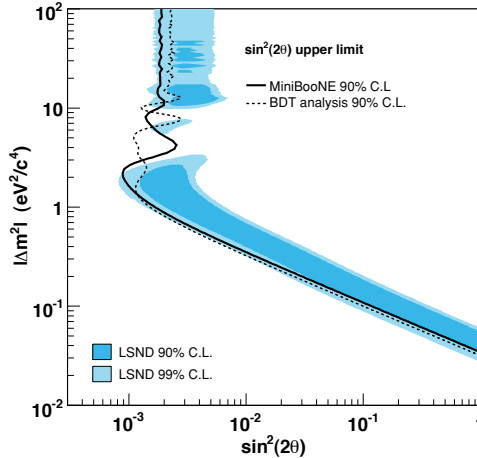


Figure 2: The MiniBooNE 90% C.L. limit (thick solid curve) from the TBL analysis for events with  $475 \text{ MeV} < E_{\nu}^{QE} < 3000 \text{ MeV}$  within a two- $\nu$  appearance only oscillations model. Also shown is the limit from the boosted decision tree (BDT) analysis (dashed curve) for events with  $300 \text{ MeV} < E_{\nu}^{QE} < 3000 \text{ MeV}$ .

Table 1: Preliminary results for the predicted background and observed data in three  $E_\nu^{QE}$  bins.

$E_\nu^{QE}$ (MeV)	200-300	300-475	475-1250
Total Background	$284 \pm 25$	$274 \pm 21$	$358 \pm 35$
$\nu_e$ intrinsic	26	67	229
$\nu_\mu$ induced	258	207	129
NC $\pi^0$	115	76	62
NC $\Delta \rightarrow N\gamma$	20	51	20
Dirt	99	50	17
other	24	30	30
Data	$375 \pm 19$	$396 \pm 19$	$380 \pm 19$
Data-Background	$91 \pm 31$	$95 \pm 28$	$22 \pm 40$

Ref. 3) with this fit. The details of the limit at high  $\Delta m^2$  are determined by how the fit responds to the specific fluctuations in the  $\nu_\mu$  and  $\nu_e$  data distributions, and in this case the analysis does not improve the limit at the highest  $\Delta m^2$  values. However, an increase of 10%-30%, depending on the  $\Delta m^2$  value, in the coverage of the region below  $\Delta m^2 < 1.2 \text{ eV}^2$  is achieved, which is a significant gain over the first publication.

## 5 Investigations of the low energy excess with the TBL analysis

The collaboration has explored several possible sources of the excess events below 475 MeV in the TBL analysis, ranging from detector reconstruction issues to incorrect or new sources of background. Explanations involving new backgrounds or signal sources could be relevant for future experiments like T2K and NOvA. All of the excess events have been visually scanned and found to be consistent with single-ring electromagnetic-like events. Since MiniBooNE cannot distinguish electrons from photons the excess could be of either type. Table 1 lists the event numbers in three  $E_\nu^{QE}$  bins detailing their background composition. In the bin corresponding to the oscillation analysis, the main background are intrinsic  $\nu_e$  from  $\mu$  and  $K$  decay. In the lower energy bins the  $\nu_\mu$ -induced backgrounds from NC  $\pi^0$ ,  $\Delta$  decays, and ‘‘Dirt’’ become dominant over the  $\nu_e$  backgrounds. MiniBooNE constrains these background types using observed events, so their enhancement beyond the systematic uncertainties shown in Table 1 would contradict these observations. One possibility are pho-

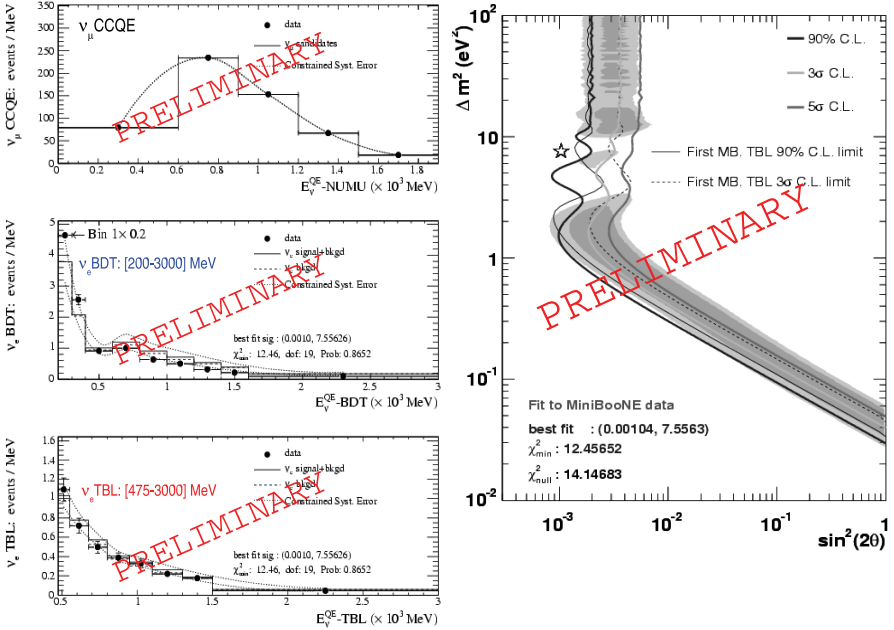


Figure 3: Left: The  $E_V^{QE}$  distributions for the  $\nu_\mu$  CCQE sample (top), the BDT  $\nu_e$  candidate sample (middle), and the TBL  $\nu_e$  candidate sample (bottom) that result from the combined fit described in the text. The dashed curves represent the total constrained systematic uncertainties. For display purposes, the first bin in the BDT distribution has been scaled to 20% of its value. Right: C.L. limits (90% in blue, 3 $\sigma$  in cyan, 5 $\sigma$  in magenta) obtained with the combined technique, compared to the previous result <sup>3)</sup> (90% in black solid and 3 $\sigma$  in black dashed), which used a different technique.

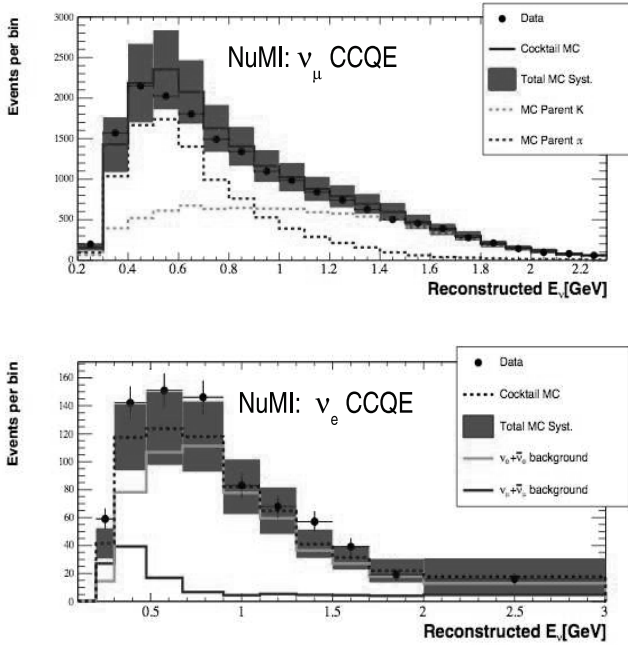


Figure 4: Data *vs.* Monte Carlo comparison of the  $E_\nu^{QE}$  distribution for  $\nu_\mu$  (top) and  $\nu_e$  (bottom) CCQE candidate events from the NuMI beam at MiniBooNE. The red bands represent the total systematic errors. The  $\pi$  and  $K$  components of the  $\nu_\mu$  distribution are displayed in the top plot. In the bottom plot the  $\nu_\mu$  and  $\nu_e$  induced components are shown.

tonuclear processes that are not currently in the simulation and could absorb one of the gammas from a NC  $\pi^0$  giving a single-gamma background. Initial estimates are at the 10-20% level in the two lowest  $E_\nu^{QE}$  bins. The standard model process of anomaly-mediated single photon production has been recently proposed <sup>8)</sup> as a possible source of the excess. This process has never been observed and the MiniBooNE excess could be the first observation if the rates and kinematic distributions are shown to be consistent.

MiniBooNE also observes off-axis neutrinos from the NuMI/MINOS beam (10, 11). These events can provide an important cross check on the nature of the low energy excess since their energy and distance is similar to those from the BNB. In addition, their background composition is significantly different, being dominated by intrinsic  $\nu_e$  at low energies. The  $E_\nu^{QE}$  distribution of observed  $\nu_\mu$  and  $\nu_e$  candidate events from the NuMI beam are shown in fig.4 compared to the simulation, showing that there is good agreement between data and Monte Carlo. The systematic uncertainties are large at this stage, leaving room for the observed discrepancies, but will be constrained by applying similar techniques to those used in the oscillation analyses in the near future.

## 6 Summary

MiniBooNE has ruled out the LSND result interpreted as two- $\nu$ ,  $\nu_\mu \rightarrow \nu_e$  oscillations described by the standard L/E dependence. At low energies outside of the oscillation search region, MiniBooNE observes an excess of  $\nu_e$  events; studies are currently underway to determine if these events are from unexpected backgrounds or possibly an indication of a new physics process. A recent analysis combining two largely independent  $\nu_e$  samples has been conducted and shown to enhance the rejection of the LSND allowed region below  $\Delta m^2 < 1.2$ .

## Acknowledgements

We acknowledge and thank Fermilab, the Department of Energy, the National Science Foundation, and Los Alamos National laboratory for their support.

## References

1. C. Athanassopoulos *et al.*, Phys. Rev. Lett. **75**, 2650 (1995); C. Athanassopoulos *et al.*, Phys. Rev. Lett. **77**, 3082 (1996); C. Athanassopoulos *et al.*

- al.*, Phys. Rev. Lett. **81**, 1774 (1998); A. Aguilar *et al.*, Phys. Rev. D **64**, 112007 (2001).
2. M. Sorel, J. M. Conrad, and M. H. Shaevitz, Phys. Rev. D **70**, 073004 (2004).
  3. A. A. Aguilar-Arevalo *et al.* [MiniBooNE Collaboration], Phys. Rev. Lett. **98**, 231801 (2007).
  4. B.P. Roe *et al.*, Nucl. Instrum. & Meth. A**543**, 577 (2005); H.J. Yang *et al.*, Nucl. Instrum. & Meth. A**555**, 370 (2005); H.J. Yang *et al.*, Nucl. Instrum. & Meth. A**574**, 342 (2007); Y. Liu *et al.*, Nucl. Instrum. & Meth. A**578**, 315 (2007).
  5. Y. Liu and I. Stancu, Nucl.Instrum.Meth.**A578**, 315-321 (2007), arXiv:Physics/0611267.
  6. A. A. Aguilar-Arevalo *et al.* [MiniBooNE Collaboration], arXiv:0803.3423 [hep-ex], Submitted to Phys. Lett. B.
  7. A. A. Aguilar-Arevalo *et al.* [MiniBooNE Collaboration], Phys. Rev. Lett. **100**, 032301 (2008).
  8. J. Harvey, C. Hill, and R. Hill, "Anomaly Mediated Neutrino-Photon Interactions at Finite Baryon Density", hep-ph0708.1281.
  9. A. A. Aguilar-Arevalo, Ph.D. Thesis, Columbia University, New York, 2008. FERMILAB-THESIS-2008-01 (2008).
  10. S.E. Kopp, Phys. Rept. **439**, 101 (2007); D. G. Michael *et al.* [MINOS Collaboration], Phys. Rev. Lett. **97**, 191801 (2006).
  11. A. A. Aguilar-Arevalo [MiniBooNE and MINOS Collaborations], AIP Conf. Proc. **842**, 834 (2006).



# OBSERVATION OF NEUTRINO INTERACTIONS IN THE OPERA DETECTOR

Alberto Garfagnini  
*Università di Padova and INFN*

## Abstract

OPERA is a long baseline neutrino oscillation experiment designed to observe  $\nu_\mu \rightarrow \nu_\tau$  oscillations by looking at the appearance of  $\nu_\tau$ 's in a quasi pure  $\nu_\mu$  beam. The beam is produced at CERN and sent towards the Gran Sasso INFN laboratories where the experiment is running. OPERA started its data taking in October 2007, when the first 38 neutrino interactions were successfully located and reconstructed. This paper reviews the status of the experiment discussing its physics potential and performances for neutrino oscillation studies.

## 1 Introduction

OPERA <sup>1)</sup> is a long baseline experiment at the Gran Sasso underground laboratories (LNGS) and is part of the CERN Neutrino to Gran Sasso (CNGS) project. The detector has been designed to observe the  $\nu_\mu \rightarrow \nu_\tau$  oscillations in the parameter region indicated by Super-Kamiokande <sup>2)</sup> through direct observation of  $\nu_\tau$  charged current interactions. The detector is based on a massive lead/nuclear emulsion target complemented by electronic detectors (scintillator bars) that allow the location of the event and drive the scanning of the emulsions. A magnetic spectrometer follows the instrumented target and measures the charge and momentum of penetrating tracks.

## 2 The CNGS neutrino beam

The Cern Neutrino to Gran Sasso(CNGS) <sup>3)</sup> facility is a wide-band neutrino beam which provides an almost pure  $\nu_\mu$  source traveling 730 km under the Earth crust from CERN to Gran Sasso. The beam parameters have been designed in order to optimize the number of  $\nu_\tau$  charge current interactions in the OPERA detector. The neutrino beam mean energy is  $\langle E_\nu \rangle = 17$  GeV with a very small  $\nu_e$  and  $\bar{\nu}_e$  contamination (less than 1%). The average  $L/E$  ratio is 43 km/GeV, far from the oscillation maximum, but it dictated by the high energy needed for  $\nu_\tau$  appearance.

The beam has been designed to provide  $45 \cdot 10^{18}$  proton-on-target/year (p.o.t./y) with a running time of 200 days per year.

The first CNGS technical run, occurred in August 2006 with a delivered luminosity of  $0.76 \cdot 10^{18}$  p.o.t. A new short run followed in October 2006, but was shortly interrupted due to a leak in the closed water cooling system of the reflector: only  $0.06 \cdot 10^{18}$  p.o.t. were delivered for the experiment. At that time only the electronic detectors were installed and under commissioning.

After repair of the reflector cooling system, a new physics run occurred in October 2007, when OPERA had 40% of the target mass installed. The beam extraction intensity was limited to 70% of the normal values due to beam losses which brought severe radiation damage of the equipment. Due to these new technical problems, only  $0.79 \cdot 10^{18}$  p.o.t. were delivered. The beam operation was interrupted due to loss of ventilation control in the CNGS area due to the radiation damage of the CNSG standard electronics.

A major revision of the project has been taken in the beginning of 2008 in order to improve the radiation shielding of the electronics and reduce the beam losses. A new physics run is going to start in summer 2008 with a planned luminosity of  $\sim 30 \cdot 10^{18}$  p.o.t. for the CNGS experiments in Gran Sasso.

### 3 The OPERA detector

OPERA is a large detector ( $10\text{ m} \times 10\text{ m} \times 20\text{ m}$ ) located in the underground experimental Hall C of LNGS. As shown in Figure 1, the detector is made of two identical super-modules, aligned along the CNGS beam direction, each one consisting of a target and a muon spectrometer. The target section combines passive elements, the lead-emulsion bricks, and electronic detectors. Each target section consists of a multi-layer array of 31 target walls followed by pairs of planes of plastic scintillator strips (Target Tracker). A magnetic spectrometer follows the instrumented target and measures charge and momentum of the penetrating tracks.

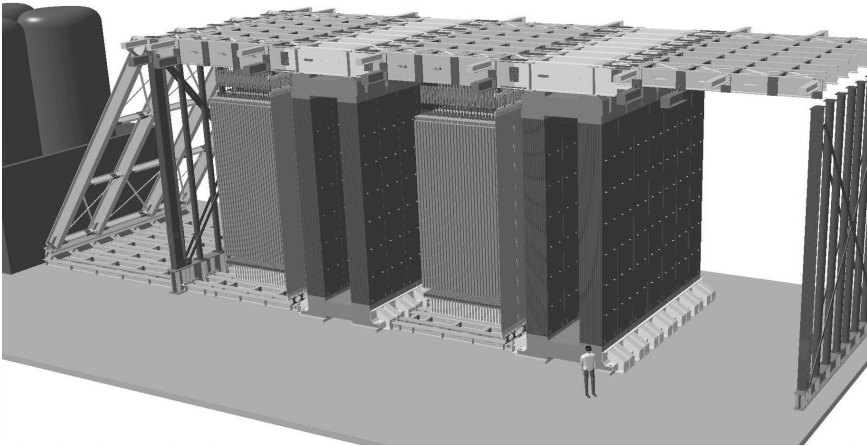


Figure 1: *Schematic view of the OPERA detector. The neutrino beam enters the detector from the left.*

#### 3.1 The Emulsion Target

The development of automatized scanning systems during the last two decades has made possible the use of large nuclear emulsion detectors. Indeed, nuclear emulsion are still successfully used nowadays, especially in neutrino experiments <sup>4)</sup> <sup>5)</sup>. The realization of a new scanning system has been carried out by two different R&D programs in the Nagoya University (Japan) and in several european laboratories belonging to the OPERA collaboration. These scanning systems <sup>6)</sup> <sup>7)</sup> <sup>8)</sup> were designed to take into account the requests

of high scanning speed (about 20 cm<sup>2</sup>/h) while keeping the extremely good accuracy provided by nuclear emulsions. The total number of emulsion films in the OPERA detector will be about 9 millions, for an area of about 110000 m<sup>2</sup>. This quantities are orders of magnitude larger than the ones used by previous experiments. That made necessary an industrial production of the emulsion films, performed by the Fuji Film company, in Japan, after an R&D program conducted jointly with the OPERA group of the Nagoya University.

The OPERA emulsions are made up of two emulsion layers of 44  $\mu\text{m}$  thick coated on both sides of a 205  $\mu\text{m}$  triacetate base. The AgBr crystal diameter is rather uniform, around 0.2  $\mu\text{m}$ , and the sensitivity is about 35 grains/100  $\mu\text{m}$  for minimum ionizing particles.

The main constituent of the OPERA target is the brick. It is a pile of 57 nuclear emulsion sheets interleaved by 1 mm thick lead plates. The brick combines the high precision tracking capabilities provided by the emulsions with the large mass given by the lead. The OPERA brick is a detector itself. In addition to the vertex identification and  $\tau$  decay detection, shower reconstruction and momentum measurements using the Multiple Coulomb Scattering can be performed, being the total brick thickness of 7.6 cm equivalent to 10  $X_0$ .

Bricks are hosted in the walls of the target. The target section is made of 31 walls interleaved with 31 target tracker walls.

The occurrence of a neutrino interaction inside the target is triggered by the electronic detectors. Muons are reconstructed in the spectrometers and all the charged particles in the target tracker. The brick finding algorithm indicates the brick where the interaction is supposed to be occurred. The trigger is confirmed in the Changeable Sheet Doublet (CSD) <sup>11)</sup>, a pair of emulsion films hosted in a box placed outside the brick, as interface between the latter and the target tracker. Before detaching the CSD from the brick, they are exposed to an XRay spot, in order to define a common reference system for the two CS and the first emulsion in the brick (with a precision of a few tens of  $\mu\text{m}$ ). Afterwards the CS are developed and the predictions from target tracker are searched for within a few cm area. If these are confirmed the brick is brought outside the Gran Sasso laboratory and exposed to cosmic ray before development.

The mechanical accuracy obtained during the brick piling is in the range of 50-100  $\mu\text{m}$ . The reconstruction of cosmic rays passing through the whole brick allows to improve the definition of a global reference frame, allowing a precision of 1-2  $\mu\text{m}$ .

All the tracks located in the CSD are subsequently followed inside the brick, starting from the most downstream film, until they stop. Then a general scanning around the stopping point(s) is performed, tracks and vertices are reconstructed, the primary vertex is located and the kinematic analysis defines the

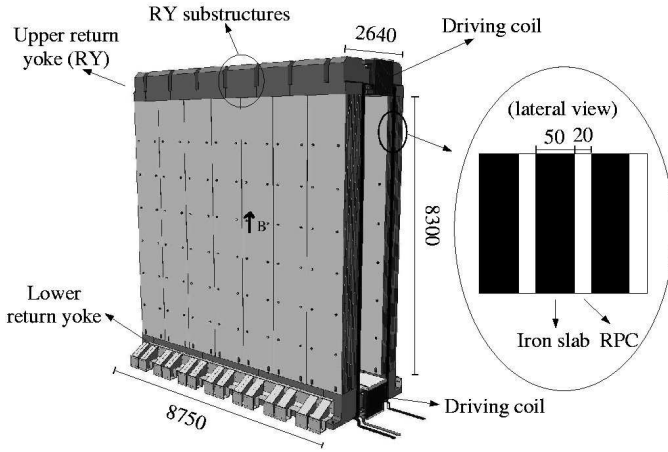


Figure 2: Three dimensional view of the OPERA magnet. Units are in mm.

event topology.

### 3.2 The Target Tracker

The main role of the target Tracker is to provide a trigger and identify the right bricks where the event vertex should be located. Each wall is composed by orthogonal planes of plastic scintillator strips ( $680 \text{ cm} \times 2.6 \text{ cm} \times 1 \text{ cm}$ ). The strips are made of extruded polystyrene with 2% p-terphenyl and 0.02% POPOP, coated with a thin diffusing white layer of  $\text{TiO}_2$ . Charged particle crossing the strips will create a blue scintillation light which is collected by wavelength-shifting fibers which propagate light at both extremities of the strip. All fibers are connected at both ends to multianode Hamamatsu PMTs. For a minimum ionizing particle, at least five photoelectrons are detected by the photomultipliers. The detection efficiency of each plane is at 99%. A detailed description of the Target Tracker design can be found in <sup>12)</sup>

### 3.3 The Spectrometer

The spectrometer allows to suppress the background coming from charm production through the identification of wrong-charged muons and contributes to the kinematic reconstruction of the event performed in the target section. The magnet <sup>13)</sup>, shown in Figure 2, is made of two vertical walls of rectangular cross section and of a top and bottom flux return path. The walls are built lining twelve iron layers (5 cm thickness) interleaved with 2 cm of air

gap, allocated for the housing of the Inner Tracker detectors, Resistive Plate Chambers, RPCs. Each iron layer is made of seven slabs, with dimensions  $50 \times 1250 \times 8200 \text{ mm}^3$ , precisely milled along the two 1250 mm long sides connected to the return yokes to minimize the air gaps along the magnetic circuit. The slabs are bolted together to increase the compactness and the mechanical stability of the magnet which acts as a base for the emulsion target support. The nuts holding the bolts serve as spacers between two slabs and fix the 20 mm air gap where the RPCs are mounted.

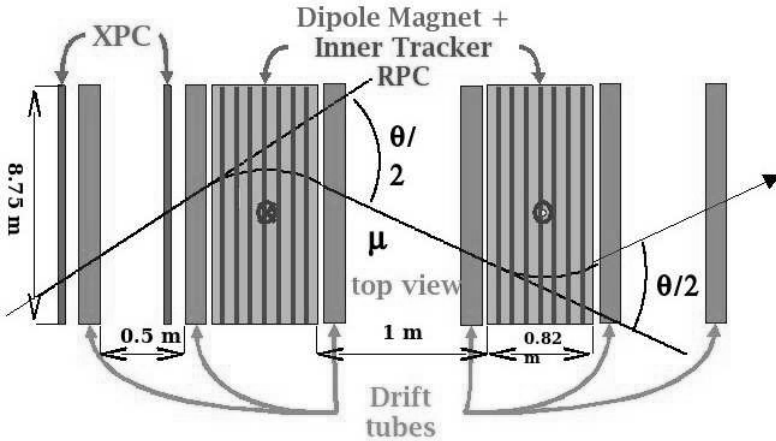


Figure 3: Top view of the OPERA muon spectrometer. The picture shows a track trajectory along the drift tube chambers, the XPCs and the RPCs inside the magnet ( $dE/dx$  losses are neglected).

The precision tracker is made of drift tube planes located in front, behind and between the two magnet walls: in total 12 drift tube planes covering an area of  $8 \text{ m} \times 8 \text{ m}$ . The tubes are 8 m long and have an outer diameter of 38 mm. The trackers allow to reconstruct the muon momentum with a resolution  $\Delta p/p \leq 0.25$ .

As shown in Fig. 3, a particle entering the spectrometer is measured by layers of vertical drift tube planes located before and after the magnet walls. Left-right ambiguities are resolved by the two dimensional measurement of the spectrometer RPCs and by two additional RPC planes, equipped with pickup strips inclined of  $\pm 42.6^\circ$  with respect to the horizon (XPC). The Inner Tracker RPCs, eleven planes per spectrometer arm, give a coarse measurement of the tracks and perform pattern recognition and track matching between the precision trackers. The OPERA RPCs<sup>14)</sup> are “standard” bakelite RPCs,

similar to those used in the LHC experiments: two electrodes, made of 2 mm plastic laminate (HPL) are kept 2 mm apart by means of polycarbonate spacers in a 10 cm lattice configuration. The double coordinate readout is performed by means of copper strip panels. The strip pitch is 3.5 cm for the horizontal strips and 2.6 cm for the vertical layers. The OPERA RPCs have a rectangular shape, covering an area of about 3.2 m<sup>2</sup>. The sensitive area between the iron slabs (8.75 × 8 m<sup>2</sup>), is covered by twenty one RPCs arranged on seven rows, each with three RPCs in a line. In total, 1008 RPCs have been installed in the two spectrometers.

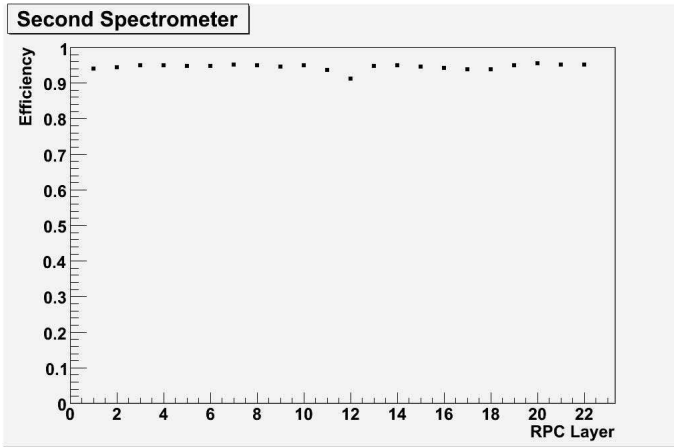


Figure 4: *Inner tracker plane efficiency. The mean value per plane, averaged over 21 RPCs, is shown.*

Recent analysis of 2007 data, both with cosmic and beam events show an average efficiency of 95% for the RPC planes. Figure 4 shows the average efficiency for the 22 layers of the second spectrometer. and <sup>15)</sup>).

#### 4 Physics performances

The OPERA detector will host 155000 bricks for a total target mass of 1350 tons. The signal of the occurrence of  $\nu_\mu \rightarrow \nu_\tau$  oscillation is the charged current interaction of the  $\nu_\tau$ 's inside the detector target ( $\nu_\tau N \rightarrow \tau^- X$ ). The reaction is identified by the detection of the  $\tau$  lepton in the final state through the decay topology and its decay modes into an electron, a muon, and a single or three charged hadrons:

$$\begin{aligned}
\tau^- &\rightarrow e^- \nu_\tau \bar{\nu}_e \\
\tau^- &\rightarrow \mu^- \nu_\tau \bar{\nu}_\mu \\
\tau^- &\rightarrow (h^- h^+) h^- \nu_\tau (n\pi^0)
\end{aligned}$$

The branching ratio for the electronic, muonic and hadronic channel are 17.8%, 17.7% and 64.7% respectively. For the typical  $\tau$  energies expected with the CNGS spectrum the average decay length is  $\sim 450 \mu\text{m}$ .

Neutrino interactions will occur predominantly inside lead plates. Once the  $\tau$  lepton is produced, it will decay either within the same plate, or further downstream. In the first case,  $\tau$  decays are detected by measuring the impact parameter of the daughter track with respect to the tracks originating from the primary vertex, while in the second case the kink angle between the charged decay daughter and the parent direction is evaluated.

The  $\tau$  search sensitivity, calculated for 5 years of data taking with a total number of  $45 \times 10^{18}$  integrated p.o.t. per year, is given in table: 1

$\tau$ decay channels	Signal $\div \Delta m^2$ (Full mixing)		Background
	$2.5 \times 10^{-3}$ (eV <sup>2</sup> )	$3.0 \times 10^{-3}$ (eV <sup>2</sup> )	
$\tau \rightarrow \mu^-$	2.9	4.2	0.17
$\tau \rightarrow e^-$	3.5	5.0	0.17
$\tau \rightarrow h^-$	3.1	4.4	0.24
$\tau \rightarrow 3h$	0.9	1.3	0.17
ALL	10.4	15.0	0.76

Table 1: Expected number of signal and background events after 5 years of data taking.

The main background sources are given by:

- Large angle scattering of muons produced in  $\nu_\mu CC$  interactions.
- Secondary hadronic interaction of daughter particles produced at primary  $\nu_\mu$  interaction vertex.
- Decay of charmed particles produced at primary  $\nu_\mu$  interaction vertex

Comparing the total number of detected  $\nu_\tau$  interaction with the estimated background it's clearly seen that OPERA is quite a background-free experiment. In Figure 5 the  $\nu_\tau$  observation probability at 3 and 4  $\sigma$  as a function of  $\Delta m^2$  is reported.

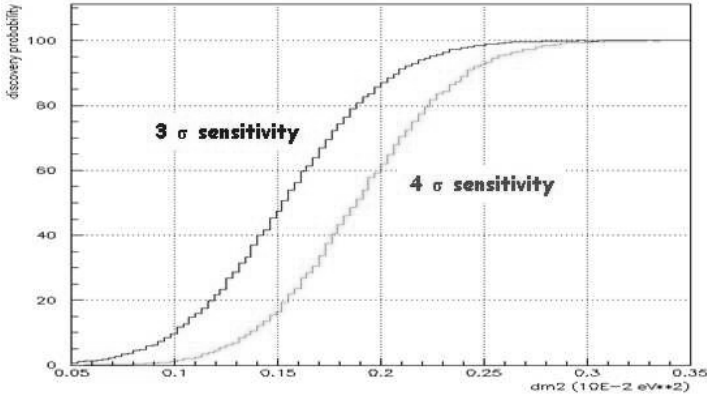


Figure 5:  $3\sigma$  and  $4\sigma$  observation probability as a function of  $\Delta m^2$ .

## 5 Results from the first runs

The first CNGS run was held in August 2006<sup>16)</sup>. At that time only electronic detectors were installed: the brick filling started indeed at the beginning of 2007. From 18 to 30 August 2006 a total intensity of  $0.76 \times 10^{18}$  p.o.t. was integrated and 319 neutrino-induced events were collected (interactions in the rock surrounding the detector, in the spectrometers and in the target walls). Thanks to this first technical run the detector geometry was fixed and the full reconstruction of electronic detectors data tested. It was also possible to fine-tune the synchronization between CERN and Gran Sasso, performed using GPS clocks. Furthermore, the zenith-angle distribution from penetrating muon tracks was reconstructed and the measured mean angle of  $3.4 \pm 0.3^\circ$  was well in agreement with the value of  $3.3^\circ$  expected for CNGS neutrinos traveling from CERN to the LNGS underground laboratories.

The first OPERA physical run was held in October 2007. At that time about 40% of the target was installed, for a total mass of about 550 tons. In about 4 days of continuous data taking  $0.79 \times 10^{18}$  p.o.t. were produced at CERN and 38 neutrino interactions in the OPERA target were triggered by the electronic detectors. The corresponding bricks indicated by the brick finding algorithm were extracted and developed after the cosmic ray exposure and their emulsions sent to the scanning laboratories. In a few hours the first neutrino interactions of the OPERA experiment were successfully located and reconstructed. In Figure 6 the display of two events is shown. The left one is a  $\nu_\mu$ CC interaction with 5 prongs and a shower reconstructed pointing to the

primary interaction vertex ( $\gamma$  conversion after a  $\pi^0$  decay). In the second a quite energetic shower (about 4.7 GeV) coming from the primary interaction vertex is visible.

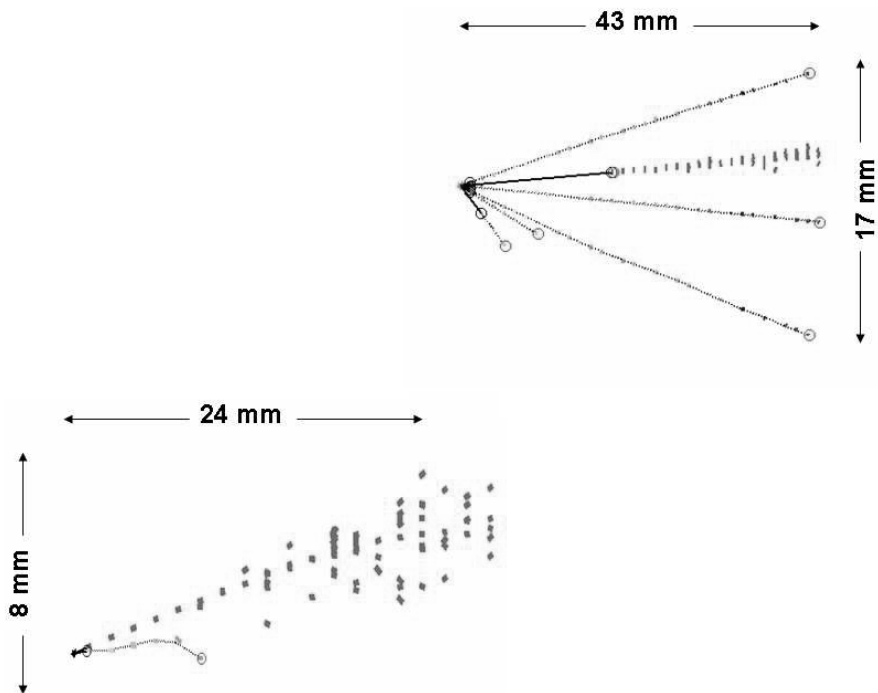


Figure 6: *Two reconstructed neutrino interaction from the OPERA 2007 run. The event displayed on the left is a  $\nu_\mu CC$  interaction. The right side shows an event where an energetic shower comes from the interaction vertex.*

This first physical run was quite short but very significant. Indeed it allowed a full testing of the electronic detectors and the data acquisition. Furthermore, the brick finding algorithm was successfully used to locate the bricks where the neutrino interaction occurred. Finally, the target tracker to brick matching was proved to be able to satisfy the expectations and the full scanning strategy validated.

## 6 Outlook and future plans

The OPERA target will be completed by May 2008. In June a first 150-day period of CNGS beam at nominal intensity is expected to start. About  $30 \times 10^{18}$  p.o.t. will be integrated, equivalent to about 3500 neutrino interactions. More than 100 charm decays will be collected, so that the capability to reconstruct  $\tau$  decays will be fully exploited. The corresponding number of expected triggered  $\nu_\tau$  is 1.3: with some luck the first  $\nu_\tau$  candidate event will be observed during the 2008 OPERA run.

## References

1. M. Guler *et al.*, “An appearance experiment to search for oscillations in the CNGS beam”, CERN/SPSC 2000-028, SPSC/P318, LNGS P25/2000, Jul. 2000
2. Y. Fukuda *et al.* “Evidence for oscillation of atmospheric neutrinos” *Phys. Rev. Lett.* vol. 81, pp. 1562-1567, Aug. 1998
3. CNGS project: <http://proj-cngs.web.cern.ch/proj-cngs/>  
G. Acquispace *et al.*, CERN-98-02 (1998)  
R. Bailey *et al.*, CERN-SL/99-034 (1999)  
A. E. Ball *et al.*, CERN-SL/Note-2000-063 (2000)
4. E. Eskut *et al.*, *Nucl. Instrum. Methods A* **401**, 7 (1997)
5. K. Kodama *et al.*, *Phys. Lett. B* **504**, 218 (2001)
6. T. Nakano (CHORUS collaboration), *International Europhysics Conference on High-Energy Physics* (HEP 2001), Budapest, Hungary, 12-18 July 2001
7. M. De Serio *et al.*, *Nucl. Instrum. Methods A* **554**, 247 (2005)
8. N. Armenise *et al.*, *Nucl. Instrum. Methods A* **551**, 261 (2005)
9. K. Borer *et al.*, *Nucl. Instrum. Methods A* **566**, 327 (2006)
10. I. Kreslo *et al.*, *JINST* **3**, P04006 (2008)
11. A. Anokhina *et al.*, submitted to JINST
12. T. Adam *et al.*, “The OPERA experiment target tracker”, *Nucl. Instrum. Meth.*, vol. A 577, pp. 523-539, Jul. 2007
13. M. Ambrosio *et al.*, “The OPERA magnetic spectrometer”, *IEEE Trans. Nucl. Sci.* vol. 51, no. 3, pp. 975-979, Jun. 2004

14. A. Bergnoli *et al.*, “Tests of OPERA RPC Detectors”, IEEE Trans. Nucl. Sci. vol. 52, no. 6, pp. 2963-2970, Dec. 2005
15. S. Dusini, “RPC performances during 2007 October run”, OPERA internal note, 86, Feb. 2008.
16. R. Acquafredda *et al.*, OPERA collaboration, *New J.Phys* **8**, 303 (2006)

# RECENT RESULTS FROM THE MINOS EXPERIMENT 1)

Alfons Weber for the MINOS Collaboration

University of Oxford, DWB, Keble Rd., OX1 3RH Oxford, United Kingdom

A.Weber@physics.ox.ac.uk

## Abstract

MINOS is a long baseline neutrino oscillation experiment. Protons from the Fermilab main injector are used to generate an intense muon neutrino beam, which is directed at the Soudan underground laboratory in Northern Minnesota. The result from two years of running with a total exposure of  $2.5 \times 10^{20}$  protons on target from the NuMI beam is reported. We made a preliminary measurement by comparing the event rate and energy spectra of charge current muon neutrino interactions in the two detectors, which are 1 and 735 km from the neutrino production target. The data is consistent with  $\nu_\mu$  to  $\nu_\tau$  oscillation in the so-called atmospheric parameter range with  $\Delta m^2 = (2.38_{-0.16}^{+0.20}) * 10^{-3} \text{eV}^2$  and  $\sin^2 2\theta = 1_{-0.08}$ .

## 1 Introduction

There is now substantial evidence that neutrinos oscillate <sup>2)</sup>. This oscillation requires having a distinct set of mass and flavour eigenstates, which are related by the PMNS matrix <sup>3, 4)</sup>. The parameters of neutrino oscillation are 3 mixing angles, a CP-violating phase and the two mass differences between the 3 mass eigenstates. The Main Injector Neutrino Oscillation Search (MINOS) has been designed to study the flavour transitions of neutrinos produced by the .Neutrinos at the Main Injector. (NuMI) beam line at the Fermi Nation Accelerator Laboratory (FNAL). MINOS employs two detectors, one on the FNAL campus only 1 km from the neutrino production target, the other in the Soudan Underground Laboratory, a further 734 km away in northern Minnesota. From the comparison of the reconstructed neutrino energy spectra and event rates at both locations the oscillation parameters  $\Delta m^2$  and  $\sin^2 2\theta$  are extracted.

### 1.1 The Beam

The NuMI neutrino beam is produced by depositing around  $2.5 * 10^{13}$  protons, with energy of 120 GeV each, every 2-3 s onto a 94 cm long, segmented carbon target. The protons are bent downward 58 mrad to point toward both MINOS detectors and are delivered in 10  $\mu$ s spills. The positively charged particles produced in the target are focused by two magnetic horns into the 675 m long evacuated decay pipe, where they are allowed to decay to produce neutrinos. The target position relative to the first horn and the horn current are variable to allow particles of different momenta to be focused into the decay volume, thus allowing modification of the neutrino energy spectrum. The recorded neutrino interactions are predicted to be 92.9%  $\nu_\mu$ , 5.8%  $\bar{\nu}_\mu$ , 1.2%  $\nu_e$  and 0.1%  $\bar{\nu}_e$ . For the results reported here, the target was inserted around 25 cm into the horn yielding a peak in the neutrino energy spectrum in the 2-6 GeV range. A total of  $2.5 * 10^{20}$  protons on target were taken in this position between May 2005 and April 2007. This roughly doubles the statistics in comparison with the result we published earlier <sup>5)</sup>.

### 1.2 The Detector

Both MINOS detectors <sup>6)</sup> are iron/scintillator tracking calorimeters with an average toroidal magnetic field of 1.3 T. The iron planes are 2.54 cm thick and are interleaved with scintillator planes. The scintillator are made up of 4.1 cm wide and 1 cm thick, TiO<sub>2</sub> coated extruded plastic scintillator strips, which are up to 8 m long. The light produced in the scintillator is captured by 1.2 mm wavelength shifting fibers, which are imbedded in a groove along the scintillator and is guided to multi-anode photomultiplier tubes (PMTs). The planes are

oriented  $45^\circ$  from the vertical and  $90^\circ$  with respect to the previous plane. The 5.4 kton far detector (FD), situated around 700 m underground in the Soudan underground laboratory, has 484 octagonal 8 m wide instrumented planes read out at both ends via Hamamatsu M16 PMTs <sup>7)</sup> and custom electronics <sup>8)</sup>. Eight WLS fibers from strips separated by about 1 m are coupled to a single PMT pixel. The coupling pattern is different on both sides of the detector to allow the resolution of ambiguities. The MINOS near detector (ND), 100 m underground, has a total mass of 0.98 kton and is located at the Fermi National Accelerator Laboratory close to Chicago. In order to cancel uncertainties in the neutrino interaction and detector modeling, the two detectors have been built as similar as possible. However, the event rate in the ND is  $\sim 10^5$  higher than in the FD, which required some design difference between them. The geometry of the ND has been optimized to contain hadronic showers, while at the same time providing sufficient flux return to achieve a magnetic field similar to the FD. The steel planes have the same thickness as the FD, but are 282 irregular  $4 \times 6 \text{ m}^2$  octagons. The scintillator strips have identical cross section and are coupled via WLS fibers to one pixel of a Hamamatsu M64 PMT <sup>9)</sup>. The ND readout system <sup>10)</sup> is dead-timeless during the spill and integrates the PMT charges at a rate of 53.1 MHz. Minimum ionizing particles produce 6-7 photoelectrons in both detectors. The data acquisition system accepts data above a threshold of around 0.25 photo-electrons. In the FD, the events are recorded in a window of 100  $\mu\text{s}$  around the beam spill, while in the ND, all data is retained during the spill. The trigger efficiency is expected to be 100% for neutrino events with a visible energy above 0.5 GeV.

The detectors are calibrated using an in-situ light injection system and cosmic ray muons. The LED light, which is monitored by PIN diodes is injected into the WLS fibers and tracks the changes in PMT and electronics response on short to medium timescales. The energy depositions of through going cosmic muons are used to calibrate the relative response of the individual strips in each detector. Stopping muons are used to fix the relative energy scale of the two detectors, which is known to about 3%. The energy scale of single hadrons and electrons was determined from the results of an experiment using a smaller un-magnetized copy of the MINOS detector in a test-beam at CERN. The uncertainty of the absolute hadronic energy scale is estimated to be 6%.

Neutrino production is calculated using a FLUKA <sup>11)</sup> simulation of the hadron production in our carbon target. These simulations have an uncertainty of 20 – 30% stemming from the lack of relevant hadron production data in thick targets. Particles are tracked through the horn and decay pipe using a GEANT3 <sup>12)</sup> based simulation. Neutrino interactions in the MINOS detector is simulated using a tuned version of NEUGEN3 <sup>13)</sup>. CC production cross sections below 10% have an uncertainty at the 20% level. The products of

the neutrino interaction are propagated out of the iron nucleus using the INTRANUKE<sup>14)</sup> code. The response of the detector is modeled using GEANT3 with the GCALOR model to simulate hadronic interactions. The effect of photon propagation, transmission through the WLS fiber, the PMT, and the electronics is also taken into account.

## 2 Data Reconstruction

The initial step in the reconstruction of the FD data is the removal of the eight-fold hit-to-strip ambiguity using information from both strip ends. In the ND, timing and spatial information are first used to separate individual neutrino interactions from the same spill. Subsequently, tracks are found and fitted and showers are reconstructed in the same way in both detectors. For muon neutrino CC events, the total reconstructed event energy is obtained by summing the muon energy and the visible energy of the hadronic system. The FD data set was left blind until the selections and analysis procedure was understood and fixed. The blinding procedure hid a substantial fraction of the FD events, with the precise fraction depending on the event length and energy being unknown. CC muon neutrino interactions were selected by requiring negatively charged tracks with a vertex in the fiducial volume. The event time must be within 50  $\mu\text{sec}$  of the spill time corrected for the time of flight. Cosmic ray events were further suppressed in the FD by requiring the track to point within  $53^\circ$  of the neutrino beam direction. A new particle identification parameter (PID) incorporating one and two dimensional probability density functions for the event length, the number of planes with just a reconstructed track, the average energy depositions along the track and the hadronic energy fraction were used to separated muon neutrino interactions from the NC background.

## 3 Data Analysis

To constrain hadron production in the NuMI target, a series of six runs with similar exposure was taken where the target position and the magnitude of the horn current, i.e. its magnetic field, was varied. Comparing the reconstructed energy spectrum of CC event in the ND with the prediction of the FLUKA based hadron production model showed an energy dependent discrepancy that changed with the beam settings and thus implying that the primary effect is cased by beam modelling, rather than detector or cross section effects. To bring data and MC into better agreement, we re-tuned the hadron production cross section as a function of longitudinal and transverse momentum, thus changing the pion and kaon production yields. In addition, potential systematic effects as beam focussing, NC background and reconstruction energy scales and offsets were allowed to vary within their uncertainties. All fitted parameters were

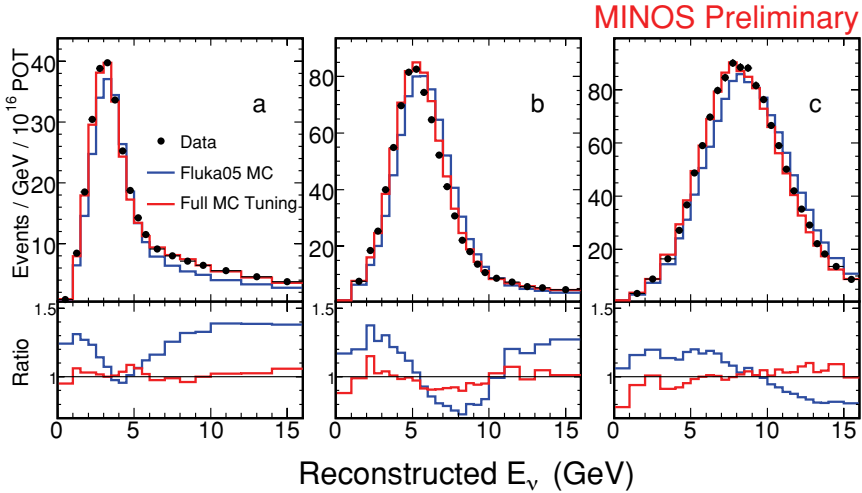


Figure 1: Comparison of the ND energy spectrum for different beam sittings with the MC expectations before and after tuning of the hadron production parameters.

found to agree well with our expectations and the resulting energy spectrum agrees well with the ND data. (See Fig. 1)

The measured ND neutrino energy spectrum is used to predict the unoscillated spectrum at the FD. The oscillation hypothesis is tested relative to this prediction. The prediction takes into account the ND and FD spectral differences that are present, even in the absence of oscillations, due to pion decay kinematics and beamline geometry. The shape differences are up to 20% on either side of the peak. We have used the so called Beam Matrix method <sup>5)</sup>, in which the agreement between data and MC is not very important as the ND data itself is used to predict the FD energy spectrum. It corrects for all effects which are common to both detectors such as beam modeling, neutrino cross sections and detector response. It utilizes the beam simulation to derive a transfer matrix that relates the neutrinos in the two detectors via their parent hadrons. The matrix elements  $M_{ij}$  give the relative probability that the distribution of secondary hadrons which produce neutrinos of a certain  $E_i$  in the ND will produce a neutrino of energy  $E_j$  in the FD. The reconstructed ND energy spectrum is first translated into a flux using efficiencies, resolution and background estimations for the ND MC. This flux is multiplied by the matrix to yield the predicted un-oscillated FD flux, which is translated into the reconstructed FD energy spectrum using the FD MC simulation. A clear

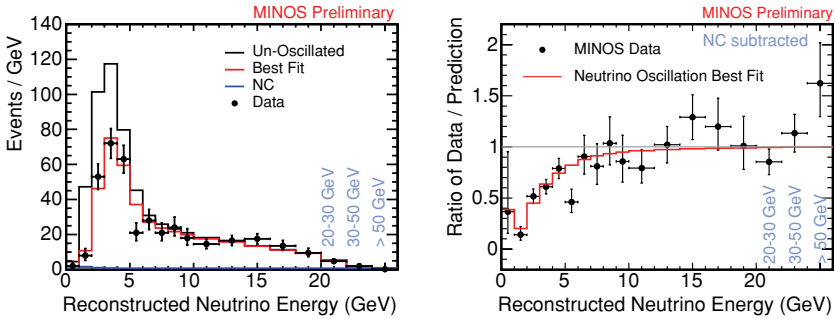


Figure 2: The left plot shows the reconstructed energy spectrum of the selected muon neutrino charge current events together with the expected un-oscillated prediction from the near detector and the best fit oscillation result. The right hand plot shows the ratio of the data and oscillated MC to the un-oscillated prediction. One can clearly see that the data nicely follows the expectation from neutrino oscillations.

deficit of neutrinos was observed, which was concentrated at low reconstructed energies. Under the assumption that the observed deficit is due to  $\nu_\mu \rightarrow \nu_\tau$  oscillations, a fit is performed to the parameters  $\Delta m^2$  and  $\sin^2 2\theta$  using the following expression for the muon neutrino survival probability:

$$P(\nu_\mu \rightarrow \nu_\mu) = 1 - \sin^2(2\theta) * \sin\left(\frac{\Delta m^2 L}{4E}\right),$$

where  $L$  is the distance travel and  $E$  the energy of the neutrino. The FD data is binned in reconstructed energy and the observed number of events in each bin is compared to the expected number of events for this hypothesis. The best fit parameters are those which minimize  $\chi^2 = -2 \ln \mathcal{L}$ , where  $\mathcal{L}$  is the likelihood ratio as defined in <sup>5</sup>). The main systematic effects (relative normalization of the ND and FD data set, absolute hadronic energy scale including effects of intra-nuclear re-scattering and the amount of NC background in the NC sample) were included as nuisance parameters in the fit. The total systematic errors are  $1.1 \times 10^{-4} \text{ eV}^2$  and 0.008 for  $\Delta m^2$  and  $\sin^2 2\theta$  respectively. The data, together with un-oscillated prediction and the best fit result are shown in Fig.2. The best fit point and 68% and 90% CL contours for the oscillation parameter are shown in Fig.3.

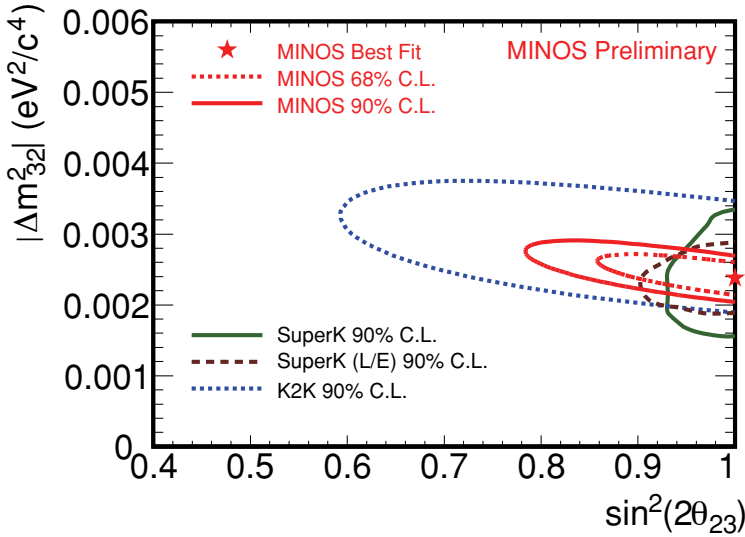


Figure 3: 68% and 90% confidence limit contours for with  $\Delta m^2$  and  $\sin^2 2\theta$  together with results from the SuperK and K2K experiments (from <sup>2)</sup> and references therein).

#### 4 Summary, Conclusion and Outlook

Using  $2.5 \times 10^{20}$  protons on target from the NuMI beam at Fermilab, MINOS has made a preliminary measurement of the “atmospheric” neutrino oscillations parameters to be  $\Delta m^2 = (2.38^{+0.20}_{-0.16}) * 10^{-3} \text{eV}^2$  and  $\sin^2 2\theta = 1_{-0.08}$ . The measurement is the world’s most precise measurement of  $\Delta m^2$  and is in good agreement with the previous measurements performed by MINOS and other experiments. The MINOS experiment expects to more than triple the data set presented in this note over the coming years and thus will drastically improve the current measurement. It will be able to limit alternative non-oscillation models and also look for alternative oscillation channels involving sterile and electron neutrinos.

#### Acknowledgement

This work was supported by the US DoE, the UK STFC; the US NSF; the State und University of Minnesota; the University of Athens, Greece and Brazil’s FAPESP and CNPq. We are grateful to the Minnesota Department of Natural Resources, the crew of the Soudan Underground Laboratory, and the Staff of Fermilab for their contributions to this effort.

**References**

1. This work is also being published in Journal of Physics: Conference Series, EPS HEP (2008)
2. W.-M. Yao et al., Journal of Physics G33, 1 (2006)
3. B. Pontecorvo, JETP (USSR) 34, 247 (1958)
4. Z. Maki, M. Nakagawa, S. Sakata, Prog.Theor.Phys. 28. 870 (1962)
5. D.G. Michael et al., Phys. Rev. Lett. 97, 191801 (2006)
6. D.G. Michael et al., The MINOS Detectors, to be submitted to NIM.
7. K. Lang et al., NIM A545, 853 (2005)
8. J. Oliver et al., IEEE Trans. Nucl. Sci. 51, 2193 (2004)
9. N. Tagg et al., NIM A539, 668 (2005)
10. T. Cundiff et al., IEEE Trans. Nucl. Sci. 53, 1347 (2006)
11. A. Fasso et al., CERN-2005-10 (2005)
12. R. Brun et al., CERN DD/EE/84-1 (1984)
13. H. Gallagher, Nucl. Phys. B (Proc. Suppl.) 112, 188 (2002)
14. A. Merenyi et al., Phys. Rev. D47, 743 (1992)

# FLAVOR SYMMETRY AND NEUTRINO MIXING

H. Fritzsch

*Sektion Physik, Ludwig-Maximilians-Universität München,  
Theresienstrasse 37, 80333 München, Germany*

## Abstract

We discuss the neutrino mixing, using the texture 0 mass matrices, which work very well for the quarks. The solar mixing angle is directly linked to the mass ratio of the first two neutrinos. The neutrino masses are hierarchical, but the mass ratios turn out to be much smaller than for quarks. The atmospheric mixing angle is  $38^\circ$ . The CP violation for leptons should be much smaller than for quarks.

The central problem in flavor physics is a deeper understanding of the quark and lepton masses. Thus far we only understand the hadron masses, e. g. the mass of the nucleon. These masses are generated in QCD <sup>1)</sup> by the quark–gluon interaction. The confinement of the colored quarks and gluons leads to the appearance of a mass for the nucleons and the other hadrons. This mass is the confined field energy of the gluons and quarks inside the hadrons. The scale parameter  $\Lambda_c$  of QCD, measured to be about 220 MeV, determines the hadronic masses. But the masses of hadrons, especially the heavy ones like the  $J/\psi$ –meson, depend also on the quark masses, and those remain mysterious.

The Standard Model has 28 fundamental parameters. 22 of these parameters are directly related to the fermion masses: 6 quark masses, 3 charged lepton masses, 3 neutrino masses, 4 flavor mixing parameters for the quarks, and 6 for the leptons.

In the Standard Model the masses of the  $W/Z$ –bosons are due to the "Higgs"–mechanism, but we still do not know, whether the "Higgs"–model <sup>2)</sup> is true. Soon we shall find out, when the new LHC–accelerator at CERN starts producing experimental data.

It remains open, whether there exist relations between the fermion mass parameters. Many years ago I proposed such relations between the quark masses and the flavor mixing angles <sup>3)</sup>. Using the parametrization, given in ref. (4), these relations are:

$$\begin{aligned}\Theta_u &= \sqrt{m_u/m_c} \\ \Theta_d &= \sqrt{m_d/m_s}.\end{aligned}\tag{1}$$

The Cabibbo angle is approximately given by

$$\Theta_c \cong \left| \sqrt{\frac{m_d}{m_s}} - e^{i\phi} \sqrt{\frac{m_u}{m_c}} \right|\tag{2}$$

Taking into account the recent experimental data, these relations work very well. Similar relations might also exist for the leptons, as discussed below.

I shall concentrate on the neutrino mixing. About 10 years ago Xing and I <sup>5)</sup> discussed the possibility that the mixing angles for the leptons are large, even maximal. The recent data support this hypothesis. But it is still unclear, what type of masses the neutrinos have. Are these masses like the masses of the charged leptons, i. e. Fermi–Dirac–masses? Or are they Majorana masses? In any case these masses are very small, probably less than 1 eV. In the Standard Model with Fermi–Dirac neutrino masses this is not understood.

If the neutrino masses are Majorana masses, one can introduce these masses, using the see-saw mechanism <sup>6)</sup>.

If the Standard Model is embedded in the Grand Unified Theory, based on  $SO(10)$  <sup>7)</sup>, the small Majorana neutrino masses reflect the heavy masses of the righthanded neutral leptons, which are part of the 16-dimensional fermion representation of  $SO(10)$ .

The relations (1) follow from an underlying texture zero mass matrix:

$$M = \begin{pmatrix} O & A & O \\ A^* & D & B \\ O & B^* & C \end{pmatrix} \tag{3}$$

We describe the neutrino mixing by the following flavor mixing matrix:

$$V = U \cdot P \tag{4}$$

$$P = \begin{pmatrix} e^{i\rho} & 0 & 0 \\ 0 & e^{i\sigma} & 0 \\ 0 & 0 & 1 \end{pmatrix} \tag{5}$$

$$U = \begin{pmatrix} c_l & s_l & 0 \\ -s_l & c_l & 0 \\ 0 & 0 & 1 \end{pmatrix} \begin{pmatrix} e^{i\varphi} & 0 & 0 \\ 0 & c & s \\ 0 & -s & c \end{pmatrix} \begin{pmatrix} c_\nu & -s_\nu & 0 \\ s_\nu & c_\nu & 0 \\ 0 & 0 & 1 \end{pmatrix} \tag{6}$$

where  $s_\nu$  stands for  $\sin\Theta_\nu$ ,  $s_l$  for  $\sin\Theta_l$ ,  $s$  for  $\sin\Theta$ , etc. The angle  $\Theta_\nu$  is the solar mixing angle ( $\Theta_{sun}$ ), the angle  $\Theta$  the atmospheric angle ( $\Theta_{at}$ ) and the angle  $\Theta_l$  describes the mixing between the electron neutrino and the third mass eigenstate.

The experiments give:

$$\Theta_\nu \approx 34^\circ \quad \Theta \approx 65^\circ \quad \Theta_l < 13^\circ \tag{7}$$

We assume that the lepton mass matrices are described, like the quarks, by a texture zero matrix (2). Thus we have:

$$\begin{aligned} \tan\Theta_l &= \sqrt{\frac{m_e}{m_\mu}} & \Theta_l &\approx 4^\circ \\ \tan\Theta_\nu &= \sqrt{\frac{m_1}{m_2}} \end{aligned} \tag{8}$$

( $m_1, m_2$  are the masses of the first, second neutrino). Using the experimental value  $\Theta_\nu \approx 34^\circ$ , we find:

$$\frac{m_1}{m_2} = (\tan 34^\circ)^2 \approx 0.45 \tag{9}$$

The neutrino masses are fixed, since the mass difference are given by the experiments, and the mixing angles are fixed by the mass matrices. Thus one finds for the neutrino masses:

$$\begin{aligned} m_1^2 &= \frac{\sin^4 \Theta_\nu}{\cos 2\Theta_\nu} \Delta m_{21}^2 \\ m_2^2 &= \frac{\cos^4 \Theta_\nu}{\cos 2\Theta_\nu} \Delta m_{21}^2 \\ m_3^2 &= m_2^2 + \Delta m_{32}^2 \end{aligned} \quad (10)$$

Taking into account the observed (mass)<sup>2</sup> differences  $\Delta m_{21}^2 \approx 8 \cdot 10^{-5} eV^2$  and  $\Delta m_{32}^2 \approx 2.3 \cdot 10^{-3} eV^2$ , we obtain the following neutrino masses:

$$\begin{aligned} m_1 &\approx 0.0046 \text{ eV} \\ m_2 &\approx 0.01 \text{ eV} \\ m_3 &\approx 0.05 \text{ eV} \end{aligned} \quad (11)$$

Note that the mass ratio  $m_2/m_3$  is:

$$m_2/m_3 \cong 0.20 \quad (12)$$

In order to calculate the atmospheric angle  $\Theta$ , we take  $\phi = \pi$  in eq. (2) and find:

$$\begin{aligned} \Theta &\cong \arctan \sqrt{\frac{m_2}{m_3}} + \arctan \sqrt{\frac{m_\mu}{m_\tau}} \\ \tan \Theta &\cong \left( \sqrt{\frac{m_2}{m_3}} + \sqrt{\frac{m_\mu}{m_\tau}} \right) / \left( 1 - \sqrt{\frac{m_2}{m_3} \cdot \frac{m_\mu}{m_\tau}} \right). \end{aligned} \quad (13)$$

The angle  $\Theta$  is about  $38^\circ$ . In eq. (13) there is a phase parameter  $e^{i\phi}$  multiplying the second term. In order to obtain  $38^\circ$ , we have to assume that  $\phi$  is close to zero, i. e. in the leptonic sector the CP violation should be very small, at least one order of magnitude smaller than for the quarks.

Our expected value  $\Theta \approx 38^\circ$  is on the low side of the experimental data, which give  $\Theta \approx 45^\circ \pm 7^\circ$ . We have  $\sin^2 \Theta \approx 0.94$ .

The matrix element  $V_{3e}$  of the mixing matrix is  $\sin \Theta_l \cdot \sin \Theta$ , and we find:  $V_{3e} \approx 0.043$ . New experiments with reactor neutrinos might detect this matrix element.

We summarize: We assume that the lepton mass matrices have the texture zero form (3) with  $D = 0$ . The three mixing angles can be calculated as functions of the lepton masses.

The three neutrino masses are

$$\begin{aligned} m_1 &\approx 0,005 \text{ eV}, m_2 \approx 0,01 \text{ eV}, \\ m_2 &\approx 0,05 \text{ eV}. \end{aligned} \quad (14)$$

There is a normal mass hierarchy:  $m_1 < m_2 < m_3$ , but the mass ratios 0.5 and 0.7 are much smaller than the mass ratios for the quarks ( $u$ -quark: 0.005, 0.006;  $d$ -quarks: 0.05, 0.04).

We obtain:

$$\begin{aligned} \tan\Theta_\nu &= \tan\Theta_{sun} = \sqrt{m_1/m_2} \\ \tan\Theta_l &= \sqrt{m_e/m_\mu} \\ \Theta &= \Theta_1 + \Theta_2 \\ \tan\Theta_1 &= \sqrt{m_2/m_3} \\ \tan\Theta_2 &= \sqrt{m_\mu/m_\tau}. \end{aligned} \quad (15)$$

We do expect that the CP violation in the lepton sector is much smaller than the CP-violation in the quark sector.

Thus in the coming experiments it will not be possible to observe a CP-violation.

## References

1. H. Fritzsch and M. Gell-Mann, *Proc. of the Int. Conf. on HEP, Chicago*, 135 – 165 (1972).
2. P. Higgs, *Phys. Rev. Lett.* 13,, 508 (1964), *Phys. Lett.* 12, 132 (1964), *Phys. Rev.* 145, 1156 (1966)  
R. Brout and F. Englert, *Phys. Rev. Lett.* 13, 321 (1964) G. S. Guralnik, C. R. Hagen, T. W. B. Kibble, *Phys. Rev. Lett.* 13, 585 (1964)
3. H. Fritzsch, *Nucl. Phys.* B155, 189, (1979).
4. H. Fritzsch and Z. Xing, and K. H. Lee, *Phys. Rev.* D57, 594 (1998)
5. H. Fritzsch and Z. Xing, *Phys. Lett.* B634, 514 (2006)

6. P. Minkowski, *Phys. Lett. B* 67 421 (1977), T. Yanagida, *Progress of Theor. Phys.* 64 1103 (1980), M. Gell-Mann, P. Ramond and R. Slansky, in: *Supergravity*, North-Holland (1979), Print-80-0576 (CERN)
7. H. Fritzsch and P. Minkowski, *Annals of Physics* 93, 193 (1975)

**DOUBLE CHOOZ**

Elizabeth Falk Harris  
*University of Sussex, UK*

Written contribution not received



## THE CURRENT STATUS OF THE RENO EXPERIMENT

Yeongduk Kim

for RENO Collaboration

*Physics Department, Sejong University, Seoul 143-747, South Korea*

*E-mail : ydkim@sejong.ac.kr*

### Abstract

An experiment, RENO (Reactor Experiment for Neutrino Oscillation), is under construction to measure the unknown neutrino mixing angle ( $\theta_{13}$ ) using anti-neutrinos emitted from the Younggwang nuclear power plant in Korea. Two identical 16.3-ton Gadolinium loaded liquid scintillator detectors will be constructed at 290 m and 1.4 km from the center of the reactor array. The sensitivity in  $\sin^2\theta_{13}$  is expected as 0.2-0.3 in 90% confidence level with three years of data.

## 1 Introduction

There have been great progresses in understanding the neutrino sector of elementary particle physics in the past few years. The discovery of neutrino oscillation is a direct indication of physics beyond the Standard Model. The smallness of neutrino masses and the large lepton flavor violation associated with neutrino mixing are both fundamental properties that give insights into modifications of current theories.

Among the three neutrino mixing angles,  $\theta_{12}$  is measured by solar neutrinos and the KamLAND reactor experiment, and another,  $\theta_{23}$ , by atmospheric neutrinos and the long-baseline accelerator experiments, K2K and MINOS. Both angles are large, unlike mixing angles among quarks. The third angle,  $\theta_{13}$ , has not yet been measured but constrained to be small ( $\sin^2\theta_{13} < 0.16$ ) by the CHOOZ reactor neutrino experiment <sup>1)</sup>. Future measurement of  $\theta_{13}$  is possible using either reactor neutrinos or long baseline accelerator neutrino beams.

The Chooz experiment had a single detector located about 1 km from the reactors. A reactor experiment using two identical detectors of 10 ~ 30 tons at near (100 ~ 200 m) and far (1 ~ 2 km) locations was proposed <sup>2)</sup> and will have significantly improved sensitivity for  $\theta_{13}$  down to the  $\sin^2(2\theta_{13}) \sim 0.01$  level <sup>3)</sup>. Reactor neutrino experiment with multi-detectors at different baseline can cancel out the systematic uncertainties associated with reactor power and detector efficiencies. In addition, reactor measurements can determine  $\theta_{13}$  without the ambiguities associated matter effects and CP violation.

## 2 Overview of RENO Experiment

### 2.1 Site

The Younggwang nuclear power plant is one of four nuclear reactor complexes in Korea which has world-second largest thermal power output of 16.4 GW. The reactor complex is located in the west coast of southern part of Korea, about ~ 250 km from Seoul. The power plant has six reactors with about equal power, and are lined up in equal distances as shown in Fig. 1. The power plant is operated by Korea Hydro & Nuclear Power Co. Ltd. (KHNP).

The near and far detectors will be located about 290 m and 1.4 km from the center of reactor array. The detectors will be constructed identically and

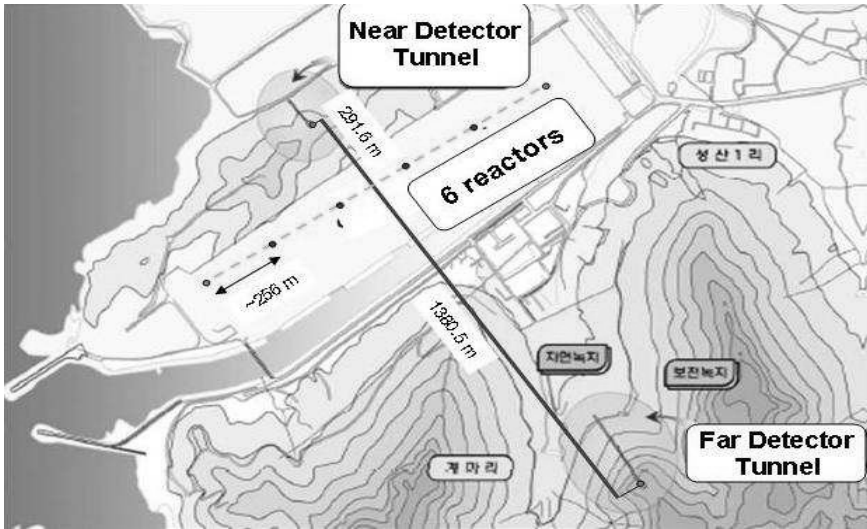


Figure 1: The layout of the Yonggwang experiment site. The reactors are roughly equally spaced at 260 m apart. The near and far detectors are 282 m and 1380 m away from the reactor array.

the Gadollinium loaded scintillator for neutrino detection will be 16.3 ton. The basic parameters for the two sites are summarized in Table 1.

## 2.2 Tunneling and Experiment Halls

The underground laboratories will be constructed with two horizontal tunnels, 100 m long for the near detector and 300 m long for the far detector, as shown in Fig. 1. The tunnel cross section is 4.5 m wide and 4.8 m high.

In order to check the suitability of constructing experimental halls and access tunnels at the experiment site, geological surveys have been performed. Four and three boreholes were drilled for near and far detector sites respectively. The rock quality at both sites was found to be solid enough for tunneling by electric and seismic tests. Bore samples are used to determine various properties of rocks, such as chemical composition, compressive strength, density, and radioactivities.

The natural radioactivities of rock samples obtained by boring at both

Table 1: *Basic parameters of near and far detectors.*

	Near	Far
Distance(m)	282	1380
Overburden(m)	46	168
# of neutrino events/day	920	82
muon flux( $m^{-2}s^{-1}$ )	5.5	0.85
$\langle E_\mu \rangle$ (GeV)	34.3	65.2

sites were measured by ICP-MASS. The U, Th, and  $^{40}K$  contents inside rock were  $2.1 \pm 0.1$ ,  $7.3 \pm 1.2$ , and 2.4 ppm respectively at near detector site. The far detector site has similar amounts of natural radioactivities.

### 3 Detector Design

The RENO detector is composed of 4 layers, starting from the center, target,  $\gamma$ -catcher, buffer and veto. The shape of each layer is cylindrical. The various design parameters have been determined for optimal performance using "Generic Liquid-scintillator Anti-Neutrino Detector Geant4 Simulation(GLG4Sim ?)". The program has been customized for the geometry of RENO detector with new event generator which provides better physics model. The simulation includes background  $\gamma$  rays from PMTs and surrounding rocks, cosmic muons and neutrons reaching the detector site as well as inverse  $\beta$  decay from the reactor anti-neutrinos. The neutrino events are characterized by time coincidence between positron signal and neutron signal. The cuts we applied was  $E_{e^+} > 1MeV$ ,  $6MeV < E_{neutron} < 12MeV$ ,  $0.3\mu s < \Delta T < 100\mu s$ . The energy resolution was applied.

The target, a cylinder of radius 1.4 m, of height 3.2 m contains 16.3 tons of 0.1% Gd and liquid scintillating material. To increase the detection efficiency of the neutron capture signal inside the target, a second layer called  $\gamma$ -catcher has been added and the thickness of  $\gamma$ -catcher is 60 cm. The neutrino detection efficiency with 60 cm thick  $\gamma$ -catcher was  $(93.0 \pm 0.6)\%$ .

The buffer is filled with non-scintillating mineral oil. 342 10" PMTs are mounted uniformly on the wall of this buffer vessel, and the thickness of mineral oil is 0.7 m to effectively reduce the radioactive backgrounds of PMTs. The

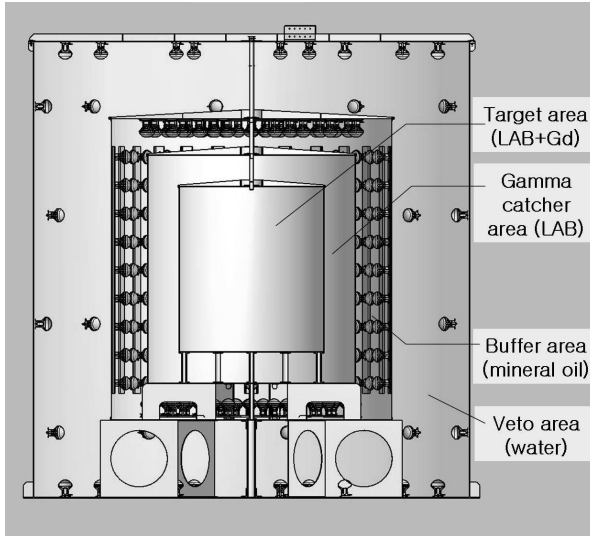


Figure 2: RENO detector. From the center, there are liquid scintillator filled target and gamma catcher with transparent acrylic vessel, mineral oil filled buffer with stainless steel vessel, and water filled veto layers. The PMTs for the inner and outer detectors are inwardly mounted buffer and veto vessels, respectively. The dimensions are given in Table 2.

outermost layer of the RENO detector is a veto layer composed of pure water. Its purpose is to reduce the background  $\gamma$  rays and neutrons from surrounding environment. The thickness of water is 1.5 m.

#### 4 Liquid Scintillator

Linear Alkyl Benzene(LAB) has been introduced by SNO group as basic liquid scintillator noting several advantageous properties such as excellent light yield, high flash point, good optical properties(transmittance and attenuation length), excellent compatibility with acrylic, as well as cheap price. LAB is composed of a linear alkyl chain of 10 ~ 13 carbon atoms attached to a benzene ring with a density of 0.86 (g/ml). In order to reduce the systematic error between near detector and far detector at RENO experiment, it is very important to know the compositions of LAB exactly. The composition of LAB is

Table 2: *Dimensions of the mechanical structure of the detector. OD and H are the out diameter and height of each layer.*

Layer	OD (cm)	H (cm)	Vessel Material	Material	Mass (tons)
Target	280	320	Acrylic	Gd-Doped LS	16.3
$\gamma$ -catcher	400	440	Acrylic	LS	28.5
Buffer	540	580	SUS	Mineral Oil	64.1
Veto	840	880	SUS	Water	352.6

measured by Gas Chromatography with Mass Spectrometry(GC-MS) at Korea Basic Science Institute with a sample of LAB supplied by a domestic company (Isu Chemical).

The optimal concentration of PPO and bis-MSB(wave length shifter) in the LAB in terms of light output was found to be 3 g/l and 30 mg/l respectively. The light yield of pure LAB with PPO and bis-MSB was found to be about 96 % relative to 100 % of pure PC. Target scintillator will be loaded with 0.1 % Gd, and it's critical to make the scintillator stable. We have studied samples of Gd complex with different additional organic ligands such as trioctyl phosphine oxide (TOPO) and 3,5,5-trimethylhexanoic acid (TMHA). The long-term stability tests are under progress. The radiopurity of domestic LAB sample was measured with ICP-MASS. The LAB, if not exposed to air, is sufficiently pure without purification. The Uranium content was less than  $8 \times 10^{-13}$ , and Thorium was less than  $1.1 \times 10^{-12}$ .

## 5 Backgrounds

From Chooz experiment, one can expect the main background events are due to the neutrons entering the scintillating liquid from outside. These neutrons produce the primary signal by a collision with the protons and captured inside the liquid scintillator. In addition, there are gamma background events from various sources containing natural radioactivities. The neutrons are mainly generated by cosmic muons inside rock and also inside water in the veto vessel.

The background event rate of energy deposit over 1 MeV from the natural background of surrounding rock was estimated as about 10 Hz for 70cm thick

Table 3: *Result of muon transport simulation for the detector candidate sites.*

Detector Site	Integrated intensity ( $\text{cm}^{-2}\text{s}^{-1}$ )	Average energy (GeV)
70 m	$5.5 \times 10^{-4}$	34.3
200 m	$8.5 \times 10^{-5}$	65.2
250 m	$2.9 \times 10^{-5}$	91.7

mineral oil and 1.5 m water veto layers. The radioactivities inside of PMTs were measured for a number of 8" and 10" PMTs provided by Hamamatsu, Photonis, and Electron Tube companies. If we use low radioactivity glass PMTs, the estimated single background rate will be also about 10 Hz for 70cm thick mineral oil layer. The radioactivities inside the liquid scintillator depends on the radiopurity of the liquid scintillator. We have measured the pure LAB sample provided by domestic chemical company without purification by ICP-MASS, and the U, Th contents were  $8 \times 10^{-13}$  and  $1.1 \times 10^{-12}$  respectively. The single background event rate will be a few Hz if we can confirm this level of radioactivity for bulk LAB. The overall accidental background event rate of energy over 1 MeV is order of 30 Hz.

We have simulated the muon intensity and energy at the underground lab using MUSIC and FLUKA packages with the modified Gaisser parameterization. Table 3 shows the rates and mean energy of the passing muons at near and far detector sites. The fast neutron backgrounds entering  $\gamma$ -catcher was simulated with the expected neutron flux and energy spectra from the parameterization by Mei et al. <sup>8)</sup> after matching to the average muon energies at RENO sites. The background event rate considering the valid neutrino event selection cuts and rejecting the multiple neutron capture and muon veto signals was found to be about 0.5 event per day for far detector.

## 6 Electronics

The gain of PMTs will be set at  $10^7$  and the electronics threshold of each PMT will be set at 0.5 photoelectron level. The main front-end electronics will be charge-to-time converting (QTC) chips recently developed by Super-Kamiokande group <sup>7)</sup>. A board housing 8 QTC chips can handle 24 PMT signals. A trigger logic based on the multiplicity of PMT hits and analogue sum is under development.

## 7 Sensitivity

The expected sensitivity of RENO experiment was calculated using the pull  $\chi^2$  method <sup>9)</sup>. Figure 3 shows the 90% confidence sensitivity in  $\sin^2\theta_{13}$ . The lines are explained in the figure caption. We expect the sensitivity of RENO experiment will be 0.2-0.3 with 3 years data taking. The relatively long spanning length of reactor array makes the sensitivity a little worse, but the effect is only about 30% level.

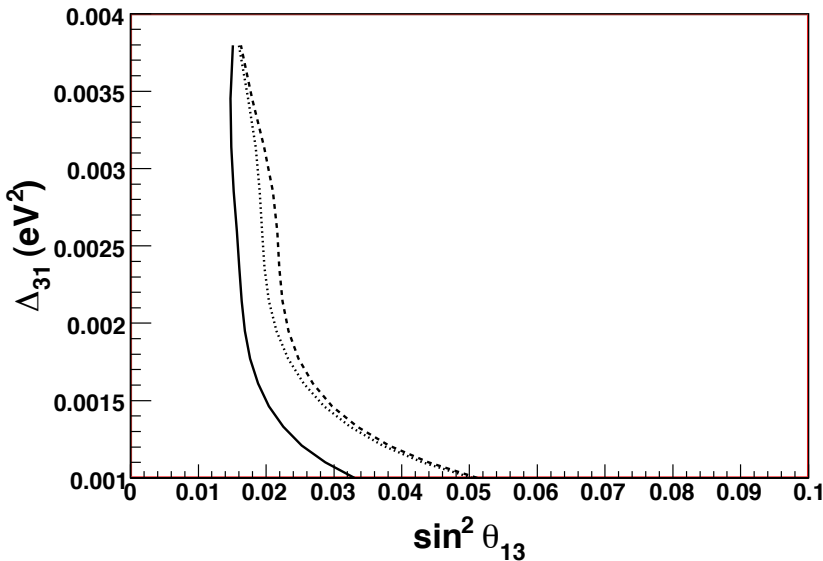


Figure 3: Two right curves shows the sensitivity with the expected parameters and the bin-by-bin relative error of 0.6%. The rightest curve shows the effect that the six reactor cores are separated and spans 1.3 km. Core fluctuation error was 2%. The solid curve was obtained with bin-by-bin relative error of 0.38%.

## 8 Acknowledgements

RENO collaboration acknowledge the financial support of Korean Science and Engineering Foundation(KOSEF).

## References

1. M. Appollonio *et al.*, Eur. Phys. J. **C27**, 331 (2003).
2. Yu. Kozlov, L. Mikaelyan, and V. Sinev, “*Two Detector Reactor Neutrino Oscillation Experiment Kr2Det at Krasnoyarsk. Status Report,*” Phys. Atom. Nucl. 66 (2003) 469-471;
3. K. Anderson *et al.* (2004), hep-ex/0402041.
4. K. Eguchi *et al.*, Phys. Rev. Lett. **90**, 021802 (2003).
5. Q. R. Ahmad *et al.*, Phys. Rev. Lett. **89**, 011301 (2002).
6. C. Bemporad, G. Gratta, and P. Vogel, Rev. Mod. Phys. 74, 297 (2002).
7. Y. Ashie *et al.*, Phys. Rev. D **71**, 112005 (2005).
8. D.-M. Mei and A. Hime Phys. Rev. D **73**, 053004 (2006)
9. G.L. Fogli, L. Lisi, A. Marrone, D. Montanino, and A. Palazzo, Phys. Rev. D **66**, 053010 (2002).



# ANTARES: TOWARDS A LARGE UNDERWATER NEUTRINO EXPERIMENT

M. Spurio, on behalf of the ANTARES collaboration  
*Dipartimento di Fisica and INFN- Bologna. spurio@bo.infn.it*

## Abstract

After a long R&D phase to validate its detector concept, the ANTARES (Astronomy with a Neutrino Telescope and Abyss environmental RESearch) collaboration<sup>1)</sup> is operating the largest neutrino telescope in the Northern hemisphere, which is close to completion. It is located in the Mediterranean Sea, offshore from Toulon in France at a depth of  $\sim 2500$  m of water which provide a shield from cosmic rays. The detector design is based on the reconstruction of events produced by neutrino interactions. The expected angular resolution for high energy  $\nu_\mu$  ( $E > 10$  TeV) is less than  $0.3^\circ$ . To achieve this good angular resolution, severe requirements on the time resolution of the detected photons and on the determination of the relative position of the detection devices must be reached.

The full 12-line detector is planned to be fully operational during this year. At present (April 2008) there are 10 lines taking data plus an instrumented line deployed at the edge of the detector to monitor environmental sea parameters. This paper describes the design of the detector as well as some results obtained during the 2007 5-line run (from March to December).

## 1 Scientific motivation

The main purpose of the ANTARES experiment is the detection of high energy neutrinos from galactic or extragalactic sources. Neutrinos are neutral and weak interacting particles and they can escape from astrophysical sources, delivering direct information about the processes taking place in the core of cosmic objects. The main scenario for the astrophysical production of high energy neutrinos involves the decay of charged pions in the beam dump of energetic protons in dense matter or photons field <sup>2)</sup>. A deep connection exists between charged cosmic rays, high energy  $\gamma$  emission and  $\nu$  production on beam dump models. Candidates for neutrino sources are in general also  $\gamma$ -ray sources, since most of the mechanisms that produce neutrinos also produce high-energy photons and cosmic rays. Indeed, rather stringent limits on the diffuse neutrino flux are based on this connection (see sec. 7).

There are many candidate neutrino sources in the cosmos; among them, supernova remnants, pulsars and micro-quasars in the Galaxy. Possible extragalactic sources include active galactic nuclei <sup>3)</sup> and  $\gamma$ -ray burst emitters <sup>4)</sup>. For such processes the neutrino energy scale is  $10^{12}$  to  $10^{16}$  eV. Neutrino sources that cannot be individually resolved or neutrinos produced in the interactions of cosmic rays with intergalactic matter or radiation produce a diffuse neutrino flux. This can be studied for neutrino energies in excess of  $10^{14}$  eV.

ANTARES is also suited for the search of dark matter in the form of WIMPs (Weakly Interacting Massive Particles). As an example in the case of supersymmetric theories with R-parity conservation, relic neutralinos are predicted to concentrate in the centre of massive bodies such as the Earth, the Sun or the Galaxy. At these sites neutralino annihilations and the subsequent decays of the resulting particles may yield  $\nu$  with energies up to  $10^{10} \div 10^{12}$ .

This paper describes the design of the ANTARES detector, as well as the experience and results obtained from the 5-line run (March to December 2007).

## 2 The ANTARES projet

The ANTARES project <sup>1)</sup> started in 1996. Today it involves about 180 physicists, engineers and sea-science experts from 24 institutes of 7 European countries. The experiment is based on the reconstruction of the direction and energy of neutrinos by detecting the Cherenkov light from particles produced in neutrino interactions. Since the neutrino interaction probability is extremely low, a huge detection volume is required to have a reasonable number of events. Secondary charged particles from cosmic rays represent the main physical background. In order to reduce it by several orders of magnitude, a large shield of kilometres of water is required.

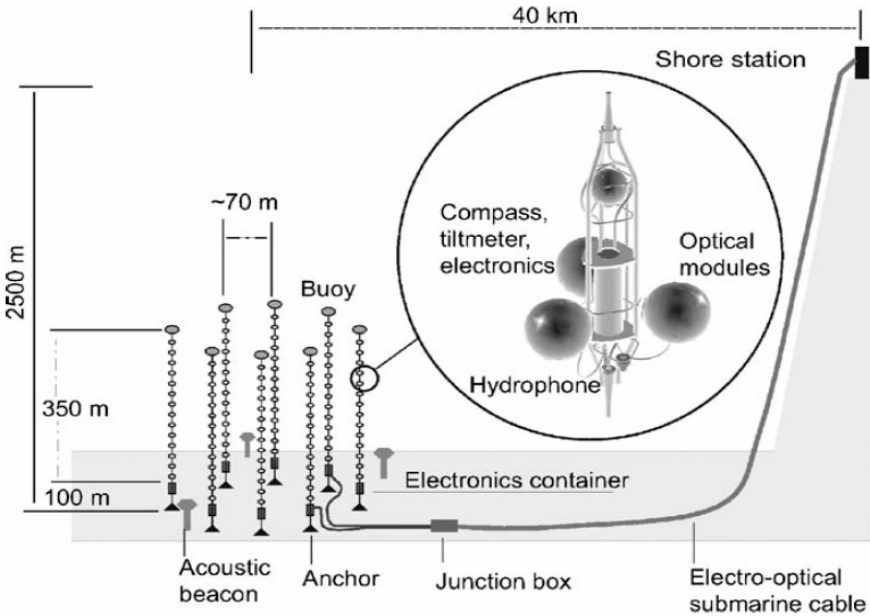


Figure 1: Schematic view of the ANTARES detector

From 1996 to 1999 an extensive R&D program has been successfully performed to prove the feasibility of the detector concept <sup>5)</sup>. Site properties that have been extensively studied are: the optical properties of the surrounding water; the biofouling on optical surfaces; the optical backgrounds due to bioluminescence and to the decay of the radioactive salts present in sea water; the geological characteristics of its ground. These studies have led to the selection of the present site, 40 km off La Seyne-sur-Mer (France) at 2475 m depth.

The full detector, which is almost completed, will consist of 12 lines made of mechanically resistant electro-optical cables anchored at the sea bed at distances of about 70 m one from each other, and tensioned by buoys at the top. Figure 1 shows a schematic view of the detector array indicating the principal components of the detector. Each line has 25 storeys, and each storey (inset in figure) contains three optical modules (OM) and a local control module for the corresponding electronics. The OM are arranged with the axis of the PMT 45° below the horizontal. In the lower hemisphere there is an overlap in angular acceptance between modules, permitting an event trigger based on coincidences from this overlap.

On each line, and on a dedicated instrumented line, there are different kinds of sensors and instrumentation (LED beacons, hydrophones, compasses/tiltmeters) for the timing and position calibration. The first storey is about 100 m above the sea floor and the distance between adjacent storeys is 14.5 m. The instrumented volume corresponds to about 0.04 km<sup>3</sup>.

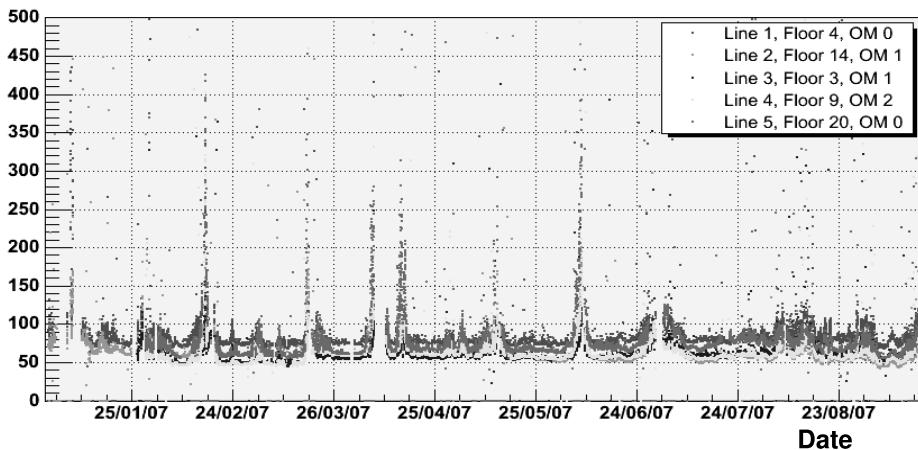


Figure 2: *Counting rates of optical modules (in kHz) from January to September, 2007. The five coloured points show the rate on 5 different storeys (numbers 4, 14, 3, 9 and 20) of the five lines. Storey 25 is the uppermost. The holes represent periods of calibration or interruptions in the data taking.*

The basic unit of the detector is the optical module (OM), consisting of a photomultiplier tube, various sensors and the associated electronics, housed in a pressure-resistant glass sphere <sup>6</sup>). Its main component is a 10-inch hemispherical photomultiplier model R7081-20 from Hamamatsu (PMT) glued in the glass sphere with optical gel. A  $\mu$ -metal cage is used to shield the PMT against the Earth magnetic field. Electronics inside the OM are the PMT high voltage power supply and a LED system used for internal calibration.

At present (April 2008) there are 10 lines taking data (plus the instrumented line, IL). The two remaining lines will be deployed and connected during 2008. The total sky coverage is  $3.5\pi$  sr, with an instantaneous overlap of  $0.5\pi$  sr with that of the IceCube experiment. The Galactic Centre will be observed 67% of the day time.

### 3 The Data Acquisition system

The Data acquisition (DAQ) system of ANTARES is extensively described in <sup>7</sup>). The PMT signal is processed by an ASIC card (the Analogue Ring Sampler, ARS) which measures the arrival time and charge of the pulse. On each OM, the counting rates exhibit a baseline dominated by optical background due to sea-water  $^{40}\text{K}$  and bioluminescence coming from bacteria as well as bursts of a few seconds duration, probably produced by bioluminescent emis-

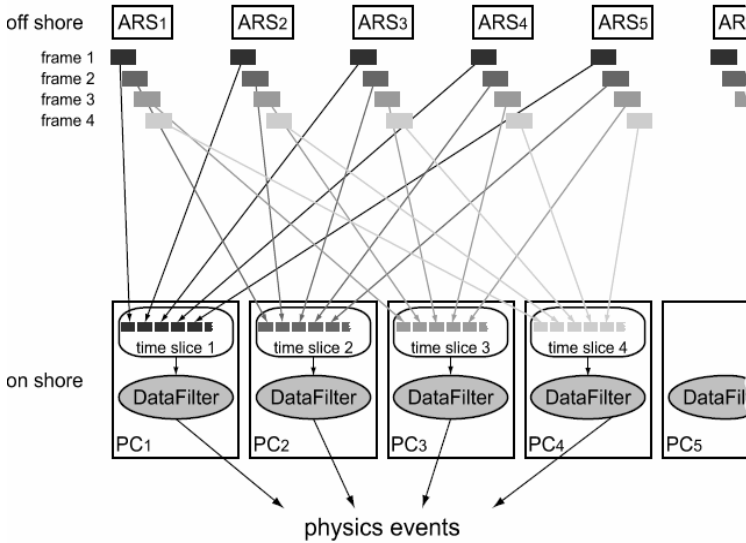


Figure 3: Scheme of the data processing based on time slices. All frames belonging to the same time window are sent to a single PC and form a time slice. The DataFilter program running on each PC processes the data in the time slice. All physics events are stored on disk.

sion of macro-organisms. Figure 2 shows the counting rates recorded by five OMs located on different storeys of each of the 5 lines during the 2007 run. The average counting rate increases from the bottom to the upper layers. The baseline is normally between 50 to 80 kHz. There can be large variations of the rate, reaching hundreds of kHz for some small periods.

The optical modules deliver their data in real time and can be remotely controlled through a Gb Ethernet network. Every storey is equipped with a Local Control Module (LCM) which contains the electronic boards for the OM signal processing, the instrument readout, the acoustic positioning, the power system and the data transmission. Every five storeys the Master Local Control Module (MLCM) also contains an Ethernet switch board which multiplexes the DAQ channels from the other storeys. At the bottom of each line, the Bottom String Socket (BSS) is equipped with a String Control Module (SCM) which contains the local readout and DAQ electronics, as well as the power system for the whole line. Both MCLM and SCM include a Dense Wavelength Division Multiplexing (DWDM) system used for data transmission in order to merge several 1Gb/s Ethernet channels on the same pair of optical fibres using different laser wavelengths. The lines are linked to the junction box by electro-optical cables which are connected using a unmanned submarine. A standard deep sea telecommunication cable links the junction box with the shore station where the data are filtered and recorded.

The trigger logic in the sea is planned to be as simple and flexible as possible. All OMs are continuously read out and the digitized information (*hits*) sent to shore. On-shore, a dedicated computer farm performs a global selection of *hits* looking for interesting physics events (DataFilter). This on-shore handling of all raw data is the main challenge of the ANTARES DAQ system, because of the high background rates.

A *hit* is a digitized PMT signal above the ARS threshold, set around 1/3 of the single photoelectron level (Level 0 hits, L0). The data output rate is from 0.3 GB/s to 1 GB/s, depending on background and on the number of active strings. A subset of L0 fulfilling particular conditions were defined for triggering purposes (Level 1 hits, L1). This subset corresponds either to coincidences within 20ns of L0 hits on the same triplet of OM of a storey, or a single high amplitude L0 (typically  $> 3$  p.e.). The DataFilter processes all data online and looks for a physics event by searching a set of correlated L1 hits on the full detector on a  $\sim 4 \mu\text{s}$  window. When an event is found, all L0 hits of the full detector during the time window are written on disk, otherwise the hits are thrown away. Each DataFilter program running on a PC, see Figure 3, has to finish processing a  $\sim 100\text{ms}$  time slice before it receives the next. This imposes an optimisation of the DataFilter programs in terms of processing speed and determines the specifications and number of the PCs required for online data processing.

During the 5-line data taking period, the trigger rate was a few Hz. The rate of reconstructed atmospheric muons is around 1 Hz. When ANTARES receives an external GRB alerts <sup>7)</sup>, all the activity of the detector is recorded for a few minutes. In addition, untriggered data runs were collected on a weekly basis. This untriggered data subset is used to monitor the relative PMT efficiencies, as well as to check the timing within a storey, using the  $^{40}\text{K}$  activity. The coincidence rate of the Cherenkov photons coming from a single  $^{40}\text{K}$  decay on 2 PMTs of a storey is estimated by a Monte Carlo calculation which include the simulation of the OM, to be  $(13 \pm 4)$  Hz. This is in very good agreement with the measured value of  $(14.5 \pm 0.4)$  Hz.

Contrary to the  $^{40}\text{K}$  background, the bioluminescence suffers from seasonal and annual variations, see Figure 2. Since September 2006 the mean rate is below 100 kHz 75% of the time. A safeguard against bioluminescence burst is applied online by means of a high rate veto, most often set to 250 kHz.

#### 4 The time and positioning calibration systems

The reconstruction of the muon trajectory is based on the differences of the arrival times of the photons between optical modules (OMs). ANTARES is expected to achieve very good angular resolution ( $< 0.3^\circ$  for muon events above 10 TeV). The pointing accuracy of the detector is determined largely by the

overall timing accuracy of each event. It is necessary to monitor the position of each OM with a precision of  $\sim 10$  cm (light travels 22 cm per ns in water). The pointing accuracy thus is limited by: *i*) the precision with which the spatial positioning and orientation of the OM is known; *ii*) the accuracy with which the arrival time of photons at the OM is measured; *iii*) the precision with which local timing of individual OM signals can be synchronised with respect to each other.

The lines are flexible and move with the sea current, with displacements being a few metres at the top for a typical sea current of 5 cm/s. The positions of the OMs are measured in real-time, typically once every few minutes, with a system of acoustic transponders and receivers on the lines and on the sea bed together with tilt meters and compasses. The shape of each string is reconstructed by performing a global fit based on all these information. Additional information needed for the line shape reconstruction are the water current flow and the sound velocity in sea water, which are measured using different equipments: an Acoustic Doppler Current Profiler; a Conductivity-Temperature-Depth sensors; a Sound Velocimeter.

The time resolution between OMs is limited by the transit time spread of the signal in the PMTs (about 1.3 ns) and by the scattering and chromatic dispersion of light in sea water (about 1.5 ns for a light propagation of 40 m). The electronics of the ANTARES detector is designed to contribute less than 0.5 ns to the overall time resolution.

Complementary time calibration systems are implemented to measure and monitor the relative times between different components of the detector at the one ns level. These time calibrations are performed by:

*i*) the internal clock calibration system. It consists of a 20 MHz clock generator on shore, a clock distribution system and a clock signal transceiver board placed in each LCM. The system also includes the synchronisation with respect to Universal Time, by assigning the the GPS timestamp to the data. This system provides the absolute timing up to the level of each LCM.

*ii*) The internal Optical Module LEDs: inside each OM there is a blue LED attached to the back of the PMT. These LEDs are used to measure the relative variation of the PMT transit time using data from dedicated runs.

*iii*) The Optical Beacons <sup>8)</sup>, which allow the relative time calibration of different OMs by means of independent and well controlled pulsed light sources distributed throughout the detector.

*iv*) Several thousands of down-going muon tracks are detected per day. The hit time residuals of the reconstructed muon tracks can be used to monitor the time offsets of the OM, enabling an overall space-time alignment and calibration cross-checks.

## 5 Atmospheric muons

Although ANTARES is located under a large water depth, a great number of atmospheric muons reach the active volume. They are produced in the decay of charged mesons produced at 10-20 km height by the interactions of primary cosmic rays (CR) with atmospheric nuclei. They represent the most abundant signal in any neutrino telescope and can be used to calibrate the detector and to check the simulated Monte Carlo response to the passage of charged particles. On the other side, atmospheric muons constitute the major background source, mainly because they can incorrectly be reconstructed as upward-going particles mimicking high energy neutrino interactions. Muons in bundles seem to be particularly dangerous.

### 5.1 Monte Carlo simulations

In ANTARES, two different Monte Carlo simulations are used to generate atmospheric muons: one based on a full Corsika simulation, and another based on a parameterisation of the underwater muon flux.

**Full Monte Carlo.** The full Monte Carlo simulation <sup>9)</sup> is based on Corsika <sup>10)</sup>, starting from the interactions of primary CR with atmospheric nuclei. An angular range from 0 to 85 degrees and an energy per nucleon range from 1 TeV to 100 PeV are considered for the primaries. At lower energies the produced muons cannot reach anymore the detector whereas at higher energies the primary flux becomes negligibly small. The package QGSJET <sup>11)</sup> for the hadronic shower development has been chosen, because it has the lowest CPU need among several packages with equivalent results. As output of the first step of the simulation, muon events at the sea surface are obtained. In the next step the muons are propagated to the detector using the muon propagation program MUSIC <sup>12)</sup>, which includes all relevant muon energy loss processes. At the end of this second step muons on the surface of a virtual underwater cylinder (*can*) are obtained. The *can* defines the limit inside which charged particles are propagated using GEANT-based programs, producing also Cherenkov photons <sup>9)</sup>. Then, the background (extracted from real data) is added and the events are feed to a program which reproduces the DataFilter trigger logic. After this step, the simulated data have the same format as the real ones.

The main advantage of the full Monte Carlo simulation is that it is done with a simple  $E^{-\gamma}$  spectrum for the primary flux for all nuclei. This allows a later re-weighting with any chosen primary flux model. The drawback is that a very large amount of CPU time is needed.

**Monte Carlo with parametric formulas.** A second data set is generated using parametric formulas <sup>13)</sup>, which allow a fast generation of a very large sample of atmospheric muons.

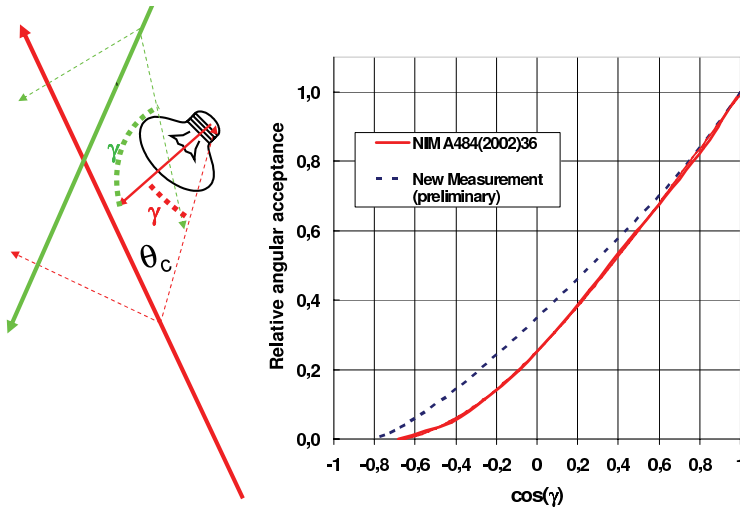


Figure 4: *Left: sketch of the photon detection. The Cherenkov angle in water is  $\sim 42^\circ$ : upward (downward) going muons produce mostly photons arriving with an angle  $\gamma$  smaller (larger) than  $90^\circ$  with respect to the PMT axis. Right: measured acceptance of the ANTARES OM. A recent measurement shows a larger acceptance with respect to that with an older configuration.*

The used parameterisation of the flux of underwater muon bundles is based on a full Monte Carlo simulation of CR interaction and shower propagation in the atmosphere using the HEMAS code <sup>14)</sup>, with DPMJET <sup>15)</sup> to calculate the hadronic shower development. The adopted primary CR flux is an un-published model which reproduces the muon flux (single and multiple muons) and energy spectrum as measured by the MACRO experiment <sup>16)</sup>. The muons reaching the sea level are then propagated using MUSIC down to 5.0 km w.e. The characteristics of underwater muon events (flux, multiplicity, radial distance from the axis bundle, energy spectrum) are described with multi-parameter formulas in the range 1.5 ÷ 5.0 km w.e. and up to  $85^\circ$  for the zenith angle. In particular, the energy spectrum of muons depends on the vertical depth  $h$ , on the zenith angle  $\theta$ , on the muon multiplicity in the shower  $m$  and on the distance of the muon from the shower axis  $R$ .

Using this parameterization, an event generator (called MUPAGE) was developed <sup>17)</sup> in the framework of the KM3NeT project <sup>18)</sup> to generate underwater atmospheric muon bundles. In the case of ANTARES, the events are generated on the *can* surface. Then, the muons are propagated with the production of Cherenkov light, the background added and the events fed to the trigger logic as in the case of the full Monte Carlo.

The main advantage of this simulation is that a large sample is produced

with a relatively small amount of CPU time (much less than the time needed to simulate the Cherenkov light inside the *can*). A data set with a livetime equivalent to one month, which is used to compare data and MC, required 300 hours of CPU time on a 2xIntel Xeon Quad core, 2.33 GHz processor. The drawback is that the primary CR composition is fixed, and the events cannot be re-weighted.

A larger data set of more energetic atmospheric muons, equivalent to one year of livetime, is generated to study the background rejection criteria in the search of diffuse flux of high energy neutrino ( $E_\nu > 100$  TeV). This sample required 232 hours of CPU time (with the aforementioned processor), when a cut on the total energy of the underwater muons is applied ( $E_{total} > 3$  TeV).

## 5.2 Results for the 5-line run

As expected, atmospheric muons were an important tool to monitor the detector status and to check the reliability of the simulation tools and data taking.

The early comparison of atmospheric muons shows a large discrepancy between data and Monte Carlo, the MC rate being about 1/3 of that measured. This pushed us for systematic checks of all sections in our Monte Carlo simulations (water absorption length and scattering models; Cherenkov light production; tracking algorithm procedure; description of the optical module effective area, etc.) as well as in the analysis data chain (efficiency of the trigger algorithm, etc.).

The main problem was found in the description of the optical module response. The three PMTs in each storey are oriented with axis  $45^\circ$  below the horizontal. They detect light with high efficiency from the lower hemisphere (from where neutrinos are expected), and has some acceptance for muons coming from above the horizontal. The OM angular acceptance used in the MC code (red line in Figure 4) was measured <sup>6)</sup> with an old configuration. It is broad, falling to half maximum at  $70^\circ$  from the axis of the PMT. When re-measured with the present OM configuration (blue line in Figure 4), it shows higher values for incoming photons angles,  $\gamma$ , larger than  $\sim 60^\circ$ . As a consequence, the number of MC reconstructed atmospheric muons increases by 200-300%, while upward going particles (neutrino induced) increases at most by  $\sim 20\%$ . Another small inefficiency was found in the data acquisition by comparing the distribution of the number of triggering hits in data and MC.

The results after the checks in the Monte Carlo and in the data acquisition chain are shown in Figure 5 and 6. Figure 5 shows the distribution of the number of hits used by the trigger process (DataFilter) to trigger the event in data and Monte Carlo (atmospheric muons from MUPAGE <sup>17)</sup>). Figure 6 shows the zenith and azimuth angle distribution of reconstructed events (without any quality cuts) in data (black) and MC (red). At present, a systematic

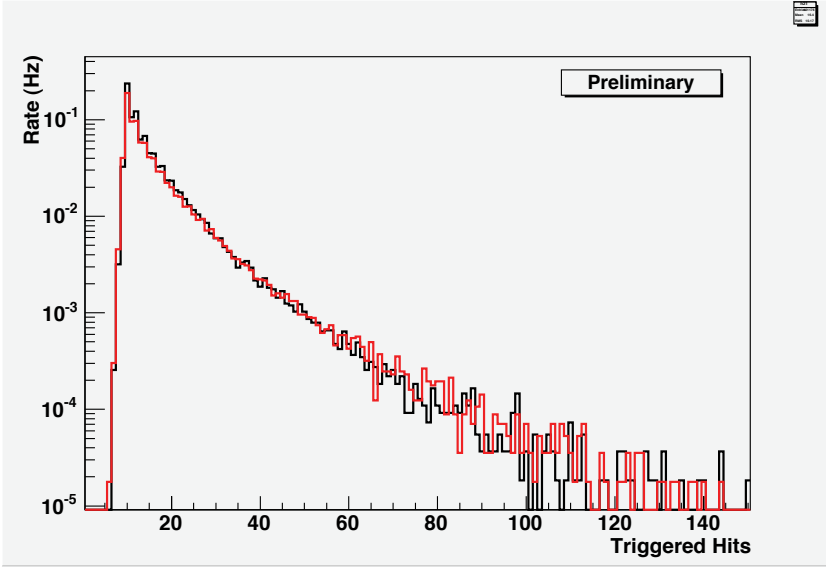


Figure 5: The trigger process (*DataFilter*) act on a subset of hits, the so called *L1 hits* (see text). When a sufficient number of correlated *L1 hits* is found, the data are considered as due to a physics event and all information from a  $\sim 4\mu\text{s}$  time window written to disk. The triggered hits are those hits which enabled the trigger logic. The figure shows the triggered event rate (in Hz) versus the number of triggered hits in the event. Black histogram: data. Red histogram: Monte Carlo (atmospheric muons).

error (constant for all bins) of  $\sim 40\%$  which include the uncertainties on the interaction model but not that on the primary CR composition is estimated for the MC predictions. In the figure, the data and MC are not normalized but the agreement in the integrated data should be consider fortuitous, due to the used CR composition model.

The quality cuts in the reconstruction applied for the selection of neutrino candidates are needed in order to reduce the badly reconstructed downward going events mimicking upward going tracks (see next section).

## 6 Neutrino candidates from the 5 Line data set

The bulk of triggered events are due to downward going atmospheric muon. A first, very preliminary, analysis has been performed on some high quality data, ignoring all storeys positioning aspects and assuming straight lines. The alignment, results of line shape fits using slow control positioning data available every 6 minutes, is currently implemented in track reconstruction, and will soon

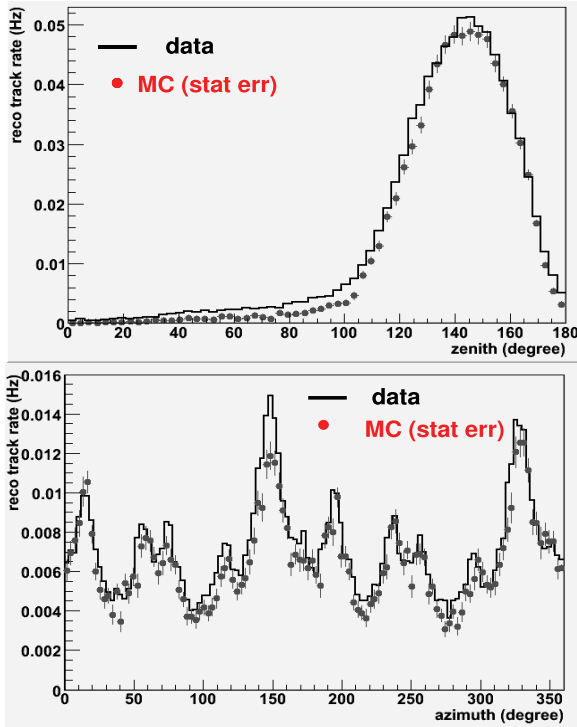


Figure 6: Zenith (upper plot) and azimuth (lower plot) distribution of atmospheric muons detected in the 5-line run. Black: experimental data. Red: MC simulation. The shape of the azimuth distribution reflects the geometry of the 5 line detector.

allows for a much efficient determination of the neutrino candidates.

Figure 7 shows the comparison between reconstructed data and Monte Carlo. The data sample consists of 36.8 days of active time from selected runs between 01/02/2007 and 25/05/2007. The atmospheric muons are from the Corsika-based Monte Carlo, with the primary CR flux of <sup>19</sup>). The neutrino events are simulated using the Bartol flux <sup>20</sup>). Only events detected at least by two lines and with at least 6 floors are considered. The integrated rates (after quality cuts) as shown on the plots are 0.07 Hz for data and 0.10 Hz for atmospheric muons. Restricting to the upward going hemisphere (neutrino candidates) this becomes 1.4 per day for data, 0.11 per day for atmospheric muons and 0.84 per day for atmospheric neutrinos. When this information is included, the number of reconstructed events per day is expected to increase by at least a factor of three, with an higher angular resolution.

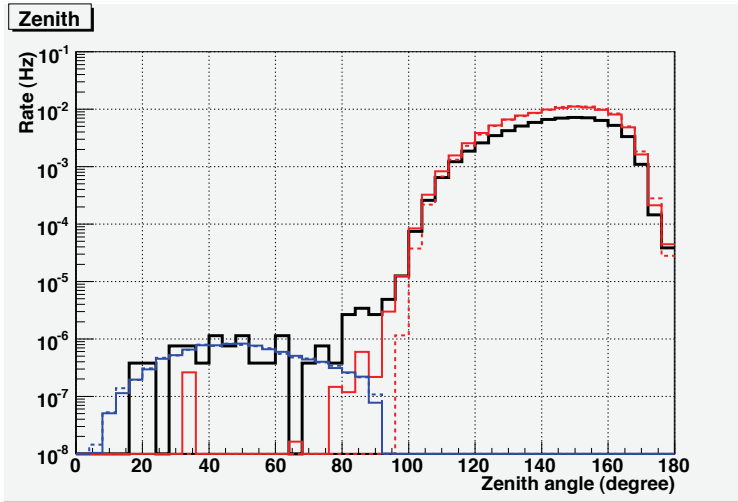


Figure 7: Zenith angle distribution of detected events after quality cuts. Upgoing events have zenith angle  $< 90^\circ$ . Black lines represent data. Red stands for atmospheric muons, and blue indicates atmospheric neutrinos. MC-truth is shown as dotted lines, full lines are reconstruction results. For this analysis, the dynamic positioning of each OM was NOT used.

## 7 Expected performances

The expected performances of the full 12-line detector have been estimated by computer simulation. The capabilities of the telescope can be characterized by several quantities. For instance, the muon effective area gives the ratio of the number of well-reconstructed (*selected*) muon events to the incoming muon flux. The effective area increases with energy: it is  $0.02(0.04) \text{ km}^2$  for  $E_\nu = 10(100) \text{ TeV}$  and reaches  $0.08 \text{ km}^2$  for neutrino energies larger than  $10^4 \text{ TeV}$ . These values assume *selected* events, in such a way that the median of the distribution of the angular difference in space between the reconstructed muon track and the original parent neutrino is better than  $0.3^\circ$ . The angle between the parent neutrino and the muon is dominated by kinematics effects up to around  $10 \text{ TeV}$ . Above that energy, the instrumental resolution is the limiting factor. A good angular resolution helps to reject the background whenever the source position is relevant, as is the case in the search of point-like sources.

The energy of the crossing muon or of secondary particles generated by neutrino interactions inside the instrumented volume is estimated from the amount of light deposited in the PMTs. Several estimators based on different techniques were developed<sup>21)</sup>. MC studies show that this resolution is between  $\log_{10}(\sigma_E/E) = 0.2 \div 0.3$  for muons with energy above  $1 \text{ TeV}$ . The event energy

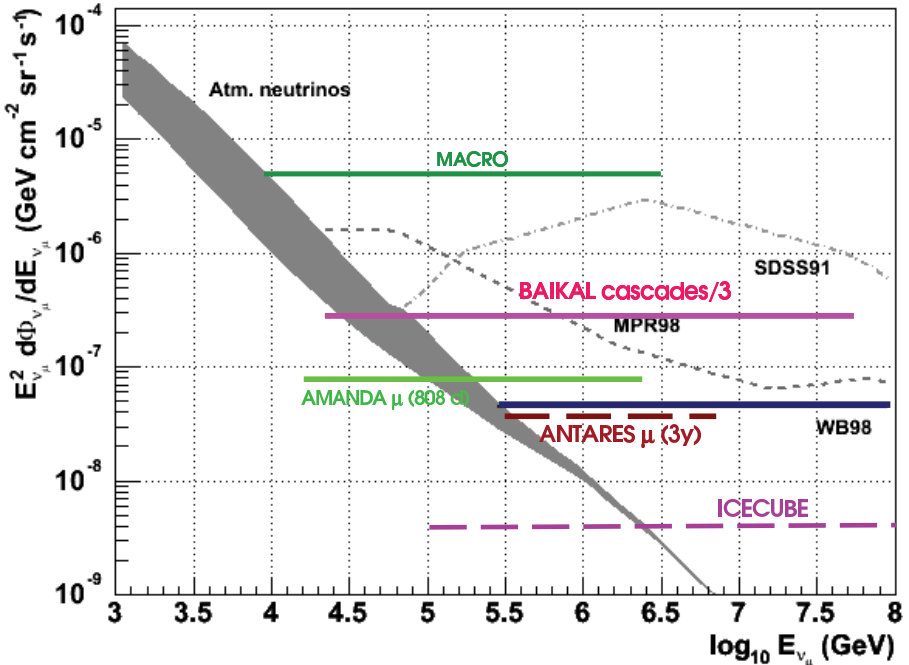


Figure 8: Diffuse flux scaled to an  $E^{-2}$  spectrum as a function of the neutrino energy. The upper limit that ANTARES can set in 3 year is indicated together with the expected atmospheric flux, some theoretical predictions and limits from other experiment.

measurement is a mandatory requirement for the study of the diffuse flux of high energy neutrinos. The link between the extra-galactic sources of cosmic rays, gamma-rays and neutrinos leads to severe limits on the neutrino diffuse flux expressed in the Waxman and Bahcall (WB98) upper limit  $E^2\Phi < 4.5 \times 10^{-8} \text{ GeV cm}^{-2} \text{ s}^{-1} \text{ sr}^{-1}$  (22). Monte Carlo simulations indicate that after 3 year of data taking ANTARES can set an upper limit for diffuse fluxes of  $E^2\Phi < 3.9 \times 10^{-8} \text{ GeV cm}^{-2} \text{ s}^{-1} \text{ sr}^{-1}$ , just below the WB98 upper limit (Figure 8). This value marks a limit for a list of known candidate sources, but must be corrected to take into account neutrino oscillations.

The ANTARES sensitivity to point-like sources is estimated as a function of the declination. The 90% C.L. upper limit for the  $\nu_\mu + \bar{\nu}_\mu$  flux from point-like sources we can set in case of a null signal after one year of data taking is  $E^2 dN/dE_\nu = 4 \times 10^{-8} \text{ GeV cm}^{-2} \text{ s}^{-1}$  for a declination of  $\delta = -90^\circ$  and rises to  $1.5 \times 10^{-7} \text{ GeV cm}^{-2} \text{ s}^{-1}$  for  $\delta = +40^\circ$ . These limits improve those of SuperKamiokande and MACRO from the Southern sky and are comparable to those obtained by AMANDA II in 1001 days from the Northern sky.

## 8 Prospective and conclusions

ANTARES is at present the largest neutrino observatory in the Northern hemisphere, which represents a privileged sight of the most interesting areas of the sky like the Galactic Centre, where neutrino source candidates are expected. It is able to explore the Southern sky hemisphere in the search for astrophysical neutrinos with a sensitivity much better than any other previous experiments.

ANTARES is also the most advanced pilot neutrino telescope in the Mediterranean sea toward the km<sup>3</sup>-scale telescope, with a strong relationship and cooperation with the NEMO <sup>23</sup>) project. Most of the theoretical models put the sensitivity for discovering neutrino sources at a level for which a telescope  $\sim 50$  times larger than ANTARES is required (or 3 times IceCube, which observes the complementary sky region). While ANTARES is taking and analyzing data, some of the collaboration activities are continuing in the framework of the KM3NeT project <sup>18</sup>).

The KM3NeT Design Study is a 3-year project (started in 2006) which is founded by the EU within the VI Framework Programme. The Design Study objective is to produce a Technical Design Report by the Summer 2009. For this report, decisions on the implementations of the different components of the Neutrino Telescope must be taken, with a full costing of the solutions. A Conceptual Design Report will be released at the end of this month. In parallel, in March 2008, the Preparatory Phase of the KM3NeT project has started and will continue until March 2011. In this phase, a small-scale engineering model of the detection unit and the sea-floor infrastructure will be produced. The final selection of the site will be pursued in the framework of the Preparatory Phase and will likely involve decisions at the political level.

## References

1. For more information and for a complete list of the ANTARES members see: <http://antares.in2p3.fr>
2. V. Berezhinsky et al., *Astrophysics of Cosmic Rays*, North-Holland, Amsterdam (1990).
3. F. Halzen and E. Zas, *Astrophys. J.*, **488**,669 (1997).
4. T. Piran, *Rev. Mod. Phys.* **76**,1143(2004).
5. P. Amram et al., *Astropart, Phys.* **13**, 127(2000); P. Amram et al., *Astropart, Phys.* **19**, 253(2003); J. A. Aguilar et al. *Astropart, Phys.* **23**, 131(2005).
6. P. Amram et al., *Nucl. Instr. and Methods A* **484**,369 (2002).

7. J.A. Aguilar et al., Nucl. Instr. and Methods **A570**, 107 (2007).
8. M. Ageron et al., Nucl. Instr. and Methods A **578**, 498 (2007).
9. J. Brunner, Antares simulation tools, VLVnT Workshop on Technical Aspects of a Very Large Volume Neutrino Telescope in the Mediterranean Sea, Amsterdam, The Netherlands, 5-8 Oct 2003. <http://www.vlvnt.nl/proceedings/>
10. D.Heck et al., CORSIKA: A Monte Carlo Code to Simulate Extensive Air Showers, Forschungszentrum Karlsruhe Report **FZKA-6019** (1998).
11. N.N.Kalmykov, S.S.Ostapchenko, A.I.Pavlov, Nucl. Phys. B (Proc. Suppl.) **52B**, 17 (1997).
12. P. Antonioli, et al., Astropart. Phys. **7**, 357 (1997).
13. Y. Becherini, A. Margiotta, M. Sioli and M. Spurio, Astrop. Phys. **25**, 1 (2006).
14. C. Forti *et al.*, Phys. Rev. D **42**, 3668 (1990).
15. J.Ranft, Phys. Rev. **D51**,64 (1995); arXiv:hep-ph/0002137 (2000).
16. M. Ambrosio et al. (The MACRO Collaboration), Phys. Rev. **D 56**, 1407 (1997); M. Ambrosio et al. (The MACRO Collaboration), Astropart. Phys. **10**,11(1999); M. Ambrosio et al. (The MACRO Collaboration), Astropart. Phys. **19**,313 (2003).
17. G. Carminati, A. Margiotta, M. Spurio. Atmospheric MUons from PArametric formulas: A Fast GEnerator for neutrino telescopes (MUPAGE). arXiv:0802.0562 .
18. <http://www.km3net.org>
19. J. Horandel, Astrop. Phys. **19**, 193 (2003).
20. V. Agrawal, T.K. Gaisser, P. Lipari, T. Stanev, Phys. Rev. **D53**,1314 (1996).
21. A. Romeyer, R. Bruijn, and J.D. de Zornoza: 2003, Proceedings of the 28th International Conference on Cosmic Rays, vol. 3, pp. 1329-1332.
22. E. Waxman and J. Bahcall, Phys. Rev. **D59** 023002-1 (1998); J. Bahcall, E. Waxman: Phys. Rev. **D64** 023002-1 (2001).
23. E. Migneco et al., Nucl. Instr. and Methods A **588**, 111 (2008).

# NEUTRINOS, GRAND UNIFIED THEORIES AND THE HIERARCHY PROBLEM

Francesco Caravaglios  
*Dipartimento di Fisica, Università di Milano, Via Celoria 16,  
I-20133 Milano, Italy*  
and *INFN sezione di Milano*

## Abstract

The Standard Model correctly describes all interactions at (and below) the electroweak scale. However it does not explain the peculiar pattern of quark, lepton and neutrino masses. Also charge quantization is not understood. These are well known motivations to go beyond the Standard Model and to build a Grand Unified Theory. This extension has several good predictions but the proton lifetime is huge compared to similar weak decays. This hierarchy problem suggests two possible extensions of the standard quantum field theory: a non linear version of the Schroedinger functional equation and Third Quantization.

## 1 Introduction

The theory that describes the strong, electromagnetic and weak interactions is based on the gauge group  $SU(3) \times SU(2) \times U(1)$ . The symmetry group is spontaneously broken and the gauge boson together with the matter fermions become massive. If and only if the scalar field responsible for electroweak symmetry breaking is a  $SU(2)$  doublet with hypercharge  $-1/2$  we get the well known relation

$$\frac{M_W^2}{M_Z^2} = \cos^2(\theta_W) \quad (1)$$

that relates the weak boson masses with the coupling constants in the interaction between weak boson and fermions. Also charge quantization comes from this peculiar choice for the Higgs hypercharge, and this choice is natural in Grand Unified Theories as we will see later. The Standard Model gives a correct description of all forces that act at and below the weak scale. In fact it provides us with several theoretical predictions for all the observables listed in Table 1.

Adding an extra  $Z'$  or additional Higgs doublets does not improve the fit of data; on the contrary these extensions of the Standard Model are strongly constrained by these data (Table 1). The the top mass obtained in this fit is in very good agreement with the direct experimental observation. The Higgs mass seems to be not very large, probably the Higgs is lighter than the top. When the top mass is very heavy, as proven by experiments, the radiative corrections to the effective potential are large. This theoretical extrapolation of the standard theory to values of the Higgs average field much higher than the weak scale, shows that the value of 246 GeV deduced from the weak boson masses is not a global minimum if  $M_H$  does not satisfy the inequality <sup>1, 2)</sup>

$$M_H \gtrsim 75 + 1.64(m_t - 140) - 3\left(\frac{\alpha_s - 0.117}{0.007}\right) \quad (2)$$

This limit holds in the standard theory. As we will see after, the effective potential is a theoretical extrapolation of the energy of the universe to quantum physical states very far from the present universe that we observe, however we know that theories often have a wide validity region that can often cover several order of magnitudes. The validity of maxwell equations, as well as quantum

mechanics have been proved in several extremely different experimental situations. If the effective potential of the standard theory has a validity extended over several order of magnitudes of the Higgs average field could be challenged not only by the limit (2) but also by the so called hierarchy problem that appears when the group  $SU(3) \times SU(2) \times U(1)$  is embedded into a unified gauge group. We mention the following arguments that motivate us to embed the standard theory into a grand unified theory. The first motivation is the charge quantization and the quantum numbers of the matter fermions. In Table 2 we give a list of some reducible representation of  $SU(3) \times SU(2) \times U(1)$  that are anomaly free. We observe that the unifying group  $SU(5)$  predicts that matter fermions correspond to the choice of the last row. On the contrary, other rows are acceptable anomaly free representations that do not immediately lead to any unified group.

Without the assumption of a unified theory that includes a flavor symmetry, it remains a mystery why nature has chosen three times the last row (Table 2) for the three families <sup>3)</sup>. Also the Higgs hypercharge, that is a completely arbitrary choice without unification hypotheses, find an obvious explanation within  $SU(5)$ . Among all possible groups of unification  $SU(5)$ ,  $SO(10)$  and  $E_6$  are the most favored candidates. These are the arguments in favor of unification, but we have not yet understood why the proton lifetime is huge, if compared with the muon decay and the neutron decay lifetime. This is the hierarchy problem, *i.e.* the need of an explanation for the gauge lepto-quark boson masses and the weak boson masses. The effective potential responsible for the symmetry breaking pattern  $SU(5) \rightarrow SU(3) \times SU(2) \times U(1) \rightarrow SU(3)_{\text{col}} \times U(1)_{\text{em}}$  is written

$$V = -\mu^2 H^2 - m^2 \Sigma^2 + \lambda_1 H^4 + \lambda_2 H \Sigma^2 H + \lambda_3 \Sigma^4 \quad (3)$$

where  $\Sigma$  and  $H$  are respectively the **24** and the **5** of  $SU(5)$ . We have to choose the arbitrary parameters  $\mu, m, \lambda_2$ , with an extreme fine tuning if we want the hierarchy  $\tau_{\text{prot}} \gg \tau_{\mu}$  between the proton and the muon lifetime. We will see how it is possible to modify the standard theory in order to obtain a simple explanation of the hierarchy problem.

Table 1: *The electroweak data and the Standard Model fit* <sup>4)</sup>.

observable	experimental value	SM prediction	pull
$M_Z$	$91.1876 \pm 0.0021$	$91.1874 \pm 0.0021$	0.1
$\Gamma_Z$	$2.4952 \pm 0.0023$	$2.4968 \pm 0.0011$	-0.7
$\sigma_{\text{had}}^0$ [nb]	$41.541 \pm 0.037$	$41.467 \pm 0.009$	2.0
$R_e$	$20.804 \pm 0.050$	$20.756 \pm 0.011$	1.0
$R_\mu$	$20.785 \pm 0.033$	$20.756 \pm 0.011$	0.9
$R_\tau$	$20.764 \pm 0.045$	$20.801 \pm 0.011$	-0.8
$R_b$	$0.21629 \pm 0.00066$	$0.21578 \pm 0.00010$	0.8
$R_c$	$0.1721 \pm 0.0030$	$0.17230 \pm 0.00004$	-0.1
$A_{FB}^e$	$0.0145 \pm 0.0025$	$0.01622 \pm 0.00025$	-0.7
$A_{FB}^\mu$	$0.0169 \pm 0.0013$		0.5
$A_{FB}^\tau$	$0.0188 \pm 0.0017$		1.5
$A_{FB}^b$	$0.0992 \pm 0.0016$	$0.1031 \pm 0.0008$	-2.4
$A_{FB}^c$	$0.0707 \pm 0.0035$	$0.0737 \pm 0.0006$	-0.8
$A_{FB}^s$	$0.0976 \pm 0.0114$	$0.1032 \pm 0.0008$	-0.5
$\bar{s}_l^2$	$0.2324 \pm 0.0012$	$0.23152 \pm 0.00014$	0.7
	$0.2328 \pm 0.0050$		-1.5
$A_e$	$0.15138 \pm 0.00216$	$0.1471 \pm 0.0011$	2.0
	$0.1544 \pm 0.0060$		1.2
	$0.1498 \pm 0.0049$		0.6
$A_\mu$	$0.142 \pm 0.015$		-0.3
$A_\tau$	$0.136 \pm 0.015$		-0.7
	$0.1439 \pm 0.0043$		-0.7
$A_b$	$0.923 \pm 0.020$	$0.9347 \pm 0.0001$	-0.6
$A_c$	$0.670 \pm 0.027$	$0.6678 \pm 0.0005$	0.1
$A_s$	$0.895 \pm 0.091$	$0.9356 \pm 0.0001$	-0.4
$M_W$			

Table 2: Representations of the Standard Model gauge group  $SU(3) \times SU(2) \times U(1)$ . The last row corresponds to the  $10 + \bar{5}$ , the minimal and anomaly free chiral representation of  $SU(5)$ .

$(3,3)(-1) + (3,2)(4) + (3,1)(-5)$
$(1,1)(-5/6) + (1,1)(-5/6) + (1,1)(-1/6) + (1,1)(1/3) + (1,1)(1/2) + (1,1)(1)$
$(3,2)(4) + (3,2)(-4) + (1,2)(1) + (1,2)(-1)$ vectorlike
$(1,2)(-1/2) + (3,1)(1/3) + (1,1)(1) + (3,1)(-2/3) + (3,2)(1/6) \subset 10 + \bar{5}$

## 2 Non linear extension of quantum field theory

The free classical hamiltonian of a scalar real field is written

$$\mathcal{H} = \int d^3x \pi^2(x) + \phi(-\nabla^2 + m^2)\phi(x). \tag{4}$$

We have to replace the functions  $\pi(x)$  and  $\phi(x)$ , defined in the three-dimensional space  $x$ , with two operators  $\hat{\pi}(x)$  and  $\hat{\phi}(x)$  that satisfy the commutation rules

$$\left[ \hat{\pi}(x), \hat{\phi}(y) \right] = i \delta^3(x - y). \tag{5}$$

This quantizes the hamiltonian above (4). We can also give a representation of the algebra (5) of the operators  $\hat{\pi}(x)$  and  $\hat{\phi}(x)$  in the space of functionals  $S[\phi]$ , replacing  $\hat{\pi}(x)$  and  $\hat{\phi}(x)$  with

$$\begin{aligned} \hat{\phi}(x)|S > &\rightarrow \phi(x) S[\phi] \\ \hat{\pi}(x)|S > &\rightarrow i \frac{\delta}{\delta\phi(x)} S[\phi] \end{aligned} \tag{6}$$

It is easy to verify that they satisfy the algebra (5)

$$\left[ i \frac{\delta}{\delta\phi(x)}, \phi(y) \right] = i \delta^3(x - y). \tag{7}$$

In the Schroedinger picture, the physical states of quantized field are described by the functional  $S[\phi, t]$ , whose time dependence  $t$ , is given by the Schroedinger equation

$$i \frac{\partial}{\partial t} S[\phi, t] = \int d^3x \left( -\frac{\delta^2}{\delta \phi^2(x)} - \phi(x) \nabla^2 \phi(x) + m^2 \phi^2(x) \right) S[\phi, t] \quad (8)$$

The equation (8) represent the quantized theory of a free scalar field. The mass  $m$  is a fundamental and arbitrary constant. In the case of a free particle,  $m$  coincides with the physical measured mass, but in the general case of an interacting field it does not coincide with the physical mass, because it also depends on the radiative corrections due to the presence of interactions, and on any possible vacuum expectation value of other scalar fields. For example in (3) the value of  $\mu$  necessary to get a very light higgs at the weak scale, is around  $10^{16}$  GeV, *i.e.* the order of magnitude of the vev of  $\Sigma$ . The fine tuning is needed to achieve a cancellation between several contributions. In other words this correspond to a very precise choice for  $\mu$ , very close to the arrow depicted in Fig.1. Since  $\mu$  is a free parameter, the choice of  $\mu$  very close to the arrow (Fig.1) is accidental and would give not natural predictions. Now we will see how this odd fine tuning can be explained in a non linear extension of the equation (8). Let us assume that we add a non linear term that modifies eq. (8) as follows

$$i \frac{\partial}{\partial t} S[\phi, t] = \hat{H} S[\phi, t] + \int d^3x J(x, t) \phi^2(x) S[\phi, t] \quad (9)$$

$$J(x, t) = \int D\phi S^\dagger[\phi, t] \phi(x)^2 S[\phi, t]$$

When the non linear term  $J(x)$  is very small and negligible the equation (9) reduces to a linear equation and it describes an ordinary quantum field theory. But in certain physical situations  $J(x)$  could be not negligible<sup>1</sup>. Let us consider the case when  $J(x)$  is small but not negligible, and we can solve the equation (9) in perturbation theory. The simplest non trivial case is when  $J(x, t)$  is a constant and does not depend on space and time. This happens when the functional  $S$  corresponds to physical systems where the field  $\phi$  has constant and non zero vev. For any fixed value of  $J$  eq.(9) is linear, and we know that such a linear equation admits a stationary solution  $S[\phi, t]$  when the expectation value of  $\phi$  minimizes the effective potential (with  $J$  fixed).  $S[\phi, t]$  is

---

<sup>1</sup>When the physical state  $S[\phi, t]$  is a system that contains one (or more) scalar particles  $\phi$ , then  $J$  is proportional to the wave function squared of this particle.

the wave functional of the state with minimal energy. The vev of  $\phi$  depends on the arbitrary choice of  $J$ , but also  $J$  (in the non linear case) is a function of the vev  $\phi$ . Thus both the vev  $\phi$  and the constant  $J$  are two variables determined by two equations (9). The non linear term in (9) can be replaced by any generic dependence on the vev  $\phi$ , in fact the second eq.(9) is an arbitrary physical choice. An illustrative choice like

$$\mu^2(\phi) = \mu^2 + J = -M_{\text{unif}}^2 \log(\phi/M_{\text{unif}}) \quad (10)$$

could even explain the hierarchy problem. In fact in the linear theory the vacuum expectation value is a function of the arbitrary constant  $\mu$  (see Fig.1), but in the non linear theory  $\mu$  is not arbitrary and depends on  $\phi$  (see eq.(9) and eq. (10)). The special dependence (10) explains why the intersection of both curves<sup>2</sup> (Figure 1 ) happens when the vev  $\phi$  is very small *i.e.* close to the arrow. This explains the hierarchy problem.

However a non linear extension of the Schroedinger functional equation shows the lack of a theory of measurement. If a state  $S$ , evolves from being the superimposition of several eigenstates toward a single eigenstate of an observable, because of a measurement, then this time evolution also affects (9) and the probability distribution of the final states is automatically modified. In other words the time evolution deduced from equation (9) can be considered valid until when no measurement is performed<sup>3</sup>.

There is another extension of the field theory that does not violate the quantum mechanical principle of linear superimposition in the evolution of physical states and that could explain in a similar way the hierarchy problem. But before introducing this new theory we deepen briefly the safety of a collider like the LHC in the context of a non linear extension.

It is not hard to realize that if we abandon the request of linearity in eq. (8), various possible extensions are possible, each one with a phenomenology

---

<sup>2</sup>The first curve is the dependence of the vev from  $\mu$  as from the minimization of (3); the second curve comes from the dependence of  $\mu$  (or equivalently  $J$ ) from the vev.

<sup>3</sup>Note that even the definition of measurement in quantum mechanics is rather ambiguous. And this put an ambiguity on the extent of validity of eq.(9).

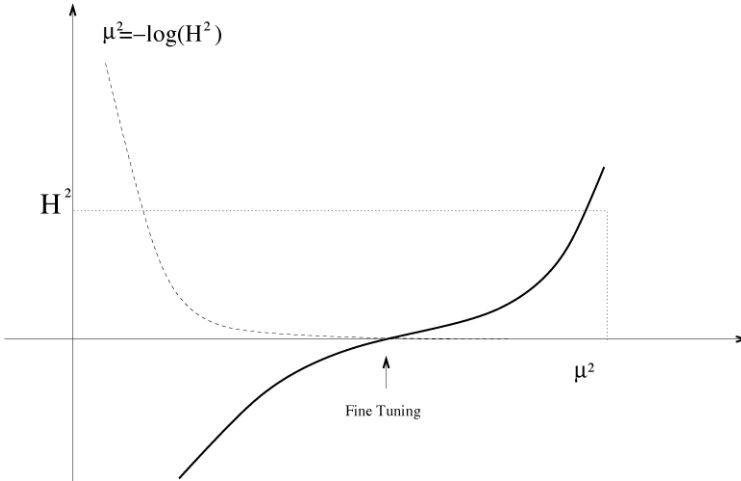


Figure 1: The Higgs doublet vev  $H^2 = \langle \phi^2 \rangle$  as a function of the bare mass  $\mu^2$  (solid curve). The dashed curve comes from the non linear term and gives the bare mass  $\mu^2$  as a function of the vev  $H$  (see eq.(10 in the text)).

and with physical consequences that are completely unexpected. Even if an exhaustive discussion of all possible cases is very difficult or even impossible, we briefly draw our attention to few cases that probably deserve more attention. Firstly, let us note that the limit <sup>1, 2)</sup> on the higgs mass due to the requirement of stability of the vacuum cannot be directly applied in a non linear extension of the standard theory. Let us now see some potential risks: the creation of a new exotic particle  $\phi$  at the collider LHC locally changes the value of  $J$  (9), that is in the region occupied by the wave packet of this scalar particle. This could modify the fundamental bare constants of the linearized theory. It would also modify the physical masses and the couplings of the standard particles: for example the photon could become massive, and all electromagnetic interactions would be turned off in a region of finite volume<sup>4</sup>.

Another risk could come from the fact that the non linear theory violates the crossing symmetry and thus the production of very light particles with

---

<sup>4</sup>The theory of quantum mechanics does not put any bound on the size of a wave packet

strong interaction with matter is not incompatible with the observation of previous accelerators. We remind also that non linear interactions with the simultaneous presence of significant amount of dark matter in the solar systems adds other dangerous scenarios.

### 3 Third Quantization

A similar but alternative explanation of the hierarchy problem is obtained embedding second quantization into third quantization <sup>5, 6</sup>). The embedding of first quantization into second quantization proceeds as follows. The Schroedinger equation for one particle is written

$$i \frac{\partial}{\partial t} \psi(x, t) = H \psi(x, t) \quad (11)$$

and in fact the quantum state of a particle in the Schroedinger picture is a wave function  $\psi(x)$ . The wave function is replaced by an operator when we go to second quantization (quantum field theory)

$$\psi(x) \Rightarrow \hat{\psi}(x) \quad (12)$$

and we set the following anticommutation rules

$$\left\{ \hat{\psi}(x), \hat{\psi}^\dagger(y) \right\} = \delta^3(x - y). \quad (13)$$

The quantum field theory analogue of eq.(11) is eq.(8). This equation (8) tells us that the quantum state of the universe is described by a functional  $S[\phi, t]$  where the variable  $t$  denotes the time evolution of the physical state. If we repeat the same steps as for going from first quantization to second quantization, and we want to embed second quantization into third quantization, then the functional  $S[\phi]$  becomes an operator

$$S[\phi] \Rightarrow \hat{S}[\phi] \quad (14)$$

that satisfies the anticommutation rules

$$\left\{ \hat{S}[\phi], \hat{S}^\dagger[\phi'] \right\} = \delta(\phi - \phi'). \quad (15)$$

As an illustrative example, the simplest hamiltonian can be written

$$\mathcal{H} = \int D\phi \, d^3x \, \hat{S}^\dagger[\phi] \left( -\frac{\delta^2}{\delta \phi^2(x)} - \phi(x) \nabla^2 \phi(x) + m^2 \phi^2(x) \right) \hat{S}[\phi]. \quad (16)$$

The vacuum state  $|0\rangle$  satisfies the condition

$$\mathcal{H}|0\rangle = 0 \quad (17)$$

and represents a state without fields and without space, while the state

$$|F\rangle = \int D\phi \, F[\phi] \, \hat{S}^\dagger[\phi] |0\rangle \quad (18)$$

with

$$F[\phi] = \exp\left(-\frac{1}{2} \int d^3x \, \phi(x) \sqrt{-\nabla^2 + m^2} \phi(x)\right) \quad (19)$$

represents the state of a universe with only one scalar field  $\phi$  and with minimal energy. It is not difficult to verify the the functional (19) minimizes the energy  $E$  among all possible states  $|F\rangle$

$$E = \langle F | \mathcal{H} | F \rangle. \quad (20)$$

Let us see why such a theory can explain the hierarchy problem.

We can add to the hamiltonian (16) new composite operators that contain a larger number of creation/annihilation  $\hat{S}, \hat{S}^\dagger$  operators. We add to the hamiltonian  $\mathcal{H}$  the following interaction

$$\mathcal{H}_{\text{int}} = \int D\phi \, d^3x \sum_{i=1}^n a_n \hat{S}^\dagger[\phi_1] \cdots \hat{S}^\dagger[\phi_n] \phi_1^2(x) \cdots \phi_n^2(x) \hat{S}[\phi_1] \cdots \hat{S}[\phi_n]. \quad (21)$$

We introduce the function  $G(J)$  defined by the sequence of  $a_n$  as follows

$$G(J) = \sum_{n=1}^{\infty} a_n J^n \quad (22)$$

We have a considerable freedom in the  $G(J)$ , and almost any choice of  $G(J)$  corresponds to a physically acceptable<sup>5</sup>  $\mathcal{H}_{\text{int}}$ . In those cases where one can

---

<sup>5</sup>Unfortunately we have not yet (in third quantization) a highly constraining theoretical principle like “renormalizability”, that applies only in second quantization. Thus we have a lot of freedom in this embedding and in the choice of  $\mathcal{H}_{\text{int}}$ .

apply the mean field approximation, the vacuum does not satisfy the trivial relation

$$S[\phi] |0\rangle = 0. \tag{23}$$

On the contrary, the action of several annihilation operators  $S$  is the following

$$\hat{S}[\phi_1] \hat{S}[\phi_2] \cdots \hat{S}[\phi_n] |0\rangle \simeq F[\phi_1] F[\phi_2] \cdots F[\phi_n] |x\rangle \tag{24}$$

where  $F$  is a functional that must be determined by the minimization of  $E$

$$E = \langle 0 | \mathcal{H} | 0 \rangle \tag{25}$$

that leads us to the equation

$$\left( -\frac{\delta^2}{\delta \phi^2(x)} - \phi(x) \nabla^2 \phi(x) + (m^2 + G(J)) \phi^2(x) + \gamma \phi^4 \right) F[\phi] = \lambda F[\phi]. \tag{26}$$

where  $J$  is given by

$$J = \int D\phi F^\dagger[\phi] \phi^2(x) F[\phi]. \tag{27}$$

The equation (26) is not linear in  $F$  but it can be solved as follows. Firstly, let us neglect eq.(27), and let us assume that  $J$  is an arbitrary constant (an external source) that does not depend on  $F$ . With this assumption, the equation (26) is much more simple, since it is linear and we know how to solve it, by means of ordinary quantum field theory methods. In fact the eq.(26) is the same equation that we solve to find out the state with minimal energy (the vacuum) in quantum field theory, we have to calculate and minimize the effective potential where  $G(J)$  appears as an external source: it corrects the bare mass with the replacement

$$m^2 \rightarrow m^2 + G(J) \equiv \mu^2. \tag{28}$$

The field  $\phi$  takes a vev if  $\mu^2 \equiv m^2 + G(J)$  is negative; the vev will be a function of  $J$ , through the dependence (28). But also  $J$  is a function of the vev as predicted by the original exact equation (27). We have two variables and two equations: both the vev  $\phi$  and  $J$  are determined. This clearly appears in Fig. 1, where the solid curve gives the dependence of the vev on the  $\mu^2$ , as predicted

by the minimization of the full effective potential (*i.e.* including all radiative corrections). The dashed curve gives the dependence of  $\mu^2$  on  $J$ , where we have assumed a logarithmic function for  $G(J)$ . In this case the intersection of the two curves occurs very close to the arrow: it is not a fine tuned and arbitrary choice, the hierarchy is enforced by the logarithmic function  $G(J)$ .

This theory of third quantization has another interesting direct prediction, concerning the flavor problem: it provides us with an explanation for the existence of fermion families. We have already mentioned that the existence of three fermion families with quantum numbers given by the last row in Table 1, hints a group of unification beyond the Standard Model. However the grand unified theory does not tell us why there are three identical families. In the past several unifying group have been studied, in the attempt to understand the three families. No convincing and significant result has been found. In third quantization our universe (made of three identical fermion families) is obtained applying three consecutive times the creation operator  $S^\dagger[\psi]$  on the vacuum state

$$\int D\psi F[\psi_1, \psi_2, \psi_3] S^\dagger[\psi_1] S^\dagger[\psi_2] S^\dagger[\psi_3] |0\rangle. \quad (29)$$

The functional  $F$  identifies the physical quantum state of our universe, and the three functions  $\psi_i$  represent the fermionic fields of the three families. In the general case the functional operators  $S^\dagger$  create new families, and we can call them family creation operators. The anticommutation rules (15) tell us that the functional  $F$  is antisymmetric when we exchange the fields  $\psi_i$ , not only at  $t = 0$ , but for the full time evolution: the hamiltonian of second quantization that describes the time evolution of  $F$  must be symmetric under permutations of the fermions  $\psi_i$ .

We have obtained a simple explanation of the family problem and a clear prediction on the flavor symmetry group. Namely the flavor symmetry is the permutation group  $S_n$  where  $n$  is the number of families. We still have to understand if the functional  $S$  only depends on the fermion field  $\psi$  or it is preferable to add the dependence on the gauge boson  $A^\mu$  too: in the last case the operator  $S^\dagger[\psi, A^\mu]$  creates universe containing  $n$  families, with the following gauge group and flavor symmetry (7, 8)

$$G^n \times S_n \quad (30)$$

where  $G$  is a unified gauge group and the permutations  $S_n$  act both on the fermionic families and the gauge bosons families, exchanging the  $n$  factors in the group  $G^n$ . It remains to understand which gauge group  $G$  to choose.  $SU(5)$  is a possible group <sup>9)</sup> but it is a symmetry that does not automatically contain righthanded neutrinos (*i.e.* gauge bosons ignore the righthanded neutrinos): we have not explored this possibility.  $SO(10)$  is the most appealing candidate <sup>8)</sup>, because it contains the righthanded neutrino in the **16**. In the simplest  $SO(10)$  model where the Higgs doublet is in the **10**, we have yukawa unification between the Dirac neutrino masses and the up quark masses. This must be discarded. There are interesting exceptions to this unification if we put the Higgs into larger irreducible representations but this study is left for another work.

We have decided to focus on the gauge group  $E_6$ . Differently from  $SO(10)$ , whose **16** contains only one Standard Model singlet, the **27** of  $E_6$  contains two singlets of the Standard Model ( $SU(3) \times SU(2) \times U(1)$ ). The lefthanded neutrino of the standard model can exchange a yukawa interaction with both singlets. While for the first singlet, precisely as in  $SO(10)$ , this interaction coincides with the yukawa interaction in the up quark sector, the coupling between the second singlet and the lefthanded neutrino does not unify with other yukawa fermion couplings. Namely, the scalar representation **351'** of  $E_6$  contains various  $SU(2)$  doublets with different quantum numbers, and a particular one gives a yukawa interaction for neutrinos only

$$\lambda_{27\,27\,351'} = \lambda_{\nu_L\nu_R} H \quad (31)$$

while all other fermions contained in the **27** have a combination of quantum numbers such that any yukawa coupling with the Higgs doublet in (31) is forbidden. The interaction (31) allows us to understand why the neutrino Dirac mass does not unify with up quark mass. After having chosen the group  $G = E_6$  we must fix the number  $n$  in (30). The simplest and more obvious choice is  $n = 3$ , but this choice does not help us in understanding why the two almost degenerate states (the first two columns in (32)) in neutrino oscillations are the  $S_3$  singlet and the component of the  $S_3$  doublet that is even under the exchange of the two heaviest families (the  $S_2$  symmetry). In other words the mass hierarchy between the even states and the odd state under  $S_2$  suggests a  $S_2$  symmetry and not  $S_3$ ; but we need  $n \geq 3$  in (30) if we want (at least)

three families. In fact even in those cases  $n > 3$ , some pattern of symmetry breaking of the group (30) lead us to the Standard Model with three families of fermionic matter. It is just in these cases that we also find an explanation for neutrino masses and mixing as observed in neutrino oscillations. For clarity, we study the case  $n = 4$ , because the generalization to the case with arbitrary  $n > 3$  is trivial. Our aim is to explain how to attain in neutrino oscillations the mixing angle matrix <sup>10)</sup>

$$\begin{pmatrix} \frac{-2}{\sqrt{6}} & \frac{1}{\sqrt{3}} & 0 \\ \frac{1}{\sqrt{6}} & \frac{1}{\sqrt{3}} & \frac{-1}{\sqrt{2}} \\ \frac{1}{\sqrt{6}} & \frac{1}{\sqrt{3}} & \frac{1}{\sqrt{2}} \end{pmatrix} \quad (32)$$

with  $\Delta m_{\text{atm}}^2 \gg \Delta m_{\text{sol}}^2$ . We have three distinct possibilities: the neutrino mass matrix is diagonal and the oscillations are due to an off-diagonal charged lepton mass matrix. The second case is when the charged lepton mass matrix is diagonal. The last possibility is when both matrices are not diagonal.

We will assume that the lepton charged matrix is diagonal, thus the columns of the matrix (32) coincide with the three mass eigenstates of neutrinos in the flavour basis. They are also eigenstates of the symmetry  $S_2$  that exchanges the last two rows in the (32). The second column is a singlet of the  $S_3$  symmetry that permutes the rows.

In the following model we will try to explain the matrix (32), and why  $|\Delta m_{\text{atm}}^2| \gg |\Delta m_{\text{sol}}^2|$ , but we will ignore the sign of  $\Delta m_{\text{sol}}^2$ , because it requires a more detailed study. The  $S_n$  symmetry ( $n \geq 3$ ) can hardly explain the pattern  $m_3^2 \gg m_1^2 = m_2^2$ , but it can more easily explain why

$$m_3^2 \gg m_1^2 \gg m_2^2. \quad (33)$$

In fact, the seesaw mechanism changes the (33) into  $m_{\text{sing}}^R \gg m_{\text{doub}}^R$ : the righthanded  $S_3$  singlet becomes the heaviest state. So the  $S_3$  symmetric righthanded neutrino matrix must be of the form

$$M_\nu^R \simeq \begin{pmatrix} m_d & m & m \\ m & m_d & m \\ m & m & m_d \end{pmatrix}. \quad (34)$$

with

$$m_d = m. \quad (35)$$

The matrix (34) descends from the  $S_3$  symmetry, while eq. (35) does not. The reason why the  $S_3$  doublet is much more light is obscure.

If we add a fourth family, we can write the following antisymmetric matrix

$$M = \begin{pmatrix} 0 & 0 & 0 & -1 \\ 0 & 0 & 0 & -1 \\ 0 & 0 & 0 & -1 \\ 1 & 1 & 1 & 0 \end{pmatrix} \quad (36)$$

that has the following properties: it is  $S_3$  symmetric, *i.e.* it is invariant under the exchange of the first three families. It couples only with  $S_3$  singlets, the only states acquiring a non zero mass. The doublet of  $S_3$  is given by the two massless states  $(-2/\sqrt{6}, 1/\sqrt{6}, 1/\sqrt{6}, 0)$  and  $(0, -1/\sqrt{2}, 1/\sqrt{2}, 0)$ .

The matrix (36) is the only  $4 \times 4$  matrix that is simultaneously  $S_3$  symmetric and antisymmetric under transposition. Instead of majorana masses, we are forced to choose a dirac mass term

$$M_{ij} \nu_R^i X_R^j \quad (37)$$

with two distinct weyl spinors  $\nu_R$  and  $X_R$ , otherwise the (37) would be identically zero, since  $M_{ij} = -M_{ji}$ . The **27** of  $E_6$  contains two different weyl spinors, that we can call  $\nu_R$  and  $X_R$ ; thus (36) and (37) are compatible with the choice of the group  $E_6^4 \rtimes S_4$ .

We complete this discussion, suggesting how to break the group  $S_3$  into  $S_2$ . We add a scalar field  $\phi^i$ , with the family index  $i = 1, 4$ . Only the first component of this field takes a vev  $\phi^1 = v$ . The state  $(-2/\sqrt{6}, 1/\sqrt{6}, 1/\sqrt{6}, 0)$  takes a mass, while the orthogonal state  $(0, -1/\sqrt{2}, 1/\sqrt{2}, 0)$  remains as the lightest righthanded neutrino. The seesaw mechanism through the diagonal yukawa interaction (31) will make the  $S_2$  odd state (last column of (32)) the heaviest neutrino. A more detailed discussion of this model can be found in 7).

## References

1. M. Sher, Phys. Lett. B **317** (1993) 159 ,Addendum-ibid. B **331** (1994) 448
2. G. Isidori, V. S. Rychkov, A. Strumia and N. Tetradis, Phys. Rev. D **77** (2008) 025034

3. H. Georgi, Nucl. Phys. B **156** (1979) 126.
4. J. Erler, AIP Conf. Proc. **857** (2006) 85
5. F. Caravaglios, arXiv:hep-ph/0211183.
6. F. Caravaglios, arXiv:hep-ph/0211129.
7. F. Caravaglios and S. Morisi, Int. J. Mod. Phys. A **22** (2007) 2469
8. K. S. Babu, S. M. Barr and I. Gogoladze, Phys. Lett. B **661** (2008) 124
9. N. Haba and K. Yoshioka, Nucl. Phys. B **739** (2006) 254
10. G. L. Fogli, E. Lisi, A. Marrone, A. Palazzo and A. M. Rotunno, arXiv:hep-ph/0506307.

**NEUTRINOS: WHAT WE KNOW, AND WHAT WE WOULD  
LIKE TO FIND OUT**

Boris Kayser  
*Fermilab*

Written contribution not received



### ***SESSION III – QCD AND HADRONIC INTERACTIONS***

<i>R. Craig Group</i>	Recent QCD Studies at the Tevatron
<i>Stanco Luca</i>	From HERA to LHC: Implications and Constraints
<i>Magnea Lorenzo</i>	Analytical Studies for Non-Perturbative QCD of Jets at Hadron Colliders
<i>Pakhlov Pasha</i>	Charmonium and New States at B Factories
<i>Mizuk Roman</i>	New Resonances at BELLE
<i>Polosa Antonello</i>	Spectrum and Decays of Diquark Antidiquark States
<i>Franco Buccella</i>	Spectrum of Positive and Negative Parity Pentaquarks, Including $SU(3)_F$ Breaking



## RECENT QCD STUDIES AT THE TEVATRON

Robert Craig Group

*Fermilab, Batavia, IL, USA*

*(On behalf of the CDF and DØ Collaborations)*

### Abstract

Since the beginning of Run II at the Fermilab Tevatron, the QCD physics groups of the CDF and DØ experiments have worked to reach unprecedented levels of precision for many QCD observables. Thanks to the large dataset - over  $3 \text{ fb}^{-1}$  of integrated luminosity recorded by each experiment - many important new measurements have recently been made public and will be summarized in this paper.

## 1 Introduction

The Tevatron collider at Fermilab provides collisions of protons with anti-protons at a center of mass energy of 1.96 TeV. This is currently the highest energy collider in the world. The multipurpose detectors of the CDF <sup>1)</sup> and DØ <sup>2)</sup> experiments are exploiting the more than  $3 \text{ fb}^{-1}$  of integrated luminosity provided by the Tevatron in order to make important progress in constraining and confirming the calculations made from quantum chromodynamics (QCD).

Precise measurements of QCD observables in hadron-hadron collisions - such as jet cross sections - constrain parton density functions (PDFs) and confirm the predictive power of theory. This results in a better control of the standard QCD production calculations which are used to predict major backgrounds for many important physical processes. In addition, the specific QCD processes which pose challenges to new physics searches such as supersymmetry and Higgs production can be measured directly with dedicated analyses.

In this paper some of the most recent measurements from the CDF and DØ collaborations will be reviewed. These measurements will be split into underlying event observables, jet cross sections, and boson plus jet cross section measurements.

## 2 Hadronic Collisions and Underlying Event Observables

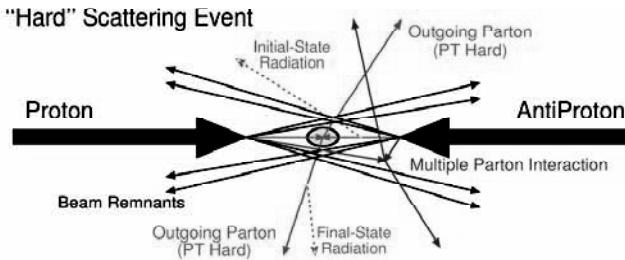


Figure 1: *Simple model for hadronic collisions.*

A brief introduction into the structure of hadronic collisions is useful as a motivation for jet definition. Hadronic collisions may be factorized into perturbative components (hard scattering and initial and final state radiation) and non-perturbative components (beam remnants and multiple parton interactions). These components are illustrated in the simple “cartoon” shown in

figure 1. This simple picture is similar to the model used by a program like PYTHIA <sup>3)</sup> to generate hadronic collisions.

Figure 1 should be thought of as occurring within the radius of the proton around the colliding partons. In fact, the picture becomes more complicated when the property of QCD color confinement and detector effects are included. The colored partons must hadronize into color neutral hadrons. All of these particles originating from the different components of the collider event are indistinguishable in the detector, and it is the job of jet algorithms to cluster these objects into jets. Figure 2 illustrates that jets may be clustered at the parton (quarks and gluons) or particle (hadrons) level when dealing with MC simulation, or detector (calorimeter towers) levels. Of course, measurements are made at the detector level, but it is useful to use the the parton and particle level jets from MC studies to derive corrections for the measured quantities.

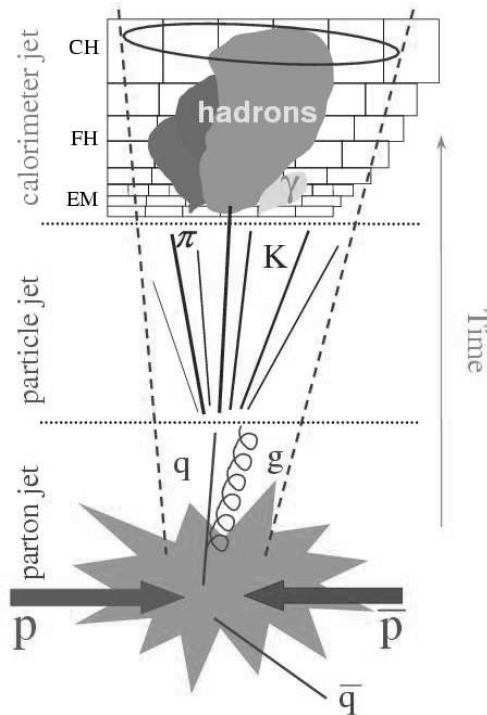


Figure 2: Jets clustering can be defined at the parton, particle, and detector levels.

Most results discussed in this note will focus on the properties of the perturbative component of the collision. However, studies of the “underlying event”<sup>4, 5)</sup> from CDF focus on measuring observables that are sensitive to the non-perturbative components such as beam remnants and multiple parton interactions. These studies provide constraints useful for the modeling of the non-perturbative regime (where pQCD fails), such as the “soft” interactions generating the underlying event which accompanies the “hard” collision.

The direction of the leading calorimeter jet is used to isolate regions of  $\eta$ - $\phi$  space that are sensitive to the underlying event. As illustrated in figure 3, the direction of the leading jet, jet#1, is used to define correlations in the azimuthal angle,  $\Delta\phi$ . The angle  $\Delta\phi = \phi - \phi_{\text{jet}\#1}$  is the relative azimuthal angle between a charged particle (or a calorimeter tower) and the direction of jet#1. The “transverse” region is perpendicular to the plane of the hard 2-to-2 scattering and is therefore very sensitive to the “underlying event”. These regions can be studied for different event topologies such as leading jet (require one or more jets), back-to-back (requiring two or more jets with the leading jets back-to-back in  $\phi$ ), and exclusive dijet (requiring only two jets which are back-to-back in  $\phi$ ). By studying different regions and event topologies components of the hadronic collision can be isolated.

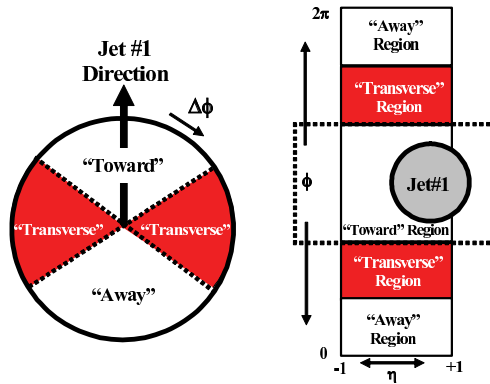


Figure 3: *Illustration of correlations in azimuthal angle  $\phi$  relative to the direction of the leading jet in the event. Observables studied in the “transverse” region are sensitive the “underlying event”.*

CDF has recently updated their UE studies for leading jet events and other event topologies are under study. As an example of the types of observables measured, the charged particle density per unit  $\eta - \phi$  in the toward, away,

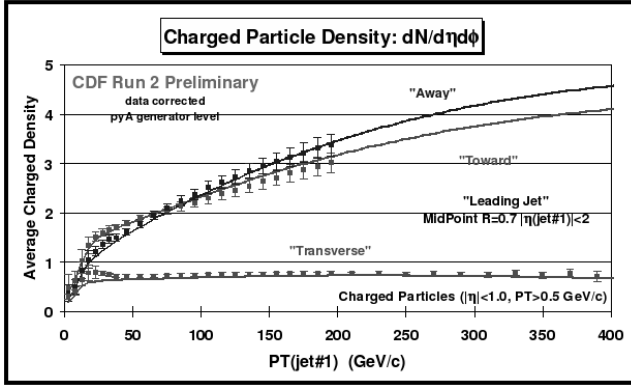


Figure 4: The charged particle density per unit  $\eta - \phi$  in the toward, away, and transverse regions. The points are the data corrected to the particle level and the lines are the PYTHIA prediction for each distribution.

and transverse regions is shown in figure 4. The goal is to publish more than one hundred distributions of observables corrected to the particle level. These results will be useful for tuning and improving theoretical models of hadronic collisions. Understanding the underlying event contribution to jet events is important for many searches at the Large Hadron Collider (LHC) and measurements of this type will likely be of the first made at the LHC <sup>6, 7</sup>).

### 3 Jet Cross Section Measurements

#### 3.1 Inclusive Jet Cross Sections

The measurement of the differential inclusive jet cross section at the Tevatron probes the highest momentum transfers in particle collisions, and thus is potentially sensitive to new physics such as quark substructure <sup>8</sup>). The measurement also provides a fundamental test of predictions of perturbative quantum chromodynamics (pQCD) <sup>9, 10</sup>). Comparisons of the measured cross section with pQCD predictions provide constraints on the parton distribution function (PDF) of the (anti)proton, in particular at high momentum fraction ( $x \gtrsim 0.3$ ) where the gluon distribution is poorly constrained <sup>11</sup>). Further constraints on the gluon distribution at high  $x$  will contribute to reduced uncertainties on theoretical predictions of many interesting physics processes both for experiments at the Tevatron and for future experiments at the LHC. Extending the

measurements to higher rapidities significantly increases the kinematic reach in the  $x$ - $Q$  space, where  $Q$  denotes the momentum transfer, and helps to place stronger constraints on the gluon PDF.

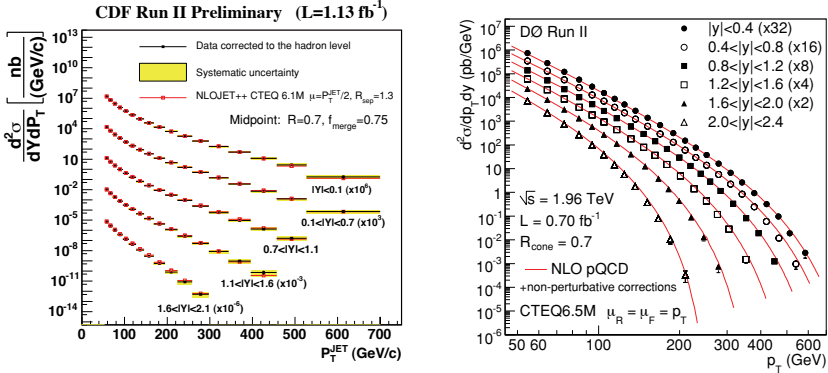


Figure 5: The inclusive jet cross section distributions recently measured by CDF (left) and DØ (right) using the Midpoint cone-jet clustering algorithm.

The inclusive jet cross section has been measured in Run II by CDF (12, 13) and DØ (14). The most recent measurements using the Midpoint cone jet clustering algorithm are shown in figure 5. The CDF result (left) compares with NLO predictions using CTEQ6.1M PDFs and 1.1 fb<sup>-1</sup> of luminosity and breaks the measurement into five rapidity regions with  $|y| < 2.1$ , while the DØ result (right) compares with CTEQ6.5M (15) using 0.7 fb<sup>-1</sup> of luminosity and splits the rapidity into six regions with  $|y| < 2.4$ . The comparison with NLO pQCD is shown by taking the ratio (DATA/THEORY) in figures 6 and 7. Both measurements observe reasonable agreement with the NLO predictions and see similar trends in the data at high rapidities. In addition the systematic uncertainties are smaller than the PDF uncertainty on the theory prediction and they should therefore be useful to constrain the proton PDFs. DØ recently reduced their absolute jet energy scale uncertainty - which yields the dominant systematic uncertainty in this measurement - to less than 2 %, and this improvement will lead to important constraints on the gluon PDF. These results are also reasonably consistent with the recently published CDF measurement (16) using the  $k_T$  clustering algorithm (17) pointing to the conclusion that the  $k_T$ -type algorithm can work well in the difficult hadron collider environment.

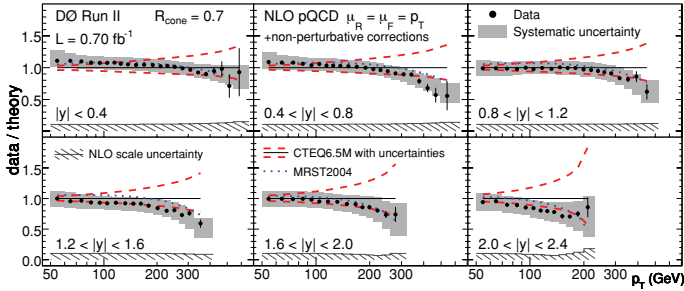


Figure 6: The inclusive jet cross section ratios to the NLO pQCD predictions from D0 using the Midpoint cone-jet clustering algorithm.

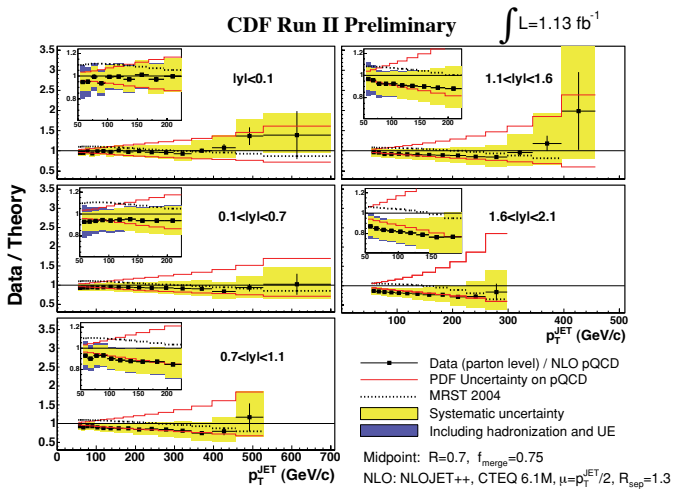


Figure 7: The inclusive jet cross section ratios to the NLO pQCD predictions from CDF using the Midpoint cone-jet clustering algorithm.

### 3.2 Dijet Mass

In addition to being a fundamental test of pQCD which can be used to constrain PDFs, the dijet mass ( $M_{jj}$ ) cross section distribution can be used to constrain new physics models which predict heavy particles decaying to dijets. A recent measurement from CDF of the high dijet mass production cross section for  $180 < M_{jj} < 1350 \text{ GeV}/c^2$  uses  $1.1 \text{ fb}^{-1}$  of luminosity. As shown in figure 8 nice agreement with the NLO predictions of NLOJET++ (18).

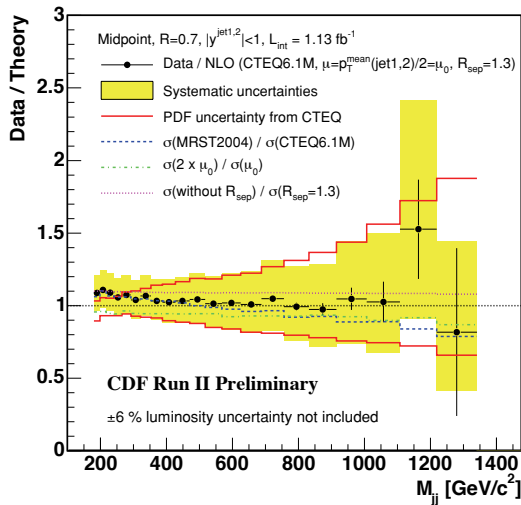


Figure 8: The dijet mass cross section ratio to the NLO pQCD prediction from CDF using the Midpoint cone-jet clustering algorithm.

### 3.3 Exclusive Dijets

In another exciting measurement the first observation of exclusive dijet production has been reported by CDF (19). In this analysis the presence of exclusively produced dijets ( $p + \bar{p} \rightarrow \bar{p}' + 2jets + p'$ ) was demonstrated by studying the distributions of the dijet mass fraction, defined as the dijet mass divided by the full system mass. The dijet mass fraction distributions and the exclusive dijet mass differential cross section distribution are given in figure 9.

This exclusive dijet result is important because it verifies that theoretical calculations (20, 21) have control over exclusive production channels like the

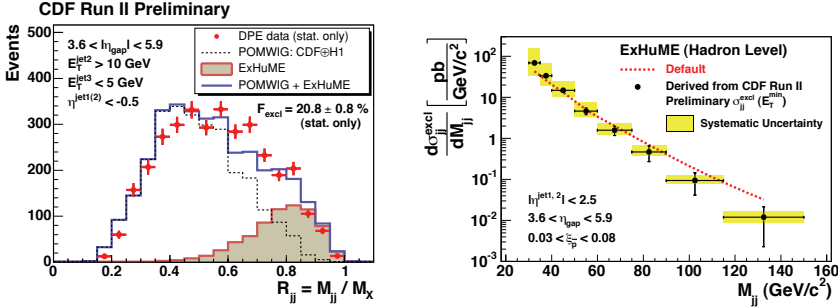


Figure 9: The Dijet mass fraction (left) and the exclusive dijet mass differential cross section distribution (right).

ones shown in figure 10. The exclusive Higgs boson production mechanism provides an exciting discovery possibility for the LHC and this exclusive dijet cross section measurement serves as a useful calibration channel for this process.

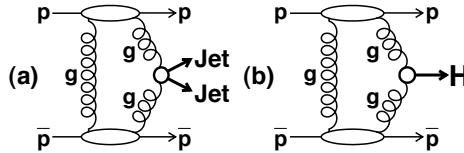


Figure 10: Production diagrams for exclusive dijet (a) and exclusive Higgs production (b).

## 4 Boson Plus Jet Measurements

Boson plus jet production processes measured at the Tevatron experiments are useful to study pQCD and in addition are some of the most important backgrounds in new physics searches. The most recent results for  $\gamma$  plus jet,  $Z$  plus jet, and  $W$  plus jet cross sections are presented next.

### 4.1 Triple Differential $\gamma + \text{Jet}$ Cross Section

Historically, inclusive direct photon cross section measurements have observed mediocre agreement with theoretical predictions (22, 23, 24). Recently, DØ

has measured the triple differential  $\gamma + \text{jet}$  cross section ( $\frac{d^3\sigma}{dp_T^\gamma d\eta^\gamma d\eta^{\text{jet}}}$ ) in an effort to understand these discrepancies (25). The analysis requires a photon in the central region ( $|\eta| < 1.0$ ) with  $p_T > 30$  GeV/c and a jet in the central ( $|\eta| < 0.8$ ) or forward ( $1.5 < |\eta| < 2.5$ ) region with  $p_T > 15$  GeV/c. The cross section measurement is then made in four distinct kinematic regions:

- Region1: Jet and  $\gamma$  in the central region and on the same side.
- Region2: Forward jet and central  $\gamma$  in the central region and on the same side.
- Region3: Jet and  $\gamma$  in the central region and on the opposite side.
- Region4: Forward jet and central  $\gamma$  on opposite sides.

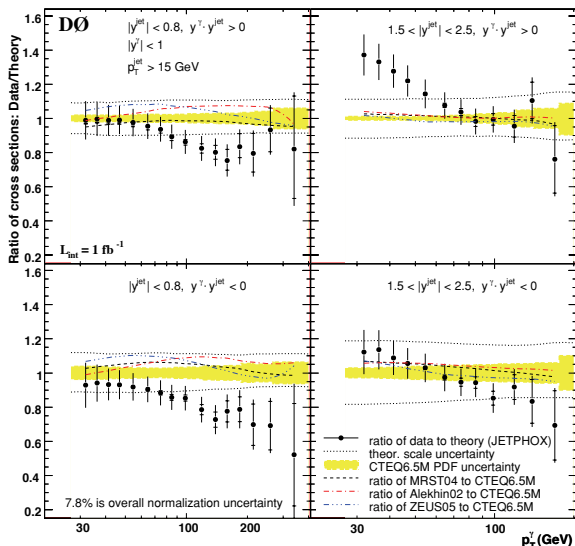


Figure 11: *Measured cross section to the NLO theory prediction is shown for each kinematic region.*

The ratio of measured cross section to the NLO theory prediction is shown in figure 11. This measurement extends the  $x$  and  $Q$  range significantly over previous measurements. In many regions the measured values are outside of the PDF uncertainty bands (CTEQ6.1). In addition, it is clear from the figure

that a simple theoretical scale variation cannot bring data and theory into agreement in all four regions. It should also be noted that the central region results are consistent with previous measurements from UA2, CDF, and DØ.

In addition to the ratios to theoretical predictions, ratios were taken between the different regions. In these ratios systematic uncertainties on the ratio largely cancel out and total experimental uncertainty is less than 9 %. The results of these studies are that shapes are reproduced by theory reasonably well, but there is a quantitative disagreement.

### 4.2 Z plus Jet Cross Sections

Z plus jet production provides a test of the properties of pQCD and this process is the dominant background for many supersymmetric searches. CDF has recently used di-electron final states to measure the inclusive jet cross sections in events with a  $Z/\gamma^*$  (26). Figure 12 shows the jet  $p_T$  distributions for  $\geq 1$  and  $\geq 2$  jets (left) and N-jet distributions (right). Good agreement is observed with the NLO predictions. The ratio to leading order shown in the N-jet study reveals that the LO-NLO “k-factor” does not exhibit strong dependence on the number of jets.

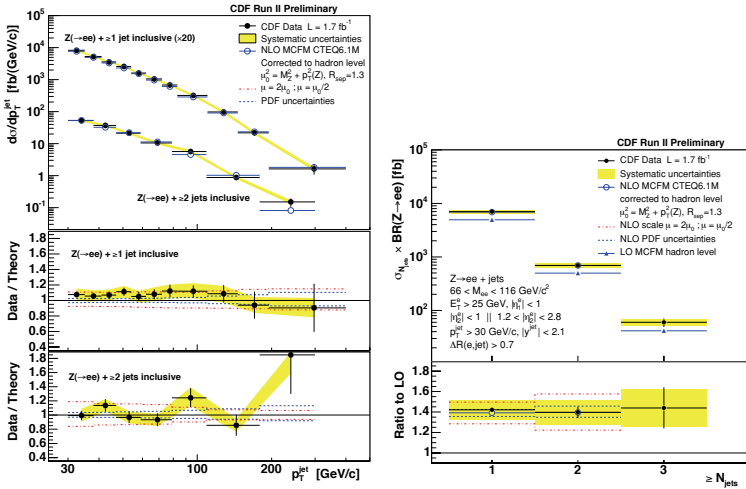


Figure 12: Results of the measurement of the Z plus jet cross section as a function of jet  $p_T$  (left) and number of jets (right).

Using di-lepton ( $e$  or  $\mu$ ) final states CDF has also recently measured the

Table 1: The measured cross section and cross section ratios of  $Z$  plus  $b$ -jet to inclusive  $Z$  and  $Z$  plus jet cross sections as well as theoretical predictions for these quantities from PYTHIA, ALPGEN, and MCFM <sup>27)</sup> with corrections for UE and hadronization affects.

	CDF Data	PYTHIA	ALPGEN	NLO +U.E+hadr.
$\sigma(Z + b\text{jet})$	$0.86 \pm 0.14 \pm 0.12$ pb	–	–	0.53 pb
$\sigma(Z + b\text{jet})/\sigma(Z)$	$0.336 \pm 0.053 \pm 0.041\%$	0.35%	0.21%	0.23 %
$\sigma(Z + b\text{jet})/\sigma(Z + \text{jet})$	$2.11 \pm 0.33 \pm 0.34\%$	2.18%	1.45%	1.71%

$Z$  plus  $b$ -jet cross section. This measurement probes the heavy flavor content of the proton and is an important background for singly produced top quark,  $ZH$ , and supersymmetric Higgs searches. For this analysis the invariant mass distribution for tracks pointing to a displaced vertex is used to separate  $b$ ,  $c$ , and light quark contributions to the  $Z$  plus jet events. In table 1 the measured cross section and cross section ratios of  $Z$  plus  $b$ -jet to inclusive  $Z$  and  $Z$  plus jet cross sections are shown.

### 4.3 $W$ plus Jet Cross Sections

$W$  plus  $c$ -jet production is an important background for supersymmetric top quark and Higgs production. In addition the measurement of its cross section tests the  $s$ -quark content of the proton. Recently  $D\bar{O}$  measured this cross section and found reasonable agreement with the ALPGEN <sup>28)</sup> prediction <sup>29, 30)</sup>.  $W$  plus  $b$ -jet production is the dominant background for single top quark and  $WH$  searches. Using a displaced vertex mass fit, CDF measured the cross section for  $W$  plus  $b$ -jet events with an electron or muon of  $p_T > 20$  GeV/ $c$  and  $|\eta| < 1.1$ , missing transverse energy greater than 25 GeV, and one or more  $b$ -tagged jets with  $p_T > 20$  GeV/ $c$  and  $|\eta| < 2.0$ . The result is  $\sigma_{W+b\text{-jets}} \times Br(W \rightarrow l\nu) = 2.74 \pm 0.27(stat) \pm 0.42(syst)$  pb. This measurement should provide useful constraints to the  $W$  boson plus  $b$ -jet backgrounds for many future searches.

## 5 QCD Conclusions

Measurements from the Tevatron Run II are defining a new level of QCD precision measurements in hadron-hadron collisions. In this note many results from the Tevatron's rich program in QCD studies have been reviewed including: jet cross sections,  $W$ +jets,  $Z$ +jets,  $\gamma$ +jets and more. The recent inclusive jet cross section measurements from CDF and  $D\bar{O}$  report nice agreement with NLO

predictions and observe similar trends in the data-theory comparison. Boson plus jet and boson plus heavy flavor cross sections are being measured. These measurements are important for tests of pQCD and they also provide important constraints they provide on important backgrounds for new physics searches for supersymmetry and the Higgs boson. To summarize, the QCD programs of the CDF and DØ experiments are dedicated to testing and constraining pQCD and also measuring cross sections of important background processes. This important effort will continue to produce improved results as the Tevatron data sample continues to grow, so stay tuned.

We thank the Fermilab staff and the technical staffs of the participating institutions for their vital contributions. This work was supported by the U.S. Department of Energy and National Science Foundation; the Italian Istituto Nazionale di Fisica Nucleare; the Ministry of Education, Culture, Sports, Science and Technology of Japan; the Natural Sciences and Engineering Research Council of Canada; the National Science Council of the Republic of China; the Swiss National Science Foundation; the A.P. Sloan Foundation; the Bundesministerium für Bildung und Forschung, Germany; the Korean Science and Engineering Foundation and the Korean Research Foundation; the Science and Technology Facilities Council and the Royal Society, UK; the Institut National de Physique Nucleaire et Physique des Particules/CNRS; the Russian Foundation for Basic Research; the Ministerio de Educación y Ciencia and Programa Consolider-Ingenio 2010, Spain; the Slovak R&D Agency; and the Academy of Finland.

## References

1. D. E. Acosta *et al.* [CDF Collaboration], *Phys. Rev. D* **71**, 032001 (2005) [arXiv:hep-ex/0412071].
2. T. LeCompte and H. T. Diehl, *Ann. Rev. Nucl. Part. Sci.* **50**, 71 (2000).
3. T. Sjostrand, P. Eden, C. Friberg, L. Lonnblad, G. Miu, S. Mrenna and E. Norrbin, *Comput. Phys. Commun.* **135**, 238 (2001) [arXiv:hep-ph/0010017].
4. T. Affolder, *et al* [CDF Collaboration], *Phys. Rev. D* **65**, 092002 (2002).
5. R. Field and R. C. Group [For The CDF Collaboration], arXiv:hep-ph/0510198, (2005).
6. D. Acosta, *et al* [The CMS Collaboration], CERN-CMS-NOTE-2006-067, (2007)

7. P. Z. Skands, Contribution to Les Houches Workshop on Physics at TeV Colliders, FERMILAB-CONF-07-706-T, (2007)
8. E. Eichten, K. D. Lane and M. E. Peskin, Phys. Rev. Lett. **50**, 811 (1983).
9. D. J. Gross and F. Wilczek, Phys. Rev. D **8**, 3633 (1973).
10. H. Fritzsch, M. Gell-Mann and H. Leutwyler, Phys. Lett. B **47**, 365 (1973).
11. D. Stump, J. Huston, J. Pumplin, W. K. Tung, H. L. Lai, S. Kuhlmann and J. F. Owens, JHEP **0310**, 046 (2003) [arXiv:hep-ph/0303013].
12. A. Abulencia *et al.* [CDF Collaboration], Phys. Rev. D **74**, 071103 (2006) [arXiv:hep-ex/0512020].
13. A. Abulencia *et al.* [CDF Collaboration], Phys. Rev. Lett. **96**, 122001 (2006) [arXiv:hep-ex/0512062].
14. Abazov, V.M. *et al.* [D0 Collaboration], arXiv:0802.2400 [hep-ex].
15. P. M. Nadolsky *et al.*, arXiv:0802.0007 [hep-ph].
16. A. Abulencia *et al.* [CDF Collaboration], Phys. Rev. D **74**, 071103 (2006) [arXiv:hep-ex/0512020].
17. S. D. Ellis and D. E. Soper, Phys. Rev. D **48**, 3160 (1993) [arXiv:hep-ph/9305266].
18. Z. Nagy, Phys. Rev. Lett. **88**, 122003 (2002) [arXiv:hep-ph/0110315].
19. T. Aaltonen *et al.* [CDF Collaboration], arXiv:0712.0604 [hep-ex].
20. V. A. Khoze, M. G. Ryskin and W. J. Stirling, arXiv:hep-ph/0607134.
21. V. A. Khoze, A. D. Martin and M. G. Ryskin, Eur. Phys. J. C **14**, 525 (2000) [arXiv:hep-ph/0002072].
22. J. Alitti *et al.* [UA2 Collaboration], Phys. Lett. B **263**, 544 (1991).
23. D. E. Acosta *et al.* [CDF Collaboration], Phys. Rev. D **65**, 112003 (2002) [arXiv:hep-ex/0201004].
24. V. M. Abazov *et al.* [D0 Collaboration], Phys. Lett. B **639**, 151 (2006) [Erratum-ibid. B **658**, 285 (2008)] [arXiv:hep-ex/0511054].
25. V. M. Abazov *et al.* [D0 Collaboration], arXiv:0804.1107 [hep-ex].

- 
26. T. Aaltonen *et al.* [CDF Collaboration], Phys. Rev. Lett. **100**, 102001 (2008) [arXiv:0711.3717 [hep-ex]].
  27. J. Campbell and R. K. Ellis, Phys. Rev. D **65**, 113007 (2002) [arXiv:hep-ph/0202176].
  28. M. L. Mangano, M. Moretti, F. Piccinini, R. Pittau and A. D. Polosa, JHEP **0307**, 001 (2003) [arXiv:hep-ph/0206293].
  29. V. M. Abazov *et al.* [D0 Collaboration], arXiv:0803.2259 [hep-ex].
  30. T. Aaltonen *et al.* [CDF Collaboration], Phys. Rev. Lett. **100**, 091803 (2008) [arXiv:0711.2901 [hep-ex]].



## FROM HERA TO LHC: IMPLICATIONS AND CONSTRAINTS

Luca Stanco

*I.N.F.N. Padova, via Marzolo 8, Padova, Italy*

### **Abstract**

Starting of LHC sometime this year and the long expected and unexpected new physics results which will be granted in the near future, will be challenged by the capacity to keep under control most of the Standard Model physics. The results from the HERA machine in terms of Parton Density Functions from very low to high  $x$ -Bjorken, jet flow and structures of the underlying event, as well as diffraction production, are all key issues to be considered by LHC community. A personal short overview of the HERA results from H1 and ZEUS experiments are given together with their connection to LHC physics.

## 1 Introduction

This year the more and more awaited LHC startup will constitute the most important event of the last decade in particle physics and one of the most relevant from the discovery of the Neutral weak Currents more than 30 years ago. In the last three decades many important theoretical and experimental discoveries raised to the horizon of the particle physics community. They can be roughly divided into two sets of discoveries: those verifying more and more deeply the Standard Model (from the proves of the ElectroWeak radiative corrections at LEP to the Top discovery at the Tevatron) and those opening new unexpected scenarios not fitting in the Standard Model (from the observation of neutrino oscillations to the dark matter to the frightening theoretical "discovery" of the superstring models). Either set is anxiously waiting for any hint may come from the first measurements of LHC experiments. To be astringent a general hope and believe is that Standard Model be living his last days, based on the lack of a SM Higgs observation around the 170 GeV region <sup>1)</sup> which should indicate a possible void observation also in the lower energy range<sup>1</sup>.

However, new physics at LHC will come together the usual Standard Model production. It is matter of consideration wether and how the SM physics will overburden the new production, without discarding the importance to study the known with much better precision and at rather different energy ranges (one for all it will be extremely interesting to measure the top-top production as hint for inclusive new physics) <sup>3)</sup>. The SM physics production as expected from previous or current experiments will constitute a multiway challenge for LHC. In this report we will focus on the challenges which come from the HERA measurements.

HERA was an electron(positron)-proton collider with a center-of-mass energy around 300 GeV. The two experiments H1 and ZEUS collected together 1  $fbarn^{-1}$  during the years 1992-2007 providing an extended gathering of data in the so called low  $x$ -Bjorken region of the Deep Inelastic Scattering regime, together with new insights in the *parallel* productions of photoproduction and diffraction. As a result completely new and exhaustive measurements of structure function  $F_2$  of the proton have been provided in many extended  $x$  regions.

We will discuss (pompously talking) the relevance of these HERA aspects for LHC. Likely the original physics aspects which happened to be studied in the  $e - p$  collisions at few hundreds of GeV may own a counterexample at

---

<sup>1</sup>This conclusion is not completely justified being formulated on the basis of SM constraints. For a exhaustive report, I like to refer to [2] and references therein. Personally I would tend to conclude no Higgs signal either SM or BSM will be found in the 100-200 GeV energy range, while the new physics would happen to emerge beyond 200 GeV.

LHC at few TeV. Throughout this short report we will discuss explicitly about this point. Moreover, it is clear that HERA themes constitute real physical constraints in case the long awaited new physics will raised up without striking signals. That is, we will focus on the constraints which experimenters at LHC have to take into account wether no *smoking-gun* analysis will be available by Nature to get the new physics understandable, and instead long exhaustive analysis will be needed to analyze primarily the Standard Model production and eventually its discrepancies from data. To this respect, HERA results will constitute an important, and unavoidable, key-corner by their restraints on the Parton Density Functions of gluons and quarks.

## 2 LHC expectations

It is much easier for me to start saying few words about LHC and eventually address the HERA issues. LHC is the *biggest* for many aspects: the biggest accelerator ever built, the biggest involvement of physicists/engineers ever tried, the biggest enterprise ever challenged in particle physics, the biggest ever potential place for new discoveries. Last but not least, LHC will also constitute a serious (experimental) wager to connect Particle Physics and Cosmology. LHC machine is supposed to start operations sometime the second part of this year<sup>2</sup>, hoping for a "Stage A" operation at 10 TeV in *c.o.m.* with a luminosity around  $10^{32} \text{cm}^{-2} \text{sec}^{-1}$  which will provide few inverse *picobarns* to ATLAS and CMS experiments.

It is by now a well known example that looking for new physics at LHC will correspond to grabble a needle in 100,000 haystacks<sup>3</sup> by comparing the relative cross sections of new particles at 1 TeV scale and electroweak coupling with the total proton-proton cross section. It is easy to identify the "needles" with particles like the Higgses (Standard Model or SuperSymmetric ones), supersymmetric particles, extradimensions, micro black holes etc., while the haystacks can be essentially fractionalized into 4 classes: total proton-proton cross section, jet (with heavy flavor) production, photon-production, Standard Model candles (W, Z and top). All these four classes may correspond to a sort of QCD **mobocracy**<sup>4</sup> to point out that QCD will pervade all the different analysis performed at LHC.

We try to think to a correspondence between QCD and New Physics at LHC, with respect to the correspondence between the first analyzed mea-

---

<sup>2</sup>At the time of this writing, it has been decided that the first circulating beams will occur on September 10<sup>th</sup>.

<sup>3</sup>See for example the presentation at plenary of EPS07 conference by J. Ellis, <http://www.hep.man.ac.uk/HEP2007/>.

<sup>4</sup>Mobocracy is the governance of mob people (plebs), opposite to oligarchy.

surements and the first signals, as well as between the most exhaustive measurements and the detailed analysis, and how these correspondences will be enlighten by HERA results. Moreover, what may be expected at LHC in term of diffraction is an open interesting issue, while few aspects of Electroweak (and nones on Heavy Flavors) Physics will be further addressed.

Actually, the presence of a QCD *mobocracy* at LHC will correspond to a much better understanding of the PDF issues, provided the huge enlargement of phase space, the jet (and heavy quarks) production, the diffraction reactions. Finally, one has not to forget the "second order priority" analysis which will take place to test QCD at high scale, smallest- $x$  ever studied (and the corresponding questions on parton saturation), possibility of new phases in QCD and, last but not least, possibility to observe non-linear phenomena.

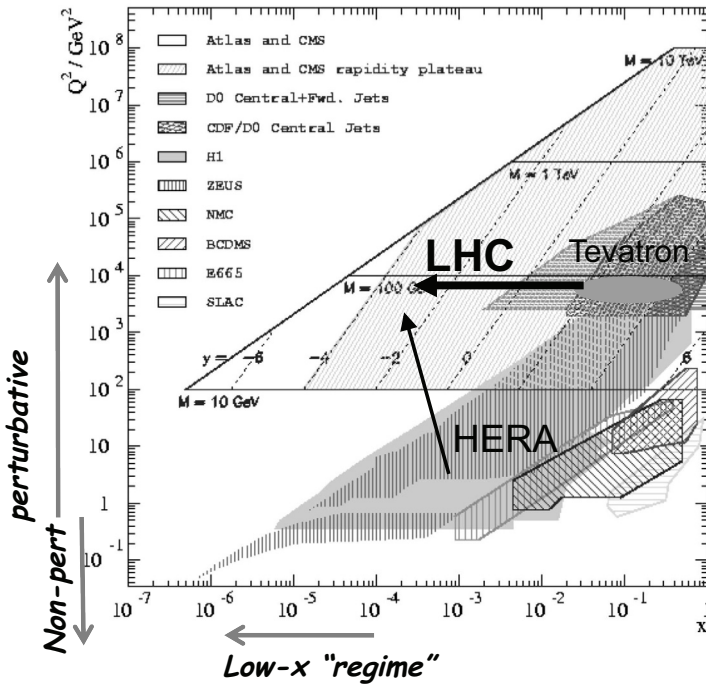


Figure 1: The phase space region in terms of  $x$  and  $Q^2$ . The LHC accessible region is largely dominated either in the high  $Q^2$  or the small- $x$  regions. Arrows on the axis indicate the usually undertaken domains of (non)perturbative and low- $x$  regimes. The two arrows inside the picture indicate the propagation by QCD evolution equations from the experimentally measured regions by HERA and Tevatron to the unexplored LHC ones.

### 3 HERA: the QCD machine

The interaction of electron(positron) and proton at HERA is described by two independent variables usually handpicked as Bjorken- $x$  and  $Q^2$ , the momentum fraction of the proton and the energy transferred on the electron side. The artwork of the available phase space in terms of  $x$  and  $Q^2$  is shown in fig.1 for different machines and experiments.

The naturalness of investigating the proton structure through a quasi-real/virtual photon probe explains easily the character of QCD testing machine for HERA. We meditate the F.Wilczek quotation "... *The most dramatic of these (experimental consequences), that proton viewed at ever higher resolution would appear more and more as a field energy (soft glue), was only clarified at HERA twenty years later* <sup>4)</sup>.

As can be noted from a careful look at fig.1 the two colliders HERA experiments were able to analyze a large new part of phase space. A real HERA's legacy is wonderfully reported in fig.2 were preliminary results on the combined data from H1 and ZEUS were reported <sup>5)</sup> together with the corresponding extracted fits of PDF<sup>5</sup>.

The studies of Standard Model signals at LHC will definitively need the HERA results on PDF. A very good example comes from the W bosons production, dominated by the sea-quark density and probably used as a source of luminosity measure. Their systematic errors will be dominated by the PDF inputs, as exhaustively reported e.g. in the paper of M. Diehl <sup>6)</sup>.

It is also time to point out that already sometime ago several groups and workshops have been settled by HERA people in touch with theorists and interested LHC community.

All references can be looked at <http://www.desy.de/~heralhc/>.

### 4 LHC and HERA interplay

The LHC studies can be temporarily divided following the years of data taking and the corresponding acquired luminosity. The first step of few *inverse picobarns* will allow the LHC experiments to have a threefold clear look at: a) charge particle production, underlying event, multipartons pile-up; b) detectors calibration and tuning and c) early (un)discovering of new physics from leptons signatures. In this context the HERA experience (as well the Tevatron one) may help a little just from human (and potentially Monte Carlo) experience.

---

<sup>5</sup>At the time of the talk the combined fits of H1 and ZEUS were not available yet. For a very recent preliminary fit result see ICHEP08 conference at the plenary session, <http://www.hep.upenn.edu/ichep08/talks/misc/schedule,talk-id=460>.

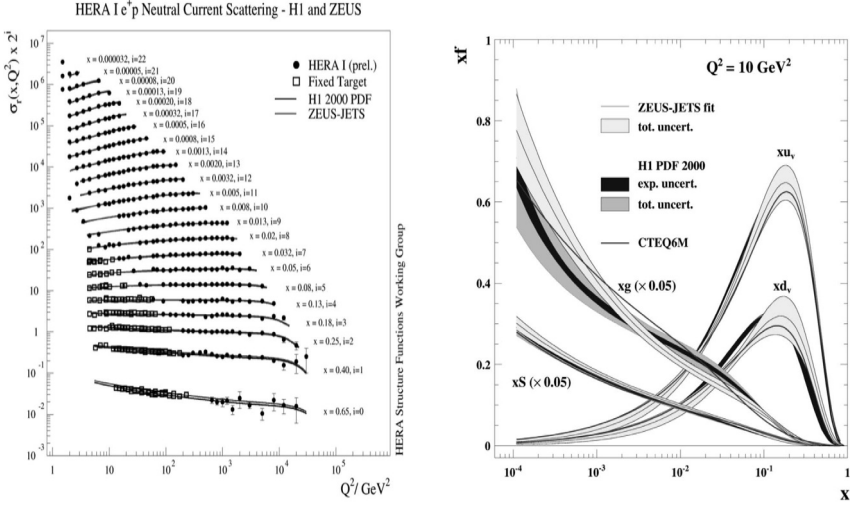


Figure 2: The full set of combined (H1 and ZEUS) measurements of the Neutral Current cross-section (left) and the corresponding extraction of PDF (right) internally arranged by either H1 or ZEUS collaboration.

Furthermore, once some tens of *inverse picobarns* will be available at LHC, analysis with jets will open up. At this moment HERA will display its full impact. Careful and exhaustive analysis interplaying between HERA PDF fits and LHC jets will have to be considered. For the time being, not all the HERA data have been used for PDF fitting yet, nor an overall analysis which takes into account data from both experiments (H1 and ZEUS) as well as other data for  $F_L$ , the longitudinal structure function, has been fully elaborated yet. The gluon density is still an open issue, especially at low- $x$  and low- $Q^2$  (low at HERA not at LHC!) <sup>7)</sup>. The radiative corrections at low- $x$  are quite important and they drive large discrepancies in the extracted theoretical fits at LO, NLO, NNLO (see fig.3).

In synthesis the issue about the small- $x$  and the  $Q^2$  evolutions as they will occur at LHC is a hot open issue. That is represented by the arrow of fig.1 which indicates the evolution path of the HERA data into the LHC domain. There have been several recent theoretical studies <sup>9)</sup> to disentangle the possible different QCD evolutions and resummations at low- $x$ . All of them seem to point towards a BFKL evolution. As all we know, life for experimenters is usually harder than antecedently foreseen. It may also happen that BFKL evolution at LHC points unto Double Unintegrated Parton Density, *id est* parton densities

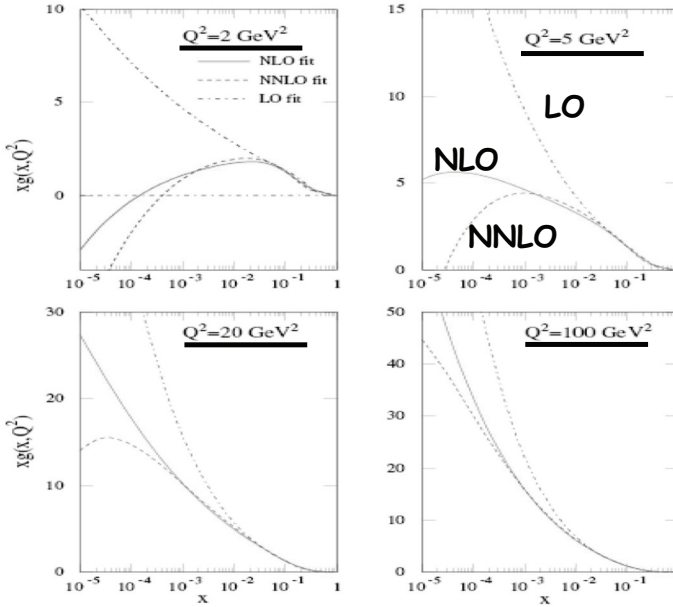


Figure 3: The gluon density function as extracted from different order approximation (from R. Thorne at HERA-LHC workshop <sup>8)</sup>) at different  $Q^2$  values.

not integrated over the usual  $k_T$  and virtuality parameters. If such be the case, a long and painful work await LHC analyzers.

The third big step in LHC analysis will be devoted to precise measurements. At this minute LHC will become a real SM factory. HERA data will probably be used only to calibrate the signals and the PDF fits, without forgetting the (second class) possible discovery of new physics by comparing data and extrapolation of HERA results at very high  $Q^2$ .

A completely different issue refers to *Diffraction*. As defined by Bjorken in 1994 after the first observations of HERA <sup>10)</sup>, ... *the diffraction reactions can be operatively termed as the class of reactions with non-exponentially suppressed large rapidity gaps* (on the longitudinal axis). In this field there are several open issues and many studies available <sup>11)</sup>. I will only write down a personal skeletal synthesis: HERA brought up to the particle physics community the attention on diffraction at high energies with new physics perspectives and ideas. Furthermore, several analysis tools have been developed, together with new parameters in analysis and physics descriptions. IF at LHC more new physical aspects (or the ones already explored but at different regions of phase space) will appear, THEN the diffractive counterbalance between HERA and LHC will be(come) extremely important.

## 5 Conclusions

The importance of the interlude between the HERA machine and LHC has been discussed and illustrated by pointing out some issues related to QCD and Parton Density Functions.

The already long history of PDF results from the two HERA experiments, H1 and ZEUS, led to important (almost final) fitting analysis. Their application to the LHC context especially in term of Standard Model physics will put somehow strong constraints on the extraction of new BSM physics as well on the prospect to make use of SM signals for the measurement of the luminosity. Although studies are progressing and LHC data will enter themselves in the analysis procedures, the first years of analysis at LHC will undergo severe limitations due to the actual knowledge of QCD in a limited phase space region. Indeed the inclusive studies at LHC could easily be overwhelmed by a so called QCD mobocracy, a fully pervaded SM production.

We also clear out the need for awareness while new portion of unexplored phase space in  $x$  and  $Q^2$  will be analyzed at LHC. Even if the evolution equations via their specific resummations underwent recent theoretical developments arranging a beneficial ground for LHC, surprises may arise up due to the small- $x$  corrections and the new regime of the parton dynamics. All that by taking note that the small- $x$  regime will be probably unsettled at HERA. Therefore it may turns out to be a big question mark at LHC.

Similarly, the diffraction production received new exciting inputs from HERA data and analysis. It may be considered as a "new story" at HERA, will it be considered as an "interesting story" at LHC ?

In summary, the first years of LHC analysis will be (probably heavily) constrained by the HERA results. This will be ulteriorly true wether the SM Higgs and no signal of new (supersymmetric)physics will be early discovered below the 200 GeV energy range. In such a case, greater energy ranges will be analyzed mostly in terms of QCD jets where its mobocracy will dominate. However at that further time the LHC data by themselves will certainly be able to overcome the SM production and perform more accomplished studies.

## 6 Acknowledgements

It is a pleasure to thanks the organizers for the invitation and the wonderful and charming ambiance. The participation has been funded by I.N.F.N. Padova.

## References

1. The last results on the SM Higgs searches from Tevatron were presented at ICHEP08 conference at the plenary session, <http://www.hep.upenn.edu/ichep08/talks/misc/schedule>, talk-id=465.
2. K. Jakobs and M. Schumacher, "Prospects for Higgs Boson Searches at the LHC", in "Perspectives on LHC physics", G.Kane and A. Pierce editors, World Scientific (2008).
3. Physics studies from the two collider experiments, ATLAS and CMS, are relevant if not conclusive. For general studies refer e.g. to CMS physics TDR, A. Ball et al, CERN-LHCC-2006-021, CMS-TDR-008-02 (2006).
4. F. Wilczek, "Asymptotic Freedom", Lecture on receipt of the Dirac Medal, hep-th/9609099 (1996).
5. E.Tassi, "Electroweak Physics Measurements at HERA", these proceedings.
6. M. Diehl, "Implications of HERA measurements for LHC", arXiv:0711.1077v2 [hep-ph] (2007).
7. See e.g. A.D.Martin et al., Phys. Lett. B **652**, 292 (2007) also in arXiv:0706.0459v3 [hep-ph] and therein fig.8 where comparison of the gluon density predictions by MSTW2006 and Alekhin2006 PDF fits at NNLO, at  $Q^2 = 5 \text{ GeV}^2$  and low- $x$  region ( $10^{-3.5}$ ), shows big discrepancy (around a factor 4) due mainly to the different treatments of the sea-quarks evolutions.
8. R. Thorne, HERA-LHC workshop of 3/07, (2007).  
The figure has been updated at the HERA-LHC workshop of 5/08, see <http://www.desy.de/~heralhlc/Agenda>, (2008).
9. For recent works see e.g. M.Ciafaloni et al., JHEP **0708**, 046 (2007) also in ar.Xiv:0707.1453 [hep-ph];  
G.Altarelli et al., ar.Xiv:0802.0032v1 [hep-ph] (2008).
10. J. Bjorken, "Hard Diffraction", SLAC-PUB 93-029 (1994).
11. For a general overview see e.g. C.Royon, arXiv:0612.153 [hep-ph] (2006).  
Very recent reports on "Diffraction from HERA to LHC" can be found in M. Diehl, ar.Xiv:0808.0970v1 [hep-ph] (2008), and  
"... from Tevatron to LHC" in C.Royon, arXiv:0805.0261v1 [hep-ph] (2008).



# ANALYTICAL STUDIES FOR NON-PERTURBATIVE QCD OF JETS AT HADRON COLLIDERS

Mrinal Dasgupta

*School of Physics and Astronomy, Oxford Road.,  
Manchester M13 3NP, England*

Lorenzo Magnea

*Dipartimento di Fisica Teorica, Università di Torino,  
and INFN, Sezione di Torino, Via P. Giuria, I-10125 Torino, Italy*

Gavin Salam

*LPTHE, CNRS UMR 7589; UPMC Univ. Paris 6;  
Université Paris Diderot (Paris 7), 75252 Paris Cedex 05, France*

## Abstract

Inspired by the success of analytical models for non-perturbative effects, used to investigate event shape variables at LEP and HERA, we apply them to a study of jets at hadron colliders such as the Tevatron and the LHC. We find that simple analytical estimates are able to shed considerable light on issues that could previously be tackled only through Monte-Carlo simulations, for example the role of different non-perturbative effects in various jet algorithms. In this context, we also provide testable numerical results for the commonly studied inclusive-jet  $p_t$  distribution, and we introduce new observables that could be employed to verify our calculations.

## 1 Introduction

With the LHC due to start later this year, there is considerable activity geared towards sharpening of theoretical and experimental tools, so as to optimize its discovery potential. A portion of this activity is directed at developing a more refined understanding of the physics of strong interactions (QCD), since they will be ubiquitous at the LHC. Since QCD has a non-perturbative aspect that is out of reach for the available tools of quantum field theory, there is an immediate challenge to the level of precision that one may hope to achieve. Inevitably, one has to deal at some level with the effects of parton hadronization, as well as with contamination from the non-perturbative underlying event that accompanies the main hard process.

In an ideal world, one may for example envisage reconstructing clear mass peaks — or other kinematic structures — for some heavy decaying particle (for instance a SUSY particle, or a  $Z'$  decaying to jets at the LHC); in the real hadron collider environment, however, these peaks will be smeared by shifts and distortions in the energy spectrum of final state jets, induced by different QCD effects, so that the signal may even be altogether washed out. The smearing effects will involve both initial and final state QCD radiation, as well as non-perturbative energy flows arising from hadronization and the underlying event. To minimise such smearing requires some understanding of the dependence of each effect on the experimental parameters involved in the study, in particular on the choice of jet-algorithm and on the choice of jet size (which is governed by a “radius” parameter  $R$ ). While perturbative contributions can be obtained using Feynman graph techniques, it is less clear how to acquire information on non-perturbative effects. This is the question that we shall focus on below: we will employ analytical models <sup>1)</sup> that have been very successful in the context of DIS and  $e^+e^-$  event shape studies to the more complex environment of hadron collisions.

## 2 Non-perturbative tools for jet physics

The toolkit for non-perturbative (NP) physics of QCD jets has been thus far rather limited, comprising almost exclusively Monte Carlo (MC) studies using mostly HERWIG and PYTHIA. While MC’s are indispensable tools in this and other regards, they have their own shortcomings, and a certain amount of analytical insight is thus, in our opinion, a welcome addition. For example, it is not straightforward to gain information from MC studies on the functional dependence of NP corrections on jet parameters such as radius, flavour and  $p_t$ , while this information is provided immediately by the analytical estimates we

will derive. The lack of parametric information, in turn, gives rise to a lore of qualitative statements that may or may not be supported by a quantitative analysis. One may hear, for example, that the  $k_t$  algorithm <sup>2)</sup> suffers more significantly from underlying event (UE) contamination, as compared to cone algorithms <sup>3)</sup>, which are supposed to be more significantly affected by hadronisation. We find that, if one chooses the same value of jet radius in either case, there are no differences between algorithms in a first-order calculation. For the UE, calculated to the next order <sup>4)</sup>, one sees as much variation between different cone algorithms as between cones and the  $k_t$  algorithm.

## 2.1 The Dokshitzer-Webber model applied to jets

We shall first examine, as an example, hadronization corrections to a jet transverse momentum  $p_t$ , and then turn to the underlying event contribution. To obtain our main analytical results for hadronization corrections, it is sufficient to use the renormalon-inspired model developed by Dokshitzer and Webber <sup>1)</sup> (DW). This model has been widely used for QCD studies at HERA and LEP, and has been followed by several theoretical developments <sup>5, 6, 7, 8, 9)</sup>, which have firmly established its physical features in the context of our understanding of perturbative QCD. To understand our central result, it is however sufficient to use the model in its original form. In the DW model, hadronization is associated to the emission of a soft gluon with transverse momentum  $k_t \sim \Lambda_{\text{QCD}}$  (“gluer”). While the strong coupling associated to such an emission,  $\alpha_s(k_t)$ , is divergent within perturbation theory, one assumes that it can be replaced, in the infrared, by a physically meaningful infrared finite and universal coupling. One then calculates the change  $\delta p_t$  in the transverse momentum of a jet due to gluer emission, and one averages this change over the gluer emission probability.

In general the calculation will depend on the details of the hard process of which the triggered jet is a part. A full calculation in the threshold limit of hadronic dijet production has been reported in Ref. <sup>10)</sup>. The calculation there reveals that the hadronization contribution is singular in the jet radius  $R$ , as  $R \rightarrow 0$ , *i.e.* in the limit of narrow jets. This most significant feature is in fact universal, and applies to jet production in any hard process; moreover, the leading behavior in  $R$  can be derived with a simple calculation, as we illustrate below.

Consider the emission of a soft gluon from a hard parton (say a quark to be definite), such that the gluon is not recombined with the quark jet. We will work in the collinear approximation, which is sufficient to reproduce the leading small- $R$  behaviour. If the transverse momentum of the quark jet was  $p_t$

before gluon emission, it becomes  $zp_t$  after the emission, with  $z$  the fraction of the initial quark momentum carried by the final quark, so that in the soft limit  $z \rightarrow 1$ . The change in  $p_t$  induced by gluon emission is then  $\delta p_t = (z - 1)p_t$ . Averaging this over phase space with the appropriate probability distribution leads to <sup>1</sup>

$$\langle \delta p_t \rangle = p_t \int \frac{d\theta^2}{\theta^2} \int dz (z - 1) P_{qq}(z) \frac{\alpha_s(\theta z(1 - z)p_t)}{2\pi} \Theta(\theta - R). \quad (1)$$

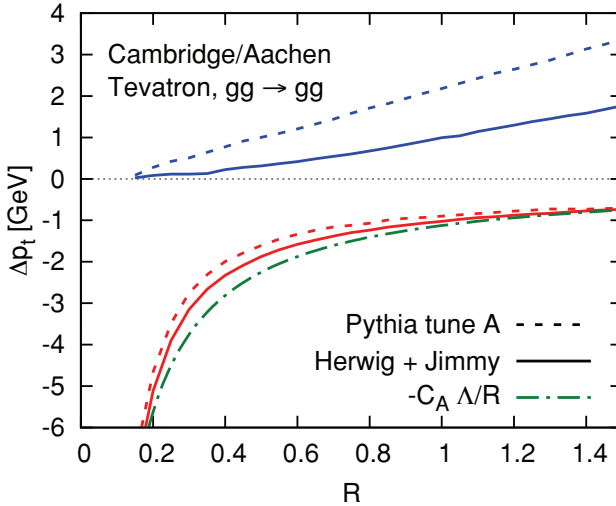


Figure 1: Hadronisation (negative) and underlying event (positive) contributions to jet  $p_t$ , as functions of the jet radius  $R$ , for gluon jets at the Tevatron.

In the perturbative regime Eq. (1) gives a  $\log R$  behaviour, which is a reflection of the collinear enhancement. To evaluate non-perturbative contributions we change variable to  $k_t = z(1 - z)\theta p_t$ , we insert the soft limit of the splitting function  $P_{qq} = 2/(1 - z)$ , and we substitute to the coupling its non-perturbative modification  $\delta\alpha_s$ , corresponding to ‘gluer’ emission. We then integrate over  $\theta$

<sup>1</sup>The condition that the gluon not be recombined with the jet reduces to  $\theta > R$  in the soft limit for all the commonly used jet algorithms.

and  $z$ , which gives

$$\langle \delta p_t \rangle^h = -\frac{4}{R} C_F \int \frac{dk_t}{k_t} k_t \frac{\delta \alpha_s(k_t)}{2\pi}, \quad (2)$$

where  $\delta \alpha_s$  is the non-perturbative QCD coupling minus its perturbative counterpart, and it is non-vanishing only in the infrared region,  $0 < k_t < \mu_I$ , with  $\mu_I$  an infrared matching scale conventionally taken to be  $\mu_I = 2 \text{ GeV}$ . The value of the integral of  $\delta \alpha_s(k_t)$  cannot be computed, but it can be extracted from event shape variables, under the assumption of universality. We arrive then at a simple result for the  $p_t$  shift of a quark jet, which amounts to  $\approx -0.5/R \text{ GeV}$ . For a gluon jet the corresponding result is obtained by replacing  $C_F$  with  $C_A$  in Eq. (2).

The behaviour of underlying event contributions to the same observable, on the other hand, is regular, and vanishes like  $R^2$  as  $R \rightarrow 0$ , in stark contrast with Eq. (2). This result is natural since the underlying event is disentangled from the dynamics of the jet, which serves merely as a receptacle for soft radiation from partons uncorrelated with the hard scattering. Assuming a uniform rapidity distribution for the soft radiation gives a contribution to  $\delta p_t$  proportional to the jet area<sup>4)</sup>, with a functional dependence on  $R$  given by  $RJ_1(R) = R^2 + \mathcal{O}(R^4)$ .

We have compared our expectations for the  $R$  dependence with Monte Carlo event generators, and the results are shown in Fig. 1. One observes that the  $1/R$  hadronization correction is in good agreement with the event generators HERWIG and PYTHIA, in both shape and normalization, over virtually the full range of  $R$  studied. In contrast, while the underlying event varies with  $R$  as expected, its normalisation is different depending on the event generator model. We also emphasize that very similar results are obtained with all commonly used jet algorithms, so that we have displayed just the Cambridge/Aachen<sup>11)</sup> algorithm. We conclude that by varying  $R$  it is possible to enhance or reduce the sensitivity to one non-perturbative effect or the other, as desired, which leads to the possibility of isolating and testing individually the different sources of non-perturbative contributions to jets at hadron colliders. We note finally that the size of the underlying event contribution, unlike that of hadronisation, is not under theoretical control, and is different for HERWIG and PYTHIA at Tevatron energies. Further work is needed to obtain a less ambiguous picture for this component of NP physics.

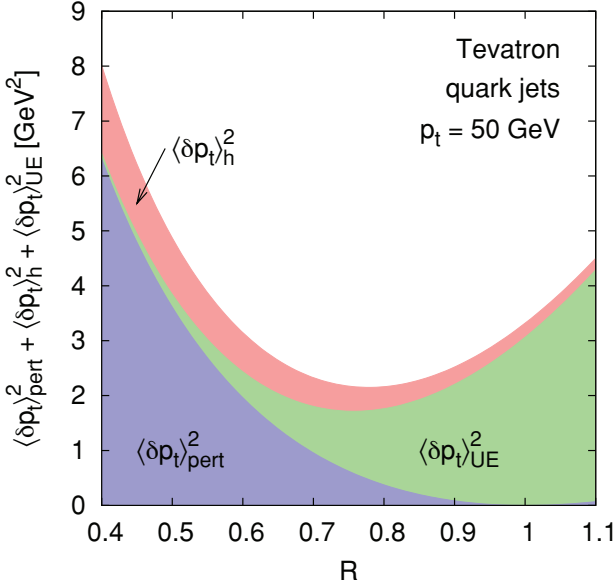


Figure 2: The dispersion of jet  $p_t$  as a function of jet radius, due to perturbative and non-perturbative QCD effects, for 50 GeV quark jets at the Tevatron. The minimum value for the total dispersion corresponds to the best value of  $R$  if one wishes to minimize all QCD effects.

### 3 Experimental tests and applications

We briefly present here some experimental avenues to corroborate and exploit the results mentioned above. A fuller account is available in our article <sup>10)</sup>. One idea that emerges from computing the different  $R$  dependencies of perturbative and non-perturbative QCD effects is that of optimal values of  $R$  for studies involving jets. In the sort of study we mentioned before, aiming at the reconstruction of the mass of a heavy particle decaying to jets, we would like to minimise the dispersion on jet  $p_t$  due to all QCD effects (perturbative and non-perturbative). A detailed study of this dispersion would require a knowledge of correlations between different physical effects, which is not available with current tools. To get a qualitative understanding, one may approximate the true dispersion with the uncorrelated sum

$$\langle \delta p_t^2 \rangle = \langle \delta p_t \rangle_h^2 + \langle \delta p_t \rangle_{\text{UE}}^2 + \langle \delta p_t \rangle_{\text{PT}}^2. \quad (3)$$

Each term in the sum has a characteristic  $R$  dependence at small  $R$ , with the perturbative piece varying as  $\log R$ , the hadronisation correction as  $-1/R$ , and

the underlying event contribution as  $RJ_1(R)$ . The result is plotted for 50 GeV quark jets at the Tevatron in Fig. 2, where we displayed the dispersion due to each effect separately, as well as the approximate total dispersion, whose minimum corresponds to the optimal  $R$ .

While Fig. 2 reflects what could be achieved with current knowledge about the  $R$  dependence, it should not be taken too literally as far as the precise value of the optimal  $R$  is concerned, since we neglected correlations, and furthermore we have oversimplified the perturbative piece, retaining only the leading small  $R$  behaviour. The general features of Fig. 2 are however robust, since they follow from the different parametric dependence on  $R$  of the various physical effects. From our studies we are also able to predict how the optimal  $R$  may change with a change of jet parameters such as “flavour” or  $p_t$ . As might be expected, a gluon jet favours a larger  $R$  value than a quark jet, and likewise the optimal  $R$  rises in a predictable manner with increasing jet  $p_t$  (see <sup>10)</sup> for details).

For QCD studies, involving, say, the determination of  $\alpha_s$  from jet observables, one may again search for an optimal  $R$ : in this case however one should seek to minimize only the non-perturbative contributions. One finds <sup>10)</sup> that the optimal  $R$ , in this case, is proportional to the cube root of the ratio of the characteristic scales for hadronization and underlying event.

Various direct experimental tests can be carried out to check our predictions. In this regard one may for example study inclusive jets at HERA, where the steeply falling  $p_t$  spectrum would be approximately shifted by the  $1/R$  hadronisation effect. Hence a study of inclusive jets with variable  $R$  would provide a valuable opportunity to confirm our results. Similarly studies at the Tevatron could lead to a direct determination from data of the scale of the underlying event, addressing the current disagreement between the MC models of HERWIG and PYTHIA. It is also possible to define operationally, and measure directly as a function of  $R$ , the change in the jet  $p_t$  due to nonperturbative effects as one changes the jet algorithm or the jet parameters; this definition can be implemented in Monte Carlo studies and could be useful to determine the non-perturbative scales associated with hadronization and underlying event.

To conclude, we would like to emphasise the role of simple analytical studies, which are however well grounded in the technology of perturbative QCD, in order to obtain information about complex non-perturbative properties of jets. This information, reflected for example in the dependence on the jet radius of various jet observables, ought to be of use in carrying out precision studies involving jets at current and future colliders. We would especially like to emphasize the importance of maintaining flexibility in the choice of jet algorithm

and jet parameters, since our results show that choices that may be very useful for one class of studies may lead to poor results for other cases.

### Acknowledgements

Work supported by MIUR under contract 2006020509\_004, by the French ANR under contract ANR-05-JCJC-0046-01 and by the European Community's Marie Curie Research and Training Network 'HEPTOOLS', under contract MRTN-CT-2006-035505.

### References

1. Y. L. Dokshitzer and B. R. Webber, *Phys. Lett. B* **352**, 451 (1995), hep-ph/9504219.
2. S. Catani, Y. L. Dokshitzer, M. H. Seymour and B. R. Webber, *Nucl. Phys. B* **406**, 187 (1993); S. D. Ellis and D. E. Soper, *Phys. Rev. D* **48**, 3160 (1993), hep-ph/9305266.
3. G. C. Blazey *et al.*, hep-ex/0005012; G. P. Salam and G. Soyez, *JHEP* **0705**, 086 (2007) arXiv:0704.0292 [hep-ph].
4. M. Cacciari, G. P. Salam and G. Soyez, *JHEP* **0804**, 205 (2008), arXiv:0802.1188 [hep-ph]; *JHEP* **0804**, 063 (2008), arXiv:0802.1189 [hep-ph].
5. Y. L. Dokshitzer, G. Marchesini and B. R. Webber, *Nucl. Phys. B* **469**, 93 (1996), hep-ph/9512336.
6. Y. L. Dokshitzer and B. R. Webber, *Phys. Lett. B* **404**, 321 (1997), hep-ph/9704298.
7. Y. L. Dokshitzer, A. Lucenti, G. Marchesini and G. P. Salam, *Nucl. Phys. B* **511**, 396 (1998), hep-ph/9707532; *JHEP* **9805**, 003 (1998), hep-ph/9802381; M. Dasgupta, L. Magnea and G. Smye, *JHEP* **9911**, 025 (1999), hep-ph/9911316.
8. G. P. Korchemsky and G. Sterman, *Nucl. Phys. B* **555**, 335 (1999), hep-ph/9902341.
9. E. Gardi, *NPB* **622**, 365 (2002), hep-ph/0108222.
10. M. Dasgupta, L. Magnea and G. P. Salam, *JHEP* **0802**, 055 (2008), arXiv:0712.3014 [hep-ph].
11. Y. L. Dokshitzer, G. D. Leder, S. Moretti and B. R. Webber, *JHEP* **9708**, 001 (1997), hep-ph/9707323; M. Wobisch and T. Wengler, hep-ph/9907280.

**CHARMONIUM AND NEW STATES AT B FACTORIES**

Pasha Pakhlov

*ITEP, Moscow*

Written contribution not received



**NEW RESONANCES AT BELLE**

Roman Mizuk  
*ITEP, Moscow*

Written contribution not received



**TITLE SPECTRUM AND DECAYS OF DIQUARK  
ANTIDIQUARK STATES**

Antonello Polosa  
*INFN-Roma 1, Italy*

Written contribution not received



**SPECTRUM OF POSITIVE AND NEGATIVE PARITY  
PENTAQUARKS, INCLUDING  $SU(3)_F$  BREAKING**

Franco Buccella

*Dipartimento di Scienze Fisiche, Università di Napoli "Federico II"  
and INFN, Sezione di Napoli, Via Cintia, I-80126 Napoli, Italy*

**Abstract**

We reproduce the spectrum of the pentaquark states of both parities proposed in the literature within a constituent model, where we consider the chromomagnetic interaction and the spin orbit term.

## 1 Introduction

I am going to describe a recent work on pentaquarks in collaboration with Mario Abud, Domenico Falcone, Giulia Ricciardi and Francesco Tramontano <sup>1)</sup>. The evidence about the existence of pentaquarks is oscillating in time. After the first  $\Theta^+$  discovery <sup>2)</sup>, there was a negative experiment <sup>3)</sup> and more recently again a positive result <sup>4)</sup>. Since many years exotic baryonic resonances in  $KN$  scattering have been found in phase shift analysis <sup>5)</sup> <sup>6)</sup> <sup>7)</sup>. Evidence has also been claimed for the existence of a narrow  $\Xi^- \pi^-$  baryon resonance with mass  $1.862 \pm 0.002$  GeV at  $4.0 \sigma$  <sup>8)</sup>. This state would be an exotic baryon  $\Xi^{--}$  with isospin  $I = 3/2$ , hypercharge  $Y = -1$  and quark content  $ddss\bar{u}$ . A  $P_{11}$  resonance has been found at  $1358$  MeV by BES <sup>9)</sup> in the study of the decay  $J/\psi \rightarrow p\bar{p}\pi^0$ .

Some years ago the lightest scalar nonet with the isovector  $A^0$  degenerate in mass with the heavier isoscalar  $f^0$  at 980 MeV has been interpreted as a tetraquark <sup>10)</sup>, as already conjectured by Jaffe in 1978 <sup>11)</sup>.

It is reasonable to expect such mesonic states to be accompanied by exotic baryonic states, consisting of four quarks ( $4q$ ) and an antiquark ( $\bar{q}$ ).

We shall show that the experimental information on these states available now complies well with what one should deduce within a constituent quark model, where the chromomagnetism plays the main role; we also include the effect of  $SU(3)_F$  flavour symmetry breaking.

The chromo-magnetic interaction has been proved remarkably successfully at describing the spectrum of the standard baryons <sup>12)</sup>, which transform as the 56 of  $SU(6)_{FS}$  <sup>13)</sup>, of the positive and negative parity  $Y = 2$  baryons <sup>14)</sup> and of the two lightest scalar nonets <sup>15)</sup>.

Here we extend the analysis to the pentaquarks with one or more strange constituents, that is to  $Y < 2$ . We shall consider  $S$  and  $P$  waves and, for the latter, the case with  $4q$  in  $P$  wave previously considered by Jaffe and Wilczek <sup>16)</sup>.

## 2 The chromomagnetic interaction

In the limit of exact  $SU(3)_F$  flavour symmetry, the hamiltonian in the chromomagnetic model for constituents in S-wave reads

$$H = \sum_i m_i - C \sum_{i < j} \lambda_i \cdot \lambda_j \sigma_i \cdot \sigma_j \quad (1)$$

where  $\sigma_i$  and  $\lambda_i$  are respectively the Pauli and Gell-Mann matrices for colour  $SU(3)_C$ , acting on the  $i^{th}$  quark (or antiquark), while  $m_i$  is its constituent mass.

The contribution of the chromomagnetic interaction (1) can be written as a combination of the  $SU(6)_{CS}$  color-spin,  $SU(3)_C$  color and  $SU(2)$  spin Casimir operators [17].

We call  $p$  the pentaquark state  $(4q)\bar{q}$  and  $t$  the tetraquark state  $4q$ . The mass of a negative parity pentaquark state is given by

$$\begin{aligned} m(s) &= \sum_{i=1}^4 m_{q_i} + m_{\bar{q}} + C_{4q,\bar{q}}^s [C_6(p) - C_6(t) + \\ &- \frac{1}{3}C_2(p) + \frac{1}{3}C_2(t) - \frac{4}{3}] + \\ &- C_{qq} \left[ C_6(t) - \frac{1}{3}C_2(t) - \frac{26}{3} \right]. \end{aligned} \quad (2)$$

Since  $p$  is a colour singlet, the tetraquark  $t$  needs to be in the fundamental representation of  $SU(3)_C$ . The last two terms contributing to  $m(s)$  express the interaction of the tetraquark with the antiquark and the interaction of the quarks in the tetraquark, respectively: the lightest states have large  $SU(6)_{CS}$  Casimir for the  $4q$  and as small as possible for the pentaquark. It applies to states with  $Y = 2$  and  $Y = 1$ , with no strange quarks.

In order to use the mass formula, given a pentaquark state with defined isospin and hypercharge, one needs to identify its group properties under  $SU(6)_{CS}$ ,  $SU(3)_C$  and  $SU(2)$  spin, as well as those of its 4-quark subsystem.

In the pentaquarks, the colour-spin part of the wave function has to be combined with the flavour part and the orbital part in such a way that the total pentaquark wave function is a colour singlet state and the four quarks obey the Pauli principle, i.e. are antisymmetric under any permutation of the four quark. When the  $4q$  are in the S wave, the request of total antisymmetry relates

the  $SU(6)_{CS}$  and the  $SU(3)_F$  properties of their wave function. The resulting correspondence is:

$$210_{CS} \leftrightarrow 3_F \quad 105_{CS} \leftrightarrow \bar{6}_F \quad 105'_{CS} \leftrightarrow 15_F \quad \bar{15}_{CS} \leftrightarrow 15'_F \quad (3)$$

An easy way to find relations (3) is to look at the Young diagram associated to each representations of the  $4q$  in  $SU(6)_{CS}$ ; the Young diagram obtained by interchanging rows and columns gives the related representation for  $SU(3)_F$ . The correspondance between the  $SU(6)_{CS}$  and the  $SU(3)_F$  transformation properties for the  $4q$  state gives the  $SU(6)_{CS}$  group properties of pentaquark states with definite hypercharge  $Y$  and isospin  $I$ . Let us show it in the case of pentaquarks with  $Y = 2$ , with quark content  $(4q)\bar{s}$ .

No  $Y = 2$  pentaquark state can be constructed starting from a representation  $3_F$  for the  $4q$  subsystem. On the contrary, the representations  $\bar{6}_F$ ,  $15_F$  and  $15'_F$  contain states with  $Y = 4/3$  and isospin  $I = 0$ ,  $I = 1$  and  $I = 2$ , respectively; therefore, by adding an antiquark  $\bar{s}$ , we can obtain  $Y = 2$  pentaquarks, without changing the value of the isospin.

Hypercharge  $Y = +2$  baryon resonances, called  $Z^*$ , have been revealed in  $KN$  interactions. The  $Z^*$  resonances  $D_{03}$  and  $D_{15}$  (the two lower indexes stand for the isospin and twice the spin, respectively), have negative parity, and have possibly been revealed within mass ranges  $m_{D_{03}} = 1788 - 1865$  and  $m_{D_{15}} = 2074 - 2160$ , respectively. While we can use Eq. (2) for the states with  $Y = 2$  and  $Y = 1$  without strange constituents,  $SU(3)_F$  breaking implies more complicate expressions for the pentaquarks containing both light (u,d) and strange quarks. In fact we assume the giro-chromomagnetic factors to be inversely proportional to the constituent masses of the quark involved.

Pentaquark with positive parity may be costructed with  $t$  in  $P$ -wave and  $\bar{q}$  in  $S$ -wave with respect to  $t$  16).

In the symmetry limit the mass of the pentaquark states is

$$\begin{aligned} m(p) = & \Sigma_{i=1,4} m_{q_i} + m_{\bar{q}} + \frac{1}{2}C [C_6(p) - C_6(t)] \\ & - \frac{1}{3}C_2(p) + \frac{1}{3}C_2(t) - \frac{4}{3} + \\ & + \Delta m_{qq}^1 + \Delta m_{qq}^2 + K_1 + a \vec{L} \cdot \vec{S}_q. \end{aligned} \quad (4)$$

Here  $\Delta m_{qq}^1$  and  $\Delta m_{qq}^2$  are the contributions of the chromomagnetic interaction for each of the two diquark clusters, and depend on the colour and spin of the pair of quarks.

$K_1$  is the kinetic term associated to the angular motion of the quarks. The spin-orbit term arises, as in electrodynamics, from the interaction of the quarks with the coloured current. It is proportional to the giro-chromomagnetic factor of the quarks in P wave as well to the product of their colour matrices : more precisely, if the representation  $3_C$  of the  $4q$  state is originated by the  $\bar{3}_C \otimes \bar{3}_C$ , or the  $6_C \otimes \bar{3}_C$  representation of the two diquark pairs, the coefficients will be in the ratio 2 : 5.

The  $SU(3)_F$  breaking in the chromomagnetic interaction and in the spin-orbit term implies the mixing between different representations of  $SU(3)_F$ . We assume the kinetic energy and the spin-orbit term to be inversely proportional to the reduced mass of the two pairs in P-wave.

While the contribution of the quarks in the two pairs depends on the colour and the spin of the pair, their interaction with the  $\bar{q}$  depends on the  $SU(6)_{CS}$  transformation property of the  $4q$  with  $L = 1$  <sup>14</sup>). The total antisymmetry with respect to the exchange of the quarks, which are in the two S-wave pairs, and of the two pairs (which are in P-wave), fixes the  $SU(3)_F$  quantum numbers of the pentaquarks.

### 3 The "open door" decay channels

It has been observed for the first time by Jaffe <sup>11</sup>) that some  $qq\bar{q}\bar{q}$  mesons may decay into two ordinary mesons (PP, PV, VV) by simple separation of the constituents: he called these channels "open door".

Many years later a group theoretical criterium has been found <sup>18</sup>) to give a necessary condition for a PP and PV channels to be "open door", according to  $SU(6)_{CS}$  symmetry. Since a pseudoscalar and a vector meson transform under the singlet  $1_{CS}$  or the adjoint  $35_{CS}$  representation of  $SU(6)_{CS}$ , respectively, only states, which transform as  $1_{CS}$  (or  $35_{CS}$ ) of  $SU(6)_{CS}$ , may have "open door" amplitudes into PP (or VP) final states.

The contributions of the chromomagnetic interaction are proportional to a combination of quadratic Casimir operators, and the most strong dependance is on

the  $SU(6)_{CS}$  Casimir operator.

Therefore the eigenstates of the mass spectrum belong to almost irreducible representations of  $SU(6)_{CS}$ . In particular, the lighter tetraquark meson scalar (or axial) states, which transform approximately as a singlet (or  $35_{CS}$ ), have large "open door" amplitudes into PP (or VP) channels.

These considerations can be extended to pentaquarks, as a consequence of the  $SU(6)_{CS}$  transformation properties of the baryon  $1/2^+$  octet and of the  $3/2^+$  decuplet, respectively in the  $70_{CS}$  and the  $20_{CS}$  representations: only pentaquarks with the same  $SU(6)_{CS}$  transformation properties have "open door" amplitudes into a channel consisting of one of these baryons and a pseudoscalar meson.

Therefore there is a correlation between smaller mass and large couplings to the final channels consisting of a baryon of the 56 of  $SU(6)_{FS}$  and a pseudoscalar meson. For these negative parity pentaquarks we expect the "open door" channels above threshold to be difficult to detect for their broad width, as the long controversy about the  $f_0$  has shown.

Instead we expect that the first pentaquarks with positive parity to be detected are the ones with large couplings to the final states. In conclusion we expect P and D-wave resonances to have been already found.

#### 4 Comparison with data

We find a good description of the present albeit controversial experimental evidence for pentaquarks with the following parameters:

$$\begin{aligned}
 C &= 74.5\text{MeV} \\
 m_u &= 346.8\text{MeV} \quad m_s = 480\text{MeV} \\
 a &= 73\text{MeV} \quad K = 110\text{MeV}
 \end{aligned}
 \tag{5}$$

In fact one gets:

$$\begin{aligned}
 m(\text{Roper}) &= 1356 \text{ MeV} & m(\Theta^+) &= 1545 \text{ MeV} \\
 m(P_{11}) &= 1732 \text{ MeV} & m(\Xi^{11}) &= 1851 \text{ MeV} \\
 m(D_{03}) &= 1858 \text{ MeV} & m(D_{15}) &= 2088 \text{ MeV}
 \end{aligned}
 \tag{6}$$

to be compared with:

$$\begin{aligned}
 m(Roper) &= 1358 \text{ MeV} & m(\Theta^+) &= 1540 \text{ MeV} \\
 m(P_{11}) &= 1720 \text{ MeV} & m(\Xi^{11}) &= 1862 \text{ MeV} \\
 m(D_{03}) &= 1788 - 1865 \text{ MeV} & m(D_{15}) &= 2074 - 2150 \text{ MeV}
 \end{aligned} \tag{7}$$

The pentaquark states already discovered are just the ones expected and a good description of their masses is obtained with reasonable values of the parameters.

## References

1. M. Abud, F. Buccella, D. Falcone, G. Ricciardi and F. Tramontano ( in preparation).
2. LEPS Collaboration, T. Nakano et al., *Phys. Rev. Lett.* **91** (2003) 012002; DIANA collaboration, V.V. Barmin et al., *Phys Atom. Nucl.* **66**, 1715 (2003).
3. CLAS Collaboration, B. Mc Kinnon et al., *Phys. Rev. Lett.* **96** (2006) 2120031.
4. V.V. Barmin et al., DIANA Coll., *Phys.Atom.Nucl.* **70** (2007) 35; A. Kubarovsky, SVD Coll., arXiv:hep-ex/0610050v1.
5. The Particle Data Group *Phys. Lett.* **B111** (1982) 1.
6. R. A. Arndt and L. D. Roper *Phys. Rev.* **D31** (1985) 2230.
7. J. S. Hyslop, R. A. Arndt , L. D. Roper and R. L. Workman *Phys. Rev.* **D46** (1992) 961.
8. NA49 Collaboration, C. Alt et al., *Phys. Rev. Lett.* **92** (2004) 042003.
9. BES Collaboration, M. Ablikim et al. *Phys. Rev. Lett.* **97** (2006) 062001.
10. L. Maiani, F. Piccinini, A.D. Polosa, V.Riquer, *Phys. Rev. Lett.* **92** (2004) 042003.
11. R. L. Jaffe, *Phys. Rev.* **D17** (1978) 1444.

12. A. De Rújula, H. Georgi and S.L. Glashow, *Phys. Rev.* **D12** (1975) 147.
13. F. Gursey and L.A. Radicati, *Phys. Rev. Lett.* **13** (1964) 173.
14. F. Buccella, D. Falcone and F. Tramontano, *Central. Eur. J. Phys.* **3** (2005) 525.
15. F. Buccella, H. Högaasen, J. M. Richard and P. Sorba, *Eur. Phys. J.* **C49** (2007) 743.
16. R. L. Jaffe and F. Wilczek, *Phys. Rev. Lett.* **91** (2003) 232003;
17. H. Högaasen and P. Sorba, *Nucl. Phys.* **B145** (1978) 119;  
M. De Crombrugghe, H. Högaasen and P. Sorba, *Nucl. Phys.* **B156** (1979) 347.
18. F. Buccella, *Mod. Phys. Lett.* **A21** (2006) 831.

## ***SESSION IV – ELECTROWEAK AND TOP PHYSICS***

<i>Andrew Askew</i>	Electroweak Measurements (Including Dibosons) at the Tevatron
<i>Tassi Enrico</i>	Electroweak Physics Measurements at HERA
<i>Adelman Jahred</i>	Top Quark Mass Measurements at the Tevatron
<i>Pleier Marc-André</i>	Top Quark Pair Production and Properties Measurements at the Tevatron
<i>Dong Peter</i>	Measurement of the Electroweak Single Top Production Cross Section at the Tevatron
<i>Bellomo Massimiliano</i>	Standard Model Physics in ATLAS at the Start of the LHC
<i>Wardrope David</i>	W and Z Measurements with the Initial CMS Data
<i>Piccinini Fulvio</i>	Drell-Yan Processes at LHC
<i>Masiero Antonio</i>	Flavour Physics in the LHC Era



# **ELECTROWEAK MEASUREMENTS (INCLUDING DIBOSONS) AT THE TEVATRON**

A. W. Askew  
*Florida State University, Fermilab MS 352,  
P.O. Box 500, Batavia, Illinois USA*

## **Abstract**

The large amounts of data being integrated by the CDF and DØ experiments at the Fermilab Tevatron allow for large samples of vector bosons to be collected. As a result precise measurements of the properties of inclusive W and Z production can be made. At the same time studies of events with multiple vector bosons may be studied for insight into the structure of the Standard Model.

## 1 Introduction

The increasing integrated luminosity being delivered to the CDF and DØ experiments at the Fermilab Tevatron, allow for many different electroweak measurements to be made. The production properties of W and Z bosons give insight into the structure of the proton, and the behavior of the Standard Model. These measurements, by their very nature, require large inclusive samples of events, since they require differential (and in some cases, double differential) cross section measurements. On the other end of the spectrum, with more data, comes an opportunity to study very low cross section processes such as ZZ, which can give information as to the structure of the underlying gauge theory. The analyses presented here make use of 0.2-1.9 fb<sup>-1</sup> of integrated luminosity.

## 2 Inclusive W measurements

The large cross section for W production at the Tevatron makes available large samples of W events, even after accounting for the branching fraction for decays to electron (and neutrino) and muon (and neutrino). Using these samples, precision measurements of the mass and width, as well as the production charge asymmetry may be made. Those summarized here are the W charge asymmetry as well as the W mass and width.

### 2.1 W Charge Asymmetry

On average, the u-quark carries more of the proton momentum than the d-quark. Thus in the production of W bosons, the  $W^+$  tends to be produced with momentum along the proton direction, and likewise the  $W^-$  is produced along the direction of the anti-proton. This charge asymmetry can be observed in two ways: one can make a hypothesis as to the unknown  $p_Z$  of the neutrino from the W decay and solve for the W rapidity directly <sup>1)</sup>, or one may assume the V-A structure of the W decay is well known, and instead measure the rapidity of the charged lepton.

The CDF experiment chooses to do the former, and selects the best hypothesis for the neutrino  $p_Z$  based on the event kinematics. Using 1 fb<sup>-1</sup> of data, CDF reconstructs the W rapidity in the electron channel (due to the large coverage of the calorimeter, which yields good acceptance for the leptons).

The DØ experiment does the latter, using the lepton charge asymmetry in the muon channel, due to the much smaller backgrounds and charge misidentification systematics in this channel. The measurement of the muon charge asymmetry uses 0.3 fb<sup>-1</sup> of integrated luminosity <sup>2)</sup>.

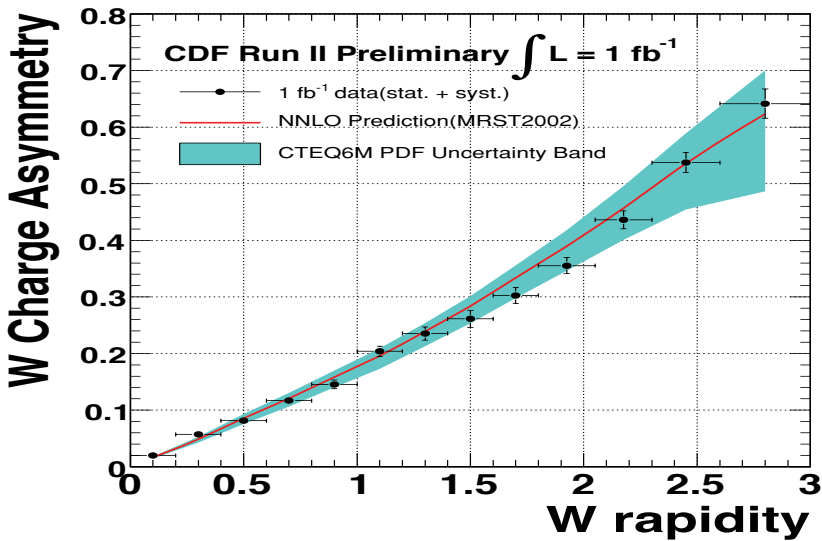


Figure 1: *CDF W charge asymmetry measurement (preliminary). The points correspond to the measured data, the red curve is the NNLO Monte Carlo prediction<sup>3)</sup> (using MRST2002 parton distribution functions), and the blue band is the uncertainty from the CTEQ6M parton distribution functions.*

## 2.2 W Mass and Width

A full discussion of the measurement of the W mass and W width is beyond the scope of these proceedings. In short, by use of the kinematic quantities sensitive to these properties (the lepton  $p_T$ , the missing transverse energy, and the transverse mass), and a detailed and precise understanding of detector response, one may generate templates for different values of the mass and width, and find the values which are most representative of the data distributions (full discussions of these measurements are detailed in<sup>4)</sup> and<sup>5)</sup>). The CDF experiment has measured the W mass with  $200 \text{ pb}^{-1}$ , and the W-width with  $350 \text{ pb}^{-1}$ . The W-mass is measured to be  $80413 \pm 34(\text{stat.}) \pm 34(\text{syst.}) \text{ MeV}/c^2$ . This is the single most precise measurement of this quantity, and improves the uncertainty on the world average by 15%. The W-Width is measured to be  $2032 \pm 73(\text{stat.}+\text{syst.}) \text{ MeV}/c^2$ . This is the most precise single direct measurement of this quantity, and decreases the uncertainty on the world average

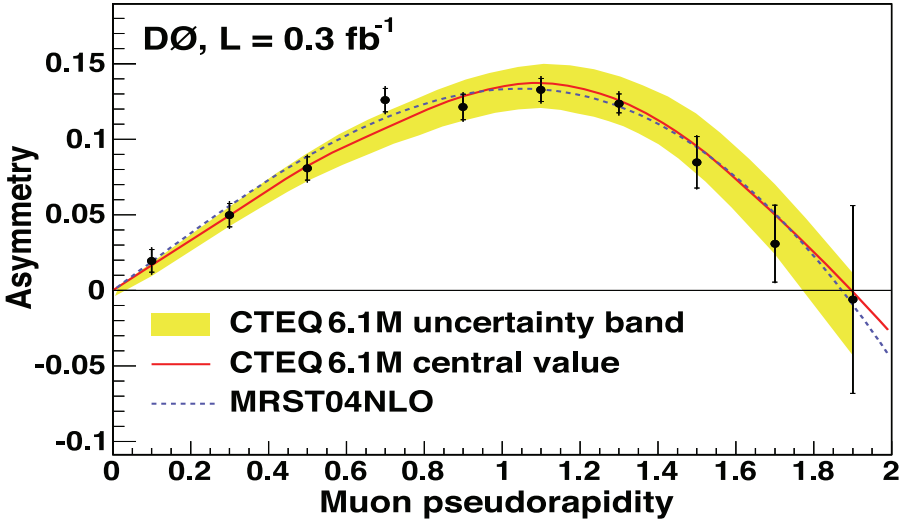


Figure 2:  $D^0$  muon charge asymmetry measurement. The points correspond to the measured data, the red line is the RESBOS plus PHOTOS central value using CTEQ6.1M parton distribution functions, the blue dotted line is the RESBOS plus PHOTOS central value using MRST2004 parton distribution functions, and the yellow band represents the uncertainty from the CTEQ6.1M parton distribution functions.

by 22%.

### 3 Inclusive Z measurements

Measurements of inclusive Z boson production can shed light on not only the parton distribution functions, but also the extent to which the merger of perturbation theory and soft gluon resummation provide a consistent description of the  $p_T$  distribution of the produced Z bosons. In addition,  $Z \rightarrow \tau\tau$  events provide an important calibration for hadronic  $\tau$  decays.

#### 3.1 $Z \rightarrow \tau\tau$ Cross Section

The measurement of Z boson decays provide a standard candle not only for studying detector performance for the reconstruction of leptons, but also to ensure that the energy scale and resolution for these leptons is properly determined. For processes such as  $Z \rightarrow \tau\tau$ , it is vital to assess both performance

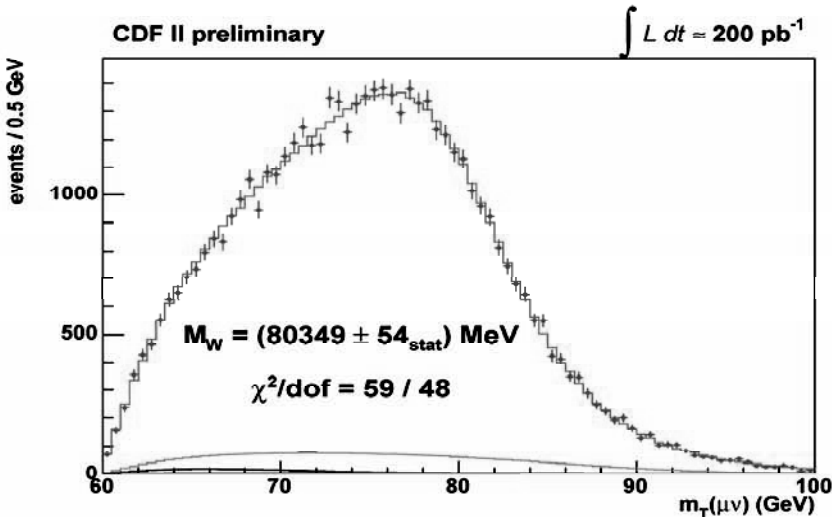


Figure 3: *Transverse mass of  $W \rightarrow \mu\nu$  from CDF  $W$ -mass measurement. The blue points are the data with statistical uncertainties. The red curve is the combined  $W$ -mass Monte Carlo (for the measured value) combined with the estimated backgrounds (the pink and grey curves).*

(of both reconstruction and triggering) and resolution/scale for further analyses involving  $\tau$  decays to hadrons (notably Higgs searches). Using  $1 \text{ fb}^{-1}$  of integrated luminosity, the  $D\bar{O}$  experiment measures the  $Z \rightarrow \tau\tau$  cross section when one  $\tau$  decays leptonically, and then other  $\tau$  decays to hadrons. The cross section is measured to be  $\sigma(p\bar{p} \rightarrow Z \rightarrow \tau\tau) = 247 \pm 8(\text{stat.}) \pm 13(\text{syst.}) \pm 15(\text{lumi.}) \text{ pb}$ , in good agreement with the Standard Model value of  $251_{-11.8}^{+5} \text{ pb}$ .

### 3.2 $Z$ Rapidity Measurement

At leading order, the  $Z$  rapidity is specified by the momentum fractions carried by the colliding partons. So natively, this is a distribution that is highly influenced by the parton distribution functions. At next-to-leading order, gluon radiation also makes changes to this distribution, making this measurement sensitive to the measurement of these effects as well.

CDF measures the differential cross section for  $Z \rightarrow ee$  events as a function of rapidity. While statistics limited, the measured distribution is in good agreement with the shape of the NLO MC theory distribution (normalized to

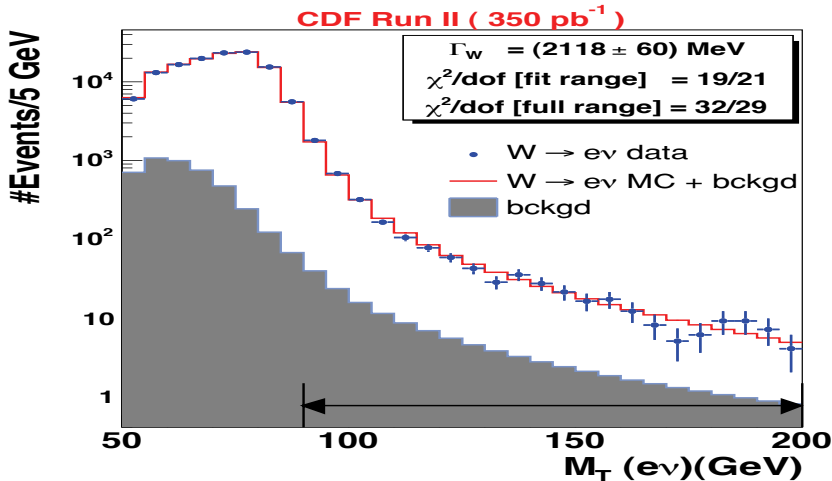


Figure 4: *Transverse mass of  $W \rightarrow e\nu$  from CDF  $W$ -width measurement. The blue points are the data with statistical uncertainties. The red curve is the combined  $W$ -width Monte Carlo (for the measured value) combined with the estimated background (the grey shaded histogram).*

the data cross section) using the CTEQ6.1M parton distribution functions.

### 3.3 $Z p_T$ Measurement

At leading order, the produced  $Z$  boson  $p_T$  is zero. Thus measuring this distribution is a direct probe of NLO QCD, which has two distinct regimes. For large  $p_T$ , the theoretical calculation can be made in perturbation theory. For very small  $p_T$  one must invoke soft gluon resummation, which involves free parameters which must be measured from the data. One of these parameters,  $g_2$ , determines the position of the peak of the distribution in  $Z p_T$  (which is the same parameter which determines the peak position for  $W p_T$ , making this an important measurement for precision tests such as  $W$ -mass).

The  $D\bar{O}$  experiment measures the shape of the  $Z p_T$  distribution using approximately  $1 \text{ fb}^{-1}$  of integrated luminosity. Using the low  $p_T$  data, the value for  $g_2$  is measured. The shape of the data at high  $p_T$  agrees well with the NNLO theory prediction from <sup>7)</sup>. In this study, the  $Z p_T$  distribution is also measured in two separate bins of  $Z$ -rapidity, a first step towards a true double

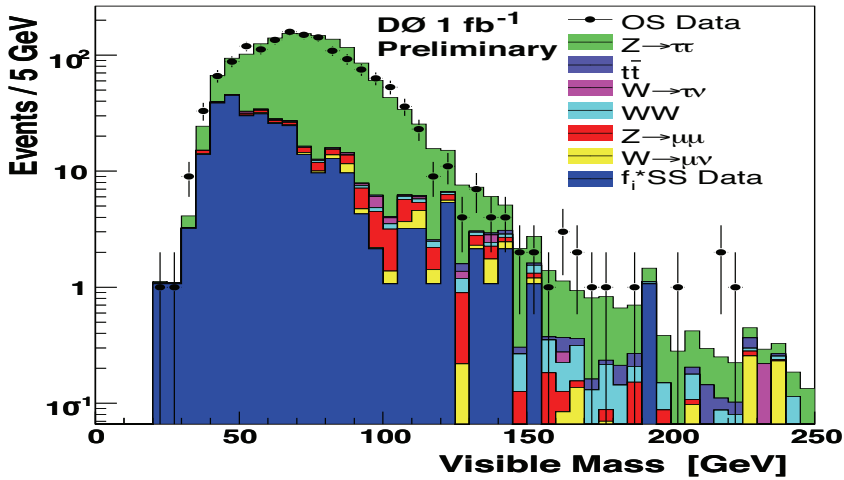


Figure 5: Visible mass of  $Z \rightarrow \tau\tau$  with subsequent decay of one  $\tau \rightarrow \mu$  and one  $\tau$  decaying hadronically, from  $D\bar{O}$  cross section measurement (preliminary). The points represent the data candidates with statistical uncertainties. The green shaded histogram is the sum of the  $Z \rightarrow \tau\tau$  Monte Carlo combined with the estimated backgrounds (QCD multijet (dark blue),  $t\bar{t}$  (blue-grey),  $W \rightarrow \tau\nu$  (pink),  $WW$  (light blue),  $Z \rightarrow \mu\mu$  (red), and  $W \rightarrow \mu\nu$  (yellow)).

differential cross section.

#### 4 Diboson Measurements

At hadron colliders, in the same manner as on-shell W production, one may produce off-shell, high mass W propagators. As a consequence of this, there is the opportunity to study such final states as WZ, which in the case of the trilinear vector boson coupling is the result of a very off-shell W radiating a Z boson to become an on-shell W boson. In the case of these trilinear vertices, the Standard Model prediction is absolute (there is no tuning possible), the coupling of the W and Z must be as predicted, and as such any deviation is evidence for new physics. In the case of ZZ production, there is no trilinear boson diagram in the Standard Model, and thus if there is anomalous production of pairs of Z bosons, then this again is evidence for new physics.

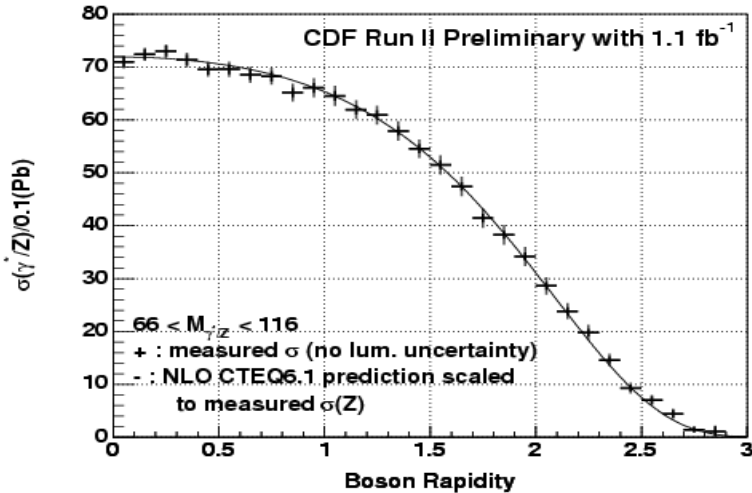


Figure 6: CDF Z rapidity measurement. The measured differential cross section (without luminosity uncertainty) is shown as the points. The solid line is the NNLO prediction from <sup>6)</sup> using CTEQ6.1M parton distribution functions, scaled to match the measured cross section.

#### 4.1 WW/WZ $\rightarrow \ell\nu jj$

At hadron colliders, in general, only leptonic decays of W and Z bosons are discernable from the large QCD dijet backgrounds. However, in the case of semileptonic decay of WW/WZ  $\rightarrow \ell\nu jj$ , the much larger branching fraction of W or Z to hadrons, produced in association with a well identified lepton and missing transverse energy, motivates an attempt to winnow out a signal. WW/WZ are combined together as the resolution on the jet transverse momentum (for both Tevatron experiments) is insufficient to separate the constituent W and Z decays to hadrons.

CDF attempts to find evidence for this diboson final state by first selecting a sample of W bosons produced in association with two or more jets. Then a neural network is used, trained on Monte Carlo, which exploits the kinematic correlations present in W and Z decays to jets, as opposed to the inclusive QCD background. Template shapes are verified in the di-jet mass bins which should have little signal contribution, and then bin by bin template fits are performed to extract the signal contribution in the range of 60-100 GeV. The number of signal extracted from these fits is  $410 \pm 212(\text{stat.}) \pm 107(\text{syst.})$  events. Since

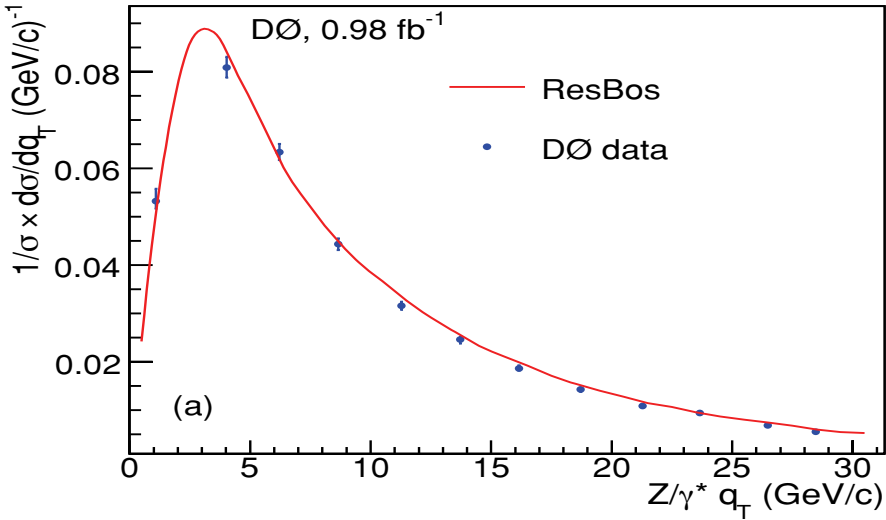


Figure 7:  $D\bar{O}$   $Z p_T$  spectrum: Low  $p_T$  region used for measurement of  $g_2$  parameter. The points are the measured data, the red line is the RESBOS prediction.

this is not sufficient to claim evidence, a limit of  $2.88 \text{ pb}$  is set on the cross section times branching fraction.

#### 4.2 $WZ \rightarrow \ell\ell\nu$

Unlike the semileptonic decay of  $WZ$ , the three charged lepton decay mode is one of the cleanest signals at a hadron collider. This comes at the cost of the branching fraction of both the  $W$  and the  $Z$  to leptons, specifically electrons and muons. Both CDF and  $D\bar{O}$  have significant samples of  $WZ \rightarrow \ell\ell\nu$ , which then can be used to set limits on anomalous  $WWZ$  couplings, by use of the  $Z$  boson  $p_T$  spectrum.

The  $D\bar{O}$  experiment uses  $1 \text{ fb}^{-1}$  of data and finds 13 candidate events, with expected signal of  $9.2 \pm 1.0$  and expected background of  $4.5 \pm 0.6$ . The measured cross section is  $2.7^{+1.7}_{-1.3} \text{ pb}$  <sup>8)</sup>. The CDF experiment uses  $1.9 \text{ fb}^{-1}$  of data and finds 25 candidate events, with expected signal of  $16.5 \pm 2.0$  and expected background of  $5.8 \pm 0.7$ . The measured cross section is  $4.3^{+1.4}_{-1.0} \text{ pb}$ .

When setting limits on anomalous  $WWZ$  couplings, both CDF and  $D\bar{O}$  use a form factor scale  $\Lambda = 2 \text{ TeV}$ . The one-dimensional limits from CDF are:  $-0.13 < \lambda_Z < 0.14$ ,  $-0.15 < \Delta g_1^Z < 0.24$ , and  $-0.82 < \Delta \kappa_Z < 1.27$ . The

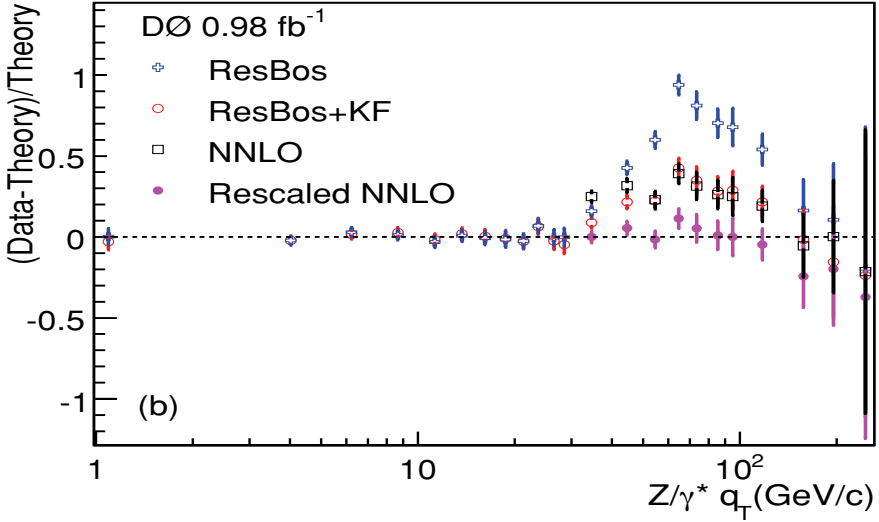


Figure 8:  $D\bar{O}$   $Z$   $p_T$  spectrum,  $(Data-Theory)/Theory$ . The blue points use *RESBOS* as the theory. The red points use *RESBOS* as the theory, along with a  $k$ -factor to adjust to NNLO effects. The black points are the NNLO prediction from  $\hat{\gamma}$ , and the pink points are the NNLO theory prediction rescaled to the data normalization.

$D\bar{O}$  one-dimensional limits, which assume  $\Delta g_1^Z = \Delta \kappa_Z$  (and are thus not directly comparable), are:  $-0.17 < \lambda_Z < 0.21$ ,  $-0.14 < \Delta g_1^Z < 0.34$ , and  $-0.12 < \Delta \kappa_Z < 0.29$ .

### 4.3 $ZZ \rightarrow lll$

The smallest cross section times branching fraction diboson process at hadron colliders is that of  $ZZ \rightarrow lll$ . In no other analysis is the acceptance times efficiency of the detector tested as in this one. Both  $D\bar{O}$  and CDF have performed searches for this process. The  $D\bar{O}$  experiment finds one candidate using  $1 \text{ fb}^{-1}$  of integrated luminosity and sets a limit on the cross section of  $\sigma_{ZZ} < 4.4 \text{ pb}$ . Limits on anomalous neutral gauge couplings are also set (for the first time at a hadron collider) <sup>9</sup>.

CDF finds three candidates with an estimated background of less than 0.1 event, and claims  $4.2\sigma$  evidence for  $ZZ$  production in the four charged lepton channel <sup>10</sup>. Thus a cross section of  $1.4_{-0.6}^{+0.7} \text{ pb}$  is measured for this

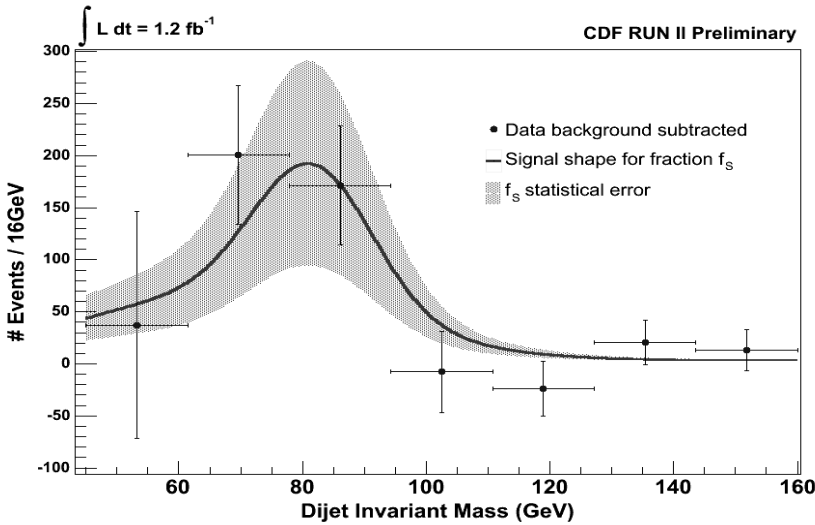


Figure 9: *CDF WW/WZ*  $\rightarrow$   $l\nu jj$ : Di-jet invariant mass after background subtraction. Each point is the result of a template fit to the neural network discriminant in the corresponding di-jet mass bins.

process. It is worth noting that substantial improvement in the identification of leptons was found by using calorimeter clusters without tracks (in areas of lower tracking coverage) and isolated tracks without calorimetry (in areas of sparse calorimeter coverage) to build a more uniform lepton acceptance.

## 5 Summary

Both of the Tevatron experiments are taking full advantage of the integrated luminosity received in Run II. Precision measurements of W and Z boson properties are becoming available, as are measurements of the smallest diboson production cross sections yet observed. All measurements will improve in uncertainty with the addition of integrated luminosity being gained at the time of these proceedings.

## References

1. A. Bodek *et al.*, “Direct measurement of W Production Charge Asymmetry at the Tevatron,” arXiv:0711.2859 [hep-ph].

2. V. M. Abazov *et al.* [D0 Collaboration], Phys. Rev. D **77**, 011106 (2008).
3. C. Anastasiou *et al.*, Phys. Rev. D **69** 094008 (2004).
4. T. Aaltonen *et al.* [CDF Collaboration], Phys. Rev. Lett. **99**, 151801 (2007).
5. T. Aaltonen *et al.* [CDF Collaboration], Phys. Rev. Lett. **100**, 071801 (2008).
6. C. Anastasiou *et al.*, Phys. Rev. D **69**, 094008 (2004).
7. K. Melnikov *et al.*, Phys. Rev. D **74**, 144017 (2006).
8. V. M. Abazov *et al.*, Phys. Rev. D **76** 111104(R) (2007).
9. V. M. Abazov *et al.* [D0 Collaboration], Accepted by PRL, arXiv:0712.0599 [hep-ex].
10. T. Aaltonen *et al.* [CDF Collaboration], Submitted to PRL, arXiv:0801.4806 [hep-ex].

**ELECTROWEAK PHYSICS MEASUREMENTS AT HERA**

Enrico Tassi

*Università della Calabria – INFN , Cosenza, Italy*

Written contribution not received



# TOP QUARK MASS MEASUREMENTS AT THE TEVATRON

Jahred Adelman

(on behalf of the CDF and DØ collaborations)

*University of Chicago. 5640 S. Ellis Avenue, Chicago, IL 60615, USA*

## Abstract

Top quark mass measurements from the Tevatron using up to  $2.0 \text{ fb}^{-1}$  of data are presented. Prospects for combined Tevatron measurements by the end of Run II are discussed.

## 1 Introduction

Discovered in 1995 by both CDF and DØ, the top quark is by far the heaviest known fundamental particle<sup>1, 2)</sup>. The mass of the top quark ( $M_{\text{top}}$ ) is of particular interest, as radiative contributions involving both the top quark and the putative Higgs boson contribute to the mass of the W boson. Thus, the masses of the top quark, the Higgs boson and the W boson are not three independent parameters in the Standard Model (SM). When and if the Higgs boson is discovered, precision measurements of the masses of the W boson and the top quark will help make a key test of the SM, helping to answer whether the new find is indeed the SM Higgs boson or some other, new scalar particle. In addition, the heavy mass of the top quark, near the electroweak scale, indicates that the top quark may play a role in helping theorists disentangle possible new sources of physics<sup>3)</sup>. This letter describes measurements of the top quark mass from the CDF and DØ collaborations using up to  $2.0 \text{ fb}^{-1}$  of data collected in Run II at the Tevatron.

## 2 Production and Decay

Top quarks at the Tevatron are produced predominantly in pairs, and decay almost always in the SM to a W boson and a b quark. The topology of  $t\bar{t}$  events depends on the subsequent decay of the two W bosons. In the dilepton channel, each W boson decays leptonically, to an electron or muon and a neutrino. The dilepton channel has the lowest background and only two jets in the leading order  $t\bar{t}$  decay, but suffers from underconstrained kinematics due to the two escaping neutrinos, as well as from having the lowest branching fraction among all decay channels. In the all-hadronic channel, the two W bosons decay hadronically to quarks. The all-hadronic channel has the largest branching fraction and no neutrinos, but also contains no charged lepton to distinguish it from the large QCD background. In the lepton+channel channel, one W boson decays hadronically and the other leptonically. Though there is an undetected neutrino, the kinematics of the system are still overconstrained.

Two tricks are used often in  $t\bar{t}$  mass analyses to increase the signal-to-background and improve systematics. Each  $t\bar{t}$  event contains two btags; if the secondary vertices from the decay of metastable B hadrons can be identified, jets arising from b quarks can be distinguished from jets arising from light flavor quarks. This significantly cuts down on the number of background events, and also helps to match the jets observed in the detector to the quarks at the hard scatter level. Lepton+Jets and all-hadronic events also contain at least one hadronically decaying W boson. The narrow decay width and well known W boson mass in these events can be used to constrain, *in situ*, the largest

systematic in top quark mass measurements, the calibration and response of calorimeters to hadronic particles, also known as the jet energy scale (JES).

### 3 Dilepton template analyses

Due to the underconstrained kinematics, measurements of  $M_{\text{top}}$  in the dilepton channel must integrate over some unknown quantities. The  $D\bar{O}$  experiment has two dilepton measurements, each using  $1 \text{ fb}^{-1}$  of data. In the matrix weighting method, each charged lepton-jet pairing is given a weight for the expectation to find, within experimental resolutions, the leptons with the measured energy, given a top quark mass and the unknown top and anti-top  $p_T$ . The  $p_T$  values are integrated over using parton distribution functions, and a likelihood fit yields  $M_{\text{top}} = 175.2 \pm 6.1 \text{ (stat.)} \pm 3.4 \text{ (syst.) GeV}/c^2$  <sup>4)</sup>, with systematics that are dominated by the jet energy scale. In the Neutrino Weighting Algorithm (NWA), the unknown pseudorapidities of the two neutrinos are integrated over. The solutions for a given top quark mass are weighted by the agreement with the missing transverse energy in the detector. The mean and RMS of the top quark mass weight distribution are used as estimators for the true top quark mass. With  $1 \text{ fb}^{-1}$  of data,  $D\bar{O}$  measures  $172.5 \pm 5.8 \text{ (stat.)} \pm 3.5 \text{ (syst.) GeV}/c^2$  <sup>5)</sup>. The above two measurements, while largely correlated, are not completely correlated. A combination using the BLUE technique <sup>6)</sup> yields  $173.7 \pm 5.4 \text{ (stat.)} \pm 3.4 \text{ (syst.) GeV}/c^2$  <sup>7)</sup>.

CDF uses the NWA measurement in the dilepton channel with  $1.9 \text{ fb}^{-1}$  of data. The most probable top quark mass, and not the mean, is taken as the first estimator; the distribution is often rather asymmetric, so these are not necessarily the same quantity. The second observable is the  $H_T$ , the scalar sum of  $\vec{E}_T$ , lepton  $p_T$  values and jet  $p_T$  values. CDF measures  $171.6^{+3.4}_{-3.2} \text{ (stat.)} \pm 3.8 \text{ (syst.) GeV}/c^2$  <sup>10)</sup>.

### 4 Other template analyses

The kinematics in the lepton+jets and dilepton channel are overconstrained, so there is no need to integrate over unknown quantities. The overconstrained kinematics are also used to select the single best assignment of jets to the quarks at the hard scatter—the single assignment most consistent with the  $t\bar{t}$  hypothesis is used. CDF has two such measurements with  $1.9 \text{ fb}^{-1}$  of data. A measurement in the all-hadronic channel uses a neural network to increase the S:B and reduce the QCD background. In addition, the W mass constraint is used to calibrate the JES, yielding  $177.0 \pm 3.7 \text{ (stat.)} \pm 1.6 \text{ (syst.) GeV}/c^2$  <sup>13)</sup>, where, as in all such measurements that contain an *in situ* JES calibra-

tion, the statistical uncertainty also includes a component for the JES systematic that now scales with  $1/\sqrt{N}$ . A measurement in the lepton+jets channel yields  $171.8 \pm 1.9$  (stat.)  $\pm 1.0$  (syst.)  $\text{GeV}/c^2$  (10), and also includes an *in situ* calibration. CDF also has the first-ever analysis combining measurements of the top quark mass across different decay topologies into the same likelihood. More-traditional combinations must assume correlations for systematics between measurements, as well as assume Gaussian behavior of the separate likelihoods. By combining the measurements into the same likelihood, these assumptions are not needed. The combination of CDF's lepton+jets and dilepton analyses described above yields  $171.9 \pm 1.7$  (stat.)  $\pm 1.0$  (syst.)  $\text{GeV}/c^2$  (10).

## 5 Matrix Element Analyses

A different class of top quark mass analyses, called matrix element (ME) analyses, try to extract as much information as possible from every event. All jet-parton assignments consistent with b-tagging are used in the likelihood, which makes use of leading order theoretical predictions for how  $t\bar{t}$  events are produced and decayed, as given by the matrix element. Typically, leptons are assumed to be perfectly measured, as are jet angles. The energies of the partons at the hard scatter level are encoded in transfer functions, which give the probability to observe a jet with energy  $j$  given a parton with energy  $p$ . The transfer functions are needed since analyses measure jets in the detector, but the matrix element knows only how to describe events at the parton level. In typical ME analyses, the probability to observe  $\vec{x}$  in the detector, given some top quark mass and JES in the detector, is given by:

$$P(\vec{x} | M_{\text{top}}, \text{JES}) = \frac{1}{N} \int d\Phi |M_{t\bar{t}}(p; M_{\text{top}})|^2 \prod_{\text{objects}} W(j|p, \text{JES}) f_{\text{PDF}}(q1, q2), \quad (1)$$

where  $P$  gives the probability to observe  $x$  in the detector, given some top quark mass (and JES in the detector, if the measurement includes an *in situ* calibration).  $N$  is a normalization term that includes effects of efficiency and acceptance, as well as the changing  $t\bar{t}$  production cross section as a function of  $M_{\text{top}}$ . The integral over  $d\Phi$  is an integral over the parton-level phase space. The matrix element  $M$  is the leading order matrix element for  $t\bar{t}$  production with partons  $p$ , given some top quark mass. The transfer functions  $W$  give the probability to observe a jet with energy  $j$  given a parton energy  $p$  (and possibly the jet calibration in the detector). Finally, there are two terms in  $f_{\text{PDF}}$  that

come from the parton distribution functions and give the probability to observe the two incoming partons with the appropriate energy.

CDF has a ME element in the dilepton channel using  $2.0 \text{ fb}^{-1}$ . The analysis uses a novel evolutionary neural network at the selection stage to improve the *a priori* statistical uncertainty on the top quark mass by 20%. Normal neural networks are trained only to minimize misclassification. As such, they can be used only to distinguish signal and background, not to improve directly the expected uncertainty on a measurement. The analysis measures  $M_{\text{top}} = 171.2 \pm 2.7 \text{ (stat.)} \pm 2.9 \text{ (syst.) GeV}/c^2$  (11).

CDF has a ME element analysis in the lepton+jets channel using  $1.9 \text{ fb}^{-1}$ . The analysis differs from typical ME analyses via the modification of the propagators in the matrix element to account for the imperfect assumptions about perfectly measured angles and intermediate particle masses that make the multi-dimensional integral tractable. The analysis also makes a cut on the peak likelihood to remove both background events as well as poorly modeled signal events where the object in the detector do not match the assumed partons at the matrix element level. The analysis includes an *in situ* JES calibration, and measures  $M_{\text{top}} = 172.7 \pm 1.8 \text{ (stat.)} \pm 1.2 \text{ (syst.) GeV}/c^2$  (12).  $D\bar{O}$  also has a ME analysis using  $0.9 \text{ fb}^{-1}$ . Unlike most lepton+jet analyses, this analysis includes events with 0 b-tags. The events are separated by charged lepton type (electron vs muon). Including an *in situ* JES calibration,  $D\bar{O}$  measures  $M_{\text{top}} = 170.5 \pm 2.4 \text{ (stat.)} \pm 1.2 \text{ (syst.) GeV}/c^2$  (8).

## 6 Future prospects

As Run II progresses at the Tevatron, top quark mass measurements are rapidly approaching systematic limits. A new set of analyses are emerging from the Tevatron that make very different assumptions to measure the top quark mass, and as such are sensitive to very different systematic uncertainties. In one such measurement,  $D\bar{O}$  measures the top quark mass via a measurement of the  $t\bar{t}$  pair production cross section. Top quark pairs at the Tevatron are produced nearly at threshold, so the cross section depends strongly on the top quark mass. The analysis depends on theoretical inputs to model this relationship; using  $0.9 \text{ fb}^{-1}$  of data (9),  $D\bar{O}$  measures  $M_{\text{top}} = 166.9^{+5.9}_{-5.2} \text{ (stat + syst.)}^{+3.7}_{-3.8} \text{ theory GeV}/c^2$  using a  $\sigma_{t\bar{t}}-M_{\text{top}}$  curve from Kidonakis and Vogt. Using a curve from Cacciari et al. gives  $M_{\text{top}} = 166.1^{+6.1}_{-5.3} \text{ (stat + syst.)}^{+4.9}_{-6.7} \text{ theory GeV}/c^2$ .

The world average Tevatron top quark mass from the Tevatron as of March 2007,  $M_{\text{top}} = 170.9 \pm 1.1 \text{ (stat.)} \pm 1.5 \text{ (syst.) GeV}/c^2$  (15), already comes close to being a 1% measurement, and does not include most of the analyses describe in this letter. Figure 1 compares the world average with

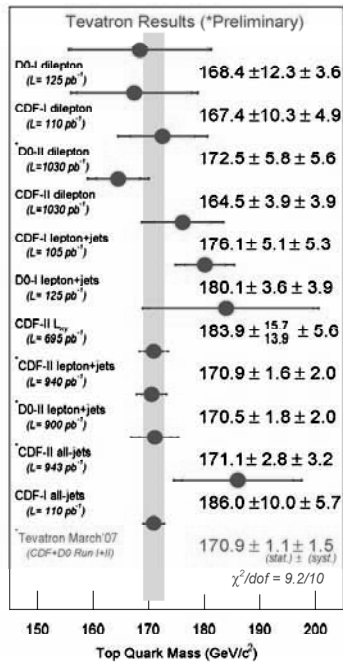


Figure 1: World-average top quark mass measurement and comparison with individual measurements from the two Tevatron experiments.

measurements from both experiments. CDF has a new combination of its own analyses, yielding  $M_{\text{top}} = 172.9 \pm 1.2$  (stat.)  $\pm 1.5$  (syst.)  $\text{GeV}/c^2$  [14], and expects by the end of Run II to have a CDF-only combination of top quark mass measurements with a precision better than 1%, as indicated in Figure 2.

## 7 Acknowledgements

I would like to thank all those in the CDF and DØ top groups who came before me in Run I and Run II (including all conveners) for setting the bar so high for top quark mass measurements. In addition, many thanks to the organizers of the La Thuile 2008 conference for all their hard work.

## References

1. Abe, F. *et al.* The CDF collaboration. *Phys Rev. Lett.*, **74**, 2626 (1995).
2. Abachi, S. *et al.* The DØ collaboration. *Phys Rev. Lett.*, **74**, 2632 (1995).
3. Hill, Christopher T. and Parke, Stephen J. *Phys. Rev. D.*, **49**, 4454 (1994).
4. The DØ collaboration. DØ Conference Note 5463 (2007).
5. The DØ collaboration. DØ Conference Note 5347 (2007).
6. Lyons, L., Gibaut, D. and Clifford, P. *Nucl. Inst. Meth.*, **A270**, 110 (1988).
7. The DØ collaboration. DØ Conference Note 5460 (2007).
8. The DØ collaboration. DØ Conference Note 5362 (2007).
9. The DØ collaboration. DØ Conference Note 5459 (2007).
10. The CDF collaboration. CDF Conference Note 9206 (2008).
11. The CDF collaboration. CDF Conference Note 9130 (2008).
12. The CDF collaboration. CDF Conference Note 9196 (2008).
13. The CDF collaboration. CDF Conference Note 9165 (2007).
14. The CDF collaboration. CDF Conference Note 9214 (2008).
15. The CDF and DØ collaborations. CDF Conference Note 8735, DØ Conference Note 5378 (2007).



# TOP QUARK PAIR PRODUCTION AND PROPERTIES MEASUREMENTS AT THE TEVATRON

Marc-André Pleier

*University of Bonn, 53115 Bonn, Germany*

On behalf of the CDF and DØ Collaborations

## Abstract

The Tevatron proton-antiproton collider at Fermilab with its centre of mass energy of 1.96 TeV is currently the only source for the production of top quarks. This report reflects the current status of measurements of the top quark pair production cross section and properties performed by the CDF and DØ Collaborations. Utilising datasets of up to two fb<sup>-1</sup>, these measurements allow unprecedented precision in probing the validity of the Standard Model.

## 1 Introduction

Since its discovery in 1995 at the Tevatron <sup>1)</sup>, the top quark remains the heaviest known fundamental particle to date. With a mass of  $172.6 \pm 1.4 \text{ GeV}/c^2$  <sup>2)</sup>, it is considered to be intimately connected with the mechanism of electroweak symmetry breaking in the Standard Model of elementary particle physics (SM) and also to be sensitive to physics beyond the framework of the SM.

This article reports recent measurements by the CDF and DØ Collaborations that probe the SM expectations for deviations both in the production and decay of the top quark. After a brief outline of the top quark properties within the SM framework in Section 2, the current status of measured top quark pair production rates is given Section 3, followed by a section on searches for top quark production beyond the SM. The subsequent three sections describe measurements probing the top quark decay in terms of branching fractions, search for flavour-changing neutral currents and the helicity of the  $W$  boson in the top quark decay, respectively. A conclusion is given in the final Section 8.

## 2 Top Quark Pair Production and Decay in the SM

Within the framework of the SM, top quark production at the Tevatron proceeds mainly in pairs:  $p\bar{p} \rightarrow t\bar{t} + X$  via the strong interaction (85%  $q\bar{q}$  annihilation and 15% gluon-gluon fusion).

The corresponding production cross section has been evaluated at next-to-leading order (NLO) QCD using two different approaches: One calculation considers soft gluon corrections up to next-to-next-to-next-to leading logarithmic (NNNLL) terms and some virtual terms in a truncated resummation, yielding  $6.77 \pm 0.42 \text{ pb}$  for a top quark mass of  $175 \text{ GeV}/c^2$  <sup>3)</sup>, while another calculation using the NLO calculation with LL and NLL resummation at all orders of perturbation theory gives  $6.70^{+0.71}_{-0.88} \text{ pb}$  for a top quark mass of  $175 \text{ GeV}/c^2$  <sup>4)</sup>. If a PDF uncertainty is combined linearly with the theoretical uncertainty for the first result – similar to what is done for the second result – both predictions exhibit not only similar central values but also similar relative uncertainties of  $\approx 12\text{-}13\%$ .

Due to its large mass, the top quark has an extremely short lifetime of approximately  $5 \cdot 10^{-25} \text{ s}$ , which makes it decay before it can form hadrons – a unique feature setting it apart from all other quarks. Since the top quark mass

is well above the threshold for  $Wq$  decays with  $q$  being one of the down-type quarks  $d, s, b$ , this two-body decay dominates the top quark decay. As each quark flavour contributes to the total decay rate proportional to the square of the respective CKM matrix element  $V_{tq}$ , top decays into  $Ws$  and  $Wd$  are strongly suppressed with respect to the dominant decay  $t \rightarrow Wb$ .

Consequently, top quark pair events contain a  $b$  and a  $\bar{b}$  quark from the  $t\bar{t}$  decay, and depending on the decay modes of the two  $W$  bosons, the observed top quark pair final states can be divided into three event classes:

- i) In *dilepton* events, both  $W$  bosons decay leptonically, resulting in a final state containing two isolated high- $p_T$  leptons, missing transverse energy  $\cancel{E}_T$  corresponding to the two neutrinos and two jets. This final state constitutes  $\approx 5\%$  of the  $t\bar{t}$  events (not counting  $\tau$  leptons) and gives the cleanest signal but suffers from low statistics.
- ii) In *lepton+jets* events, one  $W$  boson decays leptonically, the other one hadronically, resulting in one isolated high- $p_T$  lepton,  $\cancel{E}_T$  and four jets. Events in the  $e$ +jets or  $\mu$ +jets channels yield  $\approx 29\%$  of the branching fraction ( $\approx 34\%$  when including leptonic  $\tau$  decays) and provide the best compromise between sample purity and statistics.
- iii) In *all-hadronic* events, both  $W$  bosons decay to  $\bar{q}q'$  pairs, resulting in a six-jet final state. With a branching fraction of  $\approx 46\%$ , this final state represents the biggest fraction of  $t\bar{t}$  events, but it is also difficult to separate from the large background of multijet production.

All of these final states contain two  $b$ -jets from the hadronisation of the (anti-)  $b$  quarks, and additional jets can arise from initial and final state radiation.

### 3 Measurement of the Top Quark Pair Production Cross Section

Top quark pair production cross section measurements provide a unique test of the predictions from perturbative QCD calculations at high transverse momenta. Analysing all three event classes allows both the improvement of statistics of top events and studies of properties and important checks for physics beyond the SM that might result in enhancement/depletion in some particular channel via novel production mechanisms or decay modes.

The following subsections give an overview of the cross section measurements pursued at the Tevatron rather than quoting single cross section results, with the exception of the most precise single measurement to date, obtained by  $D\bar{O}$  in the lepton+jets channel. All current measurements are summarised in Figure 2.

### 3.1 Dilepton Final State

A typical selection of dilepton events requires two isolated high  $p_T$  leptons,  $\cancel{E}_T$  and at least two central energetic jets in an event. The most important physics background processes containing both real leptons and  $\cancel{E}_T$  are  $Z/\gamma^*$ +jets production with  $Z/\gamma^* \rightarrow \tau^+\tau^-$ ,  $\tau \rightarrow e, \mu$  and the production of dibosons ( $WW, ZZ, WZ$ ). Instrumental backgrounds are to be considered as well, arising from misreconstructed  $\cancel{E}_T$  due to resolution effects in  $Z/\gamma^*$ +jets production with  $Z/\gamma^* \rightarrow e^+e^-/\mu^+\mu^-$ , and also from  $W$ +jets and QCD multi-jet production where one or more jets fake the isolated lepton signature. To ensure proper description of the instrumental backgrounds, these are usually modelled using collider data, while for the physics backgrounds typically Monte Carlo simulation is used.

A further enhancement of the signal fraction in the selected data samples is possible by requiring additional kinematical event properties like the scalar sum of the jet  $p_{TS}$   $H_T$  to be above a certain threshold or rejecting events where both selected leptons have like-sign electric charge. The obtained purities in such selected samples are usually quite good with a signal to background ratio (S/B) better than 2 at least, although signal statistics are low. The acceptance for dilepton final states can be enhanced by loosening the selection to require only one fully reconstructed isolated lepton ( $e, \mu$ ) in addition to an isolated track (“ $\ell$ +track analysis”). In particular, such a selection allows the inclusion of “1 prong” hadronic  $\tau$  decays.

The top quark production cross section was recently measured for the first time also in the lepton+tau final state by  $D\bar{O}$  <sup>5)</sup>, using events with hadronically decaying isolated taus and one isolated high  $p_T$  electron or muon. To separate real taus from jets, a neural network was used, and the sample purity was enhanced by requiring  $b$ -jet identification (see Section 3.2) in the selected events. The result is shown together with the other measurements in Figure 2.

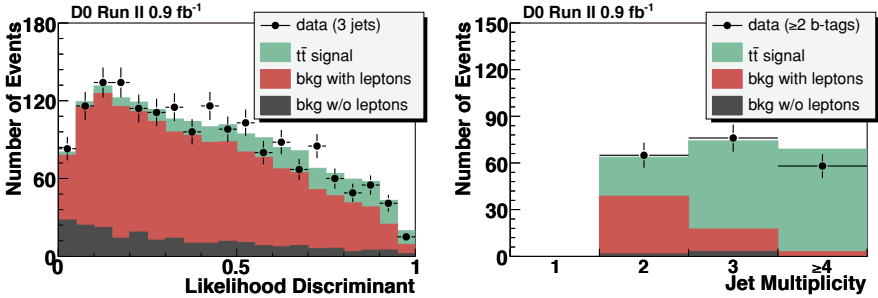


Figure 1: *Sample composition in a lepton+jets sample, requiring three jets (left) or at least two b-tagged jets (right) <sup>6</sup>.*

### 3.2 Lepton+Jets Final State

A typical lepton+jets selection requires one isolated high  $p_T$  lepton ( $e$  or  $\mu$  which includes  $\tau \rightarrow e\nu\bar{\nu}$ ,  $\tau \rightarrow \mu\nu\bar{\nu}$ ),  $\cancel{E}_T$  and at least 4 jets, yielding samples with a S/B around 1/2. The dominant physics background to be considered here comes from  $W$ +jets production while the main instrumental background arises from QCD multijet production where a jet fakes the isolated lepton signature.

The cross section can be extracted from such a selected sample either purely based on topological and kinematical event properties combined in a multivariate discriminant to separate the  $t\bar{t}$  signal from background or by adding identification of  $b$ -jets. Since topological analyses do not depend on the assumption of 100% branching of  $t \rightarrow Wb$ , they are less model-dependent than tagging analyses. On the other hand, requiring  $b$ -jet identification is a very powerful tool in suppressing the background processes, which typically exhibit little heavy flavour content. With  $b$ -jet identification, the top signal can also be easily extracted from lower jet multiplicities, where topological analyses need to impose additional selection criteria like cutting on  $H_T$  to be able to extract the signal. In addition,  $b$ -tagged analyses can provide very pure signal samples, easily exceeding a S/B > 10 in selections requiring at least four jets with two identified  $b$ -jets (see for example Figure 1).

The identification of  $b$ -jets can be based on the long *lifetime* of B hadrons resulting in significantly displaced secondary vertices with respect to the pri-

mary event vertex or large significant impact parameters of the corresponding tracks. A combination of this type of information in a neural network tagging algorithm yields  $b$ -tagging efficiencies of about 54% while only about 1% of light quark jets are misidentified as  $b$ -jets – hence the improved S/B in tagged analyses. Another way to identify  $b$ -jets is to reconstruct *soft leptons* inside a jet originating from semileptonic B decays. So far only soft- $\mu$  tagging has been deployed in  $t\bar{t}$  analyses.

The most precise  $t\bar{t}$  production cross section measurement to date with a relative uncertainty of 11% has been performed by DØ on  $0.9 \text{ fb}^{-1}$  of data in the lepton+jets channel<sup>6</sup>). For this measurement, two complementary analyses based on a kinematic likelihood discriminant and on  $b$ -tagging (see Figure 1) were combined and yield  $\sigma_{t\bar{t}} = 7.42 \pm 0.53(\text{stat}) \pm 0.46(\text{syst}) \pm 0.45(\text{lumi}) \text{ pb}$  for a top quark mass of  $175 \text{ GeV}/c^2$ . Comparing this measurement with the theory prediction, the top quark mass can be extracted as well, yielding  $170 \pm 7 \text{ GeV}/c^2$  in good agreement with the world average.

A first  $\tau$ +jets cross section analysis using events with hadronically decaying isolated taus and lifetime  $b$ -tagging was performed as well by DØ – the result is shown together with other measurements in Figure 2.

### 3.3 All-Hadronic Final State

The all-hadronic final state is studied by requiring events with at least six central energetic jets and no isolated high  $p_T$  leptons. Due to the overwhelming background from QCD multijet production with a cross section orders of magnitude above that of the signal process,  $b$ -jet identification is mandatory for this final state. Further separation of signal and background is achieved by using multivariate discriminants based on topological and kinematical event properties.

### 3.4 Summary of the Top Quark Pair Production Cross Section Measurements

Figure 2 provides an overview of recent cross section measurements performed by CDF and DØ. All measurements show good agreement with the SM prediction and with each other. The single best measurements are approaching a relative precision of  $\Delta\sigma/\sigma = 10\%$  that should be achievable for the datasets of  $2 \text{ fb}^{-1}$  already at hand and provide stringent tests to theory predictions. With increasing datasets, these measurements naturally start to become limited by

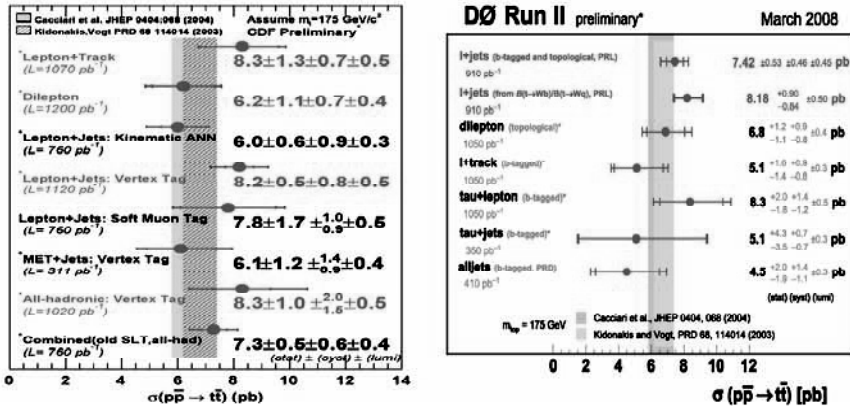


Figure 2: Top quark pair production cross section measurements performed by CDF and DØ.

systematic uncertainties rather than statistical ones, but it will be possible to further constrain the systematic uncertainties as well using additional data.

Cross section measurements form the foundation for all further property analyses like the ones described in the subsequent sections of this article by characterising the datasets enriched in top quark pairs and providing the necessary understanding of object identification, background modelling and sample composition.

## 4 Search for Top Quark Pair Production beyond the SM

### 4.1 Search for a Narrow-Width Resonance decaying into $t\bar{t}$

Various beyond the SM theories predict the existence of a massive  $Z$ -like boson that could decay into  $t\bar{t}$  and hence add a resonant production mode to the SM process. Any such additional production would be visible in the  $t\bar{t}$  invariant mass distribution provided the resonance  $X$  decaying to  $t\bar{t}$  is sufficiently heavy and narrow.

Both CDF and DØ perform a search for a generic heavy resonance  $X$  of narrow width ( $\Gamma_X = 0.012M_X$ ) compared to the detector mass resolution in  $b$ -tagged lepton+jets datasets. The  $t\bar{t}$  invariant mass spectrum is recon-

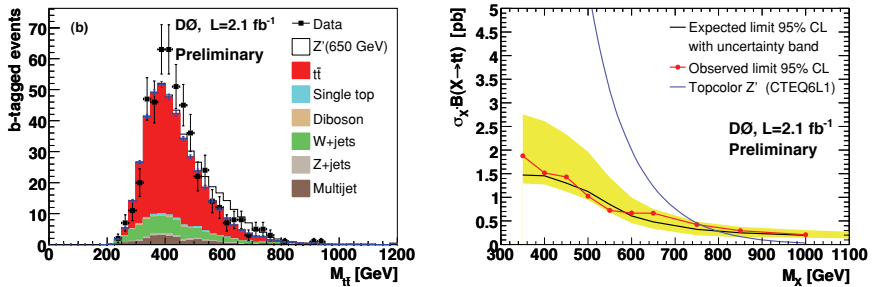


Figure 3: *Left: Expected and observed  $t\bar{t}$  invariant mass distribution in lepton+jets data with four or more jets. Right: Expected and observed 95% C.L. upper limits on  $\sigma_X \cdot \mathcal{B}(X \rightarrow t\bar{t})$  <sup>8)</sup>.*

structured using either a kinematic fit to the  $t\bar{t}$  production hypothesis (CDF) or directly from the four-momenta of the up to four leading jets, the lepton and the neutrino momentum (DØ). The latter approach was shown to provide better sensitivity for large resonance masses than the previously used constrained kinematic fit and also allows the inclusion of data with fewer than four jets in case that jets merged. As both experiments observe no significant deviation from the SM expectation, 95% C.L. upper limits on  $\sigma_X \cdot \mathcal{B}(X \rightarrow t\bar{t})$  are given for values of  $M_X$  between 450 and 900 GeV/ $c^2$  (CDF) respectively 350 and 1000 GeV/ $c^2$  (DØ, see Figure 3).

Both experiments provide 95% C.L. mass limits for a leptophobic top-colour-assisted technicolour  $Z'$  boson as a benchmark model. Using 955 pb<sup>-1</sup>, CDF finds  $M_{Z'} > 720$  GeV/ $c^2$  (expected limit: 710 GeV/ $c^2$ ) <sup>7)</sup> while DØ finds  $M_{Z'} > 760$  GeV/ $c^2$  (expected limit: 795 GeV/ $c^2$ ) <sup>8)</sup> using 2.1 fb<sup>-1</sup> of data.

#### 4.2 Search for $t\bar{t}$ Production via a Massive Gluon

Instead of a new colour singlet particle decaying into  $t\bar{t}$  as described in the previous subsection, there could also be a new massive colour octet particle  $G$  contributing to  $t\bar{t}$  production. Such a “massive gluon” production mode would interfere with the corresponding SM production process.

Assuming a SM top decay, CDF has performed a search for a corresponding contribution by comparing the  $t\bar{t}$  invariant mass distribution in a 1.9 fb<sup>-1</sup>

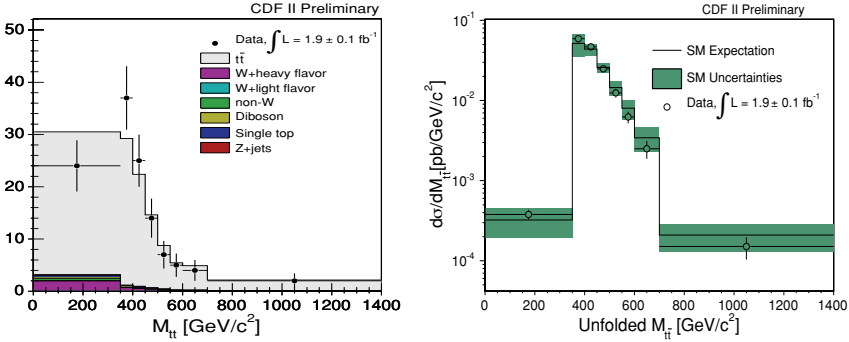


Figure 4: *Left: Reconstructed  $t\bar{t}$  invariant mass distribution in lepton+jets data with at least four jets. Right: Corresponding observed  $t\bar{t}$  differential cross section, compared to the SM expectation <sup>10)</sup>.*

$b$ -tagged lepton+jets dataset with the SM expectation. As the largest discrepancy with respect to the SM observed is  $1.7\sigma$  for the explored mass and width range  $400 \text{ GeV}/c^2 \leq M_G \leq 800 \text{ GeV}/c^2$ ,  $0.05 \leq \Gamma_G/M_G \leq 0.5$ , upper and lower limits are provided on the corresponding coupling strengths of the massive gluon <sup>9)</sup>.

### 4.3 Measurement of the $t\bar{t}$ Differential Cross Section $d\sigma/dM_{t\bar{t}}$

Contributions beyond the SM in  $t\bar{t}$  production could manifest themselves in either resonances, broad enhancements or more general shape distortions of the  $t\bar{t}$  invariant mass spectrum. A very generic way to search for such effects is to measure the  $t\bar{t}$  differential cross section  $d\sigma/dM_{t\bar{t}}$  and compare the shape with the SM expectation.

CDF reconstructs the  $t\bar{t}$  invariant mass spectrum in a  $1.9 \text{ fb}^{-1}$   $b$ -tagged lepton+jets dataset (see Figure 4) by combining the four-vectors of the four leading jets, lepton and missing transverse energy. After subtracting the background processes, the distortions in the reconstructed distribution due to detector effects, object resolutions and geometric/kinematic acceptance are corrected for by the application of a regularised unfolding technique. From the unfolded distribution, the  $t\bar{t}$  differential cross section  $d\sigma/dM_{t\bar{t}}$  is extracted and its shape is compared with the SM expectation. The shape comparison yields

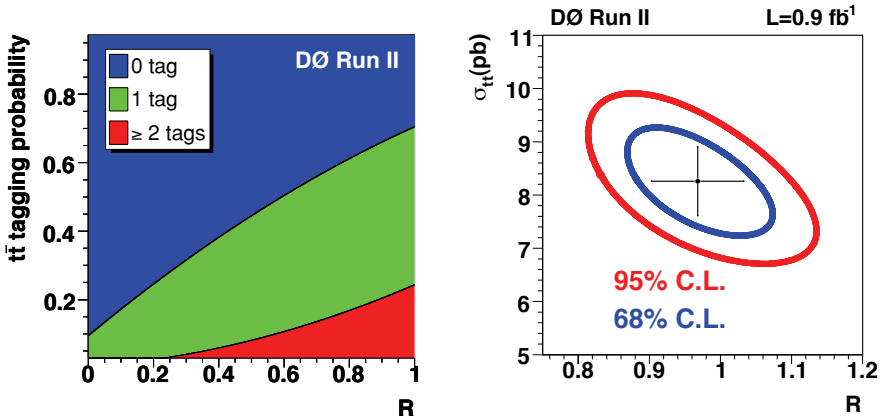


Figure 5: *Left: Fractions of events with 0, 1 and  $\geq 2$   $b$ -tags for  $t\bar{t}$  events with  $\geq 4$  jets as a function of  $R$ . Right: 68% and 95% C.L. statistical uncertainty contours in the  $R$  vs.  $\sigma_{t\bar{t}}$  plane <sup>12)</sup>.*

good agreement with the SM, yielding an Anderson-Darling p-value of 0.45 <sup>10)</sup>.

## 5 Measurement of $\mathcal{B}(t \rightarrow Wb)/\mathcal{B}(t \rightarrow Wq)$

Assuming the validity of the SM, specifically the existence of three fermion generations, unitarity of the CKM matrix and insignificance of non- $W$  boson decays of the top quark (see Section 6), the ratio of branching fractions  $R = \mathcal{B}(t \rightarrow Wb)/\sum_{q=d,s,b}\mathcal{B}(t \rightarrow Wq)$  simplifies to  $|V_{tb}|^2$ , and hence is strongly constrained:  $0.9980 < R < 0.9984$  at 90% C.L. <sup>11)</sup>. Deviations of  $R$  from unity could for example be caused by the existence of a fourth heavy quark generation.

The most precise measurement of  $R$  thus far has been performed by DØ in the lepton+jets channel using data corresponding to an integrated luminosity of  $900 \text{ pb}^{-1}$ . By comparing the event yields with 0, 1 and 2 or more  $b$ -tagged jets and using a topological discriminant to separate the  $t\bar{t}$  signal from background in events with 0  $b$ -tags,  $R$  can be extracted together with the  $t\bar{t}$  production cross section  $\sigma_{t\bar{t}}$  simultaneously (see Figure 5). This measurement allows the extraction of  $\sigma_{t\bar{t}}$  without assuming  $\mathcal{B}(t \rightarrow Wb) = 100\%$ , yielding

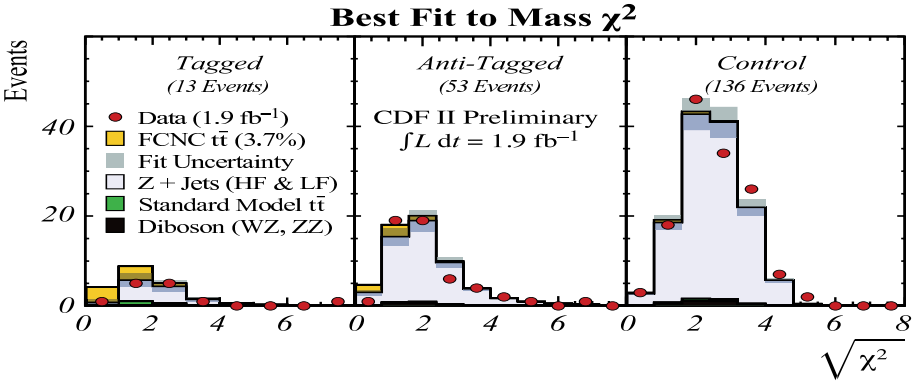


Figure 6: *Expected and observed mass  $\chi^2$  distributions of  $Z + \geq 4$  jets events in signal samples with  $\geq 1$  and  $0$   $b$ -tags and a background enriched sample to control uncertainties of the background shape and normalisation <sup>13)</sup>.*

$R = 0.97^{+0.09}_{-0.08}$  (stat+syst) and  $\sigma_{t\bar{t}} = 8.18^{+0.90}_{-0.84}$  (stat+syst)  $\pm 0.50$  (lumi) pb for a top quark mass of  $175 \text{ GeV}/c^2$  in agreement with the SM prediction <sup>12)</sup>.

### 6 Search for Flavour Changing Neutral Currents in Top Decays

The occurrence of flavour changing neutral currents (FCNC) – a decay of type  $t \rightarrow Vq$  with  $V = Z, \gamma, g$  and  $q = u, c$  – is strongly suppressed in the SM and expected to occur at a rate below  $\mathcal{O}(10^{-10})$ , well out of reach of being observed at the Tevatron. Consequently, any observation of FCNC decays would signal physics beyond the SM.

CDF has performed a search for  $t \rightarrow Zq$  in a  $1.9 \text{ fb}^{-1}$  dataset of  $Z + \geq 4$  jets events with  $Z \rightarrow e^+e^-$  or  $\mu^+\mu^-$ , assuming a SM decay of the second top quark  $t \rightarrow \bar{q}q'b$ . Since the event signature does not contain any neutrinos, the events can be fully reconstructed. The best discriminant found to separate signal from background processes is a mass  $\chi^2$  variable that combines the kinematic constraints present in FCNC decays. The signal fraction in the selected dataset is determined via a template fit in signal samples with  $0$  or  $\geq 1$   $b$ -tags and a background-enriched control sample to constrain uncertainties on the background shape and normalisation (see Figure 6).

Since the observed distributions are consistent with the SM background

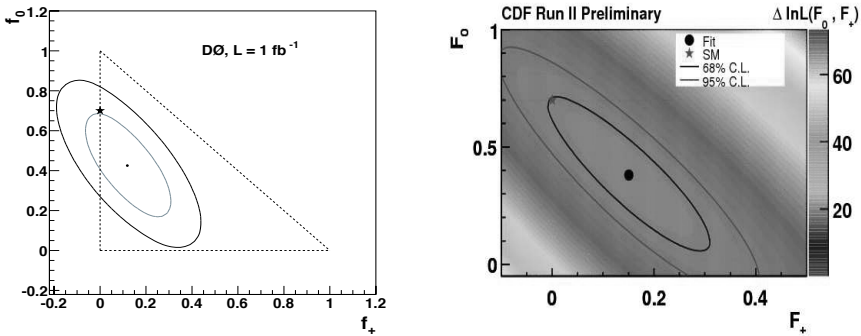


Figure 7: Results of the  $W$  boson helicity fits (left:  $D\bar{O}$  <sup>15</sup>), right: CDF <sup>14</sup>). The ellipses show the 68% and 95% C.L. contours around the measured data points. The stars show the SM expectation; the triangle denotes the physically allowed region where  $f_0$  and  $f_+$  sum to one or less.

processes, a 95% C.L. upper limit on the branching fraction  $\mathcal{B}(t \rightarrow Zq)$  of 3.7% is derived <sup>13</sup>). This is the best limit on  $\mathcal{B}(t \rightarrow Zq)$  to date.

## 7 Measurement of the $W$ Boson Helicity in Top Quark Decays

Assuming a massless  $b$ -quark, the top quark decay in the  $V-A$  charged current weak interaction proceeds only via a left-handed ( $f^- \approx 30\%$ ) and a longitudinal ( $f^0 \approx 70\%$ ) fraction of  $W$  boson helicities. The helicity of the  $W$  boson is reflected in the angular distribution  $\cos\theta^*$  of its decay products, with  $\theta^*$  being the angle of the down-type decay products of the  $W$  boson (charged lepton respectively  $d$ - or  $s$ -quark) in the  $W$  boson rest frame with respect to the top quark direction. Any observed right-handed fraction  $f^+ > \mathcal{O}(10^{-3})$  would indicate physics beyond the SM.

CDF has measured the  $W$  boson helicity fractions in  $1.9 \text{ fb}^{-1}$  of  $b$ -tagged lepton+jets data comparing the  $\cos\theta^*$  distribution of leptons in data to templates for longitudinal, right- and left-handed signal plus background templates. When fitting both  $f^0$  and  $f^+$  simultaneously, the result is  $f^0 = 0.38 \pm 0.21$  (stat)  $\pm 0.07$  (syst) and  $f^+ = 0.15 \pm 0.10$  (stat)  $\pm 0.05$  (syst) <sup>14</sup>).

$D\bar{O}$  has measured the  $W$  boson helicity fractions using the  $\cos\theta^*$  distri-

contributions in dilepton and lepton+jets events including their hadronic  $W$  boson decays in  $1 \text{ fb}^{-1}$  of data, yielding  $f_0 = 0.425 \pm 0.166$  (stat.)  $\pm 0.102$  (syst.) and  $f_+ = 0.119 \pm 0.090$  (stat.)  $\pm 0.053$  (syst.)<sup>15)</sup>.

Both measurements agree with the SM at the  $1\sigma$  level (see Figure 7).

## 8 Conclusion

A wealth of top quark analyses is being pursued at the Tevatron, probing the validity of the SM with unprecedented precision. The measured top quark pair production rates are found to be consistent with the SM expectation across the decay channels, with the most precise measurements surpassing the precision of theory predictions. There is no evidence thus far for contributions beyond the SM in either top quark production or top quark decay. However, with some measurements still being statistically limited, there is still room for surprises. More detailed descriptions of the analyses presented here and many more interesting top quark physics results can be found online<sup>16)</sup>.

Continuously improving analysis methods and using the increasing integrated luminosity from a smoothly running Tevatron that is expected to deliver more than  $6 \text{ fb}^{-1}$  by the end of Run II, we are moving towards more precision measurements and hopefully discoveries within and outside the SM.

## 9 Acknowledgements

The author would like to thank the organisers for creating a very fruitful collaborative atmosphere at the Rencontres de Physique de la Vallée d'Aoste, the CDF and DØ collaborations, the staffs at Fermilab and collaborating institutions and also the Alexander von Humboldt Foundation for their support.

## References

1. CDF Collaboration, F. Abe *et al.*, Phys. Rev. Lett. **74**, 2626 (1995);  
DØ Collaboration, S. Abachi *et al.*, Phys. Rev. Lett. **74**, 2632 (1995).
2. Tevatron Electroweak Working Group for the CDF and DØ Collaborations, FERMILAB-TM-2403-E (2008), arXiv:0803.1683.
3. N. Kidonakis and R. Vogt, Phys. Rev. D **68**, 114014 (2003).

4. M. Cacciari, S. Frixione, M. L. Mangano, P. Nason, and G. Ridolfi, *JHEP* **04**, 068 (2004).
5. DØ Collaboration, V. M. Abazov *et al.*, DØ conference note 5451 (2007).
6. DØ Collaboration, V. M. Abazov *et al.*, FERMILAB-PUB-08-064-E (2008), submitted to *Phys. Rev. Lett.*, arXiv:0803.2779.
7. CDF Collaboration, T. Aaltonen *et al.*, FERMILAB-PUB-07-576-E (2007), submitted to *Phys. Rev. D*, arXiv:0710.5335.
8. DØ Collaboration, V. M. Abazov *et al.*, DØ conference note 5600 (2008).
9. CDF Collaboration, T. Aaltonen *et al.*, CDF conference note 9164 (2008).
10. CDF Collaboration, T. Aaltonen *et al.*, CDF conference note 9157 (2008).
11. S. Eidelman *et al.*, *Phys. Lett. B* **592**, 1 (2004).
12. DØ Collaboration, V. M. Abazov *et al.*, FERMILAB-PUB-08-010-E (2008), submitted to *Phys. Rev. Lett.*, arXiv:0801.1326.
13. CDF Collaboration, T. Aaltonen *et al.*, CDF conference note 9202 (2008).
14. CDF Collaboration, T. Aaltonen *et al.*, CDF conference note 9114 (2007).
15. DØ Collaboration, V. M. Abazov *et al.*, *Phys. Rev. Lett.* **100** 062004 (2008).
16. <http://www-d0.fnal.gov/Run2Physics/top/index.html>;  
<http://www-cdf.fnal.gov/physics/new/top/top.html>

# MEASUREMENT OF THE ELECTROWEAK SINGLE TOP PRODUCTION CROSS SECTION AT THE TEVATRON

Peter Dong for the CDF and D0 Collaborations  
*University of California, Los Angeles,*  
*Dept. of Physics and Astronomy, CA 90095, USA*

## Abstract

The CDF and D0 collaborations have analyzed  $2.2 \text{ fb}^{-1}$  and  $0.9 \text{ fb}^{-1}$ , respectively, of Run II data to search for electroweak single top quark production at the Tevatron. We employ several different analysis techniques to search for a single top signal: boosted decision trees, multivariate likelihood functions, neural networks, and matrix element discriminants. Both experiments see evidence of single top production. D0 measures a combined cross section of  $4.7 \pm 1.3 \text{ pb}$  while CDF measures  $2.2_{-0.7}^{+0.8} \text{ pb}$ . D0 sets a limit at a 95% confidence level of  $|V_{tb}| > 0.68$  and measures  $|V_{tb}| = 1.3 \pm 0.2$ , while CDF calculates  $|V_{tb}| > 0.6$  and measures  $|V_{tb}| = 0.88_{-0.14}^{+0.16}(\text{stat} + \text{sys}) \pm 0.07(\text{theory})$ .

## 1 Introduction

In 1.96 TeV proton anti-proton collisions at the Tevatron, top quarks are predominantly produced in pairs via the strong force. In addition, the Standard Model predicts that single top quarks can be produced through an electroweak  $s$ - and  $t$ -channel exchange of a virtual  $W$  boson (Figure 1). The production cross sections have been calculated at next-to-leading order (NLO). For a top quark mass of  $175 \text{ GeV}/c^2$ , the results are  $1.98 \pm 0.25 \text{ pb}$  and  $0.88 \pm 0.11 \text{ pb}$  for the  $t$ -channel and  $s$ -channel processes, respectively<sup>1)</sup>. The combined cross section is about 40% of the top pair production cross section.

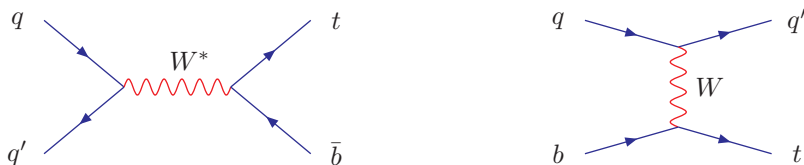


Figure 1: Leading order Feynman diagrams for  $s$ -channel (left) and  $t$ -channel (right) single top quark production.

The precise measurement of the production cross section allows the direct extraction of the Cabibbo-Kobayashi-Maskawa matrix element  $|V_{tb}|$  and offers a source of almost completely polarized top quarks<sup>2)</sup>. Moreover, the search for single top also probes exotic models beyond the Standard Model. New physics, like flavor-changing neutral currents or heavy  $W'$  bosons, could alter the observed production rate<sup>3)</sup>. Finally, single-top processes result in the same final state as the Standard Model Higgs boson process  $WH \rightarrow Wb\bar{b}$ , which is one of the most promising low-mass Higgs search channels at the Tevatron<sup>4)</sup>. Nearly all analysis tools developed for the single top search can be used for this Higgs search.

A measurement of this cross section was performed at D0 with  $0.9 \text{ fb}^{-1}$  of data and at CDF with  $2.2 \text{ fb}^{-1}$  of data. Each experiment has three analysis techniques that share a common event selection, background estimate, and statistical treatment.

## 2 Event Selection

The single top event selection exploits the kinematic features of the signal final state, which contains a real  $W$  boson, one or two bottom quarks, and possibly additional jets. To reduce multi-jet backgrounds, the  $W$  originating from the top quark decay is required to have decayed leptonically. This leads to a requirement of a high-energy electron or muon and large missing transverse energy ( $E_T$ ) from the undetected neutrino. CDF requires the electron and muon to have  $p_T > 20$  GeV and  $|\eta| < 1.6$ ; D0 requires  $p_T > 15$  GeV and  $|\eta| < 1.1$  for electrons and  $p_T > 18$  GeV and  $|\eta| < 2.0$  for muons. CDF requires  $\cancel{E}_T < 25$  GeV, while D0 requires  $15 < \cancel{E}_T < 200$  GeV.

CDF requires two or three jets with  $E_T > 20$  GeV and  $|\eta| < 2.8$ , while D0 requires from two to four jets with  $|\eta| < 3.4$ . The first jet must have  $E_T > 25$  GeV, the second jet must have  $E_T > 20$  GeV, and any additional jets must have  $E_T > 15$  GeV.

A large fraction of the background is removed by demanding that at least one of these two jets be tagged as a  $b$ -quark jet using displaced vertex information from the silicon detector. CDF's secondary vertex tagging algorithm identifies tracks associated with the jet originating from a vertex displaced from the primary vertex indicative of decay particles from relatively long-lived  $B$  mesons. D0 uses a neural network which includes seven input variables to distinguish tracks resulting from  $b$  quarks, increasing their acceptance for the same rate of mistags compared to a simple secondary-vertex tagger.

The backgrounds surviving these selections are  $t\bar{t}$ ,  $W$  + heavy-flavor jets, i.e.  $W + b\bar{b}$ ,  $W + c\bar{c}$ ,  $W + c$ ,  $Z$  + heavy-flavor jets, and the diboson processes  $WW$ ,  $WZ$ , and  $ZZ$ . Instrumental backgrounds originate from mis-tagged  $W$  + jets events ( $W$  events with light-flavor jets, i.e. with  $u$ ,  $d$ , or  $s$ -quark and gluon content, misidentified as heavy-flavor jets) and from non- $W$  + jets events (multi-jet events in which one jet is erroneously identified as a lepton).

### 2.1 Background Estimate

Estimating the background contribution after applying the event selection to the single top candidate sample is an elaborate process. NLO cross section calculations exist for diboson and  $t\bar{t}$  production, thereby making the estimation of their contribution relatively straightforward. The main background contri-

butions are from  $W + b\bar{b}$ ,  $W + c\bar{c}$  and  $W + c + \text{jets}$ , as well as mis-tagged  $W + \text{light quark jets}$ . We determine the  $W + \text{jets}$  normalization from the data and estimate the fraction of the candidate events with heavy-flavor jets using ALPGEN Monte Carlo samples<sup>5)</sup>, which were calibrated with multi-jet data<sup>6)</sup>. The probability that a  $W + \text{light-flavor jet}$  is mis-tagged is parameterized using a large, generic multi-jet data set. The instrumental background contribution from non- $W$  events is estimated using data in a control region with low  $\cancel{E}_T$ , containing very little signal, and we subsequently extrapolate the contribution into the signal region with large  $\cancel{E}_T$ . The expected signal and background yield in the signal sample is shown in Figures 2 and 3 for D0 and CDF, respectively.

The background estimate demonstrates that the expected number of single top events is much less than the large amount of expected backgrounds. In fact, the systematic uncertainty on the background estimate is larger than the expected signal, which renders a simple counting experiment impossible. The search for single top quark production requires the best possible discrimination between signal and background processes, thus motivating the use of multivariate analysis tools.

## 2.2 Neural Network Jet-Flavor Separation

Mistags and  $W + c$  events are a large class of background where no real  $b$ -quark is present and amount to about 50% of the  $W + 2 \text{ jets}$  data sample even after imposing the requirement that one jet is identified by a secondary vertex  $b$ -tagger. CDF uses a neural network tool which uses secondary vertex tracking information to distinguish jets from  $b$  quarks from jets from  $c$  and light quarks. Figure 4 shows the distribution of this jet-flavor-separating neural network in Monte Carlo events. All CDF single-top analyses use this tool to improve their sensitivity.

## 3 Analysis Techniques

No single kinematic distribution encodes all conceivable information that can separate signal from background. Sophisticated analysis techniques are needed to combine information from different variables into a single discriminant distribution which is used to extract the single top rate from the data.

Process	2 jets	3 jets	4 jets
<i>s</i> -channel	16 ± 3	8 ± 2	2 ± 1
<i>t</i> -channel	20 ± 4	12 ± 3	4 ± 1
<i>W</i> + <i>bb</i>	261 ± 55	120 ± 24	35 ± 7
<i>W</i> + <i>c</i> $\bar{c}$	151 ± 31	85 ± 17	23 ± 5
<i>W</i> + light quarks	119 ± 25	43 ± 9	12 ± 2
non- <i>W</i>	95 ± 19	77 ± 15	29 ± 6
<i>t</i> $\bar{t}$	59 ± 14	135 ± 32	154 ± 36
Total prediction	686 ± 131	460 ± 75	29 ± 6
Observed in data	697	455	246



Figure 2: Top: Expected signal and background yield for D0’s signal samples. Bottom: Graphical depiction of the expected amount of single-top signal as a function of the *W* + jets multiplicity and the presence of a *b*-tagged jet.

Process	2 jets	3 jets
$s$ -channel	$41.2 \pm 5.9$	$13.5 \pm 1.9$
$t$ -channel	$62.1 \pm 9.1$	$18.3 \pm 2.7$
$W + b$	$461.6 \pm 139.1$	$141.1 \pm 42.6$
$W + c$	$395.0 \pm 121.8$	$108.8 \pm 33.5$
$W + \text{light quarks}$	$339.8 \pm 56.1$	$101.8 \pm 16.9$
non- $W$	$59.5 \pm 23.8$	$21.3 \pm 8.5$
Diboson	$63.2 \pm 6.3$	$21.5 \pm 2.2$
$Z + \text{jets}$	$26.7 \pm 3.9$	$11.0 \pm 1.6$
$t\bar{t}$	$146.0 \pm 20.9$	$338.7 \pm 48.2$
Total prediction	$1595.1 \pm 269.0$	$776.6 \pm 91.4$
Observed in data	1535	712

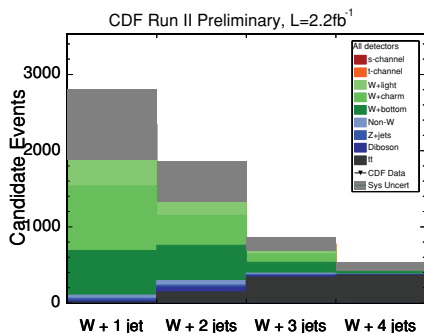


Figure 3: Top: Expected signal and background yield in CDF's signal samples. Bottom: Graphical depiction of sample composition as a function of jet multiplicity.

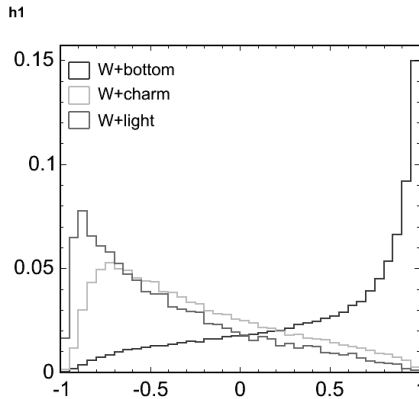


Figure 4: Distribution of the jet-flavor separator used by CDF in  $W+$  jets events. Jets likely to come from  $b$  quarks are given a high probability, while light-quark jets are assigned a low probability.

### 3.1 Boosted Decision Trees (D0)

A decision tree is a machine-learning technique that applies cuts iteratively to classify events. The discrimination power is further improved by averaging over many decision trees constructed using the adaptive boosting algorithm AdaBoost<sup>7)</sup>. This average is called a boosted decision tree. One characteristic of decision trees is that because they optimize a cut at each level, their sensitivity is not reduced by the inclusion of unnecessary variables.

D0's boosted decision tree is trained on 49 input variables, the most important of which are the invariant mass of all jets in the event, the invariant mass of the reconstructed  $W$  boson and the highest- $p_T$   $b$ -tagged jet, the angle between the highest- $p_T$   $b$ -tagged jet and the lepton in the rest frame of the reconstructed top quark ( $\cos\theta_{\ell j}^*$ )<sup>8)</sup>, and the lepton charge times the pseudorapidity of the untagged jet ( $Q \times \eta$ )<sup>9)</sup>.

### 3.2 Multivariate Likelihood Function (CDF)

A projective likelihood technique<sup>10)</sup> is used to combine information from seven input variables to optimize the separation of the single top signal from the

backgrounds in the two-jet case. The input variables  $x_i$ ,  $i = 1 \dots 7$  are measured for each event and the quantities

$$\mathcal{L}_{2n}(\{x_i\}) = \frac{\prod_{i=1}^7 p_{i,k=1}}{\sum_{k=1}^5 \prod_{i=1}^7 p_{ik}}, \text{ where } p_{ik} = \frac{f_{in_i,k}}{\sum_{m=1}^5 f_{in_i,m}} \quad (1)$$

are computed, where  $m$  and  $k$  index the five samples ( $t$ -channel signal,  $Wb\bar{b}$ ,  $Wc\bar{c} + Wc$ ,  $Wj\bar{j}$  and  $t\bar{t}$ ) and  $f_{in_i,m}$  is the normalized probability distribution in bin  $n_i$  for variable  $i$  of a template histogram constructed from a Monte Carlo (or data) model of sample  $m$ . Seven to ten input variables are chosen, including the jet-flavor separator neural network output, the mass of the reconstructed top quark,  $Q \times \eta$ , total scalar sum of transverse energy in the event  $H_T$ , the invariant mass of all jets in the event, and  $\cos\theta_{\ell_j}^*$ .

### 3.3 Matrix Element Discriminant (CDF, D0)

The matrix element method relies on the evaluation of event probability densities for signal and background processes based on calculations of the Standard Model fully differential cross sections<sup>12)</sup>. These probability densities are calculated for signal and background hypotheses for each event and quantify how likely the event is to originate either from signal or background. Given a set of observables,  $x$ , and underlying partonic quantities,  $y$ , the signal and background probability densities are constructed by integrating over the appropriate parton-level differential cross section,  $d\sigma(y)/dy$ , convolved with parton distribution functions (PDFs) and detector resolution effects:

$$P(x) = \sum_{perm.} \int \frac{d\sigma(y)}{dy} f(q_1) f(q_2) dq_1 dq_2 W(x, y) dy. \quad (2)$$

The PDFs ( $f(q_1)$  and  $f(q_2)$ ) take into account the flavors of colliding quark and anti-quark and are given by the CTEQ collaboration<sup>13)</sup>. The detector resolution effects are described by a transfer function  $W(x, y)$  relating  $x$  to  $y$ . The momenta of electrons, muons and the angles of jets are assumed to be measured exactly.  $W(x, y)$  maps parton energies to measured jet energies after correction for instrumental detector effects. This mapping is obtained by parameterizing the jet response in fully simulated Monte Carlo events, which includes effects of radiation, hadronization, measurement resolution, and energy omitted from the jet cone by the jet-reconstruction algorithm. The definition of the probability densities includes possible permutations of matching jets with partons.

The integration is performed over the energy of the partons and  $p_z'$ . Event probability densities are computed for the  $s$ -channel and  $t$ -channel signal, as well as  $Wb\bar{b}$ ,  $Wc\bar{c}$ ,  $Wcj$ ,  $Wgg$ , and  $t\bar{t}$  background hypotheses. In the specific case of the  $t\bar{t}$  matrix element, additional integrations must be performed over the momenta of particles not detected.

The event probability densities are combined into an event probability discriminant, i.e. a distribution which separates signal from background which is used to fit the data:  $P_{signal}/(P_{signal} + P_{background})$ . To better classify signal events which contain  $b$ -jets, CDF incorporates the output of the neural network jet-flavor separator,  $b$ , into the discriminant defined as:

$$\frac{b \cdot P_{st}}{b \cdot P_{st} + b(P_{t\bar{t}} + P_{Wbb}) + (1 - b)(P_{Wcc} + P_{Wcj})} \quad (3)$$

### 3.4 Neural Network (CDF)

The third multivariate approach employs neural networks, which have the general advantage that correlations between the discriminating input variables are actively identified and utilized to optimize the separation power between signal and background. The networks are developed using the NEUROBAYES analysis package <sup>11)</sup>, which combines a three-layer feed-forward neural network with a complex and robust preprocessing of the input variables. Bayesian regularization techniques are utilized to avoid over-training.

Separate networks are trained to identify different signals in distinct samples. The networks use 11 to 18 input variables, the most important ones being the reconstructed top quark mass, the neural-network jet-flavor separator, the dijet mass,  $Q \times \eta$ , the cosine of the angle between the lepton and the light quark jet, the transverse mass of the  $W$  boson, and  $H_T$ . The input variables are selected from a large list of investigated variables using an automated evaluation during the preprocessing step before the network training. In an iterative process, we determine how much the total correlation of the ensemble of variables to the target is reduced by the removal of each single variable. For the networks used in this analysis we kept those variables for which the correlation reduction was significant.

### 3.5 Bayesian Neural Network (D0)

CDF uses a traditional neural network. D0 uses a Bayesian neural network, which is a weighted sum over one hundred different neural networks sampled from the posterior probability density function of the space of network parameters. This protects the network from overtraining and gives the best average neural network for the analysis. The input variables to the Bayesian neural network are similar to those used in the boosted decision tree analysis.

## 4 Measurement Technique and Results

The cross section is extracted by a Bayesian method in which a posterior probability density function is constructed by integrating the systematic nuisance parameters for a fixed value of the single-top cross section. The maximum value of this density function is the most probable value of the cross section, and the region that contains 68% of the area marks out the uncertainty. All sources of systematic uncertainty are included in this statistical treatment, including the correlation between normalization and discriminant shape changes due to sources of systematic uncertainty (e.g. the jet-energy-scale uncertainty).

The distribution of each of D0's discriminants are shown in Figure 5. Examining  $0.9 \text{ fb}^{-1}$  of data, D0 measures values of  $4.8_{-1.4}^{+1.6}$  pb for the matrix element analysis,  $4.4_{-1.4}^{+1.6}$  pb for the Bayesian neural network analysis, and  $4.9_{-1.4}^{+1.4}$  pb for the boosted decision tree analysis<sup>14</sup>). The distribution of each of CDF's discriminants are shown in Figure 6. CDF uses  $2.2 \text{ fb}^{-1}$  of data to measure values of  $1.8_{-0.8}^{+0.9}$  pb for the likelihood function analysis,  $2.2_{-0.7}^{+0.8}$  pb for the matrix element analysis, and  $2.0_{-0.8}^{+0.9}$  pb for the neural network analysis.

D0 combines its results using a best linear unbiased estimator. This takes advantage of the fact that the different analyses, while they use the same data, use different information and are thus not fully correlated. The combination thus has a better sensitivity than any of the three analyses. D0's combination measures a cross section of  $4.7 \pm 1.3$  pb.

To quantify the signal significance of a result, pseudo-experiments are generated from events without a single top contribution. The probability ( $p$ -value) of the background-only pseudo-experiments to fluctuate to the observed result in data is the significance of the result. D0 uses the measured cross section as a test statistic. The expected sensitivity the fraction of events which have a cross

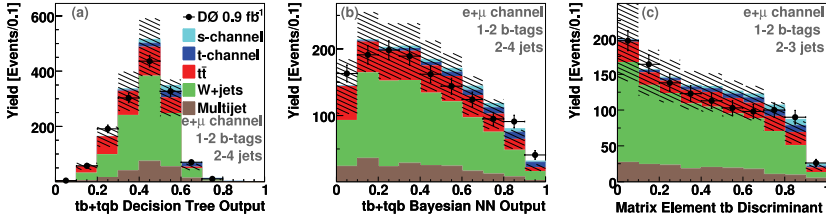


Figure 5: Discriminant distribution in Monte Carlo and data for D0’s boosted decision tree analysis (left), Bayesian neural network analysis (center), and matrix element analysis (right).

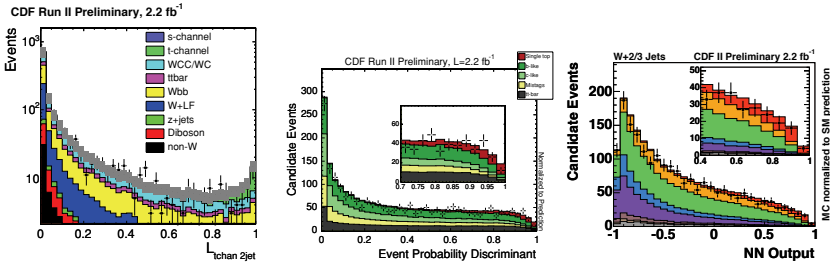


Figure 6: Discriminant distribution in Monte Carlo and data for CDF’s multivariate likelihood function analysis (left), matrix element analysis (center), and neural network analysis (right).

section higher than the Standard-Model expectation. The expected  $p$ -value of D0’s combination is 0.011, which corresponds to a  $2.3\sigma$  signal significance. The observed  $p$ -value is 0.00014, which corresponds to a  $3.6\sigma$  excess (Figure 7).

### 5 Measurement of $|V_{tb}|$

The quantity  $|V_{tb}|$  can be calculated from the single top cross section, which is directly proportional to  $|V_{tb}|^2$ . Assuming, based on branching ratio measurements on top quarks<sup>15)</sup>, that  $|V_{td}|^2 + |V_{ts}|^2 \ll |V_{tb}|^2$ , and integrating a flat prior in  $|V_{tb}|^2$ , requiring  $|V_{tb}|$  to be between 0 and 1, D0 obtains  $|V_{tb}| > 0.68$  at a 95% confidence level. Using the same method on its matrix element analysis, CDF calculates  $|V_{tb}| > 0.6$  at a 95% confidence level (Figure 8). The most

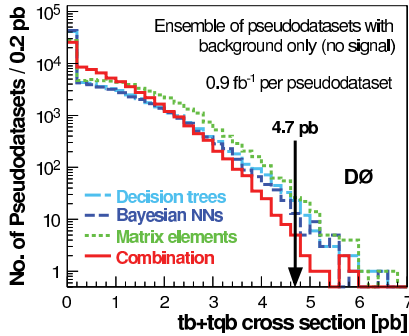


Figure 7: Distribution of cross sections for pseudo-experiments made with no signal included, showing the resulting  $p$ -value of 0.011.

probable value of  $|V_{tb}|$  is the square root of the cross section divided by the Standard Model prediction. D0 measures  $|V_{tb}| = 1.3 \pm 0.2$  and CDF measures  $|V_{tb}| = 0.88^{+0.16}_{-0.14}(\text{stat} + \text{sys}) \pm 0.07(\text{theory})$ .

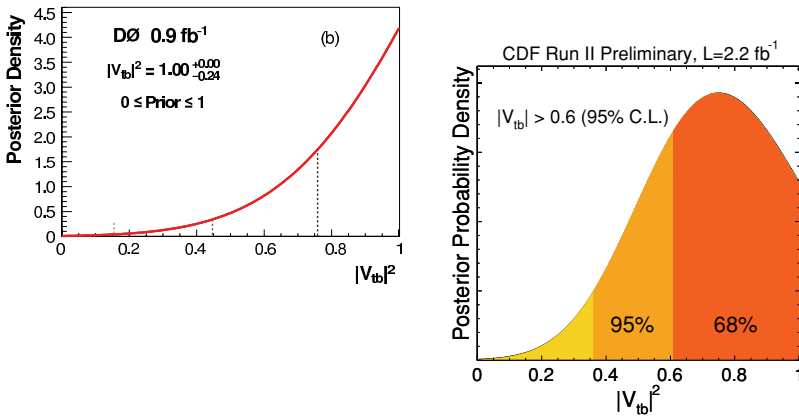


Figure 8: Likelihood curve for  $|V_{tb}|^2$ , in D0's combined analysis (left) and CDF's matrix element analysis (right), showing the limit on its value.

## 6 Conclusions

We have performed searches for electroweak single top quark production at the Tevatron using  $0.9 \text{ fb}^{-1}$  of data collected with the D0 detector and  $2.2 \text{ fb}^{-1}$  of data collected with the CDF detector. Both experiments see evidence of single top production. D0 measures a combined cross section of  $4.7 \pm 1.3 \text{ pb}$  while CDF measures cross sections between  $1.8_{-0.8}^{+0.9} \text{ pb}$  and  $2.2_{-0.7}^{+0.8} \text{ pb}$ . D0 sets a limit at a 95% confidence level of  $|V_{tb}| > 0.68$  and measures  $|V_{tb}| = 1.3 \pm 0.2$ , while CDF calculates  $|V_{tb}| > 0.6$  and measures  $|V_{tb}| = 0.88_{-0.14}^{+0.16}(\text{stat} + \text{sys}) \pm 0.07(\text{theory})$ .

## 7 Acknowledgments

We thank the Fermilab staff and the technical staffs of the participating institutions for their vital contributions.

## References

1. B. W. Harris *et al.*, *Phys. Rev. D* **66**, 054024 (2002)  
Z. Sullivan *Phys. Rev. D* **70**, 114012 (2004).
2. G. Mahlon, *Phys. Rev. D* **55**, 7249 (1997), hep-ph/0011349.
3. T. M. P. Tait and C.-P. Yuan, *Phys. Rev. D* **63**, 014018 (2002).
4. CDF and DØ Collaborations, FERMILAB-PUB-03/320-E (2003).
5. F. Caravaglios *et al.*, *Nucl. Phys. B* **632**, 343 (2002)  
M. L. Mangano *et al.*, *JHEP* 0307:001 (2003).
6. [CDF Collaboration], D. Acosta *et al.*, *Phys. Rev.* **D71**, 052003 (2005).
7. Y. Freund and R. E. Schapire, in *Machine Learning: Proceedings of the Thirteenth International Conference*, edited by L. Saitta (Morgan Kaufmann, San Francisco, 1996), p. 148.
8. G. Mahlon and S. J. Parke, “Improved spin basis for angular correlation studies in single top quark production at the Tevatron,” *Phys. Rev.* **D55**, 7249 (1997). T. Stelzer, Z. Sullivan and S. Willenbrock, “Single top quark production at hadron colliders,” *Phys. Rev. D* **58**, 094021 (1998). [arXiv:hep-ph/9807340].

9. C. P. Yuan, "A New Method to Detect a Heavy Top Quark at the Tevatron," *Phys. Rev. D* **41**, 42 (1990).
10. K. Ackerstaff *et al.* (OPAL Collaboration), "Search for the standard model Higgs boson in  $e^+e^-$  collisions at  $\sqrt{s} = 161\text{-GeV}$  to  $172\text{-GeV}$ ," *Eur. Phys. J. C* **1**, 425 (1998). [arXiv:hep-ex/9709003].
11. M. Feindt and U. Kerzel, "The NeuroBayes neural network package," *Nucl. Instrum. Methods A* **559**, 190-194 (2006).
12. [D0 Collaboration] V. M. Abazov *et al.*, "A Precision Measurement of the Mass of the Top Quark," *Nature* **429**, 638 (2004); F. Canelli, Ph.D. thesis, University of Rochester (2003); B. Stelzer, Ph.D. thesis, University of Toronto (2005); T. Gadfort, Ph.D. thesis, University of Washington (2007); J. Mitrevski, Ph.D. thesis, Columbia University (2007).
13. J. Pumplin *et al.*, *J. High Energy Phys.* **0709**, 028 (2007).
14. [D0 Collaboration] V.M. Abazov *et al.*, "Evidence for Production of Single Top Quarks and First Direct Measurement of  $|V_{tb}|$ ," *Phys. Rev. Lett.* **98**, 181802 (2007); [D0 Collaboration] V.M. Abazov *et al.*, "Evidence for Production of Single Top Quarks," accepted in *Phys. Rev. D* [arXiv:hep-ex/0803.0739].
15. [D0 Collaboration] V.M. Abazov *et al.*, accepted in *Phys. Rev. Lett.* [arXiv:hep-ex/0801.1326].

# STANDARD MODEL PHYSICS IN ATLAS AT THE START OF THE LHC

M. Bellomo on behalf of the ATLAS collaboration  
*INFN Pavia*

## **Abstract**

The upcoming start of the LHC will provide the unprecedented opportunity to explore physics beyond the TeV scale. A necessary requirement for any measurement is of course given by a good understanding and calibration of the detector response. In this note a summary of main analysis at the start of LHC within Standard Model physics is given, with particular emphasis on electroweak “standard candles” processes and inclusive cross-section measurements.

## 1 Introduction

ATLAS <sup>1)</sup> is one of the two multi-purpose detectors that are going to operate at the LHC <sup>2)</sup> to explore physics beyond the TeV scale. LHC is a proton-proton collider with 14 TeV centre-of-mass energy and  $10^{34} \text{ cm}^{-2}\text{s}^{-1}$  design luminosity, which is currently under final installation at CERN and will provide collisions from summer 2008 on.

ATLAS is a general-purpose detector with a 2 T solenoidal magnetic field in the inner tracking volume and air-core toroids for the stand-alone measurements of muons. The inner detector consists of precision silicon detectors followed by a transition-radiation tracker. The electromagnetic and the forward hadronic calorimeters exploit the LAr technology; while the barrel hadronic calorimeters are based on scintillating tile as active material with iron absorber. Muons are measured in the outer part of the detector in a spectrometer based on Monitored Drift Tubes and Resistive Plate Chambers technologies for precision and trigger measurements (Cathode Strip Chambers and Thin Gap Chambers are used in the forward regions) <sup>3)</sup>.

During the start-up phase of the LHC, the initial delivered luminosity is expected to be of the order of  $10^{31} \text{ cm}^{-2}\text{s}^{-1}$ , leading to 50-100  $\text{pb}^{-1}$  of integrated luminosity ( $\mathcal{L}$ ) per experiment on storage by the end of 2008. The main goal of each collaboration is to make best use of these data for the final commissioning of the detectors and to perform first physics measurements. The so-called “standard candle” processes are usually adopted as experimental signatures for calibration purposes. Among them there are resonances as  $J/\psi$  and  $\Upsilon$ , for the low energy region, and electroweak vector bosons. Also  $t\bar{t}$  events, characterized by an overconstrained kinematics, can be used to calibrate several aspect of the reconstruction process.

First physics measurements will be devoted to the determination of the underlying event, inclusive cross-sections in EW and QCD sectors of the Standard Model (SM) and to improve the knowledge of the Parton Distribution Functions (PDFs) looking at rapidity and angular asymmetry distributions of the leptonic decay of EW vector bosons. In the following sections these analysis will be summarized. It has to be noted that first collisions will be at 10 TeV centre-of-mass energy while following results are based on simulation at the nominal LHC energy.

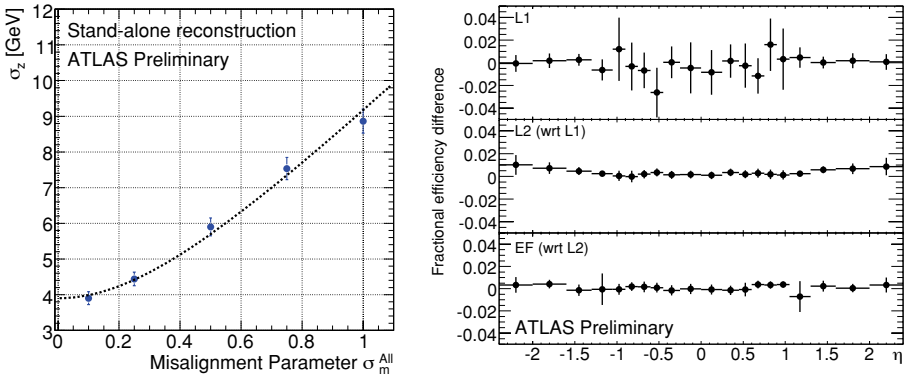


Figure 1: *The width of the gaussian smearing of the Z width as a function of the misalignment parameter  $\sigma_m^{all}$  (left). The fractional difference of trigger efficiency evaluated from data and using MC generator information as a function of  $\eta$  for each trigger level (right).*

## 2 Underlying event

At LHC soft interactions will be dominant. The remains of hard scattering, called Underlying Event, are interpreted as the result of those soft interaction. Its analysis will provide important information on the fundamental aspect of p-p collisions and for the calibration of major physics tools (pile-up, energy and momentum scales, isolation properties, etc.). Although the properties of underlying event have been extensively studied at Tevatron <sup>4)</sup>, the extrapolation at the LHC centre-of-mass energy suffers of large uncertainties between available models <sup>5)</sup>. Thus measurements of charged particles properties in the transverse plane to the leading jet, where particles from soft interactions dominate, as a function of transverse momentum  $p_T$  of the leading jet will be used to tune Monte Carlo generators accordingly.

## 3 W and Z physics in early data

W and Z are produced with high rate even in the initial phase of the LHC running and their leptonic decays represent one of the cleanest signature among the higher jet activity of an hadron collider. Their well-know masses and widths are moreover fundamental references to calibrate particle energy scales and to evaluate detector resolutions. The analysis is generally based on the reconstruction

of the  $Z$  boson resonance. In the case of the muon final state, the momentum scale of reconstructed tracks has a direct impact on the mass peak and position, while the resolution alters the width of the invariant mass distribution. This effect is shown in left side of fig. 1: the width of the gaussian smearing, convoluted with the Breit-Wigner distribution to fit the  $Z$  line shape, grows with the increasing of misalignment parameter ( $\sigma_m^{all} = 1$  means 1 mm and 1 mrad of standard deviations of random displacements). The measured  $Z$  boson mass distribution in Monte Carlo simulation is fit using smearing parameters to take into account for experimental resolutions. Results, for  $\mathcal{L} = 100 \text{ pb}^{-1}$ , have been obtained with correct geometry and magnetic field showing that a precision of few per mille can be reached. The application with also misaligned description of the detector indicates that, although adding a gaussian resolution term, the scale can be fixed at percent level. The fact that a misaligned geometry leads to a worsening of the momentum resolution and so to a broadening of the reconstructed  $Z$  boson resonance, is the starting point of an analysis performed to test the alignment of the muon spectrometer using  $Z \rightarrow \mu^+ \mu^-$  events <sup>6)</sup><sup>1</sup>. In this approach the goal is to determine the net-shift in the sagitta for each sector of the spectrometer. Preliminary results obtained with statistics corresponding to one day of data taking at  $10^{33} \text{ cm}^{-2} \text{ s}^{-1}$  luminosity, indicate that the average residuals can be corrected to zero within 2% while, after correction, a residual effect of the order of 5% is found in muon momentum resolution. However it is expected that larger statistics will make corrections within a single sector possible and therefore leading to a further reduction of this deviation.

One of the first analysis that will be carried out will be the evaluation of the inclusive cross-sections of electroweak vector bosons decaying into leptons. The measurement is based on the following formula:

$$\sigma_{V \rightarrow ll} = \frac{(N_{signal} - N_{bkg})}{\int L dt \cdot A \cdot \epsilon}, \quad (1)$$

where  $N_{signal}$  and  $N_{bkg}$  are the number of events for signal and background processes,  $\int L dt$  is the integrated luminosity,  $A$  is the geometrical and kinematical acceptance and  $\epsilon$  is the trigger and offline lepton identification efficiencies.

---

<sup>1</sup>The muon spectrometer is equipped with an optical alignment system, based on CCD cameras which monitor the movement and internal deformation of MDT chambers. Regions of the detector which are difficult to reach by the optical system will be aligned by muon tracks.

Main analysis areas are therefore dedicated to the evaluation of these parameters<sup>2</sup>, with particular attention to systematics effects that, as luminosity will start to increase, will suddenly dominate over statistical errors.

The acceptance related to the geometrical coverage of the detectors and to the kinematical selections has to be calculated using a detailed simulation of the physics process and of the detector response. Different studies have been performed using different event generators (e.g. PYTHIA<sup>7</sup>), HERWIG<sup>8</sup>), MC@NLO<sup>9</sup>), HORACE<sup>10, 11</sup>) with selections tuned for the detection of  $W$  and  $Z$  leptonic signatures. A relevant effect is expected from NLO corrections due to the enhancement of transverse momentum of the final lepton, related to the hard emissions of initial and final state radiative gluons and photons. This change in the shape of the  $p_T$  distribution leads to a not negligible effect on the acceptance of a given  $p_T$  cut, with differences up to 2% for QCD effects and  $\leq 1\%$  for EW corrections. Also the impact of PDFs uncertainty has to be taken into account, leading to not negligible effects at the percent level.

The efficiencies of the trigger and offline identifications will be derived directly from data, applying the widely used “tag and probe” technique. The method is based on the definition of a “probe-like” object, used to make the performance measurement, within a properly “tagged” sample of events. It can be applied to processes characterized by double object final state signatures, like  $Z$  boson lepton decays. Events are selected tagging one lepton with tight cuts and then selecting other lepton, defined the probe track, from  $Z$  decay with a loose requirement, excluding the detector system (e.g. muon trigger) or the analysis cut (e.g. isolation) under study. The efficiency is then evaluated using this probe object. An example of the Tag and Probe method applied to  $Z \rightarrow \mu^+\mu^-$  events is shown on the left part of fig. 1<sup>12</sup>). The trigger efficiency of each muon trigger level is studied, referred to the previous one, and values measured from  $Z \rightarrow \mu^+\mu^-$  using the tag and probe (*data*) are compared to those obtained using Monte Carlo generated information (*mc*). Comparisons are shown as fractional differences:  $\frac{data-mc}{mc}$  as a function of the reconstructed muon pseudorapidity. These results demonstrate that the systematic uncertainties of the method are at the level of 1%. Background contribution from other processes<sup>3</sup>

---

<sup>2</sup>The integrated luminosity is taken here as an input parameter, whose uncertainty is expected to be of the order of 10-20% in the start-up phase.

<sup>3</sup>These backgrounds have been considered:  $BB \rightarrow \mu\mu X$ ,  $t\bar{t} \rightarrow WbWb \rightarrow$

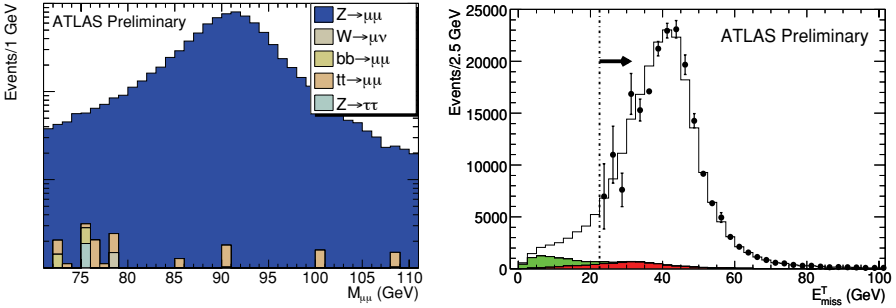


Figure 2:  $\gamma^*Z \rightarrow \mu^+\mu^-$  expected invariant mass spectrum for signal and background process selected using only Muon Spectrometer tracks isolated with Inner Detector. Selections for  $50 \text{ pb}^{-1}$  (left).  $E_T^{\text{miss}}$  spectrum from  $W \rightarrow \nu e$  events, obtained after subtraction of  $\gamma^*Z \rightarrow e^+e^-$  and data-driven jet background (blackdots) together with distributions for signal and remaining backgrounds events (right).

have been found to be quite negligible ( $\leq 0.5\%$ ). Similar analysis have been also performed in the electron channel.

Electroweak boson events are selected using as signature their leptonic decays. The main trigger criteria are therefore based on the requirement of one or two electrons or muons with high transverse momentum. Additional requirements are then imposed offline on the triggered lepton candidates<sup>13)</sup>. Leptons from  $W, Z$  decay tend to be isolated and therefore different isolation cuts can be applied based on Calorimetry and Inner Detector, to reject events coming from background process (e.g. leptons from QCD events are highly not isolated). An example of expected invariant mass spectra from  $\gamma^*Z \rightarrow \mu^+\mu^-$  process is shown in fig. 2. Different background studies have been carried out<sup>14)</sup>. As electroweak backgrounds ( $W\gamma$ ,  $WW$ ,  $ZZ$ ,  $WZ$ ,  $ZZ$ ,  $tW$ ,  $t\bar{t}$ ) give a small contribution (about few %) and most importantly are theoretically known with high accuracy: they can indeed be estimated with high precision from simulation.

On the other side the theoretical prediction for jet background (light parton di-jet and  $b\bar{b}$  events) cross-sections suffer of higher uncertainty and also different experimental aspects, as the probability of a jet to fake an electron,

---


$$\mu^+\mu^-X, Z \rightarrow \tau^+\tau^- \rightarrow \mu^+\nu_\mu\bar{\nu}_\tau \mu^-\bar{\nu}_\mu\nu_\tau \text{ and } W \rightarrow \mu\nu X.$$

are hard to estimated and control from simulation. Therefore the estimation of jet background from data is necessary. Different techniques can be applied.

In the case of  $Z$  leptonic decay background suppression is enhanced by the possibility to apply an invariant mass cut. Backgrounds from QCD events are evaluated from data using, for instance, events with same-sign leptons to parametrize the background shape. In general the more effective selection of  $Z$  events with respect to the  $W$  case, leads to a very small contamination of background events. <sup>14)</sup>

In the case of  $W$  leptonic decay, the undetectable neutrino carries out a fraction on the energy. This results in events with unbalanced energy in the transverse plane ( $E_{miss}^T$ ). The first step to obtain a QCD-enriched sample, for instance in the selection of the  $W \rightarrow e\nu$  signal, is to remove  $Z \rightarrow e^+e^-$  background events via the calculation of the invariant mass of electron pairs. Then a photon selection, based on the same calorimeter cuts as for the electron candidate, is applied requiring the absence of a match between the calorimeter cluster and an inner track. This control sample contains only a small fraction of true electrons which fail the track association cut and is kinematically very similar to a pure QCD sample (purity  $\simeq 99\%$ ) containing fake electron candidates. The QCD shape obtained is then normalized to the missing transverse energy spectrum of events containing electrons by applying an overall normalization factor (calculated in the side-band region between 10 and 22.5 GeV). In the right side of fig. 2 the  $E_{miss}^T$  spectrum, after subtraction of QCD events, is shown.

#### 4 Top pair inclusive cross-section

At the LHC, millions of top quark pairs will be produced each year, allowing for high precision determination of its properties. Top quark pair production is characterized by a well-known experimental signature that it's similar to that predicted by many models of new physics: large amounts of missing energy, multiple leptons(s) and jets. Studying events that look like top quarks is then a fundamental step in increasing the sensitivity to predictions from physics beyond SM. In addition the possibility to over-constrain the kinematics of the final state makes these events suitable to calibrate several aspect of the detector reconstruction.

A top quark decays for nearly 100% into a  $b$  quark and a  $W$  boson. The

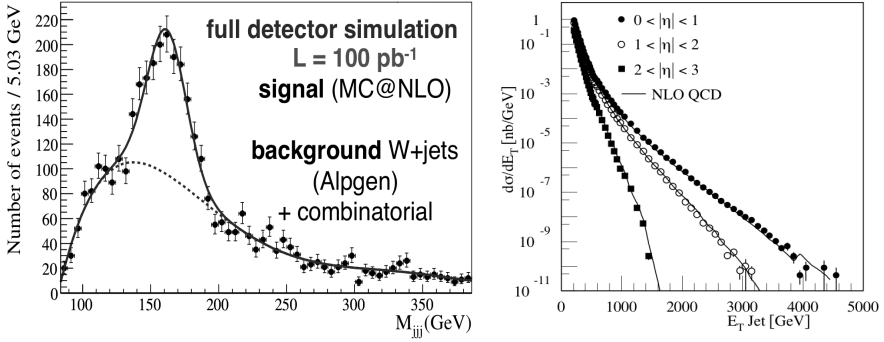


Figure 3: The expected three-jet (top mass) distribution for an integrated luminosity of  $100 \text{ pb}^{-1}$  (left). The inclusive jet cross-section as a function of the  $E_T^{\text{jet}}$  of the leading jet for various pseudorapidity intervals (right).

intermediate boson then decays either into a pair of light jet (2/3) or into a lepton and a neutrino (1/3). The semi-leptonic decay channel  $t\bar{t} \rightarrow WbWb \rightarrow (\ell\nu)b(jj)b$  (4/9 of the total) is particularly interesting: the single high- $p_T$  lepton allows to suppress the amount of Standard Model jet background while the neutrino  $p_T$  is in principle reconstructable being the unique source of missing energy in the signal event. Thus the redundant kinematics constraints can be used to study detector and reconstruction performances<sup>15)</sup>. Events where two jets are known to originate from the decay of a  $W$  boson, whose mass is known with high precision, can be used to calibrate the light jet energy scale. On the other side the missing energy coming from  $W$  leptonic decay can be used to improve the knowledge of the missing energy calibration. The presence of b-jets allow also to test the various tagging algorithms in complex events with a well known kinematics.

In preparation of early LHC data, the top quark pair selection has been studied<sup>16, 17)</sup> without using the b-tagging requirement and asking for 4 jets (cone size  $\Delta R = 0.4$ ) with  $p_T > 40 \text{ GeV}$ , an isolated lepton with  $p_T > 20 \text{ GeV}$  and missing transverse energy exceeding  $20 \text{ GeV}$ . The dominant background has been estimated using the **Alpgen**<sup>18)</sup> Monte Carlo generator (4 jets inclusive sample). The three-jets invariant mass with the additional requirement that two jets are compatible with the mass of the  $W$  boson is shown on the left side of fig. 3 for integrated luminosity of  $100 \text{ pb}^{-1}$ . Various sources of systematic uncertainties have to be taken into account: for instance, 2% and 5%

uncertainty respectively on the light-jet and on the b-jet scales would impact at the level of 3.6% on the top pair inclusive cross-section uncertainty.

## 5 Jet inclusive cross-section

The production of jets is the hard scattering process with the higher cross-section at the LHC<sup>19)</sup>. Therefore a precise measurement of the inclusive jet cross-section is particularly important to keep under control the largest background source in the search of new physics. Determination of  $\alpha_s$  is possible and tests of perturbative QCD over more than 8 orders of magnitude can be performed. The measurement of the jet cross-section is also sensitive both to the quark and gluon PDFs and to new phenomena as quark compositeness.

The expected inclusive jet cross-section as a function of the transverse energy of the leading jet in different pseudorapidity ranges is shown in the right side of fig. 3. The error bars correspond to the expected statistical uncertainty for an integrated luminosity of 300 fb<sup>-1</sup>. For only 30 fb<sup>-1</sup>, about  $4 \cdot 10^5$  events are expected with  $E_T > 1$  TeV, about  $3 \cdot 10^3$  events with  $E_T > 2$  TeV and about 40 events with  $E_T > 3$  TeV.

Especially in the  $E_T^{jet} > 1$  TeV region the dominating systematic uncertainty will be given by the knowledge of the jet energy scale<sup>20)</sup>: 1(5,10)% uncertainty in jet energy scale translates in 10(30,70)% uncertainty in the cross-section measurement. The impact of theoretical uncertainty has been also studied in terms of renormalization and factorization scale uncertainties and PDFs errors: for both in the 1 TeV region an effect of the order of 10% has been observed on the cross-section uncertainty.

## 6 PDFs constraints with LHC data

The knowledge of PDFs is crucial for reliable predictions for new physics signals and their backgrounds at LHC. Every cross section calculations is the convolution of the parton level cross-section and PDF  $f_i(x, Q^2)$ , where  $x$  is the momentum fraction of the parton involved in the hard process,  $Q$  in the energy scale of the interaction and  $i$  represents the parton flavour. Since PDFs describe the dynamics inside the proton in a non perturbative QCD regime, they can't be predicted theoretically but are extracted from experimental observables in various process, using the DGLAP evolution equation<sup>21, 22)</sup>.

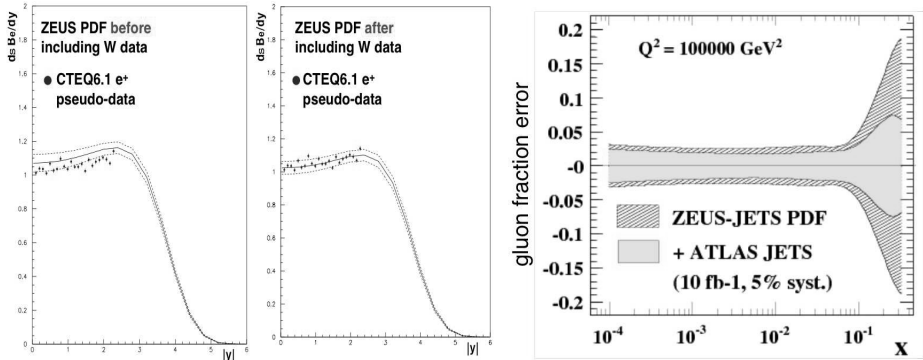


Figure 4:  $e^+$  rapidity spectra generated from CTEQ6.1 PDFs, passed through the ATLAS fast detector simulation and corrected back to generator level using ZEUS-S PDFs, compared to the analytic prediction using ZEUS-S PDFs. The same rapidity distribution is then compared to the analytic prediction after including these lepton pseudo-data in the ZEUS-S PDF fit (left). The expected improvement in gluon ZEUS PDF fit precision using ATLAS jet measurements for  $10 \text{ fb}^{-1}$  and systematics kept at the level of 5% (right).

PDFs are today available up to next-to-next-to leading order (NNLO) and in some cases also take into account experimental errors and their correlations. Given the broad LHC kinematic region, PDFs will be tested both at very low- $x$  ( $10^{-4} < x < 10^{-1}$ ), where they dominate the predictions at the EW scale, and at high- $x$ , where they are extremely important for new physics searches in the TeV energy domain.

The possibility to reduce the uncertainty on PDFs using LHC data has been explored using different processes (23, 24). The  $W$  and  $Z$  production and leptonic decay are clean signals with a very low background contamination (at the level of 1%). Here the PDFs precision can be well improved if the detector systematic uncertainties can be kept at the level of  $\sim 4\%$ . To estimate the contribution to the global PDF fit, ATLAS pseudo-data has been added to the ZEUS-S fit: as a result the error on the  $\lambda$  parameter, which controls the low- $x$  gluon, is reduced by 35% (see left fig. 4).

Other PDFs constraints can be derived from jets measurements (right fig. 4). Also in this case pseudo-data for  $0 < \eta < 1, 1 < \eta < 2, 2 < \eta < 3$  up to  $p_T = 3 \text{ TeV}$  has been used in a global ZEUS fit. Preliminary results suggest that this data can constrain the high- $x$  gluon. However this requires the control of the jet energy scale: increasing statistics from  $1 \text{ fb}^{-1}$  to  $10 \text{ fb}^{-1}$  (equal to

one year of  $\mathcal{L} = 10^{33} \text{ cm}^{-2}\text{s}^{-1}$  data taking) leads only to small changes, while a significant improvement is obtained only if systematic errors can be kept at the level of 5%.

## References

1. ATLAS Collaboration, in: CERN/LHCC, **99-15**, (1999).
2. D. Boussard et al., in: CERN/AC, **95-05**, (1995).
3. ATLAS Collaboration, Technical Design Report, in: CERN/LHCC, **97-22**, (1997).
4. T. Affolder et al., in: Phys. Lett., **D 65**, 092002, (2002).
5. A. Moraes, C. Buttar, I. Dawson, in: ATLAS Note ATL-PHYS-PUB-2005-007.
6. ATLAS Collaboration, In-Situ Determination of the Performance of the ATLAS Muon Spectrometer, in: ATLAS CSC Note, **to be published**, (2008).
7. T. Sjöstrand, P. Edén, C. Friberg, L. Lönnblad, G. Miu, S. Mrenna and E. Norrbin, in: Comput. Phys. Commun., **135**, (2001).
8. G. Corcella, I.G. Knowles, G. Marchesini, S. Moretti, K. Odagiri, P. Richardson, M.H. Seymour and B.R. Webber, in: JHEP, **0101-010**, (2001).
9. S. Frixione, B. R. Webber, in: JHEP **0206** (2002) 029, in: JHEP **0308** (2003) 007.
10. C.M. Carloni Calame, G. Montagna, O. Nicrosini, A. Vicini, in: JHEP, **12**, **016**, (2006).
11. C.M. Carloni Calame, G. Montagna, O. Nicrosini, A. Vicini, in: JHEP, **10**, **109**, (2007).
12. ATLAS Collaboration, Performance of the ATLAS Muon Trigger Slice with Simulated Data, in: ATLAS CSC Note, **to be published**, (2008).
13. ATLAS Collaboration, The ATLAS Experiment at the CERN Large Hadron Collider, in: JINST, **accepted for publication**, (2008).

14. ATLAS Collaboration, Electroweak boson cross-section measurements with ATLAS, in: ATLAS CSC Note, **to be published**, (2008).
15. I. Van Vulpen, in: ACTA PHYSICS POLONICA, **B 38**, (2007).
16. S. Bentvelsen, M. Cobal, in: ATLAS Note, ATL-PHYS-PUB-2005-024, (2005).
17. I. van Vulpen, W. Verkerke, Top Quark Physics with the ATLAS Detector During the LHC Commissioning Phase, in: ATLAS Note, in preparation.
18. M.L. Mangano, M. Moretti, F. Piccinini, R. Pittau, A.D. Polosa, in JHEP, 0307, 001, (2003).
19. H. Stenzel, S. Tapprogge, Prospects for QCD Jet Studies in ATLAS, in: ATL-PHYS-2000-003, (2000).
20. D. Clements et al., Prospects For Inclusive Jet Cross-Section Measurement With Early Data at ATLAS, in: ATL-SLIDE-2007-025, CERN-ATL-SLIDE-2007-025 (2007).
21. G. Altarelli, G. Parisi, in: Nucl. Phys., **B126, 298**, (1977)
22. V. N. Gribov, L. N. Lipatov, in: Yad. Fiz., **15, 781** (1972a); in: Sov. J. Nucl. Phys., **15, 438**, (1972).
23. A. Tricoli, A. Cooper-Sarkar, C.Gwenlan, Uncertainties on W and Z production at the LHC, in: CERN, 2005-014, (2005), [hep-ex:0509002].
24. A. Tricoli et al., in: ACTA PHYSICA POLONICA, **B37**, (2006).

# W AND Z MEASUREMENTS WITH INITIAL CMS DATA

David Wardrope  
*Imperial College London*  
*On Behalf of the CMS Collaboration*

## Abstract

The CMS analysis strategy for the early data measurement of the inclusive W and Z production cross-sections using their electron and muon decay modes, with an integrated luminosity of  $10 \text{ pb}^{-1}$ , is outlined. This measurement is expected to be among the first from the LHC and so the ultimate calibration and alignment precision will not have been obtained. To mitigate the impact of this on the analysis, focus is placed on the use of robust selections and data-driven methods. Preliminary results are presented, which were obtained using data from a detector fully simulated with miscalibration and misalignment on the level expected in the initial data-taking.

## 1 Introduction

There are several compelling reasons for measuring the inclusive W and Z production cross-sections using their decay modes to electrons <sup>1)</sup> and muons <sup>2)</sup> in the early data from CMS. The production of W and Z bosons is well understood theoretically <sup>3)</sup> and has been experimentally tested to great precision <sup>4)</sup> since their discovery in the early 1980s. The principal theoretical uncertainties that concern their production at the LHC are from radiative corrections and those arising from uncertainties on the parton density functions of the proton.

The high centre of mass energy at the LHC will allow measurements in new, unprobed energy regime. ‘Rediscovering’ the physics of the electroweak sector is a vital activity in order to understand both the physics of the LHC and the use of the CMS detector to reconstruct it. Precise measurements, together with good theoretical understanding, of W and Z production can constrain parton density functions, as these processes are sensitive to the internal structure of the proton. Furthermore, making cross-section measurements requires a good knowledge of trigger, reconstruction and selection efficiencies, useful for a wide range of analyses.

W and Z bosons are predicted to have large production cross-sections at the LHC, approximately 190 nb and 60 nb respectively <sup>3)</sup>. Their experimental signature of well-isolated leptons with high transverse momenta is very distinctive in hadron collisions and should be readily triggered and selected. Thus, an integrated luminosity of only  $10 \text{ pb}^{-1}$  is sufficient for significant analyses of W and Z production.

An inclusive cross-section measurement made with  $10 \text{ pb}^{-1}$  will be one of the first results from CMS and the LHC. For this early data, the ultimate calibration and alignment of the detector will not be available and so the analyses described here place emphasis on mitigating any effects consequent to this : simple and robust selections and data-driven methods are used to measure efficiencies and estimate signal and background yields in order to reduce sensitivity to the Monte Carlo modelling of CMS and the LHC environment.

The focus of the analyses was on developing and testing these methods as realistically as possible. To this end, the data used was from a detector simulated with miscalibrations and misalignments on the level we expect shortly after start-up.

## 2 Reconstruction and Selection of W and Z Bosons

The design of the CMS detector <sup>5)</sup> is based around a 4 T large radius solenoid, containing the silicon-based inner tracking; the homogeneous, fully active, crystal electromagnetic calorimeter (ECAL); and the sampling hadronic calorimeter (HCAL). Outside the solenoid are four layers of muon detectors, installed in the solenoid return yoke.

### 2.1 Decays to Electrons

$W \rightarrow e\nu$  and  $\gamma^*/Z \rightarrow ee$  events must pass the single isolated electron High Level Trigger requirements <sup>6)</sup>. Further offline selection of  $W \rightarrow e\nu$  requires one offline reconstructed electron within these events and  $\gamma^*/Z \rightarrow ee$  requires two. An offline reconstructed electron <sup>5)</sup> consists of a supercluster in the ECAL, matched to a track from the interaction vertex. The supercluster is a collection of clusters, extended in the azimuthal direction to gather the energy radiated by an electron traversing the tracker.

The reconstructed electrons in both event types must satisfy some robust identification criteria based on cluster shape and track-supercluster matching, which are designed to be efficient and effective at start-up when CMS is not calibrated or aligned to the ultimate precision. In order to select the high  $p_T$ , isolated electrons characteristic of W and Z decay, the electrons' superclusters must be within the fiducial volume of the ECAL ( $|\eta| < 1.44$  and  $1.56 < |\eta| < 2.5$ ), with transverse energy  $> 20$  GeV. Low charged particle activity around the electron is demanded in the tracker.

In  $W \rightarrow l\nu$  events, the presence of the neutrino is inferred by an imbalance in the transverse energy vector sum of the event,  $\cancel{E}_T$ . This missing transverse energy, calculated from calorimeter energy deposits, is used as a further discriminating variable for the estimation of signal and background event yields.

### 2.2 Decays to Muons

$W \rightarrow \mu\nu$  and  $\gamma^*/Z \rightarrow \mu\mu$  events are first triggered by the single muon trigger <sup>6)</sup>. Offline, muons are reconstructed by both the inner tracking detector and the dedicated muon chambers outside the solenoid. A global muon has its

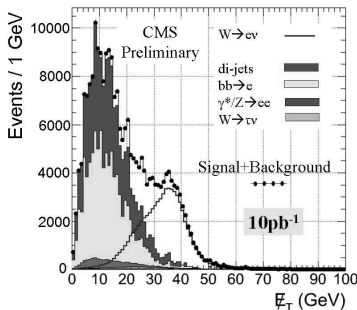


Figure 1:  $E_T$  distribution of  $W \rightarrow e\nu$  and its backgrounds, after selection. The number of events used correspond to those expected for  $10 \text{ pb}^{-1}$  of integrated luminosity. The largest background contributions are from light-flavour QCD di-jet and  $b\bar{b} \rightarrow e$  events.

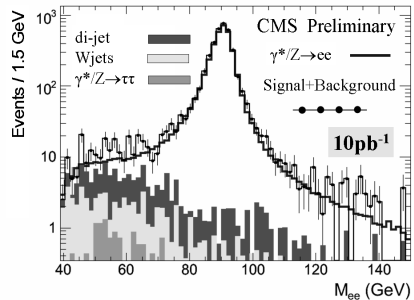


Figure 2: Invariant mass distribution of  $Z \rightarrow ee$  and its backgrounds, after selection. The number of events used correspond to those expected for  $10 \text{ pb}^{-1}$  of integrated luminosity. The largest background contributions are from light-flavour QCD di-jet and  $W$ +jet events.

trajectory reconstructed using hits in both of these subdetectors. All muons are required to have low charged particle track activity around them.

The selection of  $W \rightarrow \mu\nu$  events requires the presence of an isolated global muon with  $p_T > 25 \text{ GeV}$ , with  $|\eta| < 2$ . The transverse mass,  $m_T$ , of the  $W$  is formed, interpreting the  $E_T^{\nu}$  as the neutrino's  $p_T$ .  $m_T > 50 \text{ GeV}$  is required.

$$m_T = \sqrt{2p_T^{\mu} p_T^{\nu} (1 - \cos(p_T^{\mu}, p_T^{\nu}))} \quad (1)$$

$\gamma^*/Z \rightarrow \mu\mu$  events are selected by requiring two muons, at least one of which must be global. The other muon may be global or – in order to increase selection efficiency – may be reconstructed either in the muon chambers or inner tracker alone. Both muons must have  $p_T > 20 \text{ GeV}$  and be within the muon system fiducial volume ( $|\eta| < 2.5$ ). The invariant mass of the muon pair is required to be above  $40 \text{ GeV}$ .

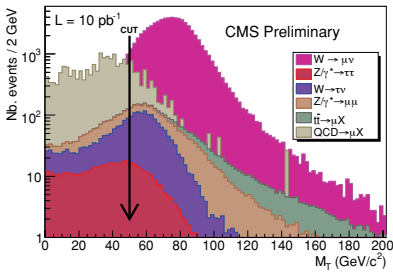


Figure 3:  $m_T$  distribution of  $W \rightarrow \mu\nu$  and its backgrounds, after selection. The number of events used correspond to those expected for  $10 \text{ pb}^{-1}$  of integrated luminosity. The cut at  $m_T = 50 \text{ GeV}$  is indicated.

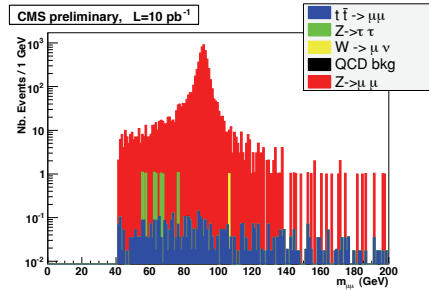


Figure 4: Invariant mass distribution of  $\gamma^*/Z \rightarrow \mu\mu$  and its backgrounds, after selection of events with two global muons. The number of events are those expected for  $10 \text{ pb}^{-1}$  of integrated luminosity.

### 3 Efficiency Determination from Data

The efficiency to reconstruct objects and to trigger and select events can be measured using the data-driven “Tag and Probe” method <sup>7)</sup>. An unbiased and pure sample of leptons is obtained from  $Z \rightarrow ll$  for measuring the efficiency of a particular cut, trigger threshold or reconstruction step. One lepton, the “tag”, meets stringent identification criteria. The other, “probe”, lepton need satisfy only loose criteria that are appropriate to the efficiency under study and leaves it unbiased with respect to it. The purity of the probe sample is ensured by restricting the invariant mass of the lepton pair to be about the Z mass pole.

The efficiencies measured using the Tag and Probe method have been validated against the true efficiencies from Monte Carlo simulations. An example of the good level of agreement found is shown in Figure 5.

### 4 Background Estimation

Electroweak backgrounds in the W and Z samples are small and sufficiently well understood theoretically, so they can be reliably estimated from simulation.

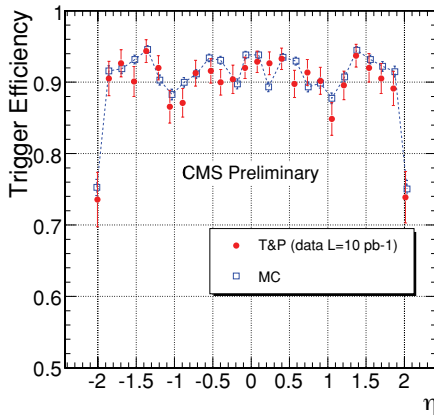


Figure 5: Efficiency as a function of the pseudorapidity,  $\eta$ , for a global muon with  $p_T > 20$  GeV in selected  $Z \rightarrow \mu\mu$  events to satisfy the single muon trigger criteria. A good level of agreement is observed between the true efficiency (open squares) and the efficiency determined using Tag and Probe (filled circles) with data corresponding to  $10 \text{ pb}^{-1}$  of integrated luminosity. Statistical uncertainties are shown for the Tag and Probe efficiencies.

However, the QCD backgrounds are much larger and more difficult to simulate, particularly in the case of  $W \rightarrow e\nu$ . As a result several data-driven background subtraction methods have been evaluated for use on data.

The template method uses predefined distributions of some background discriminating variable, “templates”. Separate templates for selected signal and background events are determined and are simultaneously fit to the distribution of the selected sample (which contains both signal and background). The templates have free normalisation and so the number of both signal and background events can be estimated. Both signal and background templates can be determined from data.

The templates for  $W \rightarrow l\nu$  are determined from data using  $Z \rightarrow ll$  events. In the muon case, the missing transverse energy distribution and the transverse energy direction resolution observed in  $Z \rightarrow \mu\mu$  are parameterised appropriately in terms of the Z momentum. These are then interpreted as predictions for the  $W \rightarrow \mu\nu E_T$ , and can be combined to form a  $m_T$  template, Figure 6.

The transverse energy magnitude and its direction are considered uncorrelated.

In the  $W \rightarrow e\nu$  channel, the template for the dominant QCD di-jet background can be determined by making the selection, but inverting the track isolation criterion. This has the effect of anti-selecting the signal and also the electroweak backgrounds, leaving a pure di-jet sample. The  $E'_T$  distribution of this sample seems to be a good template for the isolated background (Figure 7), as the isolation condition applied to the jets and  $E'_T$  are largely uncorrelated.

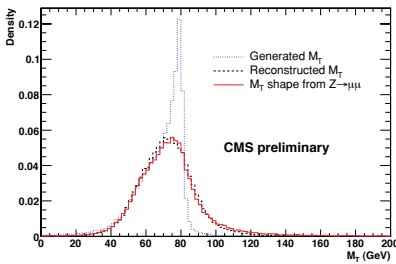


Figure 6: The  $m_T$  distribution of the selected  $W \rightarrow e\nu$  sample (dashed line) is well represented by the template derived from  $Z \rightarrow \mu\mu$  events (solid line).

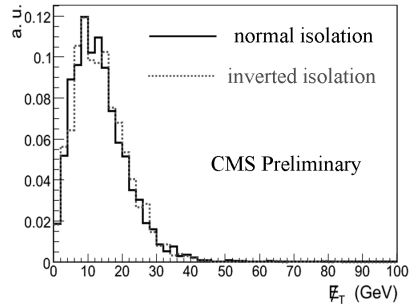


Figure 7: The  $E'_T$  distribution of QCD di-jet events passing the selection (solid line) is well represented by the template derived from the inverted isolation sample (dashed line).

### 5 Cross-section Measurement

The  $W \rightarrow l\nu$  cross section is calculated using the following formula (similarly for  $\gamma^*/Z \rightarrow ll$ ):

$$\sigma_W \times BR(W \rightarrow l\nu) = \frac{N_W^{sig} - N_W^{bkgd}}{A_W \times \epsilon_W \times \int L dt} \tag{2}$$

$N_W^{sig}$  and  $N_W^{bkgd}$  are the number of signal and background events passing the selection.  $\epsilon_W$  is the efficiency of the triggering, reconstruction and selection of the  $W \rightarrow l\nu$  events. All are measured from data using the methods described.

$A_W$  is the geometric and kinematic acceptance of  $W \rightarrow l\nu$  events, which is determined from simulation. The integrated luminosity,  $\int Ldt$ , is measured externally to these analyses.

The results of the calculations for  $W \rightarrow e\nu$  are shown in Table 1. There is good agreement between the data-driven cross-section determination and the cross-section input to the analysis. It should be noted that the uncertainties in the table are purely statistical and a systematic uncertainty of  $\sim 10\%$  is anticipated on the integrated luminosity measurement. The largest systematic uncertainty of these analyses is 5% from the signal and background yield estimation for  $W \rightarrow e\nu$ .

Table 1: Results for the  $W \rightarrow e\nu$  cross section measurement.

$N_{selected} - N_{bkgd}$	$67954 \pm 674$
Tag&Probe $\varepsilon_{total}$	$65.1 \pm 0.5 \%$
Acceptance	$52.3 \pm 0.2 \%$
Int. Luminosity	$10 \text{ pb}^{-1}$
$\sigma_W \times BR(W \rightarrow e\nu)$	$19.97 \pm 0.25 \text{ nb}$
cross section used	$19.78 \text{ nb}$

## 6 Conclusions

Analysis strategies for measuring the inclusive production cross-sections of the W and Z bosons have been formulated and tested for the early data-taking period of CMS. These strategies must handle data before precise calibration and alignment can be carried out and so use robust selections and data-driven methods to extract efficiencies and background-corrected signal yields. Significant results can be obtained with only  $10 \text{ pb}^{-1}$  of data.

Table 2: Results for the  $\gamma^*/Z \rightarrow e^+e^-$  cross section measurement.

$N_{selected}$	$3914 \pm 63$
$N_{bkgd}$	assumed 0.0
Tag&Probe $\varepsilon_{total}$	$68.1 \pm 0.6 \%$
Acceptance	$32.39 \pm 0.18 \%$
Int. Luminosity	$10 \text{ pb}^{-1}$
$\sigma_{Z/\gamma^*} \times BR(Z/\gamma^* \rightarrow e^+e^-)$	$1775 \pm 34 \text{ pb}$
cross section used	1787 pb

## References

1. CMS Collaboration, Towards a Measurement of the Inclusive  $W \rightarrow e\nu$  and  $\gamma^*/Z \rightarrow e^+e^-$  Cross Sections in pp Collisions at  $\sqrt{s}=14$  TeV, CMS PAS EWK-2007/001.
2. CMS Collaboration, Towards a Measurement of the Inclusive  $W \rightarrow \mu\nu$  and  $Z \rightarrow \mu^+\mu^-$  Cross Sections in pp Collisions at  $\sqrt{s}=14$  TeV, CMS PAS EWK-2007/002.
3. CERN, Standard Model Physics (and more) at the LHC, CERN-2000-004.
4. LEP Electroweak Working Group, Precision Electroweak Measurements and Constraints on the Standard Model, CERN-PH-EP/2007-039.
5. CMS Collaboration, Physics TDR Vol I. Detector Performance and Software, CERN/LHCC 2006-001.
6. CMS Collaboration, Data Acquisition & High-Level Trigger, TDR, CERN/LHCC 2002-26.
7. CMS Collaboration, Measuring Electron Efficiencies at CMS with Early Data, CMS PAS EGM-2007/001.



## DRELL YAN PROCESSES AT LHC

G. Balossini, G. Montagna

*Dipartimento di Fisica Nucleare e Teorica, Università di Pavia,  
and INFN, Sezione di Pavia,  
via A. Bassi 6, 27100, Italy*

C.M. Carloni Calame

*INFN, Frascati (Italy)*

*and School of Physics and Astronomy,  
Southampton University, Southampton (UK)*

M. Moretti, M. Treccani

*Dipartimento di Fisica, Università di Ferrara,  
and INFN, Sezione di Ferrara, Italy*

O. Nicrosini, F. Piccinini

*INFN, Sezione di Pavia,  
via A. Bassi 6, 27100, Italy*

A. Vicini

*Dipartimento di Fisica, Università di Milano,  
and INFN, Sezione di Milano,  
Via Celoria 16, 20133, Italy*

### Abstract

The relevance of single- $W$  and single- $Z$  production processes at hadron colliders is well known: in the present paper the status of theoretical calculations of Drell-Yan processes is summarized and some results on the combination of electroweak and QCD corrections to a sample of observables of the process  $pp \rightarrow W^\pm \rightarrow \mu^\pm + X$  at the LHC are discussed. The phenomenological analysis shows that a high-precision knowledge of QCD and a careful combination of electroweak and strong contributions is mandatory in view of the anticipated LHC experimental accuracy.

## 1 Introduction

Precision measurements of electroweak (EW) gauge boson production and properties will be a crucial goal of the physics program of proton-proton collisions at the LHC.  $W$  and  $Z$  bosons will be produced copiously and careful measurements of their observables will be important in testing the Standard Model (SM) and uncovering signs of new physics <sup>1)</sup>.

Thanks to the high luminosity achievable at the LHC, the systematic errors will play a dominant role in determining the accuracy of the measurements, implying, in particular, that the theoretical predictions will have to be of the highest standard as possible. For Drell-Yan (D-Y) processes, this amounts to make available calculations of  $W$  and  $Z$  production processes including simultaneously higher-order corrections coming from the EW and QCD sector of the SM. Actually, in spite of a detailed knowledge of EW and QCD corrections separately, the combination of their effects have been addressed only recently <sup>2, 3, 4)</sup> and need to be deeply scrutinized in view of the anticipated experimental accuracy.

In this contribution, after a review of existing calculations and codes, we present the results of a study aiming at combining EW and QCD radiative corrections to D-Y processes consistently. We do not include in our analysis uncertainties due to factorization/renormalization scale variations, as well as uncertainties in the Parton Distribution Functions arising from diverse experimental and theoretical sources, which are left to a future publication. Some results already available in this direction can be found in <sup>5)</sup>.

## 2 Status of theoretical predictions and codes

Concerning QCD calculations and tools, the present situation reveals quite a rich structure, that includes next-to-leading-order (NLO) and next-to-next-to-leading-order (NNLO) corrections to  $W/Z$  total production rate <sup>6, 7)</sup>, NLO calculations for  $W, Z + 1, 2$  jets signatures <sup>8, 9)</sup> (available in the codes DYRAD and MCFM), resummation of leading and next-to-leading logarithms due to soft gluon radiation <sup>10, 11)</sup> (implemented in the Monte Carlo ResBos), NLO corrections merged with QCD Parton Shower (PS) evolution (in the event generators MC@NLO <sup>12)</sup> and POWHEG <sup>13)</sup>), NNLO corrections to  $W/Z$  production in fully differential form <sup>14, 15)</sup> (available in the Monte Carlo program FEWZ), as well as leading-order multi-parton matrix elements generators matched with vetoed PS, such as, for instance, ALPGEN <sup>16)</sup>, MADE-

VENT<sup>17)</sup>, HELAC<sup>18)</sup> and SHERPA<sup>19)</sup>.

As far as complete  $\mathcal{O}(\alpha)$  EW corrections to D-Y processes are concerned, they have been computed independently by various authors in<sup>20, 21, 22, 23, 24</sup> for  $W$  production and in<sup>25, 26, 27, 28)</sup> for  $Z$  production. Electroweak tools implementing exact NLO corrections to  $W$  production are DK<sup>20)</sup>, WGRAD2<sup>21)</sup>, SANC<sup>23)</sup> and HORACE<sup>24)</sup>, while ZGRAD2<sup>25)</sup>, HORACE<sup>27)</sup> and SANC<sup>28)</sup> include the full set of  $\mathcal{O}(\alpha)$  EW corrections to  $Z$  production. The predictions of a subset of such calculations have been compared, at the level of same input parameters and cuts, in the proceedings of the Les Houches 2005<sup>29)</sup> and TEV4LHC<sup>30)</sup> workshops for  $W$  production, finding a very satisfactory agreement between the various, independent calculations. A first set of tuned comparisons for the  $Z$  production process has been recently performed and is available in<sup>31)</sup>.

From the calculations above, it turns out that NLO EW corrections are dominated, in the resonant region, by final-state QED radiation containing large collinear logarithms of the form  $\log(\hat{s}/m_l^2)$ , where  $\hat{s}$  is the squared partonic centre-of-mass (c.m.) energy and  $m_l$  is the lepton mass. Since these corrections amount to several per cents around the jacobian peak of the  $W$  transverse mass and lepton transverse momentum distributions and cause a significant shift (of the order of 100-200 MeV) in the extraction of the  $W$  mass  $M_W$  at the Tevatron, the contribution of higher-order corrections due to multiple photon radiation from the final-state leptons must be taken into account in the theoretical predictions, in view of the expected precision (at the level of 15-20 MeV) in the  $M_W$  measurement at the LHC. The contribution due to multiple photon radiation has been computed, by means of a QED PS approach, in<sup>32)</sup> for  $W$  production and in<sup>33)</sup> for  $Z$  production, and implemented in the event generator HORACE. Higher-order QED contributions to  $W$  production have been calculated independently in<sup>34)</sup> using the YFS exponentiation, and are available in the generator WINHAC. They have been also computed in the collinear approximation, within the structure functions approach, in<sup>35)</sup>.

A further important phenomenological feature of EW corrections is that, in the region important for new physics searches (i.e. where the  $W$  transverse mass is much larger than the  $W$  mass or the invariant mass of the final state leptons is much larger than the  $Z$  mass), the NLO EW effects become large (of the order of 20-30%) and negative, due to the appearance of EW Sudakov logarithms  $\propto -(\alpha/\pi) \log^2(\hat{s}/M_V^2)$ ,  $V = W, Z$ <sup>20, 21, 24, 25, 26, 27)</sup>. Furthermore, in this region, weak boson emission processes (e.g.  $pp \rightarrow e^+ \nu_e V + X$ ), that contribute at the same order in perturbation theory, can partially cancel

the large Sudakov corrections, when the weak boson  $V$  decays into unobserved  $\nu\bar{\nu}$  or jet pairs, as recently shown in <sup>36</sup>).

### 3 Theoretical approach

A first strategy for the combination of EW and QCD corrections consists in the following formula

$$\left[\frac{d\sigma}{d\mathcal{O}}\right]_{\text{QCD\&EW}} = \left\{\frac{d\sigma}{d\mathcal{O}}\right\}_{\text{MC@NLO}} + \left\{\left[\frac{d\sigma}{d\mathcal{O}}\right]_{\text{EW}} - \left[\frac{d\sigma}{d\mathcal{O}}\right]_{\text{Born}}\right\}_{\text{HERWIG PS}} \quad (1)$$

where  $d\sigma/d\mathcal{O}_{\text{MC@NLO}}$  stands for the prediction of the observable  $d\sigma/d\mathcal{O}$  as obtained by means of MC@NLO,  $d\sigma/d\mathcal{O}_{\text{EW}}$  is the HORACE prediction for the EW corrections to the  $d\sigma/d\mathcal{O}$  observable, and  $d\sigma/d\mathcal{O}_{\text{Born}}$  is the lowest-order result for the observable of interest. The label HERWIG PS in the second term in r.h.s. of eq. (1) means that EW corrections are convoluted with QCD PS evolution through the HERWIG event generator, in order to (approximately) include mixed  $\mathcal{O}(\alpha\alpha_s)$  corrections and to obtain a more realistic description of the observables under study. However, it is worth noting that the convolution of NLO EW corrections with QCD PS implies that the contributions of the order of  $\alpha\alpha_s$  are not reliable when hard non-collinear QCD radiation turns out to be relevant, e.g. for the lepton and vector boson transverse momentum distributions in the absence of severe cuts able to exclude resonant  $W/Z$  production. In this case, a full  $\mathcal{O}(\alpha\alpha_s)$  calculation would be needed for a sound evaluation of mixed EW and QCD corrections. Full  $\mathcal{O}(\alpha)$  EW corrections to the exclusive process  $pp \rightarrow W + j$  (where  $j$  stands for jet) have been recently computed, in the approximation of real  $W$  bosons, in <sup>37, 38</sup>), while one-loop weak corrections to  $Z$  hadro-production have been computed, for on-shell  $Z$  bosons, in <sup>39</sup>). It is also worth stressing that in eq. (1) the infrared part of QCD corrections is factorized, whereas the infrared-safe matrix element residue is included in an additive form. It is otherwise possible to implement a fully factorized combination (valid for infra-red safe observables) as follows:

$$\left[\frac{d\sigma}{d\mathcal{O}}\right]_{\text{QCD}\otimes\text{EW}} = \left(1 + \frac{[d\sigma/d\mathcal{O}]_{\text{MC@NLO}} - [d\sigma/d\mathcal{O}]_{\text{HERWIG PS}}}{[d\sigma/d\mathcal{O}]_{\text{Born}}}\right) \times \left\{\frac{d\sigma}{d\mathcal{O}}\right\}_{\text{HERWIG PS}}, \quad (2)$$

where the ingredients are the same as in eq. (1) but also the QCD matrix element residue is now factorized. Eqs. (1) and (2) have the very same  $\mathcal{O}(\alpha)$  and

$\mathcal{O}(\alpha_s)$  content, differing by terms of the order of  $\alpha\alpha_s$ . Their relative difference has been checked to be of the order of a few per cent in the resonance region around the  $W/Z$  mass, and can be taken as an estimate of the uncertainty of QCD and EW combination.

#### 4 Numerical results: $W$ and $Z$ production

In order to assess the phenomenological relevance of the combination of QCD and EW corrections, we study, for definiteness, the charged-current process  $pp \rightarrow W^\pm \rightarrow \mu^\pm + X$  at the LHC, imposing the following selection criteria

$$\begin{aligned} \text{a. } & p_\perp^\mu \geq 25 \text{ GeV}, \quad \cancel{E}_T \geq 25 \text{ GeV}, \quad |\eta_\mu| < 2.5, \\ \text{b. } & \text{the cuts as above} \oplus M_\perp^W \geq 1 \text{ TeV}, \end{aligned} \quad (3)$$

where  $p_\perp^\mu$  and  $\eta_\mu$  are the transverse momentum and the pseudorapidity of the muon,  $\cancel{E}_T$  is the missing transverse energy, which we identify with the transverse momentum of the neutrino, as typically done in several phenomenological studies. For set up b., a severe cut on the  $W$  transverse mass  $M_\perp^W$  is superimposed to the cuts of set up a., in order to isolate the region of the high tail of  $M_\perp^W$ , which is interesting for new physics searches. We also consider the neutral-current reaction  $pp \rightarrow \gamma, Z \rightarrow e^+e^- + X$ , selecting the events according to the cuts

$$p_\perp^{e^\pm} \geq 25 \text{ GeV}, \quad |\eta^{e^\pm}| < 2.5, \quad M_{e^+e^-} \geq 200 \text{ GeV}. \quad (4)$$

The granularity of the detectors and the size of the electromagnetic showers in the calorimeter make it difficult to discriminate between electrons and photons with a small opening angle. We adopt the following procedure to select the event: we recombine the four-momentum vectors of the electron and photon into an effective electron four-momentum vector if, defining

$$\Delta R(e, \gamma) = \sqrt{\Delta\eta(e, \gamma)^2 + \Delta\phi(e, \gamma)^2}, \quad (5)$$

$\Delta R(e, \gamma) < 0.1$  (with  $\Delta\eta, \Delta\phi$  the distances of electrons and photons along the longitudinal and azimuthal directions). We do not recombine electrons and photons if  $\eta_\gamma > 2.5$  (with  $\eta_\gamma$  the photon pseudo-rapidity). We apply the event selection cuts as in Eq. (4) only after the recombination procedure.

The parton distribution function (PDF) set MRST2004QED<sup>40</sup>) has been used to describe the proton partonic content. The QCD factorization / renormalization scale and the analogous QED scale (present in the PDF

set MRST2004QED) are chosen to be equal, as usually done in the literature 20, 21, 24, 25, 27), and fixed at  $\mu_R = \mu_F = \sqrt{(p_{\perp}^W)^2 + M_{\mu\nu}^2}$  (for the charged-current case), where  $M_{\mu\nu}$  is the  $\mu\nu$  invariant mass, and at  $\mu_R = \mu_F = \sqrt{(p_{\perp}^Z)^2 + M_{e^+e^-}^2}$  (for the neutral-current case), where  $M_{e^+e^-}$  is the invariant mass of the lepton pair.

In order to avoid systematic theoretical effects, all the generators used in our study have been properly tuned at the level of input parameters, PDF set and scale to give the same LO/NLO results. The tuning procedure validates the interpretation of the various relative effects as due to the radiative corrections and not to a mismatch in the setups of the codes under consideration.

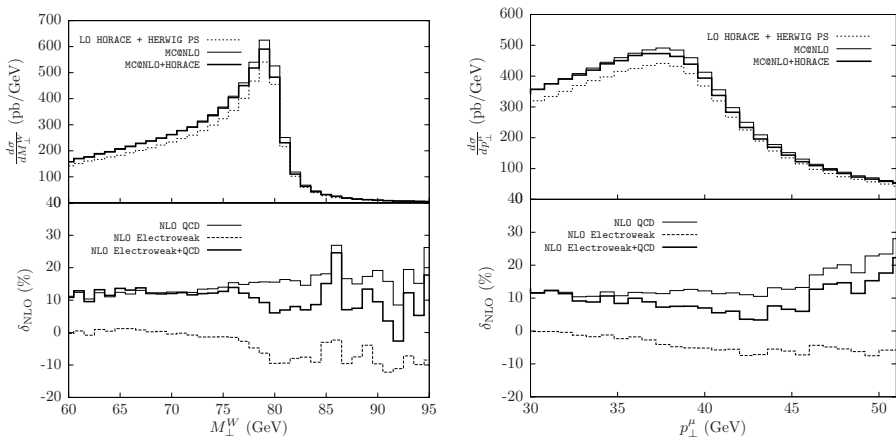


Figure 1: *Upper panel: predictions of MC@NLO, MC@NLO+HORACE and leading-order HORACE+HERWIG PS for the  $M_{\perp}^W$  (left) and  $p_{\perp}^{\mu}$  (right) distributions at the LHC, according to the cuts of set up a. of Eq. (3). Lower panel: relative effect of QCD and EW corrections, and their sum, for the corresponding observables in the upper panel.*

A sample of our numerical results is shown in Fig. 1 for the  $W$  transverse mass  $M_{\perp}^W$  and muon transverse momentum  $p_{\perp}^{\mu}$  distributions according to set up a. of Eq. (3), and in Fig. 2 for the same distributions according to set up b. In Fig. 1 and Fig. 2, the upper panels show the predictions of the generators MC@NLO and MC@NLO + HORACE interfaced to HERWIG PS (according to eq. (1)), in comparison with the leading-order result by HORACE convoluted with HERWIG shower evolution. The

lower panels illustrate the relative effects of the matrix element residue of NLO QCD and of full EW corrections, as well as their sum, that can be obtained by appropriate combinations of the results shown in the upper panels. More precisely, the percentage corrections shown have been defined as  $\delta = (\sigma_{\text{NLO}} - \sigma_{\text{Born+HERWIG PS}}) / \sigma_{\text{Born+HERWIG PS}}$ , where  $\sigma_{\text{NLO}}$  stands for the predictions of the generators including exact NLO corrections matched with QCD PS.

From Fig. 1 it can be seen that the QCD corrections are positive around the  $W$  jacobian peak, of about 10-20%, and tend to compensate the negative effect due to EW corrections. Therefore, their interplay is crucial for a precise  $M_W$  extraction at the LHC and their combined contribution can not be accounted for in terms of a pure QCD PS approach, as it can be inferred from the comparison of the predictions of MC@NLO versus the leading-order result by HORACE convoluted with HERWIG PS. It is also worth noting that the convolution of NLO corrections with the QCD PS broadens the sharply peaked shape of the fixed-order NLO QCD and EW effects.

The interplay between QCD and EW corrections to  $W$  production in the region interesting for new physics searches, i.e. in the high tail of  $M_{\perp}^W$  and  $p_{\perp}^{\mu}$  distributions, is shown in Fig. 2. For both  $M_{\perp}^W$  and  $p_{\perp}^{\mu}$ , the QCD corrections are positive and largely cancel the negative EW Sudakov logarithms. Therefore, a precise normalization of the SM background to new physics searches necessarily requires the simultaneous control of QCD and EW corrections.

Results about the combination of QCD and EW corrections for the dilepton invariant mass in the neutral-current D-Y process  $pp \rightarrow \gamma, Z \rightarrow e^+e^- + X$ , according to the cuts of Eq. (4) can be found in <sup>41</sup>). The QCD corrections are quite flat and positive with a value of about 15% over the mass range 200–1500 GeV. The EW corrections are negative and vary from about –5% to –10% and thus partially cancel the QCD contribution. Therefore, as for the charged-current channel, the search for new physics in di-lepton final states needs a careful combination of EW and QCD effects.

## 5 Conclusions

During the last few years, there has been a big effort towards high-precision predictions for D-Y-like processes, addressing the calculation of higher-order QCD and EW corrections. Correspondingly, precision computational tools

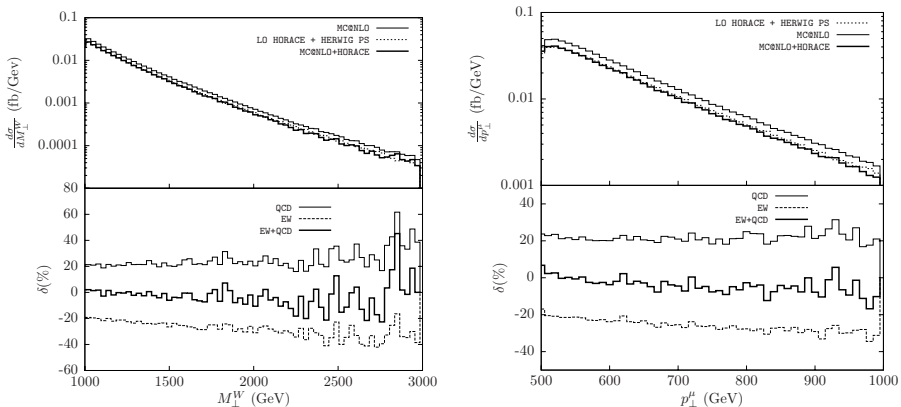


Figure 2: *Upper panel: predictions of MC@NLO, MC@NLO+HORACE and leading-order HORACE+HERWIG PS for the  $M_{\perp}^W$  (left) and  $p_{\perp}^{\mu}$  (right) distributions at the LHC, according to the cuts of set up a. of Eq. (3). Lower panel: relative effect of QCD and EW corrections, and their sum, for the corresponding observables in the upper panel.*

have been developed to keep under control theoretical systematics in view of the future measurements at the LHC.

We presented some original results about the combination of EW and QCD corrections to a sample of observables of  $W$  and  $Z$  production processes at the LHC. Our investigation shows that a high-precision knowledge of QCD and a careful combination of EW and strong contributions is mandatory in view of the anticipated experimental accuracy. We plan, however, to perform a more complete and detailed phenomenological study, including the predictions of other QCD generators and considering further observables of interest for the many facets of the  $W/Z$  physics program at the LHC.

## 6 Acknowledgments

C.M. Carloni Calame is supported by a INFN postdoc Fellowship and thanks the School of Physics&Astronomy, University of Southampton, for hospitality. We are grateful to the colleagues of the common paper <sup>41)</sup> for precious collaboration. F. Piccinini would like to thank G. Bellettini, G. Chiarelli and M. Greco for the kind invitation.

## References

1. U. Baur, Electroweak physics at the Tevatron and LHC: Theoretical status and perspectives, arXiv:hep-ph/0511064
2. Q.-H. Cao and C.-P. Yuan, Phys. Rev. Lett. **93** (2004). 042001; arXiv:hep-ph/0401171
3. B.F.L. Ward and S.A. Yost, Acta Phys. Polon. **B38** (2007) 2395.
4. S. Jadach, W. Placzek, M. Skrzypek, P. Stephens and Z. Was, Acta Phys. Polon. **B38** (2007) 2305.
5. N.E. Adam, V. Halyo and S.A. Yost, arXiv:0802.3251 [hep-ph]; S. Frixione and M.L. Mangano, JHEP **0405** (2004) 056
6. G. Altarelli, R. K. Ellis and G. Martinelli, Nucl. Phys. **B157** (1979) 461.
7. R. Hamberg, W. L. van Neerven and T. Matsuura, Nucl. Phys. **B359** (1991) 343 [Erratum Nucl. Phys. **B644** (2002) 403].
8. W.T. Giele, E.W.N. Glover and D.A. Kosower, Nucl. Phys. **B403** (1993) 633.
9. J.M. Campbell and R.K. Ellis, Phys. Rev. **D65** (2002) 113007.
10. C. Balazs and C. P. Yuan, Phys. Rev. **D56** (1997) 5558.
11. F. Landry, R. Brock, P.M. Nadolsky and C.-P. Yuan, Phys. Rev. **D67** (2003) 073016.
12. S. Frixione and B. R. Webber, JHEP **0206** (2002) 029.
13. S. Frixione, P. Nason and C. Oleari, JHEP **0711** (2007) 070.
14. K. Melnikov and F. Petriello, Phys. Rev. Lett. **96** (2006) 231803.
15. K. Melnikov and F. Petriello, Phys. Rev. **D74** (2006) 114017.
16. M.L. Mangano, M. Moretti, F. Piccinini, R. Pittau and A.D. Polosa, JHEP **0307** (2003) 001.
17. T. Stelzer and W.F. Long, Comp. Phys. Commun. **81** (1994) 357; F. Maltoni and T. Stelzer, JHEP **02** (2003) 027.
18. A. Kanaki and C.G. Papadopoulos, Comput. Phys. Commun. **132** (2000) 306; C.G. Papadopoulos and M. Worek, Eur. Phys. J. **C50** (2007) 843; A. Cafarella, C.G. Papadopoulos and M. Worek, arXiv:0710.2427 [hep-ph].
19. T. Gleisberg, S. Höche, F. Krauss, A. Schälicke, S. Schumann and J. Winter, JHEP **0402** (2004) 056.
20. S. Dittmaier and M. Krämer, Phys. Rev. **D65** (2002) 0703007.
21. U. Baur and D. Wackerth, Phys. Rev. **D70** (2004) 073015.

22. V. A. Zykunov, Eur. Phys. J. Direct **C3** (2001) 9; Phys. Atom. Nucl. **69** (2006) 1522.
23. A. Arbuzov, D. Bardin, S. Bondarenko, P. Christova, L. Kalinovskaya, G. Nanava and R. Sadykov, Eur. Phys. J. **C46** (2006) 407.
24. C.M. Carloni Calame, G. Montagna, O. Nicrosini and A. Vicini, JHEP **12** (2006) 016.
25. U. Baur, O. Brein, W. Hollik, C. Schappacher and D. Wackerroth, Phys. Rev. **D65** (2002) 033007.
26. V.A. Zykunov, Phys. Rev. **D75** (2007) 073019.
27. C.M. Carloni Calame, G. Montagna, O. Nicrosini and A. Vicini, JHEP **10** (2007) 109.
28. A. Arbuzov, D. Bardin, S. Bondarenko, P. Christova, L. Kalinovskaya, G. Nanava and R. Sadykov, arXiv:0711.0625 [hep-ph].
29. C. Buttar *et al.*, arXiv:hep-ph/0604120.
30. C.E. Gerber *et al.*, FERMILAB-CONF-07-052, arXiv:0705.3251 [hep-ph].
31. C. Buttar *et al.*, arXiv:0803.0678 [hep-ph].
32. C.M. Carloni Calame, G. Montagna, O. Nicrosini and M. Treccani, Phys. Rev. **D69** (2004) 037301.
33. C.M. Carloni Calame G. Montagna, O. Nicrosini and M. Treccani, JHEP **05** (2005) 019.
34. S. Jadach and W. Flączek, Eur. Phys. J. **C29** (2003) 325.
35. S. Brensing, S. Dittmaier, M. Krämer and A. Muck, arXiv:0710.3309 [hep-ph].
36. U. Baur, Phys. Rev. **D75** (2007) 013005.
37. W. Hollik, T. Kasprzik and B.A. Kniehl, Nucl. Phys. **B790** (2008) 138.
38. J.H. Kühn, A. Kulesza and S. Pozzorini, Nucl. Phys. **B797** (2008) 27.
39. E. Maina, S. Moretti and D.A. Ross, Phys. Lett. **593** (2004) 143, Erratum *ibid.* **614** (2005) 216.
40. A.D. Martin, R.G. Roberts, W.J. Stirling and R.S. Thorne, Eur. Phys. J. **C39** (2005) 155.
41. U. Baur *et al.*, The neutral-current Drell-Yan process in the high invariant mass region, in <sup>31</sup>.

**SESSION V – HEAVY FLAVOUR PHYSICS**

*Matthew Jones*

*Neri Nicola*

*Pedlar Todd*

*Du ShuXian*

*Yuan Ye*

*Chiang -C.Mark*

*Playfer Steve*

*Gardi Einan*

B States at the Tevatron

Charm Decays, Mixing and CP Violation at the B  
Factories

Results from CLEO-C

Recent Results from BESII

BESIII: A Status Report

Measurement of  $B^0 \rho^+ \rho^- \rho^+ \rho^-$  Decays and  
Search for  $B^0 \rho^0 \rho^0$

Radiative and Electroweak Penguins

On the Determination of  $|V_{ub}|$  from Inclusive  
Semileptonic B Decays



## **B STATES AT THE TEVATRON**

Matthew Jones

*Purdue University, 525 Northwestern Ave, West Lafayette, IN 47907, USA*

### **Abstract**

The CDF and DØ experiments at the Fermilab Tevatron collider have now accumulated sufficient integrated luminosity to allow the discovery of previously unobserved hadronic states containing bottom quarks. The analysis of fully reconstructed decays of orbitally excited  $B$ -mesons, the  $\Sigma_b$ ,  $\Sigma_b^*$  and  $\Xi_b$  baryons and the  $B_c$  meson are presented, from which precise mass measurements are obtained. The current status of  $\Lambda_b$  lifetime measurements is presented in light of a precise measurement by CDF, and a DØ analysis is described which has provided a new measurement of the  $B_c$  lifetime.

## 1 Introduction

Over the past decade the field of heavy flavor physics has been transformed from one motivated by understanding the origins of CP violation to one in which we hope to observe the influence of new physics on the properties of  $b$ -hadrons. New physics processes typically modify couplings at the quark level but precision measurements of these couplings require calculating hadronic matrix elements and form factors with comparable precision. Therefore, the discovery of new physics through the analysis of hadrons containing  $b$ -quarks requires calculations that are both accurate and precise and that have, ideally, been performed in advance of experimental measurements. Alternatively, observables that are not highly sensitive to new physics provide ways to study the accuracy of theoretical techniques without introducing intentional, or unintentional bias. For this reason, the recent discoveries of previously unobserved  $b$ -flavored hadronic states provide a unique opportunity to exercise theoretical tools in ways that are independent of any prior knowledge of the well measured properties of  $B^0$  and  $B^+$  mesons<sup>1</sup>. In the sections that follow, we describe several of these recent observations and present comparisons of their properties with some theoretical calculations.

## 2 Excited B Mesons

For over two decades, the properties of orbitally excited heavy mesons have been analyzed using QCD potential models<sup>1)</sup> which account for most of their observed properties. In these models, effects that depend on the heavy quark spin are suppressed by powers of  $1/m_Q$  leading to an approximate decoupling of the heavy- and light-quark degrees of freedom. In the limit  $m_Q \rightarrow \infty$ , the  $P$ -wave mesons, which have one unit of orbital angular momentum, form two degenerate doublets with properties characterized by the total angular momentum of the light quark,  $j_q = 1 \pm 1/2$ . The  $j_q = 1/2$  states are normally expected to be quite broad because they decay via  $S$ -wave pion emission, while the decays of the  $j_q = 3/2$  states are dominated by  $D$ -wave pion emission, leading to much narrower natural widths. The properties of  $P$ -wave charm mesons determined from the analysis of  $e^+e^-$  collision data<sup>2)</sup> are in general

---

<sup>1</sup>Additional charge conjugate states are implied throughout.

agreement with this picture, however not without some surprises<sup>2</sup>. Evidence for  $P$ -wave  $b$ -meson production was first observed in  $Z^0$  decays<sup>4</sup>), but it is only recently that the experiments at the Tevatron have accumulated sufficient statistics to study their properties in detail.

The narrow  $P$ -wave  $B$  meson states can be observed as peaks in the invariant mass distribution of  $B\pi$  combinations, or  $BK$  combinations in the case of  $P$ -wave  $B_s$  mesons. The spin-1  $B_1^0$  and  $B_{s1}^0$  states can decay only to  $B^*\pi$  or  $B^*K$ , respectively, but the spin-2  $B_2^{*0}$  and  $B_{s2}^{*0}$  mesons can also decay directly to  $B\pi$  or  $BK$ . Both types of decay lead to distinct peaks in the  $B\pi$  or  $BK$  mass distributions, but those that proceed by an intermediate  $B^*$  state will be shifted to lower masses by approximately 45 MeV due to the unobserved soft photon from the subsequent  $B^* \rightarrow B\gamma$  decay.

The DØ and CDF experiments have both collected high statistics samples of fully reconstructed  $B^+ \rightarrow J/\psi K^+$  decays using single- and dilepton triggers, respectively. In addition, CDF reconstructs  $B^+ \rightarrow \overline{D}^0 \pi^+$  and  $B^+ \rightarrow \overline{D}^0 \pi^+ \pi^- \pi^+$  in events triggered by the presence of displaced secondary vertices<sup>6</sup>). In the DØ analysis<sup>7</sup>), pions are selected from the primary event vertex and combined with  $B^+$  candidates to generate the distribution of  $\Delta M = M(B^+ \pi^-) - M(B^+)$  shown in Figure 1. The signal component is parameterized using Breit-Wigner shapes that are convoluted with the Gaussian resolution expected from a simulation of the DØ detector. The fit determines the positions and yields of  $B_J^{(*)}$  decays in the three peaks from which the masses shown in Table 1 are obtained. Systematic uncertainties in the masses are dominated by the methods used to bin the data, the imprecise knowledge of the natural widths of the states and the absolute momentum scale of the detector. The widths of the peaks are mostly determined by detector resolution effects and DØ does not attempt to measure their natural widths.

A similar analysis has been performed by CDF<sup>8</sup>), using an artificial neural network to maximize the significance of a simulated signal in a data sample dominated by the  $B\pi$  combinatorial background. The CDF analysis fits the distribution of the variable  $Q = M(B^+ \pi^-) - M(B^+) - M(\pi)$  using three peaks to represent the direct  $B_1^0 \rightarrow B^+ \pi^-$  contribution, and two overlapping peaks from  $B_1^0 \rightarrow B^{*+} \pi^-$  and  $B_2^{*0} \rightarrow B^{*+} \pi^-$ . Table 1 summarizes the  $B_1^0$

---

<sup>2</sup>The observation of narrow states decaying to  $D_s^+ \pi^0$  and  $D_s^{*+} \pi^0$ <sup>3</sup>) is one such exception.

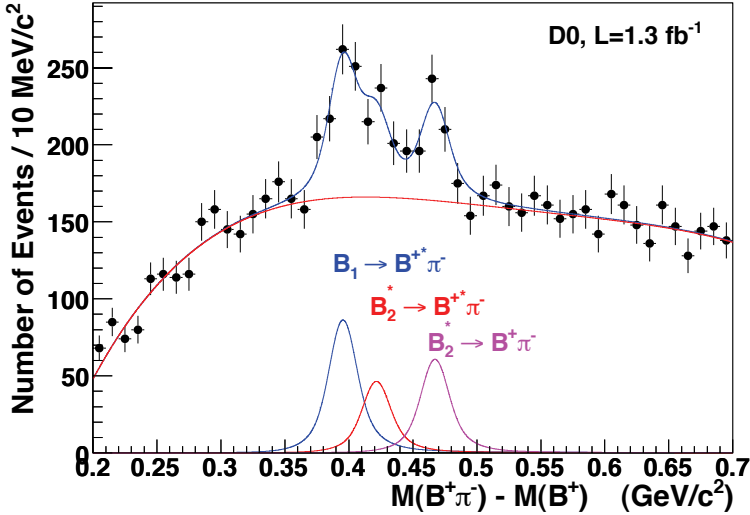


Figure 1: Mass difference distribution of  $B^+\pi^-$  pairs obtained by the  $D\bar{O}$  experiment.

and  $B_2^{*0}$  properties derived from the fit to the  $Q$  distribution. The shape of the peak from  $B_2^{*0} \rightarrow B^+\pi^-$  determines the natural width of this state, while the shape of the structure at lower  $Q$  values determines the mass splitting between the  $B_1^0$  and  $B_2^0$  states.

The CDF and  $D\bar{O}$  experiments have also observed the production of  $P$ -wave  $B_s$  mesons through the analysis of the  $B^+K^-$  final state. As was seen to be the case for the  $D_{s1}^+$  meson<sup>9, 10</sup>,  $P$ -wave  $B_s$  meson decays occur close to threshold, resulting in very narrow signal peaks. Furthermore, phase space constraints suggest that the ratio  $\text{BF}(B_{s2}^{*0} \rightarrow B^{*+}K^-)/\text{BF}(B_{s2}^{*0} \rightarrow B^+K^-)$  will be only about 7% resulting in a peak at low mass differences that is almost entirely due to the  $B_{s1}^0$  state.

Figures 3 and 4 show the mass difference distributions observed in  $D\bar{O}$  and CDF data, respectively. The  $D\bar{O}$  analysis<sup>11</sup>) provides evidence for  $B_{s2}^{*0}$  production with a significance in excess of  $4.8\sigma$ , from which the mass listed in Table 1 is determined. Although a second peak may be visible near  $Q \sim 10 \text{ MeV}/c^2$  which could be attributed to  $B_{s2}^0$  production, its significance is less than  $3\sigma$ . CDF, however, observes both of these states<sup>12</sup>) with greater than  $5\sigma$

Table 1: Properties of P-wave B mesons determined by the DØ and CDF experiments. The first and second uncertainties are statistical and systematic, respectively.

		DØ	CDF
$M(B_1^0)$	[MeV/c <sup>2</sup> ]	$5720.6 \pm 2.4 \pm 1.4$	$5725.3^{+1.6+0.8}_{-2.1-1.1}$
$M(B_2^{*0})$	[MeV/c <sup>2</sup> ]	$5746.8 \pm 2.4 \pm 1.7$	$5746.8^{+1.7+0.5}_{-1.8-0.6}$
$\Gamma(B_2^{*0})$	[MeV/c <sup>2</sup> ]	—	$22.1^{+3.6+3.5}_{-3.1-2.6}$
$M(B_{s1}^0)$	[MeV/c <sup>2</sup> ]	—	$5829.4 \pm 0.21 \pm 0.62$
$M(B_{s2}^{*0})$	[MeV/c <sup>2</sup> ]	$5839.9 \pm 1.1 \pm 0.7$	$5839.7 \pm 0.39 \pm 0.62$

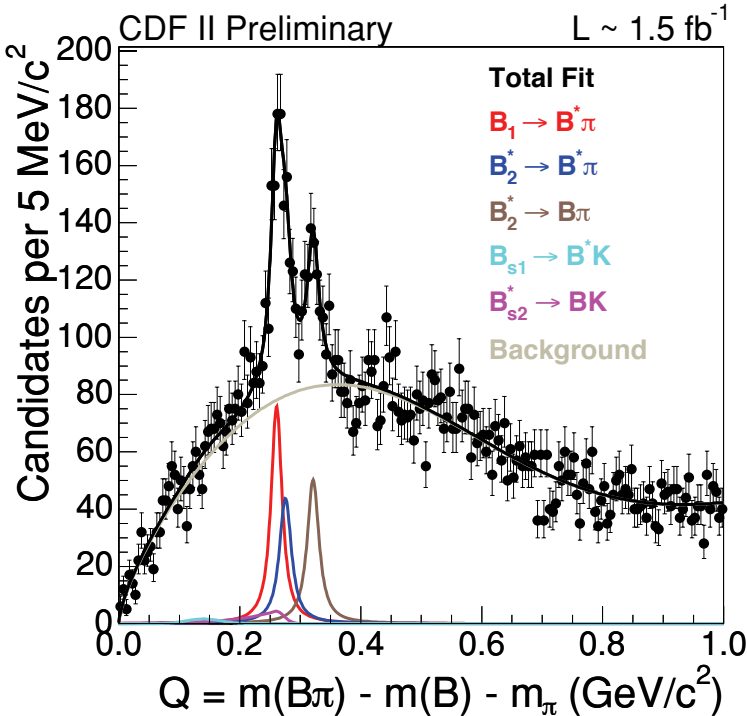


Figure 2: Mass difference distribution for  $B^+\pi^-$  pairs reconstructed by the CDF experiment. The distribution combines candidates formed using B signals reconstructed using  $J/\psi$ ,  $D^0\pi$  and  $\bar{D}^0 3\pi$  final states.

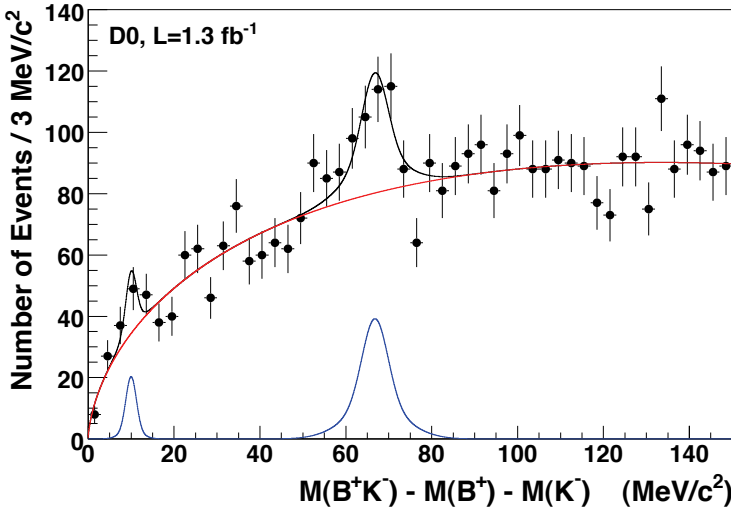


Figure 3: Mass difference distribution of  $B^+K^-$  pairs analyzed by the  $D\bar{0}$  experiment.

significance and determines the masses of the  $B_{s1}^0$  and  $B_{s2}^{*0}$  listed in Table 1.

Predictions for  $B$ -meson mass splittings obtained from the early QCD potential models have been improved <sup>5)</sup> by including  $1/m_Q$  corrections and by treating the emission of the light quanta using chiral perturbation theory. However, the splittings in the  $B$  system are still expected to scale with those measured in the charm system by the ratio  $m_c/m_b \sim 1/3$ . This rule yields expected mass splittings that are smaller than the observed  $B_2^{*0}-B_1^0$  mass difference but quite close to those observed for the  $B_{s2}^{*0}$  and  $B_{s1}^0$ . Predictions for the absolute masses of the  $P$ -wave states are higher than the measurements by about  $60 \text{ MeV}/c^2$  but the accuracy of these predictions is only of order  $40 \text{ MeV}/c^2$ . Predictions have also been made for the natural widths of the  $B_1^+$  and  $B_2^{*+}$  states, assuming decays are dominated by single pion emission. Updating the prediction for the  $B_2^*$  width using the measured masses from Table 1 suggests that  $\Gamma(B_2^*) = (14 \pm 6) \text{ MeV}/c^2$  which is smaller than, but still consistent with the observed width. Predictions for the properties of the  $B_1^0$  depend strongly on the amount of mixing with the spin-1  $j_q = 1/2$  state, which might be constrained in the future through angular analyses of the  $B\pi$  decay

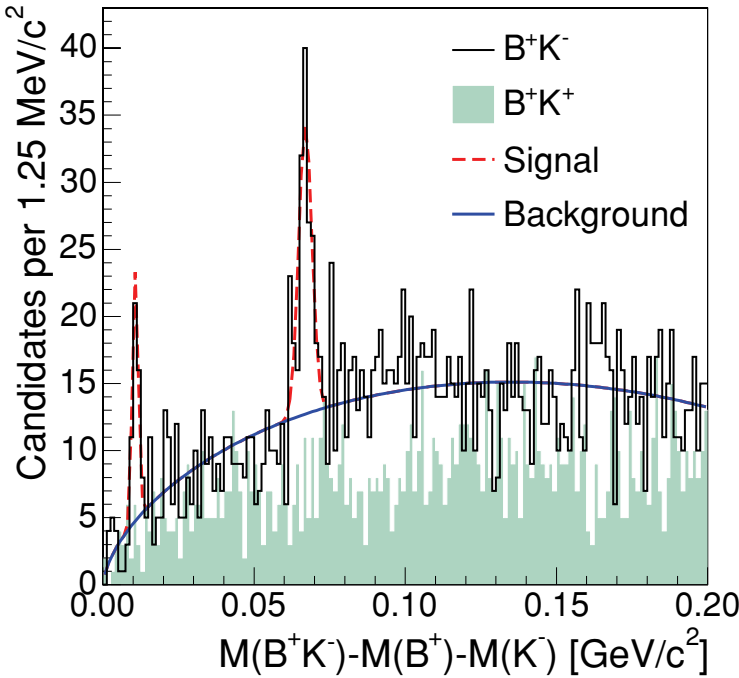


Figure 4: Mass difference distribution of  $B^+K^-$  pairs analyzed by the CDF experiment showing peaks from  $B_{s1}^0 \rightarrow B^{*+}K^-$  and  $B_{s2}^{*0} \rightarrow B^+K^-$  at low and high mass differences, respectively.

products.

### 3 B Baryon States

Baryons containing bottom quarks provide systems in which higher order corrections to the naive spectator models of  $b$ -hadron decays can be studied. Although the properties of  $\Lambda_b$  baryons have been analyzed for several years, discrepancies between the measured and predicted lifetimes have raised questions about both the experiments and the phenomenological tools used to analyze  $\Lambda_b$  decays. The recent precision measurement of the  $\Lambda_b$  lifetime presented in the following section suggests that these questions may still not be satisfactorily resolved. Thus, we are fortunate that the Tevatron experiments to have recently begun to extend our knowledge of  $b$ -flavored baryons beyond the  $\Lambda_b$

singlet state.

Observations of the first exclusive decays of  $b$ -baryon multiplet states have recently been made by both the CDF and DØ experiments. Although evidence for  $\Xi_b^-$  ( $bsd$ ) production was first obtained by studying  $\Xi^- \ell^-$  correlations at LEP <sup>13, 14</sup>), it is now feasible to reconstruct the exclusive decay  $\Xi_b^- \rightarrow J/\psi \Xi^-$  at the Tevatron, from which precise mass measurements can be obtained. The reconstruction of this decay mode is not without significant challenges, however, and both CDF and DØ have developed novel analysis techniques that are needed to reconstruct  $\Xi^- \rightarrow \Lambda \pi^-$  decays in  $p\bar{p}$  collisions.

Reconstructing the  $\Lambda \pi^-$  final state is complicated by the low momentum of the emitted pion and by the characteristic hyperon lifetime of the  $\Xi^-$ , which is short enough to allow it to decay inside the tracking volume, but still much longer than that of weakly decaying  $b$ - or  $c$ -hadrons. If a  $\Xi^-$  does decay within the volume of one of the experiment's silicon micro-vertex detectors, the soft  $\pi^-$  produced far from the primary interaction point will produce signals in silicon sensor layers that normal pattern recognition and tracking algorithms would identify with only low efficiency. The DØ analysis <sup>15</sup>) re-processes events containing  $J/\psi \rightarrow \mu^+ \mu^-$  decays using a track reconstruction algorithm developed to improve the efficiency for low  $p_T$  tracks with large impact parameters, increasing the yield of reconstructed  $\Xi^-$  decays by a factor of 5.5. The CDF analysis <sup>16</sup>) reconstructs  $\Xi^- \rightarrow \Lambda \pi^-$ ,  $\Lambda \rightarrow p \pi^-$  but then applies a technique that was first pioneered by the DELPHI experiment <sup>14</sup>) in which hits left by  $\Xi^-$  baryons decaying outside the inner layers of the silicon detector are correlated with the  $\Lambda$  and  $\pi$  trajectories. Inclusion of these hits in a fit to the  $\Xi^-$  helix yields very precise mass resolution of the resulting  $J/\psi \Xi^-$  combinations.

The  $J/\psi \Xi^-$  invariant mass distributions for the DØ and CDF analyses are shown in Figures 5 and 6, both of which show signals that have greater than  $5\sigma$  significance. DØ observes a  $\Xi_b^-$  yield of  $15.2 \pm 4.4$  candidates using a  $1.3 \text{ fb}^{-1}$  data sample, while CDF observes  $17.5 \pm 4.3$  candidates in a  $1.9 \text{ fb}^{-1}$  sample. The mass of the  $\Xi_b^-$  is determined from these distributions to be

$$M(\Xi_b^-) = \begin{cases} 5792.9 \pm 2.5 \pm 1.7 \text{ MeV}/c^2 & \text{CDF} \\ 5774 \pm 11 \pm 15 \text{ MeV}/c^2 & \text{DØ} \end{cases} \quad (1)$$

The systematic uncertainty of the DØ measurement is dominated by variations in the mass obtained using modified selection criteria rather than by the absolute mass scale, which is found to be only  $\pm 2 \text{ MeV}/c^2$  by studying  $\Lambda_b \rightarrow J/\psi \Lambda$

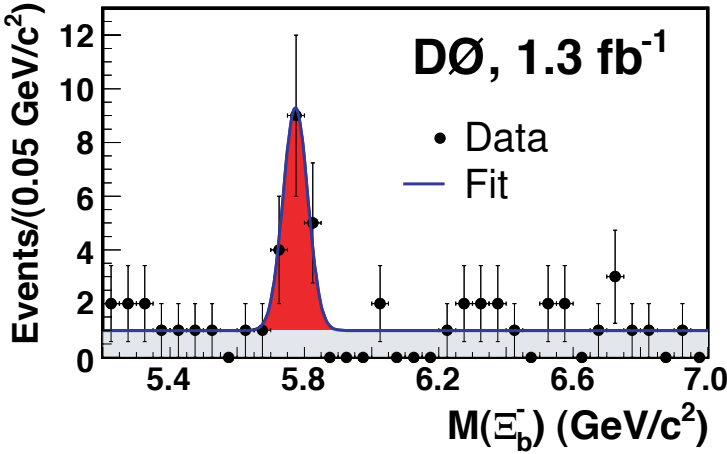


Figure 5: Invariant mass distribution of  $\Xi_b^- \rightarrow J/\psi \Xi^-$  candidates reconstructed by the  $D\bar{O}$  experiment.

and  $B^0 \rightarrow J/\psi K_S^0$  decays. The absolute mass scale, systematic uncertainties in track reconstruction and the model used to fit the  $\Xi_b^-$  mass peak, all contribute to the systematic uncertainty of the CDF measurement. Considering the size of these uncertainties, a consistent value for the  $\Xi_b^-$  mass is obtained by both experiments which is in agreement with quark model predictions <sup>17, 18)</sup> that range from 5770 to 5813 MeV/c<sup>2</sup>.

The CDF experiment has also provided the first unambiguous<sup>3</sup> observation of the  $\Sigma_b^+$  ( $buu$ ),  $\Sigma_b^-$  ( $bdd$ ) and  $\Sigma_b^{*\pm}$  states from the  $b$ -baryon multiplet by analyzing  $\Lambda_b \pi^\pm$  correlations <sup>20)</sup>. By reconstructing the decay chain  $\Lambda_b \rightarrow \Lambda_c^+ \pi^-$ , with  $\Lambda_c^+ \rightarrow p K^- \pi^+$  in events triggered by the presence of tracks from a displaced secondary vertex, CDF obtained a sample of over 3000 fully reconstructed  $\Lambda_b$  decays with only a small contamination from  $B$ -decays with mis-assigned masses of final state particles. The four  $\Sigma_b^{(*)\pm}$  states are then studied by analyzing the  $\Lambda_b \pi^+$  and  $\Lambda_b \pi^-$  invariant mass distributions.

Significant backgrounds arise from  $\Lambda_b$  decays that are produced directly in  $b$ -quark fragmentation paired with random pions produced in the primary  $p\bar{p}$  interaction. Selection criteria used for the final  $\Sigma_b^{(*)\pm}$  analysis were first determined so as to maximize the significance of a simulated  $\Sigma_b^{(*)\pm} \rightarrow \Lambda_b \pi^\pm$

<sup>3</sup>A possible observation by DELPHI <sup>19)</sup> remains unpublished.

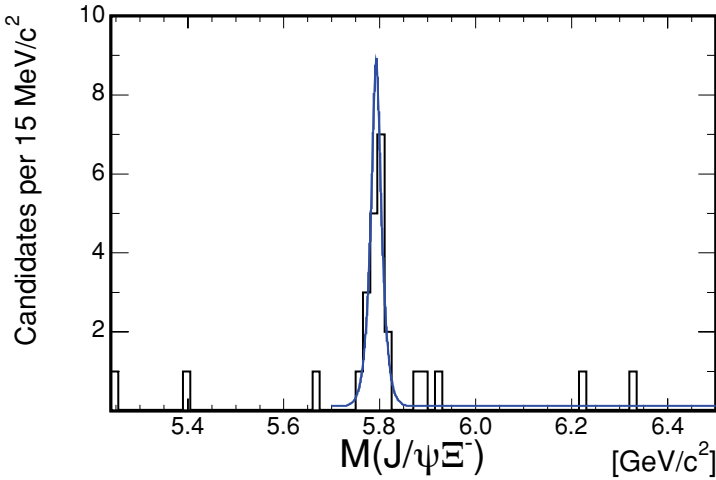


Figure 6: *Invariant mass distribution of  $J/\psi\Xi^-$  pairs reconstructed by the CDF experiment.*

signal using a background estimate from  $\Lambda_b\pi^\pm$  candidates with invariant masses outside the range expected for the  $\Sigma_b$  states. Figure 7 shows the distributions of  $Q = M(\Lambda_b\pi) - M(\Lambda_b) - M(\pi)$  that result when these criteria are applied to a data set corresponding to  $1.1 \text{ fb}^{-1}$  of integrated luminosity. The fit to the mass difference distributions determines  $Q(\Sigma_b^+)$ ,  $Q(\Sigma_b^-)$  and the mass splittings,  $\Delta(\Sigma_b^\pm)$ , between the  $\Sigma_b^*$  and  $\Sigma_b$  ground states. The absolute masses, listed in Table 2 have systematic uncertainties dominated by the understanding of the mass scale, determined at CDF by measurements of the  $Q$  values of  $D^*$ ,  $\Sigma_c$  and  $\Lambda_c^+$  hadrons. The isospin averaged  $\Sigma_b\text{-}\Lambda_b$  mass difference and  $\Sigma_b^*\text{-}\Sigma_b$  mass splitting agree well with the quark model predictions <sup>21)</sup>:

$$M(\Sigma_b) - M(\Lambda_b) = 194 \text{ MeV}/c^2 \quad (2)$$

$$M(\Sigma_b^*) - M(\Sigma_b) = 22 \text{ MeV}/c^2. \quad (3)$$

#### 4 $\Lambda_b$ Lifetime

Lifetimes of all  $b$ -hadrons are expected to be equal in the naive spectator model of  $b$ -decays. This is even true when corrections of order  $1/m_b$  are included and

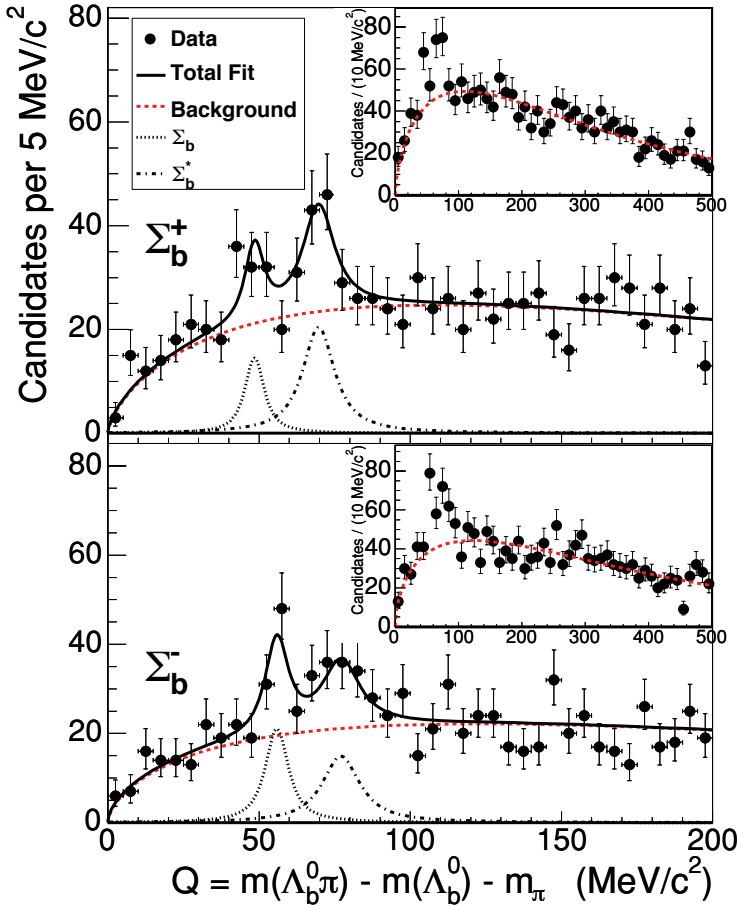


Figure 7: Mass difference distributions for  $\Lambda_b \pi^\pm$  pairs reconstructed by the CDF experiment. The inset histograms show the background-only fit hypothesis over an extended range of candidate mass differences.

only 1-2% corrections occur at order  $1/m_b^2$ , with larger corrections appearing at order  $1/m_b^3$ . Predictions for the lifetime ratios of  $b$ -mesons have generally been found to agree well with experiment, but Table 3 shows that the situation with the  $\Lambda_b$  lifetime is not so clear: theoretical predictions have only recently reached values compatible with the experimental averages. The  $\Lambda_b$  lifetime measurements have been dominated by analyses of semi-leptonic decays

Table 2: Masses, mass differences and splittings of the  $\Sigma_b$  states measured by CDF. Uncertainties are statistical and systematic, respectively.

State	Mass [MeV/ $c^2$ ]
$\Sigma_b^+$	$5807.8^{+2.0}_{-2.2} \pm 1.7$
$\Sigma_b^-$	$5815.2 \pm 1.0 \pm 1.7$
$\Sigma_b^{*+}$	$5829.0^{+1.6+1.7}_{-1.8-1.8}$
$\Sigma_b^{*-}$	$5836.4 \pm 2.0^{+1.8}_{-1.7}$
$M(\Sigma_b^+) - M(\Lambda_b)$	$188.1^{+2.0+0.2}_{-2.2-0.3}$
$M(\Sigma_b^-) - M(\Lambda_b)$	$195.5 \pm 1.0 \pm 0.2$
$M(\Sigma_b^*) - M(\Sigma_b)$	$21.2^{+2.0+0.4}_{-1.9-0.3}$

Table 3: Predictions  $^{22, 23, 24}$  and experimental measurements of the  $b$ -lifetime ratio  $\tau(\Lambda_b)/\tau(B^0)$ .

Theory		Experiment $\Lambda_b \rightarrow \Lambda_c^+ \ell^- X$	
$\mathcal{O}(1/m_b)$	1.00	OPAL, 1996	$0.84 \pm 0.08$
$\mathcal{O}(1/m_b^2)$	0.97	CDF, 1996	$0.84 \pm 0.11$
$\mathcal{O}(1/m_b^3)$	0.94	ALEPH, 1998	$0.77 \pm 0.08$
$\mathcal{O}(1/m_b^3) + NLO$	$0.90 \pm 0.05$	DELPHI, 1999	$0.73 \pm 0.13$
$\mathcal{O}(1/m_b^4) + NLO$	$0.86 \pm 0.05$	DØ, 2007	$0.83 \pm 0.10$

which, until recently, were statistically more powerful than the analysis of fully reconstructed decays such as  $\Lambda_b \rightarrow J/\psi\Lambda$ . However, lifetimes measured using semi-leptonic decays require a decay model to estimate the  $\Lambda_b$  momentum from the momenta of the observed  $\Lambda_c^+ \ell^-$  decay products which could potentially introduce a source of bias common to all experiments. For these reasons, precise, independent measurements of the  $\Lambda_b$  lifetime continue to attract interest.

Recently, CDF has produced the most precise measurement  $^{25}$ ) of the  $\Lambda_b$  lifetime by a single experiment using the fully reconstructed decay mode  $\Lambda_b \rightarrow J/\psi\Lambda$ . Selection criteria for reconstructing  $\Lambda_b \rightarrow J/\psi\Lambda$  and  $B^0 \rightarrow J/\psi K_S^0$  decays were chosen to optimize the significance,  $S/\sqrt{S+B}$ , where signal events,  $S$ , were simulated using Monte Carlo and  $J/\psi\Lambda$  or  $J/\psi K_S^0$  candidates were used to estimate the background,  $B$ . Candidates were rejected from the  $\Lambda \rightarrow p\pi^-$  sample if a  $\pi^+\pi^-$  mass assignment yielded a candidate with a mass consistent with  $K_S^0$  decay and vice versa. When applied to the data sample,  $3376 \pm 88$

$B^0 \rightarrow J/\psi K_S^0$  decays and  $538 \pm 38 \Lambda_b \rightarrow J/\psi \Lambda$  decays were observed in  $1 \text{ fb}^{-1}$  of integrated luminosity. A kinematic fit was applied to the final state particles to impose mass constraints on the  $J/\psi$  and a three dimensional geometric constraint to require that the  $\Lambda$  or  $K_S^0$  momentum vector point back to the  $J/\psi$  decay vertex. The lifetimes were then determined from a simultaneous fit using the candidate mass,  $m$ , and the proper time  $t = L_{xy}m/p_T$  on an event-by-event basis, in which  $L_{xy}$  is the distance between the primary  $p\bar{p}$  interaction vertex and the  $B^0$  or  $\Lambda_b$  decay vertex, projected into the plane transverse to the beam axis.

The resulting lifetime measurements and their ratio are

$$\tau(B^0) = 1.524 \pm 0.030 \pm 0.016 \text{ ps} \quad (4)$$

$$\tau(\Lambda_b) = 1.593_{-0.078}^{+0.083} \pm 0.033 \text{ ps} \quad (5)$$

$$\tau(\Lambda_b)/\tau(B^0) = 1.041 \pm 0.057 \quad (6)$$

where the uncertainties are statistical and systematic, respectively and have been combined in the measured lifetime ratio. Systematic uncertainties include uncertainties in the silicon vertex detector alignment, bounds on possible effects due to the decay topology fit and to different parameterizations of the models used to describe the candidate mass and proper time distributions, their resolutions and their correlations. While the measured  $B^0$  lifetime agrees well with previous measurements <sup>26)</sup>, the lifetime ratio is  $3.2\sigma$  higher than the previous world average. The  $B^0$  and  $B^+$  lifetimes were also measured using the same techniques but in the  $J/\psi K^+$ ,  $\psi' K^+$ ,  $J/\psi K^{*+}$ ,  $J/\psi K^{*0}$  and  $\psi' K^{*0}$  final states, with  $\psi' \rightarrow \mu^+ \mu^-$  and  $\psi' \rightarrow \psi \pi^+ \pi^-$ . These were found to be in good agreement with world averages and do not reveal any apparent source of experimental bias.

The  $\Lambda_b$  lifetime has also been measured by  $D\bar{O}$  using a similar analysis technique <sup>27)</sup>. Using a data sample corresponding to  $1.2 \text{ fb}^{-1}$  of integrated luminosity,  $171 \pm 20 \Lambda_b \rightarrow J/\psi \Lambda$  decays and  $717 \pm 30 B^0 \rightarrow J/\psi K_S^0$  decays were reconstructed from which the lifetimes and the lifetime ratio

$$\tau(B^0) = 1.501_{-0.074}^{+0.078} \pm 0.050 \text{ ps} \quad (7)$$

$$\tau(\Lambda_b) = 1.218_{-0.115}^{+0.130} \pm 0.042 \text{ ps} \quad (8)$$

$$\tau(\Lambda_b)/\tau(B^0) = 0.81 \pm 0.10 \text{ ps} \quad (9)$$

were determined. While  $\tau(\Lambda_b)$  differs from the CDF measurement by approxi-

mately  $2\sigma$ , the current level of precision is not sufficient to seriously challenge the measurement by CDF or the world average. Thus, in spite of significant theoretical work, in light of the most precise measurements, a complete resolution of the  $\Lambda_b$  lifetime puzzle remains elusive.

## 5 Properties of the $B_c$ Meson

The CDF experiment provided the first evidence for  $B_c$  production <sup>29)</sup> using data from Run I of the Tevatron, but the tri-lepton final state that was used in this analysis did not allow a precise determination of the  $B_c$  mass. A more precise mass measurement was made by OPAL <sup>30)</sup> using the exclusive decay  $B_c^+ \rightarrow J/\psi\pi^+$ , but this was based on only 2 events with an expected background of 0.63 events over the search range of 6.0 to 6.5 GeV/ $c^2$ . Today, both the CDF and DØ experiments have accumulated sufficient integrated luminosity for unambiguous observations of  $B_c^+$  production and precision mass measurements using the exclusive decay  $B_c^+ \rightarrow J/\psi\pi^+$ . Nevertheless, the semi-leptonic decay  $B_c^+ \rightarrow J/\psi\ell^+\nu_\ell$  remains important, since it currently has greater statistical power for lifetime measurements.

A precise measurement of the  $B_c$  mass was recently made by CDF using a  $B_c^+ \rightarrow J/\psi\pi^+$  selection that was designed to maximize the expected signal significance. This analysis used a large, relatively pure sample of  $B^+ \rightarrow J/\psi K^+$  decays to approximate the properties of the  $B_c$  signal. The optimization was performed on a subset of the reconstructed  $B^+$  decays that was chosen so that the properties of the selected candidates reflected those expected for the  $B_c$ , for example, by selecting only those with relatively short proper decay time. Figure 8 shows the invariant mass distribution of the  $J/\psi\pi^+$  candidates selected using 2.4 fb<sup>-1</sup> of integrated luminosity from which the mass was determined to be

$$M(B_c^+) = 6274.1 \pm 3.2 \pm 2.6 \text{ MeV}/c^2. \quad (10)$$

The DØ experiment has also observed  $B_c^+ \rightarrow J/\psi\pi^+$  in a data sample corresponding to 1.3 fb<sup>-1</sup> of integrated luminosity <sup>32)</sup> and obtained a compatible measurement of the mass:

$$M(B_c^+) = 6300 \pm 14 \pm 5 \text{ MeV}/c^2. \quad (11)$$

These measurements agree reasonably well with the predicted mass of  $6304 \pm$

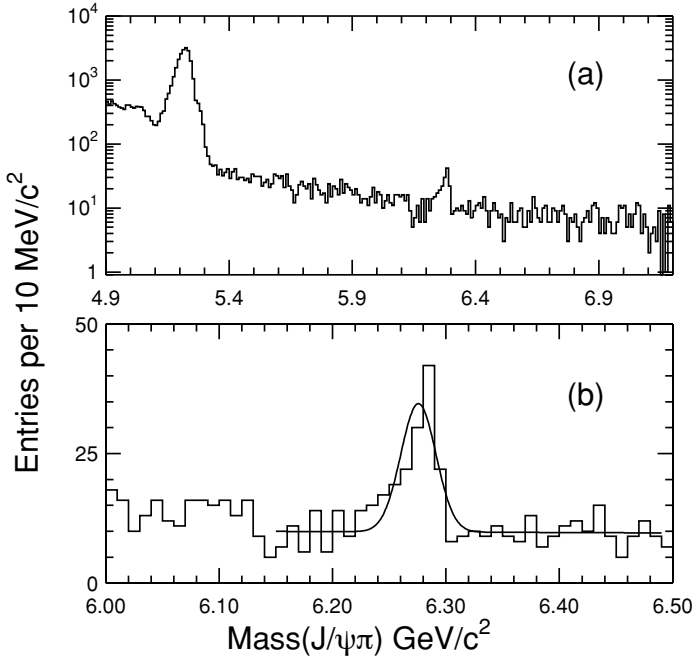


Figure 8: (a) Invariant mass distribution of  $J/\psi\pi^+$  candidates and (b) the projection of the fit used to determine the  $B_c$  mass. The large peak near  $5.2 \text{ GeV}/c^2$  in (a) is the result of  $B^+ \rightarrow J/\psi K^+$  decays reconstructed with the pion mass assignment.

$12_{-0}^{+18} \text{ MeV}/c^2$  based on recent numerical lattice QCD calculations<sup>33)</sup> that use three flavors of light sea-quarks.

The lifetime of the  $B_c$  meson is expected to be shorter than typical  $b$ -hadron lifetimes because it can proceed by  $c$ -quark decay,  $\bar{b}$ -quark decay or by  $\bar{b}$ - $c$  annihilation, which are expected to contribute about 70%, 20% and 10% to the total decay rate, respectively. Predictions<sup>28)</sup> based on QCD sum rules suggest that  $\tau(B_c^+) = 0.48 \pm 0.05 \text{ ps}$ , while those based on an operator product expansion or potential models predict that  $\tau(B_c^+) = 0.55 \pm 0.15 \text{ ps}$  with a larger uncertainty related to the appropriate choice of the charm quark mass. These were consistent with previous CDF measurements<sup>29, 34)</sup>, but are still important predictions that can now be tested using a precise measurement of the  $B_c$  lifetime that has recently been made by the  $D\mathcal{O}$  experiment.

Using  $1.35 \text{ fb}^{-1}$  of integrated luminosity, the  $D\bar{O}$  analysis identified high quality muons that formed a common vertex with a  $J/\psi \rightarrow \mu^+\mu^-$  decay. The resulting distribution of tri-lepton invariant mass contains the  $B_c$  signal, which includes both  $B_c^+ \rightarrow J/\psi\mu^-\nu_\mu$  and  $B_c^+ \rightarrow \psi(2S)\mu^-\nu_\mu$  with subsequent  $\psi(2S) \rightarrow J/\psi X$  decay, and several background components. The background consists of  $B^+ \rightarrow J/\psi K^+$  decays in which the kaon is misidentified as a muon, other  $B \rightarrow J/\psi X$  decays with fake muons,  $J/\psi$  combinatorial background, uncorrelated  $J/\psi + \mu$  production, and prompt  $J/\psi + \mu$  production. The invariant mass distributions for the background components are constrained using the fitted peak from  $J/\psi K^+$  decays,  $\mu^+\mu^-$  sidebands to model properties of the fake  $J/\psi$  component, a Monte Carlo model for  $b\bar{b}$  events in which one quark decays to  $J/\psi$  and the other to a muon, and candidates with negative decay lengths to model the prompt  $J/\psi + \mu$  background. The invariant mass distribution, with the different components indicated, is shown in Figure 9 for events with decay length significance greater than  $4\sigma$ . This distribution is only

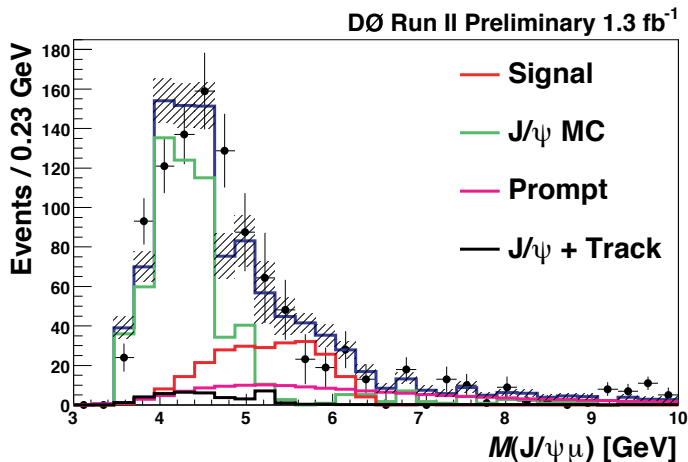


Figure 9: *Invariant mass distribution of  $J/\psi + \mu$  candidates with the classification of the different background components indicated. The dashed histogram indicates the total systematic uncertainty on the shapes of the different components.*

used to demonstrate the existence of a signal from  $B_c^+ \rightarrow J/\psi\mu\nu_\mu$  decays: the normalization of the signal component yields  $242 \pm 30 B_c$  decays, with a probability for the background to fluctuate to at least this number of events being

less than  $5\sigma$ . Without the decay length significance requirement, the yield of  $B_c$  signal events is determined to be  $858 \pm 80$ .

The  $B_c$  lifetime is measured using an un-binned likelihood fit to the  $J/\psi\mu$  mass and the pseudo-proper decay length,  $\lambda = L_{xy}m(B_c)/p_T(J/\psi\mu)$ , determined on an event-by-event basis. For the  $B_c$  signal, the distribution of pseudo-proper decay length is corrected by the expected distribution of  $K = p_T(J/\psi\mu)/p_T(B_c)$  to account for the unmeasured momentum carried away by the neutrino, or other undetected particles. Pseudo-proper decay length distributions for the background components are constrained using the data and Monte Carlo control samples. The resulting measurement of the  $B_c$  lifetime is

$$\tau(B_c^+) = 0.444^{+0.039+0.039}_{-0.036-0.034} \text{ ps} \quad (12)$$

where the second, systematic uncertainty is dominated by uncertainties in the shapes of the mass and lifetime distributions for the background components. This value is consistent with the prediction based on QCD sum rules which is of comparable precision.

## 6 Summary and Outlook

The recent observation of several new hadronic states containing  $b$ -quarks illustrates how a hadron collider can significantly extend our knowledge of  $B$  hadrons beyond what has been obtained at  $e^+e^-$  colliders operating at the  $B\bar{B}$  production threshold. The observations so far suggest that the spectroscopy of orbitally excited  $B$ -mesons is at least as rich as it is in the charm system and that the quark model can provide an very good description of the masses of states in the  $b$ -baryon multiplet. The mass of the  $B_c$  meson is now known precisely and its lifetime has been measured with sufficient precision to clearly see that it is similar to that of the weakly decaying charm hadrons. Perhaps the only unsatisfactory situation is the case of the  $\Lambda_b$  lifetime where one may continue to question the previous world averages, based on semi-leptonic decays, the current precision measurements, the most recent calculations of the lifetime, or all of these.

Most of the analyses described here were performed using between 1 and  $2 \text{ fb}^{-1}$  of integrated luminosity. By now, the CDF and DØ experiments have accumulated over  $3 \text{ fb}^{-1}$  and are expected to ultimately record between 7

and  $8 \text{ fb}^{-1}$  by the nominal end of the Tevatron run in 2010. With this increase in statistics it should be possible to measure the natural width of the  $B_1^0$  meson and to perform angular analyses of  $P$ -wave  $B$  meson decay products, constraining the amount of mixing between the  $j_q = 1/2$  and  $3/2$  bases. Observation of the decay  $\Omega_b^- \rightarrow J/\psi\Omega$  will be challenging but might be possible using techniques developed for the  $\Xi_b$  analysis when applied to the full Tevatron dataset. It should be possible to determine the lifetimes of some of the newly observed  $b$ -baryon states, but the precision of these measurements may not be sufficient to clarify the continuing  $\Lambda_b$  lifetime puzzle. Nevertheless, the full data sample should allow the  $D\bar{O}$  experiment to measure the  $\Lambda_b$  lifetime with a statistical uncertainty comparable to the current CDF measurement. CDF can also measure the  $\Lambda_b$  lifetime using other fully reconstructed final states recorded using the displaced vertex trigger, but the intrinsic trigger bias on the lifetime measurement complicates these analyses. The continuing study of  $b$ -hadron spectroscopy and lifetimes will remain interesting for several years. It remains to be seen how well suited the next generation of hadron collider experiments will be for extending the studies of these newly observed  $B$  states.

## 7 Acknowledgments

The author would like to express thanks collaborators on both CDF and  $D\bar{O}$  for their useful discussions and to the conference secretariat and organizers for all the planning that led to a very interesting and enjoyable scientific program, surrounded by the beauty of the Aosta Valley.

## References

1. S. Godfrey and N. Isgur, Phys. Rev. D **32**, 189-231 (1985).
2. J. Bartlet and S. Shukla, Ann Rev. Nucl. Part. Sci. **45**, 133-161 (1995).
3. D. Besson *et al.* (CLEO Collab.), Phys. Rev. D **68**, 032002 (2003).  
B. Aubert *et al.* (BaBar Collab.), Phys. Rev. Lett. **90**, 242001 (2003).
4. R. Akers, *et al.* (OPAL Collab.), Z. Phys. C **66** 19 (1995).  
P. Abreu, *et al.* (DELPHI Collab.), Phys. Lett. B **345**, 598 (1995).  
C. Goy, *et al.* (ALEPH Collab.), Z. Phys. C **69**, 393 (1996).

5. A.F. Falk and T. Mehen, Phys. Rev. D **53**, 231-240 (1996).
6. W. Ashmanskas *et al.*, Nucl. Inst. Meth. A **518**, 532-536 (2004).
7. V. M. Abazov *et al.* (DØ collab.), Phys. Rev. Lett. **99**, 172001 (2007).
8. CDF Collaboration, CDF Note 8945, August 7, 2007.
9. H. Abrecht, *et al.*, (ARGUS Collab.), Phys. Lett. B **230**, 162 (1989).
10. J.P. Alexander, *et al.*, (CLEO Collab.), Phys. Lett. B **303**, 377 (1993).
11. V.M. Abazov, *et al.*, (DØ collab.), Phys. Rev. Lett. **100**, 082002 (2008).
12. T. Aaltonen, *et al.* (CDF collab.), Phys. Rev. Lett. **100**, 082001 (2008).
13. D. Buskulic, *et al.* (ALEPH collab.), Phys. Lett. B **384** 449 (1996).
14. P. Abreu, *et al.* (DELPHI collab.), Zeit. Phys. C**68** 541 (1995).
15. V.M. Abazov, *et al.* (DØ collab.), Phys. Rev. Lett. **99**, 052001 (2007).
16. T. Aaltonen, *et al.* (CDF collab.), Phys. Rev. Lett. **99**, 052002 (2007).
17. M. Karliner, B. Keren-Zur, H.J. Lipkin and J.L. Rosner, hep-ph/0706.2163v1.
18. D. Ebert, R.N. Faustov and V.O. Galkin, Phys. Rev. D **72**, 034026 (2005).
19. P. Abreu, *et al.* (DELPHI collab.), DELPHI report DELPHI 95-107 PHYS542, June, 1995, presented by M. Feindt, C. Kreuter, A. Miagkov and O. Podobrin at EPS-HEP 95, Brussels, July 27-August 2, 1995 (unpublished).
20. T. Aaltonen, *et al.* (CDF collab.) Phys. Rev. Lett. **99**, 202001 (2007).
21. M. Karliner and H.J. Lipkin, hep-ph/0611306v1.
22. J.L. Rosner, Phys. Lett. B **379**, 267 (1996).
23. E. Franco, V. Lubicz, F. Mescia and C. Tarantino, Nucl. Phys. B **633**, 212-236 (2002).

24. F. Gabbiani, A. I. Onishchenko and A. A. Petrov, Phys. Rev. D **70**, 094031 (2004).
25. A. Abulencia, *et al.* (CDF Collab.) Phys. Rev. Lett. **98**, 122001 (2007).
26. W.-M. Yao, *et al.* (Particle Data Group), J. Phys. G **33**, 1 (2006).
27. V. M. Abazov, *et al.* (DØ Collab), Phys. Rev. Lett. **99**, 142001 (2007).
28. V.V. Kiselev, arXiv:hep-ph/0308214v1.
29. F. Abe, *et al.* (CDF Collab.), Phys. Rev. Lett. **81** 2432 (1998).
30. K. Ackerstaff, *et al.* (OPAL Collab.), Phys. Lett. B **420** 157 (1998).
31. T. Aaltonen, *et al.* (CDF Collab.), Fermilab-Pub-07/644-E, arXiv:0712.1506 [hep-ex], Submitted to Phys. Rev. Lett.
32. V.M. Abazov, *et al.* (DØ Collab.), Fermilab-Pub-08/047-E, arXiv:0802.4258 [hep-ex], Submitted to Phys. Rev. Lett.
33. I.F. Allison, *et al.*, Phys. Rev. Lett. **94**, 172001 (2005).
34. A. Abulencia, *et al.* (CDF Collab.), Phys. Rev. Lett. **97**, 012002 (2006).
35. DØ Collaboration, DØ Note 5824-CONF.

# CHARM DECAYS, MIXING AND VIOLATION AT THE *B* FACTORIES \*

Nicola Neri

(representing the BaBar collaboration)

*Università di Pisa and INFN Sezione di Pisa*

*Largo B. Pontecorvo, 3 - 56127, Pisa - Italy*

## Abstract

Flavor oscillation in  $D^0$ - $\bar{D}^0$  system is predicted to be of order of percent or less in the Standard Model (SM), while  $CP$  violation is predicted to be of order  $10^{-5} \div 10^{-3}$ , and therefore not measurable with the current data sample. Evidence of  $CP$  violation with present statistics would constitute evidence of New Physics as long as a measurement of the mixing parameters  $x$  and  $y$ , not consistent with the SM predictions. We report on recent results from *BABAR* and *BELLE* experiments of  $D^0$ - $\bar{D}^0$  mixing and  $CP$  violation measurements in  $D^0$  decays for the most sensitive analyses: time dependent analysis of  $D^0 \rightarrow K^+\pi^-$  wrong sign decays, the measurement of the ratio of lifetimes of the decays  $D^0 \rightarrow K^+K^-$  and  $D^0 \rightarrow \pi^+\pi^-$  relative to  $D^0 \rightarrow K^-\pi^+$ , search for mixing in semileptonic decays  $D^0 \rightarrow K^{(*)}l\nu$  where  $l = e, \mu$ . New limits on  $CP$ -violating time-integrated asymmetries in two body decays  $D^0 \rightarrow K^+K^-$ ,  $D^0 \rightarrow \pi^+\pi^-$  and in three body decays  $D^0 \rightarrow K^+K^-\pi^0$ ,  $D^0 \rightarrow \pi^+\pi^-\pi^0$  are also discussed. The analyses presented are based on  $384 \text{ fb}^{-1}$  data for the *BABAR* experiment and on  $400 \div 500 \text{ fb}^{-1}$  data for the *BELLE* experiment. Data have been collected with the *BABAR* detector at the PEP-II asymmetric-energy *B* Factory at SLAC and with the *BELLE* detector at the KEKB asymmetric-energy *B* Factory at KEK.

---

Work supported by Università di Pisa and INFN. Also supported by U.S. Department of Energy and SLAC, Stanford University.

## 1 Introduction

$B$  Factories are ideal laboratories <sup>1, 2)</sup> to study charm physics which represents an important part of their scientific program. The main topics of charm physics are:  $D^0$ - $\bar{D}^0$  mixing and  $CP$  violation ( $CPV$ ), search for rare charm decays, Dalitz plot analysis and charm spectroscopy. In the following we will focus on  $D^0$ - $\bar{D}^0$  mixing and  $CPV$ .

$D^0$ - $\bar{D}^0$  oscillations can be explained by the fact that the effective Hamiltonian which determines the time-evolution of the neutral  $D$  meson system is not diagonal in the  $|D^0\rangle$ ,  $|\bar{D}^0\rangle$  flavor defined base. The eigenstates of the effective Hamiltonian,  $|D_{1,2}\rangle$ , are therefore a linear combination of  $|D^0\rangle$  and  $|\bar{D}^0\rangle$ :

$$|D_{1,2}\rangle = p|D^0\rangle \pm q|\bar{D}^0\rangle, \quad \text{with } |p|^2 + |q|^2 = 1. \quad (1)$$

If  $CP$  is conserved, then  $q/p = 1$  and the physical states are  $CP$  eigenstates.

The mixing parameters  $x$  and  $y$  are defined as

$$x \equiv \frac{m_1 - m_2}{\bar{\Gamma}}, \quad y \equiv \frac{\Gamma_1 - \Gamma_2}{2\bar{\Gamma}}, \quad (2)$$

where  $m_{1,2}$  and  $\Gamma_{1,2}$  are the mass and the width values for the effective Hamiltonian eigenstates and  $\bar{\Gamma} = (\Gamma_1 + \Gamma_2)/2$ .

The effects of  $CPV$  in  $D^0$ - $\bar{D}^0$  mixing can be parameterized in terms of the quantities

$$r_m \equiv \left| \frac{q}{p} \right| \quad \text{and} \quad \varphi_f \equiv \arg \left( \frac{q \bar{A}_f}{p A_f} \right), \quad (3)$$

where  $A_f \equiv \langle f | \mathcal{H}_D | D^0 \rangle$  ( $\bar{A}_f \equiv \langle f | \mathcal{H}_D | \bar{D}^0 \rangle$ ) is the amplitude for  $D^0$  ( $\bar{D}^0$ ) to decay into a final state  $f$ , and  $\mathcal{H}_D$  is the Hamiltonian for the decay. A value of  $r_m \neq 1$  would indicate  $CPV$  in mixing. A non-zero value of  $\varphi_f$  would indicate  $CPV$  in the interference of mixing and decay.

In the SM  $D^0$ - $\bar{D}^0$  oscillations are predicted to proceed quite slowly. The short distance contributions to  $D^0$ - $\bar{D}^0$  mixing from the SM box diagrams are expected to be very small <sup>3, 4)</sup>. Long-distance effects from intermediate states coupling to both  $D^0$  and  $\bar{D}^0$  are expected to contribute, but are difficult to estimate precisely <sup>5)</sup>.

Within the SM,  $CPV$  is also expected to be small in the  $D^0$ - $\bar{D}^0$  system. An observation of  $CPV$  in  $D^0$ - $\bar{D}^0$  mixing with the present experimental sensitivity would be evidence for physics beyond the SM <sup>6)</sup>.

Recent results from *BABAR* <sup>7)</sup> and *BELLE* <sup>8)</sup> show an evidence of  $D^0$ - $\bar{D}^0$  oscillation at  $3.9\sigma$  and  $3.2\sigma$  level respectively. At this level of precision the measurements are compatibles with the predicted values from SM and put significant constraints on New Physics models <sup>4, 9)</sup>.

## 2 Selection of signal events

Signal events are selected via the cascade decay  $D^{*+} \rightarrow D^0 \pi_s^+ \text{ }^1$ , and the flavor of the  $D$  meson is identified at production by the charge of the soft pion ( $\pi_s$ ). The difference of the reconstructed  $D^{*+}$  and  $D^0$  masses ( $\Delta m$ ), which has an experimental resolution at the level of  $\simeq 350 \text{ keV}/c^2$ , is used to remove background events by requiring typically to be less than  $1 \text{ MeV}/c^2$  from the expected value,  $145.5 \text{ MeV}/c^2 \text{ }^{10}$ ). In order to reject background events with  $D^0$  candidates from  $B$  meson decays, the momentum of the  $D^0$ , evaluated in the center-of-mass (CM) of the  $e^+e^-$  system, is required to be greater than  $2.4 - 2.5 \text{ GeV}/c$  for most of the analyses. The  $D^0$  proper-time,  $t$ , is determined in a vertex constrained combined fit to the  $D^0$  production and decay vertices. In this fit the  $D^0$  and the  $\pi_s$  tracks are imposed to originate from the  $e^+e^-$  luminous region. The average error on the proper time,  $\sigma_t \sim 0.2 \text{ ps}$ , is comparable with half of the  $D^0$  lifetime  $\text{ }^{10}$ ). Particle identification algorithms are used to identify the charged tracks from  $D^0$  decays.

## 3 Time Dependent measurements for mixing and CP violation

### 3.1 Wrong-sign decays $D^0 \rightarrow K^+ \pi^-$

The final wrong sign (WS) state can be produced via the doubly Cabibbo-suppressed (DCS) decay or via mixing followed by the Cabibbo-favored (CF) decay  $D^0 \rightarrow \bar{D}^0 \rightarrow K^+ \pi^-$ . The time dependence of the WS decay of a meson produced as a  $D^0$  at time  $t = 0$  in the limit of small mixing ( $|x|, |y| \ll 1$ ) and  $CP$  conservation can be approximated as

$$\frac{T_{\text{WS}}(t)}{e^{-\bar{\Gamma}t}} \propto R_{\text{D}} + \sqrt{R_{\text{D}}} y' \bar{\Gamma} t + \frac{x'^2 + y'^2}{4} (\bar{\Gamma} t)^2, \quad (4)$$

where  $R_{\text{D}}$  is the ratio of doubly Cabibbo-suppressed to Cabibbo-favored (CF) decay rates,  $x' = x \cos \delta_{K\pi} + y \sin \delta_{K\pi}$ ,  $y' = -x \sin \delta_{K\pi} + y \cos \delta_{K\pi}$ , and  $\delta_{K\pi}$  is the strong phase between the DCS and CF amplitudes.

The time dependence of the WS decays is used to separate the contribution of DCS decays from that of  $D^0$ - $\bar{D}^0$  mixing. The mixing parameters are determined by an unbinned extended maximum-likelihood fit to the reconstructed  $D^0$  invariant mass  $m_{D^0}$ ,  $\Delta m$ ,  $t$ ,  $\sigma_t$  variables for WS decays.

The *BABAR* experiment has found evidence of  $D^0$ - $\bar{D}^0$  mixing at  $3.9\sigma$  level  $\text{ }^7$ ). The results of the different fits - no  $CPV$  or mixing, no  $CPV$ ,  $CPV$  allowed - including statistical and systematic errors are reported in Table 1.

---

<sup>1</sup>Consideration of charge conjugation is implied throughout this paper, unless otherwise stated.

Table 1: *BABAR* results from the different fits. The first uncertainty listed is statistical and the second systematic.

Fit type	Parameter	Fit Results ( $\times 10^{-3}$ )
No <i>CPV</i> or mixing	$R_D$	$3.53 \pm 0.08 \pm 0.04$
No <i>CPV</i>	$R_D$	$3.03 \pm 0.16 \pm 0.10$
	$x'^2$	$-0.22 \pm 0.30 \pm 0.21$
	$y'$	$9.7 \pm 4.4 \pm 3.1$
<i>CPV</i> allowed	$R_D$	$3.03 \pm 0.16 \pm 0.10$
	$A_D$	$-21 \pm 52 \pm 15$
	$x'^{2+}$	$-0.24 \pm 0.43 \pm 0.30$
	$y'^+$	$9.8 \pm 6.4 \pm 4.5$
	$x'^{2-}$	$-0.20 \pm 0.41 \pm 0.29$
	$y'^-$	$9.6 \pm 6.1 \pm 4.3$

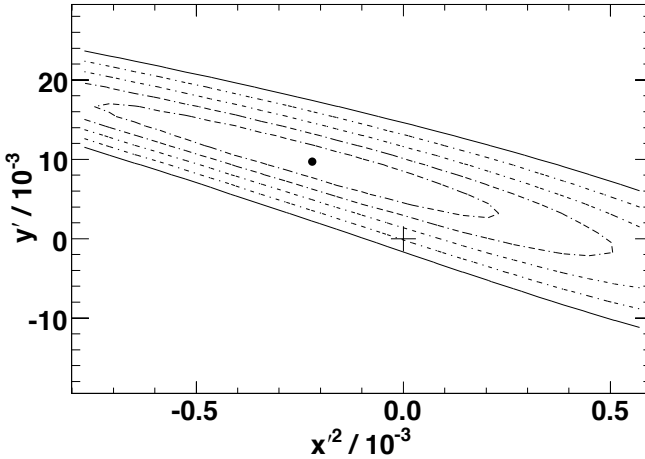


Figure 1: *BABAR* results. The central value (point) and confidence-level (CL) contours for  $1 - \text{CL} = 0.317$  ( $1\sigma$ ),  $4.55 \times 10^{-2}$  ( $2\sigma$ ),  $2.70 \times 10^{-3}$  ( $3\sigma$ ),  $6.33 \times 10^{-5}$  ( $4\sigma$ ) and  $5.73 \times 10^{-7}$  ( $5\sigma$ ), calculated from the change in the value of  $-2 \ln \mathcal{L}$  compared with its value at the minimum. Systematic uncertainties are included. The no-mixing point is shown as a plus sign (+).

The confidence level countours including systematic errors are shown in Fig. 1, where the no-mixing point  $(x', y') \equiv (0, 0)$  is shown as a plus sign (+).

The *BABAR* results have been confirmed by the CDF experiment with a significance for mixing at  $3.8\sigma$  level <sup>11)</sup>. *BELLE* experiment - on an equivalent data sample to *BABAR*- finds no evidence for mixing <sup>12)</sup>.

### 3.2 Lifetime Ratio of $D^0 \rightarrow K^+K^-$ and $D^0 \rightarrow \pi^+\pi^-$ relative to $D^0 \rightarrow K^-\pi^+$

One consequence of  $D^0$ - $\bar{D}^0$  mixing is that  $D^0$  decay time distribution can be different for decays to different CP eigenstates.  $D^0$ - $\bar{D}^0$  mixing will alter the decay time distribution of  $D^0$  and  $\bar{D}^0$  mesons that decay into final states of specific CP <sup>13)</sup>. To a good approximation, these decay time distributions can be treated as exponential with effective lifetimes  $\tau_{hh}^+$  and  $\tau_{hh}^-$ , for  $D^0$  and  $\bar{D}^0$  events respectively, decaying to CP-even final states (such as  $K^-K^+$  and  $\pi^-\pi^+$ ). The effective lifetimes measurements can be combined into the quantities  $y_{CP}$  and  $\Delta Y$ :

$$y_{CP} = \frac{\tau_{K\pi}}{\langle\tau_{hh}\rangle} - 1$$

$$\Delta Y = \frac{\tau_{K\pi}}{\langle\tau_{hh}\rangle} A_\tau,$$
(5)

where  $\langle\tau_{hh}\rangle = (\tau_{hh}^+ + \tau_{hh}^-)/2$  and  $A_\tau = (\tau_{hh}^+ - \tau_{hh}^-)/(\tau_{hh}^+ + \tau_{hh}^-)$ . Both  $y_{CP}$  and  $\Delta Y$  are zero if there is no  $D^0$ - $\bar{D}^0$  mixing. In the limit where CP is conserved in mixing and decay, but violated in the interference between them, these quantities are related to the mixing parameters  $y_{CP} = y \cos \varphi_f$  and  $\Delta Y = x \sin \varphi_f$ , with the convention that  $\cos \varphi_f > 0$ .

*BELLE* experiment measures the relative difference of the apparent lifetime of  $D^0$  mesons between decays to CP-even eigenstates and the  $K^-\pi^+$  final state to be

$$y_{CP} = (1.31 \pm 0.32(\text{stat.}) \pm 0.25(\text{syst.}))\%,$$
(6)

which represents a significance for  $D^0$ - $\bar{D}^0$  mixing at  $3.2\sigma$  level <sup>8)</sup>. The effect is presented visually in Fig. 2(d), which shows the ratio of decay time distributions for  $D^0 \rightarrow K^+K^-, \pi^+\pi^-$  and  $D^0 \rightarrow K^-\pi^+$  decays. The CPV parameter  $A_\Gamma \equiv -A_\tau$  was found to be consistent with zero:

$$A_\Gamma = (0.01 \pm 0.30(\text{stat.}) \pm 0.15(\text{syst.}))\%.$$
(7)

*BABAR* experiment measures  $y_{CP} = (1.03 \pm 0.33(\text{stat.}) \pm 0.19(\text{syst.}))\%$ , which represents evidence of mixing at  $3.0\sigma$  level, and  $\Delta Y = (-0.26 \pm 0.36(\text{stat.}) \pm 0.08(\text{syst.}))\%$  consistent with no CPV <sup>14)</sup>.

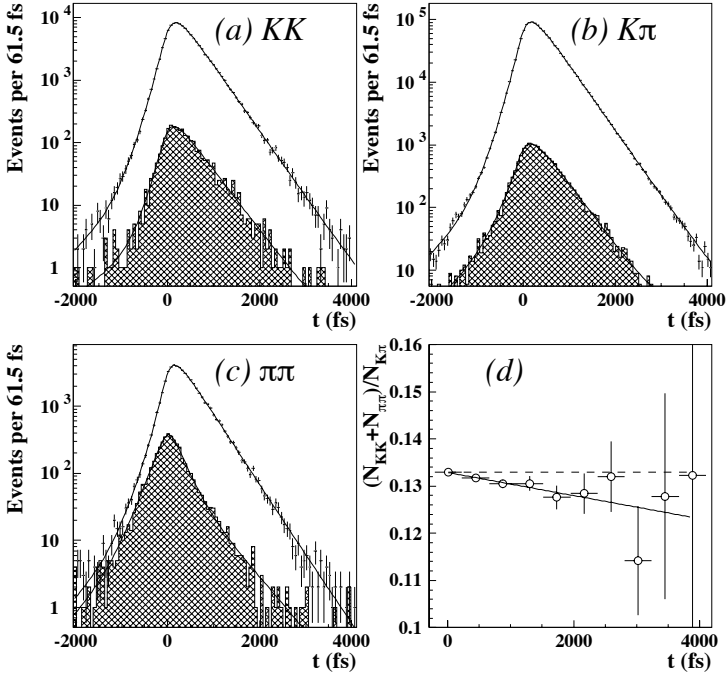


Figure 2: *BELLE* results of the simultaneous fit to decay time distributions of (a)  $D^0 \rightarrow K^+K^-$ , (b)  $D^0 \rightarrow K^-\pi^+$  and (c)  $D^0 \rightarrow \pi^+\pi^-$  decays. The cross-hatched area represents background contributions, the shape of which was fitted using  $D^0$  invariant mass sideband events. (d) Ratio of decay time distributions between  $D^0 \rightarrow K^+K^-$ ,  $\pi^+\pi^-$  and  $D^0 \rightarrow K^-\pi^+$  decays. The solid line is a fit to the data points.

## 4 Time integrated measurements for mixing and CP violation

### 4.1 Search for mixing in semileptonic decays $D^0 \rightarrow K^{(*)}l\nu$

The search for mixing in semileptonic WS decays is performed by reconstructing events from the decay chain  $D^{*+} \rightarrow D^0\pi_s^+$  with  $D^0 \rightarrow \bar{D}^0 \rightarrow K^{(*)}l^-\bar{\nu}$ , where  $l = e, \mu$ . Any WS event, characterized by the opposite charge of the  $\pi_s$  from  $D^*$  and the lepton from the neutral  $D$ , would be evidence of  $D^0$ - $\bar{D}^0$  mixing. In the approximation of small  $x$  and  $y$  and  $CP$  conservation, the decay time distribution of neutral  $D$  meson which changes flavor and decays semileptonically, and thus involves no doubly interfering Cabibbo-suppressed (DCS) amplitudes, is

$$R_{\text{mix}}(t) \simeq R_{\text{unmix}}(t) \frac{x^2 + y^2}{4} \left( \frac{t}{\tau_{D^0}} \right)^2 \quad (8)$$

where  $\tau_{D^0}$  is the characteristic  $D^0$  lifetime, and  $R_{\text{unmix}}(t) \propto e^{-t/\tau_{D^0}}$ . The time integrated mixing rate relative to the unmixed rate is

$$R_M = \frac{x^2 + y^2}{2}. \quad (9)$$

*BELLE* experiment did not find any evidence of WS events and sets the limit on the time integrated mixing rate,  $R_M < 6.1 \times 10^{-4}$  at 90% CL<sup>15)</sup>. *BABAR* experiment using a more exclusive reconstruction technique which fully reconstructs charm decays in the hemisphere opposite the semileptonic signal, sets the constraint  $R_M \in [-13, 12] \times 10^{-4}$ <sup>16)</sup>.

### 4.2 Two body decays $D^0 \rightarrow K^-K^+$ and $D^0 \rightarrow \pi^-\pi^+$

The  $CP$ -even decays  $D^0 \rightarrow K^-K^+$  and  $D^0 \rightarrow \pi^-\pi^+$  are Cabibbo suppressed, with the two neutral charmed mesons,  $D^0$  and  $\bar{D}^0$ , sharing the final states.  $CP$ -violating asymmetries in these modes are predicted to be of order 0.001%  $\div$  0.01% in the SM<sup>3, 17)</sup>. The observation of  $CP$  asymmetries at the level of current experimental sensitivity<sup>18)</sup> would indicate a clear sign of physics beyond the SM<sup>4, 19)</sup>. The *BABAR* experiment performed a search for  $CPV$  in neutral  $D$  mesons<sup>20)</sup>, produced from the reaction  $e^+e^- \rightarrow c\bar{c}$ , by measuring the time-integrated asymmetries

$$a_{CP}^{hh} = \frac{\Gamma(D^0 \rightarrow h^+h^-) - \Gamma(\bar{D}^0 \rightarrow h^+h^-)}{\Gamma(D^0 \rightarrow h^+h^-) + \Gamma(\bar{D}^0 \rightarrow h^+h^-)}, \quad (10)$$

where  $h = K$  or  $\pi$ .

Table 2:  $CPV$  asymmetries in  $D^0$  two body decays. The first error is statistical, the second systematic.

Quantity	Value
$a_{CP}^{KK}$	$(0.00 \pm 0.34 \pm 0.13)\%$
$a_{CP}^{\pi\pi}$	$(-0.24 \pm 0.52 \pm 0.22)\%$

The precise measurement of the time-integrated asymmetry is experimentally challenging due to the forward backward (FB) asymmetry in  $e^+e^- \rightarrow c\bar{c}$  production - which creates a different number of  $D^0$  and  $\bar{D}^0$  reconstructed events due to the FB detection asymmetry due to the boost of the CM system relatively to the laboratory - and to different flavor tag efficiencies for  $D^0$  and  $\bar{D}^0$ . Those effects are ruled out by using both tagged and untagged control samples to measure the relative efficiency for soft pions on data and by measuring the integrated asymmetry as a function of the cosine of the angle of the  $D^0$  in the CM,  $\cos\theta \equiv \cos\theta_{D^0}^{\text{CMS}}$ , and projecting out the even part due to  $CPV$ . The measured asymmetries, found to be consistent with zero, are listed in Table 2.

#### 4.3 Three body decays $D^0 \rightarrow \pi^-\pi^+\pi^0$ and $D^0 \rightarrow K^-K^+\pi^0$

The three body decays  $D^0 \rightarrow \pi^-\pi^+\pi^0$  and  $D^0 \rightarrow K^-K^+\pi^0$  proceed via  $CP$  eigenstates (e.g.,  $\rho^0\pi^0$ ,  $\phi\pi^0$ ) and also via flavor states (e.g.,  $\rho^\pm\pi^\mp$ ,  $K^{*\pm}K^\mp$ ), thus making it possible to probe  $CPV$  in both types of amplitudes and in the interference between them. Measuring interference effects in a Dalitz plot (DP) probes asymmetries in both the magnitudes and phases of the amplitudes, not simply in the overall decay rates.

The *BABAR* experiment searched for  $CPV$  asymmetries in both  $D^0 \rightarrow \pi^-\pi^+\pi^0$  and  $D^0 \rightarrow K^-K^+\pi^0$  decays quantifying  $D^0$ - $\bar{D}^0$  differences in four different methods: difference between Dalitz plots, difference between the angular moments, difference in phase space integrated asymmetry, difference in Dalitz plot fit results for amplitudes and phases, where only the latter is a model dependent approach. There is no evidence of  $CPV$  in any of the four different methods<sup>21</sup>). Result for phase space integrated asymmetry are reported in Table 3.

The *BELLE* experiment has measured the time integrated asymmetry in  $D^0 \rightarrow \pi^-\pi^+\pi^0$  and found no evidence of  $CPV$ <sup>22</sup>), see Table 3. *BELLE* also measured the relative branching ratio of  $D^0 \rightarrow \pi^-\pi^+\pi^0$  to  $D^0 \rightarrow K^-K^+\pi^0$  to be  $\text{BR} = (10.12 \pm 0.04(\text{stat}) \pm 0.18(\text{syst})) \times 10^{-2}$ .

Table 3: *CPV* time integrated asymmetries for  $D^0$  three body decays. The first error is statistical, the second systematic. For *BELLE* results the error is the sum of the statistical and the systematic contribution.

Quantity	<i>BABAR</i>	<i>BELLE</i>
$a_{CP}^{KK\pi^0}$	$(0.00 \pm 0.34 \pm 0.13)\%$	-
$a_{CP}^{\pi\pi\pi^0}$	$(-0.24 \pm 0.52 \pm 0.22)\%$	$(0.43 \pm 1.30)\%$

## 5 Conclusions

In conclusion, the results from *B* Factories show evidence of charm mixing in WS  $D^0 \rightarrow K^+\pi^-$  decays at  $3.9\sigma$  level (*BABAR*) and in the lifetime ratio analysis at  $3.2\sigma$  level (*BELLE*) and  $3.0\sigma$  level (*BABAR*). Significance of charm mixing exceeds  $6.7\sigma$  when combining all the available mixing results<sup>23</sup>. No evidence of *CPV* has been found in  $D^0$  decays. The above results are compatible with the Standard Model predictions and provide useful constraints for New Physics models<sup>4, 9</sup>.

## 6 Acknowledgements

I would like to thank the Istituto Nazionale di Fisica Nucleare (INFN) and the University of Pisa for the support for this work. I would like to thank also SLAC for its support and the kind hospitality.

## References

1. B. Aubert *et al.* [BABAR Collaboration], Nucl. Instrum. Meth. A **479**, 1 (2002)
2. Nucl. Instrum. Meth. A **479**, 117 (2002).
3. S. Bianco, F. L. Fabbri, D. Benson and I. Bigi, Riv. Nuovo Cim. **26N7**, 1 (2003)
4. G. Burdman and I. Shipsey, Ann. Rev. Nucl. Part. Sci. **53**, 431 (2003)
5. L. Wolfenstein, Phys. Lett. B **164**, 170 (1985). J. F. Donoghue, E. Golowich, B. R. Holstein and J. Trampetic, Phys. Rev. D **33**, 179 (1986). I. I. Y. Bigi and N. G. Uraltsev, Nucl. Phys. B **592**, 92 (2001). A. F. Falk, Y. Grossman, Z. Ligeti and A. A. Petrov, Phys. Rev. D **65**, 054034 (2002).

- 
- A. F. Falk, Y. Grossman, Z. Ligeti, Y. Nir and A. A. Petrov, Phys. Rev. D **69**, 114021 (2004).
  6. G. Blaylock, A. Seiden and Y. Nir, Phys. Lett. B **355**, 555 (1995)
  7. B. Aubert *et al.* [BABAR Collaboration], Phys. Rev. Lett. **98**, 211802 (2007)
  8. M. Staric *et al.* [Belle Collaboration], Phys. Rev. Lett. **98**, 211803 (2007)
  9. A. A. Petrov, Int. J. Mod. Phys. A **21**, 5686 (2006)
  10. W. M. Yao *et al.* [Particle Data Group], J. Phys. G **33**, 1 (2006).
  11. T. Aaltonen *et al.* [CDF Collaboration], Phys. Rev. Lett. **100**, 121802 (2008)
  12. L. M. Zhang *et al.* [BELLE Collaboration], Phys. Rev. Lett. **96**, 151801 (2006)
  13. T. h. Liu, arXiv:hep-ph/9408330.
  14. B. Aubert *et al.* [BABAR Collaboration], arXiv:0712.2249 [hep-ex].
  15. U. Bitenc *et al.* [BELLE Collaboration], arXiv:0802.2952 [hep-ex].
  16. B. Aubert *et al.* [BABAR Collaboration], Phys. Rev. D **76**, 014018 (2007)
  17. F. Buccella, M. Lusignoli, G. Miele, A. Pugliese and P. Santorelli, Phys. Rev. D **51**, 3478 (1995)
  18. D. Acosta *et al.* (CDF Collaboration), Phys. Rev. Lett. **94**, 122001 (2005);  
B. Aubert *et al.* (BABAR Collaboration), Phys. Rev. D **71**, 091101 (2005).
  19. Y. Grossman, A. L. Kagan and Y. Nir, Phys. Rev. D **75**, 036008 (2007)
  20. B. Aubert *et al.* [BaBar Collaboration], Phys. Rev. Lett. **100**, 061803 (2008)
  21. B. Aubert *et al.* [BABAR Collaboration], arXiv:0802.4035 [hep-ex].
  22. K. Arinstein [Belle Collaboration], Phys. Lett. B **662**, 102 (2008)
  23. A. J. Schwartz, arXiv:0803.0082 [hep-ex].

**RESULTS FROM CLEO-C**

Todd Pedlar  
*Luther College, USA*

Written contribution not received



**RECENT RESULTS FROM BESII**

Du Shuxian  
*IHEP-Beijing, China*

Written contribution not received



**BESIII: A STATUS**

Yuan Ye

*IHEP-Beijing, China*

Written contribution not received



# MEASUREMENT OF $B^0 \rightarrow \pi^+\pi^-\pi^+\pi^-$ DECAYS AND SEARCH FOR $B^0 \rightarrow \rho^0\rho^0$

C.-C. Chiang

*Department of Physics, National Taiwan University, Taipei*  
(The Belle Collaboration)

## Abstract

We search for the decay  $B^0 \rightarrow \rho^0\rho^0$  and other possible charmless modes with a  $\pi^+\pi^-\pi^+\pi^-$  final state, including  $B^0 \rightarrow \rho^0 f_0(980)$ ,  $B^0 \rightarrow f_0(980)f_0(980)$ ,  $B^0 \rightarrow f_0(980)\pi^+\pi^-$ ,  $B^0 \rightarrow \rho^0\pi^+\pi^-$  and non-resonant  $B^0 \rightarrow 4\pi^\pm$ . These results are obtained from a data sample containing  $656.7 \times 10^6 B\bar{B}$  pairs collected by the Belle detector at the KEKB asymmetric-energy  $e^+e^-$  collider. We measure a branching fraction of  $B^0 \rightarrow \rho^0\rho^0$  to be  $(0.4 \pm 0.4_{-0.3}^{+0.2}) \times 10^{-6}$ , where the first and second errors are statistical and systematic, respectively, or  $\mathcal{B}(B^0 \rightarrow \rho^0\rho^0) < 1.0 \times 10^{-6}$  at the 90% confidence level. The significance including systematic uncertainties is  $1.0\sigma$ , these values correspond to the final state being longitudinally polarized. With the  $B \rightarrow \rho\rho$  measurement, we obtain a  $1\sigma$  interval on the Cabibbo-Kobayashi-Maskawa quark-mixing matrix phase angle  $\phi_2 = (91.7 \pm 14.9)^\circ$ . We also measure the branching fraction of non-resonant  $B^0 \rightarrow 4\pi^\pm$  decay to be  $(12.4_{-4.6-2.2}^{+4.7+2.0}) \times 10^{-6}$  with  $2.5\sigma$  significance, and set the 90% confidence level upper limit  $\mathcal{B}(B^0 \rightarrow 4\pi^\pm) < 19.0 \times 10^{-6}$ . For  $B^0 \rightarrow \rho^0\pi^+\pi^-$  mode, we measure its branching fraction to be  $(5.9_{-3.4-2.8}^{+3.5+2.7}) \times 10^{-6}$  with  $1.3\sigma$  significance, and 90% confidence level upper limit  $\mathcal{B}(B^0 \rightarrow \rho^0\pi^+\pi^-) < 11.9 \times 10^{-6}$ .

## 1 INTRODUCTION

In the Standard Model (SM),  $CP$  violation in the weak interaction can be described by the presence of an irreducible complex phase in the three-generation Cabibbo-Kobayashi-Maskawa (CKM) quark-mixing matrix <sup>1)</sup>. Measurements of the differences between  $B$  and  $\bar{B}$  mesons decays provide an opportunity to determine the elements of CKM matrix and thus test the SM. One can extract the CKM phase  $\phi_2 \equiv \arg[-(V_{td}V_{tb}^*)/(V_{ud}V_{ub}^*)]$  from the time-dependent  $CP$  asymmetry for the decay of a neutral  $B$  meson via a  $b \rightarrow u$  process into a  $CP$  eigenstate. However, in addition to the  $b \rightarrow u$  process, there are  $b \rightarrow d$  penguin transitions that shift the  $\phi_2$  value by  $\delta\phi_2$  in the time-dependent  $CP$  violating parameter. To determine  $\delta\phi_2$ , we perform an isospin analysis <sup>2)</sup> for  $B \rightarrow \pi\pi$  <sup>3)</sup> and  $B \rightarrow \rho\rho$  <sup>4)</sup>, which are of pseudoscalar-pseudoscalar (PP) and vector-vector (VV) modes, respectively. The latter can provide additional information through an angular analysis. Polarization measurements in the  $B \rightarrow \rho^+\rho^-$  <sup>4)</sup> and  $B^\pm \rightarrow \rho^\pm\rho^0$  <sup>5)</sup> show the dominance of longitudinal polarization, thus  $B \rightarrow \rho^+\rho^-$  and  $B^\pm \rightarrow \rho^\pm\rho^0$  are  $CP$  eigenstates. Measurements of the branching fraction, polarization and  $CP$ -violating parameters in  $B^0 \rightarrow \rho^0\rho^0$  decays complete the isospin triangle. Theoretically, the tree contribution to  $B^0 \rightarrow \rho^0\rho^0$  is color-suppressed, therefore its branching fraction is much smaller than that of  $B \rightarrow \rho^+\rho^-$  or  $B^\pm \rightarrow \rho^\pm\rho^0$ , which make it sensitive to the penguin amplitude. This mode is particularly effective for the constraints on  $\phi_2$ .

Predictions for  $B^0 \rightarrow \rho^0\rho^0$  using perturbative QCD (pQCD) <sup>6)</sup> or QCD factorization <sup>7, 8)</sup> approaches suggest that the branching fraction  $\mathcal{B}(B^0 \rightarrow \rho^0\rho^0)$  is at or below  $1 \times 10^{-6}$  and its longitudinal polarization fraction,  $f_L$ , is around 0.85. A non-zero branching fraction for  $B^0 \rightarrow \rho^0\rho^0$  was first reported by the *BABAR* collaboration <sup>9)</sup>; they measured a branching fraction of  $\mathcal{B}(B^0 \rightarrow \rho^0\rho^0) = (1.07 \pm 0.33 \pm 0.19) \times 10^{-6}$  with a significance of 3.5 standard deviations ( $\sigma$ ), and a longitudinal polarization fraction,  $f_L = 0.87 \pm 0.13 \pm 0.04$ .

The effects of non-resonant  $B^0 \rightarrow 4\pi^\pm$  and  $B^0 \rightarrow \rho^0\pi^+\pi^-$  decays on  $B^0 \rightarrow \rho^0\rho^0$  measurement, according to *BABAR*'s study <sup>10)</sup>, are zero. Since the rates for non-resonant  $B^0 \rightarrow 4\pi^\pm$  and  $B^0 \rightarrow \rho^0\pi^+\pi^-$  are not well constrained in *BABAR*'s fit, they do not set the branching fractions. The theoretical prediction for the non-resonant  $B^0 \rightarrow 4\pi^\pm$  branching fraction is around  $1 \times 10^{-4}$  <sup>11)</sup>. The most recent measurement of this decay was made by the DELPHI collaboration <sup>12)</sup>, who sets a 90% confidence level upper limit on the

branching fraction of  $2.3 \times 10^{-4}$ .

## 2 DATA SET AND APPARATUS

The data sample used contains  $656.7 \times 10^6$   $B\bar{B}$  pairs collected with the Belle detector at the KEKB asymmetric-energy  $e^+e^-$  (3.5 and 8 GeV) collider<sup>13</sup>, operating at the  $\Upsilon(4S)$  resonance. The Belle detector<sup>14, 15</sup> is a large-solid-angle magnetic spectrometer that consists of a silicon vertex detector, a 50-layer central drift chamber (CDC), an array of aerogel threshold Cherenkov counters (ACC), a barrel-like arrangement of time-of-flight scintillation counters (TOF), and an electromagnetic calorimeter comprised of CsI(Tl) crystals (ECL) located inside a superconducting solenoid coil that provides a 1.5 T magnetic field. An iron flux-return located outside of the coil is instrumented to detect  $K_L^0$  mesons and to identify muons. Signal MC is generated with GEANT, which is based on full simulation with PHOTOS package to take account of final-state radiation<sup>16</sup>.

## 3 EVENT SELECTION AND RECONSTRUCTION

$B^0$  meson candidates are reconstructed from neutral combinations of four charged pions. Charged track candidates are required to have a distance-of-closest-approach to the interaction point (IP) of less than 2 cm in the opposite direction of the positron beam direction and less than 0.1 cm in the transverse plane; they are also required to have a transverse momentum  $p_T > 0.1$  GeV/ $c$  in the laboratory frame. Charged pions are identified using particle identification (PID) information obtained from the CDC ( $dE/dx$ ), the ACC and the TOF. We distinguish charged kaons and pions using a likelihood ratio  $\mathcal{R}_{\text{PID}} = \mathcal{L}_K / (\mathcal{L}_K + \mathcal{L}_\pi)$ , where  $\mathcal{L}_\pi$  ( $\mathcal{L}_K$ ) is a likelihood value for the pion (kaon) hypothesis. We require  $\mathcal{R}_{\text{PID}} < 0.4$  for the four charged pions. The pion identification efficiency is 90%, and 12% of kaons are misidentified as pions. Charged particles positively identified as an electron or a muon are removed.

To veto  $B \rightarrow D^{(*)}\pi$  and  $B \rightarrow D_s\pi$  backgrounds, we remove candidates that satisfy any one of the following conditions:  $|M(h^\pm\pi^\mp\pi^\mp) - M_{D_{(s)}}| < 13$  MeV/ $c^2$  or  $|M(h^\pm\pi^\mp) - M_{D^0}| < 13$  MeV/ $c^2$ , where  $h^\pm$  is either a pion or a kaon, and  $M_{D_{(s)}}$  and  $M_{D^0}$  are the nominal masses of  $D_{(s)}$  and  $D^0$ , respectively. Furthermore, to reduce the  $B^0 \rightarrow a_1^\pm\pi^\mp$  feeddown in the signal region, we

require that the pion with the highest momentum have a momentum in the  $\Upsilon(4S)$  center-of-mass (CM) frame within the range 1.30-2.65 GeV/ $c$ .

The signal event candidates are characterized by two kinematic variables: beam-energy constrained mass,  $M_{bc} = \sqrt{E_{\text{beam}}^2 - P_B^2}$ , and energy difference,  $\Delta E = E_B - E_{\text{beam}}$ , where  $E_{\text{beam}}$  is the run-dependent beam energy,  $P_B$  and  $E_B$  are the momentum and energy of the  $B$  candidate in the  $\Upsilon(4S)$  CM frame. In  $B^0 \rightarrow \rho^0 \rho^0 \rightarrow (\pi^+ \pi^-)(\pi^+ \pi^-)$  decays, the invariant masses  $M(\pi^+ \pi^-)$ - $M(\pi^+ \pi^-)$  are used to distinguish different modes from signal. There are two possible combinations for the invariant masses  $M(\pi^+ \pi^-)$ - $M(\pi^+ \pi^-)$ :  $(\pi_1^+ \pi_1^-)(\pi_2^+ \pi_2^-)$  and  $(\pi_1^+ \pi_2^-)(\pi_2^+ \pi_1^-)$ , where the subscripts label the momentum ordering, e.g.  $\pi_1^+(\pi_1^-)$  has a higher momentum than  $\pi_2^+(\pi_2^-)$ . Here we consider both  $(\pi_1^+ \pi_1^-)(\pi_2^+ \pi_2^-)$  and  $(\pi_1^+ \pi_2^-)(\pi_2^+ \pi_1^-)$  combinations and select candidate events if either one of the combined masses lies in the  $\rho^0 \rho^0$  signal mass window, which is  $0.55 \text{ GeV}/c^2 < M(\pi_1^+ \pi_1^-) \cap M(\pi_2^+ \pi_2^-) < 1.7 \text{ GeV}/c^2$  or  $0.55 \text{ GeV}/c^2 < M(\pi_1^+ \pi_2^-) \cap M(\pi_2^+ \pi_1^-) < 1.7 \text{ GeV}/c^2$ . If a candidate event has  $(\pi_1^+ \pi_1^-)(\pi_2^+ \pi_2^-)$  and  $(\pi_1^+ \pi_2^-)(\pi_2^+ \pi_1^-)$  combinations whose combined masses both lie in the  $\rho^0 \rho^0$  signal mass window, we cannot distinguish which  $\rho^0 \rho^0$  mass combination is correct. In such cases, we select  $(\pi_1^+ \pi_2^-)(\pi_2^+ \pi_1^-)$  pair as the correct combination; with this selection, 1.9% of the signal is incorrectly reconstructed according to the MC. For fitting, in order to symmetrize the 2-D invariant  $\pi^+ \pi^-$  mass distribution, we randomly assign  $M_1(\pi_1^+ \pi_2^-)$ - $M_2(\pi_2^+ \pi_1^-)$  or  $M_1(\pi_2^+ \pi_1^-)$ - $M_2(\pi_1^+ \pi_2^-)$ . Therefore, the probability density functions (PDF) for  $M_1(\pi^+ \pi^-)$ - $M_2(\pi^+ \pi^-)$  are symmetric in both the  $M_1(\pi^+ \pi^-)$  and  $M_2(\pi^+ \pi^-)$  projections.

## 4 BACKGROUND SUPPRESSION

The dominant background are continuum events. To distinguish signal from the jet-like continuum background, we use modified Fox-Wolfram moments<sup>17)</sup>, which are combined into a Fisher discriminant. This discriminant is combined with PDFs for the cosine of the  $B$  flight direction in the CM and the distance in the  $z$ -direction between two  $B$  mesons to form a likelihood ratio  $\mathcal{R} = \mathcal{L}_s / (\mathcal{L}_s + \mathcal{L}_{q\bar{q}})$ . Here,  $\mathcal{L}_s$  ( $\mathcal{L}_{q\bar{q}}$ ) is a likelihood function for signal (continuum) events that is obtained from the signal MC simulation (events in the sideband region  $M_{bc} < 5.26 \text{ GeV}/c^2$ ). We also use the flavor tagging quality variable  $r$  provided by a tagging algorithm<sup>18)</sup> that identifies the flavor of the accompanying

$B^0$  meson in the  $\Upsilon(4S) \rightarrow B^0 \bar{B}^0$ . The variable  $r$  ranges from  $r = 0$  (no flavor discrimination) to  $r = 1$  (unambiguous flavor assignment), and is used to divide the data sample into six  $r$  bins. Since the discrimination between signal and continuum events depends on the  $r$ -bin, we impose different requirements on  $\mathcal{R}$  for each  $r$ -bin. We determine the  $\mathcal{R}$  requirement so that it maximizes the figure-of-merit  $N_s / \sqrt{N_s + N_{q\bar{q}}}$ , where  $N_s$  ( $N_{q\bar{q}}$ ) is the expected number of signal (continuum) events in the signal region. For multiple candidates we select a single candidate having the smallest  $\chi^2$  value of the  $B^0$  decay vertex reconstruction. After the selection, 79.6% of selected events are of correct combination. The detection efficiency for the signal MC is calculated to be 9.16% (11.25%) for longitudinal (transverse) polarization.

## 5 ANALYSIS STRATEGY

Since there are large overlaps between  $B^0 \rightarrow \rho^0 \rho^0$  and other signal decay modes in the  $M_1(\pi^+\pi^-)$ - $M_2(\pi^+\pi^-)$  distribution, it is better to distinguish these modes using a simultaneous fit to a large  $M_1(\pi^+\pi^-)$ - $M_2(\pi^+\pi^-)$  region. The signal yields are extracted by performing extended unbinned maximum likelihood (ML) fits. In the fits, we use four dimensional ( $M_{bc}$ ,  $\Delta E$ ,  $M_1$ ,  $M_2$ ) information to measure the branching fraction of  $B^0$  decays into  $\rho^0 \rho^0$ ,  $\rho^0 \pi^+ \pi^-$ , non-resonant  $4\pi^\pm$ ,  $\rho^0 f_0$ ,  $f_0 f_0$  and  $f_0 \pi^+ \pi^-$ . We define the likelihood function

$$\mathcal{L} = \exp\left(-\sum_j n_j\right) \prod_{i=1}^{N_{\text{cand}}} \left(\sum_j n_j P_j^i\right), \quad (1)$$

where  $i$  is the event identifier,  $j$  indicates one of the event type categories for signals and backgrounds;  $n_j$  denotes the yield of the  $j$ -th category, and  $P_j^i$  is the probability density function (PDF) for the  $j$ -th category. For the 4D fits, the PDFs are a product of two smoothed two-dimensional functions:  $P_j^i = P_j(M_{bc}^i, \Delta E^i, M_1^i, M_2^i) = p_{\text{smoothed}}(M_{bc}^i, \Delta E^i) \times p_{\text{smoothed}}(M_1^i, M_2^i)$ .

For the  $B$  decay components, the smoothed functions  $p_{\text{smoothed}}(M_{bc}^i, \Delta E^i)$  and  $p_{\text{smoothed}}(M_1^i, M_2^i)$  are obtained from MC simulations. For the  $M_{bc}$  and  $\Delta E$  PDFs, possible differences between the real data and the MC modeling are calibrated using a large control sample of  $B^0 \rightarrow D^-(K\pi^+\pi^-)\pi^+$  decays. The signal mode PDF is divided in two parts: one is correctly reconstructed events (Right) and the other is self-cross-feed (SCF); for SCF events at least one track from the signal decay is replaced by one from the accompanying  $B$

meson decay. We use different PDFs for the SCF events and correctly reconstructed events, and employ the SCF fraction for a signal decay in the nominal fit.

For the continuum and charm  $B$  decay backgrounds, we use the product of a linear function for  $\Delta E$ , an ARGUS function<sup>20)</sup> for  $M_{bc}$  and a two-dimensional smoothed function for  $M_1$ - $M_2$ . The parameters of the linear function and ARGUS function for the continuum events are floated in the fit. Other parameters and shape of the  $M_1$ - $M_2$  functions are obtained from MC simulations and fixed in the fit. For the charmless  $B$  decay backgrounds, we construct three separate PDFs for  $B^0 \rightarrow a_1^\pm \pi^\mp$ ,  $B^+ \rightarrow \rho^+ \rho^0$  and other charmless  $B$  decays; all the PDFs are obtained using MC simulations. In the fit, while the yields of the  $B^0 \rightarrow a_1^\pm \pi^\mp$  and  $B^+ \rightarrow \rho^+ \rho^0$  are fixed to expected values obtained from measured branching fractions, the yield of other charmless  $B$  decays is floated. We fix the branching fraction of  $B^0 \rightarrow a_1^\pm \pi^\mp$  to the published value  $(33.2 \pm 3.0 \pm 3.8) \times 10^{-6}$ <sup>19)</sup>. If we float the  $B^0 \rightarrow a_1^\pm \pi^\mp$  yield in the fit; the fit result is  $\mathcal{B}(B^0 \rightarrow a_1^\pm \pi^\mp) = (33.8_{-13.2}^{+13.4}) \times 10^{-6}$ , which is consistent with the assumed value.

Table 1 and Fig. 1 show the fit results and projections of the data onto  $\Delta E$ ,  $M_{bc}$ ,  $M_1(\pi^+ \pi^-)$  and  $M_2(\pi^+ \pi^-)$  for  $B^0 \rightarrow \rho^0 \rho^0$  decay. The statistical significance is defined as  $\mathcal{S}_0 = \sqrt{-2 \ln(\mathcal{L}_0/\mathcal{L}_{\max})}$ , where  $\mathcal{L}_0$  and  $\mathcal{L}_{\max}$  are the likelihoods of the fits with the signal yield fixed at zero and at the fitted value, respectively. The 90% confidence level (C.L.) upper limit is calculated from the equation

$$\frac{\int_0^N \mathcal{L}(x) dx}{\int_0^\infty \mathcal{L}(x) dx} = 90\%, \quad (2)$$

where  $x$  indicates one of likelihood variables corresponding to the number of signal, and  $N$  is the upper bound for the yield that includes 90% of the integral of the likelihood function. The upper limit (UL) including systematic uncertainties is calculated by smearing the statistical likelihood function with a Bifurcated Gaussian, where the Bifurcated Gaussian width is the combination of two total systematic errors: one is independent of the branching fraction and the other is proportional to it. The significance including systematic uncertainties is calculated in the same way, but we only included the systematic errors related to signal yields in the convoluted Bifurcated Gaussian width.

Table 1: Fit results for each decay mode listed in the first column. The signal yields, reconstruction efficiency, significance ( $\mathcal{S}$ ), branching fractions ( $\mathcal{B}$ ) and the upper limit at the 90% confidence level (UL) are listed. For the yields and branching fractions, the first (second) error is statistical (systematic).

Mode	Yield	Eff.(%)	$\mathcal{S}$	$\mathcal{B}(\times 10^{-6})$	UL( $\times 10^{-6}$ )
$\rho^0 \rho^0$	$24.5^{+23.6+9.7}_{-22.1-16.5}$	9.16	1.0	$0.4 \pm 0.4^{+0.2}_{-0.3}$	< 1.0
$\rho^0 \pi^+ \pi^-$	$112.5^{+67.4+51.5}_{-65.6-53.7}$	2.90	1.3	$5.9^{+3.5+2.7}_{-3.4-2.8}$	< 11.9
$4\pi^\pm$	$161.2^{+61.2+26.0}_{-59.4-28.5}$	1.98	2.5	$12.4^{+4.7+2.0}_{-4.6-2.2}$	< 19.0
$\rho^0 f_0$	$-11.8^{+14.5+4.9}_{-12.9-3.6}$	5.10	—	—	< 0.6
$f_0 f_0$	$-7.7^{+4.7+3.0}_{-3.5-2.9}$	2.75	—	—	< 0.4
$f_0 \pi^+ \pi^-$	$6.3^{+37.0+18.0}_{-34.7-18.1}$	1.55	—	$0.6^{+3.6}_{-3.4} \pm 1.8$	< 7.3

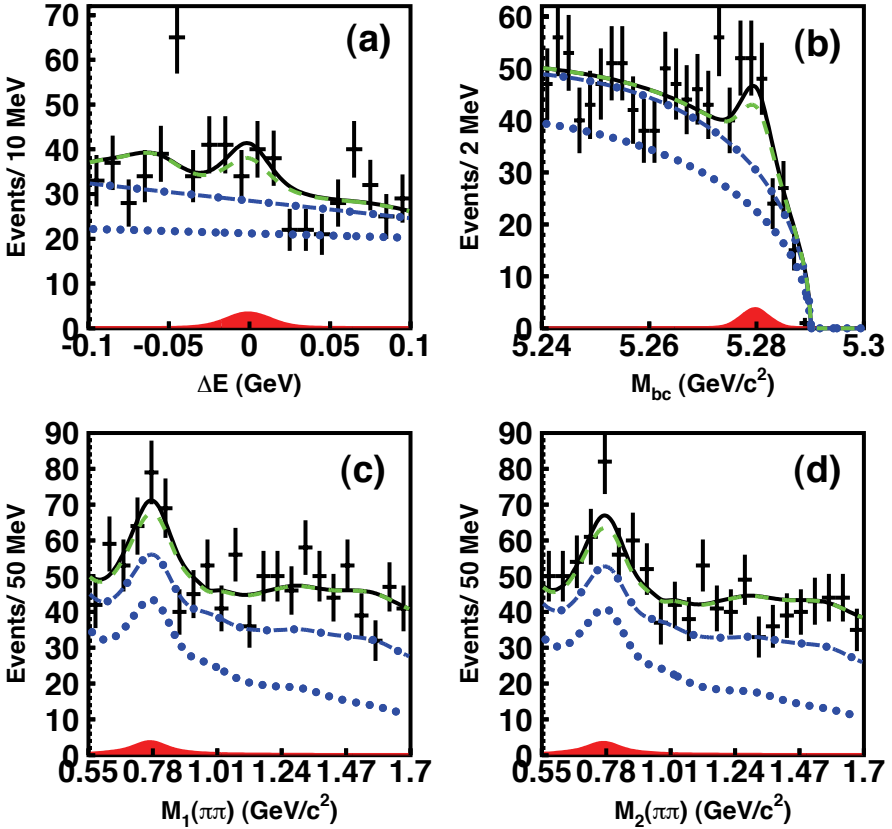


Figure 1: Projections of the four dimensional fit onto (a)  $\Delta E$ , (b)  $M_{bc}$ , (c)  $M_1(\pi^+\pi^-) \in (0.55, 1.7) \text{ GeV}/c^2$  and (d)  $M_2(\pi^+\pi^-) \in (0.55, 1.7) \text{ GeV}/c^2$ . For the  $\Delta E$  projection:  $M_{bc} \in (5.27, 5.29) \text{ GeV}/c^2$  and  $M_{1,2}(\pi^+\pi^-) \in (0.626, 0.926) \text{ GeV}/c^2$ ; for the  $M_{bc}$  projection:  $\Delta E \in (-0.05, 0.05) \text{ GeV}$  and  $M_{1,2}(\pi^+\pi^-) \in (0.626, 0.926) \text{ GeV}/c^2$ ; for the  $M_{1(2)}(\pi^+\pi^-)$  projection:  $\Delta E \in (-0.05, 0.05) \text{ GeV}$  and  $M_{bc} \in (5.27, 5.29) \text{ GeV}/c^2$  and  $M_{2(1)}(\pi^+\pi^-) \in (0.626, 0.926) \text{ GeV}/c^2$ . The fit result is shown as the thick solid curve; the hatched region represents the signal component,  $B^0 \rightarrow \rho^0 \rho^0$  decay. The dotted, dot-dashed and dashed curves represent, respectively, the cumulative background from continuum processes,  $b \rightarrow c$  decays, and charmless  $B$  backgrounds.

## 6 SYSTEMATIC ERROR

The systematic errors are summarized in the Table 2, they are represented as percentages. Because of the relatively small signal yield compared to the systematic uncertainty,  $B^0 \rightarrow f_0\pi^+\pi^-$  mode has the largest systematic error. For the systematic uncertainties of fixed branching fractions, we vary the branching fractions of  $B^0 \rightarrow a_1^\pm\pi^\mp$  ( $33.2 \pm 4.8$ , in units of  $10^{-6}$ )<sup>19)</sup> and  $B^\pm \rightarrow \rho^0\rho^\pm$  ( $18.2 \pm 3.0$ )<sup>21)</sup> by their  $\pm 1\sigma$  errors. The fits are repeated and the differences between the results and the nominal fit values are taken as systematic errors. Systematic uncertainties for the  $\Delta E$ - $M_{bc}$  PDFs used in the fit are estimated by performing the fits while varying the signal peak positions and resolutions by  $\pm 1\sigma$ . Systematic uncertainties for the  $M_1$ - $M_2$  PDFs are estimated in a similar way. A systematic error for the longitudinal polarization fraction of  $B^0 \rightarrow \rho^0\rho^0$  is obtained by changing the fraction from the nominal value  $f_L = 1$  to the most conservative value  $f_L = 0$ . According to MC, the signal SCF fractions are 20.4% for  $B^0 \rightarrow \rho^0\rho^0$ , 15.0% for  $B^0 \rightarrow \rho^0f_0$ , 9.9% for  $B^0 \rightarrow f_0f_0$ , 13.4% for  $B^0 \rightarrow f_0\pi^+\pi^-$ , 14.2% for  $B^0 \rightarrow \rho^0\pi^+\pi^-$  and 11.1% for non-resonant  $B^0 \rightarrow 4\pi^\pm$ . We estimate a systematic uncertainty for the signal SCF by setting its fraction to zero.

A MC study indicates that the fit biases are +12.5 event for non-resonant  $B^0 \rightarrow 4\pi^\pm$ , +7.2 event for  $B^0 \rightarrow \rho^0\pi^+\pi^-$ , +2.4 event for  $B^0 \rightarrow \rho^0\rho^0$ , +3.6 event for  $B^0 \rightarrow \rho^0f_0$ , -0.8 event for  $B^0 \rightarrow f_0f_0$  and +5.1 event for  $B^0 \rightarrow f_0\pi^+\pi^-$ . We find that fit biases occur due to the correlations between the two sets of variables ( $\Delta E$ ,  $M_{bc}$ ) and ( $M_1$ ,  $M_2$ ), which are not taken into account in our fit. We correct the yields in the fit for these biases and include the corrections as systematic errors.

We test the possible interference between  $B^0 \rightarrow a_1^\pm\pi^\mp$ , non-resonant  $B^0 \rightarrow 4\pi^\pm$ ,  $B^0 \rightarrow \rho^0\pi^+\pi^-$  and  $B^0 \rightarrow \rho^0\rho^0$  by toy MC. We add a simple interference model to the toy MC generation, which is, for  $\rho^0 \rightarrow \pi^+\pi^-$  decay, modified from a relativistic Breit-Wigner function. We assume that the interference term due to the amplitudes for  $B^0 \rightarrow a_1^\pm\pi^\mp$ , non-resonant  $B^0 \rightarrow 4\pi^\pm$  and  $B^0 \rightarrow \rho^0\pi^+\pi^-$  decays is constant in the  $B^0 \rightarrow \rho^0\rho^0$  signal region. Since the magnitude of the interfering amplitude and relative phase are not known, we uniformly vary these parameters and perform a fit in each case to measure the deviations from the incoherent case. The mean deviation is calculated, and we add and subtract the r.m.s. of the distribution of deviations from this value

Table 2: Summary of systematic errors (%) for the branching fraction measurements.  $f_L$  and  $f_{\text{SCF}}$  are the fractional uncertainties for longitudinal polarization and self-cross-feed.

Source	$\rho^0\rho^0$	$\rho^0\pi^+\pi^-$	$4\pi^\pm$	$\rho^0f_0$	$f_0f_0$	$f_0\pi^+\pi^-$
Fitting PDF	$\pm 10.2$	$\pm 29.8$	$\pm 12.2$	$\pm 18.6$	$\pm 31.2$	$\pm 269.8$
$\mathcal{B}(B^0 \rightarrow a_1\pi)$	$\pm 21.6$	$\pm 33.5$	$\pm 2.7$	$\pm 17.8$	$\pm 1.3$	$\pm 39.7$
$\mathcal{B}(B^\pm \rightarrow \rho^0\rho^\pm)$	$\pm 0.0$	$\pm 0.7$	$\pm 0.2$	$\pm 0.0$	$\pm 0.0$	$\pm 1.6$
$f_L$	-53.7	-	-	-	-	-
$f_{\text{SCF}}$	-17.6	-13.5	-10.3	+8.5	+9.1	-34.9
Fit bias correction	$\pm 16.3$	+6.4 -5.7	+7.8 -3.3	+30.5 -14.4	$\pm 20.8$	$\pm 82.5$
Interference	+25.7 -20.8	-	-	-	-	-
Tracking	$\pm 5.3$	$\pm 4.6$	$\pm 4.4$	$\pm 5.0$	$\pm 4.8$	$\pm 4.5$
PID	$\pm 4.8$	$\pm 3.5$	$\pm 3.2$	$\pm 4.4$	$\pm 3.9$	$\pm 3.4$
$\mathcal{R}$ requirement	$\pm 3.2$	$\pm 3.2$	$\pm 3.2$	$\pm 3.2$	$\pm 3.2$	$\pm 3.2$
$N_{B\bar{B}}$	$\pm 1.3$	$\pm 1.3$	$\pm 1.3$	$\pm 1.3$	$\pm 1.3$	$\pm 1.3$
Sum(%)	+39.5 -67.3	+45.8 -47.7	+16.1 -17.7	+41.5 -30.4	+39.3 -38.2	+285.0 -287.1

to obtain the systematic uncertainty.

The systematic errors for the efficiency arise from the tracking efficiency, particle identification (PID) and  $\mathcal{R}$  requirement. The systematic error due to the track finding efficiency is estimated to be around 1.2% per track using partially reconstructed  $D^*$  events. The systematic error due to the pion identification (PID) is around 1.0% per track estimated using an inclusive  $D^*$  control sample. The  $\mathcal{R}$  requirement systematic error is determined from the efficiency difference between data and MC using a  $B^0 \rightarrow D^+(K\pi^+\pi^-)\pi^-$  control sample. Table 2 summarizes the sources of systematic uncertainties and their quadratic sum for each of the items.

## 7 SUMMARY

In summary, we measure the branching fraction of  $B^0 \rightarrow \rho^0\rho^0$  to be  $(0.4 \pm 0.4^{+0.2}_{-0.3}) \times 10^{-6}$  with  $1.0\sigma$  significance; the 90% confidence level upper limit including systematic uncertainties is  $\mathcal{B}(B^0 \rightarrow \rho^0\rho^0) < 1.0 \times 10^{-6}$ . Since no significant signal is found, we have assumed this mode is a longitudinally polarized decay ( $f_L = 1$ ), to obtain the most conservative upper limit.

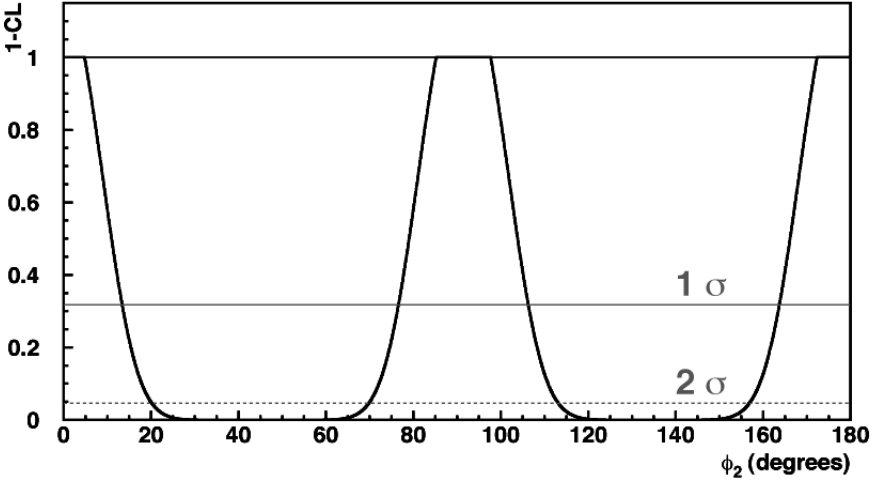


Figure 2:  $1-C.L.$  vs  $\phi_2(\alpha)$  obtained from the isospin analysis of  $B \rightarrow \rho\rho$  decays.

To constrain  $\phi_2$  using  $B \rightarrow \rho\rho$  decays, we perform an isospin analysis, and use the measured branching fractions of longitudinally polarized  $B^\pm \rightarrow \rho^\pm\rho^0$ ,  $B \rightarrow \rho^+\rho^-$  and  $B^0 \rightarrow \rho^0\rho^0$  decays as the lengths of the sides of the isospin triangles. The  $B^\pm \rightarrow \rho^\pm\rho^0$  and  $B \rightarrow \rho^+\rho^-$  branching fractions, as well as the corresponding  $f_L$  values, are obtained from the world average <sup>21)</sup>; the  $B^0 \rightarrow \rho^0\rho^0$  branching fraction is from this measurement, and we assume its  $f_L = 1$ . The  $CP$ -violating parameters  $S_L^{+-}$  and  $C_L^{+-}$  are determined from the time evolution of the longitudinally polarized  $B \rightarrow \rho^+\rho^-$  decay. Assuming the uncertainties to be Gaussian, we neglect  $I = 1$  isospin contributions and electroweak loop amplitudes <sup>22)</sup>, and the possible interference from non-resonant components. The resulting function  $1-C.L.$  is shown in Fig. 2, the  $1\sigma$  interval corresponding to the  $\phi_2$  solution expected by SM is  $(91.7 \pm 14.9)^\circ$ .

On the other hand, we find excesses in  $B^0 \rightarrow \rho^0\pi^+\pi^-$  and non-resonant  $B^0 \rightarrow 4\pi^\pm$  decays with  $1.3\sigma$  and  $2.5\sigma$  significance, respectively. We measure

the branching fraction and a 90% confidence level upper limit for non-resonant  $B^0 \rightarrow 4\pi^\pm$  decay to be  $(12.4_{-4.6-2.2}^{+4.7+2.0}) \times 10^{-6}$  and  $\mathcal{B}(B^0 \rightarrow 4\pi^\pm) < 19.0 \times 10^{-6}$ . For  $B^0 \rightarrow \rho^0\pi^+\pi^-$  mode, we measure its branching fraction to be  $(5.9_{-3.4-2.8}^{+3.5+2.7}) \times 10^{-6}$ , and 90% confidence level upper limit  $\mathcal{B}(B^0 \rightarrow \rho^0\pi^+\pi^-) < 11.9 \times 10^{-6}$ . We find no significant signal for the decays  $B^0 \rightarrow \rho^0 f_0$ ,  $B^0 \rightarrow f_0 f_0$  and  $B^0 \rightarrow f_0\pi^+\pi^-$ ; the final results and upper limits are listed in Table 1.

## 8 ACKNOWLEDGMENTS

We thank the KEKB group for the excellent operation of the accelerator, the KEK cryogenics group for the efficient operation of the solenoid, and the KEK computer group and the National Institute of Informatics for valuable computing and SINET3 network support. We acknowledge support from the Ministry of Education, Culture, Sports, Science, and Technology of Japan and the Japan Society for the Promotion of Science; the Australian Research Council and the Australian Department of Education, Science and Training; the National Natural Science Foundation of China under contract No. 10575109 and 10775142; the Department of Science and Technology of India; the BK21 program of the Ministry of Education of Korea, the CHEP SRC program and Basic Research program (grant No. R01-2005-000-10089-0) of the Korea Science and Engineering Foundation, and the Pure Basic Research Group program of the Korea Research Foundation; the Polish State Committee for Scientific Research; the Ministry of Education and Science of the Russian Federation and the Russian Federal Agency for Atomic Energy; the Slovenian Research Agency; the Swiss National Science Foundation; the National Science Council and the Ministry of Education of Taiwan; and the U.S. Department of Energy.

## References

1. N. Cabibbo, Phys. Rev. Lett. **10**, 531 (1963); M. Kobayashi, T. Maskawa, Prog. Theor. Phys. **49**, 652 (1973).
2. M. Gronau and D. London, Phys. Rev. Lett. **65**, 3381 (1990).
3. H. Ishino *et al.* (Belle Collaboration), Phys. Rev. Lett. **98** 211801 (2007); B. Aubert *et al.* (BABAR Collaboration), Phys. Rev. Lett. **99** 021603 (2007).

4. A. Somov *et al.* (Belle Collaboration), Phys. Rev. D **76**, 011104 (2007); B. Aubert *et al.* (BABAR Collaboration), Phys. Rev. D **76**, 052007 (2007).
5. J. Zhang *et al.* (Belle Collaboration), Phys. Rev. Lett. **91**, 221801 (2003); B. Aubert *et al.* (BABAR Collaboration), Phys. Rev. Lett. **97**, 261801 (2006).
6. H. Li, S. Mishima Phys. Rev. D **73** 114014 (2006).
7. M. Beneke, J. Rohrer , D. Yang, arXiv:hep-ph/0612290.
8. W. Zou, Z. Xiao, Phys. Rev. D **72** (2005) 094026, arXiv:hep-ph/0507122.
9. B. Aubert *et al.* (BABAR Collaboration), Phys. Rev. Lett. **98**, 111801 (2007).
10. B. Aubert *et al.* (BABAR Collaboration), arXiv: 0708.1630.
11. K. Berkelman, *Hadronic Decays*, in *B Decays* ed. by S. Stone, World Scientific, Singapore (1992).
12. W. Adam *et al.* (DELPHI Collaboration), Z. Phys. C72: 207-220 (1996); P. Abreu *et al.* (DELPHI Collaboration), Phys. Lett. B357: 255-266 (1995).
13. S. Kurokawa and E. Kikutani, Nucl. Instrum. and Methods Phys. Res. Sect. A **499**, 1 (2003), and other papers included in this volume.
14. A. Abashian, *et al.* (Belle Collaboration), Nucl. Instrum. and Methods Phys. Res. Sect. A **479**, 117 (2002).
15. Z. Natkaniec *et al.* (Belle SVD2 Group), Nucl. Instrum. and Methods Phys. Res. Sect. A **560**, 1 (2006).
16. E. Barberio and Z. Was, Comput. Phys. Commun. **79**, 291 (1994); P. Golonka and Z. Was, arXiv:hep-ph/0506026.
17. G. C. Fox and S. Wolfram, Phys. Rev. Lett. **41** 1581 (1978). The modified moments used in this paper are described in S. H. Lee *et al.* (Belle Collaboration), Phys. Rev. Lrtt. **91**, 261801 (2003).
18. H. Kakuno *et al.*, Nucl. Instrum. and Meth. A **533**, 516 (2004).

19. B. Aubert *et al.* (*BABAR* Collaboration), Phys. Rev. Lett. **97**, 051802 (2006).
20. H. Albrecht *et al.* (*ARGUS* Collaboration), Phys. Lett. B **241**, 278 (1990).
21. E. Barberio *et al.* (Heavy Flavor Averaging Group), arXiv:0704.3575 [hep-ex] and online update for winter 2008 at <http://www.slac.stanford.edu/xorg/hfag/rare/index.html>
22. A. Falk *et al.*, Phys. Rev. D **69**, 011502(R) (2004).

**RADIATIVE AND ELECTROWEAK PENGUINS**

Stev Playfer  
*University of Edinburgh, UK*

Written contribution not received



# ON THE DETERMINATION OF $|V_{ub}|$ FROM INCLUSIVE SEMILEPTONIC B DECAYS

Einan Gardi

*School of Physics, The University of Edinburgh,  
Edinburgh EH9 3JZ, Scotland, UK*

Abstract

Precision tests of the CKM mechanism and searches for new physics in the flavour sector require dedicated QCD calculations of decay widths and spectra. Significant progress has been achieved in recent years in computing inclusive B decay spectra into light energetic partons. I briefly review different theoretical approaches to this problem focusing on the determination of  $|V_{ub}|$  from inclusive semileptonic decays and show that this determination is robust. The largest uncertainty is associated with the value of the b quark mass. Finally I present new numerical results in the DGE resummation-based approach, now including  $\mathcal{O}(\beta_0\alpha_s^2)$  corrections. The results are presented for all relevant experimental cuts, from which a preliminary average is derived  $|V_{ub}| = (4.31 \pm 0.16(\text{exp})_{-0.15}^{+0.09}(\text{th})_{-0.33}^{+0.36}(m_b)) \cdot 10^{-3}$ , where the PDG value of the b quark mass,  $m_b^{\overline{\text{MS}}} = 4.20 \pm 0.07$  GeV, is assumed.

## 1 Introduction

Low-energy precision measurements, in particular precision determination of the CKM parameters and the branching fractions of rare decays, provide many valuable tests of the Standard Model. The resulting constraints on new physics are highly complementary to the direct searches at hadron colliders, and are expected to continue being so throughout the LHC era [1].

The experimental effort over the past few years by the B factories and the Tevatron has established the fact that CKM is the main mechanism of flavour and CP violation in the quark sector. This is now a field of precision physics. Measuring deviations from the Standard Model and further strengthening the constraints on new physics will require a continuous experimental effort [2–5] alongside corresponding progress on the theory side.

The obvious example of the progress that was made is the precise measurement of the small angle  $\beta$  of the Unitarity Triangle, and its comparison with the short side of the triangle,  $|V_{ub}/V_{cb}|$ . While the former is directly sensitive to potential CP-violation beyond the Standard Model and can be measured experimentally with high precision without any theoretical input, the latter, being determined by tree-level Weak (semileptonic) decays, is insensitive to new physics, however it heavily relies on theoretical calculations in QCD. Currently the measured  $\sin(2\beta)$  is not entirely consistent with  $|V_{ub}/V_{cb}|$ , introducing some tension into global fits [6, 7]. This comparison is a crucial element in the big picture.

Experimentally, both  $|V_{ub}|$  and  $|V_{cb}|$  can be measured either using an exclusive hadronic final state, e.g.  $\bar{B} \rightarrow D^* l \bar{\nu}$  and  $\bar{B} \rightarrow \pi l \bar{\nu}$  or by considering the inclusive rate, summing over all hadronic final states subject to some kinematical constraints. The two approaches involve different experimental and theoretical tools and are therefore complementary.

The lower rate of the  $b \rightarrow u$  transition ( $|V_{ub}/V_{cb}|^2 \sim 1/50$ ) makes the  $|V_{ub}|$  measurement more challenging. Further difficulties, common to all heavy-to-light decays, lie on the theory side. The *exclusive* determination of  $|V_{ub}|$  requires a theoretical calculation of the form factor using non-perturbative methods such as Lattice QCD [8, 9] or QCD sum-rules [10], which both have systematic uncertainties that are hard to quantify. The Lattice calculations are expected to improve in the future. In contrast the *inclusive* determination relies primarily on the Heavy Quark Expansion (HQE) and QCD perturbation theory, where a systematic improvement can be achieved and uncertainties are easier to quantify. However, the case of inclusive  $b \rightarrow u$  decay is further complicated by the fact that the final state is characterized by jet-like kinematics. This,

in conjunction with the experimental requirement to perform the measurement subject to stringent kinematic cuts (in order to suppress the charm background) implies that to extract  $|V_{ub}|$  one needs a precise calculation of the spectrum, not just the total width. This provides one of the biggest challenges in Heavy Flavour physics, a subject an intense theoretical effort over the past few years. This is the subject of the present talk.

## 2 A brief look at inclusive semileptonic $b \rightarrow c$ decay

In order to appreciate the difficulty in determining  $|V_{ub}|$ , it is useful to compare it to the much favored case of  $|V_{cb}|$ . Let us therefore briefly review the situation in inclusive semileptonic  $b \rightarrow c$  decays.

Owing to the high rate of these decays and their distinct characteristics, the B factories provide precise measurements of the branching fraction, as well as the first few moments, *over the entire phase space*. These truly-inclusive observables can be readily computed using the HQE, for example,

$$\Gamma(\bar{B} \rightarrow X_c l \bar{\nu}) = \underbrace{\Gamma(b \rightarrow X_c l \bar{\nu}; \mu)}_{\text{on-shell } b\text{-quark decay with IR cutoff}} + \frac{C_1 \mu_\pi^2(\mu) + C_2 \mu_G^2(\mu)}{m_b^2} + \frac{(\dots)}{m_b^3}, \quad (1)$$

where the first term stands for the partonic on-shell  $b$ -quark decay width  $\Gamma(b \rightarrow X_c l \bar{\nu})$ , computed with an infrared cutoff  $\mu$ , and other terms, suppressed by powers of the  $b$ -quark mass correspond to matrix elements of local operators, computed with an ultraviolet cutoff  $\mu$ ; as usual, the  $\mu$  dependence cancels out order by order. Importantly, non-perturbative corrections first appear at order  $1/m_b^2$ , where there are two non-perturbative matrix elements, the kinetic energy  $\mu_\pi^2$  and the chromomagnetic energy  $\mu_G^2$ .

Note that the partonic decay width computed to next-to-leading order (order  $\alpha_s$ ), without a cutoff, already yields a viable approximation to the measured width. This approximation is systematically improved by including non-perturbative corrections as well as higher-order perturbative corrections. There is a continuous progress on both these fronts. Recent fits to the measured moments [11–13] are based on  $\mathcal{O}(\beta_0 \alpha_s^2)$  accuracy [14] with power corrections through  $\mathcal{O}(1/m_b^3)$ , computed with leading-order coefficient functions. These fits (performed in the “kinetic” or 1S mass schemes) provide a determination of  $|V_{cb}|$ ,  $m_b$  and  $m_c$  at the 1 – 2% level together with a determination of  $\mu_\pi^2$  at the 10% level.

Very recently, complete  $\mathcal{O}(\alpha_s^2)$  corrections have become available in a fully differential form [15, 16];  $\mathcal{O}(1/m_b^4)$  corrections have been computed for the first time [17] and also the  $\mathcal{O}(\alpha_s)$  correction to the coefficient function of  $\mu_\pi^2$  [18]

was calculated. These advances will further push the accuracy, exploiting the potential of the B factory measurements for inclusive  $b \rightarrow c$  decays.

### 3 The challenge: computing the charmless semileptonic decay spectrum

Experimental measurements [19–25] of inclusive  $b \rightarrow u$  decays involve kinematic cuts in order to remove the charm background. Therefore, extracting  $|V_{ub}|$  from the data requires theoretical predictions for the fully (triple) differential  $\bar{B} \rightarrow X_u l \bar{\nu}$  spectrum.

The main difficulty in computing the spectra of heavy-to-light decays,  $\bar{B} \rightarrow X_u l \bar{\nu}$  or  $\bar{B} \rightarrow X_s \gamma$ , is in the fact that most events have a jet-like final state where the hadronic system  $X$  has a mass which is much smaller than its energy (approximately half of the energy released in the decay,  $m_b$ ). The jet kinematics is most easily described in terms of light-cone momenta  $P^\pm = E_X \mp p_X$ , where a typical event has  $P^-$  of order  $m_b$  and  $P^+$  not far above the QCD scale  $\Lambda$ . The decay process involves dynamics on scales that are far apart  $P^- \gg P^+$ , complicating the perturbative description as well as the separation and parametrization of non-perturbative effects.

It has long been recognized [26,27] that an attempt to compute the spectrum in the small- $P^+$  limit by means of the HQE would run into serious difficulties: the dynamics is dominated by gluons with momenta of  $\mathcal{O}(P^+)$ , turning the  $\Lambda/m_b$  expansion into a  $\Lambda/P^+$  one! The physical picture behind this breakdown of the expansion is clear: the small lightcone component of the jet is influenced by soft gluon radiation as well as small fluctuations in the momentum carried by the decaying heavy quark. To recover a useful heavy-quark expansion, the dominant effects, those controlled by the scale  $P^+$ , must be resummed to all orders. This sum gives rise to the well-known “shape function”, which can be interpreted as the momentum distribution function of the b quark in the B meson. Similar functions appear at higher orders in the heavy-quark expansion.

Recall that in the  $b \rightarrow c$  case one could make use of the HQE: the relevant observables were well approximated by perturbation theory and the non-perturbative corrections were restricted to a few *local matrix elements*. In contrast, when considering the  $b \rightarrow u$  case one is required to compute the spectrum at small  $P^+$ , which is proportional, *already at leading power*, to a non-perturbative object, the “shape function”. This function is defined by the

non-local matrix element:

$$S(k^+; \mu) = \int_{-\infty}^{\infty} \frac{dy^-}{4\pi} e^{-ik^+ y^-} \langle B | \bar{h}(y)[y, 0] \gamma_+ h(0) | B \rangle, \quad (2)$$

where  $k^+$  is a lightcone momentum component ( $h$  are heavy-quark effective theory fields, and  $[y, 0]$  represents a gauge link). This function describes the distribution of momentum carried by the  $b$  quark. Thus, we observe that instead of having a few unknown non-perturbative matrix elements which enter as power-suppressed corrections, one faces here an unknown *function* already at the leading order in  $\Lambda/m_b$ !

Described in these terms the problem of computing the spectrum and extracting  $|V_{ub}|$  from data may appear hopeless, or at least require a full-fledged non-perturbative approach. In fact, as we shall see below, the actual situation is significantly better. The partial branching fractions corresponding to experimentally relevant cuts, which vary between 20 to 60 percent of the total, can be still estimated reliably with very little non-perturbative input. Moreover, at present, the largest uncertainty in extracting  $|V_{ub}|$  is associated with the parametric dependence on the  $b$ -quark mass; other uncertainties (e.g. power corrections, Weak Annihilation) can be reduced by further exploiting the data and thus the prospects for an even more precise  $|V_{ub}|$  from inclusive decays are high.

In the following I will briefly describe different theoretical approaches that have been developed in the past few years to compute the fully-differential spectrum and thus extract  $|V_{ub}|$  from the  $B$  factories data. I will not enter into any technical details, just try to give the flavor of the physics involved and the principal differences between the approaches. I will also not cover all the interesting theoretical developments in this area, notably the method to express the  $b \rightarrow u$  branching fractions directly in terms of the measured photon-energy spectrum in  $\bar{B} \rightarrow X_s \gamma$ , which had some resurrection recently [28–30], incorporating subleading effects in  $\Lambda/m_b$ .

#### 4 HQE-based structure-function parametrization approach

The central idea of the HQE-based structure-function parametrization approach, which has been recently put forward and implemented by Gambino *et. al.* [31], is to first use the HQE to compute carefully-selected observables — the first few moments of the structure functions — where this expansion is expected to be most reliable, and then use these observables to constrain the parametrization of the spectrum. In this way one bypasses the need to

deal with the difficult kinematic region  $P^- \gg P^+$  where neither the HQE nor perturbation theory converge well.

To explain briefly how the calculation in this approach is set up, let us recall that the triple-differential rate can be written in terms on three hadronic structure functions  $W_i(q_0, q^2)$ :

$$\frac{d\Gamma}{dq^2 dq_0 dE_l} = \frac{G_F^2 |V_{ub}|^2}{8\pi^3} \left\{ q^2 W_1 - \left[ 2E_l^2 - 2q_0 E_l + \frac{q^2}{2} \right] W_2 + q^2 (2E_l - q_0) W_3 \right\} \quad (3)$$

where  $q_0$  and  $q^2$  are the total leptonic energy and squared invariant mass, respectively. Ref. [31] computes the shape of the physical structure functions  $W_i(q_0, q^2)$  as a convolution *at fixed*  $q^2$  between non-perturbative distribution functions  $F_i(k_+, q^2; \mu)$  and the perturbative (presently the Born-level) structure functions  $W_i^{\text{pert}}(q_0, q^2)$ :

$$W_i(q_0, q^2) = \int dk_+ F_i(k_+, q^2; \mu) W_i^{\text{pert}} \left( q_0 - \frac{k_+}{2} \left( 1 - \frac{q^2}{m_b M_B} \right), q^2; \mu \right), \quad (4)$$

where the functions  $F_i(k_+, q^2; \mu)$  are parametrized and constrained by the first few  $q_0$ -moments of  $W_i(q_0, q^2)$ .

The moments used to set these constraints are computed using the HQE, where the perturbative part currently includes corrections up to  $\mathcal{O}(\alpha_s^2 \beta_0)$  [32] and power corrections are included through  $\mathcal{O}(1/m_b^3)$ . The separation between the perturbative component and the power-correction terms is based on a hard momentum cutoff ( $\mu = 1$  GeV) in the “kinetic scheme”, which has the advantage that the input parameters (in particular  $m_b$  and  $\mu_\pi^2$ ) can be taken directly from fits to the  $b \rightarrow c$  moments.

Similarly to the  $b \rightarrow c$  analysis both the power expansion and the perturbative expansion<sup>1</sup> can be improved once higher-order corrections are known. The use of a hard cutoff on the gluon energy (the “kinetic scheme”) eliminates the sensitivity to multiple soft emission rendering the expansion better convergent. Nevertheless a single-logarithmic collinear divergence persists, and can in principle be resummed.

In this approach the parameters in  $F_i$ ,  $i = 1, 2, 3$  are fixed anew at each given value of  $q^2$ , based on the moment constraints. Thus, the way these parameters vary with  $q^2$  is indirectly determined by the HQE. This issue becomes

---

<sup>1</sup>At present fixed-order  $\mathcal{O}(\alpha_s^2 \beta_0)$  expressions are used. It is fair to say that the generalization of the hard cutoff approach beyond the level of a single gluon (possibly dressed) is difficult to implement.

crucial at large  $q^2$ , where the HQE breaks down: the final-state hadronic system is then soft. While the contribution from this phase-space region is small (it is power suppressed) the spectrum there is clearly not well under control. Ref. [31] provides an interesting analysis of the breakdown of the HQE in this region and relates it to the presence of  $\mathcal{O}(1/m_b^3)$  Weak Annihilation contributions, centered at  $q^2 \sim m_b^2$ . The contributions from the large- $q^2$  region are parametrized making a conservative estimate of their size. Even then the impact of the Weak Annihilation contributions on the average value of  $|V_{ub}|$  is just  $\sim 3\%$  [33], which is less than the parametric uncertainty due to  $m_b$  dependence. Having said that, Ref. [31] has clearly demonstrated that further experimental input on the  $q^2$  distribution and moments, measured separately for charged and neutral B mesons, would be important for reducing the uncertainty on  $|V_{ub}|$ .

To summarize, the approach of Ref. [31] is cautious: it uses the well-understood (and well tested!) theoretical framework of the HQE for carefully selected moments, and assumes very little beyond that. It relies however, on extensive parametrization, dealing with three non-perturbative functions  $F_i$  of *two kinematic variables*, whose properties are unknown. The authors of Ref. [31] therefore took special care to consider a large class of functions and further devised means to assess whether this class is large enough. In this way they managed to provide a reliable prediction for the triple differential spectrum over the entire phase space without dealing directly with the difficult kinematic region where the hadronic system is jet-like. In the following I present other theoretical approaches that instead consider directly this region.

## 5 Shape-function approach

The shape-function approach by Neubert and collaborators [34,35] deals directly with the kinematic region where  $P^+ \ll P^-$  by establishing a modified expansion in inverse powers of the mass, where at each order the dynamical effects that are associated with soft gluons,  $k^+ \sim \mathcal{O}(P^+) \sim \mathcal{O}(\Lambda)$ , are summed into non-perturbative shape functions. At leading power there is one such function, the momentum distribution function defined in (2) above; beyond this order there are several different functions with additional fields insertions. To extend the calculation beyond this particular region, it is constructed to match the standard HQE when integrated over a significant part of the phase space.

The modified expansion in shape functions is developed, following the Soft Collinear Effective Theory (SCET) methodology [36–38], for the particular kinematic region where the final-state is jet-like  $P^- \simeq m_b$ ,  $P^+ \simeq \Lambda$ ,

and thus  $m_X = \sqrt{m_b \Lambda}$ , the region into which a large fraction of the events fall. The large (parametric) hierarchy between these scales implies loss of quantum-mechanical coherence between the respective excitations, leading to factorization into three different subprocesses [39] (see also [34, 36, 40]). The result, at leading power in  $\Lambda/m_b$ , can be expressed as a convolution integral [35]:

$$\frac{d\Gamma}{dP^- dP^+ dE_l} \simeq H(y, \mu) \int_0^{P^+} dk^+ y m_b J(y m_b (P^+ - k^+), \mu) S(k^+, \mu) \quad (5)$$

where  $y \equiv (P^- - P^+)/ (M_B - P^+)$ . Here  $H$  stand for *hard*, depending on momenta of  $\mathcal{O}(m_b)$ ,  $J$  for *jet*, depending on momenta of  $\mathcal{O}(\sqrt{m_b \Lambda})$  and  $S$  for *soft*, depending on momenta of  $\mathcal{O}(\Lambda)$  and is therefore considered as a non-perturbative object, to be parametrized. Similar factorization formulae apply at subleading powers in  $\Lambda/m_b$ , leading to the following expression for the differential width:

$$\frac{d\Gamma}{dP^- dP^+ dE_l} = HJ \otimes S + \frac{\sum H_n J_n \otimes S_n}{m_b} + \dots \quad (6)$$

The matching into the standard HQE translates into constraints on the moments of the shape functions.

The authors of Ref. [35] have defined the separation between the leading term and the power corrections using a factorization procedure that is based on dimensional regularization. They parametrize the shape functions directly<sup>2</sup> at the intermediate (jet) scale  $\mu \sim \sqrt{m_b \Lambda}$  (in practice  $\mu = 1.5$  GeV is used) and thus avoid ever dealing with softer momentum scales.

Both the hard and the jet functions are computed in perturbation theory. Owing to the presence of well-separated scales, the jet energy  $\mathcal{O}(m_b)$  and its mass  $\mathcal{O}(\sqrt{m_b \Lambda})$  the perturbative expansion contains large Sudakov logarithms. Ref. [35] resum these logarithms to all orders with high logarithmic accuracy (next-to-next-to-leading log, NNLL). The hard coefficient function is currently computed at  $\mathcal{O}(\alpha_s)$ .

Variation of the matching scale is used to estimate missing higher-order corrections. This translates into about 3–4% uncertainty on the average value of  $|V_{ub}|$ .

The functional forms of the shape functions are unknown, and they are therefore parametrized. The first two moments of the leading shape function are reasonably well constrained: they are fixed by  $m_b$  and  $\mu_\pi^2$  respectively; higher

---

<sup>2</sup>Note that in this way the (known) evolution properties of the shape-function are not being used.

moments are not well constrained. Subleading shape functions are difficult to constrain.

To summarize, the method of Ref. [35] makes extensive use of the available theoretical tools, employing consistently two expansions that are valid in two different kinematic regimes: the expansion in shape functions, valid for the typical final-state momentum configuration, and the standard HQE, valid for the fully integrated width. Further to that, Sudakov resummation for the jet-scale logarithms is employed at NNLL accuracy. By using a relatively high factorization scale the perturbative calculation remains insensitive to the infrared, and converges well. All ingredients, the power expansions as well as the perturbative ones, can in principle be improved systematically by including higher-order terms.

The motivation to go to subleading powers in a completely general way, however, has a price: one needs to parametrize several different subleading shape functions on which there is no theoretical control nor experimental input. Despite this, the authors of Ref. [35] have demonstrated that the experimentally-relevant partial branching fractions remain under good control: their sensitivity to the unknown higher moments of the leading shape function as well as to the unknown functional form of the subleading shape functions is small: the estimated effect of these unknowns on the average value of  $|V_{ub}|$  is less than 1%! The largest uncertainty in the determination of  $|V_{ub}|$  is the parametric one, owing to the strong dependence on  $m_b$ .

A common feature of the two approaches described so far is the extensive use of parametrization of non-perturbative functions. The fact that these functions all have a clear field-theoretic definition does not presently help in their parametrization. To improve on that one needs to avoid introducing an explicit cutoff  $m_b \gg \mu \gg \Lambda$ . This is indeed possible. It is well-known that inclusive observables, such as moments of decay spectra, are *infrared-safe* observables. In other words, in the absence a cutoff soft-gluons divergences cancels out in the sum of real and virtual diagrams, making the moments finite at any order in perturbation theory. In the following I shall describe a resummation-based approach, where a cutoff is not used and consequently one relies less on parametrization.

## 6 Resummation-based approach

The approach of Refs. [40–43] uses resummed perturbation theory in moment-space to provide a perturbative calculation of the on-shell decay spectrum in the entire phase space without introducing any external momentum cutoff; non-

perturbative effects are taken into account as power corrections in moment space. Resummation is applied to both the ‘jet’ function and the ‘soft’ (quark distribution) function, dealing directly with the double hierarchy of scales characterizing the decay process. Consequently, the shape of the spectrum in the kinematics region where the final state is jet-like is largely determined by a calculation, and less by parametrization.

The resummation method employed, DGE<sup>3</sup>, combines Sudakov and renormalon resummation. Sudakov logarithms are resummed with high logarithmic accuracy (NNLL) for both<sup>4</sup> the ‘jet’ and the ‘soft’ functions.

Renormalon resummation is an essential element in implementing a consistent separation between perturbative and non-perturbative corrections at the power level. Refs. [41–43] have adopted the Principal Value procedure to regularized the Sudakov exponent and thus *define* the non-perturbative parameters. This is in full analogy [49] with the way a momentum cutoff is conventionally used. Most importantly, this definition applies to the would-be  $1/m_b$  ambiguity of the ‘soft’ Sudakov factor, which cancels exactly [40] against the pole–mass renormalon when considering the spectrum in physical hadronic variables. The same regularization used in the Sudakov exponent must be applied in the computation of the b-quark pole mass<sup>5</sup>. This vital mechanism is absent in a fixed–logarithmic–accuracy procedure (as employed for example in [50,51]) leading to an uncontrolled shift of the entire spectrum with  $P^+/P^-$ .

Aiming to provide a good description of the spectrum in the kinematic region where there is a large hierarchy between the lightcone momentum components,  $P^+ \ll P^-$ , it proves useful to consider the moments with respect to

---

<sup>3</sup>Dressed Gluon Exponentiation (DGE) is a general resummation formalism for inclusive distributions near a kinematic threshold [44]. It goes beyond the standard Sudakov resummation framework by incorporating renormalon resummation in the calculation of the exponent. This has proven effective [47, 48] in extending the range of applicability of perturbation theory nearer to threshold and in identifying the relevant non-perturbative corrections in a range of applications [44–48].

<sup>4</sup>The ‘jet’ logarithms are similar to those resummed in the approach of Ref. [35]; there however ‘soft’ logarithms are not resummed.

<sup>5</sup>In Eq. (10) below the cancellation of the renormalon ambiguity involves Sudakov factor of Eq. (8), on the one hand, and  $\bar{\Lambda}$  on the other.

their ratio<sup>6</sup>:

$$\frac{d\Gamma_N(p^-, E_l)}{dp^- dE_l} \equiv \int_0^{p^-} dp^+ \left(1 - \frac{p^+}{p^-}\right)^{N-1} \frac{d\Gamma(p^+, p^-, E_l)}{dp^+ dp^- dE_l}, \tag{7}$$

where the partonic lightcone momentum components  $p^\pm$  are related to the hadronic ones by:  $p^\pm = P^\pm - \bar{\Lambda}$ , where  $\bar{\Lambda} = M_B - m_b$  is the energy of the light-degrees-of-freedom in the meson.

Note that in (7) large moment index corresponds to the limit of interest, jet kinematics: the main contribution to the integral for  $N \rightarrow \infty$  comes from the region where  $p^+/p^- \rightarrow 0$ . For large  $N$  one identifies three characteristic scales, *hard*  $\mathcal{O}(p^-)$ , *jet*  $\mathcal{O}(p^-/\sqrt{N})$  and *soft*  $\mathcal{O}(p^-/N)$ . In this limit, and up to  $1/N$  corrections, the moments *factorize* [34, 36, 39, 40] to all orders as follows<sup>7</sup>:

$$\frac{d\Gamma_N(p^-, E_l)}{dp^- dE_l} = H(p^-, E_l) \underbrace{J(p^-/\sqrt{N}, \mu) S_b(p^-/N, \mu)}_{\text{Sud}(p^-, N)} + \mathcal{O}(1/N), \tag{8}$$

where the factorization-scale ( $\mu$ ) dependence cancels *exactly* in the product in the Sudakov factor  $\text{Sud}(p^-, N)$ .

To use perturbation theory one must consider  $p^-$  large enough, such that even the ‘soft’ scale  $p^-/N$  is sufficiently large compared to the QCD scale  $\Lambda$ . This hierarchy of scales is illustrated in figure 1. Here one should note a subtle but important distinction from the shape-function approach discussed above, where it was a priori assumed that the “soft” scale (here  $p^-/N$ ) is  $\mathcal{O}(\Lambda)$ , prohibiting any perturbative treatment of the corresponding dynamical subprocess. Here instead we wish to compute  $S_b(p^-/N, \mu)$  — the quark distribution inside *an on-shell heavy quark* [52, 53] — in perturbation theory, as a basis for the description of the physical distribution, the quark distribution in the B meson  $S_B(p^-/N, \mu)$ . Because  $S_b(p^-/N, \mu)$  is infrared safe  $S_B(p^-/N, \mu)$  only differs from  $S_b(p^-/N, \mu)$  by power corrections, powers of  $N\Lambda/p^-$ . Eventually, at  $N \gg p^-/\Lambda$  all these powers become relevant, recovering the “shape function” scenario. Refs. [41–43] therefore parametrize these power corrections. It

---

<sup>6</sup>Note that we consider here the moments of the *fully differential width* [42]: the moments remain differential with respect to the large lightcone component  $p^-$  as well as the lepton energy  $E_l$ . This is essential for performing soft gluon resummation. This issue has also been discussed in Ref. [51].

<sup>7</sup>Note that this factorization formula maps directly onto eq. (5) above, where the convolution integral turns into a product in moment space.

should be noted that experimentally-relevant branching fraction are not so sensitive to the high moments, and therefore the effect of these power corrections is small. The resulting effect on  $|V_{ub}|$  is typically  $\pm 2 - 3\%$ .

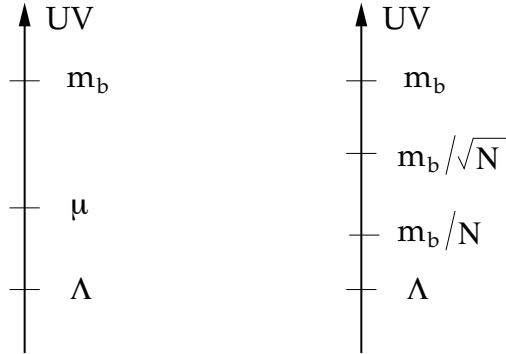


Figure 1: *The hierarchy of scales underlying factorization as conceived in a cutoff-based approach (left) vs. the moment-space resummation-based approach (right).*

Factorization facilitates the resummation of Sudakov logarithms, the corrections that dominate the dynamics at large  $N$  [34, 36, 39, 40, 51, 54, 55]. There is, however, another class of large corrections which is always important at high orders: these are running-coupling corrections, or renormalons. In the approach of Refs. [41–43] the Sudakov exponent is computed as a Borel sum, facilitating simultaneous resummation of Sudakov logarithms and running-coupling corrections. The Sudakov factor takes the form:

$$\text{Sud}(p^-, N) = \exp \left\{ \frac{C_F}{\beta_0} \int_0^\infty \frac{du}{u} \left( \frac{\Lambda}{p^-} \right)^{2u} \left[ B_S(u)G(2u, N) - B_J(u)G(u, N) \right] \right\}$$

where

$$G(u, N) = \Gamma(-u) \left( \frac{\Gamma(N)}{\Gamma(N-u)} - \frac{1}{\Gamma(1-u)} \right). \quad (9)$$

Here  $B_S(u)$  and  $B_J(u)$  are the Borel representations of the Sudakov anomalous dimensions of the quark distribution and the jet function, respectively. These

functions are known [53] to NNLO,  $\mathcal{O}(u^2)$ , facilitating Sudakov resummation with next-to-next-to-leading logarithmic accuracy [41].

Beyond that, the *analytic structure* of the integrand is indicative of power corrections. The Sudakov exponent has renormalon singularities at integer and half integer values of  $u$ , except where  $B_S, \mathcal{J}(u)$  vanish. The corresponding ambiguities, whose magnitude is determined by the residues of the poles in (9), are enhanced at large  $N$  by powers of  $N$ . They indicate the presence of non-perturbative power corrections with a similar  $N$  dependence. These power corrections *exponentiate* together with the logarithms. By evaluating the Borel integral, rather than expanding it, Refs. [41–43] make use of this additional information, defining the perturbative part of the exponent via the Principal Value (PV) prescription, and then parametrizing the dominant power corrections.

So far only non-perturbative corrections that are leading in the large  $N$  limit,  $(N\Lambda/p^-)^k$  for any  $k$ , have been taken into account in this approach. These power corrections are the non-perturbative content of the leading shape function in the approach of Sec. 5.  $\mathcal{O}(1/N)$  effects corresponding to subleading shape functions in (6) are only accounted for in Refs. [41–43] at the perturbative level. In principle, however, subleading non-perturbative effects can also be parametrized as power corrections in moment space. This would be worthwhile doing at the point where the constraints on the leading power terms would be sufficiently tight.

Moment space proves convenient for resummation and parametrization of power corrections, but at the end of the day one needs the spectrum in momentum space. The fully differential spectrum in hadronic variables is obtained by an inverse Mellin transform (*cf.* (7)):

$$\frac{d\Gamma(P^+, P^-, E_l)}{dP^+ dP^- dE_l} = \int_{c-i\infty}^{c+i\infty} \frac{dN}{2\pi i} \left(1 - \frac{p^+}{p^-}\right)^{-N} \frac{1}{p^-} \frac{d\Gamma_N(p^-, E_l)}{dp^- dE_l} \Big|_{p^\pm = P^\pm - \bar{\Lambda}} \quad (10)$$

where the integration contour runs parallel to the imaginary axis, to the right of the singularities of the integrand.

To summarize, the moment-space resummation approach of Refs. [40–43] allows to compute the fully-differential spectrum in the entire phase space as an infrared-safe quantity, without introducing any explicit cutoff scale. Non-perturbative effects are treated as power corrections, where the parameters are defined using the Principal Value prescription. This approach thus maximizes the predictive power of perturbation theory, and minimizes the role of parametrization. In the next section we shall have a quick look at the resulting

phenomenology. In particular, we will present here for the first time numerical results that are based on matching the resummation formula to  $\mathcal{O}(\beta_0\alpha_s^2)$ , incorporating the results of Ref. [32].

## 7 $|V_{ub}|$ by DGE including $\mathcal{O}(\beta_0\alpha_s^2)$ corrections

So far the calculation of the partial branching fractions from which  $|V_{ub}|$  was extracted, has been based on a NLO result: although the jet and the soft functions were resummed with NNLL accuracy, the hard coefficient function  $H(p^-, E_l)$  in (8), corresponding to constants and  $1/N$  suppressed terms at large  $N$ , was only known to NLO,  $\mathcal{O}(\alpha_s)$  [56]. In a recent paper [32] we have computed analytically the running-coupling corrections, which are the dominant corrections at the NNLO. Both real and virtual  $\mathcal{O}(\beta_0\alpha_s^2)$  corrections are now available.

Very recently I have completed the task of matching the resummed triple differential rate to the new  $\mathcal{O}(\beta_0\alpha_s^2)$  corrections, and implemented it into the DGE code. The new version of the code is available at [57]. Preliminary results based on this new version will be presented below.

Prior to describing the new results a comment is due concerning the way the partial branching fractions are computed, which has changed between the old and new implementations [57]. In the old version the triple differential width, normalized as  $1/\Gamma_0 d\Gamma/dP^+dP^-dE_l$  ( $\Gamma_0$  is the Born-level width) was integrated over the relevant phase-space, and then divided by a normalization factor corresponding to a similar integral *over the entire phase space*. In the new version, I apply the same procedure but this time evaluating at each point in phase space the (perturbatively) normalized rate  $1/\Gamma_{\text{total}}d\Gamma/dP^+dP^-dE_l$  instead of  $1/\Gamma_0d\Gamma/dP^+dP^-dE_l$ . This implies that the expression for  $\Gamma_0/\Gamma_{\text{total}}$  has been expanded, and multiplied into the hard matching coefficient. Finally the new hard matching coefficient is truncated at the required order,  $\alpha_s$  (NLO) or  $\beta_0\alpha_s^2$  (NNLO). When working at NLO this amounts to an  $\mathcal{O}(\alpha_s^2)$  difference with respect to the previous calculation, which is not small numerically (it is comparable to the  $\beta_0\alpha_s^2$  term, and has the opposite sign). The new formulation is theoretically favored as it leads to smaller renormalization-scale dependence<sup>8</sup>.

---

<sup>8</sup>Renormalization scale dependence appears in our formulation only through the hard matching coefficients, as running coupling corrections are resummed in the jet and soft functions.

Table 1: Computed values of  $R_{\text{cut}}$  for different experimentally relevant cuts. For  $R_{\text{cut}}^{\text{NLO}}$  we present the central value only, while for  $R_{\text{cut}}^{\text{NNLO}}$  the errors are broken into (an asymmetric) theory error (which includes parametric uncertainty in the input value of  $\alpha_s$ ; renormalization scale uncertainty; power corrections associated with the quark distribution function; and Weak Annihilation effect) and parametric uncertainty in the input value of  $m_b$  according to (11).

cut	Ref.	$R_{\text{cut}}^{\text{NLO}}$	$R_{\text{cut}}^{\text{NNLO}}$
$E_l > 2.1 \text{ GeV}$	[19]	0.229	$0.219^{+0.030}_{-0.009} {}^{+0.020}_{-0.022}(m_b)$
$m_X < 1.7 \text{ GeV}; q^2 > 8 \text{ GeV}$	[20]	0.376	$0.365^{+0.035}_{-0.021} {}^{+0.027}_{-0.015}(m_b)$
$E_l > 1.9 \text{ GeV}$	[21]	0.387	$0.374^{+0.025}_{-0.014} {}^{+0.016}_{-0.026}(m_b)$
$E_l > 2.0 \text{ GeV}$	[22]	0.309	$0.295^{+0.032}_{-0.010} {}^{+0.022}_{-0.017}(m_b)$
$E_l > 2.0 \text{ GeV}; S_h^{\text{max}} < 3.5 \text{ GeV}^2$	[23]	0.233	$0.228^{+0.031}_{-0.013} {}^{+0.021}_{-0.011}(m_b)$
$E_l > 1.0 \text{ GeV}; m_X < 1.7 \text{ GeV}$	[24]	0.653	$0.633^{+0.037}_{-0.047} {}^{+0.054}_{-0.063}(m_b)$
$E_l > 1.0 \text{ GeV}; m_X < 1.55 \text{ GeV}$	[25]	0.559	$0.535^{+0.049}_{-0.051} {}^{+0.066}_{-0.070}(m_b)$

Using the 2007 PDG value for the short-distance b-quark mass,

$$m_b^{\overline{\text{MS}}} = 4.20 \pm 0.07 \text{ GeV} \tag{11}$$

I have computed the normalized partial widths

$$R_{\text{cut}} = \frac{\Gamma(\bar{B} \rightarrow X_u l \bar{\nu}; \text{cut})}{\Gamma_{\text{total}}(\bar{B} \rightarrow X_u l \bar{\nu})} \tag{12}$$

for the specific cuts used by the HFAG [33] to extract  $|V_{ub}|$  based on the measurements in [19–25]. The results are summarized in table 1.

As shown in table 1 a significant contribution to the uncertainty is due to the parametric dependence on  $m_b$  for which we have taken the conservative range of (11). Other uncertainties we take into account (all summed up in quadrature in table 1) are:

- Parametric uncertainty in the input value of  $\alpha_s$ , where we take  $\alpha_s^{\overline{\text{MS}}}(M_Z) = 0.1176 \pm 0.020$ .
- Power corrections associated with the quark distribution function, estimated by varying the  $u = 3/2$  renormalon residue as well as the power terms based on the parametrization presented in Sec. 4.3 in [43]. We take  $(C_{3/2}, f^{\text{PV}}) = (1, 0)$  as default and determine the uncertainty by considering the case  $(C_{3/2}, f^{\text{PV}}) = (6.2, 0.3)$ .
- Weak Annihilation effect. We assume that Weak Annihilation effects can increase the width by up to 2%. This error is taken as unidirectional.
- The residual dependence on  $\mu$  in the matching coefficient is used to estimate higher-order perturbative corrections. We vary it from  $\mu = m_b/2$  to  $\mu = 2m_b$ , where the central value is taken at  $\mu = m_b$ .

Note that the NNLO result for each of the cuts is consistent within errors with the NLO one. For NLO we only quote the central values; the errors are similar to those at NNLO. In particular, considering here the normalized  $R_{\text{cut}}$  computed by integrating  $1/\Gamma_{\text{total}} d\Gamma/dP^+ dP^- dE_l$  the renormalization-scale dependence is low already at NLO (for most cuts it is 1–3%, and in the worse case ( $m_X < 1.55$ ) it is 5%) and there is no significant improvement going to NNLO.

Next, to extract  $|V_{ub}|$  the experimental partial branching fractions [19–25] can be directly compared to the theoretical calculation:

$$\Delta\mathcal{B}(\bar{B} \rightarrow X_u l \bar{\nu}; \text{cut}) = \tau_B \times \Gamma_{\text{total}}(\bar{B} \rightarrow X_u l \bar{\nu}) \times R_{\text{cut}}. \quad (13)$$

Using the calculation of Sec. 2 in [42] with PDG value of  $m_b$  (11) we get the following value for the total width:

$$\frac{1}{|V_{ub}|^2} \Gamma_{\text{total}}(\bar{B} \rightarrow X_u l \bar{\nu}) = 67.3 \pm 5.4 \text{ps}^{-1}. \quad (14)$$

Using the updated world average value of the B-meson life time,  $\tau_B = 1.573$  ps, together with (14) and the  $R_{\text{cut}}$  values of table 1 we obtain for  $|V_{ub}|$  the values quoted in table 2.

Note that the uncertainty in the total width is dominated by  $m_b$  and it is therefore fully correlated with the parametric uncertainty associated with  $m_b$  in  $R_{\text{cut}}$ . This is taken into account in the parametric uncertainty quoted in Table 2. Because the effect of changing  $m_b$  on  $R_{\text{cut}}$  acts in the same direction as in the total width, their product, which enters the determination of  $|V_{ub}|$

Table 2: *Extracted values of  $|V_{ub}|$  based on the measured partial branching fractions (see quoted references), using Eq. (13) with the  $R_{\text{cut}}$  values of table 1 and the total width of Eq. (14). The errors quoted for NNLO are experimental (statistic and systematic raised in quadrature); theoretical, through  $R_{\text{cut}}$ ; and parametric dependence on  $m_b$  in both the total width and through  $R_{\text{cut}}$ .*

cut	Ref.	$ V_{ub} $ NLO	$ V_{ub} $ NNLO
$E_l > 2.1 \text{ GeV}$	[19]	3.68	$3.76 \pm 0.44(\text{exp})_{-0.20}^{+0.09}(\text{th})_{-0.30}^{+0.37}(m_b)$
$m_X < 1.7 \text{ GeV}; q^2 > 8 \text{ GeV}^2$	[20]	4.30	$4.37 \pm 0.46(\text{exp})_{-0.16}^{+0.06}(\text{th})_{-0.32}^{+0.28}(m_b)$
$E_l > 1.9 \text{ GeV}$	[21]	4.55	$4.62 \pm 0.43(\text{exp})_{-0.12}^{+0.08}(\text{th})_{-0.28}^{+0.37}(m_b)$
$E_l > 2.0 \text{ GeV}$	[22]	4.18	$4.28 \pm 0.29(\text{exp})_{-0.16}^{+0.08}(\text{th})_{-0.31}^{+0.31}(m_b)$
$E_l > 2.0 \text{ GeV}; S_h^{\text{max}} < 3.5 \text{ GeV}^2$	[23]	4.22	$4.27 \pm 0.29(\text{exp})_{-0.20}^{+0.07}(\text{th})_{-0.34}^{+0.29}(m_b)$
$E_l > 1.0 \text{ GeV}; m_X < 1.7 \text{ GeV}$	[24]	4.23	$4.30 \pm 0.28(\text{exp})_{-0.08}^{+0.10}(\text{th})_{-0.33}^{+0.42}(m_b)$
$E_l > 1.0 \text{ GeV}; m_X < 1.55 \text{ GeV}$	[25]	4.47	$4.56 \pm 0.22(\text{exp})_{-0.10}^{+0.13}(\text{th})_{-0.43}^{+0.53}(m_b)$

in (13), is highly sensitive to  $m_b$ . This is clearly reflected in the parametric uncertainty quoted in the table. It is also illustrated in figure 2.

Examining the values of  $|V_{ub}|$  corresponding to different cuts one observes very good agreement. Even ignoring the theoretical and parametric uncertainties (which are correlated), they all agree very well. There is one case where the agreement is not as striking: this is the CLEO result of Ref. [19] where the central value falls below all other determinations; note however the large experimental error quoted.

Averaging the results<sup>9</sup> in table 2 we obtain

$$|V_{ub}| = \left( 4.31 \pm 0.16(\text{exp})_{-0.15}^{+0.09}(\text{th})_{-0.33}^{+0.36}(m_b) \right) \cdot 10^{-3}. \quad (15)$$

This result can be compared with other theoretical methods used to compute the partial widths (we only refer here to the two other methods that have

<sup>9</sup>Note that in this average we have neglected several correlations, assuming normal distributions. A proper updated average is being prepared by the HFAG.

been discussed above; HFAG [33] presents additional results). The HQE-based parametrization of Ref. [31] yields an average [33]

$$|V_{ub}| = \left( 3.94 \pm 0.15(\text{exp})_{-0.23}^{+0.20}(\text{th}) \right) \cdot 10^{-3}, \quad (16)$$

while the shape-function approach of Refs. [34, 35] yields [58]

$$|V_{ub}| = \left( 4.31 \pm 0.17(\text{exp}) \pm 0.35(\text{th}) \right) \cdot 10^{-3}, \quad (17)$$

where in all cases we quoted the numbers corresponding to the central value of Eq. (11) — because of the strong  $m_b$  dependence this requirement is essential for any valuable comparison. For the average value one finds very good agreement between (15) and (17) and compatibility with (16). We note that for the  $m_X$ -based cuts there is better agreement between the methods of Ref. [31] and Ref. [58], which both yield somewhat lower central values for  $|V_{ub}|$  ( $|V_{ub}| \simeq 4.0 \cdot 10^{-3}$  [33, 58] for the above  $m_b$ ) as compared to the DGE approach.

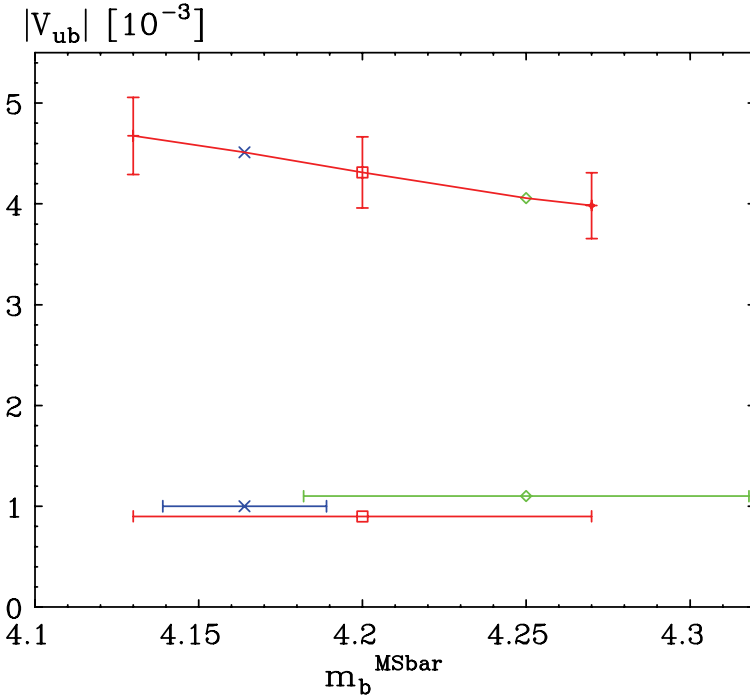


Figure 2: The extracted value of  $|V_{ub}|$ , averaged over different measurements with different kinematic cuts, as function of the  $b$  quark mass,  $m_b^{\overline{\text{MS}}}$ . The quark mass serves as an input to the calculation of the partial width; it affects the partial width through the total width,  $\sim m_b^5$ , and through  $R_{\text{cut}}$ , both acting in the same direction. The calculation of  $R_{\text{cut}}$  is done by DGE including  $\mathcal{O}(\beta_0\alpha_s^2)$  NNLO corrections. The vertical error bars are based on the remaining sources of uncertainty, theoretical and experimental, added in quadrature. The wide red horizontal bar at the bottom shows the 1-sigma range of the PDG world average value (11) setting the range of  $m_b$  values we consider. Just above it we present two specific determinations of the mass: the one extending to the right (green) based on a HQE-based fit to inclusive moments of  $b \rightarrow c$  decays [11, 12], converted to  $\overline{\text{MS}}$  [58], and the other (blue) based on a recent precise determination [59] using the total cross section in  $e^+e^- \rightarrow \text{hadrons}$  near the bottom production threshold.

## 8 Conclusions

I have given an overview of the main theoretical approaches used to compute the triple differential spectra in order to extract of  $|V_{ub}|$  from data. I have mainly emphasized the conceptual differences and the relations between the approaches, but I also reported briefly on their status, their formal accuracy and their particular sources of uncertainty.

It is evident that despite making different approximations, the various determinations are consistent with each other. Add to that the remarkable consistency between different measurements that use different kinematics cuts — which provides a valuable confirmation for the theoretical description of the spectrum — the conclusion is clear: the inclusive determination of  $|V_{ub}|$  is robust. This puts us on firm grounds coming to examine the consistency of the CKM mechanism.

Finally, the single most important source of uncertainty in the inclusive determination of  $|V_{ub}|$  is the b-quark mass. The dependence on the mass is extremely high owing to the fact that both the total width and the cut-dependence increase with increasing  $m_b$ . The effect this has on  $|V_{ub}|$  is shown in figure 2. Clearly, improving our knowledge of the b-quark mass would directly translate into more precise  $|V_{ub}|$ .

Before concluding I find it appropriate to add a few words about the field. Beyond their obvious significance to phenomenology, inclusive B decays are a remarkable source of interesting theoretical problems in QCD. We have only scratched the surface of this exciting field in this talk.

Inclusive decay are also very challenging experimentally, and although the experimental issues have not been mentioned here, it is obvious that there would not have been much point in giving this talk if not for the remarkable achievements of the B factories in this area. The on-going discussion between theory and experiment has also been extremely fruitful, and I would like to thank all those who have contributed to that.

## References

1. G. Isidori, “Flavour Physics: Now and in the LHC era,” arXiv:0801.3039 [hep-ph].
2. S. Hashimoto *et al.*, “Letter of intent for KEK Super B Factory,”
3. M. Bona *et al.*, “SuperB: A High-Luminosity Asymmetric  $e^+ e^-$  Super Flavor Factory. Conceptual Design Report,” arXiv:0709.0451 [hep-ex].

4. T. Browder, M. Ciuchini, T. Gershon, M. Hazumi, T. Hurth, Y. Okada and A. Stocchi, "On the Physics Case of a Super Flavour Factory," JHEP **0802** (2008) 110 [arXiv:0710.3799 [hep-ph]].
5. F. Muheim, Nucl. Phys. Proc. Suppl. **170** (2007) 317 [arXiv:hep-ex/0703006].
6. J. Charles *et al.* [CKMfitter Group], *Eur. Phys. J.* **C41** (2005) 1 [hep-ph/0406184].  
<http://www.slac.stanford.edu/xorg/ckmfitter/>
7. M. Bona *et al.* [UTfit Collaboration], JHEP **0603** (2006) 080 [hep-ph/0509219] <http://utfit.roma1.infn.it/>.
8. E. Dalgic, A. Gray, M. Wingate, C. T. H. Davies, G. P. Lepage and J. Shigemitsu, "B Meson Semileptonic Form Factors from Unquenched Lattice QCD," Phys. Rev. D **73** (2006) 074502 [Erratum-ibid. D **75** (2007) 119906] [arXiv:hep-lat/0601021].
9. M. Okamoto *et al.*, "Semileptonic  $D \rightarrow \pi / K$  and  $B \rightarrow \pi / D$  decays in 2+1 flavor lattice QCD," Nucl. Phys. Proc. Suppl. **140** (2005) 461 [arXiv:hep-lat/0409116].
10. P. Ball and R. Zwicky, "New results on  $B \rightarrow \pi, K, \eta$  decay formfactors from light-cone sum rules," Phys. Rev. D **71** (2005) 014015 [arXiv:hep-ph/0406232].
11. O. Buchmuller and H. Flacher, Phys. Rev. D **73** (2006) 073008 [arXiv:hep-ph/0507253].
12. O. Buchmuller and H. Flacher, "Update of Fit to Moments of Inclusive  $B \rightarrow X_c l \bar{\nu}$  and  $B \rightarrow X_s \gamma$  Decay Distributions for LP07", prepared for LEPTON - PHOTON 2007(LP07) XXIII International Symposium on Lepton and Photon Interactions at High Energy, Aug 13-18, Daegu, Korea.
13. M. Nakao, "Overview of measurements of inclusive distributions and moments in  $B \rightarrow X_c l \nu$  Decays, Results of OPE fits in different schemes", Joint workshop on  $|V_{ub}|$  &  $|V_{cb}|$  at the B-Factories, Heidelberg, December 14-16, 2007.
14. V. Aquila, P. Gambino, G. Ridolfi and N. Uraltsev, "Perturbative corrections to semileptonic b decay distributions," Nucl. Phys. B **719**, 77 (2005) [arXiv:hep-ph/0503083].

15. K. Melnikov, “ $\mathcal{O}(\alpha_s^2)$  corrections to semileptonic decay  $b \rightarrow c l \bar{\nu}_l$ ,” arXiv:0803.0951 [hep-ph].
16. A. Pak and A. Czarnecki, “Mass effects in muon and semileptonic  $b \rightarrow c l \bar{\nu}_l$  decays,” arXiv:0803.0960 [hep-ph].
17. B. M. Dassinger, T. Mannel and S. Turczyk, “Inclusive semi-leptonic B decays to order  $1/m(b)^2$ ,” JHEP **0703**, 087 (2007) [arXiv:hep-ph/0611168].
18. T. Becher, H. Boos and E. Lunghi, “Kinetic corrections to  $B \rightarrow X_c \ell \bar{\nu}$  at one loop,” JHEP **0712** (2007) 062 [arXiv:0708.0855 [hep-ph]].
19. A. Bornheim *et al.* [CLEO Collaboration], “Improved measurement of  $|V_{ub}|$  with inclusive semileptonic B decays,” Phys. Rev. Lett. **88** (2002) 231803 [arXiv:hep-ex/0202019].
20. H. Kakuno *et al.* [BELLE Collaboration], “Measurement of  $|V_{ub}|$  using inclusive  $B \rightarrow X_u l \nu$  decays with a novel X/u reconstruction method,” Phys. Rev. Lett. **92** (2004) 101801 [arXiv:hep-ex/0311048].
21. A. Limosani *et al.* [Belle Collaboration], “Measurement of inclusive charmless semileptonic B-meson decays at the endpoint of the electron momentum spectrum,” Phys. Lett. B **621** (2005) 28 [arXiv:hep-ex/0504046].
22. B. Aubert *et al.* [BABAR Collaboration], “Measurement of the inclusive electron spectrum in charmless semileptonic B decays near the kinematic endpoint and determination of  $-V(ub)$ ,” Phys. Rev. D **73** (2006) 012006 [arXiv:hep-ex/0509040].
23. B. Aubert *et al.* [BABAR Collaboration], “Determination of  $|V_{ub}|$  from measurements of the electron and neutrino momenta in inclusive semileptonic B decays,” Phys. Rev. Lett. **95** (2005) 111801 [Erratum-ibid. **97** (2006) 019903] [arXiv:hep-ex/0506036].
24. I. Bizjak *et al.* [Belle Collaboration], “Measurement of the inclusive charmless semileptonic partial branching fraction of B mesons and determination of  $|V_{ub}|$  using the full reconstruction tag,” Phys. Rev. Lett. **95** (2005) 241801 [arXiv:hep-ex/0505088].
25. B. Aubert *et al.* [BABAR Collaboration], “Measurements of Partial Branching Fractions for  $B \rightarrow X_u l \bar{\nu}$  and Determination of  $|V_{ub}|$ ,” Phys. Rev. Lett. **100** (2008) 171802 [arXiv:0708.3702 [hep-ex]].

26. I. I. Y. Bigi, M. A. Shifman, N. G. Uraltsev and A. I. Vainshtein, “On The Motion Of Heavy Quarks Inside Hadrons: Universal Distributions And *Int. J. Mod. Phys. A* **9**, 2467 (1994) [hep-ph/9312359].
27. M. Neubert, “Analysis of the photon spectrum in inclusive  $B \rightarrow X(s)$  gamma decays,” *Phys. Rev. D* **49** (1994) 4623 [hep-ph/9312311].
28. B. O. Lange, M. Neubert and G. Paz, “A two-loop relation between inclusive radiative and semileptonic B decay spectra,” *JHEP* **0510** (2005) 084 [arXiv:hep-ph/0508178].
29. B. O. Lange, “Shape-function independent relations of charmless inclusive B-decay spectra,” *JHEP* **0601** (2006) 104 [arXiv:hep-ph/0511098].
30. K. S. M. Lee, “Subleading Shape-Function Effects and the Extraction of  $|V_{ub}|$ ,” arXiv:0802.0873 [hep-ph].
31. P. Gambino, P. Giordano, G. Ossola and N. Uraltsev, “Inclusive semileptonic B decays and the determination of  $|V_{ub}|$ ,” *JHEP* **0710** (2007) 058 [arXiv:0707.2493 [hep-ph]].
32. P. Gambino, E. Gardi and G. Ridolfi, “Running-coupling effects in the triple-differential charmless semileptonic decay width,” *JHEP* **0612**, 036 (2006) [arXiv:hep-ph/0610140].
33. The Heavy Flavor Averaging Group (HFAG) update for the Particle Data Group 2008,  
<http://www.slac.stanford.edu/xorg/hfag/semi/pdg08/home.shtml>
34. S. W. Bosch, B. O. Lange, M. Neubert and G. Paz, “Factorization and shape-function effects in inclusive B-meson decays,” *Nucl. Phys.* **B699** (2004) 335 [hep-ph/0402094].
35. B. O. Lange, M. Neubert and G. Paz, “Theory of charmless inclusive B decays and the extraction of  $V(ub)$ ,” *Phys. Rev.* **D72** (2005) 073006 [hep-ph/0504071].
36. C. W. Bauer, D. Pirjol and I. W. Stewart, “Soft-collinear factorization in effective field theory,” *Phys. Rev.* **D65** (2002) 054022 [hep-ph/0109045].
37. C. W. Bauer, D. Pirjol and I. W. Stewart, “Power counting in the soft-collinear effective theory,” *Phys. Rev. D* **66** (2002) 054005 [arXiv:hep-ph/0205289].

38. M. Beneke, A. P. Chapovsky, M. Diehl and T. Feldmann, “Soft-collinear effective theory and heavy-to-light currents beyond leading power,” *Nucl. Phys. B* **643** (2002) 431 [arXiv:hep-ph/0206152].
39. G. P. Korchemsky and G. Sterman, “Infrared factorization in inclusive B meson decays,” *Phys. Lett. B* **340** (1994) 96 [hep-ph/9407344].
40. E. Gardi, “Radiative and semi-leptonic B-meson decay spectra: Sudakov resummation beyond logarithmic accuracy and the pole mass,” *JHEP* **0404** (2004) 049 [hep-ph/0403249].
41. J. R. Andersen and E. Gardi, “Taming the B to X/s gamma spectrum by dressed gluon exponentiation,” *JHEP* **0506** (2005) 030 [hep-ph/0502159].
42. J. R. Andersen and E. Gardi, “Inclusive spectra in charmless semileptonic B decays by dressed gluon exponentiation,” *JHEP* **0601** (2006) 097 [hep-ph/0509360].
43. J. R. Andersen and E. Gardi, “Radiative B decay spectrum: DGE at NNLO,” *JHEP* **0701** (2007) 029 [hep-ph/0609250].
44. E. Gardi, “Inclusive distributions near kinematic thresholds,” *In the Proceedings of FRIF workshop on first principles non-perturbative QCD of hadron jets, LPTHE, Paris, France, 12-14 Jan 2006, pp E003* [hep-ph/0606080].
45. E. Gardi and G. Grunberg, “A dispersive approach to Sudakov resummation,” *Nucl. Phys. B* **794** (2008) 61 [arXiv:0709.2877 [hep-ph]].
46. E. Gardi, “Dressed gluon exponentiation,” *Nucl. Phys. B* **622** (2002) 365 [hep-ph/0108222].
47. M. Cacciari and E. Gardi, “Heavy-quark fragmentation,” *Nucl. Phys. B* **664** (2003) 299 [hep-ph/0301047].
48. E. Gardi and J. Rathsman, “Renormalon resummation and exponentiation of soft and collinear gluon radiation in the thrust distribution,” *Nucl. Phys. B* **609** (2001) 123 [hep-ph/0103217]; “The thrust and heavy-jet mass distributions in the two-jet region,” *Nucl. Phys. B* **638** (2002) 243 [hep-ph/0201019].
49. E. Gardi and G. Grunberg, “Power corrections in the single dressed gluon approximation: The average *JHEP* **9911** (1999) 016 [arXiv:hep-ph/9908458].

50. U. Aglietti, F. Di Lodovico, G. Ferrera and G. Ricciardi, “Inclusive Measure of  $|V_{ub}|$  with the Analytic Coupling Model,” arXiv:0711.0860 [hep-ph].
51. U. Aglietti, G. Ricciardi and G. Ferrera, “Threshold resummed spectra in  $B \rightarrow X/u \ell \nu$  decays in NLO. III,” *Phys. Rev. D* **74** (2006) 034006 [arXiv:hep-ph/0509271];  
“Threshold resummed spectra in  $B \rightarrow X/u \ell \nu$  decays in NLO. II,” *Phys. Rev. D* **74** (2006) 034005 [arXiv:hep-ph/0509095];  
“Threshold resummed spectra in  $B \rightarrow X/u \ell \nu$  decays in NLO. I,” *Phys. Rev. D* **74** (2006) 034004 [arXiv:hep-ph/0507285].
52. G. P. Korchemsky and G. Marchesini, “Structure function for large  $x$  and renormalization of Wilson loop,” *Nucl. Phys.* **B406** (1993) 225 [hep-ph/9210281].
53. E. Gardi, “On the quark distribution in an on-shell heavy quark and its all-order relations with the perturbative fragmentation function,” *JHEP* **0502** (2005) 053 [hep-ph/0501257].
54. R. Akhouri and I. Z. Rothstein, “The Extraction of  $V_{ub}$  from Inclusive B Decays and the Resummation of *Phys. Rev.* **D54** (1996) 2349 [hep-ph/9512303].
55. U. Aglietti, “Resummed  $B \rightarrow X/u \ell \nu$  decay distributions to next-to-leading order,” *Nucl. Phys.* **B610**, 293 (2001) [hep-ph/0104020];
56. F. De Fazio and M. Neubert, “ $B \rightarrow X/u \ell \text{anti-}\nu/\ell$  decay distributions to order  $\alpha(s)$ ,” *JHEP* **9906** (1999) 017 [arXiv:hep-ph/9905351].
57. The new version of the code (Version 2.0) can be found at:  
<http://www.ph.ed.ac.uk/~egardi/b2uATnnlo.htm>
58. M. Neubert, “QCD Calculations of Decays of Heavy Flavor Hadrons,” arXiv:0801.0675 [hep-ph].
59. J. H. Kuhn, M. Steinhauser and C. Sturm, “Heavy quark masses from sum rules in four-loop approximation,” *Nucl. Phys. B* **778** (2007) 192 [arXiv:hep-ph/0702103].



**SESSION VI – CP VIOLATION AND RARE DECAYS**

<i>Gatti Claudio</i>	K decays Measurements with the KLOE Detector
<i>Voena Cecilia</i>	Measurements of CKM at the B-Factories
<i>Castilla Heriberto</i>	CPV and B <sub>s</sub> Physics at the Tevatron
<i>Goudzovski Evgueni</i>	New Results from the NA48/2 experiment at CERN SPS: Radiative Nonleptonic KAON Decays
<i>Blucher Ed</i>	e'/e with KTEV
<i>Barberio Elisabetta</i>	Semileptonic B Decays and Measurements of CKM Elements at B Factories



## K DECAY MEASUREMENTS WITH THE KLOE DETECTOR

Claudio Gatti\*

*Laboratori Nazionali di Frascati Via E.Fermi, 40 00044 Frascati (Rome) Italy*

### Abstract

KLOE has measured most decay branching ratios of  $K_S$ ,  $K_L$  and  $K^\pm$ -mesons. It has also measured the  $K_L$  and the  $K^\pm$  lifetime and determined the shape of the form factors involved in kaon semileptonic decays. I present here a short description of these measurements, the determination of the CKM parameter  $|V_{us}|$  and a test of the unitarity of the quark flavor matrix. I will also discuss the test of the lepton universality and new bounds on new physics based on KLOE results.

---

for the KLOE collaboration: F. Ambrosino, A. Antonelli, M. Antonelli, F. Archilli, C. Bacci, P. Beltrame, G. Bencivenni, S. Bertolucci, C. Bini, C. Bloise, S. Bocchetta, F. Bossi, P. Branchini, R. Caloi, P. Campana, G. Capon, T. Capussela, F. Ceradini, F. Cesario, S. Chi, G. Chiefari, P. Ciambrone, F. Crucianelli, E. De Lucia, A. De Santis, P. De Simone, G. De Zorzi, A. Denig, A. Di Domenico, C. Di Donato, B. Di Micco, A. Doria, M. Dreucci, G. Felici, A. Ferrari, M. L. Ferrer, S. Fiore, C. Forti, P. Franzini, C. Gatti, P. Gauzzi, S. Giovannella, E. Gorini, E. Graziani, W. Kluge, V. Kulikov, F. Lacava, G. Lanfranchi, J. Lee-Franzini, D. Leone, M. Martemianov, M. Martini, P. Massarotti, W. Mei, S. Meola, S. Miscetti, M. Moulson, S. Müller, F. Murtas, M. Napolitano, F. Nguyen, M. Palutan, E. Pasqualucci, A. Passeri, V. Patera, F. Perfetto, M. Primavera, P. Santangelo, G. Saracino, B. Sciascia, A. Sciubba, A. Sibidanov, T. Spadaro, M. Testa, L. Tortora, P. Valente, G. Venanzoni, R. Versaci, G. Xu.

## 1 Introduction

In the Standard Model (SM), the coupling of the  $W$  boson to the weak charged current is written as

$$\frac{g}{\sqrt{2}}W_\alpha^+ (\bar{U}_L V_{CKM} \gamma^\alpha D_L + \bar{e}_L \gamma^\alpha \nu_{eL} + \bar{\mu}_L \gamma^\alpha \nu_{\mu L} + \bar{\tau}_L \gamma^\alpha \nu_{\tau L}) + \text{h.c.}, \quad (1)$$

where  $U^T = (u, c, t)$ ,  $D^T = (d, s, b)$  and  $L$  is for left-handed. In the coupling above there is only one coupling constant for leptons and quarks. Quarks are mixed by the CKM matrix,  $V_{CKM}$ , which must be unitary. We can test these two predictions by comparing results from precise measurements of leptonic and semileptonic kaon decays, with pion leptonic and nuclear  $\beta$  decays. The semileptonic decay rates are given by:

$$\Gamma(K_{\ell 3}(\gamma)) = \frac{C_K^2 G_F^2 M_K^5}{192\pi^3} S_{EW} |V_{us}|^2 |f_+(0)|^2 I_{K\ell} (1 + \delta_K^{SU(2)} + \delta_{K\ell}^{EM})^2, \quad (2)$$

where the index  $K$  denotes  $K^0 \rightarrow \pi^\pm$  and  $K^\pm \rightarrow \pi^0$  transitions, and  $C_K = 1$  and  $1/2$  respectively.  $S_{EW}$  is the universal short-distance electroweak correction <sup>1)</sup> and  $\ell = e, \mu$ . Assuming lepton universality, the muon decay rate provides the value of the Fermi constant,  $G_F = 1.16637(1) \times 10^{-5} \text{ GeV}^{-2}$ . The mode dependence is contained in the  $\delta$  terms: the long-distance electromagnetic and the  $SU(2)$ -breaking corrections <sup>2)</sup>.  $I_{K\ell}$  is the integral of the Dalitz-plot density over the physical region for non radiative decays. This integral depends on the reduced form factors,  $\hat{f}_+(t)$  and  $\hat{f}_0(t)$ , while the value at zero momentum transfer,  $f_+(0)$ , appears explicitly in the above formula. The ratio of  $K$  to  $\pi$  leptonic decay widths is given by:

$$\frac{\Gamma K_{\mu 2}(\gamma)}{\Gamma \pi_{\mu 2}(\gamma)} = \frac{|V_{us}|^2 f_K^2}{|V_{ud}|^2 f_\pi^2} \frac{m_K (1 - m_\mu^2/m_K^2)^2}{m_\pi (1 - m_\mu^2/m_\pi^2)^2} (0.9930 \pm 0.0035), \quad (3)$$

where  $f_K$  and  $f_\pi$  are the kaon and pion decay constants. Radiative corrections have been evaluated in <sup>3)</sup> and <sup>4)</sup>.

In the following I will briefly describe the KLOE measurements of the main kaon branching ratios (BRs), kaon lifetimes, and of the parameters of the form factors. These are the experimental inputs needed to determine the kaon leptonic and semileptonic decay widths. These measurements are based on an integrated luminosity  $\mathcal{L} \sim 500 \text{ pb}^{-1}$  corresponding to about 500 million  $K_S K_L$  produced. At KLOE,  $K_S$ - $K_L$  and  $K^+$ - $K^-$  pairs are produced from  $\phi$  decays almost at rest. Therefore, the detection of a  $K_S$  ( $K^+$ ) signals the presence of, "tags", a  $K_L$  ( $K^-$ ) and vice versa. We determine absolute BRs either by measuring all the main kaon BRs, such that  $1 - \sum_i BR_i < 5 \times 10^{-4}$ , or by normalizing the number of signal events to the number of tagged kaons. All

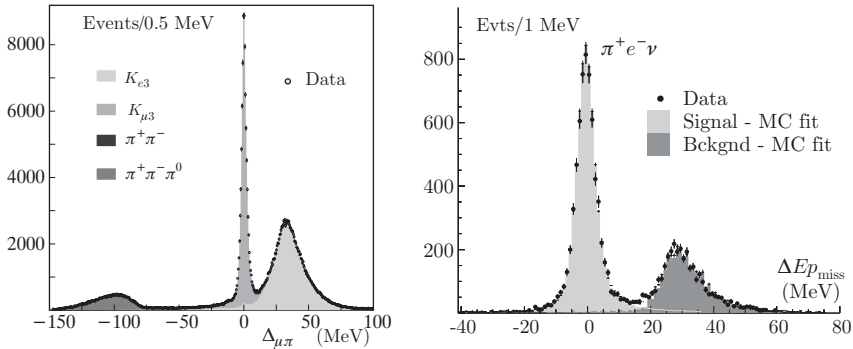


Figure 1: *Left: Distribution of  $\Delta_{\mu\pi}$  for a subsample of  $K_L$  decays leaving two tracks in the DC. Right: Distribution of  $E_{miss} - p_{miss}$  for candidate  $K_S \rightarrow \pi e \nu$  events.*

the measurements are done taking into account the presence of radiation in the final state, which is included in the Monte Carlo simulation <sup>5)</sup>.

## 2 $K^0$ decays

### 2.1 BR's and lifetime

We have measured the main  $K_L$  BRs from a sample of  $13 \times 10^6$  kaons tagged by detection of  $K_S \rightarrow \pi^+\pi^-$  decays <sup>6)</sup>.  $K_L \rightarrow 3\pi^0$  decays are identified by the presence of multiple photons reaching the calorimeter. We detect  $K_L$  decays to charged modes ( $\pi e \nu$ ,  $\pi \mu \nu$  and  $\pi^+\pi^-\pi^0$ ) by the observation of two tracks forming a vertex along the  $K_L$  path. We distinguish different decay modes by use of the smaller absolute value of the possible values of  $\Delta_{\mu\pi} = |p_{miss}| - E_{miss}$ , where  $p_{miss}$  and  $E_{miss}$  are the missing momentum and energy assuming the decay is into  $\pi^+\mu^-\bar{\nu}$  or  $\pi^-\mu^+\nu$  (Fig. 1). The geometrical efficiency for detecting  $K_L$  in the fiducial volume depends on the  $K_L$  lifetime,  $\tau_L$ . Combining this information with the condition that the sum of all BRs must equal unity, we determine the  $K_L$  lifetime and main BRs. An independent measurement of the  $K_L$  lifetime is obtained by measuring the proper decay-time distribution for  $K_L \rightarrow 3\pi^0$  events <sup>7)</sup>. These measurements are combined in a fit to determine the  $K_L$  BRs and lifetime. We also use the KLOE measurements for the decays  $K_L \rightarrow \pi^+\pi^-$  <sup>8)</sup> and  $K_L \rightarrow \gamma\gamma$  <sup>9)</sup>. The results of the fit are shown in Tab. 1. All the correlations have been taken into account. The only non-KLOE input

Table 1: *KLOE measurements of principal  $K_L$  BRs and  $\tau_L$ .*

Parameter	Value
$\text{BR}(K_{e3})$	0.4008(15)
$\text{BR}(K_{\mu3})$	0.2699(14)
$\text{BR}(3\pi^0)$	0.1996(20)
$\text{BR}(\pi^+\pi^-\pi^0)$	0.1261(11)
$\text{BR}(\pi^+\pi^-)$	$1.964(21)\times 10^{-3}$
$\text{BR}(\pi^0\pi^0)$	$8.49(9)\times 10^{-4}$
$\text{BR}(\gamma\gamma)$	$5.57(8)\times 10^{-4}$
$\tau_L$	50.84(23)ns

to the fit is the 2006 PDG ETAFIT result for  $\text{BR}(K_L \rightarrow \pi^0\pi^0)/\text{BR}(K_L \rightarrow \pi^+\pi^-) = 0.4391 \pm 0.0013$ .

We have measured the ratio  $\text{BR}(K_S \rightarrow \pi e\nu)/\text{BR}(K_S \rightarrow \pi^+\pi^-)$  <sup>11)</sup> separately for each lepton charge.  $K_{e3}$  events are selected by time of flight (TOF) and by a fit to the  $E_{\text{miss}} - p_{\text{miss}}$  distribution (Fig. 1). Combining this measurement with the value of  $\text{BR}(K_S \rightarrow \pi^+\pi^-)/\text{BR}(K_S \rightarrow \pi^0\pi^0)$  from a separate KLOE analysis <sup>10)</sup>, we determine the semileptonic branching ratio  $\text{BR}(K_S \rightarrow \pi e\nu) = (7.046 \pm 0.091) \times 10^{-4}$ .

## 2.2 Form Factors

We have measured the form factor parameters both for  $K_{e3}$  <sup>12)</sup> and  $K_{\mu3}$  <sup>13)</sup> decays. In the first case, we select a pure sample of 2 million  $K_L \rightarrow \pi e\nu$ .  $\pi$ -e separation is performed using TOF, allowing us to determine the transferred momentum  $t = (p_K - p_\pi)^2$ . The form factor parameters are then obtained from a fit to the  $t$  distribution. Since the particle identification with TOF for  $K_{\mu3}$  events is much less effective, we extract the parameters from a fit to the neutrino momentum spectrum,  $p_\nu = p_K - p_\pi - p_\mu$ , which doesn't depend on the mass assignment of the particles in the final state. The loss in sensitivity due to this choice is recovered when  $K_{e3}$  and  $K_{\mu3}$  data are fit simultaneously. The measurement is performed with about 1.7 million  $K_{\mu3}$  selected events. The results for the combined fit to  $K_{e3}$  and  $K_{\mu3}$  events are shown in Tab. 2.

## 3 $K^\pm$ decays

### 3.1 BR's and lifetime

We measure  $\text{BR}(K^+ \rightarrow \mu\nu)$  <sup>14)</sup> and  $\text{BR}(K^+ \rightarrow \pi^+\pi^0)$  <sup>15)</sup> from 4 million  $K^- \rightarrow \mu\bar{\nu}$  decays used as tags. The number of signal events is obtained from the

Table 2: *KLOE* measurement for the form factor parameters. The non-diagonal elements of the correlation matrix are also shown.

Parameter	Value		
$\lambda_+^V$	$25.6(1.7) \times 10^{-3}$	-0.95	0.29
$\lambda_+^A$	$1.5(0.8) \times 10^{-3}$		-0.38
$\lambda_0$	$15.4(2.2) \times 10^{-3}$		

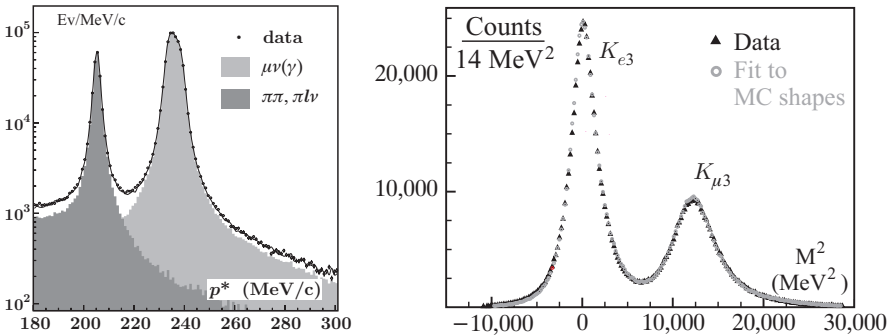


Figure 2: Left: Distribution of  $p^*$ , the charged momentum in the kaon rest frame, for  $K^\pm$  decays. The solid line is the sum of all contributions, in gray, from data control samples. Right: Distribution for  $m_\ell^2$ , from TOF information, for  $K_{\ell 3}^\pm$  events.

distribution of the  $p^*$ , the secondary particle momentum in the kaon rest frame in the pion hypothesis (Fig. 2). We obtain  $\text{BR}(K^+ \rightarrow \mu^+ \nu) = 0.6366(17)$  and  $\text{BR}(K^+ \rightarrow \pi^+ \pi^0) = 0.2065(94)$ . The BRs for semileptonic decays are measured from 60 million tagged events, for both kaon charges. Signal events are selected by first removing two-body decays, then by reconstructing the squared lepton mass,  $m_\ell^2$ , from the TOF of leptons and photons. We count the number of signal events from the distribution of  $m_\ell^2$  (Fig. 2). The measured BRs depend on the kaon lifetime,  $\tau_\pm$ , through the geometrical acceptance. Therefore, we have measured  $\tau_\pm$  from a sample of 12 million tagged kaons <sup>16</sup>). This is done using two methods. In the first method, we obtain the decay time from the kaon path length in the drift chamber, accounting for the continuous change in the kaon velocity due to the ionization energy loss. In the second method, the decay time is directly measured from the TOF of photons from  $\pi^0$  decays.

Table 3: *KLOE measurements of  $K^\pm$  semileptonic decays and lifetime.*

Parameter	Value		
BR( $K_{e3}$ )	0.04972(53)	0.63	-0.10
BR( $K_{\mu3}$ )	0.03237(39)		-0.09
$\tau_\pm$	12.347(30) ns		

The final results for lifetime and semileptonic BRs are shown in Tab. 3.

#### 4 Test of CKM unitarity and bounds on new physics

Combining all the KLOE results for semileptonic decays and lifetimes, we obtain

$$|f_+(0)V_{us}| = 0.2157 \pm 0.0006. \quad (4)$$

The only external experimental input to this analysis is the  $K_S$  lifetime. Comparison of the value of  $|f_+(0)V_{us}|$  for  $K_{e3}$  and  $K_{\mu3}$  modes provides a test of lepton universality

$$r_{\mu e} = \frac{|f_+(0)V_{us}|_{\mu3}^2}{|f_+(0)V_{us}|_{e3}^2}. \quad (5)$$

Averaging between charged and neutral modes, we find

$$r_{\mu e} = 1.000 \pm 0.008. \quad (6)$$

The sensitivity of this result may be compared with that obtained from pion and tau decays, about 0.004.

Using lattice evaluation of  $f_+(0)$  (17) and of  $f_K/f_\pi$  (18), a recent evaluation of  $|V_{ud}|$  (19) from  $0^+ \rightarrow 0^+$  nuclear beta decays, and using  $\Gamma(\pi_{\mu2})$  (20), we test the unitarity relation combining in a fit these values with the KLOE measurements of leptonic and semileptonic decay rates. The fit result ( $\chi^2/ndf = 2.34/1$ ), shown in Fig. 3, confirms the unitarity of the CKM quark mixing matrix as applied to the first row. We find:

$$1 - |V_{us}|^2 - |V_{ud}|^2 = 0.0004 \pm 0.0007 \quad (7)$$

and

$$\begin{aligned} |V_{us}| &= 0.2249 \pm 0.0010 \\ |V_{ud}| &= 0.97417 \pm 0.00026. \end{aligned} \quad (8)$$

*i.e.* the unitarity condition is verified to  $\mathcal{O}(0.1\%)$ .

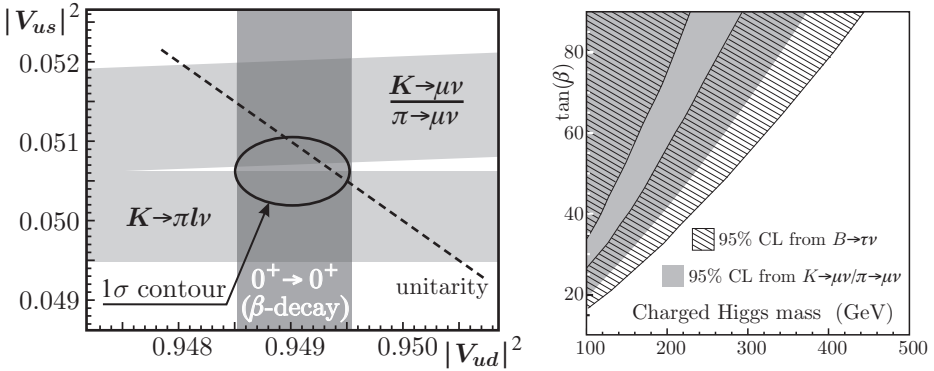


Figure 3: *Left: KLOE results for  $|V_{us}|^2$ ,  $|V_{us}|/|V_{ud}|^2$  and  $|V_{ud}|^2$  from  $\beta$ -decay measurements. The ellipse is the  $1\sigma$  contour from the fit. The unitarity constraint is illustrated by the dashed line. Right: Region in the  $m_{H^+} - \tan\beta$  plane excluded by our result from  $R_{\ell 23}$ ; the region excluded by measurements of  $BR(B \rightarrow \tau \nu)$  is also shown.*

A particularly interesting test is the comparison between the values of  $|V_{us}|$  obtained from helicity-suppressed  $K_{\ell 2}$  decays and helicity-allowed  $K_{\ell 3}$  decays. The quantity

$$R_{\ell 23} = \left| \frac{V_{us}(K_{\mu 2})}{V_{us}(K_{\ell 3})} \times \frac{V_{ud}(0^+ \rightarrow 0^+)}{V_{ud}(\pi_{\mu 2})} \right| \tag{9}$$

is unity in the SM, but would be affected by the presence of non-vanishing scalar or right-handed currents. We obtain:

$$R_{\ell 23} = 1.008 \pm 0.008, \tag{10}$$

in agreement with the SM prediction. This measurement places bounds on the charged Higgs mass and  $\tan\beta$  <sup>21)</sup>, as shown in Fig. 3.

### 5 Conclusions

KLOE has measured with very good accuracy all the main  $K_S$ ,  $K_L$  and  $K^\pm$  BRs, the  $K_L$  and  $K^\pm$  lifetimes, and the form factor parameters for semileptonic  $K_L$  decays. With these data we determine the CKM matrix element  $|V_{us}|$  with 0.5% accuracy, and we test the lepton universality and the unitarity of the first row of the CKM matrix. Furthermore, we are able to exclude a large region in

the  $m_{H^+} - \tan\beta$  plane, complementary to the one excluded by  $B \rightarrow \tau\nu$  decays. A more extended discussion of these results can be found in <sup>22)</sup>.

## References

1. A. Sirlin, Nucl. Phys. **B 196**, 83 (1982).
2. V. Cirigliano *et al.*, Eur. Phys. J. **C 23**, 121 (2002).
3. W.J. Marciano, Phys. Rev. Lett. **93**, 231803 (2004).
4. V. Cirigliano and I. Rosell, J. High Energy Phys. **0710**, 005 (2007).
5. C. Gatti, Eur. Phys. J. **C 45**, 417 (2006).
6. F. Ambrosino *et al.* (KLOE Collaboration), Phys. Lett. **B 632**, 43 (2006).
7. F. Ambrosino *et al.* (KLOE Collaboration), Phys. Lett. **B 626**, 15 (2005).
8. F. Ambrosino *et al.* (KLOE Collaboration), Phys. Lett. **B 638**, 140 (2006).
9. F. Ambrosino *et al.* (KLOE Collaboration), Phys. Lett. **B 566**, 61 (2003).
10. F. Ambrosino *et al.* (KLOE Collaboration), Eur. Phys. J. **C 48**, 767 (2006).
11. F. Ambrosino *et al.* (KLOE Collaboration), Phys. Lett. **B 636**, 173 (2006).
12. F. Ambrosino *et al.* (KLOE Collaboration), Phys. Lett. **B 636**, 166 (2006).
13. F. Ambrosino *et al.* (KLOE Collaboration), J. High Energy Phys. **12**, 105 (2007).
14. F. Ambrosino *et al.* (KLOE Collaboration), Phys. Lett. **B 632**, 76 (2006).
15. F. Ambrosino *et al.* (KLOE Collaboration), arXiv:0804.4577.
16. F. Ambrosino *et al.* (KLOE Collaboration), J. High Energy Phys. **01**, 073 (2008).
17. P. A. Boyle *et al.* (RBC/UKQCD Collaboration), arXiv:0710.5136.
18. E. Follana *et al.* (HPQCD/UKQCD Collaboration), arXiv:0706.1726.
19. I. S. Towner and J. C. Hardy, arXiv:0710.3181.
20. W. M. Yao *et al.* (Particle Data Group), J. Phys. **G 33** (2006) and 2007 web updates.
21. G. Isidori and P. Paradisi, Phys. Lett. **B 639** 499 (2006).
22. F. Ambrosino *et al.* (KLOE Collaboration), J. High Energy Phys. **04**, 059 (2008).

## MEASUREMENT OF CKM ANGLES AT THE B-FACTORIES

Cecilia Voena  
*INFN-Roma, P.le Aldo Moro 2,  
00185 Roma, Italy*

### Abstract

The experiments BaBar and Belle have collected more than 1.2 billions  $B\bar{B}$  pairs produced at the energy of the  $\Upsilon(4S)$  resonance. With this data sample it has been possible to measure precisely the CP-violating phase of the Cabibbo-Kobayashi-Maskawa (CKM) matrix that describes the CP violation pattern in the Standard Model. In this paper we present a review of the measurements of the angles  $\beta$ ,  $\alpha$  and  $\gamma$  of the unitarity triangle which are related to the CKM matrix elements, with focus on recent results.

## 1 Introduction

CP violation is present in the Standard Model due to a non irreducible phase in the Cabibbo-Kobayashi-Maskawa matrix <sup>1)</sup>,  $V_{CKM}$ , that provides the couplings of the weak charged currents to the quarks.  $V_{CKM}$  is a unitary matrix and can be parameterized by three mixing angles and one ( $CP$ -violating) phase; its elements are fundamental parameters of the Standard Model and their values are not predicted by the theory. A common parametrization of  $V_{CKM}$  has been proposed by Wolfenstein <sup>2)</sup> (fig. 1, top) in terms of the parameters  $\lambda$ ,  $A$ ,  $\rho$  and  $\eta$ . The unitary conditions can be graphically represented in a complex plane as triangles, of which the one corresponding to the relation  $V_{ud}V_{ub}^* + V_{cd}V_{cb}^* + V_{td}V_{tb}^* = 0$  has roughly equal-length sides, of the order of  $\lambda^3$ . This triangle is called *unitarity triangle* and when the sides are divided by  $V_{cd}V_{cb}^*$ , the apices are  $(0, 0)$ ,  $(1, 0)$  and  $(\rho, \eta)$  (fig. 1, bottom). The angles, expressed in terms of the  $V_{CKM}$  elements are:

$$\alpha = \arg \left[ -\frac{V_{td}V_{tb}^*}{V_{ud}V_{ub}^*} \right], \quad \beta = \arg \left[ -\frac{V_{cd}V_{cb}^*}{V_{td}V_{tb}^*} \right], \quad \gamma = \arg \left[ -\frac{V_{ud}V_{ub}^*}{V_{cd}V_{cb}^*} \right]. \quad (1)$$

$$V = \begin{pmatrix} 1 - \lambda^2/2 & \lambda & A\lambda^3(\rho - i\eta) \\ -\lambda & 1 - \lambda^2/2 & A\lambda^2 \\ A\lambda^3(1 - \rho - i\eta) & -A\lambda^2 & 1 \end{pmatrix} + \mathcal{O}(\lambda^4)$$

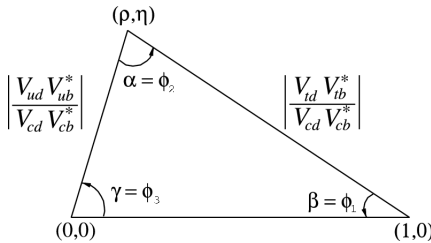


Figure 1: Top: Wolfenstein parametrization of the CKM matrix. Bottom: the unitarity triangle showing the definition of the angles  $\alpha$ ,  $\beta$  and  $\gamma$ , also known as  $\phi_1$ ,  $\phi_2$ ,  $\phi_3$ .

The  $B$  factories primary physics goal is to measure and possibly to over constrain the sides and the angles of the unitarity triangle in order to test the

CKM mechanism and to search for inconsistencies that may show evidence of physics beyond the Standard Model.

## 2 Experimental techniques for time-dependent measurements

The measurement of the angles  $\beta$  and  $\alpha$  discussed in this paper are performed through the study of time-dependent rates and CP asymmetries of neutral  $B$  mesons decays to a final state  $f$  (usually a CP eigenstate), that is accessible to both the  $B^0$  and the  $\bar{B}^0$ . The time-dependent CP asymmetry is defined as

$$\begin{aligned} A_{CP} &\equiv \frac{N(\bar{B}^0(\Delta t) \rightarrow f) - N(B^0(\Delta t) \rightarrow f)}{N(\bar{B}^0(\Delta t) \rightarrow f) + N(B^0(\Delta t) \rightarrow f)} \\ &= S_f \sin(\Delta m_d \Delta t) - C_f \cos(\Delta m_d \Delta t), \end{aligned} \quad (2)$$

where  $N(B^0(\Delta t) \rightarrow f)$  is the number of  $B^0$  mesons decayed into the CP eigenstate at a time  $\Delta t$  after (or before) the decay of the  $\bar{B}^0$  meson,  $\Delta m_d$  is the  $B^0 - \bar{B}^0$  oscillation frequency, and the coefficients  $S_f$  and  $C_f$  are functions of the  $B^0 \bar{B}^0$  mixing parameters and of the decay amplitudes:

$$S_f = \frac{2\text{Im}\lambda_f}{1 + |\lambda_f|^2}, \quad C_f = \frac{1 - |\lambda_f|^2}{1 + |\lambda_f|^2}, \quad \text{with } \lambda_f = \frac{q \bar{A}_f}{p A_f}. \quad (3)$$

The Standard Model predicts  $q/p \simeq e^{-i2\beta}$  with good precision,  $A_f$  and  $\bar{A}_f$  are the amplitudes of the  $B^0 \rightarrow f$  and the  $\bar{B}^0 \rightarrow f$  processes, respectively. If the decay is dominated by a single amplitude or by amplitudes with the same weak phase, then  $|\lambda_f| = 1$ ,  $C_f = 0$  and  $S_f = \text{Im}\lambda_f$ .

The BaBar and Belle experiments take data at the colliders PEP-II and KEKB respectively, which are  $e^+e^-$  asymmetric-energy  $B$  factories operating at the center of mass (CM) energy of the  $\Upsilon(4S)$  mass. Pairs of  $B\bar{B}$  mesons are produced almost at rest in the decay of the  $\Upsilon(4S)$  but thanks to the boost of the CM frame with respect to the laboratory frame the separation between the two decay vertices is increased to  $250 \mu\text{m}$  on average. One of the  $B$  is reconstructed exclusively in the final state  $f$  while the other  $B$  in the event is reconstructed partially to determine its flavor (that determines the flavor of the other  $B$ , given the coherence of the initial state produced). The difference of the proper decay time  $\Delta t$  is measured from the spatial separation of the two decays vertices. The effective efficiency of the tagging algorithm is  $\sim 30\%$  and the  $\Delta t$  resolution is  $\sim 1.1$  ps.

### 3 Measurement of $\beta$

The *golden* modes used to determine  $\beta$  are the  $B^0 \rightarrow (c\bar{c})K^{(*)0}$  decays. These processes have amplitudes dominated by a single weak phase, thus in the Standard Model  $S_f = -\eta_{CP}\sin 2\beta$  ( $\eta_{CP}$  is the final state CP eigenvalue) and  $C_f = 0$  with a theoretical uncertainty estimated below the 1% level. From an experimental point of view these decay modes have relatively high branching ratios ( $\sim 10^{-4}$ ) and low background. The BaBar result is based on 383 million  $B\bar{B}$  pairs, where the modes  $B^0 \rightarrow J/\psi K_S^0$ ,  $\psi(2S)K_S^0$ ,  $\chi_{c1}K_S^0$ ,  $\eta_c K_S^0$  ( $CP$ -odd),  $B^0 \rightarrow J/\psi K_L^0$  ( $CP$ -even), and  $B^0 \rightarrow J\psi K^{*0}(\pi^0 K_S^0)$  have been reconstructed.  $J\psi K^{*0}$  is a vector-vector final state and requires an angular analysis to separate the  $CP$ -even and  $CP$ -odd part. The Belle result is based on the analysis of the modes  $B^0 \rightarrow J/\psi K_S^0$  and  $B^0 \rightarrow J/\psi K_L^0$  reconstructed in 535 million  $B\bar{B}$  pairs.

Figure 2 shows the time-dependent decay rates and CP asymmetry for the two results. The amplitude of the sin-like asymmetry, corrected for the probability of wrongly assigning the flavor of the decaying  $B$  and for resolution effects measures  $\sin 2\beta$ . The BaBar result is  $\sin 2\beta = 0.714 \pm 0.032 \pm 0.018$  <sup>3)</sup> while Belle measures  $\sin 2\beta = 0.642 \pm 0.031 \pm 0.017$  <sup>4)</sup>, where the first error is statistical and the second systematic. The current world average is  $\sin 2\beta_{WA} = 0.681 \pm 0.025$  <sup>5)</sup>. Given the high experimental and theoretical precision this measurement gives the tightest constraints on the  $\rho, \eta$  parameters. Two of the four ambiguities in  $\beta$  have been resolved by measurements of  $\cos 2\beta$  <sup>6, 7, 8, 9)</sup>.

Other  $B$  decays sensitive to  $\sin 2\beta$  are those mediated by the  $b \rightarrow c\bar{c}d$  transitions <sup>10)</sup> (for example  $B^0 \rightarrow D^{(*)+}D^{(*)-}$ ) where, besides the dominant tree level amplitudes, there are non negligible penguin contributions with different weak phase. The results found by BaBar and Belle are consistent with the Standard Model expectations. A possible discrepancy has been found by Belle in the mode  $B^0 \rightarrow D^+D^-$  <sup>11)</sup> where there is evidence of direct CP violation at  $3.2\sigma$  level.

In the Standard Model CP asymmetries in  $B$  decays that proceed through  $b \rightarrow sq\bar{q}$  transitions are expected to give  $\sin 2\beta$  as the  $B^0 \rightarrow (c\bar{c})K^{(*)0}$  decays. These channels are dominated by penguin amplitudes and are potentially sensitive to contributions from new Physics (new particles in the loop). Belle and BaBar have measured time-dependent CP asymmetries in several such decays

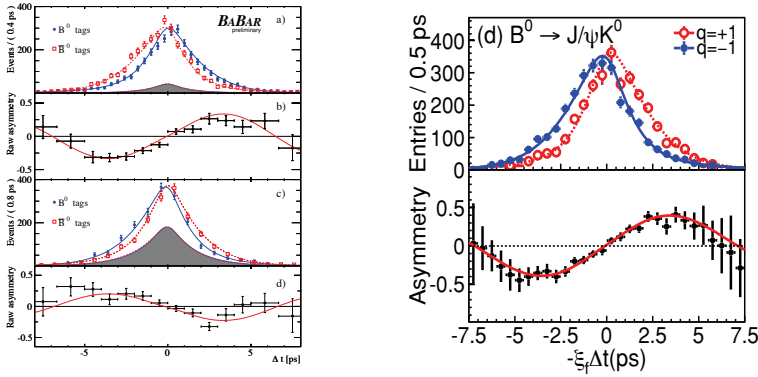


Figure 2: Left: distribution of the yields and raw CP asymmetry as functions of  $\Delta t$  for  $J/\psi K_S^0$ ,  $\psi(2S)K_S^0$ ,  $\chi_{c1}K_S^0$ ,  $\eta_c K_S^0$  (CP-odd, top) and  $J/\psi K_L^0$  (CP-even, bottom), measured by BaBar. Right: distribution of the yields and raw CP asymmetry as functions of  $-\xi_f \Delta t$  for  $J/\psi K^0$ , measured by Belle.  $\xi_f = +1(-1)$  for CP-even (CP-odd) final states,  $q = +1(-1)$  for  $B^0(\bar{B}^0)$  tag. The solid curves show the fit results.

like  $B^0 \rightarrow \phi K_s$  and  $B^0 \rightarrow \eta' K_s$ . A naive average of the  $S_f$  coefficients is consistent with the Standard Model expectation<sup>5)</sup>. Improving the precisions of these measurement is one of the main goal of future  $B$  factories experiments.

#### 4 Measurement of $\alpha$

The angle  $\alpha$  can be measured from the time-dependent rates in modes with a contribution from the tree level  $b \rightarrow u\bar{u}d$  transition like the charmless decays  $B \rightarrow h^+ h^-$  ( $h = \pi, \rho$ ), where the weak phase difference between the amplitudes of  $B^0$  and  $\bar{B}^0$  going into these final states is  $2\alpha$ . If only tree level diagrams were present, the coefficients of the time-dependent CP asymmetry would be  $S_f = \sin 2\alpha$ ,  $C_f = 0$ . Since sizable penguin contributions are present the previous relations are modified:

$$S_f = \sqrt{1 - C_f^2} \sin 2\alpha_{eff}, C_f \sim 2\text{Im}(P/T) \sin \alpha \quad (4)$$

where  $T$  and  $P$  are the parts of the amplitude depending on  $V_{ub}^* V_{ud}$  (including the tree diagram) and  $V_{tb}^* V_{td}$ , respectively, and  $\alpha_{eff}$  is unknown and equals  $\alpha$  in the limit of  $P/T \rightarrow 0$ . Once that  $C_f$  and  $S_f$  are measured with a

time-dependent analysis similar to that used to determine  $\sin 2\beta$ , the difference  $\Delta\alpha = \alpha - \alpha_{eff}$  can be obtained with an isospin analysis <sup>12)</sup>, where the penguin contribution is estimated using the isospin-related decays  $B^0 \rightarrow h^0 h^0$  and  $B^+ \rightarrow h^0 h^+$ . The method determines  $\alpha$  with an 8-fold ambiguity.

CP violation is well established in the  $\pi\pi$  system and the full isospin analysis has been performed by both the BaBar and the Belle collaborations. The BaBar result, based on 383 million  $B\bar{B}$  pairs is  $\alpha = (96_{-6}^{+10})^\circ$  <sup>13)</sup> while the Belle result, based on 535 million  $B\bar{B}$  pairs is  $\alpha = (97 \pm 11)^\circ$  <sup>14)</sup> for the solution that is not removed by other constraints on the unitary plane.

The angle  $\alpha$  can be also extracted from the decay  $B^0 \rightarrow \rho^+ \rho^-$  with a similar analysis as in  $B^0 \rightarrow \pi^+ \pi^-$ . Penguin pollution is lower with respect to the  $\pi\pi$  system allowing a more precise determination of  $\alpha$ . The final state  $\rho^+ \rho^-$  is vector-vector and an angular analysis is in principle necessary to separate the CP-odd and CP-even components. Experimentally it has been found that the state is fully longitudinal polarized (CP-even), so this channel can be analyzed as  $B^0 \rightarrow \pi^+ \pi^-$ . BaBar has recently presented the first time-dependent analysis of the  $B^0 \rightarrow \rho^0 \rho^0$  decay <sup>15)</sup> on 427 million  $B\bar{B}$  pairs. The evidence for the signal is  $3.6\sigma$  and applying the isospin analysis  $\Delta\alpha = 14.6^\circ @ 68\%$  C.L. has been obtained. Figure 3 left) shows the confidence level on  $\Delta\alpha$ . Belle has presented the result of a search of the  $B^0 \rightarrow \rho^0 \rho^0$  decay on 657 million  $B\bar{B}$  pairs where no significant signal has been found. The upper limit  $\text{BR}(B^0 \rightarrow \rho^0 \rho^0) < 1.0 \times 10^{-6} @ 90\%$  C.L. has been found <sup>16)</sup>, compatible with the BaBar result. The measurement of the  $S_f$  and  $C_f$  parameters, together with the branching fractions needed for the isospin analysis, are reported in tab. 1 <sup>17, 18, 19, 20)</sup>.

A third way to constrain  $\alpha$  is the time-dependent Dalitz plot analysis of the decay  $B^0 \rightarrow \pi^+ \pi^- \pi^0$ . The decay amplitudes of this process are dominated by the resonances  $\rho^+$ ,  $\rho^-$  and  $\rho^0$ , where  $\rho$  is the sum of the ground state  $\rho(770)$  and the radial excitations  $\rho(1450)$  and  $\rho(1700)$ . The time-dependent Dalitz plot distributions for  $B^0$  and  $\bar{B}^0$  decaying in the  $\pi^+ \pi^- \pi^0$  final state are fitted to a likelihood with 26 physical parameters related to  $\alpha$ , tree and penguin amplitudes that are subsequently determined with a least-square fit to the 26 parameters. The BaBar result, based on 375 million  $B\bar{B}$  pairs is  $\alpha = (87_{-13}^{+45})^\circ$  <sup>21)</sup>. The Belle result, based on 449 million  $B\bar{B}$  pairs is  $68^\circ < \alpha < 95^\circ @ 68.3\%$  C.L. <sup>22)</sup>. In both cases there are mirror solutions at  $+180^\circ$ . Even if with the current data sample this method alone does not constrain  $\alpha$

Table 1:  $CP$  parameters and branching fractions of  $B \rightarrow \rho\rho$ .

	BaBar	Belle
$S$	$-0.17 \pm 0.20^{+0.05}_{-0.06}$	$0.19 \pm 0.30 \pm 0.08$
$C$	$0.01 \pm 0.15 \pm 0.06$	$-0.16 \pm 0.21 \pm 0.08$
$\mathcal{B}(\rho^+\rho^-) \times 10^6$	$25.5 \pm 2.1^{+3.6}_{-3.9}$	$22.8 \pm 3.8^{+2.3}_{-2.6}$
$\mathcal{B}(\rho^+\rho^0) \times 10^6$	$16.8 \pm 2.2 \pm 2.3$	$31.7 \pm 7.1^{+3.8}_{-6.7}$
$A_{CP}(\rho^+\rho^0)$	$-0.12 \pm 0.13 \pm 0.10$	$0.00 \pm 0.22 \pm 0.03$
$\mathcal{B}(\rho^0\rho^0) \times 10^6$	$0.84 \pm 0.29 \pm 0.17$	$< 1.0$ @90%C.L.
$S(\rho^0\rho^0)$	$0.5 \pm 0.9 \pm 0.2$	—
$C(\rho^0\rho^0)$	$0.4 \pm 0.9 \pm 0.2$	—

significantly, the information is useful when added to the results in the  $\pi\pi$  and  $\rho\rho$  decay modes, in particular to remove some of the ambiguities.

#### 4.1 Global constraint on $\alpha$

Figure 3 right) shows the probability density function of  $\alpha$ , based on a bayesian analysis <sup>23)</sup> of the three measurements described above. The corresponding result is  $\alpha = (91 \pm 8)^\circ$  for the solution that is not removed by other constraints on the unitary plane.

## 5 Measurement of $\gamma$

The methods to measure  $\gamma$  exploit the interference between amplitudes corresponding to the CKM allowed  $b \rightarrow c$  transition and the CKM suppressed  $b \rightarrow u$  transition, like in the decays  $B^- \rightarrow D^{(*)0}K^{(*)-}$  and  $B^- \rightarrow \bar{D}^{(*)0}K^{(*)-}$  with  $D^{(*)0}$  and  $\bar{D}^{(*)0}$  decaying to a common final state. The sensitivity to  $\gamma$  is driven by the parameter  $r_B$ , defined as the magnitude of the ratio between the suppressed over the allowed amplitude. Since  $r_B$ , and thus the sensitivity, is in general small ( $r_B \sim 0.1-0.4$  depending on the  $B$  decay mode) the results from the different techniques must be combined to obtain a significant constraint on  $\gamma$ . The most stringent constraints come from charged  $B$  decays but BaBar has investigated methods that use neutral  $B$  decays.

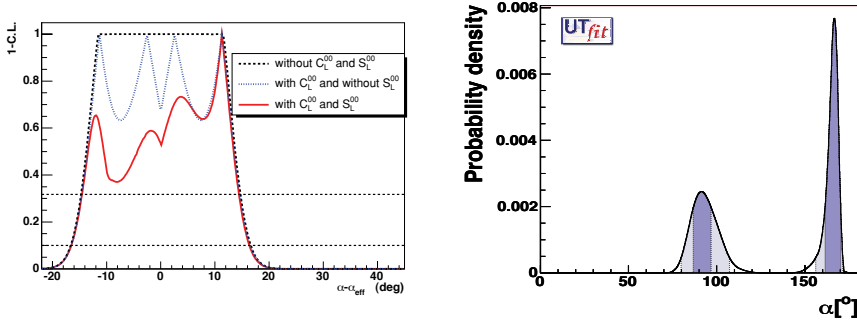


Figure 3: *Left: confidence level on  $\Delta\alpha = \alpha - \alpha_{eff}$  obtained from the isospin analysis of the  $\rho\rho$  system described in the text. The dotted line corresponds to the usual isospin analysis. The dashed line is obtained without using the CP  $S(\rho^0\rho^0)$  and  $C(\rho^0\rho^0)$  parameters. The solid line is obtained using also the information from  $S(\rho^0\rho^0)$  and  $C(\rho^0\rho^0)$ . Horizontal lines correspond to the 68% (top) and 90% (bottom) C.L. intervals. Right: probability density function of  $\alpha$  obtained from the measurements available combining BaBar and Belle described in the text. Dark and light regions correspond to 68% and 90% probability, respectively.*

### 5.1 $\gamma$ from charged $B$ decays

The  $B^- \rightarrow \tilde{D}^{(*)0}K^{(*)-}$  are used and three methods exist, depending on the  $\tilde{D}^{(*)0}$  decay: the Gronau-London-Wyler<sup>24)</sup> (GLW) method where  $\tilde{D}^{(*)0}$  decays into a CP eigenstate, the Atwood-Dunietz-Soni<sup>25)</sup> (ADS) method where  $\tilde{D}^{(*)0}$  decays into a flavor eigenstate and the Giri-Grossman-Soffer-Zupan<sup>26)</sup> (GGSZ) method where  $\tilde{D}^{(*)0}$  decays into a three-body final state. The third method is the more effective in constraining  $\gamma$  but it is not discussed here since no new results were available at the time of the conference. See<sup>5)</sup> for recent results.

BaBar recently presented an update for the GLW analysis of the  $B^- \rightarrow \tilde{D}^0 K^-$  decay on 382 million  $B\bar{B}$  pair. The  $\tilde{D}^0$  decay modes considered are  $\pi^+\pi^-$ ,  $K^+K^-$  (CP even),  $K_s\pi^0$  and  $K_s\omega$  (CP odd). The result is expressed in terms of the ratios  $R_{CP\pm}$  of charge-averaged partial rates and of the partial-rate charge asymmetries  $A_{CP\pm}$ . These observables are related to  $\gamma$ , the magnitude ratio  $r_B$  and the relative strong phase  $\delta$ . The result is:  $A_{CP+} = 0.27 \pm 0.09 \pm 0.04$ ,  $A_{CP-} = -0.09 \pm 0.09 \pm 0.02$ ,  $R_{CP+} = 1.06 \pm 0.10 \pm 0.05$ ,  $R_{CP-} =$

<sup>1</sup>The symbol  $\tilde{D}^{(*)0}$  indicates either a  $D^{(*)0}$  or a  $\bar{D}^{(*)0}$  meson.

$1.03 \pm 0.10 \pm 0.05$  <sup>27)</sup> where the first errors are statistical and the second systematic.

Belle has updated the ADS analysis of the decay  $B^- \rightarrow \tilde{D}^0 K^-$  with  $\tilde{D}^0$  decaying into the flavor eigenstate  $K^\pm \pi^\mp$  on a data sample of 657 million  $B\bar{B}$  pairs. In this case it is exploited the interference between the CKM-favored  $B^- \rightarrow D^0 K^-$  decay, followed by the doubly Cabibbo-suppressed  $D^0 \rightarrow K^+ \pi^-$  decay, with the CKM-suppressed  $B^- \rightarrow \bar{D}^0 K^-$  decay, followed by the Cabibbo-favored  $\bar{D}^0 \rightarrow K^+ \pi^-$  decay. These are called suppressed decay chains. The observables considered are the ratio of the decay rates of the suppressed decay chains over the rates of the favored decay chains (both  $B$  and  $D$  favored decays)  $R_{ADS}$ , and the CP asymmetry  $A_{ADS}$  in the suppressed decay chains. These observables are related to  $\gamma$ ,  $r_B$ ,  $\delta_B$  defined as in the GLW case and  $r_D$ ,  $\delta_D$ , the corresponding quantities for the  $D$  meson. No signal has been observed for the suppressed decays:  $A_{ADS} = -0.13_{-0.88}^{+0.97} \pm 0.26$  and  $R_{ADS} = 8.0_{-5.7-2.8}^{+6.3+2.0}$  where the first errors are statistical and the second systematic. The limit  $r_B < 0.19$  @90% C.L. has been set <sup>28)</sup>.

## 5.2 $\gamma$ from neutral $B$ decays

The angle  $\gamma$  can also be constrained using the decay  $B^0 \rightarrow \tilde{D}^0 K^{*0}$ . The  $K^{*0}$  is reconstructed in the  $K^+ \pi^-$  final state (charge conjugation is implied) where the flavor of the  $B$  meson is identified by the kaon electric charge. Neutral  $D$  mesons are reconstructed in the  $K_s \pi^+ \pi^-$  final state and analyzed with a Dalitz technique. The final states reconstructed can be reached through the  $B^0 \rightarrow \bar{D}^0 K^{*0}$  decay ( $b \rightarrow c$  mediated) and the  $B^0 \rightarrow D^0 K^{*0}$  decay ( $b \rightarrow u$  mediated). The natural width of the  $K^{*0}$  resonance has been considered by using effective variables obtained by integrating over a region of the  $B^0 \rightarrow \bar{D}^0 K^+ \pi^-$  Dalitz plot. BaBar has presented a result based on 371 million  $B\bar{B}$  pairs. An unbinned maximum likelihood technique has been applied to separate signal from background events and extract  $\gamma$  and  $r_B$ . A bias in the estimation of the error on  $\gamma$  has been observed on simulation. For this reason an external information on  $r_B$  has been combined <sup>29)</sup>. The result is  $\gamma = (162 \pm 56)^\circ$  or  $\gamma = (342 \pm 56)^\circ$ ,  $r_B < 0.55$  at 95% probability,  $\delta = (62 \pm 57)^\circ$  or  $\delta = (242 \pm 57)^\circ$  <sup>30)</sup> where  $\delta$  is the strong phase difference between the two interfering amplitudes.

Another decay mode sensitive to  $\gamma$  is  $B^0 \rightarrow D^\mp K^0 \pi^\pm$ . The three body final state is reached predominantly through the intermediate  $B^0 \rightarrow \tilde{D}^{**0} K_s$

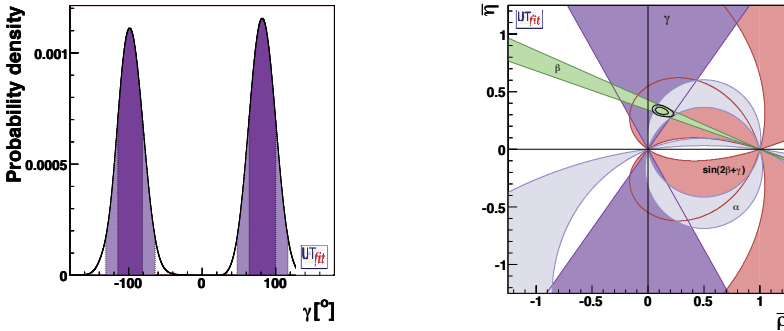


Figure 4: Left: probability density function of  $\gamma$  obtained from the all measurements available from BaBar and Belle. Dark and light regions correspond to 68% and 90% probability, respectively. Right: constraints in the  $\bar{\rho} - \bar{\eta}$  plane from the measurements of the angles  $\alpha$ ,  $\beta$  and  $\gamma$ .

and  $B^0 \rightarrow D^- K^{*+}$  decays. In the first case,  $\tilde{D}^{**0}$  indicates a  $D_0^*(2400)$  or a  $D_2^*(2460)$  state produced through  $b \rightarrow u$  and  $b \rightarrow c$  color-suppressed transitions. In the second case the  $K^*$  resonances are produced through  $b \rightarrow c$  transitions. A full time-dependent Dalitz analysis is performed and since the interference proceeds through mixing the effective measured quantity is  $2\beta + \gamma$ . The BaBar result, based on 347 million  $B\bar{B}$  pairs is:  $\gamma = (83 \pm 53 \pm 20)^\circ$  or  $\gamma = (263 \pm 53 \pm 20)^\circ$  <sup>31)</sup> where the first errors are statistical and the second systematic. With the current dataset it is not possible to determine the magnitude of the suppressed  $b \rightarrow u$  decays. Therefore the  $r_B$  parameter is fixed in the fit to 0.3 (expected value based on naive calculations) and varied by  $\pm 0.1$  in the systematic error.

### 5.3 Combined result of $\gamma$

Figure 4 left) shows the global constraint on  $\gamma$  obtained by combining all the measurements available using the bayesian approach of ref. <sup>23)</sup>. The result is  $\gamma = (82 \pm 17)^\circ$  up to a  $\pi$  ambiguity.

## 6 Conclusions

The Standard Model description of CP violation is well established and the measurements of the CKM angles are constantly improving in precision.  $\sin 2\beta$

is determined with a precision of 4% while the uncertainties on  $\alpha$  and  $\gamma$  are 10 and 20 degrees respectively. The most precisely determined angle is  $\beta$  whose measurement is nevertheless still statistics limited. Figure 4 right) shows the constraint on  $\bar{\rho}, \bar{\eta}$  ( $\bar{\rho} = \rho(1 - \lambda^2/2 + o(\lambda^2))$ ,  $\bar{\eta} = \eta(1 - \lambda^2/2 + o(\lambda^2))$ ) in the complex plane obtained by combining all the CKM angle measurements.

The  $B$  factories offer also a unique window on possible new Physics which have not been found so far. BaBar has recently stopped to take data while Belle will run to  $1ab^{-1}$  and then turn off. The future of  $B$  physics will depend on future facilities (e.g super  $B$  factories).

## References

1. N. Cabibbo, Phys. Rev. Lett. **10**, 531 (1963); M. Kobayashi and T. Maskawa, Prog. Theor. Phys. **49**, 652 (1973).
2. L. Wolfenstein, Phys. Rev. Lett. **51**, 1945 (1983).
3. BaBar Collaboration, B. Aubert *et al.*, Phys. Rev. Lett. **99**, 171803 (2007).
4. Belle Collaboration, K.-F. Chen *et al.*, Phys. Rev. Lett. **98**, 031802 (2007).
5. The Heavy Flavour Averaging Group,  
<http://www.slac.stanford.edu/xorg/hfag>.
6. BaBar Collaboration, B. Aubert *et al.*, Phys. Rev. D **71**, 032005 (2005).
7. BaBar Collaboration, B. Aubert *et al.*, Phys. Rev. Lett. **99**, 231802 (2007).
8. Belle Collaboration, R. Itoh *et al.*, Phys. Rev. Lett. **95**, 091601 (2005).
9. Belle Collaboration, P. Krokovny *et al.*, Phys. Rev. Lett. **97**, 081801 (2006).
10. *Review CP violation in meson decays*, W.-M. Yao *et al.*, Journal of Physics G **33**, 1 (2006).
11. Belle Collaboration, S. Fratina *et al.*, Phys. Rev. Lett. **98**, 221802 (2007).
12. M. Gronau *et al.*, Phys. Rev. Lett. **65**, 3381 (1990).
13. BaBar Collaboration, B. Aubert *et al.*, Phys. Rev. D **76**, 091102 (2007).
14. Belle Collaboration, H. Ishino *et al.*, Phys. Rev. Lett. **98**, 211801 (2007).

15. BaBar Collaboration, B. Aubert *et al.*, arXiv:0708.1630.
16. Belle Collaboration, result presented at La Thuile 2008.
17. BaBar Collaboration, B. Aubert *et al.*, Phys. Rev. D **76**, 052007 (2007).
18. Belle Collaboration, K. Abe *et al.*, Phys. Rev. D **76**, 011104 (2007); Belle Collaboration, A. Somov *et al.* Phys. Rev. Lett. **96**, 171801 (2006) .
19. BaBar Collaboration, B. Aubert *et al.*, Phys. Rev. Lett. **97**, 261801 (2007).
20. Belle Collaboration, J. Zhang *et al.*, Phys. Rev. Lett **91**, 221801 (2003).
21. BaBar Collaboration, B. Aubert *et al.*, Phys. Rev. D **76**, 012004 (2007).
22. Belle Collaboration, A. Kusaka *et al.*, Phys. Rev. D **77**, 072001 (2008).
23. UTfit Collaboration, <http://www.utfit.org>.
24. M. Gronau, D. Wyler, Phys. Lett. B **265**, 172 (1991); M. Gronau, D. London, Phys. Lett. B **253**, 483 (1991).
25. D. Atwood, I. Dunietz, A. Soni, Phys. Rev. Lett. **78**, 3257 (1997).
26. A. Giri, Y. Grossman, A. Soffer, J. Zupan, Phys. Rev. D **68**, 054018 (2003).
27. BaBar Collaboration, B. Aubert *et al.*, arXiv:0802.4052.
28. Belle Collaboration, Y.Horii *et al.*, arXiv:0804.2063.
29. BaBar Collaboration, B. Aubert *et al.*, Rev. D **74**, 031101 (2006).
30. BaBar Collaboration, result presented at La Thuile 2008.
31. BaBar Collaboration, B. Aubert *et al.*, Rev. D **77**, 071102 (2008) .

**CPV AND  $B_s$  PHYSICS AT THE TEVATRON**

Heriberto Castilla-Valdez  
*Cinvestav-Mexico City, Mexico*

Written contribution not received



**NEW RESULTS FROM THE NA48/2 EXPERIMENT  
AT CERN SPS: RADIATIVE NONLEPTONIC KAON DECAYS**

Evgueni Goudzovski

*INFN sezione di Pisa, Largo B. Pontecorvo 3, Pisa, 56127 Italy*

**Abstract**

The NA48/2 experiment at the CERN SPS carried out data taking in 2003 and 2004. Analysis of the selected data samples of 7,146  $K^\pm \rightarrow \pi^\pm e^+ e^-$  decay candidates with 0.6% background, 1,164  $K^\pm \rightarrow \pi^\pm \gamma \gamma$  candidates with 3.3% background, and 120  $K^\pm \rightarrow \pi^\pm \gamma e^+ e^-$  candidates with 6.1% background allowed precise measurements of branching fractions and other characteristics of these rare kaon decays.

## Introduction

Radiative nonleptonic kaon decays represent a source of information on the structure of the weak interactions at low energies, and provide crucial tests of the Chiral Perturbation Theory (ChPT). The current paper presents new results related to study of the  $K^\pm \rightarrow \pi^\pm e^+ e^-$ ,  $K^\pm \rightarrow \pi^\pm \gamma \gamma$ , and  $K^\pm \rightarrow \pi^\pm \gamma e^+ e^-$  decays by the NA48/2 experiment at the CERN SPS.

The flavour-changing neutral current process  $K^\pm \rightarrow \pi^\pm e^+ e^-$ , induced at one-loop level in the Standard Model and highly suppressed by the GIM mechanism, has been described by the ChPT<sup>1)</sup>; several models predicting the form factor characterizing the dilepton invariant mass spectrum and the decay rate have been proposed<sup>2, 3)</sup>. The decay is fairly well explored experimentally: it was first studied at CERN<sup>4)</sup>, followed by BNL E777<sup>5)</sup> and E865<sup>6)</sup> measurements.

The  $K^\pm \rightarrow \pi^\pm \gamma \gamma$  and  $K^\pm \rightarrow \pi^\pm \gamma e^+ e^-$  decays similarly arise at one-loop level in the ChPT. The decay rates and spectra have been computed at leading and next-to-leading orders<sup>7, 8)</sup>, and strongly depend on a single theoretically unknown parameter  $\hat{c}$ . The experimental knowledge of these processes is rather poor: before the NA48/2 experiment, only a single observation of 31  $K^\pm \rightarrow \pi^\pm \gamma \gamma$  candidates was made<sup>9)</sup>, while the  $K^\pm \rightarrow \pi^\pm \gamma e^+ e^-$  decay was not observed at all.

The paper is organized as follows. In Section 1, a description of the NA48/2 experiment is given. Section 2 is devoted to a rather detailed description of the  $K^\pm \rightarrow \pi^\pm e^+ e^-$  analysis and its preliminary results, which is the main topic of the paper. Section 3 briefly presents the preliminary results of the  $K^\pm \rightarrow \pi^\pm \gamma \gamma$  analysis; a more detailed discussion is reserved for the Moriond QCD 2008 conference. Section 4 briefly presents the final results of the  $K^\pm \rightarrow \pi^\pm \gamma e^+ e^-$  analysis, which have recently been published<sup>10)</sup>. Finally the conclusions follow.

## 1 The NA48/2 experiment

The NA48/2 experiment, designed to excel in charge asymmetry measurements<sup>11)</sup>, is based on simultaneous  $K^+$  and  $K^-$  beams produced by 400 GeV/c primary SPS protons impinging at zero incidence angle on a beryllium target of 40 cm length and 2 mm diameter. Charged particles with momentum  $(60 \pm 3)$  GeV/c are selected by an achromatic system of four dipole magnets with zero total deflection ('achromat'), which splits the two beams in the ver-

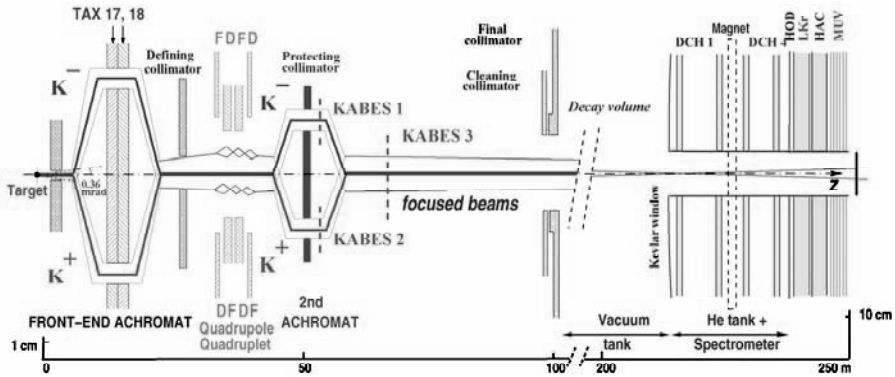


Figure 1: Schematic lateral view of the NA48/2 beam line (TAX17,18: motorized beam dump/collimators used to select the momentum of the  $K^+$  and  $K^-$  beams; FDFD/DFDF: focusing set of quadrupoles, KABES1-3: kaon beam spectrometer stations), decay volume and detector (DCH1-4: drift chambers, HOD: hodoscope, LKr: EM calorimeter, HAC: hadron calorimeter, MUV: muon veto). The vertical scales are different in the two parts of the figure.

tical plane and then recombines them on a common axis. Then the beams pass through a defining collimator and a series of four quadrupoles designed to produce focusing of the beams towards the detector. Finally the two beams are again split in the vertical plane and recombined in a second achromat. The layout of the beams and detectors is shown schematically in Fig. 1.

The beams then enter the decay volume housed in a 114 m long cylindrical vacuum tank with a diameter of 1.92 m for the first 65 m, and 2.4 m for the rest. Both beams follow the same path in the decay volume: their axes coincide within 1 mm, while the transverse size of the beams is about 1 cm. With  $7 \times 10^{11}$  protons incident on the target per SPS spill of 4.8 s duration, the positive (negative) beam flux at the entrance of the decay volume is  $3.8 \times 10^7$  ( $2.6 \times 10^7$ ) particles per pulse, of which 5.7% (4.9%) are  $K^+$  ( $K^-$ ). The  $K^+/K^-$  flux ratio is about 1.8. The fraction of beam kaons decaying in the decay volume at nominal momentum is 22%.

The decay volume is followed by a magnetic spectrometer housed in a tank filled with helium at nearly atmospheric pressure, separated from the vacuum tank by a thin ( $0.31\%X_0$ ) Kevlar composite window. A thin-walled aluminium beam pipe of 16 cm outer diameter traversing the centre of the spectrometer (and all the following detectors) allows the undecayed beam particles and the

muon halo from decays of beam pions to continue their path in vacuum. The spectrometer consists of four drift chambers (DCH): DCH1, DCH2 located upstream, and DCH3, DCH4 downstream of a dipole magnet. The magnet provides a horizontal transverse momentum kick  $\Delta p = 120 \text{ MeV}/c$  for charged particles. The DCHs have the shape of a regular octagon with a transverse size of about 2.8 m and a fiducial area of about 4.5 m<sup>2</sup>. Each chamber is composed of eight planes of sense wires arranged in four pairs of staggered planes oriented horizontally, vertically, and along each of the two orthogonal 45° directions. The spatial resolution of each DCH is  $\sigma_x = \sigma_y = 90 \text{ } \mu\text{m}$ . The nominal spectrometer momentum resolution is  $\sigma_p/p = (1.02 \oplus 0.044 \cdot p)\%$  ( $p$  in GeV/ $c$ ).

The magnetic spectrometer is followed by a plastic scintillator hodoscope (HOD) used to produce fast trigger signals and to provide precise time measurements of charged particles. The hodoscope has a regular octagonal shape with a transverse size of about 2.4 m. It consists of a plane of horizontal and a plane of vertical strip-shaped counters. Each plane consists of 64 counters arranged in four quadrants. Counter widths (lengths) vary from 6.5 cm (121 cm) for central counters to 9.9 cm (60 cm) for peripheral ones.

The HOD is followed by a liquid krypton electromagnetic calorimeter (LKr) <sup>12)</sup> used for photon detection and particle identification. It is an almost homogeneous ionization chamber with an active volume of 7 m<sup>3</sup> of liquid krypton, segmented transversally into 13248 projective cells, 2×2 cm<sup>2</sup> each, by a system of Cu–Be ribbon electrodes, and with no longitudinal segmentation. The calorimeter is 27 $X_0$  deep and has an energy resolution  $\sigma(E)/E = 0.032/\sqrt{E} \oplus 0.09/E \oplus 0.0042$  ( $E$  in GeV). Spatial resolution for a single electromagnetic shower is  $\sigma_x = \sigma_y = 0.42/\sqrt{E} \oplus 0.06$  cm for the transverse coordinates  $x$  and  $y$ .

The LKr is followed by a hadronic calorimeter (HAC) and a muon detector (MUV), both not used in the present analysis. A detailed description of the components of the NA48 detector can be found elsewhere <sup>13)</sup>. The NA48/2 experiment took data during two runs in 2003 and 2004, with about 60 days of effective running each. About  $18 \times 10^9$  events were recorded in total.

In order to simulate the detector response, a detailed GEANT-based <sup>14)</sup> Monte Carlo (MC) simulation is employed, which includes full detector geometry and material description, stray magnetic fields, DCH local inefficiencies and misalignment, detailed simulation of the kaon beam line, and time variations of the above throughout the running period. Radiative corrections are applied to kaon decays using the PHOTOS package <sup>15)</sup>.

## 2 $K^\pm \rightarrow \pi^\pm e^+ e^-$ analysis

The  $K^\pm \rightarrow \pi^\pm e^+ e^-$  rate is measured relatively to the abundant  $K^\pm \rightarrow \pi^\pm \pi_D^0$  normalization channel (with  $\pi_D^0 \rightarrow e^+ e^- \gamma$ ). The final states of the signal and normalization channels contain identical sets of charged particles. Thus electron and pion identification efficiencies, potentially representing a significant source of systematic uncertainties, cancel in the first order.

### 2.1 Event selection

Three-track vertices (compatible with the topology of  $K^\pm \rightarrow \pi^\pm e^+ e^-$  and  $K^\pm \rightarrow \pi^\pm \pi_D^0$  decays) are reconstructed using the Kalman filter algorithm<sup>16</sup>) by extrapolation of track segments from the upstream part of the spectrometer back into the decay volume, taking into account the measured Earth's magnetic field, stray field due to magnetization of the vacuum tank, and multiple scattering in the Kevlar window.

A large part of the selection is common to the signal and normalization modes. It requires a presence of a vertex satisfying the following criteria.

- Total charge of the three tracks:  $Q = \pm 1$ .
- Vertex longitudinal position is inside fiducial decay volume:  $Z_{\text{vertex}} > Z_{\text{final collimator}}$ .
- Particle identification is performed using the ratio  $E/p$  of track energy deposition in the LKr to its momentum measured by the spectrometer. The vertex is required to be composed of one pion candidate ( $E/p < 0.85$ ), and two opposite charge  $e^\pm$  candidates ( $E/p > 0.95$ ). No discrimination of pions against muons is performed.
- The vertex tracks are required to be consistent in time (within a 10 ns time window) and consistent with the trigger time, to be in DCH, LKr and HOD geometric acceptance, and to have momenta in the range  $5 \text{ GeV}/c < p < 50 \text{ GeV}/c$ . Track separations are required to exceed 2 cm in the DCH1 plane to suppress photon conversions, and to exceed 15 cm in the LKr plane to minimize particle misidentification due to shower overlaps.

If multiple vertices satisfying the above conditions are found, the one with the best fit quality is considered. The following criteria are then applied to the reconstructed kinematic variables to select the  $K^\pm \rightarrow \pi^\pm e^+ e^-$  candidates.

- $\pi^\pm e^+ e^-$  momentum within the beam nominal range:  $54 \text{ GeV}/c < |\vec{p}_{\pi ee}| < 66 \text{ GeV}/c$ .
- $\pi^\pm e^+ e^-$  transverse momentum with respect to the measured beam trajectory:  $p_T^2 < 0.5 \times 10^{-3} (\text{GeV}/c)^2$ .
- $\pi^\pm e^+ e^-$  invariant mass:  $475 \text{ MeV}/c^2 < M_{\pi ee} < 505 \text{ MeV}/c^2$ .
- Suppression of the  $K^\pm \rightarrow \pi^\pm \pi_D^0$  background defining the visible kinematic region:  $z = (M_{ee}/M_K)^2 > 0.08$ , which approximately corresponds to  $M_{ee} > 140 \text{ MeV}/c^2$ .

Independently, a presence of a LKr energy deposition cluster (photon candidate) satisfying the following principal criteria is required to select the  $K^\pm \rightarrow \pi^\pm \pi_D^0$  candidates.

- Cluster energy  $E > 3 \text{ GeV}$ , cluster time consistent with the vertex time, sufficient transverse separations from track impact points at the LKr plane ( $R_{\pi\gamma} > 30 \text{ cm}$ ,  $R_{e\gamma} > 10 \text{ cm}$ ).
- $e^+ e^- \gamma$  invariant mass compatible with a  $\pi^0$  decay:  $|M_{ee\gamma} - M_{\pi^0}| < 10 \text{ MeV}/c^2$ .
- The same conditions on reconstructed  $\pi^\pm e^+ e^- \gamma$  total and transverse momenta as used for  $\pi^\pm e^+ e^-$  momentum in the  $K^\pm \rightarrow \pi^\pm e^+ e^-$  selection.
- $\pi^\pm e^+ e^- \gamma$  invariant mass:  $475 \text{ MeV}/c^2 < M_{\pi ee\gamma} < 510 \text{ MeV}/c^2$ .

## 2.2 Signal and normalization samples

The reconstructed  $\pi^\pm e^+ e^-$  invariant mass spectrum is presented in Fig. 2 (left plot). The  $\pi^\pm e^+ e^-$  mass resolution is  $\sigma_{\pi ee} = 4.2 \text{ MeV}/c^2$ , in agreement with MC simulation. The  $e^+ e^-$  mass resolution computed by MC simulation is  $\sigma_{ee} = 2.3 \text{ MeV}/c^2$ .

In total 7,146  $K^\pm \rightarrow \pi^\pm e^+ e^-$  candidates are found in the signal region. After the kinematical suppression of the  $\pi_D^0$  decays, residual background contamination mostly results from particle misidentification (i.e.  $e^\pm$  identified as  $\pi^\pm$  and vice versa). The following relevant background sources were identified with MC simulations: (1)  $K^\pm \rightarrow \pi^\pm \pi_D^0$  with misidentified  $e^\pm$  and  $\pi^\pm$ ; (2)  $K^\pm \rightarrow \pi_D^0 e^\pm \nu$  with a misidentified  $e^\pm$  from the  $\pi_D^0$  decay. Background estimation by selecting the strongly suppressed <sup>17)</sup> lepton number violating  $K^\pm \rightarrow \pi^\mp e^\pm e^\pm$  (“same-sign”) candidates was considered the most reliable

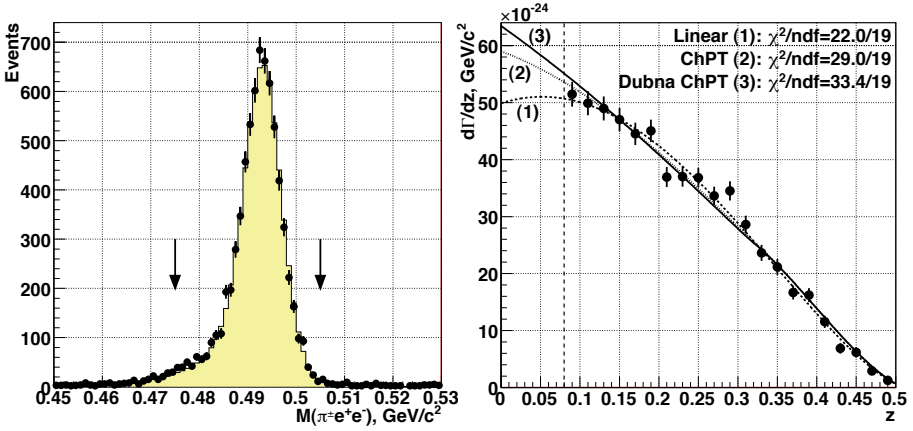


Figure 2: *Left: reconstructed spectrum of  $\pi^\pm e^+ e^-$  invariant mass; data (dots) and MC simulation (filled area). Right: the computed  $d\Gamma_{\pi ee}/dz$  (background subtracted, trigger efficiencies corrected for) and the results of fits according to the considered models.*

method. For the above two background sources, the expected mean numbers and kinematic distributions of the selected same-sign candidates are identical to those of background events (up to a negligible acceptance correction). In total 44 events pass the same-sign selection, which leads to background estimation of  $(0.6 \pm 0.1)\%$ . This result was independently confirmed with MC simulation of the two background modes.

In total  $12.228 \times 10^6$   $K^\pm \rightarrow \pi^\pm \pi_D^0$  candidates are found in the signal region. The only significant background source is the semileptonic  $K^\pm \rightarrow \pi_D^0 \mu^\pm \nu$  decay. Its contribution is not suppressed by particle identification cuts, since no  $\pi/\mu$  separation is performed. The background contamination is estimated to be 0.15% by MC simulation.

### 2.3 Trigger chain and its efficiency

Both  $K^\pm \rightarrow \pi^\pm e^+ e^-$  and  $K^\pm \rightarrow \pi^\pm \pi_D^0$  samples (as well as  $K^\pm \rightarrow 3\pi^\pm$ ) are recorded via the same two-level trigger chain. At the first level (L1), a coincidence of hits in the two planes of the HOD in at least two of the 16 non-overlapping segments is required. The second level (L2) is based on a hardware system computing coordinates of hits from DCH drift times, and a farm of asynchronous processors performing fast track reconstruction and running a

selection algorithm, which basically requires at least two tracks to originate in the decay volume with the closest distance of approach of less than 5 cm. L1 triggers not satisfying this condition are examined further and accepted nevertheless if there is a reconstructed track not kinematically compatible with a  $\pi^\pm\pi^0$  decay of a  $K^\pm$  having momentum of 60 GeV/c directed along the beam axis.

The NA48/2 analysis strategy for non-rare decay modes involves direct measurement of the trigger efficiencies using control data samples of downscaled low bias triggers collected simultaneously with the main triggers. However direct measurements are not possible for the  $K^\pm \rightarrow \pi^\pm e^+ e^-$  events due to very limited sizes of the corresponding control samples. Dedicated simulations of L1 and L2 performance (involving, in particular, the measured time dependencies of local DCH and HOD inefficiencies) were used instead. The simulated efficiencies and their kinematic dependencies were compared against measurements for the abundant  $K^\pm \rightarrow \pi^\pm\pi_D^0$  and  $K^\pm \rightarrow \pi^\pm\pi^+\pi^-$  decays in order to validate the simulations.

The simulated values of L1 and L2 inefficiencies for the selected  $K^\pm \rightarrow \pi^\pm\pi_D^0$  sample are  $\varepsilon_{L1} = 0.37\%$ ,  $\varepsilon_{L2} = 0.80\%$ . The values of the integral trigger inefficiencies for the  $K^\pm \rightarrow \pi^\pm e^+ e^-$  sample depend on the a priori unknown form factor; the corrections are applied differentially in bins of dilepton invariant mass. Indicative values of inefficiencies computed assuming a realistic linear form factor with a slope  $\delta = 2.3$  are  $\varepsilon_{L1} = 0.06\%$ ,  $\varepsilon_{L2} = 0.42\%$ . The  $K^\pm \rightarrow \pi^\pm\pi_D^0$  sample is affected by larger inefficiencies due to a smaller invariant mass of the  $e^+e^-$  system, which means that the leptons are geometrically closer.

#### 2.4 Theoretical input

The decay is supposed to proceed through one photon exchange, resulting in a spectrum of the  $z = (M_{ee}/M_K)^2$  kinematic variable sensitive to the form factor  $W(z)$  <sup>2</sup>):

$$\frac{d\Gamma}{dz} = \frac{\alpha^2 M_K}{12\pi(4\pi)^4} \lambda^{3/2}(1, z, r_\pi^2) \sqrt{1 - 4\frac{r_e^2}{z}} \left(1 + 2\frac{r_e^2}{z}\right) |W(z)|^2, \quad (1)$$

where  $r_e = m_e/M_K$ ,  $r_\pi = m_\pi/M_K$ , and  $\lambda(a, b, c) = a^2 + b^2 + c^2 - 2ab - 2ac - 2bc$ . On the other hand, the spectrum of the angle  $\theta_{\pi e}$  between  $\pi$  and  $e^+$  in the  $e^+e^-$  rest frame is proportional to  $\sin^2\theta_{\pi e}$ , and is not sensitive to  $W(z)$ .

The following parameterizations of the form factor  $W(z)$  are considered in the present analysis.

1. Linear:  $W(z) = G_F M_K^2 f_0 (1 + \delta z)$  with free normalization and slope ( $f_0, \delta$ ).
2. Next-to-leading order ChPT <sup>2)</sup>:  $W(z) = G_F M_K^2 (a_+ + b_+ z) + W^{\pi\pi}(z)$  with free parameters ( $a_+, b_+$ ), and an explicitly calculated pion loop term  $W^{\pi\pi}(z)$ .
3. The Dubna version of ChPT parameterization involving meson form factors:  $W(z) \equiv W(M_a, M_\rho, z)$  <sup>3)</sup>, with resonance masses ( $M_a, M_\rho$ ) treated as free parameters.

The goal of the analysis is extraction of the form factor parameters in the framework of each of the above models, and computation of the corresponding branching fractions  $\text{BR}_{1,2,3}$ .

## 2.5 Fitting procedure

The values of  $d\Gamma_{\pi ee}/dz$  in the centre of each  $i$ -bin of  $z$ , which can be directly confronted to the theoretical predictions (1), are then computed as

$$(d\Gamma_{\pi ee}/dz)_i = \frac{N_i - N_i^B}{N_{2\pi}} \cdot \frac{A_{2\pi}(1 - \varepsilon_{2\pi})}{A_i(1 - \varepsilon_i)} \cdot \text{BR}(K^\pm \rightarrow \pi^\pm \pi^0) \cdot \text{BR}(\pi_D^0) \cdot \frac{\Gamma_K}{\Delta z}. \quad (2)$$

Here  $N_i$  and  $N_i^B$  are the numbers of observed  $K^\pm \rightarrow \pi^\pm e^+ e^-$  candidates and background events in the  $i$ -th bin,  $N_{2\pi}$  is the number of  $K^\pm \rightarrow \pi^\pm \pi_D^0$  events (background subtracted),  $A_i$  and  $\varepsilon_i$  are geometrical acceptance and trigger inefficiency in the  $i$ -th bin for the signal sample (computed by MC simulation),  $A_{2\pi} = 2.94\%$  and  $\varepsilon_{2\pi} = 1.17\%$  are those for  $K^\pm \rightarrow \pi^\pm \pi_D^0$  events,  $\Gamma_K$  is the nominal kaon width <sup>19)</sup>,  $\Delta z$  is the chosen width of the  $z$  bin,  $\text{BR}(K^\pm \rightarrow \pi^\pm \pi^0) = (20.64 \pm 0.08)\%$  (FlaviaNet average <sup>18)</sup>),  $\text{BR}(\pi_D^0) = (1.198 \pm 0.032)\%$  (PDG average <sup>19)</sup>).

The computed values of  $d\Gamma_{\pi ee}/dz$  vs  $z$  are presented in Fig. 2 (right plot) along with the results of the fits to the three considered models.  $\text{BR}(K^\pm \rightarrow \pi^\pm e^+ e^-)$  in the full kinematic range corresponding to each model are then computed using the measured parameters, their statistical uncertainties, and correlation matrices.

In addition, a model-independent branching fraction  $\text{BR}_{\text{mi}}$  in the visible kinematic region  $z > 0.08$  is computed by integration of  $d\Gamma_{\pi ee}/dz$ .  $\text{BR}_{\text{mi}}$  is to a good approximation equal to each of the model-dependent BRs computed in the restricted kinematic range  $z > 0.08$ .

## 2.6 Systematic uncertainties

The following sources of systematic uncertainties were studied.

1. Particle identification. Imperfect MC description of electron and pion identification inefficiencies  $f_e$  and  $f_\pi$  can bias the result only due to the momentum dependence of the inefficiencies, due to identical charged particle composition, but differing momentum distributions of the signal and normalization final states. Inefficiencies were measured for the data to vary depending on particle momentum in the ranges  $1.6\% < f_\pi < 1.7\%$  and  $1.1\% < f_e < 1.7\%$  in the analysis track momentum range. Systematic uncertainties due to these momentum dependencies not perfectly described by MC were conservatively estimated assuming that MC predicts momentum-independent  $f_e$  and  $f_\pi$ .

2. Beam line description. Despite the careful simulation of the beamline including time variations of its parameters, the residual discrepancies of data and MC beam geometries and spectra bias the results. To evaluate the related systematic uncertainties, variations of the results with respect to variations of cuts on track momenta, LKr cluster energies, total and transverse momenta of the final states  $\pi^\pm e^+ e^-(\gamma)$ , and track distances from beam axis in DCH planes were studied.

3. Background subtraction. As discussed above, the same-sign event spectrum is used for background estimation in the  $\pi^\pm e^+ e^-$  sample. The method has a limited statistical precision (with an average of 2 same-sign event in a bin of  $z$ ). Furthermore, the presence of the component with two  $e^+ e^-$  pairs (due to both  $\pi_D^0$  decays and external conversions) with a non-unity expected ratio of same-sign to background events biases the method. The uncertainties of the measured parameters due to background subtraction were conservatively taken to be equal to the corrections themselves.

4. Trigger efficiency. As discussed earlier, the corrections for trigger inefficiencies were evaluated by simulations. In terms of decay rates, L1 and L2 corrections have similar integral magnitudes of a few  $10^{-3}$ . No uncertainty was ascribed to the L1 correction, due to relative simplicity of the trigger condition. On the other hand, the uncertainty of the L2 efficiency correction was conservatively taken to be equal to the correction itself.

5. Radiative corrections. Uncertainties due to the radiative corrections were evaluated by variation of the lower  $\pi^\pm e^+ e^-$  invariant mass cut.

6. Fitting method. Uncertainties due to the fitting procedure were evaluated by variation of the  $z$  bin width.

7. External input. Substantial uncertainties arise from the external input,

Table 1: Summary of corrections and systematic uncertainties (excluding the external ones).

Parameter	$e, \pi$ ID	Beam spectra	Background subtraction	Trigger efficiency	Rad. corr.	Fitting method
$\delta$	0.01	0.04	$-0.04 \pm 0.04$	$-0.03 \pm 0.03$	0.05	0.03
$f_0$	0.001	0.006	$0.002 \pm 0.002$	$0.000 \pm 0.001$	0.006	0.003
$a_+$	0.001	0.005	$-0.001 \pm 0.001$	$-0.001 \pm 0.002$	0.005	0.004
$b_+$	0.009	0.015	$0.017 \pm 0.017$	$0.016 \pm 0.015$	0.015	0.010
$M_a/\text{GeV}$	0.004	0.009	$0.008 \pm 0.008$	$0.006 \pm 0.006$	0.009	0.006
$M_b/\text{GeV}$	0.002	0.003	$0.003 \pm 0.003$	$0.003 \pm 0.003$	0.004	0.002
$\text{BR}_{1,2,3} \times 10^7$	0.02	0.02	$-0.01 \pm 0.01$	$-0.02 \pm 0.01$	0.01	0.02
$\text{BR}_{\text{mi}} \times 10^7$	0.02	0.01	$-0.01 \pm 0.01$	$-0.02 \pm 0.01$	0.01	n/a

as  $\text{BR}(\pi^\pm \pi_D^0)$  is experimentally known only with 2.7% relative precision <sup>19)</sup>. The only parameter not affected by an external uncertainty is the linear form factor slope  $\delta$  describing only the shape of the spectrum.

The applied corrections and the systematic uncertainties (excluding the external ones presented later) are summarized in Table 1.

## 2.7 Results and discussion

The measured parameters of the considered models and the corresponding BRs in the full  $z$  range, as well the model-independent  $\text{BR}_{\text{mi}}(z > 0.08)$ , with their statistical, systematic, and external uncertainties are presented in Table 2. The correlation coefficients between the pairs of model parameters, not listed in the table, are  $\rho(\delta, f_0) = -0.963$ ,  $\rho(a_+, b_+) = -0.913$ , and  $\rho(M_a, M_\rho) = 0.998$ .

Fits to all the three models are of reasonable quality, however the linear form-factor model leads to the smallest  $\chi^2$ . The data sample is insufficient to distinguish between the models considered.

The obtained form factor slope  $\delta$  is in agreement with the previous measurements based on  $K^+ \rightarrow \pi^+ e^+ e^-$  <sup>5, 6)</sup> and  $K^\pm \rightarrow \pi^\pm \mu^+ \mu^-$  <sup>20)</sup> samples, and further confirms the contradiction of the data to meson dominance models <sup>21)</sup>. The obtained  $f_0$ ,  $a_+$  and  $b_+$  are in agreement with the only previous measurement <sup>6)</sup>. The measured parameters  $M_a$  and  $M_\rho$  are a few % away from the nominal masses of the resonances <sup>19)</sup>.

The branching ratio in the full kinematic range, which is computed as the

Table 2: Results of fits to the three considered models, and the model-independent  $\text{BR}_{\text{mi}}(z > 0.08)$ .

$\delta =$	$2.35 \pm 0.15_{\text{stat.}} \pm 0.09_{\text{syst.}} \pm 0.00_{\text{ext.}}$	$=$	$2.35 \pm 0.18$
$f_0 =$	$0.532 \pm 0.012_{\text{stat.}} \pm 0.008_{\text{syst.}} \pm 0.007_{\text{ext.}}$	$=$	$0.532 \pm 0.016$
$\text{BR}_1 \times 10^7 =$	$3.02 \pm 0.04_{\text{stat.}} \pm 0.04_{\text{syst.}} \pm 0.08_{\text{ext.}}$	$=$	$3.02 \pm 0.10$
$a_+ =$	$-0.579 \pm 0.012_{\text{stat.}} \pm 0.008_{\text{syst.}} \pm 0.007_{\text{ext.}}$	$=$	$-0.579 \pm 0.016$
$b_+ =$	$-0.798 \pm 0.053_{\text{stat.}} \pm 0.037_{\text{syst.}} \pm 0.017_{\text{ext.}}$	$=$	$-0.798 \pm 0.067$
$\text{BR}_2 \times 10^7 =$	$3.11 \pm 0.04_{\text{stat.}} \pm 0.04_{\text{syst.}} \pm 0.08_{\text{ext.}}$	$=$	$3.11 \pm 0.10$
$M_a/\text{GeV} =$	$0.965 \pm 0.028_{\text{stat.}} \pm 0.018_{\text{syst.}} \pm 0.002_{\text{ext.}}$	$=$	$0.965 \pm 0.033$
$M_\rho/\text{GeV} =$	$0.711 \pm 0.010_{\text{stat.}} \pm 0.007_{\text{syst.}} \pm 0.002_{\text{ext.}}$	$=$	$0.711 \pm 0.013$
$\text{BR}_3 \times 10^7 =$	$3.15 \pm 0.04_{\text{stat.}} \pm 0.04_{\text{syst.}} \pm 0.08_{\text{ext.}}$	$=$	$3.15 \pm 0.10$
$\text{BR}_{\text{mi}} \times 10^7 =$	$2.26 \pm 0.03_{\text{stat.}} \pm 0.03_{\text{syst.}} \pm 0.06_{\text{ext.}}$	$=$	$2.26 \pm 0.08$

average between the two extremes corresponding to the models (1) and (3), and includes an uncertainty due to extrapolation into the inaccessible region  $z < 0.08$ , is

$$\text{BR} = (3.08 \pm 0.04_{\text{stat.}} \pm 0.04_{\text{syst.}} \pm 0.08_{\text{ext.}} \pm 0.07_{\text{model}}) \times 10^{-7} = (3.08 \pm 0.12) \times 10^{-7}.$$

It should be stressed that a large fraction of the uncertainty of this result is correlated with the earlier measurements. A comparison to the precise BNL E865 measurement <sup>6)</sup> dismissing correlated uncertainties due to external BRs and model dependence, and using the same external input, shows a  $1.4\sigma$  difference. In conclusion, the obtained BR is in agreement with the previous measurements.

Finally, a first measurement of the direct CP violating asymmetry of  $K^+$  and  $K^-$  decay rates in the full kinematic range was obtained by performing BR measurements separately for  $K^+$  and  $K^-$  and neglecting the correlated uncertainties:  $\Delta(K_{\pi ee}^\pm) = (\text{BR}^+ - \text{BR}^-)/(\text{BR}^+ + \text{BR}^-) = (-2.1 \pm 1.5_{\text{stat.}} \pm 0.3_{\text{syst.}})\%$ . The result is compatible to no CP violation. However its precision is far from the theoretical expectation <sup>2)</sup> of  $|\Delta(K_{\pi ee}^\pm)| \sim 10^{-5}$ .

### 3 $K^\pm \rightarrow \pi^\pm \gamma \gamma$ analysis

The  $K^\pm \rightarrow \pi^\pm \gamma \gamma$  rate is measured relatively to the  $K^\pm \rightarrow \pi^\pm \pi^0$  normalization channel. The signal and normalization channels have identical particle composition of the final states, and the only cut differing for the two channels is

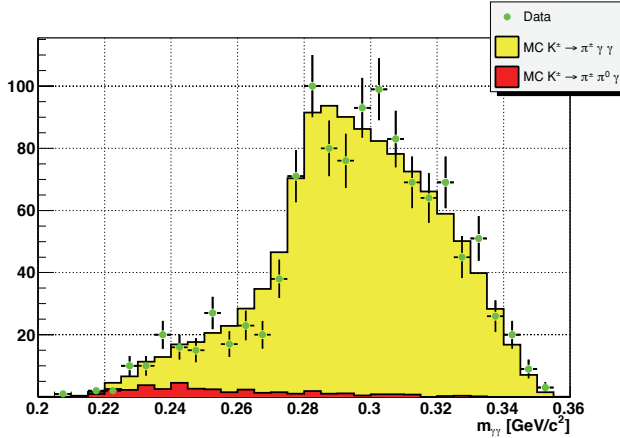


Figure 3: The reconstructed spectrum of  $\gamma\gamma$  invariant mass for the  $K^\pm \rightarrow \pi^\pm \gamma\gamma$  decay (dots), and its comparison to MC expectation assuming ChPT  $\mathcal{O}(p^6)$  distribution with  $\hat{c} = 2$  (filled area).

the one on the  $\gamma\gamma$  invariant mass. The used trigger chain involves the so called “neutral trigger” based on requirement of minimal number of energy deposition clusters in the LKr calorimeter.

About 40% of the total NA48/2 data sample have been analyzed, and 1,164  $K^\pm \rightarrow \pi^\pm \gamma\gamma$  decay candidates (with background contamination estimated by MC to be 3.3%) are found, which has to be compared with the only previous measurement<sup>9)</sup> involving 31 decay candidates. The reconstructed spectrum of  $\gamma\gamma$  invariant mass in the accessible kinematic region  $M_{\gamma\gamma} > 0.2$  GeV/ $c^2$  is presented in Fig. 3, along with a MC expectation assuming ChPT  $\mathcal{O}(p^6)$  distribution<sup>7)</sup> with a realistic parameter  $\hat{c} = 2$ . ChPT predicts an enhancement of the decay rate (cusp-like behaviour) at the  $\pi\pi$  mass threshold  $m_{\gamma\gamma} \approx 280$  MeV/ $c^2$ , independently of the value of the  $\hat{c}$  parameter. The observed spectrum provides the first clean experimental evidence for this phenomenon.

As the first step of the analysis, the partial width of the decay was measured assuming the ChPT  $\mathcal{O}(p^6)$  shape with a fixed parameter  $\hat{c} = 2$ . The following preliminary result, which is in agreement with the ChPT computation for  $\hat{c} = 2$ , was obtained:

$$\text{BR} = (1.07 \pm 0.04_{\text{stat.}} \pm 0.08_{\text{syst.}}) \times 10^{-6}.$$

A combined fit of the  $m_{\gamma\gamma}$  spectrum shape and the decay rate is foreseen to measure the  $\hat{c}$  parameter.

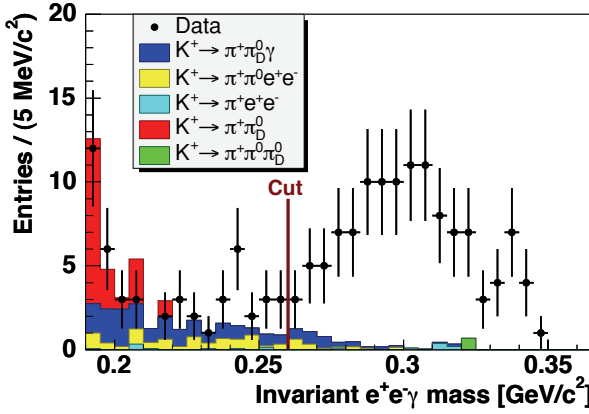


Figure 4: The reconstructed spectrum of  $\gamma e^+ e^-$  invariant mass for the  $K^\pm \rightarrow \pi^\pm \gamma e^+ e^-$  decay (dots), and MC background expectations (filled areas).

#### 4 $K^\pm \rightarrow \pi^\pm \gamma e^+ e^-$ analysis

The  $K^\pm \rightarrow \pi^\pm \gamma e^+ e^-$  rate is measured relatively to the  $K^\pm \rightarrow \pi^\pm \pi_D^0$  normalization channel. The signal and normalization channels have identical particle composition of the final states. The same trigger chain as for the collection of  $K^\pm \rightarrow \pi^\pm e^+ e^-$  is used.

With the full NA48/2 data sample analyzed, 120  $K^\pm \rightarrow \pi^\pm \gamma e^+ e^-$  decay candidates (with the background estimated by MC to be 6.1%) are found in the accessible kinematic region  $M_{\gamma ee} > 0.26 \text{ GeV}/c^2$ . This is the first observation of this decay mode. The reconstructed spectrum of  $\gamma e^+ e^-$  invariant mass is presented in Fig. 4, along with MC expectations for background contributions. The spectrum provides another evidence for the rate enhancement at the  $\pi\pi$  mass threshold.

The final results of the analysis have recently been published <sup>10)</sup>. The model-independent partial width in the accessible kinematic region is measured to be

$$\text{BR}(M_{\gamma ee} > 0.26 \text{ GeV}/c^2) = (1.19 \pm 0.12_{\text{stat.}} \pm 0.04_{\text{syst.}}) \times 10^{-8}.$$

The ChPT parameter  $\hat{c}$  assuming  $\mathcal{O}(p^4)$  distribution <sup>8)</sup> was measured to be  $\hat{c} = 0.90 \pm 0.45$ .

## Conclusions

A precise study of the  $K^\pm \rightarrow \pi^\pm e^+ e^-$  decay has been performed. The data sample and precision are comparable to world's best ones, the preliminary results are in agreement with the previous measurements, and the first limit on CP violating charge asymmetry has been obtained.

A precise study of the  $K^\pm \rightarrow \pi^\pm \gamma \gamma$  has been performed. The first clear evidence for a rate enhancement at  $\pi\pi$  mass threshold has been obtained. The preliminary measurement of BR agrees with the ChPT prediction. A detailed spectrum shape study is foreseen.

The first observation of the  $K^\pm \rightarrow \pi^\pm \gamma e^+ e^-$  decay, and measurement of its parameters, including the BR, have been performed. The  $M_{\gamma ee}$  spectrum provides an independent evidence for the cusp at the  $\pi\pi$  mass threshold.

## References

1. G. Ecker, A. Pich, E. de Rafael, Nucl. Phys. **B291** (1987) 692.
2. G. D'Ambrosio *et al.*, JHEP **8** (1998) 4.
3. A.Z. Dubničková *et al.*, Phys. Part. Nucl. Lett. **5**, vol. 2 (2008) 76 [hep-ph/0611175].
4. P. Bloch *et al.*, Phys. Lett. **B56** (1975) 201 (1975).
5. C. Alliegro *et al.*, Phys. Rev. Lett. **68** (1992) 278 (1992).
6. R. Appel *et al.*, Phys. Rev. Lett. **83** (1999) 4482.
7. G. D'Ambrosio, J. Portolés, Phys. Lett. **B386** (1996) 403.
8. F. Gabbiani, Phys. Rev. **D59** (1999) 094022.
9. P. Kitching *et al.*, Phys. Rev. Lett. **79** (1997) 4079.
10. J.R. Batley *et al.*, Phys. Lett. **B659** (2008) 493.
11. J.R. Batley *et al.*, Eur. Phys. J. **C52** (2007) 875.
12. G.D. Barr *et al.*, Nucl. Inst. Methods **A370** (1996) 413.
13. V. Fanti *et al.*, Nucl. Inst. Methods **A574** (2007) 433.

14. GEANT detector description and simulation tool, CERN program library long writeup W5013 (1994).
15. E. Barberio and Z. Was, *Comp. Phys. Comm.* **79** (1994) 291.
16. R. Frühwirth, *Nucl. Inst. Methods* **A262** (1987) 444.
17. R. Appel *et al.*, *Phys. Rev. Lett.* **85** (2000) 2877.
18. M. Antonelli *et al.*, arXiv:0801.1817.
19. W.-M. Yao *et al.* (PDG), *J. Phys.* **G33** (2006) 1.
20. H. Ma *et al.*, *Phys. Rev. Lett.* **84** (2000) 2580.
21. P. Lichard, *Phys. Rev.* **D60** (1999) 053007.

**$e^+e^-$  WITH KTEV**

Edward Blucher  
*University of Chicago, USA*

Written contribution not received



**SEMILEPTONIC  $B$  DECAYS AND MEASUREMENTS OF CKM  
ELEMENTS AT THE B FACTORIES**

E. Barberio

*School of Physics, University of Melbourne, Parkville, Victoria 3010,  
Australia*

We present the most recent results on the determination of CKM parameters from B semileptonic decays.

## 1 Introduction

Within the framework of the Standard Model (SM) of electroweak interactions, the elements of the Cabibbo-Kobayashi-Maskawa (CKM) mixing matrix<sup>1)</sup> are free parameters, constrained only by the requirement that the matrix be unitary. The CKM matrix element cannot be predicted and their values must be determined by experiment. Their magnitudes are extracted by confronting experimental measurements to SM theoretical expressions.

Since the first reports of CP violation in the  $B$  sector by the B-factory experiments BaBar and Belle in 2001, the precision to which the angle  $\sin 2\phi_1$  ( $\sin 2\beta$ ) has reached is approximately 4%. The length of the side of the unitarity triangle opposite the well-measured angle  $\phi_1$  is proportional to the ratio  $|V_{ub}|/|V_{cb}|$ , making its determination a high priority in flavour physics. Both of these elements can be measured using semileptonic  $B$  meson decays. Using charmed semileptonic decays, the precision to which  $|V_{cb}|$  has been determined is of order 2%. On the other hand  $|V_{ub}|$ , which can be measured using charmless semileptonic decays, is the most poorly known of all CKM matrix elements with a precision of order 7%.

At quark level the  $b \rightarrow c(u)$  transitions can be described by the CKM elements  $|V_{xb}|$  and by perturbative QCD. However quarks are bound inside hadrons, and non-perturbative long distance interactions must be taken into account when extracting  $|V_{xb}|$  from the decay rates. Consequently, the main error in the extraction of the CKM elements derives from the understanding of the long distance contribution.

## 2 $|V_{cb}|$

HQET provides a means to determine  $|V_{cb}|$  with small theoretical uncertainties, by studying the decay rates of semileptonic  $b$ -quark decays. There are two experimental methods to determine  $|V_{cb}|$ : the **exclusive** method, where  $|V_{cb}|$  is extracted by studying the exclusive  $\bar{B}^0 \rightarrow D^{*+} \ell^- \bar{\nu}_\ell$  decay process; and the **inclusive** method, which uses the semileptonic decay width of  $b$ -hadron decays. In both methods, the extraction of  $|V_{cb}|$  is systematics limited and the dominant errors are from theory. In this review both methods are discussed.

## 3 Exclusive $|V_{cb}|$

In the exclusive method, the value of  $|V_{cb}|$  is extracted by studying the decay rate for the process  $\bar{B}^0 \rightarrow D^{*+} \ell^- \bar{\nu}_\ell$  as a function of the recoil kinematics of the  $D^{*+}$  meson. The decay rate is parameterised as a function of the variable

$w$ , defined as the product of the four velocities of the  $D^{*+}$  and the  $\bar{B}^0$  mesons. Hence,  $w$  is a function of the  $B \rightarrow D^*$  momentum transfer squared,  $q^2$ .

The semileptonic  $B \rightarrow D^* \ell \nu$  decay rate can be described by three form factors are specified by two ratios  $R_1$  and  $R_2$ , and by a single parameter  $\rho^2$ . The first measurements of these three parameters were made by the CLEO collaboration <sup>2)</sup>. BaBar recently improved upon these measurements <sup>3)</sup>. BaBar measured the dependence of  $\bar{B}^0 \rightarrow D^{*+} e^- \bar{\nu}_e$  on the decay angles and momentum transfer. They determined  $R_1$ ,  $R_2$ , and  $\rho^2$ . In this analysis it is crucial to correctly evaluate the contribution of the background from  $B \rightarrow D^{**} \ell \nu$  decays. The results are  $R_1 = 1.396 \pm 0.060 \pm 0.035 \pm 0.027$ ,  $R_2 = 0.885 \pm 0.040 \pm 0.022 \pm 0.013$ , and  $\rho^2 = 1.145 \pm 0.059 \pm 0.030 \pm 0.035$ . The stated uncertainties are the statistical from the data, statistical from the size of the Monte Carlo sample and the systematic uncertainty, respectively.

Prior to this measurement by BaBar all the measurements relied on the form factor ratios  $R_1$  and  $R_2$  as measured by the CLEO collaboration <sup>2)</sup>. The world average takes into account the new BaBar measurements, and returns the following values for the two parameters of interest <sup>4)</sup>:

$$F(1)|V_{cb}| = (35.9 \pm 0.6) \times 10^{-3},$$

$$\rho^2 = 1.19 \pm 0.06,$$

with a much smaller error with respect to previous averages on  $\rho^2$ . Using  $F(1) = 0.92 \pm 0.04$  <sup>5)</sup>, one gets:

$$|V_{cb}| = (39.0 \pm 0.7_{exp} \pm 1.7_{theo}) \times 10^{-3}.$$

### 3.1 $B \rightarrow D^{**} \ell \nu$ decays

It is important to understand the composition of the inclusive B semileptonic decay rate in terms of exclusive final states for use in semileptonic B decay analyses. The  $B \rightarrow D^{(*)} \ell \nu$  decays are well measure, but a sizeable fraction of the semileptonic B decay rate is, however, not accounted for by the measured branching ratios of  $B \rightarrow D^{(*)} \ell \nu$ . Details of the various  $B$  decays to higher mass  $D^{(*)}$  resonances are less well known.

At present, measurements of the composition of semileptonic  $B$  decays involving  $D^{**}$  are incomplete. The ALEPH <sup>15)</sup>, CLEO, DELPHI <sup>15)</sup>, and D0 experiments have reported evidence of the narrow resonant states ( $D_1$  and  $D_2^*$ ) in semileptonic decays, whereas more recent measurements by the BaBar <sup>16)</sup> and Belle <sup>17)</sup> experiments provide semi-inclusive measurements to  $D^{(*)} \pi \ell \nu$  final states <sup>14)</sup>, <sup>16)</sup>. The total branching fractions of the  $\bar{B} \rightarrow D^{(*)} \pi \ell \nu$  decays

are calculated assuming isospin symmetry,  $B(\bar{B} \rightarrow D^{(*)}\pi^0\ell\nu) = 1/2B(\bar{B} \rightarrow D^{(*)}\pi^\pm\ell\nu)$ , to estimate the branching fractions of the  $D^{(*)}\pi^0$  final states:

$$\begin{aligned} B(B^- \rightarrow D^{(*)}\pi\ell\nu) &= (1.52 \pm 0.12_{stat} \pm 0.10_{syst})\% \\ B(\bar{B}^0 \rightarrow D^*\pi\ell\nu) &= (1.37 \pm 0.17_{stat} \pm 0.10_{syst})\%. \end{aligned}$$

The differences between the measured inclusive semileptonic branching fraction and the sum of all exclusive  $B$  semileptonic measurements give  $(2.22 \pm 0.38)\%$  for the  $\bar{B}^0$  and  $(1.27 \pm 0.37)\%$  for  $B^+$  decays. In both cases the sum of the exclusive components does not saturate the  $B$  semileptonic rate.

#### 4 Inclusive Determination of $|V_{cb}|$

The most precise determinations of  $|V_{cb}|$  are obtained using combined fits to inclusive  $B$  decay distributions <sup>6, 7</sup>). These determinations are based on calculations of the semileptonic decay rate in the frameworks of the Operator Product Expansion (OPE) <sup>8</sup>) and Heavy Quark Effective Theory (HQET) <sup>6, 9</sup>). These calculations predict the semileptonic decay rate in terms of  $|V_{cb}|$ , the  $b$ -quark mass  $m_b$ , and non-perturbative matrix elements that enter at the order  $1/m_b^2$ . The spectator model decay rate is the leading term in a well-defined expansion controlled by the parameter  $\Lambda_{\text{QCD}}/m_b$  <sup>9, 10, 11, 12</sup>) with non-perturbative corrections arising to order  $1/m_b^2$ . The key issue in this approach is the ability to separate non-perturbative corrections and perturbative corrections (expressed in powers of  $\alpha_s$ ). Perturbative and non-perturbative corrections depend on the  $m_b$  definition, *i.e.* the expansion scheme. High precision comparison of theory and experiment requires a precise determination of the heavy quark masses, as well as the non-perturbative matrix elements that enter the expansion. Heavy Quark Expansions (HQE) <sup>6, 12, 13</sup>) express the semileptonic decay width  $\Gamma_{\text{SL}}$ , moments of the lepton energy and hadron mass spectra in  $B \rightarrow X_c\ell\nu$  decays in terms of the running kinetic quark masses  $m_b^{\text{kin}}$  and  $m_c^{\text{kin}}$  as well as the  $b$ -quark mass  $m_b^{1\text{S}}$  in the 1S expansion scheme. These schemes should ultimately yield consistent results for  $|V_{cb}|$ . The precision of the  $b$ -quark mass is also important for  $|V_{ub}|$ , a limiting factor in the unitarity triangle. The shape of the lepton spectrum and of the hadronic mass spectrum provide constraints on the heavy quark expansion, which allows for the calculation of the properties of  $B(B \rightarrow X_c\ell\nu)$  transitions. So far, measurements of the hadronic mass distribution have been made by BaBar <sup>31</sup>), Belle <sup>18</sup>), CLEO <sup>19</sup>), DELPHI <sup>32</sup>) and CDF <sup>33</sup>). The leptonic spectrum has been measured by BaBar <sup>22</sup>), Belle <sup>23</sup>), CLEO <sup>19</sup>) and DELPHI <sup>32</sup>).

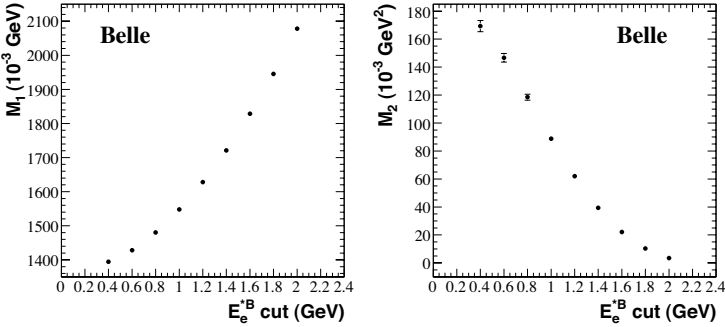


Figure 1: Belle: first (top) and second (bottom) moments as a function of the electron energy cut-off,  $E_{e\text{ cut}}^{*B}$  (referred to as  $E_{\min}$  in the text).

The most recent measurement of the electron energy spectrum is from Belle. Events are selected by fully reconstructing one of the  $B$  mesons, produced in  $\Upsilon(4S)$  decays. Belle determines the true electron energy spectrum by unfolding the measured spectrum from detector effects, in the  $B$  meson rest frame, denoted  $E_e^{*B}$ . The unfolded spectrum is corrected for QED radiative effects. Belle measures the  $B^0$  and  $B^+$  average partial branching fractions  $\mathcal{B}(B \rightarrow X_c \ell \nu)_{E_\ell < E_{\min}}$  and the first four moments of the electron energy spectrum for electron energy thresholds,  $E_{\min}$ , from 0.4 to 2.0 GeV<sup>23)</sup> (Fig.1). The main systematic errors originate from event selection, electron identification, background estimation and signal model dependence.

Belle<sup>18)</sup>, BaBar<sup>31)</sup> and CLEO<sup>19)</sup> explored the moments of the hadronic mass spectrum,  $M_X^2$ , as a function of the lepton momentum cuts. DELPHI<sup>32)</sup> measured  $M_X^2$  over the full lepton momentum and CDF<sup>33)</sup> measured the hadronic mass spectrum above 0.6 GeV lepton momentum. Both BaBar and Belle used a fully reconstructed  $B$  sample. Belle measures the first, second central and second non-central moments of the unfolded  $M_X^2$  spectrum in  $B \rightarrow X_c \ell \nu$ , for lepton energy thresholds,  $E_{\min}$ , from 0.7 to 1.9 GeV<sup>18)</sup>. BaBar measures the first, second central and second non-central moments of the  $M_X^2$  spectrum i, for lepton energy thresholds,  $E_{\min}$ , from 0.9 to 1.9 GeV<sup>18)</sup>. Principal systematic errors originate from background estimation, unfolding and signal model dependence.

Using these measurements, it is possible to determine the CKM matrix element  $|V_{cb}|$ , and HQE parameters by performing global fit analyses in the kinetic and 1S  $b$ -quark mass schemes<sup>24)</sup>. To further constrain the  $b$ -quark

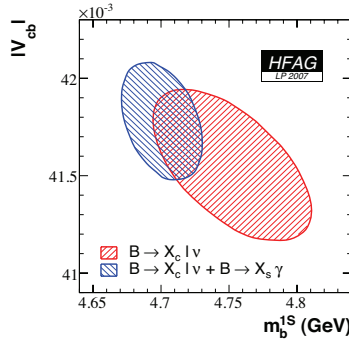


Figure 2: Fit results for  $|V_{cb}|$  and  $m_b^{1S}$  to  $B \rightarrow X_c \ell \nu$  data only (dashed line) and  $B \rightarrow X_c \ell \nu$  and  $B \rightarrow X_s \gamma$  data combined (solid line). The ellipses are  $\Delta\chi^2 = 1$  (26).

mass the photon energy moments in  $B \rightarrow X_s \gamma$  decays (25) are also included. Measurements that do not have corresponding theoretical predictions and those with high cutoff energies are excluded.

#### 4.1 1S expansion

The inclusive spectral moments of  $B \rightarrow X_c \ell \nu$  decays have been derived in the 1S scheme up to  $\mathcal{O}(1/m_b^3)$  (6). The theoretical expressions for the truncated moments are given in terms of HQE parameters with coefficients determined by theory, as functions of  $E_{\min}$ . One finds the following results for the fit parameters, if all measured moments of inclusive distributions in  $B \rightarrow X_c \ell \nu$  and  $B \rightarrow s \gamma$  decays are used (Fig. 2) (26):

$$\begin{aligned} |V_{cb}| &= (41.78 \pm 0.33_{fit} \pm 0.08_{\tau_B}) \times 10^{-3}, \\ m_b^{1S} &= (4.708 \pm 0.030) \text{ GeV}. \end{aligned}$$

#### 4.2 Kinetic mass expansion

Spectral moments of  $B \rightarrow X_c \ell \nu$  decays have been derived up to  $\mathcal{O}(1/m_b^3)$  in the kinetic scheme (12). The theoretical expressions used in the fit contain improved calculations of the perturbative corrections to the lepton energy moments (27) and account for the  $E_{\min}$  dependence of the perturbative corrections

to the hadronic mass moments<sup>28)</sup>. For the  $B \rightarrow X_s \gamma$  moments, the (biased) OPE prediction and the bias correction have been calculated<sup>13)</sup>. All these expressions depend on the  $b$ - and  $c$ -quark masses  $m_b(\mu)$  and  $m_c(\mu)$ . The CKM element  $|V_{cb}|$  is a free parameter in the fit, related to the semileptonic width  $\Gamma(B \rightarrow X_c \ell \nu)$ <sup>9)</sup>. A fit was performed for all measured moments (excluding new BaBar measurements) of inclusive distributions in  $B \rightarrow X_c \ell \nu$  and  $B \rightarrow s \gamma$  decays to extract  $|V_{cb}|$  and the  $b$ - and  $c$ -quark masses. The  $|V_{cb}|$  and  $m_b$  values obtained are:

$$\begin{aligned} |V_{cb}| &= (41.91 \pm 0.19_{\text{exp}} \pm 0.28_{\text{HQE}} \pm 0.59_{\Gamma_{\text{SL}}}) \times 10^{-3}, \\ m_b &= 4.613 \pm 0.022_{\text{exp}} \pm 0.027_{\text{HQE}} \text{ GeV}, \end{aligned}$$

where the errors are experimental and theoretical (HQE and  $\Gamma_{\text{SL}}$ ) respectively.

## 5 $|V_{ub}|$

The experimental and theoretical issues surrounding the determination of  $|V_{ub}|$  are complex and sometimes controversial. Progress in the last few years nonetheless has made it a concrete possibility that  $|V_{ub}|$  will soon be determined with a precision of 7% or better. Both inclusive and exclusive methods of measuring  $|V_{ub}|$  have been pursued, with the inclusive methods giving values with approximately 7-8% precision. The exclusive determination of  $|V_{ub}|$  currently has a precision of about 10%. The aim of the ongoing programme of measurements is to improve this precision to better than 5%, for comparison with the inclusive results. In addition to having different efficiencies and signal-to-background ratios, the inclusive and exclusive measurements depend on different types of theoretical calculations. Pursuing both approaches and comparing the results will help us verify the robustness of the theoretical errors, which limit the current precision of  $|V_{ub}|$ .

## 6 Exclusive Determination

Measurements of exclusive charmless semileptonic  $B$  meson decays, can most readily be performed at electron-positron storage rings, where large numbers of  $B\bar{B}$  pairs are produced through the process  $e^+e^- \rightarrow \Upsilon(4S) \rightarrow B\bar{B}$ . The aim is to measure the rate of the tree level quark transition  $b \rightarrow u\ell\nu$ , whose amplitude depends on  $V_{ub}$ .

The situation is complicated by strong interaction effects, as the  $b$  and  $u$  quarks are bound into mesons, which require factors depending on  $q^2$ . The most promising decays for measuring  $|V_{ub}|$  are those where the final state meson is spinless, as only two form factors are required to describe the branching

fraction, and only one if the mass of the final state lepton is neglected. If the final state meson is a pion, the differential branching fraction can be written as:

$$\frac{d(B \rightarrow \pi \ell \nu)}{dq^2} = \frac{G_F^2}{24\pi^3} |V_{ub}|^2 p_\pi^3 |f_+(q^2)|^2$$

where  $p_\pi$  is the pion momentum and  $f_+(q^2)$  is the form factor. Thus experiment determines the product  $|V_{ub}|f_+(q^2)$ , and to extract  $|V_{ub}|$ , both the shape and normalization of  $f_+(q^2)$  are required. Input to  $f_+(q^2)$  comes from theory (37).

Fig. 3 lists the measurements of the branching fractions compiled and averaged by HFAG. Note that presently the untagged methods still give the best experimental precision for the branching fraction.

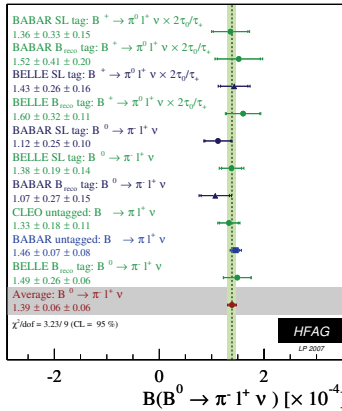


Figure 3: Branching fractions compiled and averaged by HFAG, 2007

Most of the recent measurements provide some information on the  $q^2$  dependence.

Using the measurement of branching fraction, one can extract  $|V_{ub}|$  from:

$$|V_{ub}| = \sqrt{\frac{B(B \rightarrow \pi^+ \ell \nu)}{\Gamma_{th} \tau_B}},$$

where  $\Gamma_{thy}$  is the form factor normalization provided by theory and is the  $B$  meson lifetime. The branching fraction measurements from all of the analyses are combined to give a global average in three  $q^2$  ranges: the full range which extends to approximately  $25 \text{ GeV}^2$ , the ranges  $q^2 < 16 \text{ GeV}^2$ , to which LCSR apply, and  $q^2 > 16 \text{ GeV}^2$ , to which Lattice QCD applies.  $|V_{ub}|$  is calculated using the predictions of LCSR (40), HPQCD lattice (38) FNAL lattice (39) and their stated theoretical errors.

## 7 Inclusive Determination

In an inclusive measurement of  $|V_{ub}|$ , one measures the rate of the charmless semileptonic  $B$  decay,  $B \rightarrow X_u \ell \nu$ . Since the  $u$ -quark is much lighter than the  $c$ -quark, the  $B \rightarrow X_u \ell \nu$  signal can be separated from the more abundant  $B \rightarrow X_c \ell \nu$  background by taking advantage of the differences in decay kinematics. The decay rate for  $B \rightarrow X_u \ell \nu$  is proportional to  $|V_{ub}|^2$  and  $m_b^5$ . The theoretical description of inclusive  $B \rightarrow X_u \ell \nu$  decays is based on the Heavy Quark Expansion, as for  $B \rightarrow X_c \ell \nu$  decays, which predicts the total decay rate with uncertainties of about 5%.

Experimentally, the principal challenge is to separate the signal  $B \rightarrow X_u \ell \nu$  decays from the 50 times larger  $B \rightarrow X_c \ell \nu$  background. This can be achieved by selecting regions of phase space in which this background is highly suppressed. In these regions the spectra are affected by the distribution of the  $b$ -quark momentum inside the  $B$  meson, which can be described by a structure or "shape function" (SF), in addition to weak annihilation and other non-perturbative effects. Extrapolation from the limited momentum range near the endpoint to the full spectrum is a difficult task. The shape function is a universal property of  $B$  mesons at leading order. Several functional forms for the SF have been proposed. The values and precise definitions of these parameters depend on the specific ansatz for the SF, the mass renormalization scheme, and the renormalization scale chosen.

In inclusive measurements, the most common kinematic variables discussed in the literature, each having their own advantages, are the lepton energy ( $E_e$ ), the hadronic invariant mass ( $M_X$ ), the leptonic invariant mass squared ( $q^2$ ) and the light-cone momentum component  $P_+ = E_X - |P_X|$ . In all cases, the experiments need to model  $B \rightarrow X_u \ell \nu$  decays in order to calculate acceptances and efficiencies. The rate of inclusive charmless semileptonic  $B$  decays is obtained experimentally from:

$$\Delta\Gamma_{u\ell\nu}(\Delta\Phi) = \mathcal{B}_{u\ell\nu}(\Delta\Phi)/\tau_B,$$

where  $\Delta\Phi$  is the measured region of phase space, and  $\tau_B$  is the  $B$  lifetime. The theoretical treatment is implemented as a numerical calculation of  $\mathcal{R}(\Delta\Phi)$ , related to  $|V_{ub}|$  in the following formula:

$$|V_{ub}| = \sqrt{\frac{\Delta\Gamma_{u\ell\nu}(\Delta\Phi)}{\mathcal{R}(\Delta\Phi)}}.$$

Various theoretical models have been developed to convert measured partial rates into values of  $|V_{ub}|$ .

Because of the presence of the  $B \rightarrow X_c \ell \nu$  background, the inclusive  $B \rightarrow X_u \ell \nu$  decay width cannot be directly measured. The experiments measure,

instead, partial decay widths in limited regions of the phase space that are relatively free from the  $B \rightarrow X_c \ell \nu$  background. This is achieved by a cut on one or more of the three kinematic variables of the  $X \ell \nu$  final state: the lepton energy, the hadronic mass  $m_X$ , and the lepton-neutrino invariant mass squared  $q^2$ . The fraction,  $f_u$ , of the  $B \rightarrow X_u \ell \nu$  events that pass the experimental cut needs to be accurately known in order to determine  $|V_{ub}|$ . The OPE framework can reliably predict the inclusive  $B \rightarrow X_u \ell \nu$  decay rate as long as it is integrated over a large region of the phase space. The experimental cuts required to suppress the  $B \rightarrow X_c \ell \nu$  background violate this requirement. Hence, one must use a distribution function, known as the shape function, that cannot be computed perturbatively, and must be determined experimentally.

The first  $|V_{ub}|$  measurement performed with the endpoint technique was by CLEO. In the rest frame of the  $B$  meson, the kinematic endpoint of the lepton momentum spectrum is about 2.3 GeV for the dominant  $B \rightarrow X_c \ell \nu$  decays and about 2.6 GeV for  $B \rightarrow X_u \ell \nu$  decays. The spectrum above 2.3 GeV is dominated by leptons from  $B \rightarrow X_u \ell \nu$  transitions, and this allows for a relatively precise measurement, largely free from  $B\bar{B}$  background, in a 300 MeV interval that covers approximately 10% of the total electron spectrum for charmless semileptonic  $B$  decays. Belle extracts the  $B \rightarrow X_u \ell \nu$  signal in the momentum region 1.9–2.6 GeV, BaBar covers 2–2.6 GeV and CLEO 2.3–2.6 GeV.

The analyses that involve the reconstruction of the hadron system are typically performed on samples of events where one of the  $B$  mesons from the  $\Upsilon(4S)$  decay is fully reconstructed, while the semileptonic decay of the signal side  $B$  meson is identified by a high momentum electron or muon. With this sample all of the kinematic variables that describe the signal decay can be reconstructed, the invariant meson mass  $M_X$ , the lepton neutrino mass squared  $q^2$ , and the hadronic light-cone momentum  $P_+$ , which are the best available discriminators of signal and background in inclusive  $|V_{ub}|$  analyses. BaBar selected semileptonic  $B \rightarrow X_u \ell \nu$  decays using an approach based on simultaneous requirements for the electron energy,  $E_e$ , and the invariant mass squared of the  $e\nu$  pair,  $q^2$  <sup>41</sup>). The dominant charm background is suppressed by selecting a region of the  $q^2 - E_e$  phase space where correctly reconstructed  $B \rightarrow X_c \ell \nu$  events are kinematically excluded.

It is possible to reduce the theoretical error on the extrapolation by applying simultaneous cuts on  $M_X$  and  $q^2$  in inclusive  $B \rightarrow X_u \ell \nu$  decays <sup>42</sup>). The  $M_X$  distribution has a large usable fraction of events, of the order of 70%, it depends on the shape function describing the Fermi motion of the  $b$  quark inside the  $B$  meson. Unfortunately, only a small fraction of events (about 20%) are usable with a pure  $q^2$  selection. The study in <sup>42</sup>) shows that combined cuts on  $M_X$  and  $q^2$  mitigate the drawbacks of the two methods while retaining

good statistical and systematic sensitivities. BaBar performed a measurement of the  $|V_{ub}|$  CKM matrix element, on the fully reconstructed B sample, by using the combined information of the  $M_X$ - $q^2$  distribution to discriminate signal and background and to minimize the theoretical uncertainties<sup>43)</sup>. Belle and BaBar have measured partial rates with cuts on  $M_X$ ,  $q^2$ ,  $E_e$ , but the highlight is the first measurement of the light-cone momentum  $P_+$ <sup>44)</sup>. Belle measures the partial branching fraction in the kinematic region:  $P_+ < 0.66$  GeV. BaBar<sup>29)</sup> measured  $M_X$ ,  $P_+$  and  $q^2$  spectra with  $M_X < 1.7$  GeV<sup>2</sup>, Figure 4.

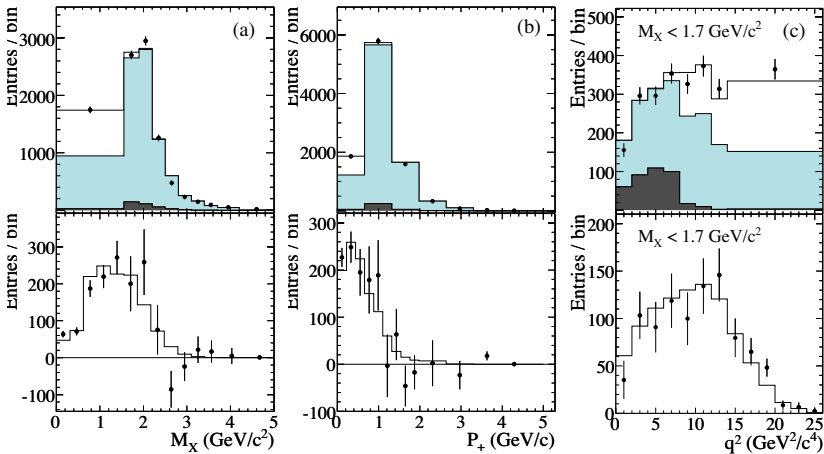


Figure 4: Upper row: measured  $M_X$  (a),  $P_+$  (b) and  $q^2$  with  $M_X < 1.7$  GeV<sup>2</sup> (c) spectra (data points). The result of the fit to the sum of three MC contributions is shown in the histograms:  $B \rightarrow X_u \ell \nu$  decays generated inside (no shading) and outside (dark shading) the selected kinematic region, and backgrounds (light shading). Lower row: corresponding spectra for  $B \rightarrow X_u \ell \nu$  after background subtraction

### 7.1 $|V_{ub}|$ extraction

The global fits to  $B \rightarrow X_c \ell \nu$  and  $B \rightarrow s \gamma$  moments discussed earlier provide input values for the heavy quark parameters needed in calculating  $B \rightarrow X_u \ell \nu$  partial rates and to constrain the first and second moments of the shape function. Additional information is obtained from the photon energy spectrum in  $B \rightarrow s \gamma$  decays. The world average is determined by HFAG. We have chosen the value extracted using the BLPN<sup>45)</sup> theoretical framework as the world

average of the CKM parameter  $|V_{ub}|$ . The value of  $m_b$  used in the world average is from the global fit in the Kinetic scheme to measurements of  $B \rightarrow X_c \ell \nu$  and  $B \rightarrow s \gamma$  decays.

HFAG also extracts  $|V_{ub}|$  using the Dressed Gluon Exponentiation <sup>46)</sup> framework, a recent new addition to the phenomenology landscape of inclusive  $B$ -meson decays. That the value of  $|V_{ub}|$  obtained within the DGE framework agrees very well with the BLNP determination. At present, as indicated by the average given above, the uncertainty on  $|V_{ub}|$  is at the 7% level. The current estimates of these uncertainties contribute to a theoretical error of 5% on  $|V_{ub}|$ . The  $|V_{ub}|$  world average is calculated by comparing the measured partial branching fractions in selected regions of phase-space to theoretical calculations of the corresponding rates, which are proportional to  $|V_{ub}|^2$ . HFAG extracts  $|V_{ub}|$  using three theoretical frameworks, described in ref. <sup>45)</sup>–<sup>46)</sup>. In Fig. 5 the different  $|V_{ub}|$  are listed.

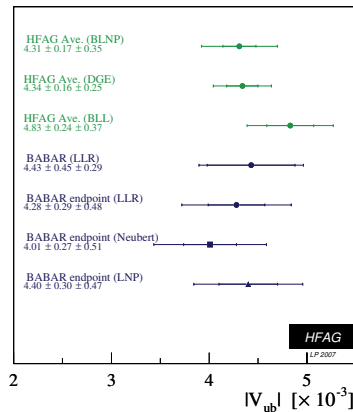


Figure 5: The world average for  $|V_{ub}|$

The dominant errors on  $|V_{ub}|$  are theoretical.

## 7.2 Weak annihilation

Weak annihilation contributions affect neutral and charged  $B$  mesons differently, because of flavour dependence. Little is known about the scale of this violation since it is fundamentally non-perturbative. Currently, only limits are available for the magnitude of weak annihilation. BaBar <sup>47)</sup> measured the partial branching fraction of charmless semileptonic  $B^0$  decays for several over-

lapping intervals in the lepton momentum spectrum. In the momentum range from 2.3 to 2.6 GeV they measure  $\Delta B(B^0 \rightarrow X_u \ell \nu) = (1.30 \pm 0.21 \pm 0.07)^{-4}$ . One can also express the result in terms of the charge asymmetry,

$$A^{+/0} = \frac{\Delta\Gamma^+ - \Delta\Gamma^0}{\Delta\Gamma^0 + \Delta\Gamma^+} = 0.08 \pm 0.15 \pm 0.08$$

which is compatible with zero, for the same momentum interval. This result is consistent with the limit set by the CLEO 48) .

### 7.3 inclusive vs exclusive

Precision determinations of  $|V_{ub}|$  and  $|V_{cb}|$  are central to testing the CKM sector of the Standard Model, and complement the measurements of CP asymmetries in  $B$  decays. The current compatibility between measurements of the CP-violation angles and the inclusive and exclusive contributions suggests tension between the inclusive determination and all other results, although this depends on the choice of theory used to extract  $|V_{ub}|$ .

## 8 CONCLUSIONS

In semileptonic  $B$  decays, the measurement of  $V_{cb}$  is now below 2% error. The difference between inclusive and exclusive measurements is less than  $2\sigma$ . The error on  $|V_{ub}|$  is about 8%, up from last year, due to a new estimate of the  $b$ -quark mass. A lot of experimental and theoretical effort is going into improving this error.

## References

1. M. Kobayashi, T. Maskawa, *Prog. Theor. Phys.* **49** (1973) 652.
2. J. E. Duboscq *et al.* (CLEO Collab.), *Phys. Rev. Lett.* **76** (1996) 3898.
3. B. Aubert *et al.* (BaBar Collab.), *Phys. Rev. D* **74** (2006) 092004.
4. Heavy Flavor Averaging Group (HFAG),  
<http://www.slac.stanford.edu/xorg/hfag/>
5. W. M. Yao *et al.* (Particle Data Group), *J. Phys. G* **3** (2006) 1.
6. C. W. Bauer *et al.*, *Phys. Rev. D* **70** (2004) 94017.
7. O. Buchmuller, H. Flacher, *Phys. Rev. D* **73** (2006) 73008.
8. K. Wilson, *Phys. Rev.* **179** (1969) 1499.
9. D. Benson *et al.*, *Nucl. Phys. B* **665** (2003) 367.
10. M. Gremm and A. Kapustin, *Phys. Rev. D* **55** (1997) 6924.
11. A. F. Falk *et al.* *Phys. Rev. D* **53** (1996) 2491; A. F. Falk and M. Luke,  
*Phys. Rev. D* **57** (1998) 424.
12. P. Gambino and N. Uraltsev, *Eur. Phys. J. C* **34** (2004) 181.
13. D. Benson *et al.*, *Nucl. Phys. B* **710** (2005) 371.
14. . Abe *et al.* (Belle Collaboration), *Phys. Rev. Lett.* **94**, 221805 (2005);  
K. Abe *et al.* (Belle Collaboration), *Phys. Rev. D* **69**, 112002 (2004).
15. D. Abbaneo *et al.* [ALEPH, CDF, DELPHI, L3, OPAL, SLD], arXiv:hep-ex/0112028. See references there.
16. B. Aubert *et al.* (BaBar Collaboration) Measurement of the Branching Fractions of Exclusive  $B \rightarrow D/D^*/D^{(*)}\pi\ell\nu$  Decays in Events Tagged by a Fully Reconstructed B Meson. arXiv:0708.1738 [hep-ex].
17. D. Liventsev, T. Matsumoto *et al.* (Belle Collaboration), *Phys. Rev. D* **72**, 051109(R) (2005).
18. C. Schwanda *et al.* (Belle Collab.), *Phys. Rev. D* **75** (2007) 032005.
19. A.H Mahmood *et al.* (CLEO Collab.), *Phys. Rev. D* **70** (2004) 32002.
20. J. Abdallah *et al.* (DELPHI Collab.), *Eur. Phys. J. C* **45** (2006) 35.

21. D. Acosta *et al.* (CDF Collab.), Phys. Rev. **D 71** (2005) 51103.
22. B. Aubert *et al.* (BaBar Collab.), Phys. Rev. **D 69** (2004) 111104.
23. P. Urquijo *et al.* (Belle Collab.), Phys. Rev. **D 75** (2007) 032001.
24. K. Abe *et al.* (Belle Collab.), arXiv:hep-ex/0611047.
25. K. Abe *et al.* (Belle Collab.), arXiv:hep-ex/0508005.
26. P. Urquijo, “Inclusive Determination of  $|V_{cb}|$ ”, in proceeding of CKM 2006, Nagoya, Japan.
27. P. Gambino, private communication (2006).
28. N. Uraltsev, Int. J. Mod. Phys. **A 20** (2005) 2099.
29. B. Aubert *et al.* (BaBar Collab.), Measurements of Partial Branching Fractions for  $B \rightarrow X_u \ell \nu$  and Determination of  $|V_{ub}|$ , arXiv:0708.3702v1
30. Belle Collaboration, hep-ex/0408139; hep-ex/0409015;
31. B. Aubert *et al.* BABAR Collaboration, Phys. Rev. D69,111104, 2004.
32. DELPHI Collaboration, ICHEP04 contribution.
33. CDF Collaboration, contribution to ICHEP2004
34. O. Buchmueller, H. Flaecher, [hep-ph/0507253].
35. C. W. Bauer *et al.*, Phys. Rev. D68, 094001 (2003); C. W. Bauer *et al.*, Phys. Lett. B543, 261 (2002).
36. M. Beneke *et al.*, JHEP 0506, 071 (2005).
37. D. Scora and N. Isgur, Phys. Rev. D 52,2783 (1995).
38. HPQCD Collaboration, E. Gulez *et al.*, hep-lat/0601201.
39. FNAL Collaboration, M. Okamoto *et al.*, hep-lat/ 0409116.
40. P. Ball and R. Zwicky, Phys. Rev. D 71, 014015 (2005).
41. BABAR Collaboration, Phys. Rev. Lett. 95, 111801 (2005).
42. C. W. Bauer, Z. Ligeti and M. E. Luke, Phys. Rev. D 64, 113004 (2001).
43. BABAR Collaboration, contribution to the XXII International Symposium on Lepton-Photon Interactions at High Energy, 2005, Uppsala, Sweden [hep-ex/0507017].

44. Belle Collaboration, Phys. Rev. Lett. 95, 241801 (2005).
45. B.O. Lange, M. Neubert and G. Paz. Phys. Rev. D72:073006 (2005)
46. J.R. Andersen and E. Gardi. JHEP 0601:097 (2006)
47. B. Aubert *et al.* (BaBar Coll.) 0708.1753 [hep-ex]
48. J. L. Rosner et al. (CLEO Collaboration), Phys. Rev. Lett 96:121801 (2006).

## ***SESSION VII – SEARCHING THE HIGGS***

- Sanders Michiel P.* Search For Low Mass SM Higgs at The Tevatron
- Whiteson Daniel* Search for the Standard Model Higgs with  $m_h > 130 - 200$  GeV at the Tevatron
- Nikolopoulos Konstantinos* Search for the Standard Model *Higgs*  $\tau ZZ^{(*)}\tau$  4 leptons Searches in ATLAS
- Ronga Frederic* Prediction for the Lightest Neutral Higgs Boson in MSSM
- Gentile Simonetta* Detect MSSM Neutral Higgs Bosons at LHC
- St. Denis Rick* Searching for the Higgs at the Tevatron and the LHC. A Critical Assessment
- Khoze Valery* Testing Predictions for Central Exclusive Processes in the Early LHC Runs



## SEARCH FOR LOW MASS SM HIGGS AT THE TEVATRON

Michiel P. Sanders

*LPNHE/IN2P3/CNRS, Paris, France*

For the DØ and CDF Collaborations

### Abstract

The only place in the world where at this time standard model Higgs bosons can be produced and detected is the Tevatron at Fermilab. In this contribution, the most recent results on the search for a low mass Higgs boson are presented, using datasets of up to  $1.9 \text{ fb}^{-1}$ . In the absence of signal, the combined Tevatron cross section limit at a Higgs boson mass of 115 GeV is determined to be 6.2 (4.3 expected) times the standard model (SM) expectation, at 95% confidence level. The expected gain in sensitivity from the forthcoming larger dataset and improved analysis methods will likely make an exclusion or observation at low mass possible in the near future.

## 1 Introduction

The standard model of particle physics as we know it has been very successful. Many precision measurements have given excellent agreement with the model, and many processes predicted by the standard model have been observed. However, the success of the standard model depends on a mechanism to break the electroweak symmetry. Without that, the W and Z bosons would remain massless.

The Higgs mechanism is the most promising way to break the electroweak symmetry. It gives mass to the electroweak bosons and it leaves the photon massless. The same Higgs field can be used to give mass to the quarks and leptons. An essential prediction of the Higgs mechanism is the existence of a yet unobserved particle: the Higgs boson (H).

Through radiative corrections, the mass of the top quark and the mass of the W boson depend on the mass of the Higgs boson. Precision measurements of these parameters, and many others, at LEP, SLD and the Tevatron can thus be interpreted in the standard model as a prediction for the mass of the Higgs boson. At the time of this meeting, the central value for this prediction <sup>1)</sup> was  $m_H = 76_{-24}^{+33}$  GeV, leading to an upper limit <sup>1</sup> of 144 GeV. Including the direct Higgs mass limit from LEP <sup>2)</sup> of 114.4 GeV raises this upper limit to 182 GeV. The Higgs boson is thus expected to have a relatively low mass, within reach of the Tevatron experiments.

## 2 Low mass Higgs and the Tevatron

The Tevatron is a  $p\bar{p}$  collider at Fermilab, near Chicago, running at a centre-of-mass energy of 1.96 TeV. The two general-purpose experiments D0 and CDF have collected a data sample corresponding to an integrated luminosity of about  $3.7 \text{ fb}^{-1}$ . The results shown in the following are based on datasets of up to  $1.9 \text{ fb}^{-1}$ .

At the Tevatron, the dominant production mode for a low mass Higgs boson ( $m_H \lesssim 140 \text{ GeV}$ ) is the gluon fusion process. The dominant decay mode for the Higgs boson is to the kinematically allowed heaviest particle, in this case to a  $b\bar{b}$  quark pair. Experimentally the combination of gluon fusion and  $b\bar{b}$  decay is unfeasible due to the enormous background from dijet production. The next most dominant production modes are those where the Higgs is produced in association with a W or Z boson. In this case the  $H \rightarrow b\bar{b}$  decay mode is accessible, using the leptonic or invisible decay modes of the W and Z bosons.

The search for a low mass Higgs boson at the Tevatron is thus a search for a pair of jets originating from b-quarks in association with a leptonic or

---

<sup>1</sup>All limits quoted in this contribution are given at 95% C.L.

invisible W or Z signature. For  $WH \rightarrow \ell\nu b\bar{b}$ , the expected cross section times branching ratio (for one lepton flavour) is of the order of 20 fb at a Higgs mass of 105 GeV down to 4 fb at 140 GeV. The same quantity for ZH production with the Z decaying invisibly to neutrinos is essentially the same as that for WH for one lepton flavour. ZH production with the Z decaying to an e,  $\mu$ , or  $\tau$  pair is about a factor of five below that.

Tagging a jet as originating from a b-quark is an important ingredient of this search. Both experiments use combinations of variables sensitive to the presence of B-mesons, such as a reconstructed secondary vertex, large track impact parameters with respect to the primary vertex and the secondary vertex mass, to obtain efficient b-tagging algorithms. As an example, D0's neural net tagger<sup>3)</sup> obtains a 50% b-tag efficiency for a mis-tag rate of 0.5% ("tight" tag) and 74% efficiency at 5% mis-tag rate ("loose" tag). Typically, in analyses either two loose b-tags or one tight b-tag are required (exclusively).

### 3 Low mass Higgs searches at the Tevatron

In the following sections, the current state of the various low mass Higgs searches at D0 and CDF is described. Common to all analyses is the clean signature of the decay of a Z or W boson as one or two high momentum leptons (only electrons and muons are considered; leptonic  $\tau$  decays are typically included) and/or large missing transverse energy due to undetected neutrinos. The Higgs boson decay has the signature of two or more (due to initial or final state radiation) jets.

Background sources include production of a W or Z boson in association with jets (including b-quark jets), production of top-quark pairs or a single top, and diboson production (WW, WZ, ZZ). The amount of background from these processes is estimated from Monte Carlo simulation of the physics process (with generators like ALPGEN, PYTHIA and HERWIG) and the detector response. Another source of background is that where a jet in a multijet event, which are abundantly produced, is misidentified as a lepton from a W or Z boson decay, and where energy mismeasurements lead to missing transverse energy. This source of background is typically estimated from the data itself.

#### 3.1 Two charged leptons: $ZH \rightarrow \ell\ell b\bar{b}$

The event signature of  $ZH \rightarrow \ell\ell b\bar{b}$  production is very clean: two isolated leptons with an invariant mass close to the Z boson mass, and two jets. Both D0 and CDF have analyzed datasets corresponding to  $\simeq 1 \text{ fb}^{-1}$  of integrated luminosity. No updates were made recently.

The CDF collaboration applies a constrained fit using the measured jet energies and missing transverse energy to improve the jet energy measurement.

To gain acceptance, D0 has rather low transverse momentum cuts on the leptons. In spite of these differences between the analyses, the final sensitivity to a Higgs boson signal is similar. Both collaborations use neural networks to improve the sensitivity over that obtained using the dijet invariant mass.

The dijet mass distribution found by D0, after requiring both jets to be b-tagged is shown in fig.1 (left). The expected Higgs boson mass peak is clearly visible, but the amount of background, in particular from  $Z+b\bar{b}$  production is large. CDF uses a two dimensional neural network, trained against  $Z$ +jets and top-quark pair production. A slice of the final CDF neural network output distribution is shown in fig.1 (right). The Higgs boson signal clearly peaks towards large output values.

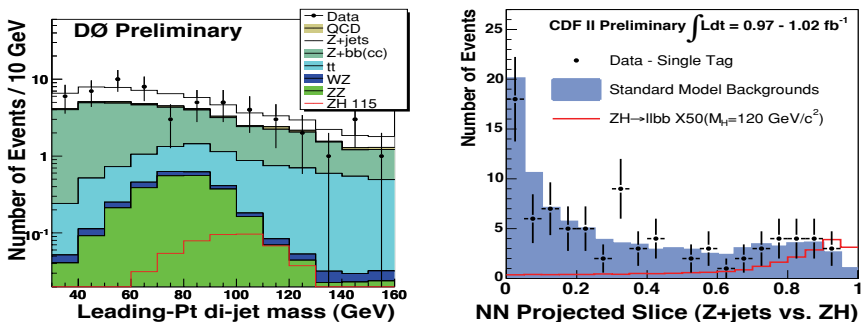


Figure 1: Dijet mass distribution obtained by D0 in the  $ZH \rightarrow \ell\ell b\bar{b}$  analysis after requiring two b-tags in the event (left) and a slice of CDF's neural network output in the same search channel (right).

Neither D0 nor CDF finds an excess, and the data agree well with the background model. The neural network distributions are then used to derive limits on the Higgs boson production cross section. At a Higgs mass of 115 GeV, D0 finds a limit of 18 (20 expected) times the expected standard model cross section times branching ratio of  $H \rightarrow b\bar{b}$ , whereas CDF finds 16 (16 expected).

### 3.2 One charged lepton: $WH \rightarrow \ell\nu b\bar{b}$

Removing a lepton from the final state described in the previous section, and instead requiring some missing transverse energy leads to the final state corresponding to  $WH \rightarrow \ell\nu b\bar{b}$  decays.

In this channel, D0 has analyzed a data set corresponding to an integrated luminosity of  $1.7 \text{ fb}^{-1}$ . Fig.2 (left) shows an example of the total background levels and the contribution from multijet production, in events with a W boson

candidate and two jets. For an expected WH signal contribution ( $m_H = 115$  GeV) of 9.9 events, a background of 33.5k events is expected. The dominant background source is production of a W boson in association with jets (white histogram), and the next most significant background source is that of multijet production (red histogram). The final discriminant variable in the D0 analysis is the output of a neural network, trained to separate Higgs boson signal from background. The distribution is shown in fig.2 (right), for events where both jets are b-tagged. At this analysis stage, the expected number of signal events is 2.3, with a background of 204 events.

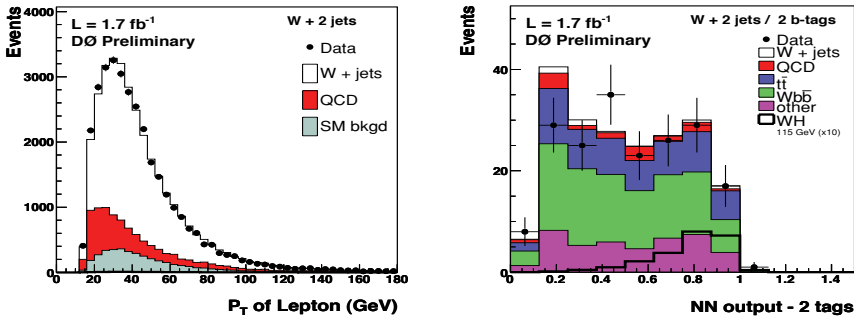


Figure 2: Distribution of the transverse momentum of the lepton in the D0  $WH \rightarrow \ell\nu b\bar{b}$  analysis, before b-tagging requirements are applied to the two jets (left), and the final neural network output distribution for events where both jets are b-tagged (right).

The CDF collaboration has released new results in this search channel with a slightly larger integrated luminosity ( $1.9 \text{ fb}^{-1}$ ). The b-tagging classification was extended to two double-tag and one single tag category (all exclusive). Moreover, CDF has already included the forward-going electrons (“plug” electrons) in the analysis. An example of that is shown in fig.3 where on the left the final neural network output distribution is shown for the events with a “central” electron or muon, and on the right that for events with a “plug” electron. The expectation is to find 0.09 WH events in the plug region (electron only), to be compared to 0.94 in the central region (electron and muon combined). This 10% increase in signal acceptance comes at the cost of larger relative background levels (14.2 events in the plug region versus 80.4 in the central region).

Again, both D0 and CDF find good agreement between the data and the expected background, without any sign of a Higgs boson signal. Therefore, cross section limits for Higgs boson production are derived using the final neural network output distributions. D0 finds, at an assumed Higgs mass of 115 GeV,

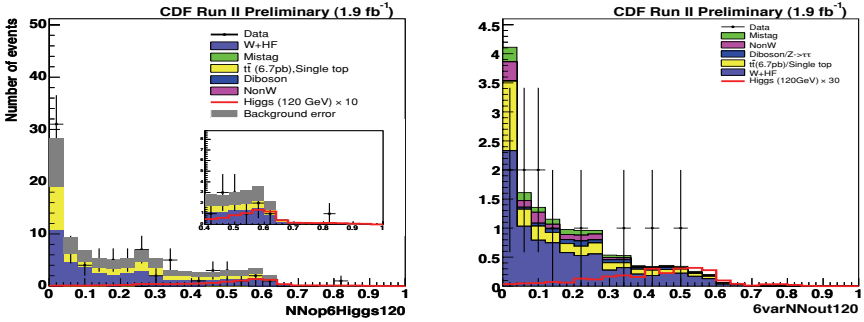


Figure 3: Neural network output distributions obtained by CDF in the  $WH \rightarrow \ell\nu b\bar{b}$  analysis for central electrons and muons (left) and forward going electrons (right).

a limit of 11.1 (9.1 expected) times the standard model expectation, and CDF find 8.2 (7.3 expected). The CDF result is better than the current D0 result, but an improved analysis from D0, using forward electrons, three-jet events and an improved neural network, will be finalized in the near future.

### 3.3 No charged leptons: $ZH \rightarrow \nu\nu b\bar{b}$

Removing the lepton from the final state described in the previous section leads to the signature of  $ZH \rightarrow \nu\nu b\bar{b}$  events.

In this case, the multijet background in the analysis is caused by events in which the energy of the jets is mismeasured, leading to missing transverse energy. The level of this background contribution can be estimated by using the fact that if the energy of one jet is mismeasured, the missing transverse energy will point in the jet direction. Also, the missing energy calculated using tracks will be different from the calorimeter based missing energy in the case of a calorimeter mismeasurement. The D0 collaboration also uses the asymmetry between missing energy calculated with all calorimeter information and missing energy using the reconstructed jets as a measure of multijet production (as shown in fig.4 (left)). CDF has used a dedicated neural network to separate the multijet background from others (shown in fig.4 (right)).

Both D0 and CDF train a neural network to improve the sensitivity of the analysis, as compared to considering the dijet mass distribution only. In the absence of a signal excess, D0 finds a cross section limit at a Higgs boson mass of 115 GeV of 13 (12 expected) times the standard model expectation, using a relatively small dataset of  $0.9 \text{ fb}^{-1}$ . A new analysis from the CDF collaboration, using an integrated luminosity of  $1.7 \text{ fb}^{-1}$ , leads to a limit of 8.0 (8.3 expected) times the standard model expectation.

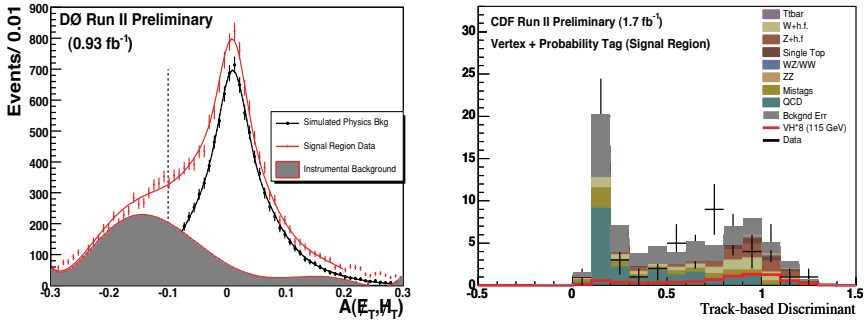


Figure 4: Distribution of the missing transverse energy asymmetry as defined by D0 in the  $ZH \rightarrow \nu\nu b\bar{b}$  analysis, before b-tagging (left) and distribution of the neural network output used by CDF to isolate multijet production, after b-tagging (right).

### 3.4 Tevatron combination

All analyses presented in the preceding sections specifically search for a standard model Higgs boson (at low mass). For optimal sensitivity, the individual search results of the two experiments can then be combined, assuming standard model branching ratios and cross sections. At the time of this meeting, the new CDF results in the  $WH \rightarrow \ell\nu b\bar{b}$  and  $ZH \rightarrow \nu\nu b\bar{b}$  channels were not included yet in the most recent Tevatron combination <sup>4)</sup>.

The log-likelihood-ratio test statistic of the Tevatron combined Higgs boson search is shown in fig.5 (left), for both a pure-background hypothesis (black dashed line) and a signal-plus-background hypothesis (red dashed line). The separation between these two gives a measure for the sensitivity, and from the figure it becomes clear that the sensitivity of the low mass Higgs boson searches is smaller than that for a high mass Higgs boson. This is mostly due to the different production and decay processes, and consequently background levels for low and high mass searches. In fig.5 (right) the combined cross section limit is given, as a ratio to the expected standard model cross section. At a Higgs boson mass of 115 GeV, the combined limit is a factor 6.2 (4.3 expected) times the standard model cross section.

## 4 Conclusion and outlook

In spite of extensive searches the Higgs boson has not been observed yet by the Tevatron experiments CDF and D0. However, the combined cross section limit for a Higgs boson mass of 115 GeV is only a factor 6.2 (4.3 expected) away from the cross section predicted by the standard model.

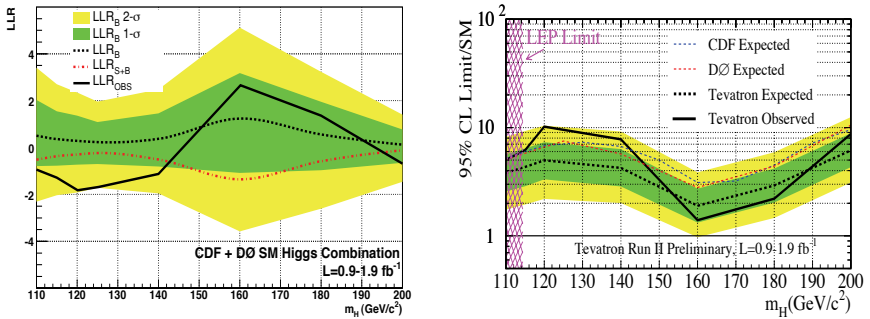


Figure 5: Tevatron combined Higgs boson search result given as the measured and expected log-likelihood-ratio test statistic (left), and as the cross section limit divided by the expected standard model cross section (right).

The prospects for an exclusion of the existence, or even an observation of the Higgs boson over a wide mass range are very good. The data sample accumulated by 2010 is expected to have a size of 7 to 9 fb<sup>-1</sup>, which is a factor four to eight more than what was used for the results presented here. Also, the improvements of the analyses over the last few years have shown an increase in sensitivity proportional to the accumulated integrated luminosity. For the near future, this trend is expected to continue, with additional improvements in, e.g., b-tagging, jet energy resolution, multivariate techniques and lepton identification.

## References

1. The LEP Collaborations: ALEPH Collaboration, DELPHI Collaboration, L3 Collaboration, OPAL Collaboration, the LEP Electroweak Working Group, arXiv:0712.0929 [hep-ex]
2. ALEPH, DELPHI, L3 and OPAL Collaborations and the LEP working group for Higgs boson searches, R. Barate *et al.*, Physics Letters B **565**, 61 (2003)
3. T. Scanlon, Ph.D. thesis, FERMILAB-THESIS-2006-43.
4. Tevatron New Phenomena and Higgs Working group, for the CDF and D0 Collaborations, arXiv:0712.2383 [hep-ex]

**SEARCH FOR THE STANDARD MODEL HIGGS WITH  
 $m_h > 130 - 200$  GeV AT THE TEVATRON**

Daniel Whiteson

*University of California, Irvine*

*Irvine, CA 92607*

*On behalf of the CDF and D0 collaborations*

Abstract

We present the latest results in searches for the Standard Model Higgs boson in the range  $m_h > 130 - 200$  GeV. No evidence of Higgs production is observed, and limits on its cross section approach the Standard Model prediction near  $m_h = 160$  GeV.

## 1 Introduction

The Standard Model requires a Higgs boson to explain the origins of Electro-Weak symmetry breaking and to regulate strong WW scattering.

The most sensitive direct searches for the Higgs boson have been performed with the detectors at LEP, which give a limit of  $m_h > 114.1 \text{ GeV}^{-1}$ ). However, the current energy and luminosity frontier is at the FermiLab Tevatron, a 1.96 TeV center-of-mass accelerator which collides protons and anti-protons at the center of two detectors, CDF and D0.

The primary Higgs production mechanism at the Tevatron is  $gg \rightarrow h$ . Cross sections for associated production  $p\bar{p} \rightarrow Wh$ ,  $p\bar{p} \rightarrow Zh$  are lower by an order of magnitude.

The primary decay mode below Higgs mass of 130 GeV is  $h \rightarrow b\bar{b}$ , while above 130 GeV the Higgs decays predominantly as  $h \rightarrow WW$ . In the lower mass region, production by gluon fusion is nearly impossible to observe due to the large backgrounds to the primary decay mode to  $b$  pairs. Analysis of the associated production modes is challenging but possible.

In the high mass region, however, the decay to  $W$  pairs makes a search for  $gg \rightarrow h$  feasible. The associated production  $p\bar{p} \rightarrow Vh \rightarrow VWW$  where  $V = Z, W$  gives additional sensitivity. This note presents results of searches by CDF and D0 in the high mass region,  $m_h = 130 - 200 \text{ GeV}$  using datasets with integrated luminosity of up to  $2 \text{ fb}^{-1}$ .

## 2 Final State Objects

In the high mass searches, the most sensitive searches for both production mechanisms  $gg \rightarrow h \rightarrow WW$  and  $p\bar{b} \rightarrow VH \rightarrow VWW$  involve final states with leptons. Leptonic  $W$  decay gives a powerful rejection of the QCD background in the hadronic environment.

For the  $WW$  final state, the signature is two opposite-signed leptons and missing transverse energy. The major backgrounds are discussed below.

For the  $VWW$  final state, the greatest power comes from the final state which includes two same-signed leptons. Backgrounds are described below.

The power of the analysis is closely tied to the ability to observe the final state leptons. To boost the sensitivity of the analyses, significant work has been done to extend the leptonic acceptance of the CDF and D0 detectors, by

loosening the identification requirements and adding new categories of identified leptons based on charged tracks rather than electromagnetic deposits or tracks in muon systems.

### 3 $h \rightarrow WW$

Searches at D0 and CDF for  $h \rightarrow WW$  require observation of two opposite sign high  $p_T$  electrons or muons as well as significant missing transverse energy due to the escaping neutrinos (2, 3).

Major backgrounds come from diboson ( $WW, WZ, ZZ$ ), where additional leptons are lost to give missing energy; dilepton top quark events, which can be suppressed due to their jet production; Drell-Yan events ( $Z \rightarrow ll$ ), which are highly suppressed by requiring missing energy; and  $W\gamma$  events, in which the photon can give a final state electron. In addition, the Higgs signal is distinguished by small lepton opening angle, due to the spin correlation between the  $W$  bosons decaying from a spin-0 Higgs.

The analysis at CDF calculates an event probability, by convoluting the matrix element for higgs or background processes with detector resolution functions and numerically integrating over unknown parton-level quantities. Some assumptions are made to retain computational tractability, but the event probability is a powerful discriminator and naturally captures, for example, the difference in lepton opening angles between the signal and the backgrounds.

Both CDF and D0 use a neural network as their final stage of analysis; at CDF the event probabilities are used as inputs to the neural network. To validate the simulation of the data, many adjacent control regions are checked and good agreement is seen, see Fig. 1.

The two experiments have sensitivity such that they expect to set an upper limit on the production cross-section which is 2.8 times the SM prediction. CDF's observed limit is 1.6, and D0's is 2.4 times the SM prediction.

### 4 $Vh \rightarrow VWW$

While the production cross section for  $Vh$  is significantly smaller than for  $gg \rightarrow h$ , the final state of  $VWW$  has a striking signature of like-signed leptons, for which the Standard Model backgrounds are small.

Dominant backgrounds at CDF and D0 are diboson production ( $ZZ, Z\gamma, W$

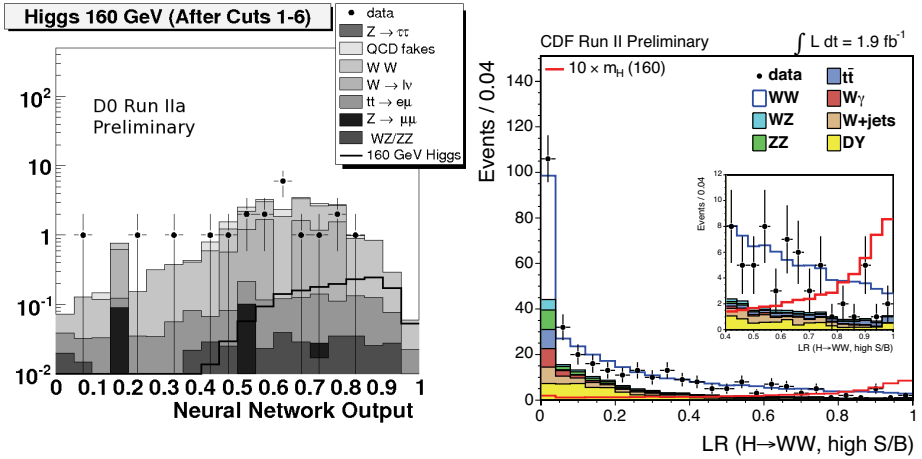


Figure 1: *Higgs and backgrounds predictions in the  $h \rightarrow WW$  analyses at D0 (left) and CDF (right), compared to observed data.*

in which some of the leptons are lost, and misidentified leptons from jets. The backgrounds are described using a combination of Monte Carlo and data-driven techniques.

CDF and D0's limits are shown in Figure 2.

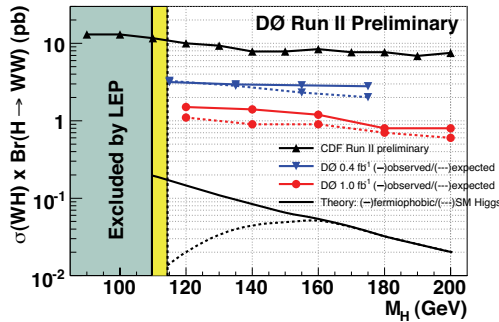


Figure 2: *Upper limits on Standard Model Higgs production from searches for  $Vh \rightarrow VWW$  with same-signed leptons.*

## 5 Combination

The results from all channels at both CDF and D0 have been combined for maximum sensitivity <sup>6)</sup>. At the most sensitive Higgs mass,  $m_h = 160$  GeV, the combined analysis expects to set an upper limit on the production cross section at 1.9 times the SM prediction. The observed limit is 1.4 times larger than the SM rate.

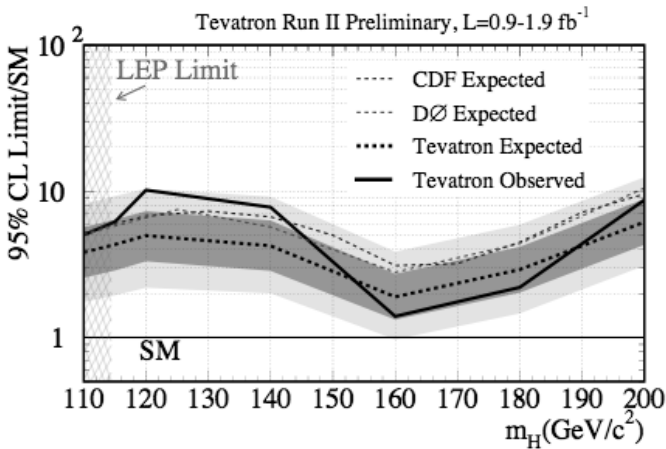


Figure 3: *Combined results from CDF and D0 Higgs searches.*

## 6 Conclusions

CDF and D0 have presented their analyses of data in searches for the Higgs boson with masses between 130 and 200 GeV. No evidence of a Higgs signal is seen, but upper limits on the cross section are rapidly approaching the predictions of the Standard Model around  $m_h = 160$  GeV.

Additional improvements currently being developed, including consideration of contributions from vector boson fusion, should yield important increases in sensitivity.

**References**

1. LEP higgs result.
2. [http://www-cdf.fnal.gov/physics/new/hdg/results/hwmmenn\\_080229/WW\\_2fb\\_public\\_note.ps](http://www-cdf.fnal.gov/physics/new/hdg/results/hwmmenn_080229/WW_2fb_public_note.ps)
3. <http://www-d0.fnal.gov/Run2Physics/WWW/results/prelim/HIGGS/H45/H45.pdf>
4. [http://www-cdf.fnal.gov/physics/exotic/r2a/20041014.lsdilep\\_whwww/note\\_7307.pdf](http://www-cdf.fnal.gov/physics/exotic/r2a/20041014.lsdilep_whwww/note_7307.pdf)
5. <http://www-d0.fnal.gov/Run2Physics/WWW/results/prelim/HIGGS/H37/H37.pdf>
6. Tevatron New Phenomena And Higgs Working Group, hep-ex/0712.2383.

## SEARCH FOR THE STANDARD MODEL

*Higgs*  $\rightarrow ZZ^{(*)} \rightarrow 4$  leptons **IN ATLAS**

Konstantinos Nikolopoulos

*University of Athens, Athens, GR 15771, Greece*

*Brookhaven National Laboratory, Upton, NY 11973, USA*

On behalf of the ATLAS collaboration

### Abstract

The sensitivity of the ATLAS experiment to possible discovery channels has been recently re-evaluated using complete - “as built” - detector simulation, latest theoretical cross-section calculations, optimized selection criteria and appropriate statistical treatment. In this contribution, the sensitivity to  $H \rightarrow ZZ^{(*)} \rightarrow 4l$ , which covers the Standard Model Higgs discovery in the mass range from  $\approx 120$  GeV to  $\approx 700$  GeV, is presented. The four lepton signature makes this channel very promising, even for the detector start-up phase, while it poses stringent requirements in terms of lepton identification and measurement capabilities.

## 1 Introduction

The Standard Model of electroweak and strong interactions has been proved to be in excellent agreement with the numerous experimental measurements performed over the last thirty years. However, the underlying dynamics of the electroweak symmetry breaking is still not known. Within the Standard Model, the electroweak symmetry is spontaneously broken via the Higgs mechanism. A doublet of complex scalar fields is introduced, out of which only a single neutral scalar particle, the Higgs boson, remains after symmetry breaking.

The Higgs boson is the only piece of the Standard Model lacking experimental verification. Indeed, the discovery of the Higgs boson, or the explanation of the electroweak symmetry breaking by other means, is one of the main Large Hadron Collider (LHC) goals.

Although the Higgs boson mass is not predicted in the Standard Model, it can be constrained by virtue of the loop corrections to the electroweak observables. Assuming the overall validity of the Standard Model, a global fit is performed to the high precision electroweak data which leads to  $m_H = 76^{+33}_{-24} GeV$ , favoring a light Higgs boson with  $m_H < 144 GeV$  at 95% confidence level <sup>1)</sup>.

On the direct searches for the Higgs boson the best lower limit  $m_H > 114.4 GeV$  at 95% confidence level comes from LEP-2 <sup>2)</sup>. Using this direct limit in the global electroweak fit,  $m_H < 182 GeV$  at 95% confidence level. Currently, direct searches for the Higgs boson are conducted at the Tevatron, where CDF and DØ might exclude a mass region around 160 GeV before LHC comes into play.

## 2 The ATLAS experiment at the LHC

The LHC is a  $pp$  accelerator installed in the pre-existing, 27 km long, LEP (Large Electron Positron) tunnel. It will operate at  $\sqrt{s} = 14 TeV$  with nominal luminosity of  $L = 10^{34} cm^{-2} s^{-1}$ . According to the current <sup>1</sup> LHC schedule, the first pilot physics run at  $\sqrt{s} = 10 TeV$  and  $L \approx 10^{32} cm^{-2} s^{-1}$  will take place in 2008.

The ATLAS (A Toroidal LHC ApparatuS) experiment <sup>3)</sup> is a general-purpose detector designed to fully exploit the physics potential of the LHC by

---

<sup>1</sup>May 2008.

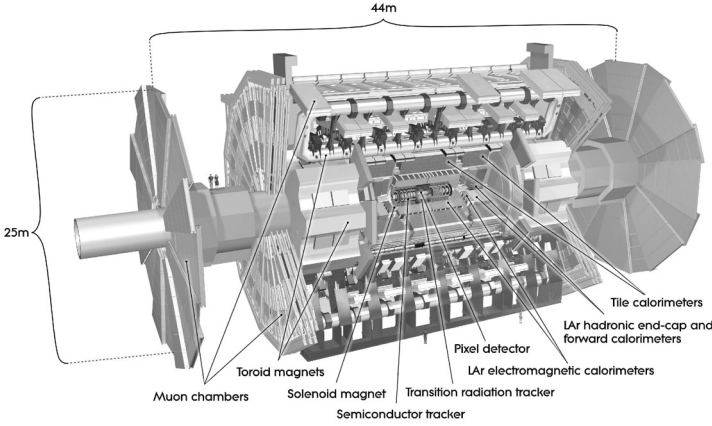


Figure 1: Schematic view of the ATLAS detector.

providing efficient and precise measurements of electrons, photons, muons, taus, light flavor and b-quark jets and missing transverse momentum. A schematic view of the ATLAS detector is given in Fig. 1, while its main characteristics are summarized in Table 1.

Table 1: Main features of the ATLAS detector.

Inner detector	Si pixels and strips Transition Radiation Tracker 2 T solenoid magnetic field $\sigma_{p_T}/p_T = 0.05\% \cdot p_T \oplus 1\%$
Electromagnetic calorimeter	Pb-liquid Argon Longitudinal and lateral segmentation $\sigma_E/E \approx 10\%/\sqrt{E(\text{GeV})} \oplus 0.7\%$
Hadronic calorimeter	Fe-scintillator + Cu-liquid Argon $\sigma_E/E \approx 50\%/\sqrt{E(\text{GeV})} \oplus 3\%$
Muon Spectrometer	Air-core toroid magnetic field Stand-alone triggering and measurement $\sigma_{p_T}/p_T \approx 10\%$ at $p_T = 1000 \text{ GeV}$ (stand-alone) $\sigma_{p_T}/p_T \approx 2.3\%$ at $p_T = 50 \text{ GeV}$ (with inner detector)

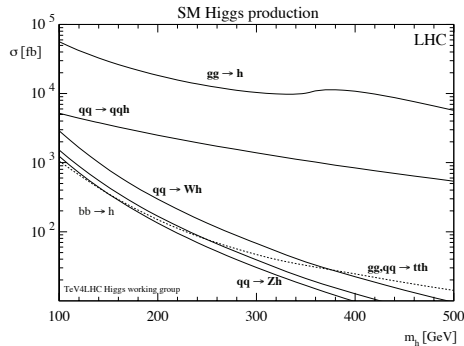


Figure 2: *Higgs boson production cross sections for the most relevant mechanisms as a function of the Higgs mass* <sup>4)</sup>.

### 3 Standard Model Higgs production and decay

The Higgs boson couples preferentially to the heavy particles and this determines its production mechanisms and decay modes. At the LHC the dominant production mechanism for the Standard Model Higgs boson is the gluon fusion,  $gg \rightarrow H$ , which at lowest order proceeds via a heavy quark loop. The vector boson fusion,  $qq \rightarrow qqH$ , follows with the exclusive signature of two forward quark jets and the lack of color exchange between those quarks. Other production mechanisms are the associated production with weak gauge bosons,  $q\bar{q} \rightarrow WH/ZH$ , and the associated production with heavy quarks, for example  $gg, q\bar{q} \rightarrow t\bar{t}H$ . These latter mechanisms are mainly relevant for low mass Higgs searches. The production cross-sections are summarized in Fig. 2 as a function of the Higgs mass.

The decay modes of the Standard Model Higgs as a function of its mass are summarized in Fig. 3(a). The branching ratios to  $WW$  and  $ZZ$  are dominant when kinematically accessible. The total Higgs decay width, which is negligible compared to the experimental resolution for low masses, increases rapidly and becomes significant above the  $ZZ$  production threshold, as shown in Fig. 3(b).

#### 4 The $H \rightarrow ZZ^{(*)} \rightarrow 4l$ channel

This is a powerful and simple but yet demanding channel for discovering the Standard Model Higgs in the mass range from 120 GeV to about 700 GeV.

In the high mass region it exhibits the striking signature of two on-shell Z bosons decaying to lepton pairs, while for lower masses - due to phase space constraints - one Z boson is on-shell and the other is pushed to lower masses. Furthermore, the Z bosons decay to lepton pairs,  $e^+e^-/\mu^+\mu^-$ , provide a very clean signature with only electrons and muons in the final state. This is a very important aspect, especially in the initial LHC phase where the leptons will be the first objects that will be understood.

By virtue of having only electrons and muons in the final state, the event can be fully reconstructed and a narrow mass peak can be observed in most of the mass interval. Furthermore, the smooth distribution of the background below the mass peak allows for its direct estimation from data.

However, due to the relatively low cross-section and the presence of four leptons in the final state, excellent lepton detection, identification and measurement is of paramount importance. The  $H \rightarrow ZZ^{(*)} \rightarrow 4l$  is a benchmark channel for the detector performance and constituted a design consideration for the ATLAS detector. In Fig. 4 the electron and muon detection efficiency is shown as a function of their transverse momentum.

The main backgrounds to this channel are the irreducible  $ZZ^{(*)}/\gamma^{(*)} \rightarrow 4l$  and the reducible  $Zb\bar{b} \rightarrow 4l$  and  $t\bar{t} \rightarrow W^+bW^-\bar{b} \rightarrow 4l$ . Other secondary backgrounds like  $WZ \rightarrow 3l + fake\ lepton$  were found to be negligible. The inclusive Z boson production  $Z \rightarrow 2l + X \rightarrow 4l$ , with one lepton pair produced

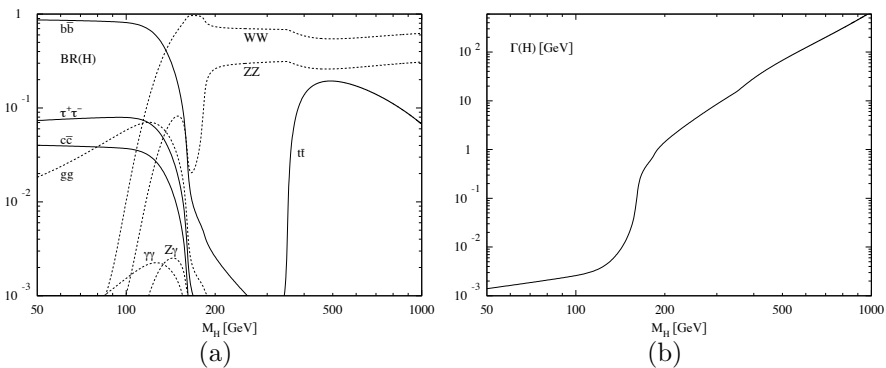
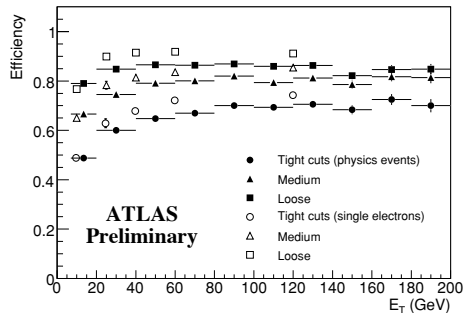
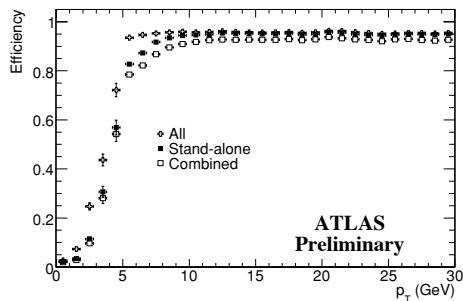


Figure 3: The Standard Model Higgs boson decay branching fractions (a) and total width (b) as a function of the Higgs mass <sup>5</sup>.



(a)



(b)

Figure 4: The efficiency in detecting and identifying electrons (a) and muons (b) in ATLAS as a function of their transverse momentum <sup>6)</sup>.

by the Z boson decay and the second lepton pair originating from charged hadrons misidentified as electrons, by photon conversions or by muons from meson decays, needs to be reduced well below the irreducible background level.

## 5 Sensitivity study

The discovery potential of the  $H \rightarrow ZZ^{(*)} \rightarrow 4l$  channel has been revisited recently. The signal and background cross-sections have been normalized to the Next-to-Leading Order calculations, including mass dependent K-factors where appropriate. Furthermore, the performance of the trigger chain has

been studied for the first time, while the effects of low luminosity pile-up<sup>2</sup> and cavern background<sup>3</sup> have been estimated. Finally, the layout of the as-built detector, including a detailed material description, has been used.

Three distinct final states can be defined: the  $H \rightarrow 4\mu$  which is the cleanest with only muons present in the final state, the  $H \rightarrow 4e$  and the  $H \rightarrow 2e2\mu$  which has two times higher branching ratio with respect to the other two final states.

### 5.1 Event triggering and lepton preselection

In order to trigger the experiment on  $H \rightarrow ZZ^{(*)} \rightarrow 4l$  events it is foreseen to use dilepton triggers, where the leptons are required to exceed a certain transverse momentum threshold. For the low luminosity phase high- $p_T$  single lepton triggers are also feasible. The two approaches are equally efficient, reaching a signal trigger efficiency close to 100% for the events selected by the offline analysis.

For considering a lepton in the offline analysis it should fulfill certain quality criteria, for example concerning the shape of the electromagnetic shower associated with an electron. Then, similarly to the Physics Performance Technical Design Report analysis<sup>3)</sup>, each candidate event should have at least four leptons passing the quality criteria in the pseudorapidity range  $|\eta| < 2.5$  and  $p_T > 7\text{ GeV}$ . Furthermore, at least two of the leptons should exceed the high- $p_T$  threshold of  $20\text{ GeV}$  as well.

The selected leptons of the event are used to form two same flavor but opposite sign dilepton candidates. Each event is required to have a dilepton with invariant mass consistent with the Z boson mass,  $|M_{l+l-} - M_Z| < 15\text{ GeV}$  for  $m_H = 130\text{ GeV}$ , in order to suppress non-resonant backgrounds like  $t\bar{t}$ . The second dilepton is required to have a mass higher than a threshold,  $M_{l+l-} > 20\text{ GeV}$  for  $m_H = 130\text{ GeV}$ , which eventually evolves in requiring two on-shell dileptons in searches at the high mass region.

---

<sup>2</sup>At “low luminosity” the instantaneous luminosity is  $10^{33}\text{ cm}^{-2}\text{ s}^{-1}$  and there are  $\approx 2.3$  interactions per bunch crossing.

<sup>3</sup>Spurious hits due to photons and thermal neutrons produced in the shielding material and machine elements.

## 5.2 Rejection of reducible backgrounds

To further reject the reducible backgrounds, the topology difference with the signal, which is the presence of two b-jets in the final state, can be exploited. In this case, the semileptonic decays of b and c quarks result in non-isolated leptons from displaced vertices.

### 5.2.1 Isolation

The calorimeter isolation is defined as the sum of the transverse energy deposited in the calorimeter inside a cone of radius  $\Delta R = \sqrt{\Delta\eta^2 + \Delta\phi^2}$ , in the pseudorapidity-azimuthal angle space, around the lepton. The energy deposition of the lepton itself is subtracted from the isolation energy. The isolation energy of the less isolated lepton is used as the discriminating variable.

Correspondingly, the track isolation is defined as the sum of the transverse momentum of the inner detector tracks in a cone of radius  $\Delta R$ , around the lepton. The tracks of the four leptons forming the two dilepton pairs are excluded from the sum. The maximum track isolation energy of all leptons in the event is used as the discriminant

A cone size of 0.2 represents a good compromise between the jet physics, which requires a large cone, and the event pile-up, requiring small cone size. The background rejection, especially in the case of  $Zb\bar{b}$ , improves substantially when the isolation energy is normalized to the transverse momentum of the lepton under examination.

In Fig. 5 the distributions of normalized calorimeter and track isolation for the Higgs signal,  $m_H = 130 \text{ GeV}$ , and the two main reducible backgrounds are presented for the  $4\mu$  channel. The difference between the signal and the backgrounds is evident.

### 5.2.2 Impact parameter

Leptons from  $t\bar{t}$  and  $Zb\bar{b}$  backgrounds are most likely to originate from displaced vertices. This characteristic can be exploited by using the transverse impact parameter significance of the leptons, which is defined as the ratio of the transverse impact parameter over its measurement error. The impact parameter is measured with respect to the primary vertex of the event, the latter being estimated from a set of tracks reconstructed in the Inner Detector. This

accounts for the spread of the vertex position, which at LHC is  $15 \mu m$  on the transverse plane and  $\approx 55 mm$  along the beam axis. In the case of electrons, bremsstrahlung affects the impact parameter distribution, hence reducing the discriminating power of this variable with respect to muons.

In Fig. 6, the maximum normalized transverse impact parameter significance for signal,  $m_H = 130 GeV$ , and the main reducible backgrounds in the  $4\mu$  channel is shown.

### 5.3 Mass reconstruction

As presented in Fig. 3(b), for Higgs masses larger than  $\approx 230 GeV$  the Higgs natural width dominates over the detector resolution. On the other hand, for lower Higgs masses the Higgs natural width is negligible and the mass resolution becomes crucial for discovery. To further improve the mass resolution a Z mass constraint is applied to the on-shell Z boson, taking into account the natural Z width. In Fig. 7 the Higgs mass resolution in the  $4\mu$  channel is presented before and after the application of the Z mass constraint demonstrating a 10% improvement in the Higgs mass resolution for  $m_H = 130 GeV$ .

### 5.4 Mass distributions and expected significance

Using the isolation and impact parameter criteria a further rejection of  $O(10^2)$  for  $Zb\bar{b}$  and  $O(10^3)$  for  $t\bar{t}$  is achieved for a signal efficiency of  $O(80\%)$ . The effect of the low luminosity pile-up was estimated to be less than 5%. The

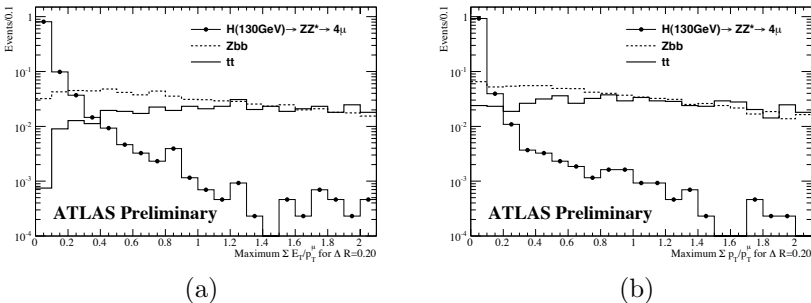


Figure 5: Normalized calorimeter (a) and track (b) isolation for the signal,  $m_H = 130 GeV$ , and the main reducible backgrounds for the  $4\mu$  channel.

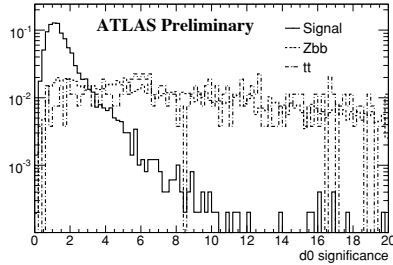


Figure 6: *Maximum impact parameter significance for the signal ( $m_H = 130$  GeV) and reducible backgrounds in the  $4\mu$  channel.*

mass distributions, including all three topologies, for signal and background after event selection are presented in Fig. 8 for three different Higgs masses. In all three cases, the expected signal is clearly seen above the background.

The updated analysis is in its final stages, where possible improvements from the use of multivariate techniques are being studied. The estimation of the experimental backgrounds from the data is also under study, while the expected significance is treated rigorously taking into account the systematic effects. In Fig. 9 the expected significance, based on older studies<sup>3, 7)</sup>, for all the Higgs channels as a function of the Higgs mass is summarized to provide

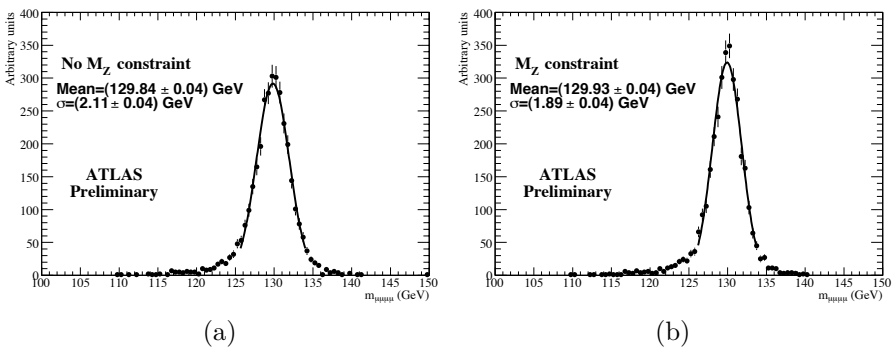
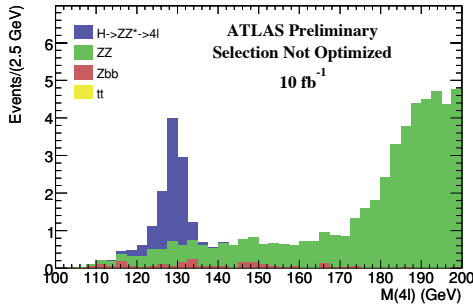
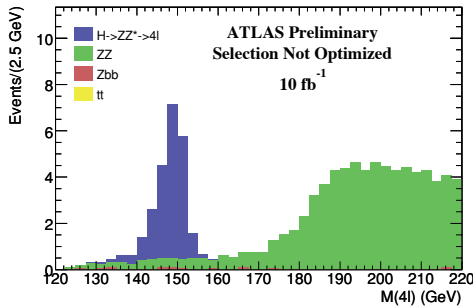


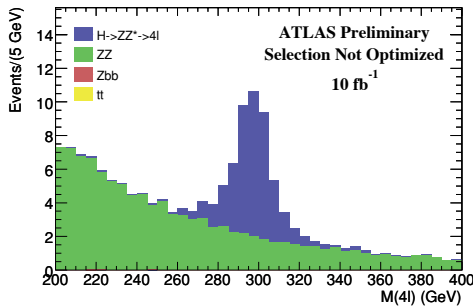
Figure 7: *The reconstructed Higgs boson mass distribution in the  $H \rightarrow ZZ^* \rightarrow 4\mu$  channel for  $m_H = 130$  GeV before (a) and after (b) the  $Z$  mass constraint is applied.*



(a)



(b)



(c)

Figure 8: Four lepton reconstructed mass distributions for the Higgs signal and backgrounds, including all three topologies, after the selection, for Higgs masses 130 GeV(a), 150 GeV(b) and 300 GeV (c).

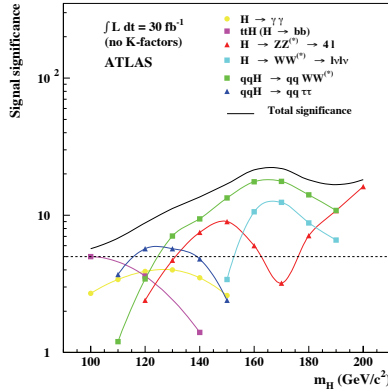


Figure 9: *ATLAS* sensitivity for the discovery of the Standard Model Higgs boson for an integrated luminosity of  $30fb^{-1}$ . The significance of the individual channels and their combination is presented as a function of the Higgs mass. No *K*-factors are used. <sup>3, 7</sup>).

some hints on the expected results. However, in this significance estimation no Next-to-Leading Order *K*-factors were used. Indeed, the preliminary results show that, depending on the Higgs mass, discoveries are already possible with few  $fb^{-1}$  of integrated luminosity.

## 6 Measurement of Higgs parameters

In the case where the Standard Model Higgs boson is discovered at the LHC, the effort will be concentrated in the measurement of its properties, both in order to understand the nature of the newly discovered particle and to test the Standard Model - which after fixing the Higgs mass can give predictions for all its properties. The  $H \rightarrow ZZ^{(*)} \rightarrow 4l$  channel is one of the most promising channels for many of these measurements.

As shown in Fig. 10(a), the Higgs mass will be measured in a wide mass range to the 0.1% level with  $300fb^{-1}$  of integrated luminosity, with the main systematic uncertainty being the energy scale of the leptons. The direct measurement of the natural width of the Higgs boson is only possible for high Higgs boson masses, where an uncertainty of  $\approx 8\%$  is to be expected for Higgs masses above 270 GeV, Fig. 10(b). The Higgs production rate,  $\sigma \times BR$ , will be measured to  $\approx 10\%$ , Fig. 10(c), with the ultimate precision being limited

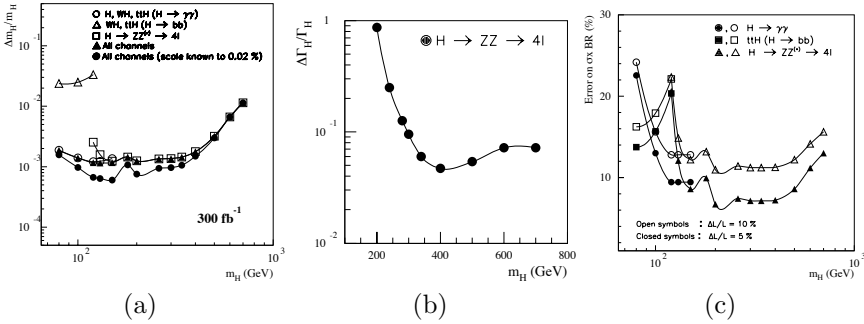


Figure 10: Relative precision on the measured Higgs boson mass (a) total decay width (b) and production rate (c) as a function of the Higgs mass for  $300 \text{ fb}^{-1}$  of integrated luminosity <sup>3)</sup>.

by the precision of the absolute luminosity measurement at the LHC.

The spin and CP quantum numbers of the Higgs boson will be determined in the  $H \rightarrow ZZ \rightarrow 4l$  channel by exploiting the correlations in the angular distributions of the leptons <sup>8)</sup>. While, the  $H \rightarrow ZZ^{(*)} \rightarrow 4l$  will be combined with other channels, like the  $H \rightarrow WW^{(*)}$ , to estimate ratios of Higgs couplings <sup>9)</sup>.

### 7 Summary

The  $H \rightarrow ZZ^{(*)} \rightarrow 4l$  channel has a large discovery potential in the LHC. It is the “gold-plated” channel for Standard Model Higgs discovery in the high mass region ( $M_H > 200 \text{ GeV}$ ) with the distinctive signature of two on-shell Z bosons decaying to leptons, while it is a very important channel in the Standard Model favored low mass region, especially during the start-up phase. If the Standard Model Higgs is discovered, then the  $H \rightarrow ZZ^{(*)} \rightarrow 4l$  channel will be used to measure its properties and fully verify the Standard Model, provided there is enough integrated luminosity.

The ATLAS detector, with its excellent lepton identification and measurement capabilities, is well-suited for this analysis. The first results of the updated analysis indicate that the combination of different decay channels allows the discovery of a signal with a  $fb^{-1}$  of well understood data.

However, before being able to extract discovery signals from LHC collisions the ATLAS collaboration will perform extensive measurements of the

main Standard Model processes in order to prove the good performance of the detector and the required understanding of the data.

## 8 Acknowledgements

The author would like to thank the organizers of the Rencontres de Physique de la Vallée d'Aoste for the excellent organization of this stimulating conference and the support provided through the grant for young physicists.

The support of the ATLAS Higgs working group is acknowledged and greatly appreciated. The author is particularly indebted to A. Nisati, L. Fayard, S. Paganis, S. Rosati, D. Rebuffi, C. Kourkoumelis, D. Fassouliotis and V. Polychronakos for their useful comments during the preparation of the talk and of this manuscript.

## References

1. J. Alcaraz *et al.* [LEP Collaborations], arXiv:hep-ex/0712.0929.
2. R. Barate *et al.* [LEP Working Group for Higgs boson searches], Phys. Lett. B **565** (2003) 61.
3. ATLAS Collaboration, ATLAS detector and physics performance Technical Design Report, CERN/LHCC 99-14/15 (1999).
4. U. Aglietti *et al.*, Tevatron-for-LHC Report: Higgs, FERMILAB-CONF-0-467-E-T, arXiv:hep-ph/0612172 (2006).
5. A. Djouadi, J. Kalinowski and M. Spira, Comput. Phys. Commun. **108** (1998) 56.
6. ATLAS Collaboration, The ATLAS Experiment at the CERN Large Hadron Collider, submitted to JINST.
7. S. Asai *et al.*, Eur. Phys. J. C **32S2** (2004) 19.
8. C. P. Buszello, I. Fleck, P. Marquard and J. J. van der Bij, Eur. Phys. J. C **32** (2004) 209.
9. M. Dürrssen, Prospects for the measurement of Higgs boson coupling parameters in the mass range from  $110 - 190 \text{ GeV}/c^2$ , ATLAS note, ATLAS-PHYS-2003-030.

**PREDICTION FOR THE LIGHTEST NEUTRAL HIGGS  
BOSON IN MSSM**

Frederic Ronga  
*ETH-Zurich, Switzerland*

Written contribution not received



# DETECT MSSM NEUTRAL HIGGS BOSONS AT LHC

Simonetta Gentile

*Dipartimento di Fisica, Università La Sapienza, Sez. I.N.F.N., Roma*

## Abstract

Discovery potential for MSSM neutral Higgs bosons in various MSSM scenarios are discussed. The region of between 5 and 50 and mass between  $\approx 95$  and few hundred 100 is considered in the framework of the experiments at the Large Hadron Collider (LHC), for a centre-of-mass energy  $= 14$  TeV. This parameter region is not fully covered by the present data either from LEP or from Tevatron. The h/A/H bosons search in decay channels in SM and supersymmetric particles is reviewed and the studies of the two LHC experiments ready to take data in the next future are discussed.

## 1 Introduction

The Minimal Supersymmetric Standard Model (MSSM) is the most investigated extension of the Standard Model (SM).

The theory requires two Higgs doublets giving origin to five Higgs bosons: two CP-even neutral scalars,  $h$  and  $H$  ( $h$  is the lighter of the two), one CP-odd neutral scalar,  $A$ , and one pair of charged Higgs bosons,  $H^\pm$  (1, 2, 3). The discovery of any one of these particles is a crucial element for the confirmation of the model. This is a key point in the physics program of future accelerators and in particular of the LHC.

After the conclusion of the LEP program in the year 2000, the experimental limit on the mass of the Standard Model Higgs boson  $H$  was established at 114.4 GeV with 95% CL (4). Limits were also set on the mass of neutral (5) and charged (6) MSSM Higgs bosons for most of the representative sets of model parameters.

In this paper is discussed the potential of the LHC detectors for the discovery of neutral MSSM Higgs bosons in the parameter region not excluded by the LEP and Tevatron data. We will discuss the  $A$ ,  $H$  and  $h$ , the lightest of the neutral Higgs bosons. Its mass, taking account of radiative corrections, is predicted to be smaller than 140 GeV, see (5) and references therein.

In the first part of this paper we review the MSSM framework, the production mechanism in hadron collisions, the present experimental situation and the discovery potential at the LHC.

In the second part, examples of their search in some decays channel are discussed

In the conclusion, results are presented on the neutral MSSM Higgs bosons discovery potential at the LHC based on the ATLAS (7) and CMS (8) detectors.

## 2 Minimal Supersymmetric Standard Model

In this paragraph the fundamental points of the model, useful for the following discussion, are summarized, referring to elsewhere for a complete review (9, 2).

The mass of the five Higgs bosons required by the MSSM, the two CP-even ( $h, H$ ), the CP-odd  $A$  and the two charged  $H^\pm$ , at tree level can be expressed in terms of two independent input parameters, the ratio of the vacuum expectation values of the two Higgs fields,  $\tan\beta$ , and the pseudoscalar Higgs-boson mass,  $m_A$ . A simple relation holds between these particle masses :

$$m_{H,h}^2 = \frac{1}{2} [m_A^2 + m_Z^2 \pm \sqrt{(m_A^2 + m_Z^2)^2 - 4m_A^2 m_Z^2 \cos^2 2\beta}] \quad (1)$$

$$m_{H^\pm}^2 = m_W^2 + m_A^2$$

Table 1: *CP-conserving benchmark scenarios.*

Parameter	$m_h - max$	<i>no-mixing</i>	<i>large-<math>\mu</math></i>
$M_{SUSY}$ [GeV]	1000	1000	400
$\mu$ [GeV]	-200	-200	1000
$M_2$ [GeV]	200	200	400
$X_t = A - \mu \cot\beta$	$2M_{SUSY}$	0	- 300
$m_{\tilde{g}}$ [GeV]	$0.8M_{SUSY}$	$0.8M_{SUSY}$	200
$m_A$ [GeV]	0.1-1000	0.1-1000	0.1-400
$\tan\beta$	0.4-50	0.4-50	0.7-50

(Recent precise measurements of W and Z masses,  $m_W$  and  $m_Z$ , are available 10)).

In comparison with the SM, the MSSM requires more free parameters. However, the assumption that the scalar fermions masses, the gaugino masses and the trilinear Higgs-fermion couplings must unify at the Grand Unification scale (GUT) reduces the number of free parameters. In one of the possible constrained models the parameters chosen are:

- $M_{SUSY}$ , a common mass for all sfermions (scalar fermions) at the electroweak scale.
- $M_2$ , a common  $SU(2)_L$  gaugino mass at the electroweak scale.
- $\mu$ , the strength of the supersymmetric Higgs mixing.
- $\tan\beta$ , the ratio of the vacuum expectation values of the two Higgs fields .
- $A = A_t = A_b$  a common trilinear Higgs-squarks coupling at the electroweak scale. It is assumed to be the same for up-type squarks and for down-type squarks.
- $m_A$ , the mass of the CP-odd Higgs boson.
- $m_{\tilde{g}}$ , the gluino mass.

Three of these parameters define the stop and sbottom mixing parameters  $X_t = A_t - \mu \cot\beta$  and  $X_b = A_b - \mu \cot\beta$ .

For the Higgs boson search, two extremes of the stop mixing are considered: the maximal mixing  $X_t = 2 M_{SUSY}$ , and the minimal mixing, when  $X_t$  is zero. Usually a set of benchmarks are applied and also in this case there are only two free parameters:  $\tan\beta$  and  $m_A$ . In this search three CP-conserving benchmark scenarios are considered (Tab.1).

The characteristics of the three scenarios are as follows.

- *m<sub>h</sub> – max*

As the name indicates, it allows in the model the maximum value of  $m_h$  5). For fixed values of  $m_t$  and  $M_{\text{SUSY}}$ , it gives the most conservative range of excluded  $\tan\beta$  values. A negative search of the h boson implies an exclusion of the model.

- *no-mixing*

It assumes no-mixing between the scalar partners of the left-handed and the right-handed top quarks. The highest value of  $m_h$  can be 114 GeV.

- *large- $\mu$*

It is designed such that the h boson doesn't decay into pairs of b quarks due to large corrections from SUSY loop processes. The dominant decay modes are to  $c\bar{c}$ ,  $g\bar{g}$ ,  $W^+W^-$ ,  $\tau^+\tau^-$ . The highest value of  $m_h$  can be 108 GeV.

The difference between *m<sub>h</sub> – max* and *no-mixing* scenario is mainly due to the fact that to the same point of the parameter space ( $m_A$ ,  $\tan\beta$ ) corresponds a different mass of the h boson, thus a different sensitivity of the channel under consideration.

### 3 Production in hadronic interaction

#### 3.1 Signal processes: the lightest Supersymmetric Higgs boson

The neutral h boson and the other Higgs bosons are important elements of the MSSM model. Their couplings at tree level to fermions and massive gauge bosons are easily obtained from the SM Higgs boson couplings (shown in Tab. 2 11)) via correction factors summarized in Tab. 3 11). These correction factors depend on the parameters  $\alpha$  and  $\beta$  which were introduced in Sec. 2 and are related by the following expression:

$$\cos 2\alpha = -\cos 2\beta \frac{m_A^2 - m_Z^2}{m_H^2 - m_h^2} \quad (2)$$

At high  $\tan\beta$  the MSSM correction factors to the SM Higgs bosons couplings to fermions and massive gauge bosons (see Tab. 3) are larger for down-type quarks (b) and leptons ( $\tau$  and  $\mu$ ) than for up type-quarks. This fact implies that the MSSM coupling to down-type quarks and leptons are strongly enhanced in this region.

Since the MSSM and SM couplings differ only by a correction factor, the most natural choice is to explore the decay channels common to both,

Table 2: *Standard Model Higgs boson couplings at tree level to fermions and massive gauge bosons.*

SM	Fermions	$W^+W^-$	$ZZ$
H	$\frac{igm_f}{2m_W}$	$igm_W g^{\mu\nu}$	$\frac{igm_Z}{2 \cos \theta_W} g^{\mu\nu}$

Table 3: *MSSM correction factors to the SM Higgs boson couplings to fermions and massive gauge bosons at tree level.*

MSSM	$d\bar{d}, s\bar{s}, b\bar{b}$ $e^+e^-, \mu^+\mu^-, \tau^+\tau^-$	$u\bar{u}, c\bar{c}, t\bar{t}$	$W^+W^-, ZZ$
h	$-\sin \alpha / \cos \beta$	$\cos \alpha / \sin \beta$	$\sin(\beta - \alpha)$
H	$\cos \alpha / \cos \beta$	$\sin \alpha / \sin \beta$	$\cos(\beta - \alpha)$
A	$-i\gamma_5 \tan \beta$	$-i\gamma_5 \cot \beta$	0

as mentioned in Sec. 4.2. The h, A, H decay channels  $b\bar{b}$  and  $gg$  are extensively studied <sup>7)</sup>. Other decay channels deserving consideration are  $\tau^+\tau^-$  and  $\mu^+\mu^-$ . It should be mentioned that the identification of hadronic decays and jet showers of the third generation fermions ( $\tau$  and  $b$ ) may be problematic in hadronic environment as LHC either SM either for MSSM Higgs. The MSSM Higgs bosons have an alternative: decays of these Higgs bosons into sparticles, in particularly, charginos and neutralinos.

Before concluding this section it should be reminded <sup>11)</sup> that the CP-odd supersymmetric boson A in the region of high  $\tan \beta$  and  $m_h$  around 100 GeV has a mass slightly higher than the CP-even h and a competitive branching ratio (Tab. 3) in the corresponding decay channel. The same situation is reproduced at high  $m_A$  mass between H and A bosons. The cross-section, the mass and width difference, which are functions of the parameters  $\tan \beta$  and  $m_A$ , are close at low  $m_A$  mass of the parameters space between h A and at higher mass H and A. Thus in these points the CP-odd and CP-even bosons

are indistinguishable from the experimental point of view. Therefore, it is more correct to think in terms of h/A search and at higher mass H/A.

## 4 Experimental search for Minimal Supersymmetric Standard Model Higgs

### 4.1 LEP and Tevatron results

High precision tests of the Standard Model have been performed at LEP setting a combined limit of  $m_H > 114.4$  GeV for the mass of the SM Higgs boson <sup>4)</sup>.

Again at LEP, the validity of the Minimal Supersymmetric Standard Model has been investigated within the constrained framework of Sec. 2. For the mass of the charged MSSM Higgs bosons a combined limit  $m_{H^\pm} > 78.6$  GeV was obtained <sup>6)</sup>. Searching for neutral CP-even and CP-odd MSSM Higgs bosons, no indication of signal was found up to a center-of-mass energy of 209 GeV <sup>5)</sup>. The corresponding lower limits on the masses were set as a function of  $\tan\beta$  for several scenarios. In the  $m_h$ -max scenario (Fig. 1) with a top mass  $m_t=174.3$  GeV the limits for  $\tan\beta > 10$  at 95% CL are approximately :

$$m_h, m_A \geq 93 \text{ GeV}$$

A complementary search, providing sensitivity in the region  $\tan\beta > 50$  has been performed at the Tevatron Collider at  $\sqrt{s}=1.96$  TeV. In the MSSM scenario, a significant portion of the parameter space has been excluded by the D0 Collaboration, down to  $\tan\beta = 50$  as a function of  $m_A$ , by studying the associated production with two b quarks of h/A/H bosons and their decay into  $b\bar{b}$  <sup>12)</sup>. Comparable results have been obtained by the CDF Collaboration exploring the h/A/H decays to  $\tau^+\tau^-$ , but extending the excluded region to higher values of  $m_A$  <sup>13)</sup>.

### 4.2 LHC discovery perspectives

The LEP and Tevatron data don't exclude the parameter space defined by  $\tan\beta$  larger than 10 and smaller than 50. Therefore, a natural continuation of the LEP and Tevatron physics is the investigation of the possible existence of MSSM Higgs bosons in this region of  $\tan\beta$ . The ATLAS <sup>7)</sup> and CMS <sup>8)</sup> experiments starting in the near future at the Large Hadron Collider (LHC), at CERN, constitute an excellent laboratory for such search.

The prospect for the detection of MSSM Higgs bosons at LHC was evaluated for benchmark sets preventing Higgs boson decays to SUSY particles <sup>11, 7)</sup> and focusing on the discovery potential of decay modes common to MSSM and SM Higgs bosons <sup>7)</sup>. It was concluded that the complete region of

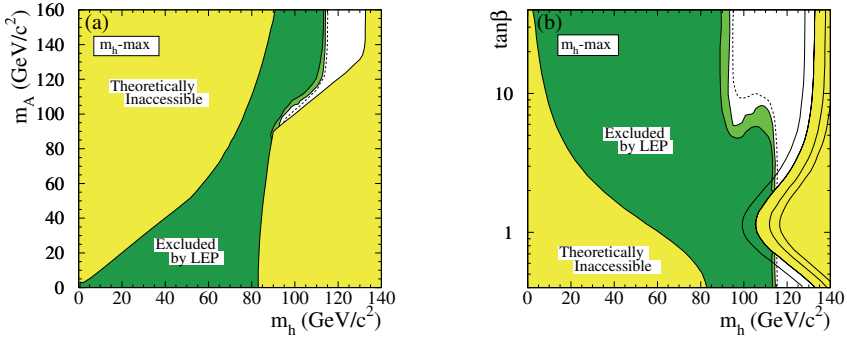


Figure 1: *The combined LEP results for the search for the MSSM neutral Higgs bosons (from Ref. 5). The figure shows the theoretically inaccessible regions (light-grey/yellow) and the regions experimentally excluded by LEP searches, at 95% C.L. (medium-grey/light-green) and 99.7% C.L. (dark-grey/dark-green), for the  $m_h$ -max scenario with the top mass  $m_t = 174.3$  GeV, in two projections of the MSSM parameters  $(m_h, m_A)$ ,  $(m_h, \tan\beta)$ . The dashed lines indicate the boundaries of the regions which are expected to be excluded, at 95% C.L., on the basis of Monte Carlo simulations with no signal. In the  $(m_h, \tan\beta)$  projection, the upper boundary of the parameter space is indicated for four values of the top mass; from left to right:  $m_t = 169.3, 174.3, 179.3$  and  $183.0$  GeV.*

parameter space  $m_A = 50 - 500$  GeV and  $\tan\beta = 1 - 50$  is open to Higgs boson discovery by the ATLAS experiment, already with an integrated luminosity of  $\int \mathcal{L} dt = 30 \text{ fb}^{-1}$ , and that over a large part of this region more than one Higgs boson and more than one decay mode could be observed – the detection of a signal in more than one decay channel would constitute strong evidence for the MSSM model. It was also found that the region in the  $(m_A, \tan\beta)$  plane which corresponds to  $m_h \approx 100$  GeV and  $\tan\beta > 10$  is only accessible by a neutral h/A boson decaying to  $\mu^+\mu^-$  or  $\tau^+\tau^-$  (11, 7), and by a charged  $H^\pm$  boson decaying to  $\tau\nu$  (14).

More recently the MSSM boson discovery potential in the MSSM scenario has been investigated (15) at two luminosities,  $\int \mathcal{L} dt = 30 \text{ fb}^{-1}$  and  $\int \mathcal{L} dt = 300 \text{ fb}^{-1}$ . At low luminosity the  $\tau^+\tau^-$  decay mode represents the main contribution to the discovery potential and covers most of the parameter space not yet explored. However the contribution of  $b\bar{b}h \rightarrow \mu^+\mu^-$  appears to be crucial in the region of moderate  $\tan\beta$  and mass close to  $m_Z$ .

At high luminosity channels such as:  $h/A/H \rightarrow \gamma\gamma$ ,  $h/A/H \rightarrow ZZ \rightarrow 4\ell$  and  $h \rightarrow b\bar{b}$  in associated production with  $t\bar{t}$  give a significant contribution. The channel  $h \rightarrow \gamma\gamma$ , which requires an excellent  $M_{\gamma\gamma}$  mass resolution and jet/ $\gamma$  separation, corresponds to MSSM rates suppressed with respect to the SM case but for a limited region of the parameter space where they could even be slightly enhanced. As for the channel  $h \rightarrow b\bar{b}$ , only the  $t\bar{t}h$  production followed by the  $h \rightarrow b\bar{b}$  decay can be observed clearly above the background, thus the extraction of the signal requires the identification of four b-jets and an excellent b-tagging performance. In the MSSM case the rates could be enhanced by 10-20% over the SM rates.

To complete all possible scenarios also the search channel in supersymmetric particles have been explored and discovery region in  $(m_A, \tan\beta)$  plane defined. I would like to underline that the two different scenarios are based different hypothesis; in the first the sparticle decays are forbidden in the second allowed, as consequence their results can't be combined.

## 5 Discovery channels

In the scenario where only the MSSM neutral Higgs bosons can decay only in SM particles a relevant importance have final states containing leptons,  $e$ ,  $\mu$ , for their clear identification in a hadronic environment.

Fig.(2) shows the  $5\sigma$  discovery regions for neutral Higgs boson  $\Phi$  ( $\Phi=h,H,A$ ) produced in association with b quarks  $pp \rightarrow b\bar{b}\phi$  with  $\Phi \rightarrow \mu^+\mu^-$  and  $\Phi \rightarrow \tau^+\tau^-$  modes in  $m_h - max$  scenario, as predicted from CMS Collaboration (8). Large fraction of this space is accessible to more than a channel with a possibility to achieve a more robust evidence in case of discovery.

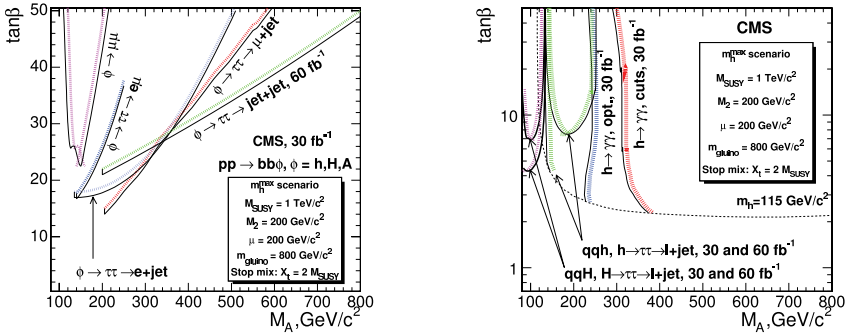


Figure 2: The 5  $\sigma$  discovery region for neutral Higgs bosons  $\Phi$  ( $\Phi=h,H,A$ ) produced in association with  $b$  quarks for  $pp \rightarrow bb\phi$  with  $\Phi \rightarrow \mu^+\mu^-$  and  $\Phi \rightarrow \tau^+\tau^-$  modes in  $m_h - \max$  scenario (on the left) <sup>8)</sup>. The 5  $\sigma$  discovery region for light neutral Higgs boson  $h$  from inclusive  $pp \rightarrow h + X$  with  $h \rightarrow \gamma\gamma$  decay for light and heavy scalar Higgs bosons,  $h$  and  $H$ , produced in the  $m_h - \max$  scenario (on the right) <sup>8)</sup>

Among the large variety of channels studied from ATLAS and CMS, we would focus the discussion few of them, representative of different categories:

- $p\bar{p} \rightarrow b\bar{b} h/H/A \rightarrow \mu^+\mu^-, \tau^+\tau^-$ , at moderate and high  $\tan\beta$ . These channels cover a large range of  $m_A$  region and may give the possibility of a  $h/A$  discovery even at mass close to  $Z$  pole.
- $p\bar{p} \rightarrow A$  at low  $\tan\beta$   $A \rightarrow Zh$  and  $Z \rightarrow \ell^+\ell^-$  ( $\ell = e, \mu$ )  $h \rightarrow b\bar{b}$  this channel has the capability to extend the search to very low  $\tan\beta$  regions.
- $p\bar{p} \rightarrow A, H \rightarrow \tilde{\chi}_2^0\tilde{\chi}_2^0$  and  $p\bar{p} \rightarrow A, H \rightarrow \tilde{\chi}_2^0\tilde{\chi}_3^0, \tilde{\chi}_2^0\tilde{\chi}_4^0, \tilde{\chi}_3^0\tilde{\chi}_3^0, \tilde{\chi}_3^0\tilde{\chi}_4^0, \tilde{\chi}_4^0\tilde{\chi}_4^0$  as well as  $A, H \rightarrow \tilde{\chi}_1^\pm\tilde{\chi}_2^\mp, \tilde{\chi}_2^+\tilde{\chi}_2^-$   
These search channels explore the MSSM Higgs decaying in supersymmetric particles.

### 5.1 $bbh/A \rightarrow bb\mu^+\mu^-$

The associated  $b\bar{b}$  ( $h,A,H$ ) production is enhanced and becomes the dominant process in the production of MSSM bosons in the high  $\tan\beta$  region. The Feynman diagrams contributing to the process  $gg \rightarrow b\bar{b}h \rightarrow b\bar{b}\mu^+\mu^-$  and  $q\bar{q} \rightarrow b\bar{b}h \rightarrow b\bar{b}\mu^+\mu^-$  are shown in Fig. 3.

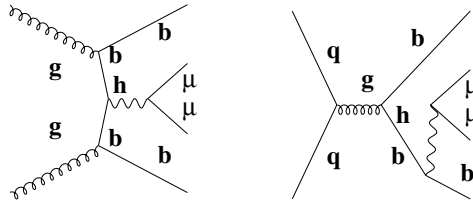


Figure 3: *Typical diagrams contributing at “tree level” to the process  $gg \rightarrow b\bar{b}h \rightarrow b\bar{b}\mu^+\mu^-$  and  $q\bar{q} \rightarrow b\bar{b}h \rightarrow b\bar{b}\mu^+\mu^-$ .*

Indeed, although the Higgs boson couplings are proportional to the fermion mass, thus resulting in a branching ratio to  $\tau^+\tau^-$  higher than to  $\mu^+\mu^-$  by a factor  $(\frac{m_\tau}{m_\mu})^2$ , the experimental conditions favor the  $\mu^+\mu^-$  channel<sup>1</sup>. These reasons encouraged both experiments to perform this search.

The signature of the h/A channel is a pair of well isolated high-energy muons with opposite charge and two hadronic jets containing b quarks. The invariant mass of the reconstructed muons is supposed to originate from a h or A boson and must be compatible, within the mass resolution, with the corresponding mass,  $m_h$  or  $m_A$ . The main backgrounds to this process are:

- $b\bar{b}Z \rightarrow b\bar{b}\mu^+\mu^-$ .
- $t\bar{t} \rightarrow b\bar{b}\mu^+\mu^-\nu\bar{\nu}$ .
- $ZZ \rightarrow b\bar{b}\mu^+\mu^-$ .

A search for neutral Higgs bosons h/A has been performed in the  $(m_A, \tan\beta)$  plane<sup>21)</sup>. Fig. 4 shows the distributions of the reconstructed  $\mu^+\mu^-$  invariant mass for signal (h and A) and background (Z,  $t\bar{t}$  and ZZ added up) events. The h/A signal (light blue) is clearly visible on top of the remaining background events (Z,  $t\bar{t}$  and ZZ added up, dark brown).

We conclude that if  $m_h = 110.00$  GeV and consequently  $m_A = 110.31$  GeV there is a high probability for these bosons to be discovered at the beginning of data taking.

---

<sup>1</sup>The production advantage of the  $\tau^+\tau^-$  channel is counterbalanced by the difficulty of identifying the hadronic decay of a  $\tau$ -jet in hadronic events, by a smaller acceptance of the detector and by a worse mass resolution due to the presence of neutrinos in the final state. Instead, with a final state like  $h \rightarrow \mu^+\mu^-$  the experiments would exploit the excellent combined performance of the muon spectrometer and inner detector.

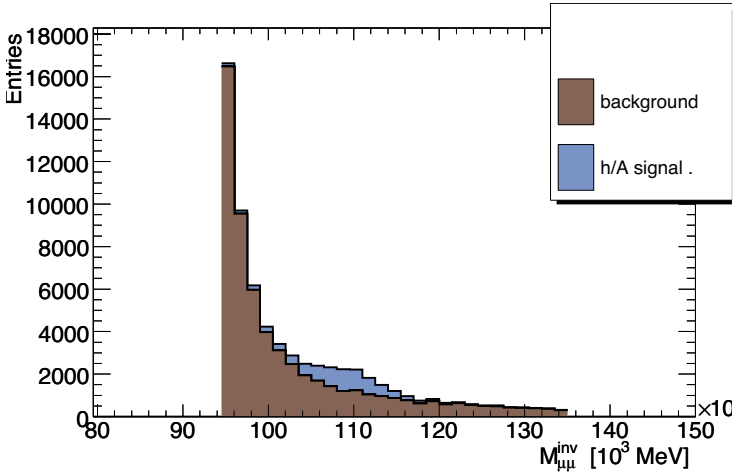


Figure 4: *Distributions of the reconstructed  $\mu^+\mu^-$  invariant mass,  $M_{\mu\mu}^{\text{inv}}$ , for signal and backgrounds events, after the selection cuts at the point ( $\tan\beta = 45$ ,  $m_A = 110.31$  GeV,  $m_h = 110.00$  GeV). The two distributions are normalized at  $\int\mathcal{L} dt = 300 \text{ fb}^{-1}$ . The h/A signal (light blue) emerge over the background (Z,  $t\bar{t}$  and ZZ) (dark brown). Entries are per bin width of  $1.5 \cdot 10^3 \text{ MeV}$  (21), (16).*

The search significance for the h/A neutral boson is shown as a function of  $m_A$  up to highest allowed value of  $m_h$ , in Fig. 5 for all scanned values of  $\tan\beta$  and three luminosities,  $\int\mathcal{L} dt = 300 \text{ fb}^{-1}$  ( $S_{h,A}^{300}$ ),  $30 \text{ fb}^{-1}$  ( $S_{h,A}^{30}$ ) and  $10 \text{ fb}^{-1}$  ( $S_{h,A}^{10}$ ) (21), (16). The values for the two lower luminosities were derived from the first one, which corresponds to the highest statistics.

One should note that large h/A masses are penalized by a small cross section, thus implying a lower significance, while the masses near to  $m_Z$  suffer from the difficulty in disentangling the neutral Higgs boson signal from the Z background.

The best mass range for an early discovery of h is between 100 and 120 GeV at any given  $\tan\beta$ . If  $\tan\beta > 30$  a large range of masses is accessible to discovery even after the first year of data taking. More integrated luminosity, between  $\approx 30$  and  $50 \text{ fb}^{-1}$ , is needed for  $\tan\beta$  between 30 and 20. The discovery at  $\tan\beta = 15$  demands a luminosity of  $\approx 150 \text{ fb}^{-1}$ , making the exploration of this region possible only after a few years of data taking.

With a  $\int\mathcal{L} dt \approx 10 \text{ fb}^{-1}$ , corresponding to one year of data taking, most of the masses are accessible if  $\tan\beta > 30$ . More integrated luminosity is needed

for  $\tan\beta = 20$  and  $\tan\beta = 15$ . Low masses need as well more luminosity in order to extract the evidence of a signal from the most copious Z background.

Discovery contours in the  $(\tan\beta, m_A)$  plane are shown, in Fig. 6 (on the left), in different  $\int \mathcal{L} dt$  scenarios for a significance of 5 as predicted from ATLAS experiment. Analogous contour plot has been derived from CMS Collaboration ( Fig. 6, the right) with an integrated luminosity of  $30 \text{ fb}^{-1}$  8).

## 5.2 Method for $b\bar{b}Z \rightarrow b\bar{b}\mu^+\mu^-$ background subtraction

The most copious background in the search of much new physics beyond Standard Model results from the production of the resonant  $b\bar{b}Z \rightarrow \mu^+\mu^-$  final state.

The Monte Carlo simulation of these processes, taking account of all correction loops, is complex and will demand an enormous theoretical effort and a careful tuning on experimental data. As a consequence, the systematic error in the background evaluation, due to the theoretical uncertainty, has to be taken in account. A review of the up-to-dated Monte Carlo implementations for LHC is summarized in Ref. 17). A strategy has been developed from ATLAS on the combined use of Monte Carlo and data to allow a realistic evaluation of that background at LHC. The method proposed in 18) exploits the two following points (at the level of particle generation):

- a) the rate of  $h/A \rightarrow e^+e^-$  is expected to be suppressed with respect to the signal  $h/A \rightarrow \mu^+\mu^-$  by a factor  $\left(\frac{m_\mu}{m_e}\right)^2$ ,
- b) the rate of the background  $b\bar{b}Z \rightarrow b\bar{b}\mu^+\mu^-$  is equal to the rate of  $b\bar{b}Z \rightarrow b\bar{b}e^+e^-$  because of the production diagrams which are the same, and of the lepton coupling universality in the Z decay.

In this context the associated Z production and decay in the channel  $b\bar{b}Z \rightarrow \mu^+\mu^-$  has been studied using a control sample of  $b\bar{b}Z \rightarrow e^+e^-$  events. The effect of *inner bremsstrahlung* (IB) radiation has been investigated and corrected for; the impact in the event reconstruction is not large. The ratio of the number of reconstructed events from the two samples in the region of mass higher than  $m_Z$ , interesting for new physics search, is stable and implies correction factors close to one as can be seen in Fig. (7)straight line is drawn for reader's eye 18) .

As a result, barring corrections for different *inner bremsstrahlung* and detector response, the number of  $b\bar{b}Z \rightarrow b\bar{b}e^+e^-$  gives directly the number of background events  $b\bar{b}Z \rightarrow b\bar{b}\mu^+\mu^-$ .

## 5.3 $bbh/A \rightarrow b\bar{b}\tau^+\tau^-$

The discovery potential for the supersymmetric Higgs boson  $h/H/A$  in final state  $\tau^+\tau^-$  has been investigated from both Collaboration with both tau leptons

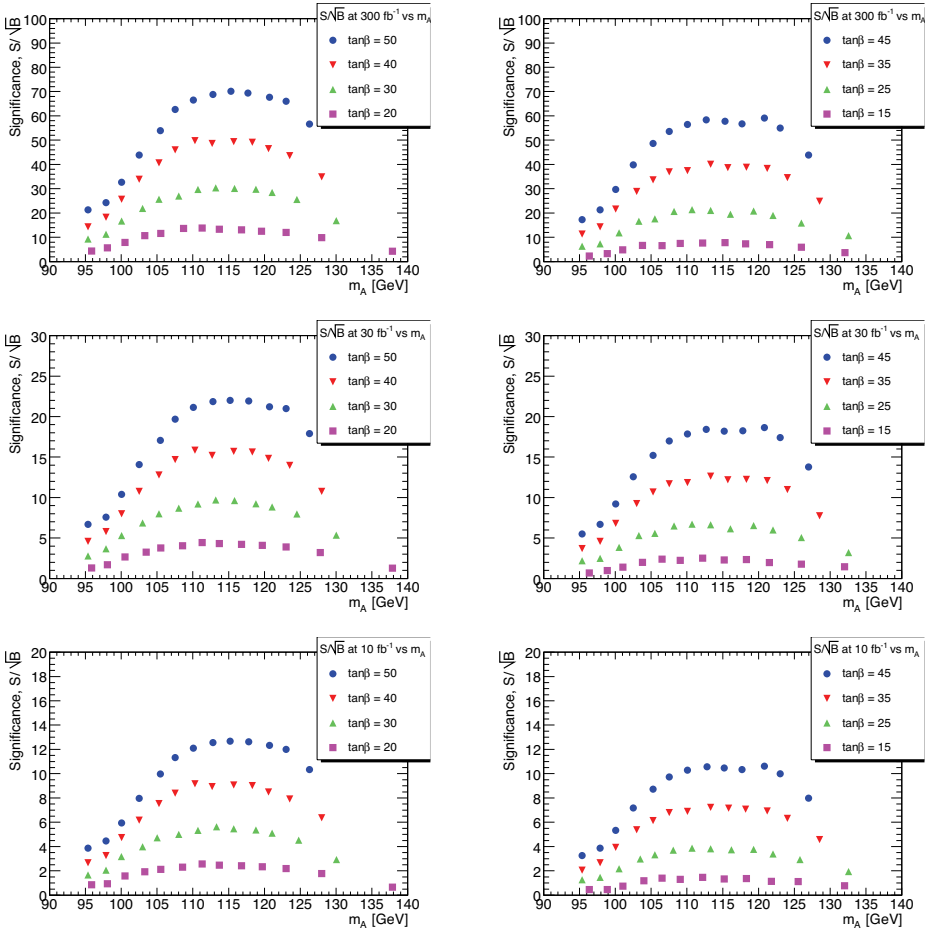


Figure 5: Search significance  $\frac{S}{\sqrt{B}}$  for a h/A neutral Higgs boson, as a function of  $m_A$  up to the largest allowed value of  $m_h$  in three different data taking scenarios,  $\int \mathcal{L} dt = 300, 30$  and  $10 \text{ fb}^{-1}$  (S is the number of h/A signal events, B is the number of background events). On the left the results for  $\tan\beta = 50, 40, 30, 20$ , and on the right the results for  $\tan\beta = 45, 35, 25, 15$ . The data are listed in Ref. <sup>16</sup>).

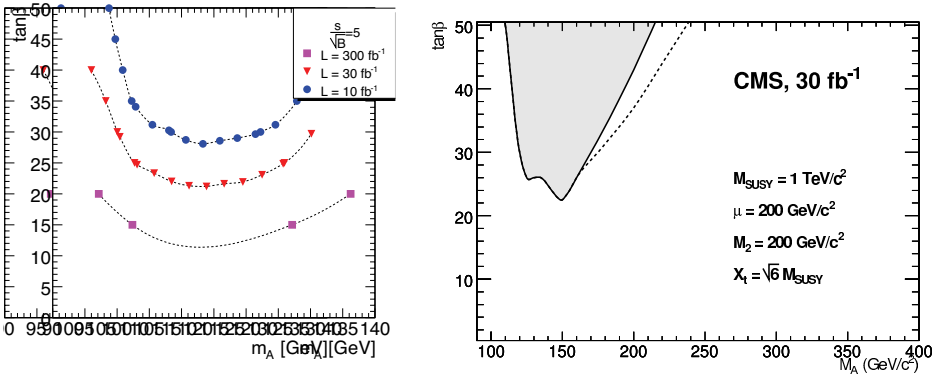


Figure 6: Discovery potential for a neutral Higgs boson  $h/A$  of mass  $m_A$  decaying to  $\mu^+\mu^-$ , accompanied by two  $b$ -jets, in the  $m_h - \max$  scenario (Sec. 2), as a function of  $m_A$ : contours are drawn for a search significance  $\frac{S}{\sqrt{B}} = 5$  (left) with an integrated luminosity of  $\int \mathcal{L} dt = 300$  (top), 30 (center) and 10 (bottom)  $\text{fb}^{-1}$  (ATLAS) <sup>21</sup>, <sup>16</sup>). Discovery contour plot for the MSSM neutral Higgs di muon analysis. the signal significance inside the gray area is  $> 5$  with an integrated luminosity of  $30 \text{ fb}^{-1}$  (CMS) <sup>8</sup>.

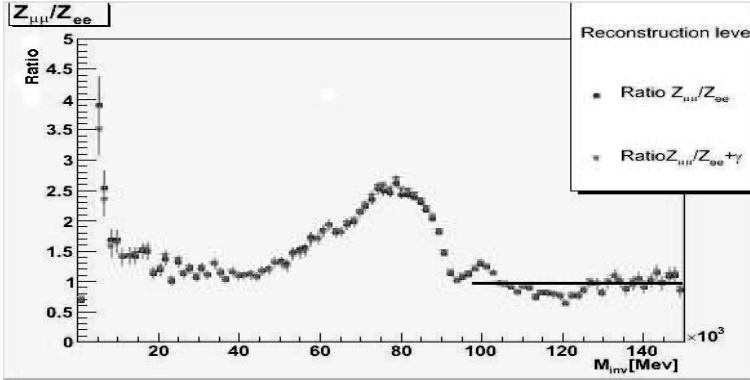


Figure 7: Ratio between the number of events decaying in  $\mu^+\mu^-$  and the number of events decaying in  $e^+e^-$ ,  $\left(\frac{N_{Z \rightarrow e^+e^-}}{N_{Z \rightarrow \mu^+\mu^-}}\right)$ , before IB correction (blue symbols), and after (red symbols). All events of the reconstructed sample are included. The black solid line is for viewing purposes.

decaying leptonically or in one lepton and one jet or both jets. As in the case  $\mu^+\mu^-$  both Collaborations have studied the MSSM Higgs production either in inclusive mode either in  $bb$  association.

Compared with hadronic and semileptonic final state, the fully leptonic final states are suppressed by relatively small branching ratio  $br(\tau \rightarrow \mu\nu\nu) \approx 0.174$  and  $br(\tau \rightarrow e\nu\nu) \approx 0.178$ , but the signal is clean.

The signal consists of events in which the Higgs boson decays into two tau leptons which in turn decay leptonically. One possible choice any final state in two leptons or  $\mu$ - $e$  final state, which is characterized from a lower background. The  $\tau^+\tau^-$  reconstructed mass with  $30\text{fb}^{-1}$  after all selections, but mass window, is shown in Fig. (8, right) for  $m_A = 140$  GeV and  $\tan\beta = 20$  in  $m_h - max$  scenario, as CMS collaboration<sup>8)</sup>. The Fig.(8, left) shows the discovery reach in  $m_A$ ,  $\tan\beta$  plane in  $m_h - max$  scenario. The lower curve correspond to the case when the background systematic uncertainty is taken in account.

## 6 Others discovery Channels

### 6.1 Search for the $A \rightarrow Zh$ decay with $Z \rightarrow \ell^+\ell^-$ , $h \rightarrow b\bar{b}$

The observation of the CP-odd pseudo-scalar Higgs (A) via its decay into a Z boson and the lighter CP-even scalar Higgs (h) followed by  $Z \rightarrow e^+e^-$ ,

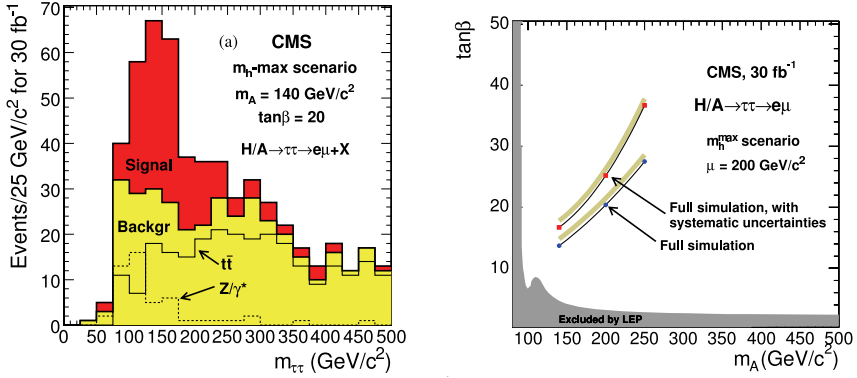


Figure 8: The  $\tau^+\tau^-$  reconstructed mass with  $30 \text{ fb}^{-1}$  after selection but mass window, in the  $m_h$  - max scenario (Sec. 2) and background  $m_A = 140 \text{ GeV}$ . The discovery region for  $gg \rightarrow b\bar{b}H/A, H/A \rightarrow \tau^+\tau^- \rightarrow e\mu + X$  in  $m_A$  -  $\tan\beta$  plane in the  $m_h$  - max scenario a search significance 5 (left) with an integrated luminosity of  $\int \mathcal{L} dt = 30 \text{ fb}^{-1}$  (8).

$\mu^+\mu^-$  and  $h \rightarrow b\bar{b}$  decays provides an interesting way to detect A and h simultaneously. The branching ratio of  $A \rightarrow Zh$  appears for the low  $\tan\beta$  and  $m_Z + m_h \leq m_A \leq 2m_{\text{top}}$  mass region.

The decays of A into charginos and neutralinos ( $A \rightarrow \chi\chi$ ), however, can dominate at certain value of  $\mu$  and  $M_2$ . Large values of these parameters are more favorable for this channel.

An interesting perspective in  $m_h$  - max scenario, with  $\mu = M_2 = 600 \text{ GeV}$  has been studied from CMS collaboration (8). The signal and background distributions of  $M_{b\bar{b}}$  are shown in Fig. 9 (left) for  $30 \text{ fb}^{-1}$ . Fig. 9 (right) shows the  $5\sigma$  discovery contours in  $(m_A, \tan\beta)$  plane for 30 and  $60 \text{ fb}^{-1}$ .

## 6.2 Search for the $A/H \rightarrow \tilde{\chi}_2^0 \tilde{\chi}_2^0 \rightarrow \ell^+ \ell^- \ell^+ \ell^-$

In all studies discussed so far, the interaction only between MSSM Higgs and SM particles were considered, in other words the SUSY mass scale was set heavy and it has been assumed no interaction between Higgs and sparticle sector. If this condition is released, different scenarios are opened and in some region of SUSY parameter space, heavy neutral Higgs bosons can be searched into supersymmetric particles. This may cover regions, which are not accessible to other SM Model particle decays. Few studies have been performed as pioneer works in this direction (19) (8). Recently a study possible decays of H/A

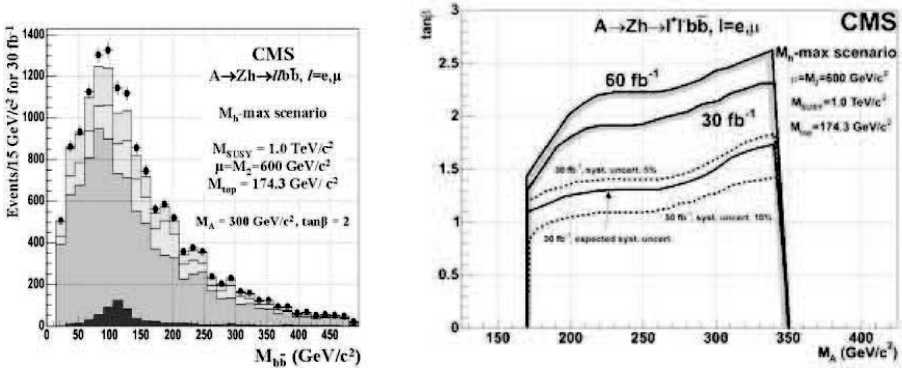


Figure 9: Distributions of  $M_{b\bar{b}}$  for signal and background after event selection for 30 fb<sup>-1</sup> of integrated luminosity. Blue (black) distribution of signal ( $m_A=300, \tan\beta=2$ ), black dots sum of signal+background (on the left) <sup>8)</sup> in the  $m_h$  - max scenario (Sec. 2) and background. The 5  $\sigma$  discovery contour for  $\int \mathcal{L} dt = 30$  and 60 fb<sup>-1</sup>. The effect of background systematic uncertainty can be seen in the curve of 30 fb<sup>-1</sup> (right) <sup>8)</sup>.

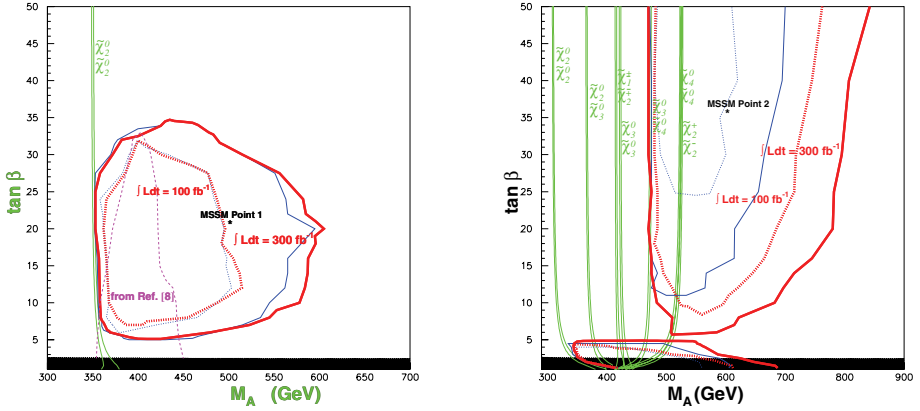


Figure 10: Discovery region in red ( $m_A, \tan\beta$ ) plane for  $-ino/spleton$  parameters  $\mu \approx 500$  GeV  $M_2=180$  GeV (Set1) as in MSSM Point1 (located with an asterisk), where  $\tilde{\chi}_2^0\tilde{\chi}_2^0$  is the dominating decay. Solid (dashed) red border delineate the discovery region for  $\int \mathcal{L} dt=300$  fb $^{-1}$  ( 100 fb $^{-1}$ ) (on the left). Discovery region in red ( $m_A, \tan\beta$ ) plane for  $-ino/spleton$  parameters  $\mu \approx 200$  GeV  $M_2=200$  GeV (Set2) as in MSSM Point2 (located with an asterisk), where Higgs boson decays to a variety of higher mass  $-inos$  (see text) constitute the majority of signal events. Solid (dashed) red border delineate the discovery region for  $\int \mathcal{L} dt= 300$  fb $^{-1}$  ( 100 fb $^{-1}$ ) (right). For complete set of MSSM parameters see Ref. 20).

bosons in MSSM and mSugra has been developed 20) as:  $H, A \rightarrow \tilde{\chi}_2^0\tilde{\chi}_2^0$ , as well  $H, A \rightarrow \tilde{\chi}_2^0\tilde{\chi}_3^0, \tilde{\chi}_2^0\tilde{\chi}_4^0, \tilde{\chi}_3^0\tilde{\chi}_3^0, \tilde{\chi}_3^0\tilde{\chi}_4^0, \tilde{\chi}_4^0\tilde{\chi}_4^0$  as well as  $H^0, A^0 \rightarrow \tilde{\chi}_1^\pm\tilde{\chi}_2^\mp, \tilde{\chi}_2^+\tilde{\chi}_2^-$ . The final state considered in this search is  $4\ell$  and missing energy. The  $m_A$  discovery reach for A and H is largely extended. Two sets of values of  $M_2$  and  $\mu$  have been chosen (Set1, Set2) to define two bench mark points in MSSM framework and this choice has been driven from consideration to have a point (Point1) where the signal most the signal events results from  $H, A \rightarrow \tilde{\chi}_2^0\tilde{\chi}_2^0$  and another (Point2), whereas decays including heavier- $inos$  make dominant contribution.

## 7 Conclusions

The ready to run experiments at LCH, ATLAS and CMS, will produce a harvest of enormous number of data. Based on these data the possibility to discover the

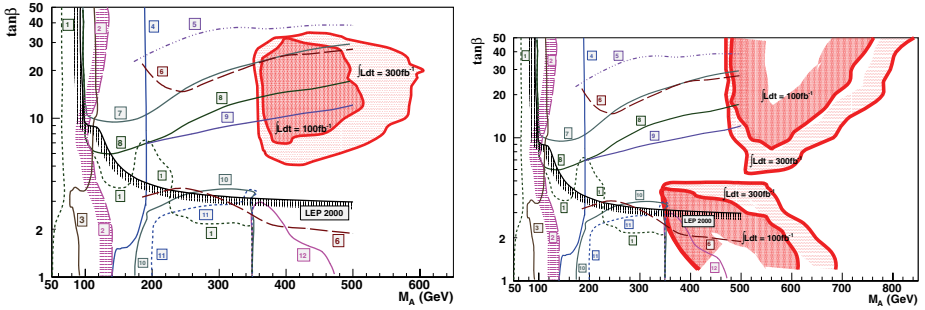


Figure 11: *On the left.* Discovery region in  $(M_A, \tan\beta)$  plane, here with a logarithmic  $\tan\beta$  scale, for MSSM Parameter Set 1 and  $\mathcal{L}_{int} = 100 \text{ fb}^{-1}$  and  $300 \text{ fb}^{-1}$  for MSSM Higgs bosons'  $4l$  signals from their decays into neutralino or chargino pairs (here  $H^0, A^0$  decays to  $\tilde{\chi}_2^0 \tilde{\chi}_2^0$  totally dominate), shown together with regions for other MSSM Higgs boson signatures from decays to SM particles based upon LEP results and ATLAS simulations  $^{(7)}$  (which assume  $\mathcal{L}_{int} = 300 \text{ fb}^{-1}$ ) where labels represent: 1.  $H^0 \rightarrow Z^0 Z^{0*} \rightarrow 4 \text{ leptons}$ ; 2.  $t \rightarrow bH^+, H^+ \rightarrow \tau^+\nu + c.c.$ ; 3.  $t\bar{t}H^0, h^0 \rightarrow b\bar{b}$ ; 4.  $h^0 \rightarrow \gamma\gamma$  and  $W^\pm h^0/t\bar{t}h^0, h^0 \rightarrow \gamma\gamma$ ; 5.  $b\bar{b}H^0, b\bar{b}A^0$  with  $H^0/A^0 \rightarrow b\bar{b}$ ; 6.  $H^+ \rightarrow t\bar{b} + c.c.$ ; 7.  $H^0/A^0 \rightarrow \mu^+\mu^-$ ; 8.  $H^0/A^0 \rightarrow \tau^+\tau^-$ ; 9.  $g\bar{b} \rightarrow \bar{t}H^+, H^+ \rightarrow \tau^+\nu + c.c.$ ; 10.  $H^0 \rightarrow h^0 h^0 \rightarrow b\bar{b}\gamma\gamma$ ; 11.  $A^0 \rightarrow Z^0 h^0 \rightarrow \ell^+\ell^- b\bar{b}$ ; 12.  $H^0/A^0 \rightarrow t\bar{t}$ . Note that SM discovery regions are not for the same input parameters: they presume Higgs bosons cannot decay into sparticles, so more accurate estimates may well be smaller. For the  $4l$  signals from  $\tilde{\chi}_i^0 \tilde{\chi}_j^0, \tilde{\chi}_m^+ \tilde{\chi}_n^-$  decays, the  $-ino/slepton$  parameters are  $\mu = -500 \text{ GeV}$ ,  $M_2 = 180 \text{ GeV}$ ,  $M_1 = 90 \text{ GeV}$  and  $m_{\tilde{\ell}_{soft}} = m_{\tilde{\tau}_{soft}} = 250 \text{ GeV}$ .

*On the right.* Discovery region in  $(M_A, \tan\beta)$  plane for for MSSM Parameter Set 2 and  $\mathcal{L}_{int} = 100 \text{ fb}^{-1}$  and  $300 \text{ fb}^{-1}$  for MSSM Higgs bosons'  $4l$  signals from their decays into neutralino or chargino pairs (here Higgs boson decays to higher-mass neutralinos typically dominate), shown together with regions for MSSM Higgs boson signatures from decays to SM particles as in Fig. 11. For the  $4l$  signals from  $\tilde{\chi}_i^0 \tilde{\chi}_j^0, \tilde{\chi}_m^+ \tilde{\chi}_n^-$  decays, the  $-ino/slepton$  parameters are  $\mu = -200 \text{ GeV}$ ,  $M_2 = 200 \text{ GeV}$ ,  $M_1 = 100 \text{ GeV}$ ,  $m_{\tilde{\ell}_{soft}} = 150 \text{ GeV}$  and  $m_{\tilde{\tau}_{soft}} = 250 \text{ GeV}$ , as in MSSM Point 2. Here Higgs boson decays to a variety of higher mass  $-inos$  (see text) constitute the majority of the signal events. Solid (dashed) red border delineates the discovery region for  $\mathcal{L}_{int} = 300 \text{ fb}^{-1}$  ( $100 \text{ fb}^{-1}$ ). Other signal delineations from the ATLAS TDR all assume  $\mathcal{L}_{int} = 300 \text{ fb}^{-1}$ . Note also that, since ATLAS discovery regions presume Higgs bosons cannot decay into sparticles, more accurate estimates may well be smaller (from Ref.  $^{(20)}$ ).

neutral MSSM h/A/H Higgs in few representative decay channels are discussed in these pages, involving SM final states and MSSM final states, in different  $(m_A, \tan\beta)$  regions.

Among the SM final state channels, a recent ATLAS study of the b-associated production of h/A and the following decay in  $\mu^+\mu^-$  is discussed <sup>21)</sup>. In this channel a detection of neutral MSSM Higgs even in the region close to Z pole is possible, exploiting the high resolution of  $\mu$  detectors. The other decay channels involving  $\tau^+\tau^-$  decaying in  $\ell^+\ell^-$  with the  $\ell=e, \mu$  <sup>8)</sup>, characterized from a clean signal due to a low background final state, and the  $\tau^+\tau^-$  decay channel in  $\ell$  and one jet with a larger significance for discovery especially in large  $m_A$  mass are also discussed.

In very low  $\tan\beta$  region, an interesting channel  $A \rightarrow Zh$  decay with  $Z \rightarrow \ell^+\ell^-$  and  $h \rightarrow b\bar{b}$  <sup>8)</sup> can have access to discovery of MSSM neutral Higgs and simultaneously discovery of A and h.

A recent study <sup>20)</sup> involving A H decays in supersymmetric particles has demonstrated that for many interesting choices of the basic input parameters of the MSSM, heavier Higgs boson decay modes of the type  $H, A \rightarrow \tilde{\chi}_i^0 \tilde{\chi}_j^0$ , with  $i, j \neq 1$  could be possible channel to detect MSSM. The neutralinos' subsequent leptonic decays, as  $\tilde{\chi}_i^0 \rightarrow \ell^+\ell^-\tilde{\chi}_1^0$ , can yield a four-isolated-lepton (where here  $\ell$  refers to electrons and/or muons) plus missing-transverse-energy signature. Such leptonic neutralino decays may proceed via either an intermediate charged slepton or via an intermediate  $Z^{0(*)}$ , where in either case this intermediate state may be on- or off-mass-shell.

We can conclude that this variety of channels will give a possibility to explore in the next future the complete region of  $m_A \tan\beta$  for a discovery of MSSM region with LHC data.

**References**

1. H.-P. Nilles, Phys. Rep. **110** (1984) 1.
2. H. E. Haber and G. L. Kane, Phys. Rep. **117** (1985) 75.
3. R. Barbieri, Riv. Nuovo Cim. **11** (1988) n. 4.
4. ALEPH Collaboration, DELPHI Collaboration, L3 Collaboration, OPAL Collaboration and LEP Working Group for Higgs boson searches, Phys. Lett. **B565** (2003) 61.
5. The LEP Collaborations ALEPH, DELPHI, L3 and OPAL, and LEP Working Group for Higgs boson searches, Eur. Phys. J. **C47** (2006) 547.
6. ALEPH, DELPHI, L3, OPAL Collaboration and LEP Working Group for Higgs boson searches, Search for charged Higgs bosons: Preliminary combined results using LEP data collected at energies up to 209 GeV, 2001, hep-ex/0107031.
7. ATLAS Coll., ATLAS detector and Physics Performance: Technical Design Report, Volume 2, report CERN/LHCC/99-15 (1999).
8. CMS Coll., CMS detector and Physics Performance: Physics Technical Design Report, Volume 1, report CERN/LHCC/2006-001 (2006).
9. Stephen P. Martin, A supersymmetry primer, 1997, hep-ph/9709356.
10. W.-M. Yao *et al.*, J. Phys. **G33** (2006) 1.
11. E. Richter-Was *et al.*, Int. J. Mod. Phys. **A13** (1998) 1371.
12. V. Abazov, Phys. Rev. Lett. **95** (2005) 151801.
13. A. Abulenci, Phys. Rev. Lett. **96** (2006) 011802.
14. K.A. Assamagan, *et al.*, Eur. Phys. J. direct **C4** (2002) 9.
15. M. Schumacher, Investigation of the discovery potential for Higgs bosons of the minimal supersymmetric extension of the standard model (MSSM) with ATLAS, 2004, hep-ph/0410112.
16. S. Gentile, H. Bilokon, V. Chiarella, G. Nicoletti, Search for MSSM neutral Higgs bosons decaying to a muon pair in the mass range up to 130 GeV, 2007, Università La Sapienza, Sez. I.N.F.N., Roma, Laboratori Nazionali di Frascati, I.N.F.N, Frascati Italy, ATL-PHYS-PUB-2007-001.

17. M.A.Dobbs, *et al.*, Les Houches guidebook to Monte Carlo generators for hadron collider physics, 2004, hep-ph/0403045, submitted to Eur.Phys.J.C.
18. S. Gentile, H. Bilokon, V. Chiarella, G. Nicoletti, Data based method for  $Z \rightarrow \mu^+ \mu^-$  background subtraction in ATLAS detector at LHC, 2006, Università La Sapienza, Sez. I.N.F.N., Roma, Laboratori Nazionali di Frascati, I.N.F.N, Frascati Italy, ATL-PHYS-PUB-2006-019.
19. Moortgat, Filip and Abdullin, Salavat and Denegri, Daniel, (2001).
20. Bisset, Mike and Li, Jun and Kersting, Nick and Moortgat, Filip and Moretti, Stefano, (2007).
21. Gentile, Simonetta and Bilokon, Halina and Chiarella, Vitaliano and Nicoletti, Giovanni, Eur. Phys. J. **C52** (2007) 229–245.

# SEARCHING FOR THE HIGGS AT THE TEVATRON AND THE LHC. A CRITICAL ASSESSMENT

Richard St. Denis

*University of Glasgow – Department of Physics and Astronomy  
Glasgow G12 8QQ – United Kingdom*

## Abstract

In this paper an update of the rapid progress in measurements of the top quark, W mass and in direct searches for the Higgs at the Tevatron is examined and compared to the observations from one year before. The indirect measurements of the Higgs mass indicate that it has a value of  $m_H < 190 \text{ GeV}/c^2$  at 95% confidence when the current direct search limits are taken into account. In direct searches, the sensitivity to the Standard Model Higgs is shown to be below a factor of six times the Standard Model cross section prediction for  $110 < m_H < 200$  and a limit of 1.1 times the Standard Model cross section is set for  $m_H = 160 \text{ GeV}/c^2$ . The physics strategy for studying electroweak symmetry breaking at the LHC and Tevatron in the next years is reconsidered and changes plus progress are noted.

## 1 Overview

Over the last four years the Tevatron experiments have enjoyed an annual doubling of the integrated luminosity delivered and recorded. This has led to an avalanche of new results in the area of electroweak symmetry breaking and in particular in direct searches for the Higgs. At the same time, completion of the Large Hadron Collider (LHC) and the associated experiments nears. In this paper an examination of the results at hand is made with a view to anticipate how the picture of electroweak symmetry breaking may evolve in the next years. The discussion is organized as follows. First the Tevatron physics reach is reviewed. This is followed by a discussion of virtual and direct Higgs detection. The situation with the SUSY Higgs is considered with a larger data sample than last year at this conference. Finally a scenarios for the development of the research environment for electroweak symmetry breaking are discussed, based on the projected schedule for the LHC and expectations for the performance of the Tevatron experiments.

## 2 The Tevatron Physics Reach

The physics reach of the Tevatron is built on a mountain of measurements that confirm the ability of the collaborations to use their detectors to do physics. Each measurement is for itself a significant result. Measurements begin with the largest cross section processes, those of B physics, but focusing in on measurements having small branching ratios and difficult backgrounds. While last year saw the new measurement of  $B_s$  oscillations <sup>1)</sup>, this year has seen evidence for single top production <sup>2)</sup>, the discovery of WZ production <sup>3)</sup>, and evidence for the ZZ production <sup>4)</sup>, the final base camp from which the Higgs summit is in sight. The ZZ cross section is only a factor of three larger than the Higgs cross section for  $m_H = 160 \text{ GeV}/c^2$ . New techniques in the Higgs analysis have brought the combined CDF and D0 Tevatron limit on production of a Standard Model Higgs with mass,  $m_H = 160 \text{ GeV}/c^2$ , to within 10% of the Standard Model predicted cross section. Processes such as single top and ZZ act as important messengers heralding the impending arrival of the Higgs. This journey through lower and lower cross section processes represents one approach to provide convincing evidence of these processes, first as discovery then as measurements constraining the Standard Model. The precision measurements themselves provide confidence in the experimental method and at the same time give insight into rare processes through their contribution to virtual mass corrections. Discussion of this approach is the subject of Section 3. The advances in direct Higgs searches are discussed in Section 4. Along the way, some new physics may well appear, with Supersymmetry being the most

popular candidate and a discussion of this in light of the updated search for SUSY Higgs is mentioned in Section 6. Finally there is an entirely different approach. This is a search for Higgs production in diffractive scattering discussed elsewhere in these proceedings <sup>5)</sup>.

### 3 Indirect Searches for Higgs

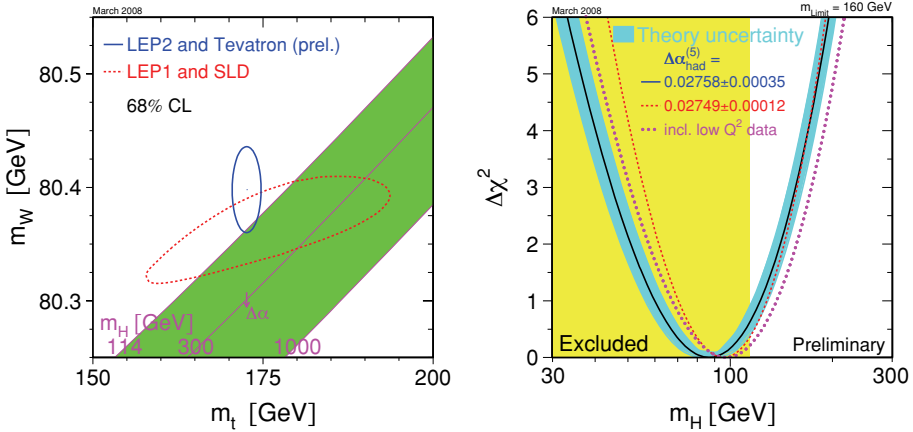


Figure 1: Mass of the top quark vs Mass of the W boson compared to MSSM SUSY and Standard Model expectations (left) and best fit Higgs mass to the electroweak data.

Measurements of the W and top mass amount to indirect searches for the Higgs since the masses are related within the Standard Model by loop corrections containing the Higgs and thus depend on its mass. SUSY particles or other new physics. In February 2006, the situation was as follows <sup>6)</sup>. The best fit mass of the Standard Model Higgs was  $M_h = 91^{+45}_{-32}$  GeV/c<sup>2</sup> with  $M_h < 186$  GeV/c<sup>2</sup> with 95% confidence and  $M_h < 210$  GeV/c<sup>2</sup> with 95% if the LEP limits on a direct search for the Higgs <sup>7)</sup> are included. By last year, the most probable value of of the Higgs mass was  $M_h = 80$  GeV/c<sup>2</sup> and  $M_h < 156$  GeV/c<sup>2</sup> with 95% confidence. This year the results are given in fig. 1 <sup>8)</sup>, with the most probable value at 87 GeV/c<sup>2</sup> and  $M_h < 190$  GeV/c<sup>2</sup> with 95% confidence (including LEP limits). These observations give strong indications for the search strategies that one should undertake when looking

for the Standard Model Higgs. While it remains true that that the  $1\sigma$  contour has crept into the SUSY-favored region, it is important to realize that the  $3\sigma$  contours overlap the Standard Model portion of the  $m_{top}-m_W$  plane.

#### 4 Direct Searches for the Standard Model Higgs

There are four main production mechanisms for the Standard Model Higgs when searching at hadron colliders: gluon fusion, which dominates at the Tevatron and LHC; associated production or ‘‘Higgsstrahlung’’, the mechanism holding the best hope for Higgs in the range up to about  $130\text{ GeV}/c^2$  and is most actively pursued at the Tevatron; and vector boson fusion and  $t\bar{t}H^0$  production which are of interest particularly at LHC.

The strategy for direct searches at the Tevatron continues to be influenced by the tantalizing results from LEP where ALEPH claimed  $3\sigma$  evidence for a Standard Model Higgs at  $M_h = 115\text{ GeV}/c^2$  <sup>9)</sup>. In light of a lack of confirmation by the other LEP experiments, the boundary for direct searches for the Higgs is set at  $M_h > 114.4\text{ GeV}/c^2$  at 95% confidence <sup>7)</sup>. The current experimental searches at the Tevatron focus on the gluon fusion process  $gg \rightarrow H^0 \rightarrow W^+W^- \rightarrow \ell^+\ell^-\bar{\nu}_{\ell^+}\nu_{\ell^-}$  and the associated production processes  $q\bar{q} \rightarrow (W^\pm/Z^0)H^0$  where  $W^\pm \rightarrow \ell^\pm\nu_\ell$ ,  $Z^0 \rightarrow \nu_\ell\bar{\nu}_\ell$  or  $Z^0 \rightarrow \ell^+\ell^-$  and  $H^0 \rightarrow b\bar{b}$ . The leptons  $\ell$  may be electrons, muons or taus. In the case of taus current searches are limited to the  $\tau$  decay channels  $\tau^- \rightarrow e^-\bar{\nu}_e$  or  $\tau^- \rightarrow \mu^-\bar{\nu}_\mu$  and charge conjugate channels. These search modes divide experimentally into two major camps of effort: those that need precise measurement of particle decay vertices employing silicon tracking and those that do not. The associated production channels fall into the first camp and the W boson pair production modes fall into the second camp.

The sensitivity of these searches to the Standard Model Higgs cross section is increasing rapidly with time. Results that were presented in all the various search modes for the Summer 2005 conferences are shown in fig. 2a and by September of 2005 had changed to those shown in fig. 2b, with sensitivity in the region around  $M_h \simeq 160\text{ GeV}/c^2$  improved by over an order of magnitude with about twice the integrated luminosity analyzed. This illustrates that the rapid progress is made not only based on an increase in the amount of data analyzed but also by the techniques employed and the understanding of the detectors. For the decay of Higgs into W pairs, the handling of leptons having transverse momenta between 10 and 20 GeV/c led to significant improvements in acceptance and hence sensitivity to smaller cross sections. By February of 2006, further improvements were made and this is illustrated in fig. 2c where the sensitivity at  $M_h = 160\text{ GeV}/c^2$  has come to within a factor of 12 of the Standard Model expectation. Since that time there are improve-



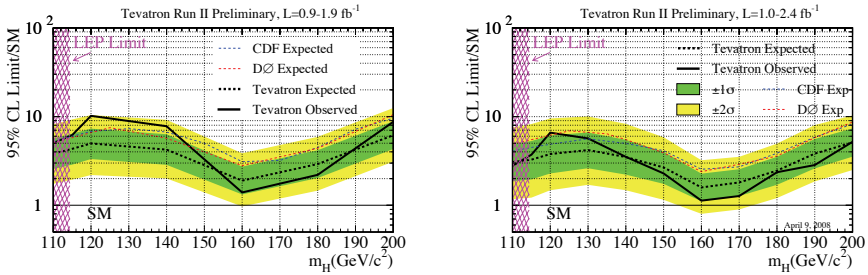


Figure 3: 95% Confidence Limits on Standard Model Higgs production cross sections from a. Summer 2007 (left) b. March 2008 (right). The y-axis is the limit relative to the expected Standard Model Higgs cross section.

at  $160 \text{ GeV}/c^2$  is now within 1.6 (1.1). All of these results are for an integrated luminosity of  $2 \text{ fb}^{-1}$  or less. This rapid progress is expected to continue as the Tevatron performance has been exceptional, with both CDF and D0 having recorded more than  $3 \text{ fb}^{-1}$  of integrated luminosity.

This progress is examined in more detail in fig. 4. The points on the figures are the actual 95% exclusion limit sensitivities achieved, given in units of the Standard Model cross section, at the integrated luminosities indicated. The curves show the projections for sensitivity assuming only an improved statistical precision. It can be seen that the progress is much more rapid than statistical improvements. In the last year this has had major improvements due to increased use of acceptance and the use of the multivariate techniques described in Section 5. Further improvements in acceptance, additional channels whose analysis are nearing completion and updating analyses with more luminosity are items that go into the projection given by the yellow band. It shows that within the next year with the data on hand, sensitivity to the Standard Model Higgs at  $m_H = 160 \text{ GeV}/c^2$  should be accomplished. If the Tevatron continues to perform well, then by the time the integrated luminosity is doubled, sensitivity at the Standard Model Cross section to a Higgs having a mass,  $m_H = 115 \text{ GeV}/c^2$ , should be achieved.

To illustrate the experimental issues and hence gain insight into the prospects for improvements, some of the challenges are considered in each of the various channels. First in associated production for the ZH mode where the Z decays to neutrinos, the trigger is 35 GeV of missing energy and two jets above 20 GeV with one jet having  $|\eta| < 0.7$ . The dominant background is QCD production of b jets with mismeasurement leading to apparent missing

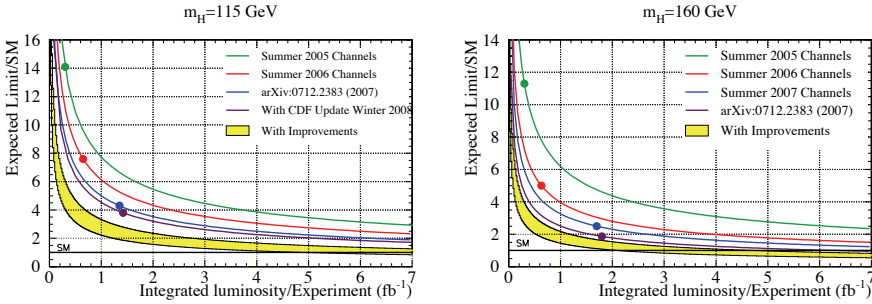


Figure 4: *Projected 95% confidence limits in Tevatron sensitivity to the Standard Model Higgs in units of the Standard Model Higgs cross section shown as a function of integrated luminosity for  $m_H = 115$  and  $160 \text{ GeV}/c^2$ . The points are the sensitivities that have been achieved and the curves are based on statistical projections of the sensitivity.*

energy. For the WZ production, the trigger is an electron or muon with transverse momentum,  $p_t > 20 \text{ GeV}/c$ . The topology is characterized by the lepton, missing energy and one or two identified b jets. The dominant background is top production. Finally, for WZ production where the Z decays to leptons, the trigger is again an electron or muon with  $p_t > 20 \text{ GeV}/c$ . The topology is distinguished by the two leptons and one or two identified b jets. In this case there is also a kinematic distinction of the leptons forming a Z mass. In all these associated production channels there are additional kinematic constraints on the b jets forming a Higgs mass. Acceptance for the leptons, improving the trigger and missing energy resolution in the trigger, and recognizing the topological and kinematic properties are all areas for experimental improvement. Of particularly acute importance is the efficient and correct recognition of b jets, a topological constraint, plus the measurement of the invariant mass with the b jets, a kinematic constraint. Efficient exploitation of the kinematic and topological features of Higgs events can be obtained from use of more sophisticated matrix element or Artificial Neural Network techniques. Whereas at the time of this conference last year the neural net method was employed only in the case of ZH where Z decays to leptons, these methods have now been applied to all the search channels. Control over systematic uncertainties and gain in sensitivity is obtained through the combination of these various channels. There are common uncertainties associated with b jet identification and Higgs mass determination from b jets at low mass searches.

Results for the various associated production modes are summarized in

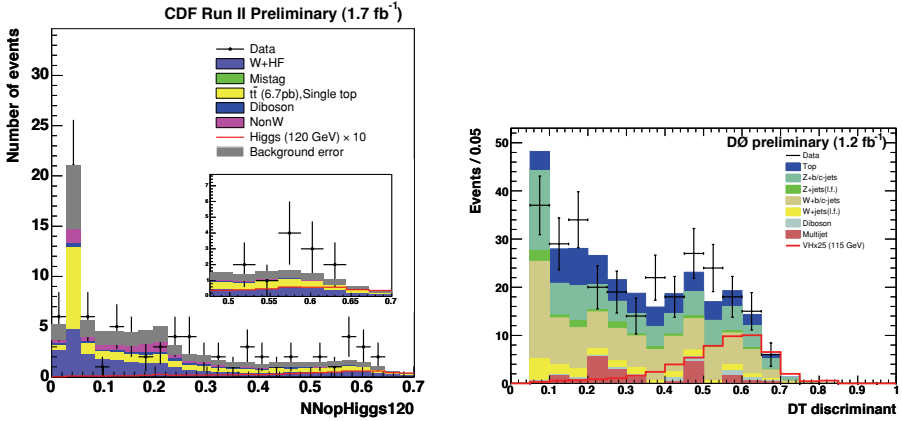


Figure 5: Neural net output distribution in Higgs search by CDF in WH mode and  $D0$  in ZH mode with Z decaying to neutrinos.

fig. 5 for WH, ZH production where the Z decays to neutrinos.

The search for the decay of Higgs to W boson pairs which decay to leptons has sensitivity that is comparable to the associated production modes down to a Higgs mass of about  $M_h = 120$  to  $130$   $\text{GeV}/c^2$  and a reach above  $170$   $\text{GeV}/c^2$  with the best sensitivity around  $M_h = 2M_w$ , where  $M_w$  is the W boson mass. This mode is characterized by two high transverse momentum leptons which have a spin correlation that lead to angular correlations between the leptons that distinguish from other Standard Model modes of dilepton production. A simple cut on a dilepton mass at  $M_{\ell\ell} > 16$   $\text{GeV}/c^2$  removes the large number of dileptons from B decays as evidenced by the fact that the kinematics of the remaining dilepton events are well described by the Drell-Yan predictions. Thus Drell-Yan production becomes the dominant source of lepton pairs at the Tevatron. These leptons tend to have an azimuthal separation of 180 degrees and these events are easily distinguished from Higgs events. The sample of events with azimuthal separation smaller than 180 degrees is dominated by W pair production without an intermediate Higgs. These leptons tend not to have the strong azimuthal correlation offered by the Higgs decay. Results for the high mass Higgs are shown in fig. 6. It can be seen that all analyses use the advanced techniques described in the next section.

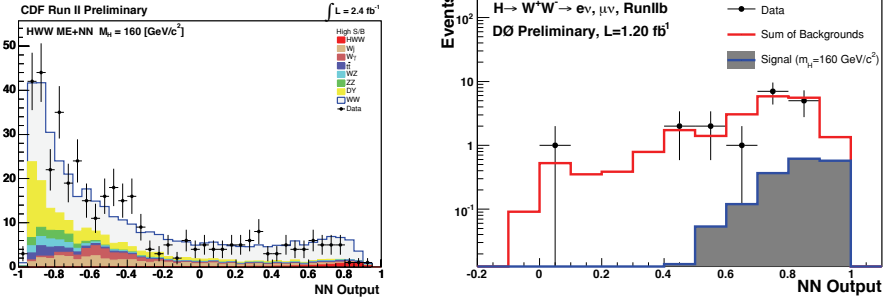


Figure 6: Results for high mass Higgs searches: NN scores for  $gg \rightarrow H \rightarrow WW$  production for CDF and D0. The CDF results combines all decays into electrons and muons whereas the D0 plot is shown for muons only. Plots for other channels may be found at [11](#)).

### 5 Multivariate Techniques

The advances in the last year included a complete transition of all analyses to using multivariate techniques. The major techniques in use were the Matrix Element (ME) and the Neural Net (NN). The next year will see a consolidation of the understanding of the intricacies of these techniques. The ME and NN techniques are compared and contrasted here.

The ME method employs leading order computations of the matrix elements for the signals and backgrounds. The inputs are the measured four-vectors of the leptons and jets. The probability that these values represent each physics process is computed by integrating over the matrix element while convolving the matrix element quantities with a *transfer function* that converts them to values that are observable. This transfer function represents the detector resolution and may include initial state radiation effects. A likelihood discriminator is formed by taking the ratio of the probability that the observed quantities represent the signal, divided by the total probability that the event is signal plus the probabilities that the event is background. The background probabilities are weighted according to their relative abundances. The computation of these probabilities is carried out on a set of simulated background and signal events. The distribution of the ME computation for each background and the signal is used to form a *template*.

At this point the analysis proceeds as for any cut analysis, with the likelihood ratio being used in place of a kinematic quantity such as the invariant mass of two b quarks, as in the low mass Higgs search, or the angular separation of the leptons in the high Mass Higgs search. The data distribution is com-

puted and the data are fitted to the templates with the signal normalization allowed to vary freely and the background normalizations constrained within the estimated systematic uncertainties. The probability that the background represents the data compared to the probability that the background plus the signal represents the data is evaluated by performing a number of pseudoexperiments on the background alone to represent the statistical accuracy of the data in the absence of a signal and the distribution of the cross sections is formed. This distribution is compared to the fit result for the actual data and the probability that the data are consistent with background is computed by determining the number of pseudoexperiments that have a value less than or equal to that observed. If the data lie within 95% of the experiments performed, a limit is set. If the data exceed expectations then a cross section can be determined.

The basic element of the NN approach is a *neuron* which takes a set of input values, applies weights to them, and uses these weighted values as input to a function of some form, such as a sigmoid. The output of this element may then be the input to another stage where another weight is applied before the response function is computed. The input to the network is some choice of variables selected on the basis that they will provide some discrimination of signal and background. The output is a number, normally 1 if the event is a signal event and 0 if it is a background event. The weights are adjusted until the difference between the output and the expected outcome is minimized as the network response to a set of events of signal and background is computed. Once the weights are established, the distributions of neural net responses to a set of simulated events for the various backgrounds and the signal are computed. These form a set of templates as in the ME approach and the same fitting procedure is used.

Both approaches contain similar elements. First there is a matrix element computation performed in both followed by a conversion of values from the ideal four vectors to the observed quantities. These values are sampled over a some region of phase space. In the case of the ME, the phase space is spanned by using a program that performs an integral numerically over that space whereas in the NN, simulated events that are meant to span a sufficient portion of the phase space are generated and the minimization of the NN determines the overall response. Each has limitations in numerical methods of the integration and in the representation of the response of the detector. Either of the methods can be computationally intensive.

The two approaches also contain complementary characteristics. While the four vectors that are input to the ME are easy to identify, the functional form that characterizes the physics is not obvious. This becomes important in understanding how to determine the systematic uncertainties. For example,

the Higgs to WW decay mode must depend on the angle of the leptons and hence it is important to determine how well the detector measures these angles. For the NN it is less obvious what values to choose and one must make a guess at what will be the important variables. Simply giving the same four vectors that were input to the ME may fail to work well if the statistics for populating the phase space is poor and variables that are not helpful in discriminating are examined by the NN. However, the most sensitive variables can be determined and the systematic uncertainties are evaluated by a straightforward variation of the most important discriminator and examination of the change of the output distribution.

The differences in the approaches can be exploited to help determine the quantities that are important in the ME computation while at the same time providing evidence that the quantities needed in the NN computation have been included. This is accomplished by including the ME computation as input to the NN. If this shows significant improvement, then important values have been missed in the NN inputs. If there is little change, then values can be removed from the input list of the NN until a change is noticed, or conversely, they can be added one at a time. This shows which quantities are most important in the ME. For most analyses, using the matrix element computation as input to the neural net is often done but the analysis of the interplay of the two methods is likely to be characteristic of the maturation of the analysis over the next year.

## 6 SUSY

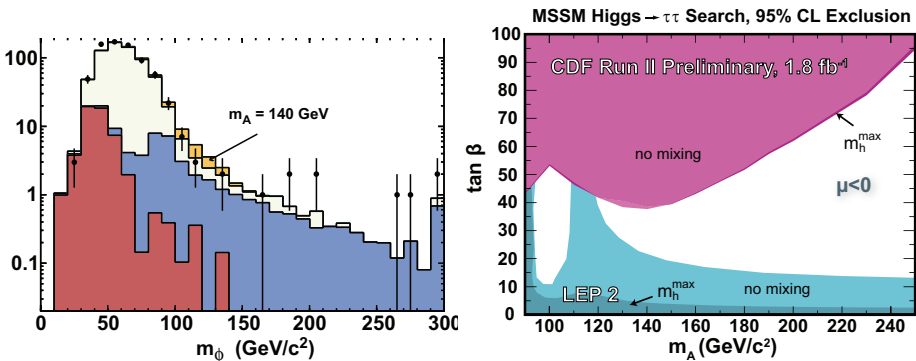


Figure 7: *Distribution of the invariant mass of the visible products of tau decays in the CDF search for SUSY Higgs and resulting exclusion limits for SUSY Higgs. The results for the higher statistics sample where one tau decays  $e$  or  $\mu$  and the other hadronically is shown. The results are preliminary.*

A recent search for neutral SUSY Higgs<sup>10)</sup> was made in the mode where the SUSY Higgs decays to tau pairs. The MSSM SUSY model has five Higgs particles,  $H^0$ ,  $h^0$ ,  $A^0$  and  $H^\pm$ . The phenomenology is characterized by the ratio of the down and up type quark vacuum expectation values expressed as the parameter  $\tan\beta$ . The b quark enhances both production and decay of these neutral Higgs particles and when  $\tan\beta$  is large, of order 50, the rate becomes sufficient to detect the neutral SUSY Higgs at the Tevatron. In this model, either the  $H^0$  is light and Standard-Model-like with the  $h^0$  and  $A^0$  degenerate and enhanced by  $\tan\beta$  or the  $h^0$  is light and Standard-Model-like with the  $H^0$  and  $A^0$  degenerate and enhanced by  $\tan\beta$ . The lighter Higgs must have a mass less than about  $130 \text{ GeV}/c^2$ . The degenerate state is denoted by the symbol  $\phi$ . The search is conducted on decays of  $\phi \rightarrow \tau^+\tau^-$  where one tau decays to a muon or electron plus neutrinos and the other either again to muon or electron plus neutrinos, or to hadrons and a neutrino. The invariant mass of the taus is examined but due to the unmeasured neutrinos, only a visible portion of the mass is measured. Last year the results for for CDF<sup>10)</sup> showed small deviation around  $M_\phi = 160 \text{ GeV}/c^2$ . The updated results with twice the data are shown in fig. 7 and are consistent with the study by D0<sup>10)</sup> which has shown no deviation.

## 7 LHC and a Scenario

The progress outlined in the last sections has been based mainly on results from the Tevatron. As the LHC comes into play the question arises as to how the understanding of electroweak symmetry breaking will continue to evolve. A broad comparison of the physics output of the LHC with  $1 \text{ fb}^{-1}$  of data to the total statistics from previous colliders<sup>1</sup> has been given<sup>12)</sup> and is reproduced in Table 1. The potential for Higgs discovery at LHC is shown in fig. 8 for an integrated luminosity of  $30 \text{ fb}^{-1}$ . From this figure, one observes that the higher mass regions may well be excluded by the Tevatron both by direct search in the W pair decay channel and by virtual measurements coming from precision top and W masses. At the Tevatron there is great potential to exclude or see deviations in the intermediate mass range,  $130 < M_h < 170 \text{ GeV}/c^2$ . This leaves the low mass range where both the Tevatron and the LHC will require more time to exclude or discover the Higgs.

In February 2006, this led to the following scenario:

- **LHC 2007:** The LHC has its first pilot run. Calibrations with Z,W are completed and an integrated luminosity of  $200 \text{ pb}^{-1}$  is accumulated.

---

<sup>1</sup>A total integrated luminosity of  $8 \text{ fb}^{-1}$  has been assumed for the Tevatron.

Table 1: *Examples of production rates of some benchmark physics processes for the LHC and past colliders.*

Channel(s)	Ev/Exp/fb <sup>-1</sup> (LHC)	Total Statistics from Previous Colliders
$W \rightarrow \mu\nu$	$7 \times 10^6$	$10^4$ (LEP) $10^6$ (TeV)
$Z \rightarrow \mu\mu$	$10^6$	$10^6$ (LEP) $10^5$ (TeV)
$t\bar{t} \rightarrow \mu\nu + X$	$10^5$	$10^4$ (TeV)
gluino-gluino ( $m = 1$ TeV)	$10^2 - 10^3$	–

- **LHC 2008:** The first full LHC physics run is completed with an integrated luminosity of  $1 \text{ fb}^{-1}$ .
- **TEV 2007:** The Tevatron has accumulated  $4 \text{ fb}^{-1}$  total. The WW decay mode is sensitive in the region  $140 < M_h < 170 \text{ GeV}/c^2$ . The W and top mass accuracy narrows in on Higgs mass so that:
  - Deviations are building in the higher mass range. LHC focusses on this in 2009.
  - Standard Model fits exclude the upper range ( $M_h > 170 \text{ GeV}/c^2$ ) and  $M_h < 150 \text{ GeV}/c^2$ .
- If the exclusion of higher masses is in fact the case then:
  - **TEV 2009:** Evidence for a Higgs for  $M_h = 115 \text{ GeV}/c^2$  is seen at  $3\sigma$  level.
  - **LHC/TEV 2011:** With  $30 \text{ fb}^{-1}$  of integrated luminosity, the LHC experiments confirm the discovery of Higgs at  $M_h = 115 \text{ GeV}/c^2$  in the  $\gamma\gamma$  decay mode.
- If deviations are seen at higher masses:
  - **LHC 2010:** With  $10 \text{ fb}^{-1}$  of integrated luminosity, the LHC experiments claim discovery of a higher mass Higgs.

In this scenario then it seems that the Tevatron should continue to run well into 2009/2010. This is especially true if the low mass Higgs emerges as the favored value.

Turning to February 2007, the situation has developed rapidly and changed, as was stated in the previous sections. The end result is to simply add approximately six months to one year to the estimates above. The evidence from

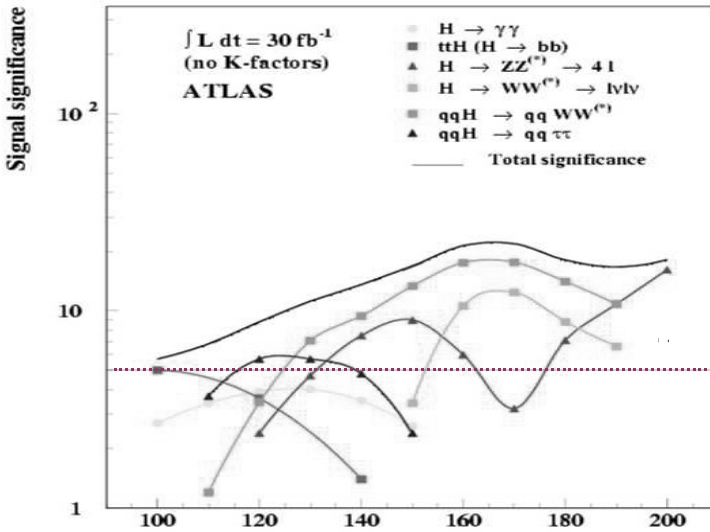


Figure 8: *Discovery potential of LHC for Higgs.*

precision fits favors somewhat more strongly the lower mass region. As of February 2008, the LHC has suffered another six month delay and the Tevatron is expected to run until October 2010 if the funding is sufficient.

## 8 Conclusions

This conference is held at a remarkable moment in the understanding of electroweak symmetry breaking. Rapid changes in data collection and more sophisticated experimental technique are leading to a constantly changing picture. The evidence presented here included the following highlights:

- The ALEPH  $3\sigma$  evidence for Higgs at a mass of  $115 \text{ GeV}/c^2$ ;
- Active searches for SUSY Higgs with the  $2\sigma$  effects at the Tevatron resolved as promised in last year's proceedings<sup>13)</sup> and evidence not found.
- New top mass measurements leading to new constraints on the Standard Model and other models of new physics, especially of SUSY.

- Evidence and discovery of channels in WZ, ZZ and single top, the messengers that the Higgs is in reach.
- Promise of a huge new increase in data collected in the next couple of years at both the Tevatron and LHC.

The changes in the understanding of the electroweak symmetry breaking at the Tevatron results are happening on the time scale of months and there is promise of a significant narrowing of the range of masses in which the Higgs boson may lie. If the scenarios play out to favor the low mass Higgs, this period of rapid development will be followed by a longer period of improving analyses as the Tevatron and LHC attempt to deal with the challenges of these low mass searches. In this case it is particularly interesting to note that the main search modes for the Tevatron are not pursued at the LHC and that only the  $H^0 \rightarrow \gamma\gamma$  mode is being investigated there. It is unlikely that this will remain the case for long as opportunities for innovation and exploitation of the data will clearly be pursued with vigor as the summit of the Higgs is finally claimed.

## 9 Acknowledgements

The author would like to thank the organizers for this invitation to speak and the wonderful atmosphere of the conference.

## References

1. A. Abulencia *et al*, Phys. Rev. Lett. **97**, 242003 (2006).
2. P. Dong, these proceedings.
3. A. Abulencia *et al*, Phys. Rev. Lett. **98**, 161801 (2007).
4. A. Abulencia *et al*, FERMILAB-PUB-08-022-E, <http://arxiv.org/abs/0801.4806v1>, Submitted to Phys. Rev. Lett.
5. V. Khoze, these proceedings.
6. The ALEPH, DELPHI, L3, OPAL, SLD Collaborations, the LEP Electroweak Working Group, the SLD Electroweak and Heavy Flavour Groups, Phys. Rept. **427** (2006) 257.
7. ALEPH, DELPHI, L3 and OPAL Collaborations  
The LEP Working Group for Higgs Boson Searches, Search for the Standard Model Higgs Boson at LEP, CERN-EP-2003-011.

8. Lep Electroweak Working Group, Winter 2008 update,  
<http://lepewwg.web.cern.ch/LEPEWWG/plots/winter2008/>.
9. A. Heister *et al*, Physics Letters B **526**, Issues 3-4, (2002) 191.
10. P. Verdier, these proceedings.
11. <http://www-d0.fnal.gov/Run2Physics/WWW/results/prelim/HIGGS/H51>
12. F. Gionatti, Probing The Hierarchy Problem with the LHC, in: Proc. XXII International Symposium on Lepton and Photon Interactions at High Energies (ed. R. Brenner, C. P. de los Heros, and J. Rathsman, Uppsala, June 2005), International Journal of Modern Physics A, **21**, Nos. 8-9 (2006)
13. R. St. Denis, On the Brink of Revelation and Revolution: Electroweak Symmetry Breaking in 2008/2009, Les Rencontres de Physique de la Valle' d'Aoste - Results and Perspectives in Particle Physics, Ed. M. Greco, La Thuile, Aosta Valley, February 28, March 5, 2007.

# TESTING PREDICTIONS FOR CENTRAL EXCLUSIVE PROCESSES IN THE EARLY LHC RUNS

V.A. Khoze, A.D. Martin and M.G. Ryskin

*IPPP, Department of Physics, University of Durham, DH1 3LE, UK*

## **Abstract**

We show that the early LHC measurements can provide crucial checks of the different components of the formalism used to predict the cross sections of central exclusive processes.

## 1 Introduction

The benefits of using forward proton detectors as a tool to study Standard Model (SM) and New Physics at the LHC have been fully appreciated only recently, see for instance, (1) - (4). The measurements of central exclusive production (CEP) is a prime target of the FP420 project (5), which aims at the installation of forward detectors in the LHC tunnel 420 m from the interaction points of the ATLAS and CMS experiments. The combined detection of both outgoing protons and the centrally produced system gives access to a rich programme of studies in QCD, electroweak, Higgs and BSM physics. Importantly, these measurements will provide valuable information on the Higgs sector of MSSM and other popular BSM scenarios, see (6) - (9). In particular, the CEP process allows for the unique possibility to study directly the coupling of Higgs-like bosons to bottom quarks (1, 10).

The theoretical formalism (11) - (13) for the description of a CEP process contains quite distinct parts, shown symbolically in Fig. 1. We first have to calculate the  $gg \rightarrow A$  subprocess,  $H$ , convoluted with the gluon distributions  $f_g$ . Next we must account for the QCD corrections which reflect the absence of additional radiation in the hard subprocess – that is, for the Sudakov factor  $T$ . Finally, we must enter soft physics to calculate the survival probability  $S^2$  of the rapidity gaps.

The uncertainties of the CEP predictions are potentially not small. Therefore, it is important to perform checks using processes that will be accessible in the first runs of the LHC (14). We first consider measurements which do not rely on proton tagging and can be performed through the detection of rapidity gaps.

The main uncertainties of the CEP predictions are associated with

- (i) the probability  $S^2$  that additional secondaries will not populate the gaps;
- (ii) the probability to find the appropriate gluons, that are given by generalized, unintegrated distributions  $f_g(x, x', Q_t^2)$ ;

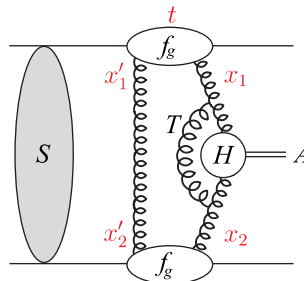


Figure 1: *The central exclusive production of a system A.*

- (iii) the higher order QCD corrections to the hard subprocess, where the most important is the Sudakov suppression;
- (iv) the so-called semi-enhanced absorptive corrections (see 15, 16) and other effects, which may violate the soft-hard factorization.

## 2 Gap survival probability $S^2$

As a rule, the gap survival probability is calculated within a multichannel eikonal approach 17). The probability of elastic  $pp$  rescattering, can be evaluated in a model independent way once the elastic cross section  $d\sigma_{el}/dt$  is measured at the LHC. However there may be some excited states between the blob  $S$  and the amplitude on the right-hand-side of Fig. 1. The presence of such states enlarges the absorptive correction. In order to experimentally check the role of this effect, we need to consider a process with a bare cross section that can be reliably calculated. Good candidates are the production of  $W$  or  $Z$  bosons with rapidity gaps.

In the case of ‘ $W$ +gaps’ production the main contribution comes from the diagram shown in Fig. 2(a) 18). One gap,  $\Delta\eta_1$ , is associated with photon exchange, while the other,  $\Delta\eta_2$ , is associated with the  $W$ . The cross section is proportional to the quark distribution at a large scale and not too small  $x$ , where the uncertainties of the parton densities are small. To select these events in the early runs, we can use the rapidity gap trigger combined with a high  $p_t$  lepton or jet.

An important point here is that the minimum value of  $|t|$  of the exchanged photon,  $|t_{min}| \simeq \frac{m_N^2 \xi^2}{1-\xi}$ , is not negligible ( $\xi$  defines the momentum fraction carried by the photon). As illustrated in Fig. 3 the rescattering reduces the cross section by the factor  $S^2$ .

In the first LHC data runs the ratio ( $W$ +gaps/ $W$  inclusive) will be measured first. This measurement is a useful check of the models for soft rescat-

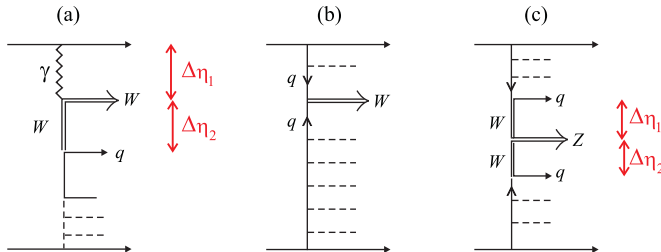


Figure 2: Diagrams for (a)  $W$  production with 2 gaps, (b) inclusive  $W$  production, and (c)  $Z$  production with 2 gaps.

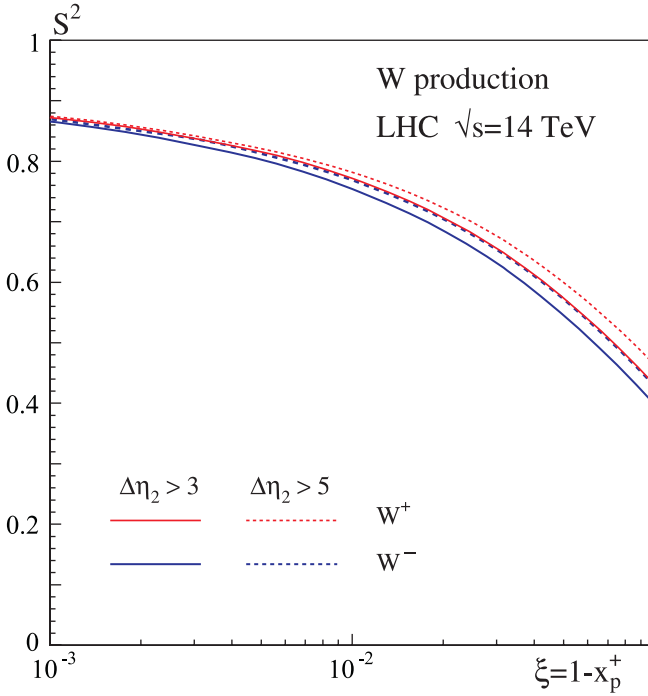


Figure 3: *The gap survival factor  $S^2$  as a function of  $\xi$  calculated using the model of <sup>12)</sup>, assuming that the valence (sea) quarks are associated with the weak (strong) absorptive components.*

tering. A good way is to observe  $Z$  boson production via  $WW$  fusion, see Fig. 2(c). Here, both of the rapidity gaps originate from heavy boson exchange, and the corresponding  $b_t$  region is similar to that for exclusive Higgs production. The expected  $Z$ +gaps cross section is of the order of 0.2 pb, and  $S^2=0.3$  for  $\Delta\eta_{1,2} > 3$  and for quark jets with  $E_T > 50$  GeV <sup>19)</sup>.

When the forward proton detectors become operational we can do more. Both the longitudinal and transverse momentum of the protons can be measured, and we can study the  $k_t$  behaviour of the cross section sections and scan the proton opacity <sup>18)</sup>.

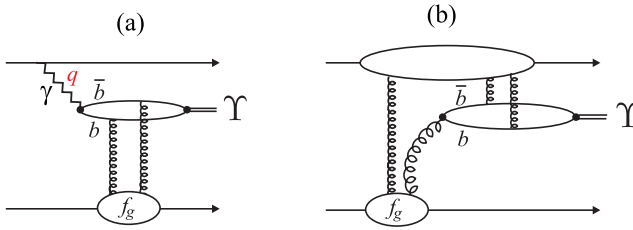


Figure 4: *Exclusive  $\Upsilon$  production via (a) photon exchange, and (b) via odderon exchange.*

### 3 Generalized, unintegrated gluon distribution $f_g$

The cross section for the CEP of a system  $A$  essentially has the form <sup>11)</sup>

$$\sigma(pp \rightarrow pAp) \simeq \frac{S^2}{b^2} \left| \frac{\pi}{8} \int \frac{dQ_t^2}{Q_t^4} f_g(x_1, x'_1, Q_t^2, \mu^2) f_g(x_2, x'_2, Q_t^2, \mu^2) \right|^2 \hat{\sigma}(gg \rightarrow A) \tag{1}$$

Here the factor  $1/b^2$  arises from the integration over the proton transverse momentum. Also,  $f_g$  denotes the generalized unintegrated gluon distribution in the limit of  $p_t \rightarrow 0$ . The  $f_g$  has not yet been measured explicitly. However, in our case it can be obtained from the conventional diagonal gluon distribution,  $g$ , known from the global parton analyses, see <sup>11, 14)</sup> for details. The main uncertainty here comes from the lack of knowledge of the integrated gluon distribution  $g(x, Q_t^2)$  at low  $x$  and small scales. For example, taking  $Q_t^2 = 4 \text{ GeV}^2$  we find that a variety of recent MRST <sup>20)</sup> and CTEQ <sup>21)</sup> global analyses give a spread of  $xg = (3 - 3.8)$  for  $x = 10^{-2}$  and  $xg = (3.4 - 4.5)$  for  $x = 10^{-3}$ . These are big uncertainties bearing in mind that the CEP cross section depends on  $(xg)^4$ .

To reduce the uncertainty associated with  $f_g$  we can measure exclusive  $\Upsilon$  production. The process is shown in Fig. 4(a). The cross section for  $\gamma p \rightarrow \Upsilon p$  <sup>22)</sup> is given in terms of exactly the same unintegrated gluon distribution  $f_g$  that occurs in Fig. 1.

There may be competition between production via photon exchange, Fig. 4(a), and via odderon exchange, see Fig. 4(b). To date, odderon exchange has not been observed. On the other hand, a lowest order calculation indicates that the odderon process (b) may be comparable to the photon-initiated process (a) (for example, <sup>23)</sup>). If the upper proton is tagged, it will be straightforward

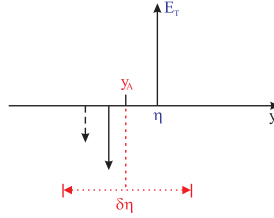


Figure 5: *The rapidities of the three jets in the central system.*

to separate the two mechanisms.

The expression for  $\sigma(\gamma p \rightarrow \Upsilon p) \propto f_g^2$  is given in <sup>22)</sup>. In order to use this process to constrain the gluon distribution it would be preferable to tag the lower proton.

#### 4 Three-jet events as a probe of the Sudakov factor

Traditionally, the search for the exclusive dijet signal at the Tevatron,  $p\bar{p} \rightarrow p + jj + \bar{p}$ , is performed <sup>24)</sup> by plotting the cross section in terms of the variable  $R_{jj} = M_{jj}/M_A$ . The  $R_{jj}$  distribution is strongly smeared out by QCD bremsstrahlung, hadronization, the jet searching algorithm and other experimental effects <sup>24, 25)</sup>. To weaken the role of smearing it was proposed in Ref. <sup>25)</sup> to study the dijet distribution in terms of a new variable

$$R_j = 2E_T (\cosh \eta^*)/M_A, \quad (2)$$

where only the transverse energy and the rapidity  $\eta$  of the jet with the *largest*  $E_T$  are used in the numerator. Here  $\eta^* = \eta - y_A$  where  $y_A$  is the rapidity of the whole central system. At leading order, it is sufficient to consider the emission of a third jet, as shown in Fig. 5, where we take all three jets to lie in a specified rapidity interval  $\delta\eta$ .

The cross section  $d\sigma/dR_j$ , as a function of  $R_j$ , for the exclusive production of a high  $E_T$  dijets accompanied by a third jet was calculated and discussed in <sup>25, 14)</sup>. It was shown that the measurements of the exclusive two- and three-jet cross sections *as a function of*  $E_T$  of the highest jet allow a detailed check of the Sudakov physics; with much more information coming from the observation of the  $\delta\eta$  dependence. A clear way to observe the effect of the Sudakov suppression is just to study the  $E_T$  dependence of exclusive dijet production. On dimensional grounds we would expect  $d\sigma/dE_T^2 \propto 1/E_T^4$ .

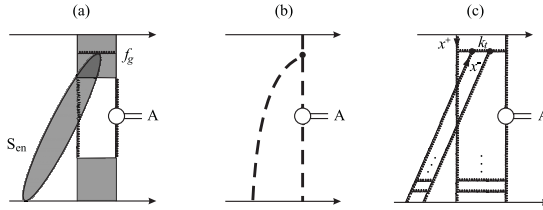


Figure 6: (a) A typical enhanced diagram, where the shaded boxes symbolically denote  $f_g$ , and the soft rescattering is on an intermediate parton, giving rise to a gap survival factor  $S_{en}$ ; (b) and (c) are the Reggeon and pQCD representations, respectively.

This behaviour is modified by the anomalous dimension of the gluon and by a stronger Sudakov suppression with increasing  $E_T$ . Already the existing CDF dijet data <sup>24)</sup> exclude predictions which omit the Sudakov effect.

### 5 Soft-hard factorization: enhanced absorptive effects

The soft-hard factorization implied by Fig. 1 could be violated by the so-called enhanced Reggeon diagrams, caused by the rescattering of an intermediate parton generated in the evolution of  $f_g$ . Such a diagram is shown in Fig. 6(a).

The contribution of the first Pomeron loop diagram, Fig. 6(b) was calculated in pQCD in Ref. <sup>16)</sup>. A typical diagram is shown in Fig. 6(c). For LHC energies it was found that the probability of such rescattering may be numerically large. The reason is that the gluon density grows in the low  $x$  region and, for low  $k_t$  partons, approaches the saturation limit. However, as shown in <sup>14)</sup>, the enhanced diagram should affect only the very beginning of the QCD evolution – the region that cannot be described perturbatively and which, in calculations of <sup>12, 13)</sup>, is already included phenomenologically.

Experimentally, we can study the role of semi-enhanced absorption by measuring the ratio  $R$  of diffractive events for  $W$  (or  $\Upsilon$  or dijet) production as compared to the inclusive process <sup>14)</sup>. That is

$$R = \frac{\text{no. of } (A + \text{gap}) \text{ events}}{\text{no. of (inclusive } A) \text{ events}} = \frac{a^{\text{diff}}(x_P, \beta, \mu^2)}{a^{\text{incl}}(x = \beta x_P, \mu^2)} \langle S^2 S_{en}^2 \rangle_{\text{over } b_t}, \quad (3)$$

where  $a^{\text{incl}}$  and  $a^{\text{diff}}$  are the parton densities determined from the global analyses of inclusive and diffractive DIS data, respectively. For  $W$  or  $\mu^+ \mu^-$  pro-

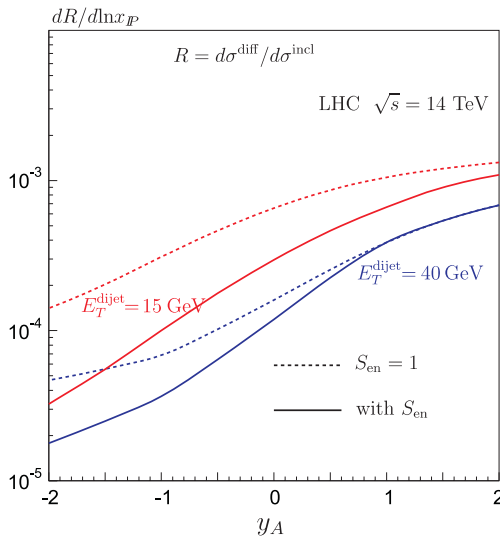


Figure 7: The predictions of the ratio  $R$  of (3) for the production of a pair of high  $E_T$  jets with (continuous curves) and without (dashed curves) enhanced soft rescattering.

duction the parton densities  $a$  are quark distributions, whereas for dijet or  $\Upsilon$  they are mainly gluon densities.

Experimentally, we can observe a double distribution  $d^2\sigma^{\text{diff}}/dx_{\mathbb{P}}dy_A$ , and form the ratio  $R$  using the inclusive cross section,  $d\sigma^{\text{incl}}/dy_A$ . If we neglect the enhanced absorption, it is quite straightforward to calculate the ratio  $R$  of (3). The results for a dijet case are shown by the dashed curves in Fig. ?? as a function of the rapidity  $y_A$  of the dijet system. The enhanced rescattering reduce the ratios and lead to steeper  $y_A$  distributions, as illustrated by the continuous curves.

Perhaps the most informative probe of  $S_{\text{en}}^2$  is to observe the ratio  $R$  for dijet production in the region  $E_T \sim 15 - 30$  GeV. For example, for  $E_T \sim 15$  GeV we predict  $S_{\text{en}}^2 \sim 0.25, 0.4$  and  $0.8$  at  $y_A = -2, 0$  and  $2$  respectively.

## 6 Conclusion

The addition of forward proton detectors to LHC experiments will add unique capabilities to the existing LHC experimental programme. For certain BSM scenarios, the tagged-proton mode may even be the Higgs discovery channel.

There is also a rich QCD, electroweak, and more exotic physics, menu.

The uncertainties in the prediction of the rate of a CEP process are potentially not small. Therefore, it is crucial to perform checks of the theoretical formalism using processes that will be experimentally accessible in the first runs of the LHC<sup>14)</sup>.

Most of the diffractive measurements described above can be performed, without detecting the forward protons, by taking advantage of the relatively low luminosity in the early LHC data runs. This allows the use of a veto trigger to select events with the large rapidity gap(s). In this way we are able to probe the various individual components of the formalism used to predict the CEP cross sections.

To summarise, the gap survival factor,  $S^2$ , caused by eikonal rescattering, may be studied as illustrated in Fig 3 and the possible enhanced,  $S_{\text{en}}^2$ , contributions as shown in Figs. 6 and 7. The relevant unintegrated gluon distribution,  $f_g$ , can be constrained by observing  $\Upsilon$  production, see Fig. 4, and the QCD radiative effect,  $T$ , may be checked by observing exclusive two- and three-jet events.

When the forward proton detectors are operating much more can be done. First, it is possible to measure directly the cross section  $d^2\sigma_{\text{SD}}/dtdM_X^2$  for single diffractive dissociation and also the cross section  $d^2\sigma_{\text{DPE}}/dy_1dy_2$  for soft central diffractive production. These measurements will strongly constrain the models used to describe diffractive processes and the effects of soft rescattering. The recent predictions can be found in<sup>13)</sup>. Next, a study of the transverse momentum distributions of both of the tagged protons, and the correlations between their momenta, is able to scan the proton optical density<sup>18, 26)</sup>.

Finally, let us emphasise that the selection of central exclusive dijet production in the kinematic region corresponding to the sought-after Higgs signal ( $E_T \sim M_H/2$ ) provides an ideal “standard candle”. At leading log accuracy, this process includes all the components of the theoretical formalism used to predict the central exclusive Higgs signal; the same parton densities in the same kinematic region, the same gap survival factors  $S^2$  and the same QCD radiative effects.

## 7 Acknowledgements

VAK is very grateful to Giorgio Bellettini, Giorgio Chiarelli and Mario Greco for the kind invitation and warm hospitality at La Thuile.

## References

1. V.A. Khoze, A.D. Martin and M.G. Ryskin, *Eur. Phys. J.* **C23**, 311 (2002).

2. A. De Roeck et al., *Eur. Phys. J.* **C25**, 391(2002).
3. J.R. Forshaw, PoS DIFF2006, 055 (2006) [arXiv:hep-ph/0611274].
4. V.A. Khoze, A.D. Martin and M.G. Ryskin, arXiv:0705.2314 [hep-ph].
5. M. Albrow et al., CERN-LHCC-2005-025.
6. A.B. Kaidalov et al, *Eur. Phys. J.* **C33**, 261 (2004).
7. S. Heinemeyer et al., *Eur. Phys. J.* **C53**, 231 (2008).
8. B. Cox, F. Loebinger and A. Pilkington, *JHEP* **0710**, 090 (2007).
9. J.R. Forshaw et al., arXiv:0712.3510 [hep-ph].
10. V.A. Khoze, A.D. Martin and M. Ryskin, *Eur. Phys. J.* **C19**, 477 (2001).
11. V.A. Khoze, A.D. Martin and M.G. Ryskin, *Eur. Phys. J.* **C14**, 525 (2000).
12. V.A. Khoze, A.D. Martin and M.G. Ryskin, *Eur. Phys. J.* **C18**, 167 (2000).
13. V.A. Khoze, A.D. Martin and M.G. Ryskin, *Eur. Phys. J.* **C54**, 199 (2008).
14. V.A. Khoze, A.D. Martin and M.G. Ryskin, arXiv:0802.0177 [hep-ph].
15. A.B. Kaidalov et al., *Eur. Phys. J.* **C21**, 521 (2001).
16. J. Bartels et al., *Phys. Rev.* **D73**, 093004 (2006).
17. For a review see: E. Gotsman et al., arXiv:hep-ph/0511060.
18. V.A. Khoze, A.D. Martin and M.G. Ryskin, *Eur. Phys. J.* **C24**, 459 (2002).
19. V.A. Khoze et al., *Eur. Phys. J.* **C26**, 429 (2003).
20. A.D. Martin et al., *Phys. Lett.* **B652**, 292 (2007) and references therein.
21. W.-K. Tung et al., *JHEP* **0702**:053 (2007) and references therein.
22. A.D. Martin, M.G. Ryskin and T. Teubner, *Phys.Lett.* **B454**, 339 (1999).
23. A. Bzdak et al., *Phys. Rev.* **D75**, 094023 (2007).
24. T. Aaltonen et al., [CDF Collaboration], arXiv:0712.0604.
25. V.A. Khoze, A.D. Martin and M.G. Ryskin, *Eur. Phys. J.* **C48**, 467 (2006).
26. V.A. Khoze, A.D. Martin and M.G. Ryskin, *Eur. Phys. J.* **C24**, 581 (2002).

## ***SESSION VIII – SEARCHES FOR NEW PHYSICS***

*Sasha Pronko*

Non-SUSY Exotics Searches at the Tevatron

*Verdier Patrice*

Search for SuperSymmetry at the Tevatron

*List Jenny*

Searches for New Physics at HERA

*Manoni Elisa*

Lepton Flavor Violation in  $\tau$  and  $B$  Decays at BaBar

*Norbert Neumeister*

Physics Beyond the Standard Model in CMS at the Startup of the LHC

*Mateev Matey*

A Maximal Mass Model

*Sannino Francesco*

(Near) Conformal Technicolor: What is Really New?



# NON-SUSY EXOTICS SEARCHES AT THE TEVATRON

Alexandre Pronko  
*Fermilab, Batavia, IL, USA*  
(For the CDF and DØ Collaborations)

## Abstract

We present results of searches for signs of physics beyond the Standard Model. The focus of this paper is on analyses not driven by SUSY models. Most of the presented results are based on  $\sim 2 \text{ fb}^{-1}$  of data and obtained since summer of 2007. No significant excess of data over predicted background is observed. We report kinematic distributions, data and background counts, as well as limits on some parameters of selected models of new physics.

## 1 Introduction

Experimental results of the past few decades have demonstrated a phenomenal success of the Standard Model (SM). Nonetheless, we also know that our picture of particle physics is incomplete. There are many questions that the Standard Model fails to answer. For example, we do not know why there are only three generations of fermions, why the masses of particles have values we observe, what are dark energy and matter, or what explains the hierarchy between the electroweak and gravitational scales. Although supersymmetry (or SUSY) is one of the most popular extensions of the Standard Model, there are other equally well-motivated models of new physics, such as extra dimensions, compositeness, and technicolor. In this paper, we focus on non-SUSY searches for signs of new physics beyond the Standard Model. We present recent results of signature-based and model-dependent measurements performed by the CDF and DØ Collaborations. The event selection in model-inspired analyses is optimized to gain the best sensitivity for a model of interest. The result of such measurements is usually a limit on some parameters of a selected model. The analysis strategy for signature-based searches is to apply generic selection criteria to reduce backgrounds in order to be sensitive to as wide range as possible of scenarios for new physics (some of them yet unknown) with a signature of interest. Observation of an excess of data over the predicted background in such analyses would indicate the presence of new physics. In signature-based searches, increased attention is also given to examining kinematic distributions.

## 2 Search for High-Mass $e^+e^-$ Resonances

Lepton-antilepton pairs have been discovery signatures for new particles such as the  $J/\psi$ ,  $\Upsilon$  mesons, and the  $Z$  boson. Even though leptonic decay rates are usually smaller than hadronic ones, leptons have relatively low background contamination at a hadron collider. Many models beyond the SM predict the existence of new particles decaying into lepton-antilepton pairs. Examples of such new resonances are  $Z'$  bosons in the  $E_6$  model <sup>1)</sup> and Randall-Sundrum (RS) gravitons <sup>2)</sup>. The CDF Collaboration has performed a search for high mass  $e^+e^-$  resonances in 2.5 fb<sup>-1</sup> of data collected in Run II between March 2002 and August 2007. In this analysis, events are required to have two well measured electrons of opposite sign with transverse energy of  $E_T \geq 25$  GeV. Both electron candidates are required to have tracks pointing to energy depositions in the calorimeter and originating from the same collision vertex. One of the electrons must be in the central part of the calorimeter (pseudorapidity range of  $|\eta| < 1.1$ ) and the second electron can be either central or forward (pseudorapidity range of  $|\eta| < 2$ ). The search for resonances is performed in the invariant mass range  $150 \text{ GeV}/c^2 < M_{e^+e^-} < 1000 \text{ GeV}/c^2$  using

an unbinned likelihood ratio. The dominant source of background is Drell-Yan production, which is estimated using the Pythia <sup>3)</sup> event generator. The other sources of background are di-boson production and events where one or two jets are mis-identified as an electron. Figure 1 shows the measured invariant mass spectrum of  $e^+e^-$  pairs from  $2.5 \text{ fb}^{-1}$  of data. The most significant excess of data over the total SM background is found in the window  $228 \text{ GeV}/c^2 < M_{e^+e^-} < 250 \text{ GeV}/c^2$ . It corresponds to 3.8 standard deviations from the SM prediction. The probability of observing a background fluctuation with significance  $S/\sigma_B > 3.8$  anywhere in the mass range  $150 \text{ GeV}/c^2 < M_{e^+e^-} < 1000 \text{ GeV}/c^2$  is about 0.6%. The upper limits on  $\sigma \cdot BR(X \rightarrow e^+e^-)$  at 95% C.L. are set as a function of mass for a  $Z'$  with SM coupling and six eigenstates of  $Z'$  bosons in  $E_6$  model. These results are presented in Table 1. The lower mass limits for  $Z'$  bosons with SM coupling and in  $E_6$  model are  $966 \text{ GeV}/c^2$  and  $737/933$  (lightest/heaviest)  $\text{GeV}/c^2$ , respectively.

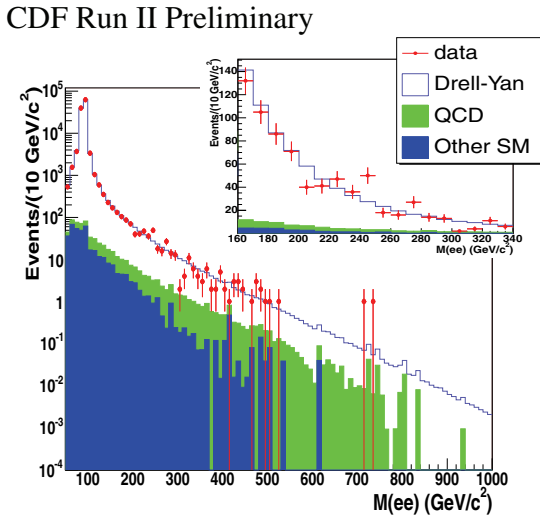


Figure 1: *Invariant mass distribution of  $e^+e^-$  pairs in data (red dots) compared to background predictions. The insert shows the same distribution for  $160 \text{ GeV}/c^2 < M_{e^+e^-} < 340 \text{ GeV}/c^2$  using a linear scale.*

### 3 Search for High-Mass Di-Jet Resonances

The di-jet mass spectrum is sensitive to new high-mass particles decaying into a pair of partons (quarks or gluons). Many beyond-the-SM scenarios predict

Table 1: Observed and expected 95% C.L. lower limits on  $Z'$  masses.

	$Z'_{SM}$	$Z'_\psi$	$Z'_\chi$	$Z'_\eta$	$Z'_I$	$Z'_{sq}$	$Z'_N$
Exp. Limit (GeV/ $c^2$ )	965	849	860	932	757	791	834
Obs. Limit (GeV/ $c^2$ )	966	853	864	933	737	800	840

much larger production cross sections for new particles decaying into hadrons rather than leptons, photons, or electroweak bosons (in some models the latter decay modes can be completely suppressed). Examples of such particles include axiglons <sup>4)</sup> ( $A \rightarrow q\bar{q}$ ), excited quarks <sup>5)</sup> ( $q^* \rightarrow qg$ ), color octet technirhos <sup>6)</sup> ( $\rho_T \rightarrow q\bar{q}, gg$ ),  $W'/Z' \rightarrow q'\bar{q}/q\bar{q}$  <sup>7)</sup>, di-quarks ( $D/D^c \rightarrow qq/\bar{q}\bar{q}$ ) in the  $E_6$  model <sup>1)</sup>, and RS gravitons <sup>2)</sup> ( $G \rightarrow q\bar{q}, gg$ ). Searches for resonances in di-jet channel are challenging due to the huge QCD background. However, the earlier observation of  $W$  and  $Z$  bosons in the hadronic decay mode by the UA2 Collaboration demonstrated the feasibility of finding di-jet resonances at hadron colliders.

The CDF Collaboration has performed a search for high-mass di-jet resonances in  $1.1 \text{ fb}^{-1}$  of data. In this analysis, events are required to have at least two central ( $|y| < 1.0$ ) jets with invariant mass  $M_{jj} > 180 \text{ GeV}/c^2$  and no significant transverse energy imbalance. Jet energy is corrected to the hadron level. The background for this analysis is completely dominated by regular QCD di-jet production. The search for resonances is performed by fitting the measured  $M_{jj}$  spectrum by a smooth function and looking for data points with a significant excess over the fit. The shape of the smooth background parameterization is motivated by the shape of the  $M_{jj}$  spectrum predicted by Pythia and Herwig Monte Carlo and LO and NLO calculations by the NLOJET++ program:

$$\frac{d\sigma}{dM_{jj}} = \frac{p_0(1-x)^{p_1}}{x^{p_2+p_3 \ln x}}, \quad x = M_{jj}/\sqrt{s}. \quad (1)$$

Figure 2 shows the measured  $M_{jj}$  spectrum and a fit by the function from Eq. 1. No significant excess of data over the fit is observed; therefore CDF has set upper limits on new-particle production cross sections. Table 2 presents the observed 95% C.L. exclusion limits on masses of new particles. These results are currently the world best limits.

#### 4 Search for Long-lived Particles Decaying into $Z$ Bosons

The DØ Collaboration has performed a search for long-lived particles that travel tens of centimeters before decaying into  $Z$  bosons. There are many models that predict the existence of such particles, for example: gauge mediated

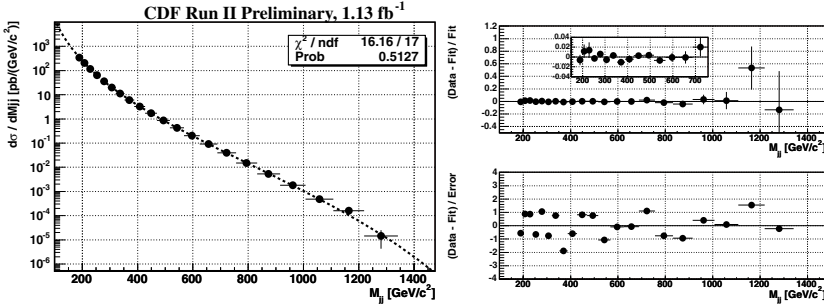


Figure 2: *Left: measured  $M_{jj}$  spectrum fitted to Eq.1. Right top:  $(data-fit)/fit$  as a function of  $M_{jj}$ . Right bottom:  $(data-fit)/\sigma_{stat}$  as a function of  $M_{jj}$ .*

Table 2: *Observed 95% C.L. exclusion limits on masses of new particles.*

Model	Observed mass exclusion ( $\text{GeV}/c^2$ )
Excited quarks	260-870
Color octet technirho	260-1110
Axigluon and coloron	260-1250
$E_6$ diquarks	260-630

SUSY <sup>8)</sup>; hidden valley models <sup>9)</sup>; models with an extended Higgs sector <sup>10)</sup>; and fourth generation quarks ( $b'$ ) <sup>11)</sup>.

The search is performed with  $1.1 \text{ fb}^{-1}$  of data. Events are required to have two central ( $|\eta| < 1.1$ ) isolated electromagnetic (EM) objects with  $E_T \geq 20 \text{ GeV}$  and invariant mass of  $M > 75 \text{ GeV}/c^2$ . The analysis is based on the unique capability of the DØ detector to reconstruct a vertex of origin for two EM clusters by using solely the position and shape of electromagnetic showers in the calorimeter and preshower system, with a resolution of  $\approx 2 \text{ cm}$ . In this search, displaced vertices of  $Z$  bosons are reconstructed in the azimuthal ( $xy$ ) plane only. The presence of long-lived particles would reveal itself as an excess of events with positive radii  $R_{xy}$  compared to negative  $R_{xy}$ . Figure 3 shows the measured  $R_{xy}$  distribution. No excess of events with  $R_{xy} > 0$  is observed, therefore DØ has set 95% C.L. limits on the production cross-section and lifetime of a fourth generation quark ( $b'$ ). The exclusion region can be found in Fig.4.

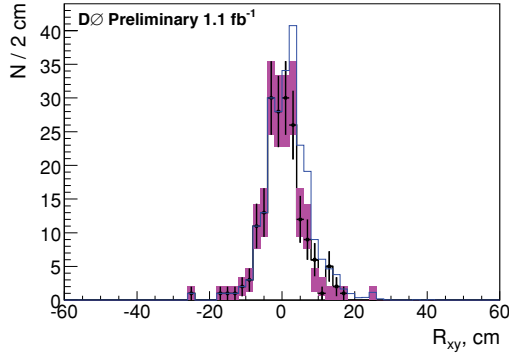


Figure 3: Vertex radius ( $R_{xy}$ ) distribution. Points with errors bars are data, the purple histogram is a reflection of the negative part of the distribution, and the blue line corresponds to an expected signal from  $b'$ -quark with mass of  $160 \text{ GeV}/c^2$  and  $c\tau$  of  $30 \text{ cm}$ .

## 5 Search for Anomalous Production of Exclusive $\gamma + \cancel{E}_T$ Events

The exclusive production of a photon in association with a large imbalance in transverse energy ( $\cancel{E}_T$ ) is a relatively rare process in the Standard Model dominated by  $Z\gamma \rightarrow \nu\bar{\nu} + \gamma$ . Such a signature is a promising way to observe the production of high-energy invisible particles <sup>17)</sup>, since a photon or gluon radiated by incoming quarks is the only detectable evidence of this process in a given event. Exclusive  $\gamma + \cancel{E}_T$  events also appear in models of Large Extra Dimensions <sup>12)</sup> (LED), where an undetectable Kaluza-Klein (KK) graviton is produced in association with a photon ( $q\bar{q} \rightarrow \gamma G_{KK}$ ).

The CDF and DØ Collaborations have performed a search for signs of the anomalous production of exclusive  $\gamma + \cancel{E}_T$  events in  $2 \text{ fb}^{-1}$  and  $1 \text{ fb}^{-1}$  of data, respectively, optimizing the analyses for maximum sensitivity to the benchmark model of KK graviton production. Both experiments select events with only one central ( $|\eta| < 1/1.1$  at CDF/DØ) photon with  $E_T > 90 \text{ GeV}$ . Events with energetic jets ( $E_T > 15 \text{ GeV}$ ) and tracks ( $P_T > 10/6.5 \text{ GeV}/c$  at CDF/DØ) are rejected. The DØ Collaboration also requires events to have  $\cancel{E}_T > 70 \text{ GeV}$ . The exclusive  $\gamma + \cancel{E}_T$  signature suffers from large non-collision backgrounds such as cosmic rays depositing significant amount of energy in the electromagnetic calorimeter. This search would not be possible without an effective rejection of cosmic-ray events. For this purpose, the CDF Collaboration requires an EM shower to be in time with a  $p\bar{p}$  collision. The DØ Collaboration rejects cosmic rays by vetoing events where an EM shower is aligned with hits in

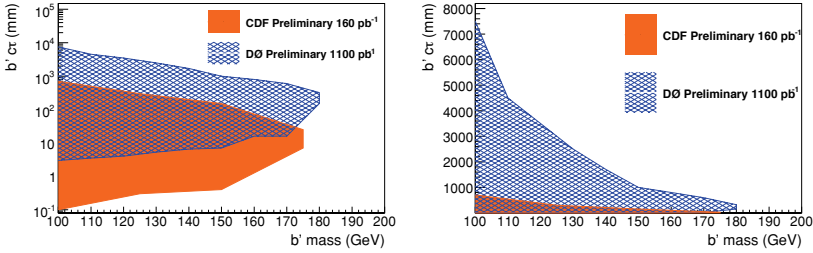


Figure 4: The 95% C.L. exclusion limits on the  $b'$ -quark lifetime versus its mass (left: log scale; right: linear scale).

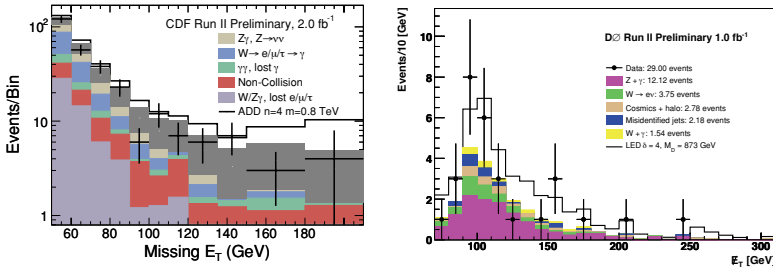


Figure 5: The  $E_T$  distribution is exclusive  $\gamma + E_T$  events (left: CDF results; right:  $DØ$  results).

the muon system. Figure 5 shows the observed  $E_T$  distributions in exclusive  $\gamma + E_T$  events. Neither of the experiments see any significant excess of data over the predicted background. Therefore, 95% C.L. lower exclusion limits are set on the fundamental Planck mass scale <sup>12)</sup>,  $M_D$ , as a function of the number of extra dimensions,  $N_{ED}$ . The results can be found in Fig. 6. The CDF Collaboration also combines the results of the exclusive  $\gamma + E_T$  analysis with an earlier search in the exclusive  $jet + E_T$  channel. The combined limit exceeds earlier world-best results obtained at LEP for  $N_{ED} > 4$ .

### 6 Search for Anomalous Production of $\gamma\gamma + E_T$ Events

The  $\gamma\gamma + E_T$  signature is predicted in many well-motivated models of new physics beyond the Standard Model. Examples include gauge-mediated SUSY <sup>13)</sup> fermiophobic Higgs <sup>16, 10)</sup>,  $4^{th}$  generation fermions <sup>14)</sup>, and the  $E_6$  model <sup>15)</sup>. Rather than trying to optimize for these or other models, the CDF Collabo-

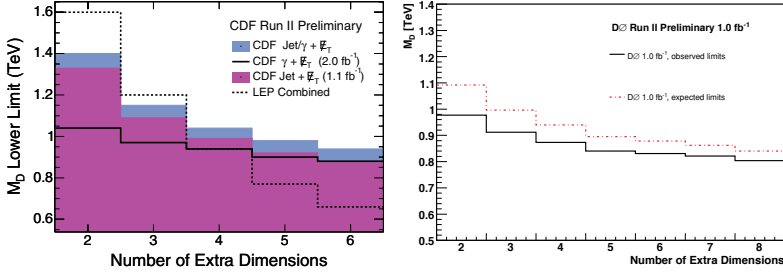


Figure 6: The observed exclusion limits on the fundamental mass scale,  $M_D$ , as a function of the number of extra dimensions (left: CDF results; right:  $DØ$  results).

ration takes a model-independent approach. The analysis is performed with 2 fb $^{-1}$  of data. Events are required to have two central photons ( $|\eta| < 1.1$ ) with  $E_T > 13$  GeV. Both photons are required to be in time with a  $p\bar{p}$  collision to reduce a contamination from non-collision sources. The dominant backgrounds are regular di-photon and QCD jet events with fake  $\cancel{E}_T$  due to energy mis-measurement in the calorimeter, and electroweak (EWK) processes with real  $\cancel{E}_T$ . In this search, the CDF Collaboration applies a novel approach to discriminate events with unobserved particles producing the  $\gamma\gamma + \cancel{E}_T$  signature. Events are selected based on a significance of the measured  $\cancel{E}_T$ , unlike the majority of similar analyses where a fixed cut (usually with a large value) on  $\cancel{E}_T$  is applied. The  $\cancel{E}_T$ -significance is estimated on an event-by-event basis according to the measured resolution for jet and soft unclustered (due to the underlying event and multiple interactions) energy, and helps to efficiently separate events with fake and true  $\cancel{E}_T$ . Figure 7 shows the observed  $\cancel{E}_T$ -significance distribution in  $\gamma\gamma$  events, and Fig. 8 illustrates how a cut on significance  $> 5$  helps to select EWK events with  $\cancel{E}_T$  as low as 20 GeV, which otherwise would be buried under the huge di-photon and QCD jet background. This plot demonstrates the major advantage of the  $\cancel{E}_T$ -significance method: it allows sensitivity to new physics processes even with moderate values of  $\cancel{E}_T$  ( $\cancel{E}_T \approx 20$ –40 GeV). Table 3 shows the observed and predicted numbers of  $\gamma\gamma + \cancel{E}_T$  events for three values of the  $\cancel{E}_T$ -significance cut. The data agree with the predicted background for all values of the significance cut.

## 7 Search for Anomalous Production of $jj + \cancel{E}_T$ Events

The search for anomalous production of  $jj + \cancel{E}_T$  is sensitive to processes not accessible by the previously discussed  $\gamma\gamma + \cancel{E}_T$  analysis. Events with large

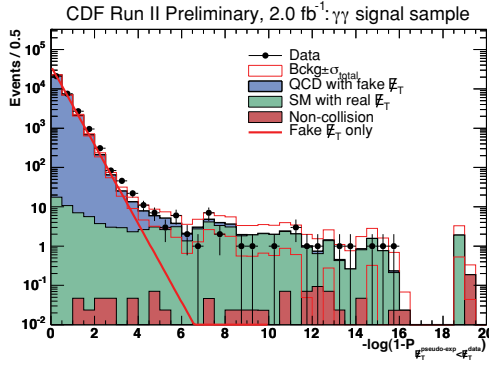


Figure 7: The  $E_T$ -significance distribution in  $\gamma\gamma$  events.

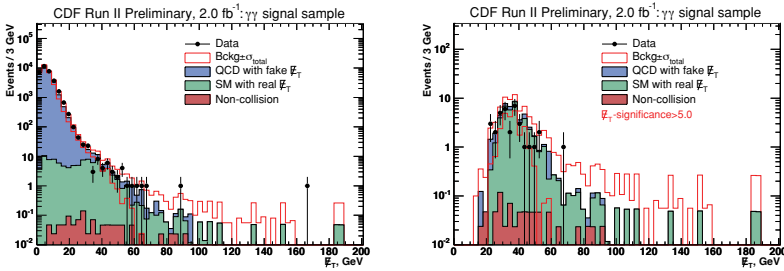


Figure 8: The observed  $E_T$  distribution in all (left)  $\gamma\gamma$  events and events with  $E_T$ -significance  $> 5$  (right).

Table 3: Observed and expected number of  $\gamma\gamma + E_T$  events for three values of the  $E_T$ -significance cut. Systematic and MC statistical uncertainties of the background are added in quadrature.

	$E_T$ -sig $>3$	$E_T$ -sig $>4$	$E_T$ -sig $>5$
Non-collision	$0.90 \pm 0.32$	$0.85 \pm 0.30$	$0.80 \pm 0.27$
QCD (fake $E_T$ )	$52.1 \pm 11.5$	$15.4 \pm 3.8$	$6.2 \pm 2.7$
EWK (real $E_T$ )	$53.6 \pm 8.9$	$47.3 \pm 8.0$	$41.6 \pm 7.0$
Total background	$106.6 \pm 14.5$	$63.6 \pm 8.9$	$48.6 \pm 7.5$
Data	120	52	34

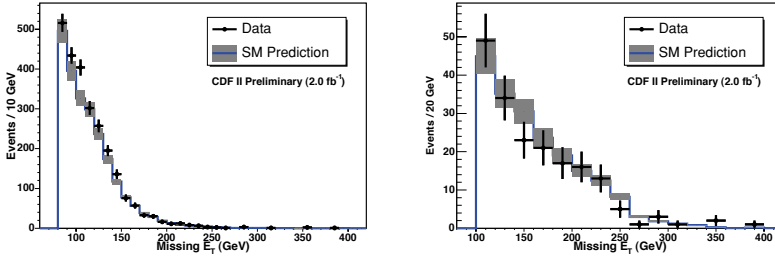


Figure 9: The observed  $\cancel{E}_T$  distribution in  $jj + \cancel{E}_T$  events from region 1 (left) and region 2 (right).

$\cancel{E}_T$  and one or more energetic jets can be produced in models of new physics beyond the Standard Model. The CDF Collaboration has previously performed a signature-based search for exclusive  $jet + \cancel{E}_T$  events<sup>18)</sup> and now extends the analysis to an exclusive  $jj + \cancel{E}_T$  channel. This signature, for example, appears in MSSM<sup>19)</sup>, Universal Extra Dimensions<sup>20)</sup>, and Littlest Higgs<sup>21)</sup> models. In this search, events are required to have exactly two jets with  $E_T > 15$  GeV and  $|\eta| < 2.4$ . The second jet has to satisfy the requirement of  $E_T > 30$  GeV. Clean-up cuts are applied to remove events with poorly measured jets and events due to cosmic rays. The data sample is split into two regions that can be sensitive to different models: events in region 1 must have  $\cancel{E}_T > 80$  GeV and  $H_T = E_T^{jet1} + E_T^{jet2} > 125$  GeV, and events in region 2 must have  $\cancel{E}_T > 100$  GeV and  $H_T > 225$  GeV. The dominant background in this search are  $W/Z + jets$  events. Figure 9 shows the observed  $\cancel{E}_T$  distributions for  $jj + \cancel{E}_T$  events from the two kinematic regions. Data agree well with the total predicted background: region-1 has 2,506 events compared to  $2,312 \pm 140$  predicted events; region-2 contains 186 events compared to  $196 \pm 29$  expected events. The CDF Collaboration has recently used these results to set limits on the leptoquark production<sup>22)</sup>.

## 8 Search for 3<sup>rd</sup> Generation Scalar Leptoquarks Using the $b\tau b\tau$ Final State

The observed symmetry between leptons and quarks leads to prediction of existence of the Leptoquark bosons in models of new physics such as grand unification<sup>23)</sup>, Technicolor<sup>24)</sup>, and compositeness<sup>25)</sup>. Since flavor-changing currents have not been observed, it is expected that there are three generations of leptoquarks (LQ), and each couples only to fermions of the same generation.

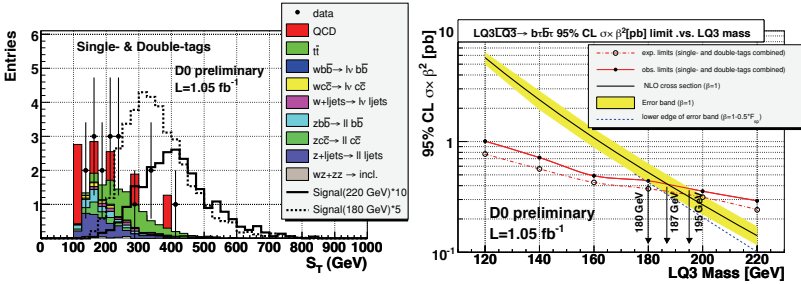


Figure 10: The observed  $S_T$  distribution (left plot) and the cross section upper limits as a function of  $LQ_3$  mass (right plot).

The  $D\mathcal{O}$  Collaboration has performed a search for  $3^{rd}$  generation scalar leptoquarks in the  $b\tau b\tau$  final state with  $1.1 \text{ fb}^{-1}$  of data. Selected events are required to have a muon with  $P_T > 15 \text{ GeV}/c$ , hadronic tau with visible  $P_T > 15 \text{ GeV}/c$ , at least two good jets with  $E_T > 25, 20 \text{ GeV}$  and  $|\eta| < 2.6$ , and transverse mass  $M_T(\cancel{E}_T, \mu) < 50 \text{ GeV}/c^2$ . At least one of the reconstructed jets is required to be tagged as a  $b$ -jet with a displaced decay vertex. The dominant backgrounds are QCD,  $t\bar{t}$ , and  $W/Z + jets$  events. In this search,  $D\mathcal{O}$  finds 17 data events, which agrees well with the expected background of  $18.4 \pm 0.5$  events. Since no excess is observed,  $D\mathcal{O}$  excludes  $3^{rd}$  generation scalar leptoquarks with masses up to  $180 \text{ GeV}/c^2$  at 95% C.L. Figure 10 shows the observed distribution of the  $S_T = P_T(\mu) + P_T(\tau) + E_T(\text{jet}1) + E_T(\text{jet}2) + \cancel{E}_T$  parameter (left plot) and the cross section upper limits as a function of  $LQ_3$  mass (right plot).

## 9 Search for $H^{++}H^{--} \rightarrow \mu^+\mu^+\mu^-\mu^-$

Doubly-charged Higgs bosons appear in such scenarios of new physics as left-right symmetric models (26), Higgs triplet models (27), and little Higgs models (28). The major production mechanism of a doubly-charged Higgs at the Tevatron is via  $p\bar{p} \rightarrow Z/\gamma^* \rightarrow H^{++}H^{--} + X$ . Since the  $H^{\pm\pm}$  coupling to  $W$  pairs is suppressed by the measured  $m_{W'}^2/(\cos^2\theta_W m_Z^2) \approx 1$ , the dominant final states are expected to be like-sign lepton pairs. Since these decays violate lepton flavor conservation, mixed flavor states are also possible. Left-handed and right-handed states are distinguished by their decays into left-handed and right-handed leptons.

The  $D\mathcal{O}$  Collaboration has performed a search for pair production of doubly-charged Higgs bosons in the  $\mu^+\mu^+\mu^-\mu^-$  final state with  $1.1 \text{ fb}^{-1}$  of data. Events are required to have three isolated muons with  $P_T > 15 \text{ GeV}/c$  and  $|\eta| < 2.0$ . At least one muon pair should satisfy  $M_{\mu\mu} > 30 \text{ GeV}/c^2$  and  $\Delta\phi_{\mu\mu} < 2.5$

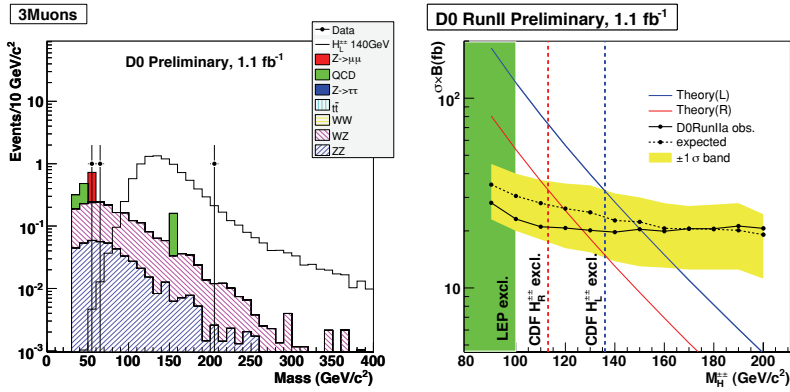


Figure 11: The observed and predicted  $M_{\mu\mu}$  distribution (left plot) and the cross section limit as a function of the Higgs mass ( $M_{H^{\pm\pm}}$ ) at 95% C.L. (right plot).

requirements to suppress  $Z \rightarrow \mu^+\mu^-$  and QCD events. The largest background comes from  $WZ$  events. Other backgrounds include  $ZZ$ ,  $Z \rightarrow \mu^+\mu^-$ , and QCD events, each at about the same level. After all cuts,  $D\emptyset$  finds 3 data events, which is in good agreement with an expected background of  $3.1 \pm 0.5$  events. Since no excess is observed, the  $D\emptyset$  Collaboration sets limits on the production of doubly-charged Higgs bosons. At 95% C.L., the left-handed state is excluded with masses up to  $150 \text{ GeV}/c^2$ , and the right-handed state is excluded with masses up to  $126.5 \text{ GeV}/c^2$ . This analysis significantly extends the previous CDF result. Figure 11 shows the observed and predicted invariant mass distribution for  $\mu\mu$  pairs (left plot) and the cross section limit as a function of the Higgs mass ( $M_{H^{\pm\pm}}$ ) at the 95% confidence level (right plot).

## 10 Search for $H \rightarrow \gamma\gamma + X$

There exist models of new physics where, unlike in the Standard Model and most common MSSM scenarios, the Higgs coupling to fermions is greatly suppressed. Such a “fermiophobic” Higgs appears in top-color models<sup>16, 10)</sup>, theories with large extra dimensions<sup>29)</sup>, and even in the MSSM where decays to  $b\bar{b}$  can be suppressed by 1-loop SUSY corrections<sup>30)</sup>. In all these cases, a light Higgs boson ( $m_h < 100 \text{ GeV}/c^2$ ) will predominantly decay into a  $\gamma\gamma$  pair. Decays are mediated by either a  $W$  or a heavy quark loop. The  $D\emptyset$  Collaboration has looked for signs of “fermiophobic” Higgs produced via two mechanisms:  $p\bar{p} \rightarrow VV \rightarrow h_f \rightarrow \gamma\gamma + X$  and  $p\bar{p} \rightarrow h_f V \rightarrow \gamma\gamma + X$ , where  $V = W, Z$ . The analysis is done with  $1.1 \text{ fb}^{-1}$  of data. Events are re-

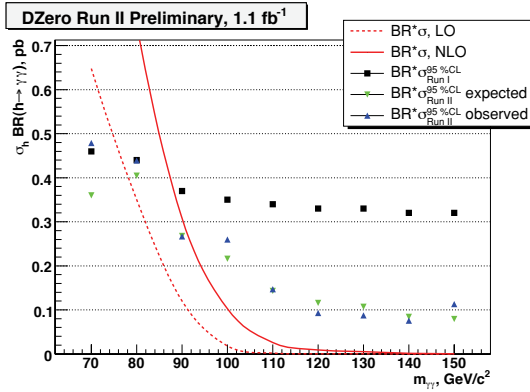


Figure 12: The cross section limit as a function of the “fermiophobic” Higgs mass at 95% C.L.

quired to have two central ( $|\eta| < 1.1$ ) photons with  $E_T > 25$  GeV and  $M_{\gamma\gamma} > 65$  GeV/ $c^2$ . The data sample is split in two parts according to the di-photon pair momentum ( $q_T$ ): signal sample with  $q_T > 35$  GeV/ $c$ , and control sample with  $q_T < 35$  GeV/ $c$ . The backgrounds are regular QCD and QED events:  $\gamma\gamma$ ,  $\gamma + jet \rightarrow \gamma\gamma_{fake}$ , and  $jet + jet \rightarrow \gamma_{fake}\gamma_{fake}$ . The control sample is used to test and tune the background estimation technique. The  $\gamma\gamma$  background template is taken from MC simulation. The  $\gamma + jet$  and di-jet background templates are derived from data. Since no excess of data over the predicted background is observed, the 95% C.L. limit on the production cross section is set. A “fermiophobic” Higgs boson with mass up to 92 GeV/ $c^2$  is excluded in this study. The limits obtained are shown at Fig. 12.

## 11 Summary and Conclusion

The CDF and DØ Collaborations continue to search for signs of new physics beyond the Standard Model in both signature-based and model-dependent analyses. Many signatures have been explored, but no significant excess of data over the predicted background is observed. An interesting result is found by the CDF Collaboration in the  $M_{e^+e^-}$  spectrum using 2.5 fb $^{-1}$  of data. In this study, the most significant excess of data over the total background is observed in the window  $228 \text{ GeV}/c^2 < M_{e^+e^-} < 250 \text{ GeV}/c^2$ . It corresponds to 3.8 standard deviations from the SM prediction. The probability of observing a background fluctuation with significance  $S/\sigma_B > 3.8$  anywhere in the mass range  $150 \text{ GeV}/c^2 < M_{e^+e^-} < 1000 \text{ GeV}/c^2$  is about 0.6%. More data and a similar analysis in the  $\mu^+\mu^-$  channel and by the DØ Collaboration should reveal

whether this is a sign of new physics or just a rare statistical fluctuation.

Both the CDF and DØ Collaborations continue to explore new signatures and analysis techniques. This increases our potential to see something new. One example of signatures that were not thoroughly explored before is the search for “delayed”  $Z$  bosons by the DØ Collaboration. Photon pointing (DØ),  $\cancel{E}_T$ -significance (CDF), and EM-timing (CDF) are examples of new promising analysis techniques.

The Tevatron has already delivered  $3.7 \text{ fb}^{-1}$  of data per experiment and continues to set performance records. With  $2\text{-}5 \text{ fb}^{-1}$  still to come in the Run II program, we can expect many new interesting results.

## 12 Acknowledgments

We thank the Fermilab staff and the technical staffs of the participating institutions for their vital contributions. This work was supported by the U.S. Department of Energy and National Science Foundation; the Italian Istituto Nazionale di Fisica Nucleare; the Ministry of Education, Culture, Sports, Science and Technology of Japan; the Natural Sciences and Engineering Research Council of Canada; the National Science Council of the Republic of China; the Swiss National Science Foundation; the A.P. Sloan Foundation; the Bundesministerium für Bildung und Forschung, Germany; the Korean Science and Engineering Foundation and the Korean Research Foundation; the Science and Technology Facilities Council and the Royal Society, UK; the Institut National de Physique Nucleaire et Physique des Particules/CNRS; the Russian Foundation for Basic Research; the Ministerio de Educación y Ciencia and Programa Consolider-Ingenio 2010, Spain; the Slovak R&D Agency; and the Academy of Finland.

## References

1. D. London and J.L. Rosner, Phys. Rev **D34**, 1530 (1986); J.L. Hewett and T.G. Rizzo, Phys. Rep. **183**, 193 (1989).
2. L. Randall and R. Sundrum, Phys. Rev. Lett. **83**, 3370 (1999).
3. T. Sjöstrand *et al.*, Comput. Phys. Commun. **135**, 238 (2001).
4. J. Bagger, C. Schmidt, and S. King, Phys. Rev **D37**, 1188 (1988); P.H. Frampton and S.L. Glashow, Phys. Lett. B **190**, 157 (1987).
5. U. Baur, I. Hinchliffe, and D. Zeppenfeld, Int. J. Mod. Phys. A **2**, 1285 (1987); U. Baur, M. Spira, and P.M. Zerwas, Phys. Rev **D42**, 815 (1990).

6. K.D. Lane and M.V. Ramana, Phys. Rev **D44**, 2678 (1991); E. Eichten and K.D. Lane, Phys. Lett. B **327**, 129 (1994); K.D. Lane and S. Mrenna, Phys. Rev **D67**, 115011 (2003).
7. E. Eichten *et al.*, Rev. Mod. Phys. **56**, 579 (1984); *Addendum-ibid.* **58**, 1065 (1986).
8. P. Fayet, Phys. Lett. B **70**, 461 (1977); *ibid.* **86**, 272 (1979); *ibid.* **175**, 471 (1986).
9. M. Strassler and K. Zurek, arXiv:hep-ph/0604261v2.
10. B. Dobrescu, G. Landsberg, and K. Matchev, Phys. Rev **D63**, 075003 (2001).
11. H. Frampton, P.Q. Hung, and M. Sher, Phys. Rep. **330**, 263 (2000).
12. N. Arkani-Hamed, S. Dimopoulos, and G. Dvali, Phys. Lett. B **429**, 263 (1998).
13. S. Dimopoulos, S.D. Thomas and J.D. Wells, Nucl. Phys. B **488**, 39 (1997); S. Ambrosanio, G.D. Kribs and S.P. Martin, Phys. Rev. D **56**, 1761 (1997); G.F. Giudice and R. Rattazzi, Phys. Rep. **322**, 419 (1999); S. Ambrosanio, G.L. Kane, G.D. Kribs, S.P. Martin and S. Mrenna, Phys. Rev. D **55**, 1372 (1997);
14. G. Bhattacharyya and R.N. Mohapatra , Phys. Rev. D **54**, 4204 (1996).
15. J.L. Rosner, Phys. Rev. D **55**, 3143 (1997).
16. B. Dobrescu, Phys. Rev. **D63**, 015004 (2001).
17. S. Ambrosanio *et al.*, Phys. Rev. Lett. **76**, 3498 (1996); B.C. Allanach *et al.*, hep-ph/0112321.
18. A. Abulencia *et al.* [CDF Collaboration], Phys. Rev. Lett. **97**, 171802 (2006).
19. H. Goldberg, Phys. Rev. Lett. **50**, 1419 (1983); J.R. Ellis *et al.*, Nucl. Phys. B **238**, 453 (1984).
20. G. Servant and T.M.P. Tait, Nucl. Phys. B **650**, 391 (2003); H.C. Cheng, J.L. Feng, and K.T. Matchev, Phys. Rev. Lett. **89**, 211301 (2002).
21. H.C Cheng and I. Low, JHEP **0309**, 051 (2003).
22. P.H. Beachemin, "Searches for Leptoquarks", talk presented at the *Deep Inelastic Scattering (DIS 08)* conference, London, 2008.

23. J.C. Pati and A. Salam, Phys. Rev **D10**, 275 (1974); H. Georgi and S.L. Glashow, Phys. Rev. Lett. **32**, 438 (1974).
24. S. Dimopoulos and L. Susskind, Nucl. Phys. B **155**, 237 (1979); S. Dimopoulos, *ibid.* **168**, 69 (1980); E. Eichten and K. Lane, Phys. Lett. B **90**, 125 (1980).
25. B. Schrempp and F. Schrempp, Phys. Lett. B **153**, 101 (1985); W. Buchmüller, R. Rückl, and D. Wyler, *ibid.* **191**, 442 (1987); *Erratum-ibid.* **448**, 320 (1999).
26. N.G. Deshpande, J.F. Gunion, and B. Kayser, Phys. Rev. **D44**, 837 (1991); J.G. Gunion *et al.*, *ibid.* **D40**, 1546 (1989); T. Rizzo, *ibid.* **D25**, 1355 (1982), *Addendum-ibid.* **D27**, 657 (1983); C.P. Hays, “Doubly-Charged Higgs Boson”, in *Search for the Higgs Boson*, Ed. J.V. Lee (Nova Science Publishers, 2006).
27. J.F. Gunion, C. Loomis, and K.T. Pitts, hep-ph/9610237 (1996); J.F. Gunion, R. Vega, and J. Wudka, Phys. Rev. **D42**, 1673 (1990); E. Accomando *et al.*, “CP Studies and Non-Standard Higgs Physics”, hep-ph/0608079.
28. N. Arkani-Hamed *et al.*, JHEP **0208**, 021 (2002).
29. L. Hall and C. Kolda, Phys. Lett. B **459**, 213 (1999); H.-C. Cheng, B.A. Dobrescu, and C.T. Hill, Nucl. Phys. B **589**, 249 (2000).
30. M. Carena, S. Mrenna, and C.E. Wagner, Phys. Rev **D60**, 075010 (1999).

**SEARCH FOR SUPERSYMMETRY AT THE TEVATRON**

Patrice Verdier  
*IPN-Lyon, France*

Written contribution not received



## SEARCHES FOR NEW PHYSICS AT HERA

Jenny List

*DESY, Notkestr. 85, 22607 Hamburg, Germany*  
on the behalf of the H1 and ZEUS Collaborations

### Abstract

Until the end of HERA operation in June 2007, the H1 and ZEUS experiments collected high quality data sets corresponding to an integrated luminosity of  $0.5 \text{ fb}^{-1}$  each. With these data sets, which comprise electron-proton as well as positron-proton data with longitudinal lepton polarisation of 30-40% for both helicity states, many searches for phenomena beyond the Standard Model have been performed, including both model driven and signature based searches. Since no significant deviations from the Standard Model have been found, preliminary exclusion limits are presented here.

## 1 Introduction

### 1.1 HERA

The world's only  $ep$  collider HERA operated between the years 1993 and 2007. The two collider experiments H1 and ZEUS collected close to  $500 \text{ fb}^{-1}$  of high quality data. About 70% of these data were taken during the HERA II phase with substantially upgraded detectors, where protons with an energy of 920 GeV collided with longitudinally polarised electrons or positrons with an energy of 27.6 GeV. The HERA II data set comprises all four possible combinations of lepton charge and helicity with roughly the same amount of integrated luminosity. The longitudinal polarisation routinely reached 30-40%.

The searches for physics beyond the Standard Model presented here use either the complete data set or substantial parts of it. All exclusion limits are given at 95% CL.

### 1.2 Deep Inelastic Scattering

Since new phenomena are usually expected to appear at high values of the momentum transfer  $Q^2$ , selections of deep inelastic scattering events are the basis for many searches. In the Neutral Current case, mediated by photon or  $Z^0$  exchange, the hadronic final state is balanced by the scattered electron<sup>1</sup>. This allows a calibration of the jet energy scale to about 1% (above  $E_{jet} > 25 \text{ GeV}$ ). In the Charged Current case  $W^\pm$  exchange leads to a neutrino in the final state, which gives a signature with significant missing transverse energy. In the Standard Model the Charged Current cross section vanishes for right-handed electrons and left-handed positrons. Therefore the lepton beam polarisation can be used either to enhance or to suppress Charged Current events. The precise measurements of the neutral and Charged Current cross sections performed by H1 and ZEUS can be used to constrain various extensions of the Standard Model. Some examples will be discussed in the next section before turning to searches for new physics with other signatures.

## 2 Searches for New Physics in Deep Inelastic Scattering

### 2.1 Quark Radius

With the maximal momentum transfer possible at HERA,  $Q_{max}^2 \simeq 10000 \text{ GeV}^2$ , one can expect a spatial resolution down to about  $r^2 \simeq \hbar c/Q \simeq 10^{-18} \text{ m}$ . A more careful analysis fits a hypothetical quark form factor  $F_q = (1 - R_q^2 Q^2/6)$  to the  $Q^2$ -dependence of the Neutral Current cross section. This method has

---

<sup>1</sup>In the following “electron” is used to refer to both electrons and positrons wherever the charge sign doesn't matter.

been applied to both H1 and ZEUS data. H1 excludes values of  $R_q > 0.74 \cdot 10^{-18} \text{ m}^1$ , whereas ZEUS excludes quark radii down to  $0.67 \cdot 10^{-18} \text{ m}^2$ .

### 2.2 Large Extra Dimensions

The same  $Q^2$  dependence has been used by the ZEUS collaboration to constrain models with large extra dimensions, where electron–quark scattering can be mediated by multiple graviton exchange in addition to the Standard Model gauge boson contributions. Assuming either constructive or destructive interference with the Standard Model, the large extra dimension mass scale can be constrained to be larger than 0.88 TeV or 0.9 TeV, respectively <sup>2)</sup>.

### 2.3 Contact Interactions

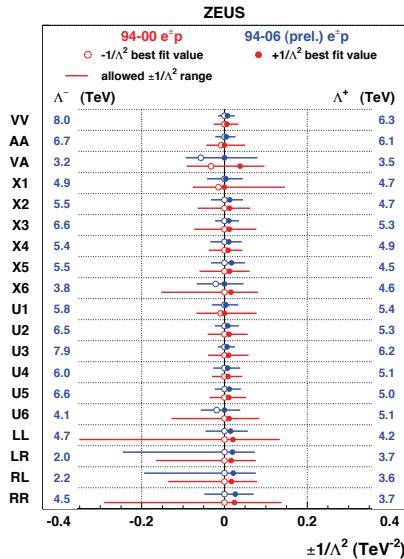


Figure 1: Limits on new phenomena in various extensions of the standard model, generically parametrised by the contact interaction scale  $\Lambda$ .

Other possible contributions to the Neutral Current cross section can be parametrised in terms of contact interactions, i.e. assuming some effective four–fermion vertex with a coupling proportional to the inverse of the energy scale  $\Lambda$  of the new contribution. The ZEUS collaboration has set lower limits on  $\Lambda$  in various scenarios which are summarised in figure 1. These lower limits range between 2 and 8 TeV, depending on the model under consideration <sup>2)</sup>.

This is a very nice example of the fact that precision measurements can probe for new physics at energy scales far above the center-of-mass energy.

### 3 Model-based Searches

#### 3.1 First Generation Leptoquarks

Leptoquarks are bosons carrying both color charge and lepton number and are predicted by many types of Grand Unified Theories. The phenomenological Buchmüller–Rückl–Wyler model <sup>3)</sup> classifies all 14 possible types of leptoquarks which respect basic experimental facts like a very long proton life time. The H1 experiment recently updated its search results for leptoquarks coupling to first generation fermions <sup>1)</sup>.

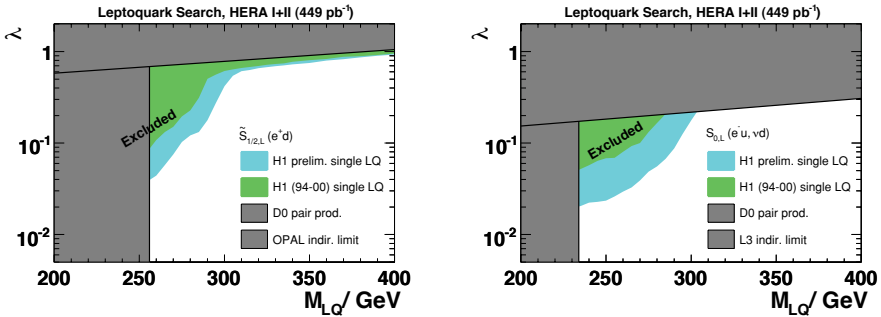


Figure 2: Upper limits on the first generation leptoquark coupling  $\lambda_{eq}$  as a function of the leptoquark mass  $M_{LQ}$  within the BRW model.

Left: for the  $F = 0$  scalar leptoquark  $\tilde{S}_{1/2,L}$

Right: for the  $F = 2$  scalar leptoquark  $S_{0,L}$ .

Figure 2 shows as an example upper limits on the leptoquark-lepton-quark coupling  $\lambda$  as a function of the leptoquark mass for two of the 14 leptoquark types. The left plot applies to a scalar leptoquark with fermion number  $F = 0$ , coupling to down quark and right-handed positron <sup>2)</sup>, whereas the right plot shows the situation for a scalar  $F = 2$  leptoquark which couples either to an up quark and a lefthanded electron or to a down quark and a neutrino. In both cases the coloured area is excluded by H1, where the blue area shows the improvement with respect to the published results from the HERA I phase <sup>4)</sup>. The upper hatched area is excluded by indirect searches performed at LEP,

<sup>2)</sup>The helicity index  $L$  or  $R$  always refers to an electron

while the hatched area at low masses comes from the (coupling independent) search for pair production of leptoquarks at D0.

### 3.2 Lepton Flavour Violation

If the leptoquark is not restricted to couple only to first generation fermions, the decay lepton could be a muon or a tau lepton instead of an electron. In this case, the leptoquark would mediate lepton flavour violation, since it has to be produced from an electron-quark initial state at HERA. The resulting signature of an energetic isolated muon balancing the hadronic final state does not exist in the Standard Model, so that this search is free from irreducible background. The H1 experiment recently updated the results for the muon channel including all HERA II  $e^-p$  data.

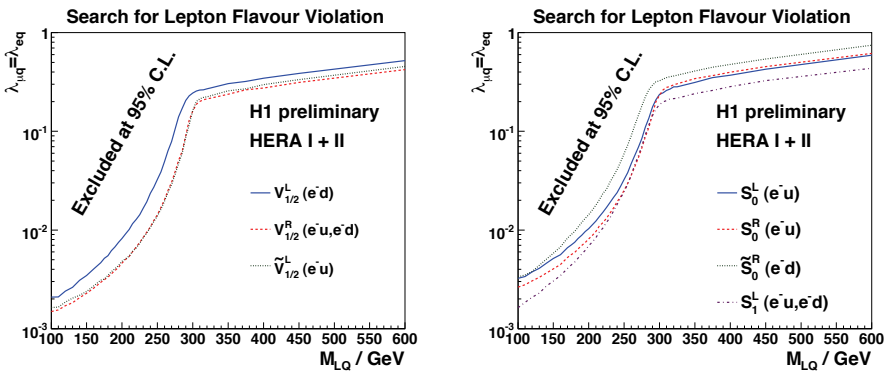


Figure 3: Upper limits on the leptoquark coupling  $\lambda_{\mu q}$  as a function of the leptoquark mass  $M_{LQ}$ , assuming  $\lambda_{\mu q} = \lambda_{eq}$  i.e. that the leptoquark mediates maximal lepton flavour violation.

Left: for the three  $F = 2$  vector leptoquarks

Right: for the four  $F = 2$  scalar leptoquarks of the BRW model.

Figure 3 shows upper limits on the coupling for the seven  $F = 2$  leptoquarks in the Buchmüller–Rückl–Wyler model as a function of the leptoquark mass assuming  $\lambda_{\mu q} = \lambda_{eq}$  and  $\lambda_{\tau q} = 0$ . The left figure addresses the three vector leptoquark types, whereas the right figure shows the results for the four scalar types. Note that at low masses, the limits are typically one order of magnitude more stringent than in the first generation case due to the extremely low background.

### 3.3 Excited Fermions

Most recently the H1 collaboration published a search for excited neutrinos based on the full HERA  $e^-p$  dataset of  $184 \text{ pb}^{-1}$  <sup>5)</sup>. On a dataset corresponding to an integrated luminosity of  $435 \text{ pb}^{-1}$  a search for excited electrons has been performed <sup>1)</sup>. If fermions have a substructure at a compositeness scale  $\Lambda$ , they would have excited states which decay into the ground state via emission of an electroweak gauge boson, i.e. a photon, a  $Z^0$  or  $W^\pm$ . All possible signatures from these decays have been searched for, but since no excess over the SM expectation has been found, limits are calculated in terms of the  $U(1)$  and  $SU(2)$  form factors  $f$  and  $f'$  over  $\Lambda$  as a function of the mass of the excited state.

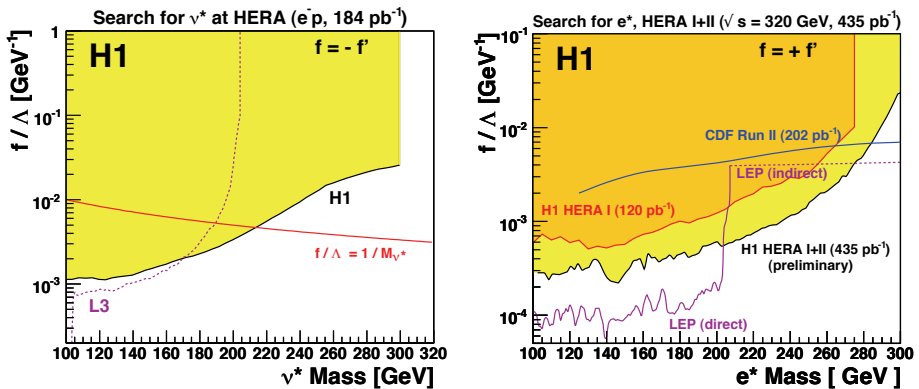


Figure 4: *Upper limits on the magnitude of the excited lepton's  $U(1)$  and  $SU(2)$  form factors  $f$  and  $f'$  over the compositeness scale  $\Lambda$  as function of the excited lepton's mass.*

*Left: for excited neutrinos assuming (assuming  $f = -f'$ )*

*Right: for excited electrons assuming (assuming  $f = f'$ )*

Figure 4 shows the resulting limits for excited neutrinos assuming  $f = -f'$  on the left side and for excited electrons assuming  $f = f'$  on the right side. In both cases substantial regions beyond the LEP limits are excluded by these searches.

## 4 Signature-based Searches

### 4.1 High $P_t$ Leptons with missing $P_t$

In the Standard Model, events with isolated high  $P_t$  leptons and missing transverse momentum are predominantly produced via single  $W^\pm$  production. In

$e^+p$  data, the H1 experiment observes a  $3\sigma$  excess of such events with a transverse momentum of the hadronic final state  $P_T^X > 25$  GeV with 21 events observed compared to an expectation of  $9 \pm 1.5$  events. This observation triggered a common analysis of the H1 and ZEUS data in the phase space region accessible to both experiments. While the excess in the H1 data doesn't change significantly when reducing the phase space, it shrinks to 1.8 standard deviations in combination with the ZEUS data (23 events observed versus  $15 \pm 2$  expected). In the complete HERA data set (H1 and ZEUS,  $e^+p$  and  $e^-p$ ), corresponding to an integrated luminosity of  $0.97 \text{ fb}^{-1}$ , the observations agree very well with the Standard Model expectations.

### 4.2 Anomalous Top Quark Production

One possible phenomenon which could enhance single  $W^\pm$  production at HERA is an anomalous coupling between top-quark, up-quark and photon  $\kappa_{tu\gamma}$ <sup>3</sup>. The H1 collaboration therefore performed a search for isolated lepton events with a b-jet in the hadronic final state<sup>1)</sup> including all data corresponding to an integrated luminosity of  $482 \text{ pb}^{-1}$ .

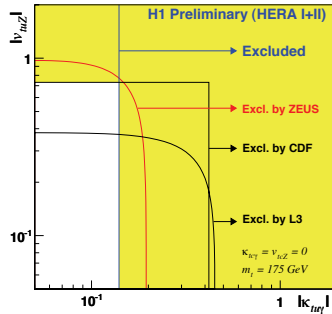


Figure 5: Limits on the size of the anomalous top-quark couplings  $|\kappa_{tu\gamma}|$  and  $|v_{tuZ}|$ . The blue line indicates the upper limit from H1, which is the world's most stringent limit on  $|\kappa_{tu\gamma}|$ .

From this analysis cross sections  $\sigma_{ep \rightarrow etX} < 0.1 \text{ pb}$  can be excluded. The resulting limit on  $|\kappa_{tu\gamma}| < 0.14$  is the most stringent one as can be seen from figure 5, where the H1 limit is shown as vertical line in the  $|v_{tuZ}|$ - $|\kappa_{tu\gamma}|$  plane in comparison with results from ZEUS, CDF and L3.

<sup>3</sup>As a flavour changing *neutral* current anomalous top quark production cannot explain the observed difference between  $e^+p$  and  $e^-p$  data in the isolated lepton analysis

### 4.3 Multi-Leptons

Another signature for which an excess has been previously observed is that of events with two or three isolated leptons (i.e. electrons and muons). For the sum of leptons' transverse momenta larger than 100 GeV, the H1 collaboration observed 4 events compared to an expectation of  $1.2 \pm 0.2$  events in  $286 \text{ pb}^{-1}$  of  $e^+p$  data, of which 3 compared to  $0.6 \pm 0.1$  events are multi-electron events<sup>1)</sup>. For the two and three electron classes, H1 and ZEUS again performed a search in a common phase space. The combined result for the  $e^+p$  data yields 5 events observed over an expectation of  $1.8 \pm 0.2$ , whereas the agreement for  $e^+p$  and  $e^-p$  data combined is significantly better with 6 events observed compared to  $3 \pm 0.3$  expected.

## 5 Conclusions

After the end of HERA operation in June 2007, nearly  $500 \text{ fb}^{-1}$  of high quality data per experiment are available for data analysis. Many preliminary search results based on the full data set have been presented here. No significant deviations from the Standard Model have been found. The analyses of isolated lepton events and of multi-electron events have been performed by the H1 and ZEUS collaborations in a common phase space. The combinations agree well with the Standard Model expectations for  $e^+p$  and  $e^-p$  data combined, but some excess is still observed in the H1  $e^+p$  data sets.

## 6 Acknowledgements

Many thanks to the ZEUS High  $Q^2$  group and the H1 REX group for the material and useful discussions!

## References

1. [http://www-h1.desy.de/publications/H1preliminary.short\\_list.htm](http://www-h1.desy.de/publications/H1preliminary.short_list.htm)
2. [http://www-zeus.desy.de/public\\_results/publicsearch.html](http://www-zeus.desy.de/public_results/publicsearch.html)
3. W. Buchmüller, R. Rückl and D. Wyler, Phys. Lett. B **191** (1987) 442 [Erratum-ibid. B **448** (1999) 320].
4. A. Aktas *et al.* [H1 Collaboration], Phys. Lett. B **629**, 9 (2005) [arXiv:hep-ex/0506044].
5. F. D. Aaron *et al.* [H1 Collaboration], arXiv:0802.1858 [hep-ex].

**LEPTON FLAVOR VIOLATION IN  $\tau$  AND  $B$  DECAYS AT  
*BABAR***

Elisa Manoni

*Università di Perugia and I.N.F.N. sezione di Perugia,  
via A. Pascoli, 06123, Perugia, Italy*  
(on behalf of the *BABAR* Collaboration)

**Abstract**

This article summarizes the search for lepton flavor violating  $\tau$  and  $B$  decays, using data collected by the *BABAR* detector at the PEP-II asymmetric-energy  $B$  factory.

## 1 Introduction

In the Standard Model (SM) with massless neutrinos, the lepton number is conserved separately for each generation. In this framework, Lepton Flavor (LF) conservation differs from other conservation laws because it is not associated with an underlying conserved current symmetry. As a consequence extension of the SM or New Physics (NP) scenarios often include LF violation, as is also suggested by the discovery of neutrino oscillations<sup>1)</sup>. In a modest extension of the SM incorporating finite  $\nu$  mass, the branching ratios (BRs) of decays with LF violation are many orders of magnitude below the experimental accessibility. On the other hand, NP models predict enhancements on the BRs within the current experimental reaches and observation of LF violating processes would be a clear signature of NP and would allow to constraint parameters of such models. As an example, in Table 1 the predictions for  $BR(\tau \rightarrow \ell\gamma)$  and  $BR(\tau \rightarrow \ell\ell\ell)$  within several beyond-SM scenarios are shown; hereafter  $\ell$  refers to a muon or an electron.

Here we present the most recent results on LF violating  $\tau$  and  $B$  decays at the *BABAR* experiment:  $\tau^- \rightarrow \ell^- \ell^+ \ell^-$  and  $\tau^\pm \rightarrow \ell^\pm \omega$ ,  $B^0 \rightarrow e^\pm \mu^\mp$ ,  $B^0 \rightarrow \ell^\pm \tau^\mp$ , and  $B^+ \rightarrow K^+ \tau^\mp \mu^\pm$ . The *BABAR* detector, described in details elsewhere<sup>2)</sup>, collects data at the PEP-II asymmetric-energy  $e^+e^-$  collider that operates at a center of mass (CM) energy of 10.58 *GeV*. The cross section production for  $e^+e^- \rightarrow \tau^+\tau^-$  is  $\sigma_{\tau\tau} \simeq 0.9$  *nb*, and is comparable with the  $e^+e^- \rightarrow B\bar{B}$  cross section production ( $\sigma_{B\bar{B}} \simeq 1.05$  *nb*): almost as many  $\tau$  pairs as  $B$  pairs are produced. Moreover, event shape variables allow to distinguish the jet-like topology of  $\tau^+\tau^-$  from the sphericity of  $B\bar{B}$  events. As a consequence,  $B$  factories represent an optimal framework for this kind of investigation due to the high statistics and the clean environment in which both  $\tau^+\tau^-$  and  $B\bar{B}$  pair can be produced and distinguished by each other and by other events.

## 2 $\tau$ decays

### 2.1 Analysis Method

The analysis discussed in this paper concerning  $\tau$  decays follow a common strategy. One  $\tau$  is reconstructed in SM decays containing 1 or 3 tracks (“1-prong” or “3-prongs” topology) and from 1 to 2 neutrinos. The 1-prong category in-

Table 1: Predictions for  $BR(\tau \rightarrow \ell\gamma)$  and  $BR(\tau \rightarrow \ell\ell\ell)$  decays within several beyond-SM scenarios.

model	$BR(\tau \rightarrow \ell\gamma)$	$BR(\tau \rightarrow \ell\ell\ell)$
SM + $\nu$ mixing <sup>3)</sup>	$10^{-54} - 10^{-40}$	$10^{-14}$
SUSY Higgs <sup>4)</sup>	$10^{-10}$	$10^{-7}$
SM + heavy Majorana $\nu_R$ <sup>5)</sup>	$10^{-9}$	$10^{-10}$
Non-universal $Z'$ <sup>6)</sup>	$10^{-9}$	$10^{-8}$
SUSY SO(10) <sup>7)</sup>	$10^{-8}$	$10^{-10}$
mSUGRA+seesaw <sup>8)</sup>	$10^{-7}$	$10^{-9}$

cludes:  $\tau \rightarrow \ell\nu_\ell\nu_\tau, \pi\nu_\tau, \rho\nu_\tau$ , while the 3-prongs embodies  $\tau \rightarrow 3\pi n\pi^0\nu_\tau$ : all these modes covers roughly 99% of  $\tau$  decays. The other  $\tau$  is reconstructed in LF violating final states. The event is divided in two hemisphere using the plane perpendicular to the thrust of the event. The sign of scalar product of the given track momentum with the thrust direction determines the hemisphere to which the track belongs to. The thrust is calculated using charged and neutral candidates in the CM frame. The side in which a 1- or 3-prong(s) decay is reconstructed is called “tag” side, while the other is the “signal” side. In Fig. 1 a sketch of a  $\tau\tau$  event in the CM frame is shown. In the tag side at least one  $\nu$  is present and the missing energy should be non zero, while on the signal hemisphere all the  $\tau$  decay products are reconstructed. This condition allow to request that the reconstructed invariant mass ( $m_{rec}$ ) and the CM energy ( $E_{rec}^*$ ) for the signal side candidates are consistent with the nominal  $\tau$  mass ( $m_\tau^{PDG}$ ) and with the beam energy in the CM frame ( $\sqrt{s}/2$ ) respectively. For signal events, the distribution of the two following variables:

$$\begin{aligned}\Delta m &= m_{rec} - m_\tau^{PDG} \\ \Delta E &= E_{rec}^* - \sqrt{s}/2\end{aligned}\tag{1}$$

should peak at zero, with non Gaussian tails due to initial and final state radiation. For  $\tau^- \rightarrow \ell^- \ell^+ \ell^-$  channel values of the resolutions in  $\Delta E$  and  $\Delta m$  are 10 MeV and 20 – 30 MeV/c<sup>2</sup> (depending on the 3 $\ell$  combination) respectively. The resolution on  $\Delta m$  can be improved by replacing  $m_{rec}$  with the beam-energy constrained mass  $m_{EC}$ , computed from a fit to the reconstructed  $\tau$  candidate decay products in which the  $\tau$  energy in the CM is fixed to  $\sqrt{s}/2$ . This method

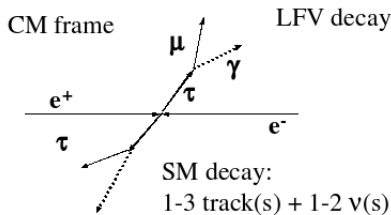


Figure 1: *Sketch of a  $\tau\tau$  event in the CM frame: a SM decay in the tag side and a neutrinoless NP decay, i.e.  $\tau \rightarrow \mu\gamma$ , in the signal hemisphere are represented.*

is adopted in the  $\tau^\pm \rightarrow \ell^\pm \omega$  analysis where the resolution in  $\Delta m_{EC}$  ( $\Delta E$ ) is  $6 - 7 \text{ MeV}/c^2$  ( $31 - 32 \text{ MeV}$ ) for  $\ell = \mu, e$  respectively. Tracks used in the  $\tau$ 's reconstruction should satisfy particle identification (PID) criteria and a cut on their minimum momentum is applied. The total charge of the events is required to be zero. Events with tracks from gamma-conversion are rejected. Cuts on the kinematic properties of the tag side, such as momentum of the prong track(s), module and direction of the missing momentum, are applied. The selection criteria are optimized by using fully simulated signal and background Monte Carlo (MC) samples. The signal MC is also used to determine the signal efficiency, whose typical values are between 2% and 12%. Background MC and data and MC control samples are used to check the data-MC agreement and to model the background shapes of the relevant variables fitted with the purpose of estimating and subtracting the final background contribution. To avoid biases in the analysis a “blind” strategy is adopted: a signal region in the  $\Delta E$ - $m_{rec}$  (or  $\Delta E$ - $m_{EC}$ ) plane is defined around their central values with a width of 2 – 3 standard deviations. The analysis procedure is tested outside the signal region (sideband); the same sample is also used for the background yield estimation, whose normalization is obtained from sideband data. Once the strategy is defined a 2-dimensional Maximum Likelihood (ML) fit is performed, the expected background yield and the fitted one are compared: if they are compatible, a 90% Confidence Level (CL) Upper Limit (UL) is set.

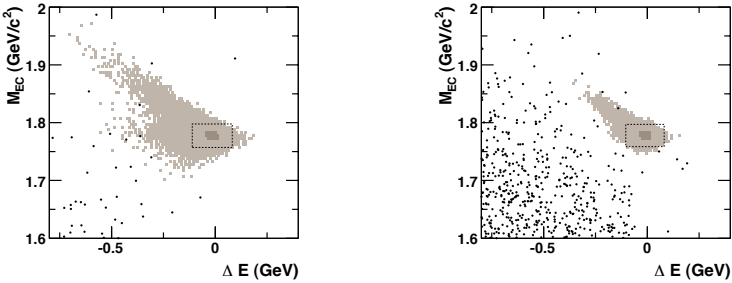


Figure 2: Selected candidates (dots) in the  $\Delta E - m_{EC}$  plane for  $\tau^\pm \rightarrow e^\pm \omega$  (left) and  $\tau^\pm \rightarrow \mu^\pm \omega$  (right). The signal box is shown by a dashed rectangle. The dark and light shading indicate contours containing 50% and 90% of the selected MC signal candidates respectively.

## 2.2 New *BABAR* results on $\tau^- \rightarrow \ell^- \ell^+ \ell^-$ (10) and $\tau^\pm \rightarrow \ell^\pm \omega$ (11)

The  $\tau^- \rightarrow \ell^- \ell^+ \ell^-$  analysis has been performed on  $376.0 \text{ fb}^{-1}$  corresponding to 346 million  $\tau\tau$  pairs. All possible 3-lepton combinations, according to the charge conservation, are reconstructed. The signal signature consist of three charged tracks satisfying PID selection, whose invariant mass and energy are consistent with the  $\tau$  hypothesis. For the tag side, the 1-prong topology is required. A 2 dimensional ML fit to the  $m_{rec} - \Delta E$  distributions is performed. The search for  $\tau \rightarrow (e, \mu)\omega$  has been performed on  $384.1 \text{ fb}^{-1}$  (353 million  $\tau^+\tau^-$  events). Signal decays are identified by a lepton track and a  $(\pi^+\pi^-\pi^0)$  system in which the  $\omega$  meson is reconstructed. The three charged tracks are fitted to a common vertex and the two photons from the  $\pi^0$  are assumed to originate from the same point. Also a mass constraint on the  $\pi^0$  is applied. The yield extraction is done by fitting the  $\Delta E - m_{EC}$  distributions. A scatter plot of  $\Delta E$  vs  $m_{EC}$  after the selection is shown in Fig.2. The results of these two analysis are presented in Table 2.

## 2.3 Overview of measurements on $\tau$ decays and LF violation at *BABAR*

In Table 3 the results of the measurements performed by the *BABAR* collaboration on LF violation in  $\tau$  decays are listed. A comparison with Belle is also reported. No evidence for signal is found in any of the channels under inves-

Table 2: Results for  $\tau^- \rightarrow \ell^- \ell^+ \ell^-$  and  $\tau^\pm \rightarrow \ell^\pm \omega$  analysis: signal efficiency ( $\epsilon$ ), number of expected background events ( $Nb_{exp}$ ), number of observed events ( $N_{obs}$ ), 90% CL UL on the BR ( $UL(BR)$ ).

channel	$\epsilon(\%)$	$Nb_{exp}$	$N_{obs}$	$UL(BR) \times 10^{-8}$
$\tau^- \rightarrow e^- e^+ e^-$	$8.9 \pm 0.2$	$1.33 \pm 0.25$	1	4.3
$\tau^- \rightarrow \mu^- e^+ e^-$	$8.3 \pm 0.6$	$0.89 \pm 0.27$	2	8.0
$\tau^- \rightarrow \mu^+ e^- e^-$	$12.4 \pm 0.8$	$0.30 \pm 0.55$	2	5.8
$\tau^- \rightarrow e^+ \mu^- \mu^-$	$8.8 \pm 0.8$	$0.54 \pm 0.21$	1	5.6
$\tau^- \rightarrow e^- \mu^+ \mu^-$	$6.2 \pm 0.5$	$0.81 \pm 0.31$	0	3.7
$\tau^- \rightarrow \mu^- \mu^+ \mu^-$	$5.5 \pm 0.7$	$0.33 \pm 0.19$	0	5.3
$\tau^- \rightarrow e^- \omega$	$2.96 \pm 0.13$	$0.35 \pm 0.06$	0	11.0
$\tau^- \rightarrow \mu^- \omega$	$2.56 \pm 0.16$	$0.73 \pm 0.03$	0	10.0

tigation, the experimental limits are going down to  $10^{-8}$  and in some cases constraints on NP parameters can be set.  $\tau$  physics will also be exploited in a future Super  $B$  factory project, preliminary studies<sup>9)</sup> have shown that improvements on the UL of factors 10–100 with respect to the  $B$  factories results can be achieved, with an integrated luminosity of  $75 \text{ ab}^{-1}$ .

### 3 $B$ decays

#### 3.1 $B^0 \rightarrow e^\pm \mu^\mp$ 20)

$B^0 \rightarrow \ell^+ \ell'^-$  decays (where  $\ell^+ \ell'^-$  stands for  $e^+ e^-$ ,  $\mu^+ \mu^-$ ,  $e^\pm \mu^\mp$ ) happen through a  $b \rightarrow d$  transition with an internal quark annihilation and are helicity suppressed by a factor  $(m_\ell/m_\tau)^2$ . Such processes are sensitive to NP in a large set of Minimal Flavor Violation models<sup>21)</sup>. In addition,  $B^0 \rightarrow e^\pm \mu^\mp$  violates the LF conservation: while it is predicted to have null BR within the SM, NP can enhance its decay rate up to  $10^{-10} - 10^{-16}$ <sup>22)</sup>. The analysis has been performed on a dataset of  $347 \text{ fb}^{-1}$  ( $384 \times 10^6 B\bar{B}$  pairs). Signal  $B$  candidates are reconstructed by identifying two oppositely charged tracks originating from the same vertex. Two main variables are used to select good  $B$  candidates:

$$\begin{aligned}
 m_{ES} &= \sqrt{E_{beam}^{*2} - p_B^{*2}} \\
 \Delta E &= E_B^* - \sqrt{s}/2
 \end{aligned}
 \tag{2}$$

Table 3: Overview of measurements on LF violating  $\tau$  decays at BABAR and comparison with Belle: for each channel the 90% CL UL on the BR and the luminosity  $\mathcal{L}$  are listed for both experiments.  $h$  and  $h'$  to a  $K$  or a  $\pi$ .

channel	BABAR		Belle	
	$UL(BR) \times 10^{-8}$	$\mathcal{L} (fb^{-1})$	$UL(BR) \times 10^{-8}$	$\mathcal{L} (fb^{-1})$
$\tau \rightarrow e\gamma$	11.0 <sup>12)</sup>	232.2	12.0 <sup>15)</sup>	535.0
$\tau \rightarrow \mu\gamma$	6.8 <sup>12)</sup>	232.2	4.5 <sup>15)</sup>	535.0
$\tau \rightarrow \ell(\pi^0, \eta, \eta')$	11.0 – 16.0 <sup>13)</sup>	339.0	7.0 – 12.0 <sup>16)</sup>	401.0
$\tau \rightarrow \ell hh'$	7.0 – 48.0 <sup>14)</sup>	221.4	20.0 – 160.0 <sup>17)</sup>	158.0
$\tau \rightarrow \ell\ell\ell$	3.7 – 8.0 <sup>10)</sup>	376.0	2.0 – 4.1 <sup>18)</sup>	535.0
$\tau \rightarrow (e, \mu)\omega$	10.0 – 11.0 <sup>11)</sup>	384.1	9.0 – 18.0 <sup>19)</sup>	543.0

where the subscripts beam and  $B$  refer to the  $\Upsilon(4S)$  and  $B$  candidate, while the asterisk denotes the  $\Upsilon(4S)$  rest frame. For well reconstructed  $B$ ,  $m_{ES}$  ( $\Delta E$ ) should be close to the  $B$  meson mass (0 GeV). A signal region in  $m_{ES}$  and  $\Delta E$  is defined. Contamination from  $q\bar{q}$  is suppressed by cutting on event shape variables. The main  $B\bar{B}$  background comes from  $B^0 \rightarrow \pi\pi, \pi K$  decay in which there is lepton-hadron misidentification; this contamination is suppressed by applying PID requirements. QED background in which  $e$  and  $\mu$  come directly from  $e^+e^-$  interaction is fought by cutting on the minimum number of charged tracks in the event. To extract the signal yields for each  $\ell\ell'$  combination a ML fit is performed: the variable used are  $m_{ES}$ ,  $\Delta E$  and a Fisher discriminant constructed by the momentum and the angle in the CM frame of each particle reconstructed in the event and not used in the signal side. The signal Probability Density Function (PDF) shapes are obtained from the MC sample while for the background control data sample are used. Table 4 summarizes the results of the analysis: no signal is found for any of the three  $\ell\ell'$  combination and a 90% probability UL on the BR is set.

### 3.2 $B^0 \rightarrow \ell^\pm\tau^\mp$ <sup>23)</sup>

$B^0 \rightarrow \ell^\pm\tau^\mp$  is potentially sensitive to NP effects due to contribution from neutral and charged non-SM Higgs mediated diagrams <sup>4)</sup> <sup>24)</sup>. In these frameworks the BR for  $B^0 \rightarrow \ell^\pm\tau^\mp$  is enhanced up to  $2 \times 10^{-10}$ . The search is performed

on  $342 \text{ fb}^{-1}$  ( $378 \times 10^6 B\bar{B}$  pairs). The analysis technique consist on exclusively reconstructing one  $B$  ( $B_{tag}$ ) in specific hadronic mode and then searching in the rest of the event for the  $\ell\tau$  signature that identify the signal  $B$  ( $B_{sig}$ ). The hadronic channels are of the form  $B \rightarrow D^{(*)}X$  where  $X$  is a combination of up to nine kaons and pions. Cuts on  $\Delta E$  and  $m_{ES}$  of the reconstructed  $B_{tag}$  are applied to check the consistency with a  $B$  meson. The signal hemisphere should contain a high momentum electron or muon not belonging to the tag side. The second highest momentum track is assumed to be a  $\tau$  daughter and should have opposite charge with respect to the primary signal lepton. Six  $\tau$  decay modes are considered:  $\tau \rightarrow e\nu_e\nu_\tau, \mu\nu_\mu\nu_\tau, \pi\nu_\tau, \pi\pi^0\nu_\tau, \pi 2\pi^0\nu_\tau, 3\pi\nu_\tau$ . Once the electron or the muon is reconstructed, the  $\tau$  kinematics is inferred by assuming the nominal energy and momentum of the  $\tau$  for a 2-body  $B^0$  decay. Background from non resonant  $e^+e^- \rightarrow q\bar{q}$  decays is suppressed by exploiting event shape variables; contamination from beam background, unassociated hadronic shower fragments, reconstruction artifacts, bremsstrahlung, and photon conversion are reduced by cutting on the number of extra tracks and neutrals, the missing momentum and the extra energy. The latter describe the amount of energy recorded by the detector, not used in the  $B_{tag}$  nor  $B_{sig}$  reconstruction, while the missing momentum is associated to the undetected neutrinos. The signal yield is extracted by an unbinned ML fit to the distribution of the signal lepton momentum in the  $B_{sig}$  rest frame (Fig.3); both signal and background PDF parametrization are determined from simulated events. The results of the analysis are presented in Table 4: these ULs represent the most stringent results on  $B^0 \rightarrow (e, \mu)^\pm \tau^\mp$ .

### 3.3 $B^+ \rightarrow K^+ \tau^\mp \mu^\pm$ 25)

*BABAR* has recently published the first search for  $B^+ \rightarrow K^+ \tau^\mp \mu^\pm$ . The process has higher sensitivity to NP with respect to  $B^0 \rightarrow \ell^\pm \tau^\mp$ , that is both helicity and CKM suppressed by a factor  $|V_{td}/V^{cb}|^2$ . In the frameworks of grand unified theories <sup>26)</sup> with non-SM Higgs, the flavor changing neutral current Yukawa couplings between the  $i^{th}$  and  $j^{th}$  generations are proportional to  $\sqrt{m_i m_j}/m_\tau$ , leading to largest contributions in processes involving the second and third generation, as the  $B^+ \rightarrow K^+ \tau^\mp \mu^\pm$  do (both in the lepton and in the quark sector). A data sample of  $347 \text{ fb}^{-1}$  ( $383 \times 10^6 B\bar{B}$  pairs) has been used. The  $B_{tag}$  meson is fully reconstructed in hadronic final states,

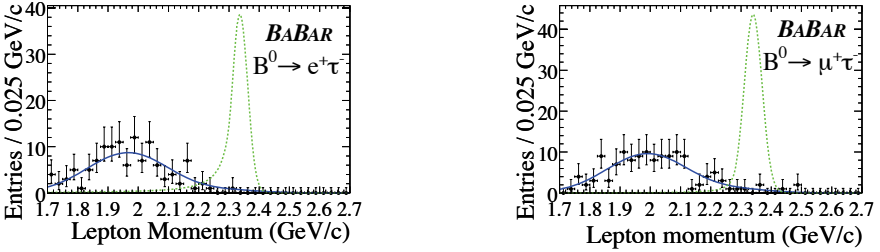


Figure 3: *The unbinned ML fits on the lepton momentum in the  $B_{sig}$  rest frame (e-channel on the left,  $\mu$ -channel on the right), for  $B^0 \rightarrow (e, \mu)^\pm \tau^\mp$  analysis. The dashed line represent the signal PDF with an arbitrary normalization, the solid line shows the background shape and the dots are the data.*

while in the signal side a kaon candidate with opposite charge with respect to the  $B_{tag}$ , a muon and a third track with opposite charge with respect to the muon (identified as one of the  $\tau$  daughter) are required. Only 1-prong  $\tau$  decays ( $\tau \rightarrow e\nu_e\nu_\tau, \mu\nu_\mu\nu_\tau, \pi\nu_\tau$ ) are considered, in order to reject combinatorial background. Having computed the  $B_{sig}$  momentum in the CM frame as  $-\vec{p}_{B_{tag}}$ , the kinematics of the  $\tau$  is completely inferred by  $B_{sig}$ ,  $K$  and  $\mu$  momenta. PID criteria are required in the three tracks reconstruction. The main  $B\bar{B}$  background contributions that survive the selection, are semileptonic  $B$  decays with signature identical to the signal one, mainly  $B^+ \rightarrow \bar{D}^0\mu^+\nu_\mu$  (where the  $\bar{D}^0$  decays to  $K^+\pi^-$  or to  $K\ell\nu_\ell$  and the  $\pi$  or the  $\mu$  coming from the  $D$  meson is identified as the  $\tau$  daughter) and  $B \rightarrow (c\bar{c})K$  decays (in which the  $c\bar{c}$  resonance produce a muon pair). To reject this two contributions, cuts on the invariant masses of the kaon and the oppositely charged tracks and of the two non-kaon tracks are applied. The continuum background is suppressed using a likelihood ratio defined by event shape information, PID on the leptons and the signal side neutral energy. Signal yield is estimated by cutting and counting in the  $m_\tau$  signal region ( $[1.65, 1.90] GeV/c^2$ ), the background is evaluated from the number of events outside this region (sideband) and the signal-to-sideband ratio obtained from background MC. The number of observed events in data is consistent with the background-only hypothesis and an upper limit on the BR of  $7.7 \times 10^{-5}$  is set. The results are summarized in Table 4.

Table 4: Results for  $B^0 \rightarrow \ell^+ \ell'^-$ ,  $B^0 \rightarrow \ell^\pm \tau^\mp$ , and  $B^+ \rightarrow K^+ \tau^\mp \mu^\pm$  analysis: efficiency, number of signal events, 90% CL UL on the BR are listed. Note that  $\epsilon_{\ell\ell'}$  and  $\epsilon_{K\tau\mu}$  represent the signal efficiency while  $\epsilon$  for the  $B^0 \rightarrow \ell^\pm \tau^\mp$  incorporates also the tag efficiency.

$B^0 \rightarrow \ell^+ \ell'^-$			
channel	$\epsilon_{\ell\ell'}(\%)$	$N_{\ell\ell'}$	$UL(BR) \times 10^{-8}$
$B^0 \rightarrow e^+ e^-$	$16.6 \pm 0.3$	$0.6 \pm 2.1$	11.3
$B^0 \rightarrow \mu^+ \mu^-$	$15.7 \pm 0.2$	$-4.9 \pm 1.4$	5.2
$B^0 \rightarrow e^\pm \mu^\mp$	$17.1 \pm 0.2$	$1.1 \pm 1.8$	9.2
$B^0 \rightarrow \ell^\pm \tau^\mp$			
channel	$\epsilon(\times 10^5)$	$N_{\ell\tau}$	$UL(BR) \times 10^{-5}$
$B^0 \rightarrow e^+ \tau^-$	$32 \pm 2$	$0.02 \pm 0.01$	2.8
$B^0 \rightarrow \mu^+ \tau^-$	$27 \pm 2$	$0.01 \pm 0.01$	2.2
$B^+ \rightarrow K^+ \tau^\mp \mu^\pm$			
$\tau$ channel	$\epsilon_{K\tau\mu}(\%)$	$Nb_{exp}; N_{obs}$	$UL(BR) \times 10^{-5}$
electron	$3.28 \pm 0.25$	$0.5 \pm 0.3; 1$	7.7
muon	$2.09 \pm 0.21$	$0.6 \pm 0.3; 0$	
pion	$2.18 \pm 0.26$	$1.8 \pm 0.6; 2$	
all			

## 4 Conclusions

Observation of LF violation in  $\tau$  and  $B$  decays would be an unambiguous signature of NP, anyhow stringent UL can constraint NP parameters and disentangle between different scenario. In this article we have presented the latest results from *BABAR*. Two analysis on  $\tau$  channel have recently been published:  $\tau^- \rightarrow \ell^- \ell^+ \ell^-$  and  $\tau^\pm \rightarrow (e, \mu)^\pm \omega$ . Many other neutrinoless  $\tau$  transitions have been investigated: no evidence for signal has been found and ULs of the order of  $10^{-8}$  have been set. Some of these analysis will be updated on the full *BABAR* dataset, and a consistent improvement can be achieved by a Super Flavor factory. On the  $B$  sector three results have been shown and the following UL have been set:  $BR(B^0 \rightarrow e^\pm \mu^\mp) < 9.2 \times 10^{-8}$ ,  $BR(B^0 \rightarrow (e, \mu)^\pm \tau^\mp) < (2.8, 2.2) \times 10^{-5}$ , and  $BR(B^+ \rightarrow K^+ \tau^\mp \mu^\pm) < 7.7 \times 10^{-5}$ . Preliminary studies show that a Super Flavor Factory can push the last two ULs down to  $10^{-7}$  with a datasample of  $75 ab^{-1}$  9).

## 5 Acknowledgments

The author wishes to thank the conference organizers for an enjoyable and well organize workshop. This work is supported by DOE and NSF (USA), NSERC (Canada), IHEP (China), CEA and CNRS-IN2P3 (France), BMBF and DFG (Germany), INFN (Italy), FOM (The Netherlands), NFR (Norway), MIST (Russia), MEC (Spain), and PPARC (United Kingdom).

## References

1. Y. Fukuda *et al* [Super-Kamiokand Collab.], Phys. Rev. Lett. **81**, 1562 (1998); Q.R. Ahmad *et al* [SNO Collab.], Phys. Rev. Lett. **89**, 011301 (2002); M.H. Ahn *et al* [K2K Collab.], Phys. Rev. Lett. **90**, 041801 (2003); K. Eguchi *et al* [KamLAND Collab.], Phys. Rev. Lett. **90**, 021802 (2003);
2. B. Auber *et al* [BABAR Collab.], Nucl. Instrum. Methods Phys. Res. Sec. A **479**, 1 (2002)
3. B.W. Lee and R.E. Shrock, Phys. Rev. D **16**, 1444 (1997); T.C. Cheng and L. Li, Phys. Rev. Lett. **45**, 1908 (1980); X. Pham, Eur. Phys. J. **C8**, 513 (1999);
4. A. Dedes, J.R. Ellis, and M. Raidal, Phys. Lett. B **549**, 159 (2002); A. Brignole and A. Rossi, Phys. Lett. B **566**, 217 (2003);
5. G. Cvetič, C.O. Dib, C. Kim, and J. Kim, Phys. Rev. D **74**, 93011 (2006)
6. C. Yue, Y. Zhang, L. Liu Phys. Lett. B **547**, 252 (2002);
7. A. Masiero, S.K. Vempati, and O. Vives, AIP Conf. Proc. **805**, 99 (2006); T. Fukuyama, T. Kikuchi, and N. Okada, Phys. Rev. D **68**, 33012 (2003)
8. J.R. Ellis, J. Hisano, M. Raidal, and Y. Shimizu Phys. Rev. D **66**, 115013 (2002)
9. M. Bona *et al*, hep-ex/07090451 (2007)
10. B. Aubert *et al* [BABAR Collab.], Phys. Rev. Lett. **99**, 251803 (2007)
11. B. Aubert *et al* [BABAR Collab.], Phys. Rev. Lett. **100**, 071802 (2008)

12. B. Aubert *et al* [*BABAR* Collab.], Phys. Rev. Lett. **96**, 041802 (2006)
13. B. Aubert *et al* [*BABAR* Collab.], Phys. Rev. Lett. **98**, 061803 (2007)
14. B. Aubert *et al* [*BABAR* Collab.], Phys. Rev. Lett. **95**, 191801 (2005)
15. B. Aubert *et al* [Belle Collab.], hep-ex/07050650
16. B. Aubert *et al* [Belle Collab.], Phys. Lett. B **648**, 341 (2007)
17. B. Aubert *et al* [Belle Collab.], Phys. Lett. B **640**, 138 (2006)
18. B. Aubert *et al* [Belle Collab.], Phys. Lett. B **660**, 154 (2008)
19. B. Aubert *et al* [Belle Collab.], hep-ex/07083276
20. B. Aubert *et al* [*BABAR* Collab.], Phys. Rev. D **77**, 032007 (2008)
21. A.J. Buras *et al*, Phys. Lett. B **500**, 161 (2001)
22. A.J. Buras, Acta Phys. Polon. B **34**, 5615 (2003); G. D'Ambrosio *et al*, Nucl. Phys. B **645**, 155 (2002)
23. B. Aubert *et al* [*BABAR* Collab.], hep-ex/08010697
24. W.S. Hou, Phys. Rev. D **48**, 2342 (1993)
25. B. Aubert *et al* [*BABAR* Collab.], Phys. Rev. Lett. **99**, 201801 (2007)
26. M. Sher and Y. Yuan, Phys. Rev. D **44**, 1461 (1991); T.P. Cheng and M. Sher, Phys. Rev. D **35**, 3484 (1987)

# PHYSICS BEYOND THE STANDARD MODEL IN CMS AT THE START OF THE LHC

Norbert Neumeister

*Department of Physics, Purdue University, West Lafayette IN, USA*

## **Abstract**

While the Standard Model of Particle Physics has been well tested and verified with high precision within the current energy limits of present day colliders, there are several reasons to expect that the Standard Model is an incomplete theory and that new phenomena should appear at the TeV energy scale. The Large Hadron Collider (LHC) is in its final stage of commissioning and first collisions are expected by mid-2008. The CMS detector is a general purpose experiments at the LHC and will be used to search for signatures of new Gauge Bosons, Extra Dimensions and other processes beyond the Standard Model. The potential of CMS to observe possible new physics at this new energy frontier and the challenges and strategies for these searches are discussed. The focus will be on searches for new physics with the initial data collected at the LHC.

## 1 Introduction

The Compact Muon Solenoid (CMS) experiment <sup>1)</sup> is one of the two general-purpose experiments, which will operate at the LHC and is currently in the construction phase at CERN. Its prime goals are to explore physics at the TeV scale and to study the mechanism of electroweak symmetry breaking. The LHC is designed to provide proton-proton collisions with a luminosity of up to  $10^{34} \text{ cm}^{-2}\text{s}^{-1}$  and a center-of mass energy of 14 TeV. Here we will focus on a start-up luminosity of  $\mathcal{L} = 10^{32} \text{ cm}^{-2}\text{s}^{-1}$ .

High-mass resonances decaying into lepton or photon pairs provide some of the most important discovery potentials beyond the Standard Model at the LHC. They are predicated in numerous models. Extra dimension models <sup>4, 5, 6)</sup> propose ways to solve one of the most fundamental problems of the Standard Model – the hierarchy problem. Basically all extra dimension models predict new resonances that can be accessible at the LHC.

In order to extract the new physics at an early stage of LHC, the key point is to understand the detector and any unanticipated limitations as soon as possible. Since both the machine and the detector comprise new challenges, it is essential to concentrate on signatures, which can be understood already with a partially commissioned detector and only a few  $\text{pb}^{-1}$  of data. The main signatures of interest for discoveries of new physics are high momentum leptons, photons, jets and missing transverse energy. The CMS detector was designed with a flexible, robust and redundant muon system. Therefore dimuons are an ideal signature for the initial phase of research at the LHC. We will discuss the search for dimuon resonances as an example for a search for new physics in the first data-taking phase with a rather low luminosity.

## 2 Dimuon Searches

Many scenarios beyond the Standard Model are expected to manifest themselves through modifications in the mass spectrum of high-mass dimuon pairs. The experiments at the LHC are going to be the first opportunity to search for new resonances in a mass range significantly larger than  $1 \text{ TeV}/c^2$ .

We discuss the potential of the CMS experiment to discover a representative set of additional heavy neutral gauge bosons  $Z'$  (spin 1) predicted by grand unified theories <sup>3)</sup>, as well as gravitons  $G^*$  (spin 2) arising in the Randall-

Sundrum (RS) model of extra dimensions<sup>5, 6</sup>). Two different  $Z'$  models are considered:  $Z_{SSM}$  within the Sequential Standard Model (SSM), which has the same couplings as the Standard Model  $Z^0$  and is often used as a benchmark by experimentalists and  $Z_\psi$ , arising in  $E_6$  and  $SO(10)$  GUT groups. The RS model suggests that excited massive graviton states are strongly coupled to ordinary particles (not suppressed below the Planckian scale like for the ordinary graviton in the usual description of gravity) and can significantly contribute to the Standard Model processes above the fundamental scale. The ability to test experimentally the RS predictions depends on the model parameter  $c = k/\bar{M}_{\text{Pl}}$ , which controls the coupling of the RS graviton to ordinary particles: both graviton production cross section and its decay width scale as  $c^2$ . The RS model graviton can decay in the dilepton, dijet or diboson channel. In the dilepton case the signature would be a series of narrow resonances in the dilepton invariant mass distribution. Here we focus on the CMS discovery potential for the *start-up luminosity*  $\mathcal{L} = 10^{32} \text{ cm}^{-2} \text{ s}^{-1}$ . To include systematic uncertainties in a realistic way we use the description of the detector alignment and calibration expected at the early stages of data-taking.

The dimuon decay is a golden channel for  $Z'$  and  $G^*$  discoveries. In both cases the dominant background arises from Drell-Yan lepton pair production, whereas contributions from  $t\bar{t}$  and from vector boson pair production are significantly smaller and are highly suppressed by selection cuts. The momentum resolution of the detector plays a key role in separating the signal from the background. The accurate momentum reconstruction of very high- $p_T$  (TeV) muons is challenging because of catastrophic energy loss and severe electromagnetic showers in the muon system. The CMS muon reconstruction algorithms have been optimized to deal with this problem.

Once a new high-mass resonance is discovered, its observables can be used in the attempt to identify the theoretical framework to which it belongs. The measurement of the forward-backward asymmetries of leptonic decay products, both at the resonance peak and off the peak, is a powerful tool to identify a  $Z'$ . Spin discrimination of new heavy resonances based on an unbinned likelihood ratio statistic incorporating the angles of the decay products typically require more signal events than one could hope to collect with the initial LHC luminosity and are therefore not discussed.

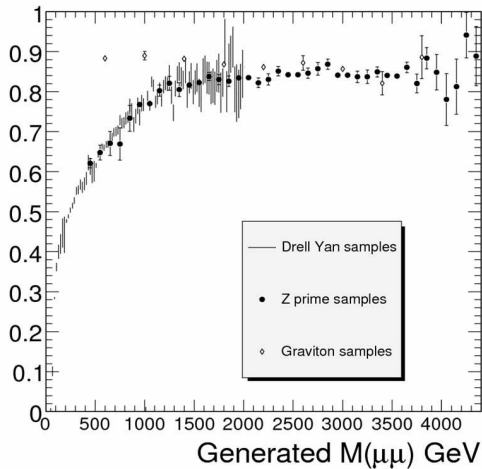


Figure 1: Overall selection and reconstruction efficiency for Drell-Yan (bars),  $Z_{SSM}$  (closed circles), and  $G^*$  (open circles) dimuon events as a function of the  $\mu^+\mu^-$  invariant mass.

## 2.1 Event Selection and Acceptance

In order to select efficiently a pure sample of high-mass dimuon candidates, the following requirements are imposed:

- The event passes the logical OR of single-muon and dimuon non-isolated trigger paths.
- It contains at least one pair of oppositely-charged muons reconstructed offline.
- The transverse momentum  $p_T$  of each muon track in a pair is larger than 20 GeV/ $c$ .
- Both muons are isolated in the tracker.

The overall selection efficiency, including acceptance effects, is shown in Fig. 1. Efficiencies for Drell-Yan and  $Z'$  dimuon events are very similar: they increase from about 50% at 200 GeV/ $c^2$  to about 80% at 2 TeV/ $c^2$ . Efficiency

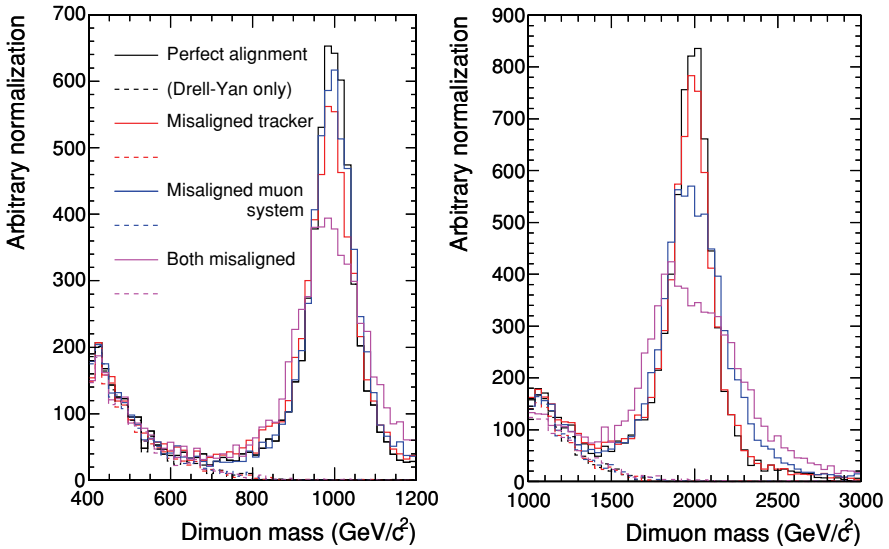


Figure 2: *Dimuon invariant mass spectra for 1 and 2 TeV/c<sup>2</sup> Z<sub>SSM</sub> resonances and the Drell-Yan background for different alignment scenarios: using ideal alignment of both the silicon tracker and the muon system; assuming ideal alignment for one detector and applying the misalignment expected at the initial stages of the data taking to the other one; and for the case when both detectors are misaligned. All histograms within each panel represent the same events under different misalignment scenarios, and are therefore normalized to the same (arbitrary) integrated luminosity.*

for  $G^* \rightarrow \mu^+ \mu^-$  events is close to 90% at masses below 1 TeV/c<sup>2</sup>, in accordance with a high geometrical acceptance in this region.

Once a sample of candidate events is selected, a search for new particles is performed by comparing the observed invariant-mass distribution of opposite-sign muon pairs,  $M_{\mu\mu}$ , with that expected from Standard Model processes for  $M_{\mu\mu} > 200$  GeV/c<sup>2</sup>. If more than one dimuon candidate can be formed in the selected event (in the absence of pile-up, this happens in less than 1% of events), the one with the highest value of  $M_{\mu\mu}$  is used.

The geometrical acceptance for the signal and backgrounds is determined by the acceptance of the muon system used to identify muons. The fraction of

Drell-Yan  $\mu^+\mu^-$  events with both muons within the full geometrical acceptance of the CMS muon system ( $|\eta| < 2.4$ ) increases from 56% at an invariant mass of 200 GeV/ $c^2$  to about 95% at very high masses. The acceptance of  $Z' \rightarrow \mu^+\mu^-$  events is very similar to that of the Drell-Yan dimuons, whereas the acceptance of  $G^* \rightarrow \mu^+\mu^-$  events is noticeably higher: the difference is as big as 25% at the mass values of a few hundred GeV/ $c^2$  and gets smaller with increasing mass. The explanation of this difference lies in the different production mechanisms for  $Z'$  bosons and  $G^*$ . At leading order, the only production mechanism for  $Z'$  bosons is the quark-antiquark scattering,  $q\bar{q} \rightarrow Z' \rightarrow \mu^+\mu^-$ . Gravitons are produced mainly via the  $gg \rightarrow G^* \rightarrow \mu^+\mu^-$  gluon-gluon fusion process at lower masses, while the  $q\bar{q} \rightarrow G^* \rightarrow \mu^+\mu^-$  contribution dominates at higher masses. The dimuons produced via quark-antiquark processes have on average lower acceptance than the ones produced via gluon-gluon fusion. This is due to the presence of forward events where a high-momentum valence quark interacts with an antiquark to produce a resonance boosted along the  $z$ -axis, resulting in lower acceptance. In addition, there is a small difference arising from the different angular distributions for the decay products of spin-1  $Z'$  bosons and spin-2  $G^*$ .

## 2.2 Invariant Mass Resolution and Detector Misalignment

The precision of reconstructed dimuon masses, and therefore the statistical significance of a possible resonance peak, would be impaired by imperfect alignment of the silicon tracker and the muon system. Small curvatures of high-momentum tracks are poorly constrained if the alignment of sensor positions is uncertain, a situation we expect to improve with data. To study the influence of misalignment effects on detector performance and the resulting physics reach, tools to displace and rotate the silicon tracker modules and muon chambers at the reconstruction level were implemented in the reconstruction software. To describe the expected misalignments and their improvement with time and integrated luminosity, several misalignment scenarios were developed in the CMS reconstruction framework and subsequently used in performance studies. These scenarios simulate the detector alignment expected to be achieved with 10 and 100 pb $^{-1}$  of integrated luminosity.

The dimuon mass spectra for 1 and 2 TeV/ $c^2$   $Z_{SSM}$  resonances and the corresponding Drell-Yan background are shown in figure 2, illustrating the

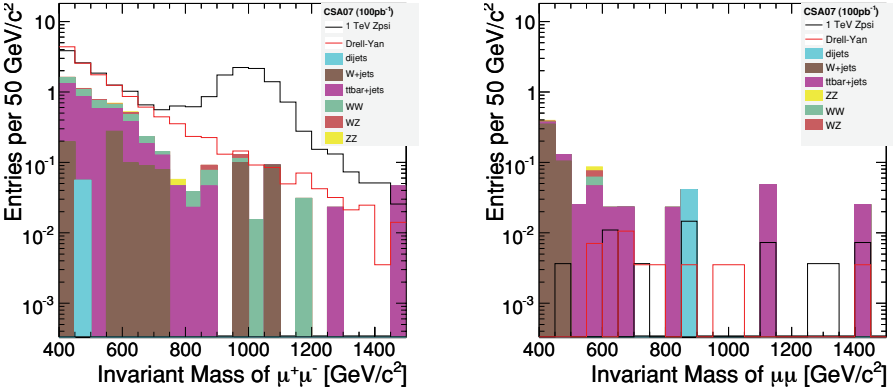


Figure 3: *Invariant-mass distributions for opposite-sign (left) and same-sign (right) dimuons from 1 TeV/c<sup>2</sup> Z<sub>ψ</sub> and different background sources expected for L<sub>int</sub> = 100 pb<sup>-1</sup> after applying all event-selection criteria. The spectrum is shown in the mass range 400 < M<sub>μμ</sub> < 1500 GeV/c<sup>2</sup>. All histograms except for Drell-Yan and Z<sub>ψ</sub> are stacked.*

relative importance of tracker alignment and muon system alignment in the expected alignment scenarios. The effect of muon alignment has a stronger dependence on momentum at these scales because long lever arms are needed to resolve small track curvatures. While the expected misalignment smears the distribution of the signal peak, the shape of the Drell-Yan mass spectrum remains largely unaffected.

### 2.3 Backgrounds

The dominant (and irreducible) source of background to new high-mass dimuon resonances is the Drell-Yan production of muon pairs,  $pp \rightarrow \gamma^*/Z^0 \rightarrow \mu^+\mu^-$ . In addition to the Drell-Yan production a variety of backgrounds from other sources have been studied. Invariant-mass distributions for opposite-sign and same-sign dimuons from different background sources passing all selection criteria and weighted to correspond to an integrated luminosity of 100 pb<sup>-1</sup> are shown in figure 3 in comparison with the mass spectrum expected for a 1 TeV/c<sup>2</sup> Z<sub>ψ</sub>. In the mass range  $M_{\mu\mu} > 400$  GeV/c<sup>2</sup>, the most significant background after the Drell-Yan is  $t\bar{t}$ . The dijet background is strongly suppressed by the

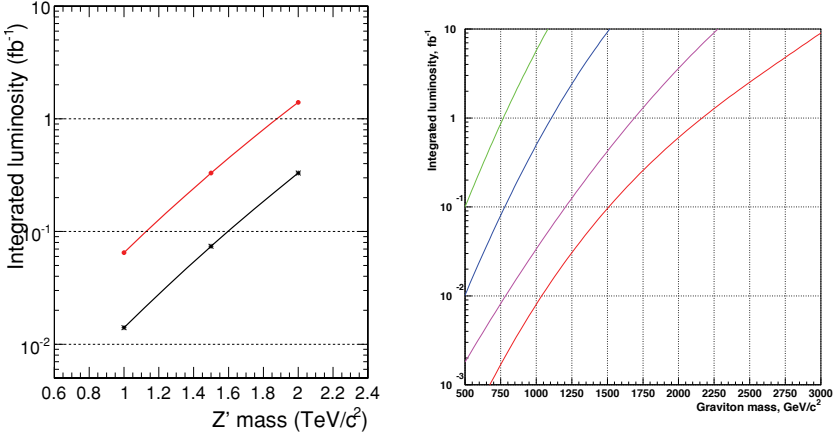


Figure 4: *Integrated luminosity needed to reach  $5\sigma$  significance ( $S_{\mathcal{L}} = 5$ ) as a function of the mass of the resonance for a)  $Z_\psi$  (top) and  $Z_{SSM}$  (bottom), and b) RS gravitons with the coupling constant  $c$  of (from top to bottom) 0.01, 0.02, 0.05, and 0.1.*

soft isolation cut, whereby the sum of the  $p_T$  of all tracks around each muon in a cone of  $\Delta R = \sqrt{(\Delta\phi)^2 + (\Delta\eta)^2} < 0.3$  is required to be less than 10 GeV/ $c$ . The remaining admixture of dijet events can be evaluated in data from samples of same-sign and opposite-sign events rejected by the isolation cut. Another useful control sample for studies of misidentified and mismeasured muons is the sample of same-sign dimuons passing all selection criteria. Non-Drell-Yan backgrounds can be further suppressed by muon-quality cuts, jet-veto criteria, missing- $E_T$  cuts, requirements that the two muons be back-to-back in the plane transverse to the beam direction and originate from a common vertex, and others.

## 2.4 Discovery Potential

The fitting procedure and the significance estimators described in <sup>2)</sup> are used to evaluate the CMS discovery potential for new high-mass resonances in the dimuon decay mode. The integrated luminosity needed to reach  $5\sigma$  significance as a function of the mass of the resonance is shown in figure 4 for a) two studied  $Z'$  models and b) Randall-Sundrum gravitons with various values of the model parameter  $c$ .

An unbinned likelihood fitter with a fitting function very similar to that of the signal-significance technique is used to set limits in the absence of a

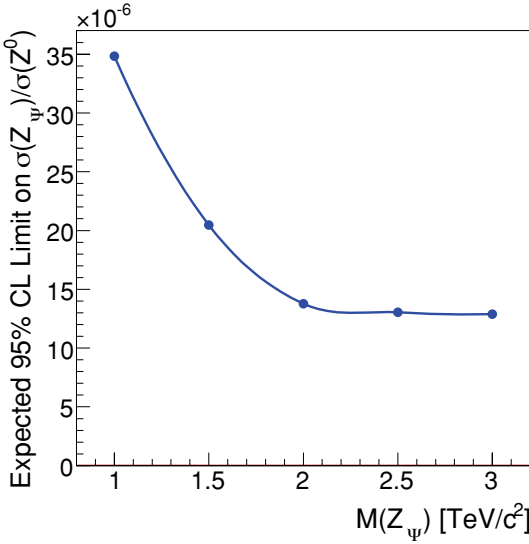


Figure 5: *Expected 95% CL limits on the ratio  $(\sigma(pp \rightarrow Z') \cdot \mathcal{B}(Z' \rightarrow \mu^+\mu^-))/(\sigma(pp \rightarrow Z^0) \cdot \mathcal{B}(Z^0 \rightarrow \mu^+\mu^-))$  as a function of  $Z'$  mass, assuming no signal events present in the sample.*

signal. Limits on the number of signal events are set using the same likelihood-ratio-based discriminant, and then translated to the limits on the ratio of cross sections for production of new resonances relative to  $Z^0$  production. Expected limits for  $Z'$  bosons are shown in figure 5, for the detector alignment expected to be achieved with  $100 \text{ pb}^{-1}$  of integrated luminosity.

The main sources of systematic uncertainties are expected to be a) theoretical uncertainties (parton distributions, higher-order corrections, etc.), b) uncertainties arising from an imperfect knowledge of the detector (alignment, calibration, magnetic field), and c) uncertainties in the fitting procedure (background shape, functional forms of pdfs, mass resolution, etc.). Evaluation of these uncertainties and of their impact on the signal observability is discussed in 2).

### 3 Conclusions

The initial phase of running will be crucial for CMS. All sub-detectors have to be understood and calibrated and the Standard Model processes have to be measured. The CMS collaboration is in the process of getting ready for this exciting period, by validating the software and preparing data analysis while installing and commissioning the detector. It has been demonstrated that signals of new physics could already be discovered with an integrated luminosity of about  $1 \text{ fb}^{-1}$ . Dilepton signatures are one of the most promising signatures for the search for new physics in the initial phase of the LHC.

### References

1. CMS Collaboration, CERN-LHCC-94-38 (1994).
2. CMS Collaboration, CMS Technical Design Report, volume II: Physics Performance, *J. Phys.* **G34**, 995–1579 (2007).
3. A. Leike, The Phenomenology of Extra Neutral Gauge Bosons, *Phys. Rept.* **317**, 143–250 (1999).
4. N. Arkani-Hamed, S. Dimopoulos and C. Dvali, *Phys. Lett.* **B 429**, 261 (1998).
5. L. Randall and R. Sundrum, *Phys. Rev. Lett.* **83**, 3370–3373 (1999).
6. L. Randall and R. Sundrum, *Phys. Rev. Lett.* **83**, 4690–4693 (1999).

## A MAXIMAL MASS MODEL\*

Vladimir Kadyshevsky

*Joint Institute for Nuclear Research, Dubna*

Matey Mateev

*University of Sofia "St. Kliment Ohridsky"*

Vasyliy Rodionov

*Moscow State Geological Prospecting University*

Alexander Sorin

*Moscow State Geological Prospecting University*

### Abstract

We investigate the possibility to construct a generalization of the Standard Model which we call the Maximal Mass Model because it contains a limiting mass  $M$  for its fundamental constituents. The parameter  $M$  is considered as a new universal physical constant of Nature and, therefore, is called the fundamental mass. It is introduced in a purely geometric way, like the velocity of light as a maximal velocity in the special relativity. If one chooses the Euclidean formulation of quantum field theory, the adequate realization of the limiting mass hypothesis is reduced to the choice of the de Sitter geometry as the geometry of the 4-momentum space. All fields defined in de Sitter p-space in configurational space obey five dimensional Klein-Gordon type equation with the fundamental mass  $M$  as a mass parameter. The role of dynamical field variables is played by the Cauchy initial conditions given at  $x_5 = 0$ , guaranteeing the locality and gauge invariance principles. The formulation of the theory of scalar and spinor fields corresponding to the geometrical requirements is considered in some detail. By a simple example it is demonstrated that the spontaneous symmetry breaking mechanism leads to renormalization of the fundamental mass  $M$ . A new geometric concept of the chirality of the fermion fields is introduced. It would be responsible for new measurable effects at high energies  $E \geq M$ . Interaction terms of a new type are revealed due to the existence of the Higgs boson. The most intriguing prediction of the new approach is the possible existence of exotic fermions with no analogues in the SM, which may be a candidate for dark matter constituents.

## 1 Introductory remarks

For decades we have witnessed the impressive success of the Standard Model (SM) in explaining properties and regularities observed in experiments with elementary particles. The mathematical basis of the SM is local Lagrangian quantum field theory (QFT). The very concept of an elementary particle assumes that it does not have a composite structure. In agreement with the contemporary experimental data this structure has not been disclosed for any fundamental particles of the SM, up to distances of the order of  $10^{-16} - 10^{-17}$  cm. The adequate mathematical images of point like particles are the local quantized fields - boson and spinor. Particles are the quanta of the corresponding fields. In the framework of the SM these are leptons, quarks, vector bosons and the Higgs scalar, all characterized by certain values of mass, spin, electric charge, colour, isotopic spin, hypercharge, etc.

Intuitively it is clear that an elementary particle should carry small enough portions of different "charges" and "spins". In the theory this is guaranteed by assigning the local fields to the lowest representations of the corresponding groups.

As for the mass of the particle  $m$ , this quantity is the Casimir operator of the *noncompact* Poincaré group and in the unitary representations of this group, used in QFT, they may have arbitrary values in the interval  $0 \leq m < \infty$ . In the SM one observes a great variety in the mass values. For example, t-quark is more than 300000 times heavier than the electron. In this situation the question naturally arises: up to what values of mass one may apply the concept of a local quantum field? Formally, the contemporary QFT remains a logically perfect scheme and its mathematical structure does not change at all up to arbitrarily large values of masses of quanta. For instance, the free Klein-Gordon equation for the one component real scalar field  $\varphi(x)$  has always the form

$$(\square + m^2)\varphi(x) = 0. \quad (1)$$

Hence, after standard Fourier transform

$$\varphi(x) = \frac{1}{(2\pi)^{3/2}} \int e^{-ip_\mu x^\mu} \varphi(p) d^4p \quad (p_\mu x^\mu = p^0 x^0 - \mathbf{p} \cdot \mathbf{x}) \quad (2)$$

we find the equation of motion in the Minkowski momentum 4-space:

$$(m^2 - p^2)\varphi(p) = 0, \quad p^2 = p_0^2 - \mathbf{p}^2. \quad (3)$$

From a geometric point of view  $m$  is the radius of the "mass shell" hyperboloid

$$m^2 = p_0^2 - \mathbf{p}^2, \quad (4)$$

where the field  $\varphi(p)$  is defined and in the Minkowski momentum space one may embed hyperboloids of type (4) of an arbitrary radius.

In 1965 M. A. Markov <sup>1)</sup> pioneered the hypothesis according to which the mass spectrum of the elementary particles should be cut off at the Planck mass  $m_{Planck} = 10^{19} GeV$  :

$$m \leq m_{Planck}. \quad (5)$$

The particles with the limiting mass  $m = m_{Planck}$ , named by the author "maximons", should play a special role in the world of elementary particles. However, Markov's original condition (5) was purely phenomenological and he used standard field theoretical techniques even for describing the maximon.

In <sup>2) - 8)</sup> a more radical approach was developed. Markov's idea of the existence of a maximal value for the masses of elementary particles was understood as a new fundamental principle of Nature, which similarly to the relativistic and quantum postulates should underlie QFT. Doing this the condition of finiteness of the mass spectrum should be introduced by the relation:

$$m \leq M, \quad (6)$$

where the maximal mass parameter  $M$  called the "**fundamental mass**" is a **new universal physical constant**.

A **new concept** of a local quantum field has been developed on the basis of (6) and on simple geometric arguments the corresponding Lagrangians were constructed and an adequate formulation of the principle of local gauge invariance was found. It was also demonstrated that the fundamental mass  $M$  in the new approach plays the role of an independent universal scale in the region of ultrahigh energies  $E \geq M$ .

It is worth emphasizing that here, due to eq(6), the Compton wave length of a particle  $\lambda_C = \hbar/mc$  cannot be smaller than the "**fundamental length**"  $l = \hbar/Mc$ . According to Newton and Wigner <sup>15)</sup>, the parameter  $\lambda_C$  characterizes the dimensions of the region of space in which a relativistic particle of mass  $m$  can be localized. Therefore, the fundamental length  $l$  introduces into the theory a universal limit on the accuracy of localization in space of elementary particles.

The objective of the present work, in few words, is to include the principle of maximal mass (6) into the basic principles of the Standard Model. The new scheme appearing in this way, which we called the Maximal Mass Model, from our point of view is interesting already because in it the trusted methods of the local gauge QFT are organically bound to the elegant, though not as popular, geometric ideas.

## 2 Boson fields in de Sitter momentum space

Let us go back to the free one component real scalar field we considered above (1 - 3). We shall suppose that its mass  $m$  satisfies the condition (6). How should one modify the equations of motion in order that the existence of the bound (6) should become as evident as it is the limitation  $v \leq c$  in the special theory of relativity? In the latter case everything is explained in a simple way: the relativization of the 3-dimensional velocity space is equivalent to transition in this space from Euclidean to Lobachevsky geometry realized on the 4-dimensional hyperboloid <sup>1</sup>(4). Let us act in a similar way and substitute the 4-dimensional Minkowski momentum space, which is used in the standard QFT, by the anti de Sitter momentum space realized on the 5-hyperboloid:

$$p_0^2 - \mathbf{p}^2 + p_5^2 = M^2. \quad (7)$$

We shall suppose that in the p-representation our scalar field is defined just on the surface (7), i.e., it is a function of five variables  $(p_0, \mathbf{p}, p_5)$ , which are connected by the relation (7):

$$\delta(p_0^2 - \mathbf{p}^2 + p_5^2 - M^2)\varphi(p_0, \mathbf{p}, p_5). \quad (8)$$

The energy  $p_0$  and the 3-momentum  $\mathbf{p}$  here preserve their usual meaning and the mass shell relation (4) is satisfied as well. Therefore, for the field considered  $\varphi(p_0, \mathbf{p}, p_5)$  the condition (6) is always fulfilled.

Clearly in eq. (8) the specification of a single function  $\varphi(p_0, \mathbf{p}, p_5)$  of five variables  $(p_\mu, p_5)$  is equivalent to the definition of two independent functions  $\varphi_1(p)$  and  $\varphi_2(p)$  of the 4-momentum  $p_\mu$ :

$$\varphi(p_0, \mathbf{p}, p_5) \equiv \varphi(p, p_5) = \begin{pmatrix} \varphi(p, |p_5|) \\ \varphi(p, -|p_5|) \end{pmatrix} = \begin{pmatrix} \varphi_1(p) \\ \varphi_2(p) \end{pmatrix}, |p_5| = \sqrt{M^2 - p^2}. \quad (9)$$

The appearance of the new discrete degree of freedom  $p_5/|p_5|$  and the associated doubling of the number of field variables is important feature of the new approach. It must be taken into account in the search for the equation of motion for the free field in de Sitter momentum space. Due to the mass shell relation (4) the Klein - Gordon equation (3) should also be satisfied by the field  $\varphi(p_0, \mathbf{p}, p_5)$  :

$$(m^2 - p_0^2 + \mathbf{p}^2)\varphi(p_0, \mathbf{p}, p_5) = 0. \quad (10)$$

From our point of view this relation is unsatisfactory for two reasons:

1. It does not reflect the bounded mass condition (6).

---

<sup>1</sup>To be exact on the upper sheet of this hyperboloid.

2. It can not be used to determine the dependence of the field on the new quantum number  $p_5/|p_5|$  in order to distinguish between the components  $\varphi_1(p)$  and  $\varphi_2(p)$ .

Here we notice that, because of (7), eq.(10) can be written as:

$$(p_5 + M \cos \mu)(p_5 - M \cos \mu)\varphi(p, p_5) = 0, \quad \cos \mu = \sqrt{1 - \frac{m^2}{M^2}}. \quad (11)$$

Now, following the Dirac trick we postulate the equation of motion under question in the form:

$$2M(p_5 - M \cos \mu)\varphi(p, p_5) = 0. \quad (12)$$

Clearly, eq. (12) has none of the enumerated defects of the standard Klein-Gordon equation (3). However, equation (3) is still satisfied by the field  $\varphi(p, p_5)$ .

From eqs. (12) and (9) it follows that

$$2M(|p_5| - M \cos \mu)\varphi_1(p) = 0, \quad (13)$$

$$2M(|p_5| + M \cos \mu)\varphi_2(p) = 0,$$

and we obtain:

$$\begin{aligned} \varphi_1(p) &= \delta(p^2 - m^2)\tilde{\varphi}_1(p) \\ \varphi_2(p) &= 0 \end{aligned} \quad (14)$$

Therefore, the free field  $\varphi(p, p_5)$  defined in the anti de Sitter momentum space (7) describes the same free scalar particles of mass  $m$  as the field  $\varphi(p)$  in the Minkowski p-space, with the only difference that now we necessarily have  $m \leq M$ . The two-component structure (9) of the new field does not manifest itself on the mass shell, owing to (14). However, it will play an important role when the fields interact, i.e., off the mass shell.

Now we face the problem of constructing the action corresponding to eq. (12) and transforming it to the configuration representation.

Due to mainly technical reasons <sup>2</sup> in the following we shall use the Euclidean formulation of the theory, which appears as an analytical continuation to purely imaginary energies:

$$p_0 \rightarrow ip_4. \quad (15)$$

In this case, instead of the anti de Sitter p-space (7), we shall work with de Sitter p-space

$$-p_n^2 + p_5^2 = M^2, \quad n = 1, 2, 3, 4. \quad (16)$$

---

<sup>2</sup>The corresponding comments on the topic will be given a bit later.

Obviously,

$$p_5 = \pm \sqrt{M^2 + p^2}. \quad (17)$$

If one uses eq. (16), the Euclidean Klein-Gordon operator  $m^2 + p^2$  may be written, similarly to (11), in the following factorized form:

$$m^2 + p^2 = (p_5 + M \cos \mu)(p_5 - M \cos \mu). \quad (18)$$

Clearly, the nonnegative functional

$$S_0(M) = \pi M \times$$

$$\int \frac{d^4 p}{|p_5|} [\varphi_1^+(p) 2M(|p_5| - M \cos \mu) \varphi_1(p) + \varphi_2^+(p) 2M(|p_5| + M \cos \mu) \varphi_2(p)], \quad (19)$$

$$\varphi_{1,2}(p) \equiv \varphi(p, \pm |p_5|), \quad (20)$$

plays the role of the action integral of the free Euclidean field  $\varphi(p, p_5)$ . The action may be written also as a 5 - integral:

$$S_0(M) = 2\pi M \times$$

$$\int \varepsilon(p_5) \delta(p_L p^L - M^2) d^5 p [\varphi^+(p, p_5) 2M(p_5 - M \cos \mu) \varphi(p, p_5)], \quad (21)$$

$$L = 1, 2, 3, 4, 5,$$

where

$$\varepsilon(p_5) = \frac{p_5}{|p_5|}. \quad (22)$$

The Fourier transform and the configuration representation have a special role in this approach. First, we note that in the basic equation (16) which defines de Sitter p-space, all the components of the 5-momentum enter on equal footing. Therefore, the expression  $\delta(p_L p^L - M^2) \varphi(p, p_5)$ , which now replaces (8), may be Fourier transformed

$$\frac{2M}{(2\pi)^{3/2}} \int e^{-ip_K x^K} \delta(p_L p^L - M^2) \varphi(p, p_5) d^5 p = \varphi(x, x_5), \quad K, L = 1, 2, 3, 4, 5. \quad (23)$$

This function obviously satisfies the following differential equation in the **5-dimensional configuration space**:

$$\left( \frac{\partial^2}{\partial x_5^2} - \square + M^2 \right) \varphi(x, x_5) = 0. \quad (24)$$

Integration over  $p_5$  in (23) gives:

$$\varphi(x, x_5) = \frac{M}{(2\pi)^{3/2}} \int e^{ip_n x^n} \frac{d^4 p}{|p_5|} \left[ e^{-i|p_5|x^5} \varphi_1(p) + e^{i|p_5|x^5} \varphi_2(p) \right], \tag{25}$$

$$\varphi^+(x, x_5) = \varphi(x, -x_5),$$

from which we get:

$$\frac{i}{M} \frac{\partial \varphi(x, x_5)}{\partial x_5} = \frac{1}{(2\pi)^{3/2}} \int e^{ip_n x^n} d^4 p \left[ e^{-i|p_5|x^5} \varphi_1(p) - e^{i|p_5|x^5} \varphi_2(p) \right], \tag{26}$$

The four dimensional integrals (25) and (26) transform the fields  $\varphi_1(p)$  and  $\varphi_2(p)$  to the configuration representation. The inverse transforms have the form:

$$\varphi_1(p) = \frac{-i}{2M(2\pi)^{5/2}} \int e^{-ip_n x^n} d^4 x \left[ \varphi(x, x_5) \frac{\partial e^{i|p_5|x^5}}{\partial x_5} - e^{i|p_5|x^5} \frac{\partial \varphi(x, x_5)}{\partial x_5} \right],$$

$$\varphi_2(p) = \frac{i}{2M(2\pi)^{5/2}} \int e^{-ip_n x^n} d^4 x \left[ \varphi(x, x_5) \frac{\partial e^{-i|p_5|x^5}}{\partial x_5} - e^{-i|p_5|x^5} \frac{\partial \varphi(x, x_5)}{\partial x_5} \right]. \tag{27}$$

We note that the independent field variables

$$\varphi(x, 0) \equiv \varphi(x) = \frac{M}{(2\pi)^{3/2}} \int e^{ip_n x^n} d^4 p \frac{\varphi_1(p) + \varphi_2(p)}{|p_5|} \tag{28}$$

and

$$\frac{i}{M} \frac{\partial \varphi(x, 0)}{\partial x_5} \equiv \chi(x) = \frac{1}{(2\pi)^{3/2}} \int e^{ip_n x^n} d^4 p [\varphi_1(p) - \varphi_2(p)] \tag{29}$$

can be treated as initial Cauchy data on the surface  $x_5 = 0$  for the hyperbolic-type equation (24).

Now substituting eq.(27) into the action (19) we obtain

$$S_0(M) = \frac{1}{2} \int d^4 x \left[ \left| \frac{\partial \varphi(x, x_5)}{\partial x_n} \right|^2 + m^2 |\varphi(x, x_5)|^2 + \left| i \frac{\partial \varphi(x, x_5)}{\partial x_5} - M \cos \mu \varphi(x, x_5) \right|^2 \right]$$

$$\equiv \int L_0(x, x_5) d^4 x. \tag{30}$$

It is easily verified that due to eq. (24) the action (30) is independent of  $x_5$ :

$$\frac{\partial S_0(M)}{\partial x_5} = 0. \tag{31}$$

Therefore the variable  $x_5$  may be arbitrarily fixed and  $S_0(M)$  may be viewed as a functional of the corresponding initial Cauchy data for the equation (24).

For example, for  $x_5 = 0$  we have:

$$S_0(M) = \frac{1}{2} \int d^4 x \left[ \left( \frac{\partial \varphi(x)}{\partial x_n} \right)^2 + m^2 (\varphi(x))^2 + M^2 (\chi(x) - \cos \mu \varphi(x))^2 \right] \equiv \int L_0(x, M) d^4 x. \quad (32)$$

We have thus shown that in the developed approach the property of locality of the theory does not disappear, moreover it becomes even deeper, as it is extended to dependence on the extra fifth dimension  $x_5$ .

The new Lagrangian density  $L_0(x, x_5)$  [see (30)] is a Hermitian form constructed from  $\varphi(x, x_5)$  and the components of the 5-component gradient  $\frac{\partial \varphi(x)}{\partial x_L}$ , ( $L = 1, 2, 3, 4, 5$ ). It is clear that although  $L_0(x, x_5)$  depends explicitly on  $x_5$ , the theory essentially remains **four-dimensional** [see eq. (31) and (32)].

As may be seen from the transformations which have been made, the dependence of the action (32) on the two functional arguments  $\varphi(x)$  and  $\chi(x)$  is a direct consequence of the fact that in momentum space the field has a doublet structure  $\begin{pmatrix} \varphi_1(p) \\ \varphi_2(p) \end{pmatrix}$  due to the two possible values of  $p_5$ . However, the Lagrangian  $L_0(x, M)$  does not contain a kinetic term corresponding to the field  $\chi(x)$ . Therefore, this variable is just auxiliary.

The special role of the 5-dimensional configuration space in the new formalism is determined by the fact that the gauge symmetry transformations are localized now in it. The initial data for the equation (24)

$$\begin{pmatrix} \varphi(x, x_5) \\ \frac{i}{M} \frac{\partial \varphi(x, x_5)}{\partial x_5} \end{pmatrix}_{x_5 = \text{fixed value}} \quad (33)$$

are subject to these transformations.

Let us now discuss this point in more detail, supposing that the field  $\varphi(x, x_5)$  is not Hermitian and some internal symmetry group is associated with it:

$$\varphi' = U\varphi. \quad (34)$$

Upon localization of the group in the 5-dimensional x-space:

$$U \rightarrow U(x, x_5), \quad (35)$$

the following gauge transformation law arises for the initial data (33) on the

plane  $x_5 = 0$ :

$$\varphi'(x) = U(x, 0)\varphi(x), \tag{36}$$

$$\chi'(x) = \frac{i}{M} \frac{\partial U(x, 0)}{\partial x_5} \varphi(x) + U(x, 0)\chi(x).$$

The group character of the transformations (36) is obvious. The specific form of the matrix  $U(x, x_5)$  can be determined in the new theory of vector fields, which is a generalization of the standard theory in the spirit of our approach ( see 5).

It is clear that the equation (24) may be represented as a system of two equations of first order in the derivative  $\frac{\partial}{\partial x_5}$  10):

$$\left\{ \frac{i}{M} \frac{\partial}{\partial x_5} - \left[ \sigma_3 \left( 1 - \frac{\square}{2M^2} \right) - i\sigma_2 \frac{\square}{2M^2} \right] \right\} \phi(x, x_5) = 0, \tag{37}$$

where

$$\phi(x, x_5) = \begin{pmatrix} \frac{1}{2} \left[ \varphi(x, x_5) + \frac{i}{M} \frac{\partial \varphi(x, x_5)}{\partial x_5} \right] \\ \frac{1}{2} \left[ \varphi(x, x_5) - \frac{i}{M} \frac{\partial \varphi(x, x_5)}{\partial x_5} \right] \end{pmatrix} \equiv \begin{pmatrix} \phi_I(x, x_5) \\ \phi_{II}(x, x_5) \end{pmatrix}, \tag{38}$$

( $\sigma_i, i = 1, 2, 3$  are the Pauli matrices). If we compare (38) with (28) and (29) we find relations between the initial Cauchy data for the equation (24) and the system (37):

$$\phi(x, 0) = \begin{pmatrix} \phi_I(x, 0) \\ \phi_{II}(x, 0) \end{pmatrix} = \begin{pmatrix} \frac{1}{2}(\varphi(x) + \chi(x)) \\ \frac{1}{2}(\varphi(x) - \chi(x)) \end{pmatrix} \equiv \phi(x). \tag{39}$$

It easy to show that in the basis (39) the Lagrangian  $L_0(x, M)$  from (32) looks like

$$L_0(x, M) = \frac{\partial \phi(x)}{\partial x_n} (1 + \sigma_1) \frac{\partial \phi(x)}{\partial x_n} + 2M^2 \phi(x) (1 - \cos \mu \sigma_3) \phi(x). \tag{40}$$

Let us discuss now the question about the conditions for the transition of the new scheme into the standard Euclidean QFT (the so called "correspondence principle"). The Euclidean momentum 4-space is the "flat limit" of the de Sitter p-space and may be associated with the approximation

$$\begin{aligned} |p_n| &\ll M \\ p_5 &\simeq M \end{aligned} \tag{41}$$

In the same limit, in the configuration space we have

$$\begin{aligned}\varphi(x, x_5) &= e^{-iMx_5} \varphi(x) \\ \chi(x) &= \varphi(x)\end{aligned}\quad (42)$$

or

$$\phi(x) = \begin{pmatrix} \varphi(x) \\ 0 \end{pmatrix}\quad (43)$$

With the help of (37) it is not difficult to obtain <sup>11, 12)</sup> the corrections of the order of  $O(\frac{1}{M^2})$  to the zero approximation (43)

$$\phi(x) = \begin{pmatrix} (1 - \frac{\square}{4M^2}) \varphi(x) \\ \frac{\square}{4M^2} \varphi(x) \end{pmatrix}\quad (44)$$

from which ( see eq. (39)) we have

$$\varphi(x) - \chi(x) = \frac{\square \varphi(x)}{2M^2}\quad (45)$$

Taking into account (45) and (11) one may conclude that in the "flat limit" (formally when  $M \rightarrow \infty$ ) the Lagrangian  $L_0(x, M)$  from (32) coincides with its Euclidean counterpart.

A key role in the SM belongs to the scalar Higgs field, the interactions with which allow the other fields to get masses. As far as in our model the masses of all particles, including the mass of the Higgs boson itself, should obey the condition (6), one would presume that there exists a deep internal connection between the Higgs field and the fundamental mass  $M$ . As a matter of fact, before the Higgs mechanism is switched on, all fields by definition are massless <sup>3</sup> and because of that the bound (6) at this stage has no physical meaning. Only, together with the appearance of the mass spectrum of the particles the condition (6) makes sense and, therefore, the magnitude of  $M$  should be essentially fixed by the same Higgs mechanism.

In order to get some orientation in this situation, let us consider in the framework of our approach the example of the simplest mechanism, connected with the spontaneous breaking of a discrete symmetry. At the beginning, in order to describe the scalar field, let us use the doublet (39). The total Lagrangian  $L_{tot}(x)$ , in analogy with the traditional approach, will include a free part (40) at  $\mu = 0$  and the well known interaction Lagrangian:

$$L_{int}(x) = \frac{\lambda^2}{4} (\phi^2 - v^2)^2.\quad (46)$$

---

<sup>3</sup>Higgs boson, as it is known, at this stage is with mass of a tachyon.

Therefore, we have:

$$L_{tot}(x) = \frac{\partial\phi(x)}{\partial x_n}(1 + \sigma_1)\frac{\partial\phi(x)}{\partial x_n} + 2M^2\phi(x)(1 - \cos \mu \sigma_3)\phi(x) + \frac{\lambda^2}{4}(\phi^2 - v^2)^2. \tag{47}$$

Here we used the field  $\phi(x)$  only to write the interaction (46) in the known symmetric form. Now in (47) we may go back to the variables  $\varphi(x)$  and  $\chi(x)$  (see (39)):

$$L_{tot}(x) = \frac{1}{2}\left(\frac{\partial\varphi(x)}{\partial x_n}\right)^2 + \frac{M^2}{2}(\varphi(x) - \chi(x))^2 + \frac{\lambda^2}{4}\left(\frac{\varphi^2(x) + \chi^2(x)}{2} - v^2\right)^2 \tag{48}$$

The Lagrangian (48) remains invariant under the transformation

$$\begin{aligned} \varphi(x) &\rightarrow -\varphi(x) \\ \chi(x) &\rightarrow -\chi(x) \end{aligned} \tag{49}$$

However, this symmetry is spontaneously broken. The transition to a stable "vacuum" is realized by the transformations

$$\begin{aligned} \varphi(x) &= \varphi'(x) + v \\ \chi(x) &= \chi'(x) + v \end{aligned} \tag{50}$$

In the new variables  $\varphi'(x)$  and  $\chi'(x)$  the part of the Lagrangian (48) quadratic in the fields takes the form:

$$\frac{1}{2}\left(\frac{\partial\varphi'(x)}{\partial x_n}\right)^2 + \frac{1}{2}\left(M^2 + \frac{\lambda^2 v^2}{2}\right)(\varphi'^2(x) + \chi'^2(x)) - \left(M^2 - \frac{\lambda^2 v^2}{2}\right)\varphi'(x)\chi'(x). \tag{51}$$

Comparing (51) and (32) we may conclude that

1. As a result of the spontaneous breaking of the symmetry (49) the fundamental mass  $M$  experiences renormalization:

$$M^2 \rightarrow M^2 + \frac{\lambda^2 v^2}{2} \tag{52}$$

2. The considered scalar particle acquires mass:

$$m = \sqrt{2}\lambda v \frac{1}{\sqrt{1 + \frac{\lambda^2 v^2}{2M^2}}}, \tag{53}$$

which satisfies the condition <sup>4</sup>:

$$m \leq \sqrt{M^2 + \frac{\lambda^2 v^2}{2}}. \tag{54}$$

---

<sup>4</sup>Let us note that (54) is equivalent to the inequality  $\left(1 - \frac{\lambda v}{\sqrt{2}M}\right)^2 \geq 0$ .

Therefore, if we, in advance, take into account the renormalization (52) due to the Higgs mechanism we may write the Lagrangian (48) in the form <sup>5</sup>:

$$L_{tot}(x) = \frac{1}{2} \left( \frac{\partial \varphi(x)}{\partial x_n} \right)^2 + \frac{1}{2} (M^2 - \frac{\lambda^2 v^2}{2}) (\varphi(x) - \chi(x))^2 + \frac{\lambda^2}{4} \left( \frac{\varphi^2(x) + \chi^2(x)}{2} - v^2 \right)^2. \quad (55)$$

In this way instead of (53) we have

$$m = \sqrt{2} \lambda v \sqrt{1 - \frac{\lambda^2 v^2}{2M^2}} \equiv m_0 \sqrt{1 - \frac{m_0^2}{4M^2}} \quad (56)$$

The quantity  $m_0 = \sqrt{2} \lambda v$  is the maximal value of the mass of the considered scalar particle. It may be reached only in the "flat limit"  $M \rightarrow \infty$ , when the Lagrangian (55) because of (42) and (45) takes the usual form:

$$L_{tot}(x) = \frac{1}{2} \left( \frac{\partial \varphi(x)}{\partial x_n} \right)^2 + \frac{\lambda^2}{4} (\varphi^2(x) - v^2)^2. \quad (57)$$

At the end of this section, we would like to explain why we prefer to develop our approach in Euclidean terms and pass from the anti de Sitter p-space (7) to the the de Sitter p-space (16).

Let us apply to (8) the 5-dimensional Fourier transform (compare with (23))

$$\varphi(x, x_5) \equiv \frac{2M}{(2\pi)^{3/2}} \int e^{-ip_0 x_0 + \mathbf{p}\mathbf{x} - ip_5 x_5} \delta(p_0^2 - \mathbf{p}^2 + p_5^2 - M^2) \varphi(p, p_5) d^5 p. \quad (58)$$

From here we find (compare with (28) and (29))

$$\varphi(x, 0) \equiv \varphi(x) = \frac{M}{(2\pi)^{3/2}} \int_{p^2 \leq M^2} e^{-ipx} d^4 p \frac{\varphi(p, |p_5|) + \varphi(p, -|p_5|)}{|p_5|} \quad (59)$$

$$\frac{i}{M} \frac{\partial \varphi(x, 0)}{\partial x_5} \equiv \chi(x) = \frac{1}{(2\pi)^{3/2}} \int_{p^2 \leq M^2} e^{-ipx} d^4 p [\varphi(p, |p_5|) - \varphi(p, -|p_5|)].$$

The principal difference of these expressions in comparison with (28) and (29) is that in (59) there is a limitation on the integration region:  $p_0^2 - \mathbf{p}^2 \leq M^2$ . This fact sharply restricts the class of functions  $\varphi(x)$  and  $\chi(x)$  and does not allow, in particular, to construct from them local Lagrangians or to apply to them local gauge transformations. Rigorously speaking eqs. (59) can not be treated

---

<sup>5</sup>In order the Lagrangian (47) remains positively definite, it is natural to suppose that  $M^2 > \frac{\lambda^2 v^2}{2}$ .

( without special reservations ) as Cauchy data for the "ultra-hyperbolic" equation:

$$\left( \frac{\partial^2}{\partial x_0^2} + \frac{\partial^2}{\partial x_5^2} - \frac{\partial^2}{\partial \mathbf{x}^2} + M^2 \right) \varphi(x, x_5) = 0, \tag{60}$$

which is satisfied by the field (58). In mathematical physics there are developed methods which allow one to use partial differential equations of ultra-hyperbolic type with Cauchy initial data. From a technical point of view we consider this a more complicated procedure, than to work in the framework of Euclidean QFT. Moreover, thanks to the locality of the Euclidean formulation, coming back to the relativistic description is not a problem.

### 3 De Sitter fermion fields

As far as the new QFT is elaborated on the basis of the de Sitter momentum space (16) it is natural to suppose that in the developed approach the fermion fields  $\psi_\alpha(p, p_5)$  have to be de Sitter spinors, i.e., to transform under the four dimensional representation of the group  $SO(4, 1)$ . Further on we shall use the following  $\gamma$  - matrix basis ( $\gamma^4 = i\gamma^0$ ):

$$\begin{aligned} \gamma^L &= (\gamma^1, \gamma^2, \gamma^3, \gamma^4, \gamma^5) \\ \{\gamma^L, \gamma^M\} &= 2g^{LM}, \\ g^{LM} &= \begin{pmatrix} -1 & 0 & 0 & 0 & 0 \\ 0 & -1 & 0 & 0 & 0 \\ 0 & 0 & -1 & 0 & 0 \\ 0 & 0 & 0 & -1 & 0 \\ 0 & 0 & 0 & 0 & 1 \end{pmatrix}. \end{aligned} \tag{61}$$

Obviously we have:

$$\begin{aligned} M^2 - p_L p^L &= M^2 + p_n^2 - p_5^2 = (M - p_L \gamma^L)(M + p_L \gamma^L) = \\ &= (M + p^n \gamma^n - p^5 \gamma^5)(M - p^n \gamma^n + p^5 \gamma^5). \end{aligned} \tag{62}$$

In the "flat limit"  $M \rightarrow \infty$  the quantities  $\psi_\alpha(p, p_5)$  become Euclidean spinor fields which are used in the construction of different versions of the Euclidean QFT for fermions.

It is clear that the relations (23) - (29) , which we considered in the theory of boson fields, exist also in its fermion version. Let us write some of them without comments

$$\psi(x, x_5) = \frac{2M}{(2\pi)^{3/2}} \int e^{-ip_\kappa x^\kappa} \delta(p_L p^L - M^2) \psi(p, p_5) d^5 p, \tag{63}$$

$$\left(\frac{\partial^2}{\partial x_5^2} - \square + M^2\right)\psi(x, x_5) = 0, \quad (64)$$

$$\begin{aligned} \psi(x, 0) \equiv \psi(x) &= \frac{M}{(2\pi)^{3/2}} \int e^{ip_n x^n} d^4 p \frac{\psi_1(p) + \psi_2(p)}{|p_5|} = \\ &= \frac{1}{(2\pi)^{3/2}} \int e^{ip_n x^n} \psi(p) d^4 p \end{aligned} \quad (65)$$

$$\begin{aligned} \frac{i}{M} \frac{\partial \psi(x, 0)}{\partial x_5} \equiv \chi(x) &= \frac{1}{(2\pi)^{3/2}} \int e^{ip_n x^n} d^4 p [\psi_1(p) - \psi_2(p)] = \\ &= \frac{1}{(2\pi)^{3/2}} \int e^{ip_n x^n} \chi(p) d^4 p. \end{aligned} \quad (66)$$

The next step is the construction of the action integral for the fermion field  $\psi_\alpha(p, p_5)$ . Here we will not follow our work <sup>6)</sup>, where this problem was solved in the spirit of the Schwinger's approach <sup>13)</sup> with the use of 8-component real spinors and preserving the reality of the action. Now we shall follow the formulation of Osterwalder and Schrader <sup>14)</sup> and write the Euclidean fermion Lagrangian in the form:

$$\begin{aligned} L_E(x) &= \bar{\zeta}_E(x) \left(-i\gamma_n \frac{\partial}{\partial x^n} + m\right) \psi_E(x), \\ \{\gamma^n, \gamma^m\} &= -2\delta^{nm} \quad (m, n = 1, 2, 3, 4). \end{aligned} \quad (67)$$

Here the spinor fields  $\bar{\zeta}_E(x) = \zeta_E^+(x)\gamma^4$  and  $\psi_E(x)$  are independent Grassmann variables, which are not connected between themselves by Hermitian or complex conjugation. Correspondingly, the action is not Hermitian. The Osterwalder and Schrader approach has been widely discussed in the literature <sup>14)</sup><sup>6)</sup> and here we shall not go into details. It is easy to convince oneself that the expression  $2M(p_5 - M \cos \mu)$ , which in our approach substitutes (see eq.(32)) the Euclidean Klein-Gordon operator  $p_n^2 + m^2$ , may be represented as

$$\begin{aligned} &2M(p_5 - M \cos \mu) = \\ &= [p_n \gamma^n - (p_5 - M)\gamma^5 + 2M \sin \frac{\mu}{2}] [-p_n \gamma^n + (p_5 - M)\gamma^5 + 2M \sin \frac{\mu}{2}] \end{aligned} \quad (68)$$

In the Euclidean approximation (41) the relation (68) takes the form:

$$p_n^2 + m^2 = (p_n \gamma^n + m)(-p_n \gamma^n + m). \quad (69)$$

---

<sup>6)</sup>By the way, in the paper <sup>15)</sup> the so called Wick rotation is interpreted in terms of the 5-dimensional space.

Therefore, we may use the expression

$$\mathcal{D}(p, p_5) \equiv p_n \gamma^n - (p_5 - M) \gamma^5 + 2M \sin \frac{\mu}{2} \tag{70}$$

like the new Dirac operator.

As a result, we come to an expression for the action of the Fermion field in the de Sitter momentum space

$$S_0(M) = 2\pi M \int \varepsilon(p_5) \delta(p_L p^L - M^2) d^5 p \times \left[ \bar{\zeta}(p, p_5) (p_n \gamma^n - (p_5 - M) \gamma^5 + 2M \sin \frac{\mu}{2}) \psi(p, p_5) \right], \tag{71}$$

In the integral (71) it is possible to pass to the field variables

$$\begin{aligned} \psi(p) &= \frac{M}{|p_5|} (\psi(p, |p_5|) + \psi(p, -|p_5|)) \equiv M \frac{\psi_1(p) + \psi_2(p)}{|p_5|} \\ \chi(p) &= \psi_1(p) - \psi_2(p) \\ \bar{\zeta}(p) &= M \frac{\bar{\zeta}_1(p) + \bar{\zeta}_2(p)}{|p_5|} \\ \bar{\xi}(p) &= \bar{\zeta}_1(p) - \bar{\zeta}_2(p), \end{aligned} \tag{72}$$

which are the Fourier amplitudes of the local fields  $\psi(x)$ ,  $\chi(x)$ ,  $\bar{\zeta}(x)$  and  $\bar{\xi}(x)$  (compare with (65) and (66)). As a result, we get:

$$\begin{aligned} S_0^D &= -\pi \int d^4 p \left( M + \frac{p_n^2}{M} \right) \bar{\zeta}(p) \gamma^5 \psi(p) + \\ &+ \pi \int d^4 p \bar{\zeta}(p) (\not{p} + M \gamma^5 + 2M \sin \frac{\mu}{2}) \chi(p) + \\ &+ \pi \int d^4 p \overline{\xi(p)} (\not{p} + M \gamma^5 + 2M \sin \frac{\mu}{2}) \psi(p) - \\ &- \pi \int d^4 p M \overline{\xi(p)} \gamma^5 \chi(p) \end{aligned} \tag{73}$$

In the configuration space we have, correspondingly,

$$\begin{aligned}
 S_0^{\mathcal{D}} &= \int L_0^{\mathcal{D}}(x, M) d^4x = \\
 &= \frac{1}{2} \int d^4x \bar{\zeta}(x) \left( \frac{\square}{M^2} - 1 \right) \gamma^5 \psi(x) + \\
 &+ \frac{1}{2} \int d^4x \bar{\zeta}(x) \left( i\gamma^n \frac{\partial}{\partial x^n} + M\gamma^5 + 2M \sin \frac{\mu}{2} \right) \chi(x) + \\
 &+ \frac{1}{2} \int d^4x \overline{\xi(x)} \left( i\gamma^n \frac{\partial}{\partial x^n} + M\gamma^5 + 2M \sin \frac{\mu}{2} \right) \psi(x) - \\
 &- \frac{1}{2} \int d^4x \overline{\xi(x)} \gamma^5 \chi(x).
 \end{aligned} \tag{74}$$

Hence, the modified Dirac Lagrangian  $L_0^{\mathcal{D}}(x, M)$  is a local function of the spinor field variables  $\psi(x)$ ,  $\chi(x)$ ,  $\bar{\zeta}(x)$  and  $\bar{\xi}(x)$ . Here there is an obvious analogy with the boson case (compare with (32) and (??)).

However, the fermion Lagrangian  $L_0^{\mathcal{D}}(x, M)$  may be represented in a different form, if one uses the relations (62). Indeed, let us put

$$\begin{aligned}
 \frac{1}{2M}(M - p_K \gamma^K) \psi(p, p_5) &\equiv \Pi_L \psi(p, p_5) \equiv \psi_L(p, p_5) \\
 \frac{1}{2M}(M + p_K \gamma^K) \psi(p, p_5) &\equiv \Pi_R \psi(p, p_5) \equiv \psi_R(p, p_5)
 \end{aligned} \tag{75}$$

Due to (16) the operators  $\Pi_L$  and  $\Pi_R$  are projectors:

$$\begin{aligned}
 \Pi_L + \Pi_R &= 1, \\
 \Pi_L^2 &= \Pi_L \quad \Pi_R^2 = \Pi_R, \\
 \Pi_L \Pi_R &= \Pi_R \Pi_L = 0.
 \end{aligned} \tag{76}$$

On the other hand they are the 5- analogue of the Dirac operator, and the fields  $\psi_L(p, p_5)$  and  $\psi_R(p, p_5)$  obviously satisfy the corresponding 5-dimensional Dirac equations

$$\begin{aligned}
 (M + p_K \gamma^K) \psi_L(p, p_5) &= 0, \\
 (M - p_K \gamma^K) \psi_R(p, p_5) &= 0.
 \end{aligned} \tag{77}$$

Therefore, in this way the fermion field  $\psi(p, p_5)$ , given in the de Sitter momentum space (16), may be presented as a sum of two fields  $\psi_L(p, p_5)$  and  $\psi_R(p, p_5)$

$$\psi(p, p_5) = \psi_L(p, p_5) + \psi_R(p, p_5), \tag{78}$$

which obey the 5-dimensional Dirac equations (77). Obviously, the decomposition (78) is *de Sitter invariant procedure*.

It is easy to verify that in the flat limit (41)

$$\Pi_{L,R} = \frac{1 \mp \gamma^5}{2}, \tag{79}$$

This is the reason that we consider the fields  $\psi_L(p, p_5)$  and  $\psi_R(p, p_5)$  as the "chiral" components in the developed approach (12). The new operator of chirality  $\frac{\not{p}_L \not{\gamma}^L}{M}$ , similarly to its "flat counterpart", has eigenvalues equal to  $\pm 1$ , but **depends on the energy and momentum**. The last circumstance, as we hope, should be revealed experimentally (see section 4).

It is worthwhile to pass in (77) to the configurational representation. Applying (63) we get :

$$\begin{aligned} \psi_L(x, x_5) &= \frac{1}{2} \left( 1 - \frac{i\gamma^n}{M} \frac{\partial}{\partial x^n} - \frac{i\gamma^5}{M} \frac{\partial}{\partial x^5} \right) \psi(x, x_5) \\ \psi_R(x, x_5) &= \frac{1}{2} \left( 1 + \frac{i\gamma^n}{M} \frac{\partial}{\partial x^n} + \frac{i\gamma^5}{M} \frac{\partial}{\partial x^5} \right) \psi(x, x_5) \end{aligned} \tag{80}$$

Setting in (80)  $x_5 = 0$  and taking into account (65) and (66) we shall have:

$$\begin{aligned} \psi_L(x, 0) \equiv \psi_{(L)}(x) &= \frac{1}{2} \left( 1 - \frac{i\gamma^n}{M} \frac{\partial}{\partial x^n} \right) \psi(x) - \frac{\gamma^5}{2} \chi(x), \\ \psi_R(x, 0) \equiv \psi_{(R)}(x) &= \frac{1}{2} \left( 1 + \frac{i\gamma^n}{M} \frac{\partial}{\partial x^n} \right) \psi(x) + \frac{\gamma^5}{2} \chi(x). \end{aligned} \tag{81}$$

As far as the field  $\psi(x, x_5)$  obeys equation (24), the relations, we obtained for the scalar field in the "flat" approximation and in particular (45), may be applied to it. Taking this into account, we find that in this approximation the equalities (81) become

$$\begin{aligned} \psi_{(L)}(x) &= \frac{1}{2}(1 - \gamma_5)\psi(x) - \frac{i\gamma^n}{2M} \frac{\partial}{\partial x^n} \psi(x) + \frac{\gamma^5}{2}(\psi(x) - \chi(x)) \simeq \\ &\simeq \frac{1}{2}(1 - \gamma_5)\psi(x) - \frac{i\gamma^n}{2M} \frac{\partial}{\partial x^n} \psi(x) + \frac{\gamma^5}{4M^2} \square \psi(x), \\ \psi_{(R)}(x) &\simeq \frac{1}{2}(1 + \gamma_5)\psi(x) + \frac{i\gamma^n}{2M} \frac{\partial}{\partial x^n} \psi(x) - \frac{\gamma^5}{4M^2} \square \psi(x). \end{aligned} \tag{82}$$

Representation, analogous to (78), may be introduced for the field  $\bar{\zeta}(p, p_5)$  appearing in (71)

$$\bar{\zeta}(p, p_5) = \bar{\zeta}_L(p, p_5) + \bar{\zeta}_R(p, p_5), \tag{83}$$

where

$$\begin{aligned} \bar{\zeta}_L(p, p_5) &= \bar{\zeta}(p, p_5) \Pi_R, \\ \bar{\zeta}_R(p, p_5) &= \bar{\zeta}(p, p_5) \Pi_L. \end{aligned} \tag{84}$$

Further it is not difficult to obtain relations similar to (80) - (82) for the fields  $\bar{\zeta}_L(x)$  and  $\bar{\zeta}_R(x)$ :

$$\bar{\zeta}_{(L)}(x) = \frac{1}{2}\bar{\zeta}(x) + \frac{i}{2M} \frac{\partial \bar{\zeta}(x)}{\partial x^n} \gamma^n + \bar{\xi}(x) \frac{\gamma^5}{2}, \quad (85)$$

$$\bar{\zeta}_{(R)}(x) = \frac{1}{2}\bar{\zeta}(x) - \frac{i}{2M} \frac{\partial \bar{\zeta}(x)}{\partial x^n} \gamma^n - \bar{\xi}(x) \frac{\gamma^5}{2},$$

$$\bar{\zeta}_{(L)} \simeq \bar{\zeta}(x) \frac{1}{2} (1 + \gamma_5) + \frac{i}{2M} \frac{\partial}{\partial x^n} \bar{\zeta}(x) \gamma^n - \frac{\square}{4M^2} \bar{\zeta}(x) \gamma^5, \quad (86)$$

$$\bar{\zeta}_{(R)} \simeq \bar{\zeta}(x) \frac{1}{2} (1 - \gamma_5) - \frac{i}{2M} \frac{\partial}{\partial x^n} \bar{\zeta}(x) \gamma^n + \frac{\square}{4M^2} \bar{\zeta}(x) \gamma^5.$$

Now substituting (81) and (85) in the action integral (74) we may pass to new variables  $\psi_{(L)}(x)$ ,  $\psi_{(R)}(x)$ ,  $\bar{\zeta}_L(x)$  and  $\bar{\zeta}_R(x)$ :

$$\begin{aligned} S_0^{\mathcal{D}} &= \int L_0^{\mathcal{D}}(x, M) d^4x = \\ &= \int d^4x \left[ \bar{\zeta}_{(L)}(x) i \gamma^n \frac{\partial}{\partial x^n} \psi_{(L)}(x) + \bar{\zeta}_{(R)}(x) i \gamma^n \frac{\partial}{\partial x^n} \psi_{(R)}(x) \right] + \\ &\quad + \int d^4x \bar{\zeta}_{(L)}(x) \left[ i \gamma^n \frac{\partial}{\partial x^n} + M(1 - \gamma^5) \right] \psi_{(R)}(x) + \\ &\quad + \int d^4x \bar{\zeta}_{(R)}(x) \left[ i \gamma^n \frac{\partial}{\partial x^n} - M(1 + \gamma^5) \right] \psi_{(L)}(x) + \\ &\quad + 2M \sin \frac{\mu}{2} \int d^4x \left[ \bar{\zeta}_{(L)}(x) \gamma^5 \psi_{(R)}(x) - \bar{\zeta}_{(R)}(x) \gamma^5 \psi_{(L)}(x) \right] \end{aligned} \quad (87)$$

The obtained expression is the basis for constructing a gauge theory of interacting fermion field. This topic will shortly be discussed in the next section. Concluding this part we would like to make one important remark <sup>6)</sup>.

The point is that for the quantity  $2M(p^5 - M \cos \mu)$ , which substituted in our approach the Euclidean Klein-Gordon operator together with (68) there exists **one more decomposition to matrix factors**:

$$\begin{aligned} &2M(p^5 - M \cos \mu) = \\ &= (p_n \gamma^n - \gamma^5(p^5 + M) + 2M \cos \frac{\mu}{2})(p_n \gamma^n - \gamma^5(p^5 + M) - 2M \cos \frac{\mu}{2}) \end{aligned} \quad (88)$$

Therefore, if our approach is considered to be realistic, it may be assumed that in Nature there exists some **exotic** fermion field whose free action integral has the form

$$\begin{aligned} S_0^{(exotic)}(M) &= 2\pi M \int \varepsilon(p_5) \delta(p_L p^L - M^2) d^5p \times \\ &\times \left\{ \bar{\xi}_{exotic}(p, p_5) \left[ p_n \gamma^n - (p_5 + M) \gamma^5 + 2M \cos \frac{\mu}{2} \right] \psi_{exotic}(p, p_5) \right\} \end{aligned} \quad (89)$$

Applying the above developed procedure it is easy to obtain  $S_0^{(exotic)}(M)$  in a form analogous to (87). However, in contrast to  $S_0^D$  this quantity does not have a limit as  $M \rightarrow \infty$ , which justifies the name chosen by us for this field. The polarization properties of the exotic field, evidently, differ sharply from standard ones.

We would like to conjecture that the quanta of the exotic fermion field have a direct relation to the structure of the "dark matter."

#### 4 The new geometrical approach to the Standard Model

To the complete formulation of the Standard Model, consistent with the principle of maximal mass (6) and its geometrical realization in terms of de Sitter momentum space <sup>7</sup> (16) we shall devote a separate paper. Now we intend to make only several remarks important for the understanding of our general strategy.

##### 1. $SU_L(2) \otimes U_Y(1)$ - symmetry

The gauge  $SU_L(2) \otimes U_Y(1)$  - symmetry is one of the most important elements of the SM which guaranteed its success. This is why it should be assumed as necessary to apply it also in our approach, taking into account our new definition of the chiral fields. However, in the new fermion Lagrangian  $L_0^D$  (see (87)) even for  $m = 0$  there are crossed terms:

$$\begin{aligned} & \bar{\zeta}_{(L)} \left[ i\gamma^n \frac{\partial}{\partial x^n} + M(1 - \gamma^5) \right] \psi_{(R)}(x) + \\ & + \bar{\zeta}_{(R)} \left[ i\gamma^n \frac{\partial}{\partial x^n} - M(1 + \gamma^5) \right] \psi_{(L)}(x) \end{aligned} \tag{90}$$

which, at first glance, are a insurmountable obstacle for the use of the group  $SU_L(2) \otimes U_Y(1)$ . The solution of this difficulty is to make the expression (90) invariant form with the help of the Higgs field. In this way, considering as before the Higgs boson to be a  $SU_L(2)$ -doublet, introducing the doublet structure for the  $L$ -component of the fermion field and passing to covariant derivatives with the rules of the SM, we may write (90) in the form:

$$\begin{aligned} & \frac{1}{v} \left( \bar{\zeta}_{(L)} \cdot H(x) \right) \left[ i\gamma^n D_n^R + M(1 - \gamma^5) \right] \psi_{(R)}(x) + \\ & + \frac{1}{v} \bar{\zeta}_{(R)} \left\{ H^+(x) \cdot \left[ i\gamma^n D_n^L - M(1 + \gamma^5) \right] \psi_{(L)}(x) \right\} + conj., \end{aligned} \tag{91}$$

where  $H(x)$  is the SM Higgs doublet and  $D^R$  and  $D^L$  are the SM covariant derivatives. After the Higgs mechanism is switched on from (91) separate our

---

<sup>7</sup>Let us recall that namely this **geometrized** SM is called in advance the Maximal Mass Model.

cross terms (90) and appear terms with interactions which are not present in the SM. Together with the corrections, caused by the difference between the new and old definitions of chirality (see (82) and (86)) they may be the ground for predictions which may be verified experimentally.

2. **Chirality** In the SM it is prescribed that the boson fields transform as representations of the group  $SU_L(2)$ , which for the vector fields is three-dimensional and two-dimensional for the Higgs scalar. Naively reasoning one may ask himself how the mentioned bosons should know about the existence of the  $4 \times 4$  matrix  $\gamma^5$  one of the eigenvalues of which corresponds to the index  $L$ ? In our approach all fields, boson and fermion, are given in the de Sitter p-space on equal footing, with the only difference that the boson fields obey the 5-equation of Klein-Gordon (see (24)), and the fermion 5-equations of Dirac (77). There is nothing strange that the field  $\psi_{(L)}(x)$  and the Higgs scalar  $\varphi(x)$  simultaneously have a doublet structure with respect to the  $SU_L(2)$ -symmetry. This has already happened in the old isospin symmetry. Let us recall the nucleon doublet and the K-meson doublet.

The new geometrical concept of chirality allows us to think that the parity violation in weak interactions discovered fifty years ago was a manifestation of the de Sitter nature of momentum 4-space.

### 3. *Higgs mechanism*

This important element of the SM, as we can see already now, is conserved in the generalized SM without considerable changes. The role of the spontaneous symmetry breaking mechanism in the formation of the fundamental mass  $M$  has been studied by a simple example in section 2.

## 5 Concluding remarks

Concluding this article, we would like to pay attention to one peculiarity of the developed here approach. All fields, independently of their spins, charges, masses etc. satisfy the free 5-equation of hyperbolic type, and the role of "time" is played by the coordinate " $x_5$ ". The interaction between the fields is realized at the level of the Cauchy data given on the plane  $x_5 = 0$ , i.e., in the four-dimensional (Euclidean) world. Only the elementary particles, described by local fields and with masses, obeying the limitation  $m \leq M$  have the right of such a "*free gliding*" in the 5-space.

### Acknowledgements

M. Mateev would like to thank the organizers of Les Rencontres de Physique de la Vallée d'Aoste Profs. Mario Greco, Giorgio Bellettini and Giorgio Chiarelli

for the invitation, support and hospitality. V. G. K. and M. D. M. would like to thank Luis Alvarez-Gaumé and the PH - TH division of CERN, where major part of this work was done, for the kind hospitality and stimulating atmosphere. Both authors would like to thank warmly Alvaro De Rújula for fruitful and highly useful discussions. The authors would like to thank also M. V. Chizhov and E. R. Popitz for discussions. This work has been supported in part by the Bulgarian National Science Fund under contract Ph-09-05 (M.D.M.) and by the Russian Foundation for Basic Research (Grant No. 05-02-16535a) and the Program for Supporting Leading Scientific Schools (Grant No. NSh-5332.2006.2) (V. G. K. and V. N. R.).

## References

1. Markov M. A., Prog. Theor. Phys. Suppl., Commemoration Issue for the Thirtieth Anniversary of Meson Theory and Dr. H. Yukawa, p. 85 (1965); Sov. Phys. JETP, **24**, p. 584 (1967).
2. Kadyshevsky V.G., Nucl. Phys., **B141**, p. 477 (1978); in Proceedings of International Integrative Conference on Group Theory and Mathematical Physics, Austin, Texas, 1978; Fermilab-Pub. 78/70-THY, Sept. 1978; Phys. Elem. Chast. Atom. Yadra, **11**, p. 5 (1980).
3. Kadyshevsky V.G., Mateev M. D., Phys. Lett., **B106**, p. 139 (1981).
4. Kadyshevsky V.G., Mateev M. D., Nuovo Cimento, **A87**, p324, (1985).
5. Chizhov M. V., Donkov A.D., Ibadov R. M., Kadyshevsky V.G., Mateev M. D., Nuovo Cimento, 1985, **A87**, p. 350 (1985).
6. Chizhov M. V., Donkov A.D., Ibadov R. M., Kadyshevsky V.G., Mateev M. D., Nuovo Cimento, **A87**, p. 373, (1985).
7. Kadyshevsky V.G., Phys. Part. Nucl. **29**, p. 227 (1998).
8. Kadyshevsky V.G., Mateev M. D., Rodionov, V. N., Sorin A. S. Doklady Physics **51**, p.287 (2006), e-Print: hep-ph/0512332.
9. Newton T. D., Wigner E. P., Rev. Mod. Phys., **21**, p.400 (1949).
10. Kadyshevsky V. G., Fursaev D. V., JINR Rapid Communications, N 6, p.5 (1992).
11. Ibadov R.M., Kadyshevsky V.G., Preprint JINR-P2-86-835 (1986).
12. Kadyshevsky V. G., Fursaev D. V. JINR-P2-87-913 (1987); Sov.Phys.Dokl.**34**, p. 534 (1989).

13. Schwinger J., Phys. Rev. **115**, p.721 (1959).
14. Osterwalder K., Schrader R., Phys. Rev. Lett. **29**, p. 1423 (1973); Helv. Phys. Acta, **46**, p.277 (1973), CMP **31**,83 (1973); CMP **42**,281 (1975).
15. Van Nieuwenhuizen P. and Waldron A. Phys. Lett. B, **389**, p. 29 (1996).

# (NEAR) CONFORMAL TECHNICOLOR: WHAT IS REALLY NEW

Francesco Sannino

*HEP Center, University of Southern Denmark.*

## Abstract

The knowledge of the phase diagram of strongly coupled theories as function of the number of colors, flavors and matter representation plays a fundamental role when constructing viable extensions of the standard model (SM) featuring dynamical electroweak symmetry breaking. Here I summarize the state-of-the-art of the phase diagram for  $SU(N)$  gauge theories with fermionic matter transforming according to arbitrary representations of the underlying gauge group. I critically report on the latest results from first principle lattice simulations and then review the principal models of (near) conformal technicolor such as (Next) Minimal Walking Technicolor (MWT) and Partially Gauged Technicolor (PGT). I finally show that the incarnation of the conformal technicolor model is nothing but the simplest PGT model.

## 1 Background

Models of electroweak symmetry breaking via new strongly interacting theories of technicolor type <sup>1, 2)</sup> are gaining momentum. The most updated review on the subject has just appeared <sup>3)</sup> while earlier ones are <sup>4, 5)</sup>. There is no doubt that the main difficulty in constructing such extensions of the SM is the very limited knowledge about generic strongly interacting theories. This has led theorists, in the past, to construct models of technicolor resembling ordinary quantum chromodynamics <sup>1, 2)</sup>. Unfortunately the simplest version of this type of models are at odds with electroweak precision measurements. New strongly coupled theories with dynamics very different from the one featured by a scaled up version of QCD are needed as summarized in <sup>3)</sup>.

In this mini-review I summarize first the state-of-the-art of the phase diagram <sup>6, 7, 8)</sup> for  $SU(N)$  gauge theories and then present the most recent models of dynamical electroweak symmetry breaking <sup>9, 10, 11, 12)</sup>.

## 2 Phase Diagram

First principle lattice simulations are now capable to investigate the spectrum and the dynamics of various four dimensional gauge theories which are of interest in our pursue of a dynamical origin of the stabilization of the Fermi scale <sup>13, 14, 15)</sup>. It is, however, very useful to provide an analytical study of the dynamics and/or spectrum of a generic nonsupersymmetric gauge theory applying, for example, the proposal of the all-order beta function for non-supersymmetric gauge theories with fermionic matter <sup>6)</sup>. This new method constitutes a true step forward with respect to the very rough method based on the truncated Schwinger-Dyson equation (SD) <sup>16, 17, 18)</sup> (referred also as the ladder approximation in the literature) or even conjectures such as the Appelquist-Cohen-Schmaltz (ACS) one <sup>19)</sup> which makes use of the counting of the thermal degrees of freedom at high and low temperature. The ACS conjecture is, in fact, unable to constrain the phase diagram for vector-like theories with matter in higher dimensional representations as I have shown in <sup>20)</sup>. The ACS conjecture has been tested also for chiral gauge theories <sup>21)</sup>. There it was also found that to make definite predictions a stronger requirement is needed <sup>22)</sup>.

### 2.1 All-order beta function

Let's start from the proposal of the beta function for nonsupersymmetric  $SU(N)$  gauge theories with fermionic matter <sup>6)</sup>. It is written in a form useful

for constraining the phase diagram of strongly coupled theories. The form is inspired by the Novikov-Shifman-Vainshtein-Zakharov (NSVZ) beta function for supersymmetric theories <sup>23, 24)</sup> and the renormalization scheme coincides with the NSVZ one. We proposed the following form <sup>6)</sup> of the beta function:

$$\beta(g) = -\frac{g^3}{(4\pi)^2} \frac{\beta_0 - \frac{2}{3} T(r) N_f \gamma(g^2)}{1 - \frac{g^2}{8\pi^2} C_2(G) \left(1 + \frac{2\beta'_0}{\beta_0}\right)}, \tag{1}$$

with

$$\beta_0 = \frac{11}{3} C_2(G) - \frac{4}{3} T(r) N_f, \quad \beta'_0 = C_2(G) - T(r) N_f. \tag{2}$$

We have also defined  $\gamma = -d \ln m / d \ln \mu$  and  $m$  the renormalized fermion mass. The generators  $T_r^a$ ,  $a = 1 \dots N^2 - 1$  of the gauge group in the representation  $r$  are normalized according to  $\text{Tr} [T_r^a T_r^b] = T(r) \delta^{ab}$  while the quadratic Casimir  $C_2(r)$  is given by  $T_r^a T_r^a = C_2(r) I$ . The adjoint representation is denoted by  $G$ .

### 2.1.1 Free Electric Phase

This is the region of  $N_f$  for which  $\beta_0$  is negative and asymptotic freedom is lost. The theory behaves like QED and hence it becomes strongly coupled at high energy.  $N_f^I$  is the number of flavors above which the theory is no longer asymptotically free. This corresponds to  $\beta_0[N_f^I]=0$ . For values of  $N_f$  larger than  $N_f^I$  the theory is in a non-Abelian QED theory. We obtain

$$N_f^I = \frac{11}{4} \frac{C_2(G)}{T(r)}. \tag{3}$$

### 2.1.2 Coulomb Phase

As we decrease the number of flavors from just below the point where asymptotic freedom is lost one expects a perturbative (in the coupling) zero in the beta function to occur <sup>25)</sup>. From the expression proposed above one finds that at the zero of the beta function, barring zeros in the denominator, one must have

$$\gamma = \frac{11C_2(G) - 4T(r)N_f}{2T(r)N_f}. \tag{4}$$

The dimension of the chiral condensate is  $D(\bar{\psi}\psi) = 3 - \gamma$  which at the IR fixed point value reads

$$D(\bar{\psi}\psi) = \frac{10T(r)N_f - 11C_2(G)}{2T(r)N_f}. \tag{5}$$

To avoid negative norm states in a conformal field theory one must have  $D \geq 1$  for non-trivial spinless operators (26, 27, 28).

Here the critical number of flavors below which the unitarity bound is violated is

$$N_f^{\text{II}} = \frac{11}{8} \frac{C_2(G)}{T(r)}, \quad (6)$$

which corresponds to having set  $\gamma = 2$ . The analysis above is similar to the one for supersymmetric gauge theories (29). The actual size of the conformal window may be smaller than the one presented here which is the bound on the size of the window. The reason being that chiral symmetry breaking could be triggered for a value of  $\gamma$  lower than two.

A value of  $\gamma$  larger than one, still allowed by unitarity, is a welcomed feature when using this window to construct walking technicolor theories (30, 31, 32, 33). It may allow for the physical value of the mass of the top while avoiding a large violation of flavor changing neutral currents which were investigated in (34) for the minimal walking model.

## 2.2 Conformal Window

I now compare and combine analytical predictions for the conformal window with lattice results (14, 35, 15, 36). The first exhaustive perturbative analysis relevant to start a systematic study of gauge theories with fermions in any given representation of the  $SU(N)$  on the lattice has just appeared (13).

### 2.2.1 Two-index symmetric representation

Two and three colors with two Dirac flavors transforming according to the two index symmetric (2S) representation of the gauge group have been investigated on the lattice respectively in (14) and (35). For  $SU(2)$  the spectrum of the theory (14) has been studied and confronted with the theory with two colors and two Dirac flavors in the fundamental representation. The lattice studies indicate that either the theory is very near an infrared stable fixed point or the fixed point is already reached. These are only preliminary results and more refined investigations are needed. Nevertheless let's compare them directly with analytical results. According to ladder results we should be below the conformal window but very near conformal (9). According to the all-order beta function the anomalous dimension of the mass operator, if the IR fixed point is reached, assumes the value:

$$\gamma = \frac{3}{4}, \quad SU(2) \text{ model with 2 (2S) Flavors.} \quad (7)$$

The all-order beta function shows that one has not yet reached  $\gamma$  equal one and suggests that the  $SU(2)$  model is indeed conformal in the infrared if one uses  $\gamma = 1$  as an indication of when the conformal window ceases to exist. However, as explained above, the constraint coming from unitarity of the conformal theories allows  $\gamma$  to take even larger values, i.e. up to 2, before losing conformality.

The situation is very intriguing for the  $SU(3)$  theory. Recent lattice results <sup>35)</sup> suggest that this theory may already have achieved an IR fixed point. Here, as well, more studies are needed. The ladder approximation predicts, however, this theory to be near conformal (i.e. walking) but further away from conformality than the  $SU(2)$  theory. If the theory were indeed conformal in the infrared, via the all-order beta function, we predict the anomalous dimension of the fermion condensate to assume the following value:

$$\gamma = 1.3, \quad SU(3) \text{ model with 2 (2S) Flavors.} \quad (8)$$

The anomalous dimension of the mass operator turns out to be larger than one! This would be quite an important result since large anomalous dimensions are needed when constructing extended technicolor models able to account for the heavy quark masses. In fact the common lore is that the anomalous dimension of the quark operator does not exceed one. If the  $SU(3)$  generates an infrared fixed point then the  $SU(2)$  would also generate it since fermions screen even more there.

### 2.2.2 Fundamental representation

The all-order beta function *predicts* that the conformal window cannot be achieved for a number of flavors less than 8.25 in the fundamental representation of  $SU(3)$ . This is supported by the latest lattice results <sup>37, 15)</sup>. If this theory develops an infrared fixed point we predict the anomalous dimension of the quark mass operator to be:

$$\gamma = \frac{3}{4}, \quad SU(3) \text{ model with 12 Fundamental Flavors} \quad (9)$$

Amusingly the theories with 12 fundamental flavors in  $SU(3)$  and 2 adjoint Dirac flavors in  $SU(2)$  (adjoint fermions here correspond to the 2S in this case) have the same anomalous dimension if both develop the infrared fixed point. What is extremely interesting to know is if a fixed point is generated for a number of flavors less than eleven but higher than eight since according to the all-order beta function this corresponds to an anomalous dimension larger than one but still smaller than two.

The phase diagram is summarized in figure 1.

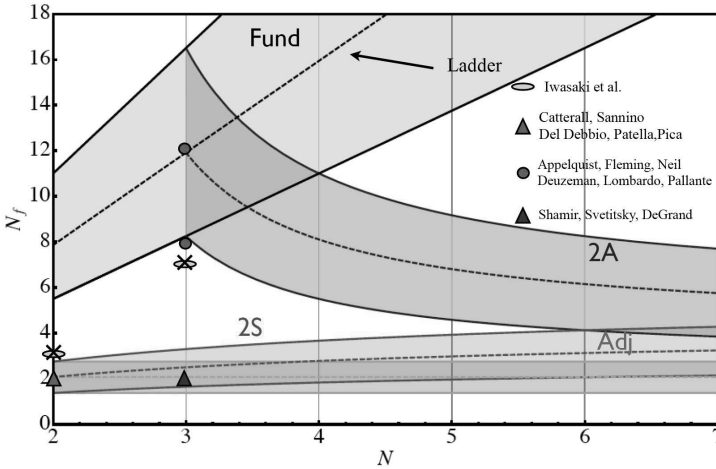


Figure 1: Phase diagram for nonsupersymmetric theories with fermions in various representations with superimposed for which theories the lattice simulations were performed. The dashed lines correspond to the ladder approximation boundary of the conformal window which correspond to  $\gamma$  about one. While the bound from the all-order beta function is obtained for  $\gamma = 2$ . Note that if we were to use  $\gamma = 1$  constraint with the all-order beta function the conformal window would be a little larger than the ladder one. Oval and round circles denote early lattice studies<sup>38)</sup> with fermions in the fundamental representation. Triangles denote the lattice results for fermions in the two index representation. The cross on the ovals denote that the conclusion of the theories already being conformal is in disagreement with the theoretical predictions.

### 2.3 Schrödinger zeros: Are they physical?

The beta function derived on the lattice using the Schrödinger functional<sup>39, 40, 41, 42)</sup> has exactly the same limitations of the 't Hooft beta function. For example the presence or absence of a zero in these schemes does not demonstrate the presence or the absence of a physical fixed point. More information is needed, such as the knowledge of the anomalous dimension of the fermion mass at the fixed point. One can infer the existence of an infrared fixed point when correlators of gauge-invariant operator show power law behaviors. Note that differently from the 't Hooft and the Schrödinger functional case the all-order beta function presented above predicts the anomalous dimensions

at the fixed point. These are physical quantities, i.e. independent from the scheme.

### 3 Better Models of Technicolor

Having shed light on the phase diagram of strongly coupled theories we are now entitled to investigate possible (near) conformal technicolor models.

The simplest technicolor model has  $N_{Tf}$  Dirac fermions in the fundamental representation of  $SU(N)$ . These models, when extended to accommodate the fermion masses through the extended technicolor interactions, suffer from large flavor changing neutral currents. This problem is alleviated if the number of flavors is sufficiently large such that the theory is (almost) conformal. This is estimated to happen, for fermion in the fundamental representation, for  $N_{Tf} \sim 4N$  <sup>30)</sup>. This, in turn, implies a large contribution to the oblique parameter  $S$  <sup>43)</sup> when all of the flavor symmetries are gauged under the electroweak group. Although near the conformal window <sup>44, 45)</sup> the  $S$  parameter is reduced due to non-perturbative corrections, it is still too large if the model has a large particle content. In addition, such models may have a large number of pseudo Nambu-Goldstone bosons. By choosing a higher dimensional technicolor representation for the new technifermions one can overcome these problems <sup>9, 43)</sup>.

To have a very low  $S$  parameter one would ideally have a technicolor theory which with only one doublet breaks dynamically the electroweak symmetry but at the same time being walking (near conformal) to reduce the  $S$  parameter. The walking nature then also enhances the scale responsible for the fermion mass generation.

According to the phase diagram exhibited earlier the promising candidate theories with the properties required are either theories with fermions in the adjoint representation or two index symmetric one.

The relevant feature, found first in <sup>9)</sup> is that the S-type theories can be near conformal already at  $N_{Tf} = 2$  when  $N = 2$  or 3. This should be contrasted with theories in which the fermions are in the fundamental representation for which the minimum number of flavors required to reach the conformal window is eight for  $N = 2$ . The critical value of flavors increases with the number of colors for the gauge theory with S-type matter: the limiting value is 4.15 at large  $N$ .

We refer with minimal theories for which the number of flavors needed to achieve an infrared fixed point is very small compared to the case of matter in the fundamental representation of the gauge group.

### 3.1 Minimal Walking Technicolor (MWT)

The dynamical sector we consider, which underlies the Higgs mechanism, is an  $SU(2)$  technicolor gauge theory with two adjoint technifermions <sup>9)</sup>. The theory is asymptotically free if the number of flavors  $N_f$  is less than 2.75 according to the ladder approximation. The two adjoint fermions are conveniently written as

$$Q_L^a = \begin{pmatrix} U^a \\ D^a \end{pmatrix}_L, \quad U_R^a, \quad D_R^a, \quad a = 1, 2, 3, \quad (10)$$

with  $a$  being the adjoint color index of  $SU(2)$ . The left handed fields are arranged in three doublets of the  $SU(2)_L$  weak interactions in the standard fashion. The condensate is  $\langle \bar{U}U + \bar{D}D \rangle$  which correctly breaks the electroweak symmetry.

The model as described so far suffers from the Witten topological anomaly. This can be fixed by adding a new weakly charged fermionic doublet which is a technicolor singlet <sup>10)</sup>. Schematically:

$$L_L = \begin{pmatrix} N \\ E \end{pmatrix}_L, \quad N_R, \quad E_R. \quad (11)$$

The low-energy effective theory to be tested at the LHC, the comparison with precision data and a first study of the unitarity of  $WW$  longitudinal scattering can be found in <sup>12, 46, 47)</sup>. In <sup>48)</sup> we discussed the unification issue within this model. Further studies appeared in <sup>49, 50)</sup>.

### 3.2 Next to Minimal Walking Technicolor Theory

The theory with three technicolors contains an even number of electroweak doublets, and hence it is not subject to a Witten anomaly. The doublet of technifermions, is then represented again as:

$$Q_L^{\{C_1, C_2\}} = \begin{pmatrix} U^{\{C_1, C_2\}} \\ D^{\{C_1, C_2\}} \end{pmatrix}_L, \quad Q_R^{\{C_1, C_2\}} = \left( U_R^{\{C_1, C_2\}}, D_R^{\{C_1, C_2\}} \right).$$

Here  $C_i = 1, 2, 3$  is the technicolor index and  $Q_{L(R)}$  is a doublet (singlet) with respect to the weak interactions. Since the two-index symmetric representation of  $SU(3)$  is complex the flavor symmetry is  $SU(2)_L \times SU(2)_R \times U(1)$ . Only three Goldstones emerge and are absorbed in the longitudinal components of the weak vector bosons. More information about this theory can be found in <sup>11)</sup>.

### 3.3 Partially Gauged Technicolor (PGT)

A small modification of the traditional technicolor approach, which neither involves additional particle species nor more complicated gauge groups, allows constructing several other viable candidates. It consists in letting only one doublet of techniquarks transform non-trivially under the electroweak symmetries with the rest being electroweak singlets, as first suggested in <sup>10)</sup> and later also used in <sup>51)</sup>.

Still, all techniquarks transform under the technicolor gauge group. Thereby, only one techniquark doublet contributes directly to the oblique parameter which is thus kept to a minimum for theories which need more than one family of techniquarks to be quasi-conformal. It is the condensation of that first electroweakly charged family that breaks the electroweak symmetry. We provided in <sup>8)</sup> an exhaustive list, given the knowledge about the phase diagram, of the possible underlying gauge theories one can use to construct PGT models. It is obvious that to be phenomenologically viable PGT requires the introduction, by hand, of mass terms for the flavors not gauged under the electroweak symmetry. The simplest model is an  $SU(N)$  gauge theory with a number of flavors in the fundamental representations sufficiently large that the massless theory is (near) conformal.

### 3.4 Conformal Technicolor = PGT

Luty in <sup>52)</sup> constructed a model of conformal technicolor <sup>53)</sup> using, in practice, the PGT model described above. We repeat once more that the addition of a mass term for the flavors not gauged under the electroweak symmetry is a necessity for any phenomenologically viable PGT model. In fact if the underlying PGT is near conformal the large chiral symmetry group breaks spontaneously and one must give mass to the phenomenologically unacceptable electroweak neutral Goldstone bosons. If the underlying theory is conformal a mass term must be introduced as well to generate the scale responsible for the breaking the electroweak symmetry in the first place. In <sup>8)</sup> we discussed the precision constraints for PGT while the bound of the large anomalous dimensions for the fermion condensate and its impact on the conformal window for nonsupersymmetric theories as well as the generation of a realistic top mass is present below equation (17) of <sup>6)</sup>.

### Acknowledgments

I am happy to thank T.A. Ryttov for discussions and careful reading of the manuscript. D.D. Dietrich, R. Foadi, M.T. Frandsen and M. Järvinen are thanked for discussions. I am partially supported by the Marie Curie Excellence

Grant under contract MEXT-CT-2004-013510.

## References

1. S. Weinberg, *Phys. Rev. D* **19**, 1277 (1979).
2. L. Susskind, *Phys. Rev. D* **20**, 2619 (1979).
3. F. Sannino, arXiv:0804.0182 [hep-ph].
4. C. T. Hill and E. H. Simmons, *Phys. Rept.* **381**, 235 (2003) [Erratum-ibid. **390**, 553 (2004)] [arXiv:hep-ph/0203079].
5. K. Lane, arXiv:hep-ph/0202255.
6. T. A. Ryttov and F. Sannino, arXiv:0711.3745 [hep-th].
7. T. A. Ryttov and F. Sannino, *Phys. Rev. D* **76**, 105004 (2007) [arXiv:0707.3166 [hep-th]].
8. D. D. Dietrich and F. Sannino, *Phys. Rev. D* **75**, 085018 (2007) [arXiv:hep-ph/0611341].
9. F. Sannino and K. Tuominen, *Phys. Rev. D* **71**, 051901 (2005) [arXiv:hep-ph/0405209].
10. D. D. Dietrich, F. Sannino and K. Tuominen, *Phys. Rev. D* **72**, 055001 (2005) [arXiv:hep-ph/0505059].
11. D. D. Dietrich, F. Sannino and K. Tuominen, *Phys. Rev. D* **73**, 037701 (2006) [arXiv:hep-ph/0510217].
12. R. Foadi, M. T. Frandsen, T. A. Ryttov and F. Sannino, *Phys. Rev. D* **76**, 055005 (2007) [arXiv:0706.1696 [hep-ph]].
13. L. Del Debbio, M. T. Frandsen, H. Panagopoulos and F. Sannino, *JHEP* **0806**, 007 (2008) [arXiv:0802.0891 [hep-lat]].
14. S. Catterall and F. Sannino, *Phys. Rev. D* **76**, 034504 (2007) [arXiv:0705.1664 [hep-lat]].
15. T. Appelquist, G. T. Fleming and E. T. Neil, *Phys. Rev. Lett.* **100**, 171607 (2008) [arXiv:0712.0609 [hep-ph]].
16. T. Appelquist, K. D. Lane and U. Mahanta, *Phys. Rev. Lett.* **61**, 1553 (1988).
17. A. G. Cohen and H. Georgi, *Nucl. Phys. B* **314**, 7 (1989).

18. V. A. Miransky and K. Yamawaki, Phys. Rev. D **55**, 5051 (1997) [Erratum-  
ibid. D **56**, 3768 (1997)] [arXiv:hep-th/9611142].
19. T. Appelquist, A. G. Cohen and M. Schmaltz, Phys. Rev. D **60**, 045003  
(1999) [arXiv:hep-th/9901109].
20. F. Sannino, Phys. Rev. D **72**, 125006 (2005) [arXiv:hep-th/0507251].
21. T. Appelquist, A. G. Cohen, M. Schmaltz and R. Shrock, Phys. Lett. B  
**459**, 235 (1999) [arXiv:hep-th/9904172].
22. T. Appelquist, Z. y. Duan and F. Sannino, Phys. Rev. D **61**, 125009 (2000)  
[arXiv:hep-ph/0001043].
23. V. A. Novikov, M. A. Shifman, A. I. Vainshtein and V. I. Zakharov, Nucl.  
Phys. B **229**, 381 (1983).
24. M. A. Shifman and A. I. Vainshtein, Nucl. Phys. B **277**, 456 (1986) [Sov.  
Phys. JETP **64**, 428 (1986 ZETFA,91,723-744.1986)].
25. T. Banks and A. Zaks, Nucl. Phys. B **196**, 189 (1982).
26. G. Mack, Commun. Math. Phys. **55**, 1 (1977).
27. M. Flato and C. Fronsdal, Lett. Math. Phys. **8**, 159 (1984).
28. V. K. Dobrev and V. B. Petkova, Phys. Lett. B **162**, 127 (1985).
29. N. Seiberg, Nucl. Phys. B **435**, 129 (1995) [arXiv:hep-th/9411149].
30. K. Yamawaki, M. Bando and K. i. Matumoto, Phys. Rev. Lett. **56**, 1335  
(1986).
31. B. Holdom, Phys. Lett. B **150**, 301 (1985).
32. B. Holdom, Phys. Rev. D **24**, 1441 (1981).
33. T. W. Appelquist, D. Karabali and L. C. R. Wijewardhana, Phys. Rev.  
Lett. **57**, 957 (1986).
34. N. Evans and F. Sannino, arXiv:hep-ph/0512080.
35. Y. Shamir, B. Svetitsky and T. DeGrand, arXiv:0803.1707 [hep-lat].
36. L. Del Debbio, A. Patella and C. Pica, arXiv:0805.2058 [hep-lat].
37. A. Deuzeman, M. P. Lombardo and E. Pallante, arXiv:0804.2905 [hep-lat].
38. Y. Iwasaki, K. Kanaya, S. Kaya, S. Sakai and T. Yoshie, Phys. Rev. D **69**,  
014507 (2004) [arXiv:hep-lat/0309159].

39. M. Luscher, R. Narayanan, P. Weisz and U. Wolff, Nucl. Phys. B **384**, 168 (1992) [arXiv:hep-lat/9207009].
40. M. Luscher, R. Sommer, P. Weisz and U. Wolff, Nucl. Phys. B **413**, 481 (1994) [arXiv:hep-lat/9309005].
41. S. Sint, Nucl. Phys. B **421**, 135 (1994) [arXiv:hep-lat/9312079].
42. A. Bode, P. Weisz and U. Wolff [ALPHA collaboration], Nucl. Phys. B **576**, 517 (2000) [Erratum-ibid. B **600**, 453 (2001 ERRAT,B608,481.2001)] [arXiv:hep-lat/9911018].
43. D. K. Hong, S. D. H. Hsu and F. Sannino, Phys. Lett. B **597**, 89 (2004) [arXiv:hep-ph/0406200].
44. T. Appelquist and F. Sannino, Phys. Rev. D **59**, 067702 (1999) [arXiv:hep-ph/9806409].
45. R. Sundrum and S. D. H. Hsu, Nucl. Phys. B **391**, 127 (1993) [arXiv:hep-ph/9206225].
46. R. Foadi, M. T. Frandsen and F. Sannino, Phys. Rev. D **77**, 097702 (2008) [arXiv:0712.1948 [hep-ph]].
47. R. Foadi and F. Sannino, arXiv:0801.0663 [hep-ph].
48. S. B. Gudnason, T. A. Rytto and F. Sannino, Phys. Rev. D **76**, 015005 (2007) [arXiv:hep-ph/0612230].
49. N. Chen and R. Shrock, arXiv:0805.3687 [hep-ph].
50. N. D. Christensen and R. Shrock, Phys. Rev. D **72**, 035013 (2005) [arXiv:hep-ph/0506155].
51. N. D. Christensen and R. Shrock, Phys. Lett. B **632**, 92 (2006) [arXiv:hep-ph/0509109].
52. M. A. Luty, arXiv:0806.1235 [hep-ph].
53. M. A. Luty and T. Okui, JHEP **0609**, 070 (2006) [arXiv:hep-ph/0409274].

***SESSION IX – PERSPECTIVES***

*Latino Giuseppe*

The TOTEM Experiment at LHC

*Kayser Boris*

PROJECT X AND THE FUTURE FERMILAB  
PROGRAM

*Mangano Michelangelo*

Physics with High Intensity Facilities (Project  
X, SLHC)



## THE TOTEM EXPERIMENT AT LHC

Giuseppe Latino

(for the TOTEM Collaboration)

*Siena University & Pisa INFN, Physics Dept., Via Roma, 56 - 53100 Siena,  
e-mail: giuseppe.latino@pi.infn.it*

### Abstract

The TOTEM experiment at the CERN LHC is here presented. After an overview of the experimental apparatus, the measurement of the total  $pp$  cross section, elastic scattering and diffractive phenomena is described. This physics programme will allow to distinguish among different models of soft proton interactions.

## 1 Introduction

The TOTEM experiment <sup>1)</sup> at the LHC is designed and optimized to measure the total  $pp$  cross section with a precision of about  $1 \div 2\%$ , to study the nuclear elastic  $pp$  cross section over a wide range of the squared four-momentum transfer  $-t^1$  ( $10^{-3} \text{ GeV}^2 < |t| < 10 \text{ GeV}^2$ ) and to perform a comprehensive physics programme on diffractive dissociation processes partially in cooperation with the CMS experiment. In order to fulfill its physics programme, complementary to the programme of the general-purpose experiments at the LHC, the TOTEM experiment has to cope the challenge of triggering and recording events in the very forward region with a good acceptance for particles produced at very small angles with respect to the beam. Based on the “luminosity independent” method the evaluation of the total cross section with such a small error will in particular require simultaneous measurement of the  $pp$  elastic scattering cross section  $d\sigma/dt$  down to  $|t| \sim 10^{-3} \text{ GeV}^2$  (to be extrapolated to  $t = 0$ ) as well as of the  $pp$  inelastic interaction rate. In particular, the detection of elastically scattered protons at a location very close to the beam (indeed inside the beam-pipe itself) is required together with particle detection with the largest possible coverage in order to reduce losses on inelastic events detection to a few percent.

The TOTEM apparatus is located on both sides of the interaction point IP5, the same LHC experimental area as CMS <sup>2)</sup>. The T1 and T2 tracking detectors are embedded inside the forward region of CMS (see fig.1, top). Charged track reconstruction in the pseudo-rapidity<sup>2</sup> range of  $3.1 \leq |\eta| \leq 6.5$  is performed by these two inelastic telescopes and complemented at very high  $|\eta|$  by detectors located in special movable beam-pipe insertion called “Roman Pots” (RP) which, being placed about 147 m and 220 m from IP5 (see fig.1, bottom), are designed to detect “leading” protons (scattered elastically or quasi-elastically from the interaction) at few mm from the beam center with a scattering angle down to few  $\mu\text{rad}$ .

The combination of the CMS and TOTEM experiments represents the largest acceptance detector ever built at a hadron collider which will also allow the study of a wide range of physics processes in diffractive interactions with an unprecedented coverage in rapidity. For this purpose the TOTEM data

---

<sup>1)</sup>In the relativistic limit and for small scattering angles:  $|t| \sim (p\theta)^2$ , where  $p$  is the proton momentum and  $\theta$  is the scattering angle with respect to the original beam direction.

<sup>2)</sup>Pseudo-rapidity is defined as  $\eta = -\ln(\tan \frac{\theta}{2})$ .

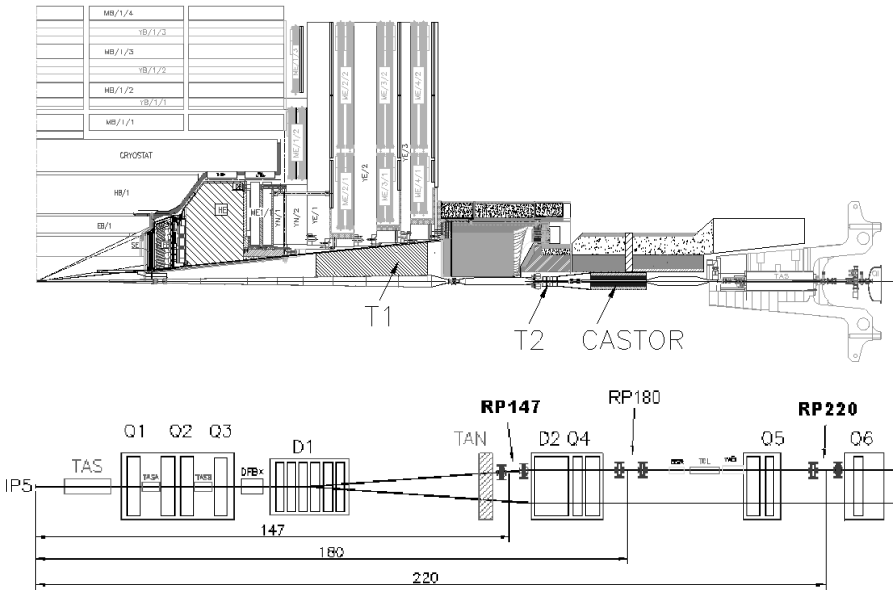


Figure 1: *Top: the TOTEM forward trackers T1 and T2 embedded into the forward region of the CMS detector. Bottom: TOTEM Roman Pots location along the LHC beam line at a distance about 147 m (RP147) and 220 m (RP220) from the interaction point IP5, RP180 being another possible location at the moment not equipped. All TOTEM detector components are located on both sides of IP5.*

acquisition system (DAQ) is designed to be compatible with the CMS DAQ in order to make common data taking possible at a later stage.

In the following, after a brief description of the experimental apparatus, the main features of the TOTEM physics programme will be presented.

## 2 Detector Overview

The TOTEM experimental setup comprises “Roman Pots” detectors to measure leading protons elastically scattered at very small angles within the beam pipe and the T1 and T2 inelastic telescopes providing charged track reconstruction for  $3.1 < |\eta| < 6.5$  with a  $2\pi$  coverage and with a very good efficiency in order to minimize losses (see fig.1). T1 and T2 track reconstruction will also allow trigger capability with acceptance greater than 95% for all inelastic events

<sup>3</sup> as well as the reconstruction of the event interaction vertex so that background events (mainly from beam-gas interactions and halo muons) <sup>3)</sup> can be rejected. Furthermore, the T1 and T2 detectors will provide tracking in front of the CMS HF (T1) and Castor (T2) very forward calorimeters so that the combination of these detectors can allow, for instance, a more complete study of “rapidity gaps”<sup>4</sup> and particle/energy flows in the very forward region.

The read-out of all TOTEM sub-detectors is based on the digital VFAT chip <sup>4)</sup> which is a tracking front-end ASIC specifically designed for the TOTEM experiment and characterized by trigger capabilities.

## 2.1 Roman Pots

The detection of very forward protons is performed by movable beam insertions, called “Roman Pots” (RP), hosting silicon detectors inside a secondary vacuum vessel (called “Pot”) which are moved very close to the beam into the primary vacuum of the machine through vacuum bellows. In this way the detectors can be put in a safe position when conditions of not stable beams are present (like at the very begin of a run), while are kept at the same time separated from the primary vacuum of the machine which is so preserved from an uncontrolled out-gassing of the detector materials. Two RP stations are installed on both sides from the interaction point IP5 on the beam pipe of the outgoing beam at a distance of about 147 m and at 220 m, a position chosen according to the constraints given by the space available among the LHC machine components and by the special optics used by TOTEM. A magnetic dipole between the two RP stations provides a magnetic spectrometer allowing an accurate proton momentum reconstruction. Each RP station is composed of two units (see fig.2, left) in order to have a lever arm for local track reconstruction and trigger selections by track angle. Each unit consists of 3 pots, 2 approaching the beam vertically from the top and the bottom and one horizontally which completes the acceptance for diffractively scattered protons (see fig.2, right). The overlap of the detectors in the horizontal pots with the ones in the vertical pots allows

---

<sup>3</sup>About 99.5% of all non-diffractive minimum bias events and about 84 % of all diffractive events have charged particles within the geometrical acceptance of T1 and T2 so that they are triggerable with these detectors.

<sup>4</sup>A rapidity gap, a region of pseudo-rapidity devoid of particles, is a typical signature for diffractive processes which are characterized by a hadronic color singlet exchange with vacuum quantum numbers, for which the Pomeron is one model.

a correlation of their positions via common particle tracks. This is used for the alignment of the three pots in an unit, the absolute alignment with respect to the beam being given by Beam Position Monitors (BPM) located in the vacuum chamber of the vertical pots.

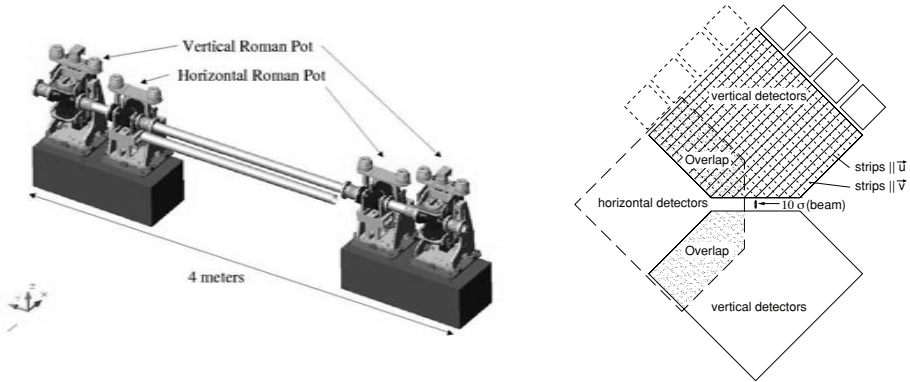


Figure 2: *Left: one TOTEM Roman Pot station. Right: arrangement of silicon detectors inside two vertical and one horizontal pots at a RP unit.*

Each pot contains a stack of 10 planes of novel silicon strip “edgeless” detectors, half of which have their strips oriented at an angle of  $+45^\circ$  and half at an angle of  $-45^\circ$  with respect to the edge facing the beam. Each plane has 512 strips with a pitch of  $66 \mu\text{m}$  allowing a single hit resolution of about  $20 \mu\text{m}$ . In order to detect protons elastically scattered at angles down to few  $\mu\text{rad}$  at the RPs locations, these detectors need to have their active area edge moved as close to the beam as  $\sim 1 \text{ mm}$ . Consequently, their edge dead area had to be greatly minimized so that a new “edgeless planar silicon” detector technology has been developed for TOTEM RPs where a current terminating structure allows to reduce to only  $50 \mu\text{m}$  the insensitive decoupling area detector edge and sensitive volume <sup>5)</sup>. For the same reason the stainless steel bottom foil of the pot (the one facing the beam) has been reduced to a thickness of  $150 \mu\text{m}$ , while the pot window in front of the detector active area is  $500 \mu\text{m}$  thick.

Irradiation studies on these silicon detectors, performed at the TRIGA reactor in Ljubljana at different neutron fluxes up to  $10^{14} \text{ 1 MeV n/cm}^2$  and with  $24 \text{ GeV}$  protons at CERN with a radiation up to  $1.4 \times 10^{14} \text{ p/cm}^2$ , have shown similar aging effects as for devices using standard voltage terminating structures. Calculations of the diffractive proton flux hitting the detectors indicate that the present detectors will probably be working up to an integrated

luminosity of about  $1 \text{ fb}^{-1}$ . To cope with higher luminosities, TOTEM has initiated an INTAS project to develop radiation harder edgeless detectors <sup>6)</sup>.

## 2.2 T1 and T2 tracking detectors

The T1 telescope covers the pseudo-rapidity range  $3.1 < |\eta| < 4.7$  on both sides of IP5. Each telescope arm consists of five planes, equally spaced in  $z$ , formed by six trapezoidal “Cathode Strip Chambers” (CSC) <sup>1)</sup> (see fig.3, left). The detector sextants in each plane are rotated with respect to each other by angles varying from  $-6^\circ$  to  $+6^\circ$  in steps of  $3^\circ$  in order to improve the pattern recognition for track reconstruction and to reduce the localized concentration of material in front of the CMS HF calorimeter. The TOTEM CSCs have a detector design similar to CMS CSC muon chambers with a gas gap of 10 mm and a gas mixture of Ar/CO<sub>2</sub>/CF<sub>4</sub> (40%/50%/10%). In these detectors the segmentation of cathode planes into parallel strips gives, combining their read-out with the one from anode wires, three measurements of the coordinates of the particle traversing the detector plane. Anode wires (with a pitch of 3 mm) give radial coordinate measurement which is also used for level-1 trigger information, while cathode strips (with a pitch of 5 mm) are rotated by  $\pm 60^\circ$  with respect to the wires. Beam tests on final prototypes have shown a spatial resolution of about 0.8 mm when using VFAT digital read-out. Aging studies performed at the CERN Gamma Irradiation Facility have shown no loss of performance after an irradiation resulting in a total charge integrated on the anode wires of 0.065 C/cm, which corresponds to an accumulated dose equivalent to about 5 years of running at luminosities of  $10^{30} \text{ cm}^{-2} \text{ s}^{-1}$ .

The T2 telescope, based on novel “Gas Electron Multiplier” (GEM) technology <sup>7)</sup>, extends charged track reconstruction to the rapidity range  $5.3 < |\eta| < 6.5$  <sup>1)</sup>. Placed 13.5 m away from both sides of IP5, each T2 arm consists of a set of 20 triple-GEM detectors having an almost semicircular shape with an inner radius matching the beam pipe. Ten aligned detectors planes, mounted “back-to-back”, are combined to form one T2 semi-arm on each side of the vacuum pipe (see fig.3, right). To avoid efficiency losses, the angular coverage of each detector is more than  $180^\circ$ . GEMs are gas-filled detectors, already successfully adopted in other experiments such as COMPASS and LHCb, which have been considered for the design of the TOTEM very forward T2 telescopes thanks to their characteristics, in particular: good spatial resolution, excellent rate capability and good resistance to radiation. Furthermore, GEM detectors are also characterized by the advantageous decoupling of the charge amplifica-

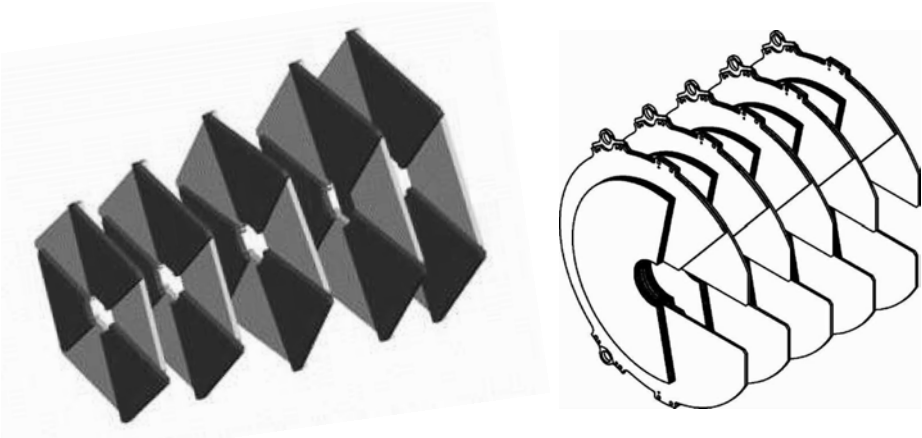


Figure 3: *Left: one arm of the TOTEM T1 telescope. Right: one half-arm of the TOTEM T2 telescope.*

tion structure from the charge collection and read-out structure which allows an easy implementation of the design for a given apparatus. The T2 GEMs <sup>8)</sup> use the same baseline design as the ones adopted in COMPASS with a triple-GEM structure, realized by separating three GEM foils by thin (2 mm) insulator spacers, adopted in order to reduce sparking probabilities while reaching typical total gas gains of about  $8 \times 10^3$  with a relatively low voltage (around 500 V) applied to each GEM foil. The gas mixture is Ar/CO<sub>2</sub> (70%/30%). The read-out board, explicitly designed for TOTEM, has two separate layers with different patterns: one with 256x2 concentric circular strips, 80  $\mu\text{m}$  wide and with a pitch of 400  $\mu\text{m}$ , allowing track radial reconstruction, and the other with a matrix of 24x65 pads varying in size from 2x2 mm<sup>2</sup> to 7x7 mm<sup>2</sup> (for a constant  $\Delta\eta \times \Delta\phi \sim 0.06 \times 0.017\pi$ ) providing level-1 trigger information as well as track azimuthal reconstruction. Final production detectors have been successfully tested in the 2007 beam test showing a spatial resolution in radial coordinate of about 100  $\mu\text{m}$  with digital VFAT read-out. COMPASS triple-GEM detectors aging tests have shown that a charge up to 20 mC/mm<sup>2</sup> can be integrated on the read-out board without aging effects. This corresponds to run TOTEM for at least 1 year at luminosities of  $10^{33}\text{cm}^{-2}\text{s}^{-1}$ . It is so assumed that TOTEM T2 triple-GEM can be operated during the first 3 years of LHC running.

### 3 Physics Programme

Given its unique coverage for charged particles at high rapidities, TOTEM is an ideal detector for studying forward phenomena, including elastic and diffractive scattering. Its main physics goals, precise measurements of the total  $pp$  cross section  $\sigma_{tot}$  and of the elastic scattering over a large range in  $t$ , are of primary importance in order to distinguish among different models of soft proton interactions. Furthermore, as energy flow and particle multiplicity of inelastic events peak in the forward region, the large rapidity coverage and the proton detection on both sides of the interaction point allow the study of a wide range of physics processes in inelastic and diffractive interactions.

#### 3.1 Total $pp$ cross section

Fig. 4 summarizes the existing measurements of  $\sigma_{tot}$  from low energies up to collider and cosmic ray energies, also showing recent predictions for the energy dependence of  $\sigma_{tot}$  by fitting all available  $pp$  and  $p\bar{p}$  scattering data according to different models <sup>9)</sup>. The dark error band shows the statistical errors to the best fit ( $\sigma_{tot} = 111.5 \pm 1.2^{+4.1}_{-2.1}$  mb for the LHC energy), the closest dashed curves near it give the sum of statistical and systematic errors to the best fit due to the discrepancy of the two Tevatron measurements, and the highest and lowest dotted curves show the total error bands (ranging in the 90–130 mb interval) from all models considered. This large theoretical uncertainty is due to the current lack of a fully satisfactory theoretical explanation of the cross section in low momentum transfer collisions, their description relying on phenomenological models to be tuned on existing data. The large uncertainties of the cosmic ray data and the 2.6 standard deviations discrepancy between the two final results from the Tevatron give an extrapolation to the LHC energy ( $\sqrt{s} = 14$  TeV) which is characterized by a wide range for the expected value of  $\sigma_{tot}$ , typically from 90 to 130 mb, depending on the model used for the extrapolation. More recent studies by other authors give predictions substantially within this range, with the exception of models with an explicit “hard” pomeron which give predictions at higher values <sup>10)</sup>. TOTEM aims to measure  $\sigma_{tot}$  with a precision down to  $\sim 1\%$  (or  $\sim 1$  mb), therefore allowing to discriminate among the different models.

In absence of an accurate determination of the LHC luminosity the measurement of  $\sigma_{tot}$  will be based on the “luminosity independent” method which combines the optical theorem, relating  $\sigma_{tot}$  to the imaginary part of the forward

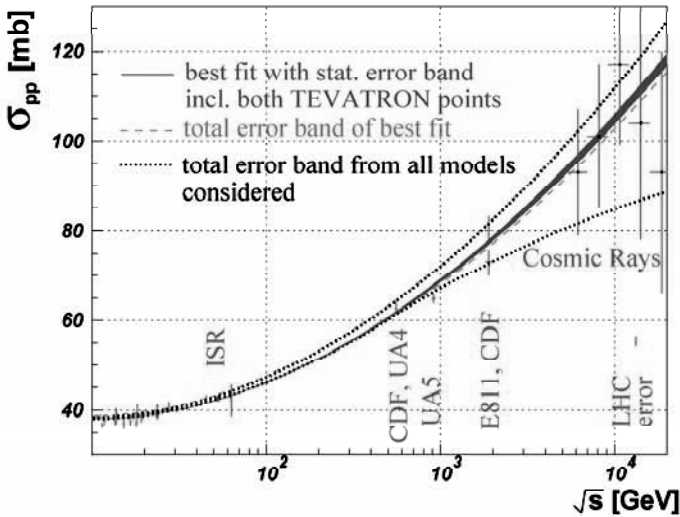


Figure 4: Fits from the COMPETE collaboration to all available  $pp$  and  $p\bar{p}$  scattering data <sup>9)</sup>.

scattering amplitude and leading to the following equation:

$$\mathcal{L} \sigma_{tot}^2 = \frac{16\pi}{1 + \rho^2} \cdot \left. \frac{dN_{el}}{dt} \right|_{t=0} \tag{1}$$

with the total rate equation:

$$\mathcal{L} \sigma_{tot} = N_{el} + N_{inel} \tag{2}$$

resulting in a system of 2 equations which can be solved for  $\sigma_{tot}$  and  $\mathcal{L}$ , which are so expressed as a function of measurable rates:

$$\sigma_{tot} = \frac{16\pi}{1 + \rho^2} \cdot \frac{dN_{el}/dt|_{t=0}}{N_{el} + N_{inel}} \tag{3}$$

$$\mathcal{L} = \frac{1 + \rho^2}{16\pi} \cdot \frac{(N_{el} + N_{inel})^2}{dN_{el}/dt|_{t=0}} \tag{4}$$

TOTEM will then measure  $\sigma_{tot}$  and the luminosity  $\mathcal{L}$  independently by experimentally measuring: the inelastic rate  $N_{inel}$  consisting of non-diffractive minimum bias events ( $\sim 65$  mb at LHC) and diffractive events ( $\sim 18$  mb at LHC) which will be measured by T1 and T2; the total nuclear elastic rate  $N_{el}$

( $\sim 30$  mb at LHC) and the nuclear part of the elastic cross section extrapolated to  $t = 0$  (optical point)  $dN_{el}/dt|_{t=0}$ , measured by the Roman Pot system. For the rate measurements it is important that all TOTEM detector systems have trigger capability. The expected uncertainty of the extrapolation to  $t = 0$  depends on the acceptance for elastically scattered protons at small  $t$ -values, hence on the beam optics. The  $\rho$  parameter, defined by:

$$\rho = \frac{\mathcal{R}[f_{el}(0)]}{\mathcal{I}[f_{el}(0)]} \quad (5)$$

where  $f_{el}(0)$  is the forward nuclear elastic scattering amplitude, has to be taken from external theoretical predictions, e.g. <sup>9)</sup>. Since  $\rho \sim 0.14$  enters only in a  $1 + \rho^2$  term, its impact is small.

A precise measurement of small scattering angles for the protons requires the beam angular divergence to be as small as possible, hence special runs with high machine optics  $\beta^*$  are required. The consequent increase in beam size at the interaction point and the zero crossing angle technically related to this optics configuration also require a small number of bunches, in order to avoid extra interactions between the colliding beams inside the common vacuum chamber. Consequently the typical instantaneous luminosity for the TOTEM  $\sigma_{tot}$  measurement at level of  $\sim 1\%$ , obtained with an approved optics characterized by  $\beta^* = 1540$  m and 43 bunches, will be of the order of  $10^{28}$   $\text{cm}^{-2}\text{s}^{-1}$ . The requirement of a special injection optics for the optimal  $\beta^* = 1540$  m configuration makes it probably not available at the early beginning of LHC. Another approved special beam optics with  $\beta^* = 90$  m (and a luminosity close to  $10^{30}$   $\text{cm}^{-2}\text{s}^{-1}$ ), achievable without modifying the standard LHC injection optics, will allow a preliminary  $\sigma_{tot}$  measurement at the level of about 5% uncertainty as well as an excellent measurement of the momentum loss of diffractive protons, opening the studies of soft and semi-hard diffraction, the latter in combination with the CMS detectors. After having understood the initial measurements and with improved beams at  $\beta^* = 1540$  m, a precision around 1% should be achievable, provided an improved knowledge of the optical functions<sup>5</sup> and an alignment precision of the RP station better than 50  $\mu\text{m}$  are obtained.

---

<sup>5</sup>The optical functions determine the explicit path of the particle through the magnetic elements and depend mainly on the position along the beam line (i.e. on all the magnetic elements traversed before reaching that position and their setting which is optics dependent) but also on the particle parameters at the IP.

Given the high value of measured rates, the statistical error on  $\sigma_{tot}$  measurement will be substantially negligible after few hours of data taking even at low luminosity runs. The vertex reconstruction will allow to largely reject the background from beam-gas (dominant) and beam halo events to a negligible rate. The systematic error for the measurement with  $\beta^* = 90$  m will be dominated by the extrapolation of nuclear elastic cross section to  $t = 0$  ( $\sim 4\%$  for  $|t|$  measured down to about  $|t| = 10^{-2}$  GeV<sup>2</sup>), while for the  $\beta^* = 1540$  m measurement the total inelastic rate will give the main systematic uncertainty which will be dominated by trigger losses in Single Diffraction events ( $\sim 0.8\%$ )<sup>6</sup>. The theoretical uncertainty related to the estimate of the  $\rho$  parameter is expected to give a relative uncertainty contribution of less than 1.2% (considering for instance the full error band on  $\rho$  extrapolation as derived in ref <sup>9</sup>). Combining all relevant uncertainties by error propagation for the equations 3 and 4, also taking into account the correlations, gives a relative error of about 5% (7%) for the measurement of  $\sigma_{tot}(\mathcal{L})$  with  $\beta^* = 90$  m and of about  $1\div 2\%$  (2%) for  $\sigma_{tot}(\mathcal{L})$  with  $\beta^* = 1540$  m <sup>6</sup>.

### 3.2 Nuclear elastic $pp$ scattering

Most of the interest in large impact parameter collisions is related to nuclear (hadronic) elastic scattering and to soft inelastic diffraction, both characterized, e.g., by the exchange of hadronic colour singlets. Fig. 5 shows the differential cross section of elastic  $pp$  interactions at  $\sqrt{s} = 14$  TeV <sup>11</sup>) as predicted by different models <sup>12</sup>). Several regions with different behavior can be distinguished when different  $t$ -ranges are considered at increasing  $|t|$  (which means looking deeper into the proton at smaller distance). The Coulomb region, where elastic

---

<sup>6</sup>Dedicated studies have shown that Single and Double Diffraction events are responsible for the major loss in the inelastic rate. With a single-arm trigger (in coincidence with a leading proton in the opposite side RP for the single diffractive events) a fraction of these events, corresponding to  $\sim 2.8$  mb, escapes detection. The lost events are mainly those with a very low mass (below  $\sim 10$  GeV/ $c^2$ ), since all their particles are produced at pseudo-rapidities beyond the T2 tracker acceptance. The fraction of these lost events can be estimated by extrapolation to low masses so to allow the determination of the total inelastic rate. For Single Diffraction, the extrapolated number of events differs from the simulation expectations by 4%, corresponding to a 0.6 mb uncertainty on the total cross-section. The same estimate for Double Diffraction and Double Pomeron Exchange gives a 0.1 mb and 0.2 mb uncertainty, respectively.

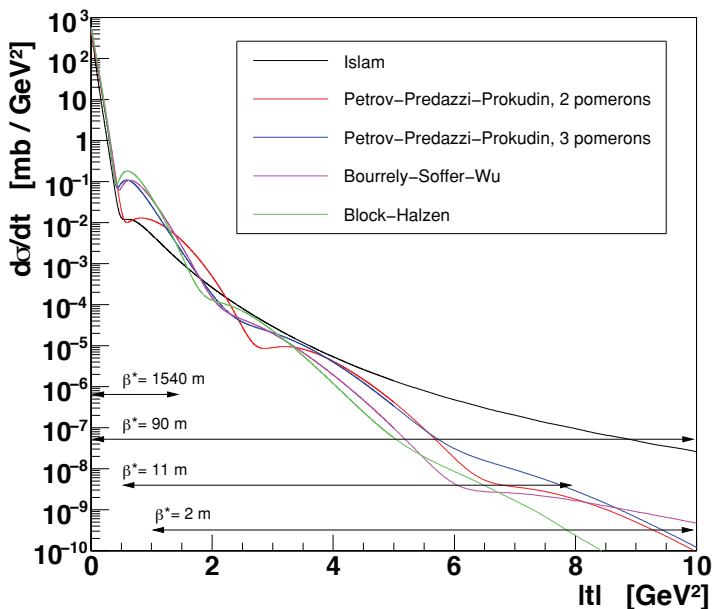


Figure 5: *Differential cross section of elastic scattering at  $\sqrt{s} = 14$  TeV as predicted by different models <sup>12)</sup>. The  $t$ -acceptance ranges for different optics settings are also shown.*

scattering is dominated by one photon exchange ( $d\sigma/dt \sim 1/t^2$ ), is characterized by  $|t| \leq 10^{-5} \text{ GeV}^2$ . In the intermediate region for  $|t|$  up to  $0.002 \text{ GeV}^2$ , the hadronic and Coulomb scattering interfere, complicating the extrapolation of the nuclear cross section to  $t = 0$ . The hadronic region, described in a simplified way, e.g., by “single-Pomeron exchange” with an approximately exponential cross section ( $d\sigma/dt \sim e^{-B|t|}$ ) at its lower border, is expected for  $0.002 < |t| < 0.4 \text{ GeV}^2$ .

The predictions of different models shown in Fig. 5 have been obtained by fitting the differential cross section data at lower measured energies starting at the ISR energies. The shown results are based on the eikonal model. The influence of the Coulomb scattering at lower  $|t|$  values has been described with the help of West and Yennie type of the total elastic scattering amplitude <sup>11)</sup>. It is still an open question if a different approach could be used in order to remove the discrepancy on the elastic impact parameters introduced by the West and Yennie approach <sup>11, 13)</sup>.

It is evident that the interference region and the beginning of hadronic

region are important for the extrapolation of hadronic  $dN_{el}/dt$  to  $t = 0$ , needed for determination of  $\sigma_{tot}$ . The  $t$ -dependence of  $B(t) = \frac{d}{dt} \ln \frac{d\sigma}{dt}$ , shows slight model dependent deviations <sup>11)</sup> from exponential shape, giving a theoretical uncertainty contribution to the systematic error of the total cross section measurement. The fit is typically performed with a quadratic polynomial parametrization in the  $|t|_{min} < |t| < 0.25 \text{ GeV}^2$  interval, where  $|t|_{min}$  depends on the acceptance for protons elastically scattered at small angles, which is related to the beam angular divergence. The expected uncertainty on the extrapolation to  $t = 0$  will be related to  $|t|_{min}$  ( $|t|_{min} \sim 0.002 (0.04) \text{ GeV}^2$  for  $\beta^* = 1540 (90) \text{ m}$ ), hence it will depend on the beam optics. The diffractive structure of the proton is then expected in the  $|t| > 0.4 \text{ GeV}^2$  region. Finally, for  $|t| \geq 1.5 \div 3 \text{ GeV}^2$  there is the domain of central elastic collisions at high  $|t|$  which might be described by perturbative QCD, e.g., in terms of three gluon exchange with a predicted cross section proportional to  $|t|^{-8}$  <sup>14)</sup>.

We can see from fig. 5 that there is a model dependence of the predictions which is very pronounced at high  $|t|$ . To discriminate among different models it is thus important to precisely measure the elastic scattering over the largest possible  $t$ -region. As shown in fig. 5 TOTEM can study different  $t$ -ranges depending on the LHC optics setting. Under different beam optics and running conditions TOTEM will cover the  $|t|$ -range from  $2 \times 10^{-3} \text{ GeV}^2$  to about  $10 \text{ GeV}^2$  spanning the elastic cross section measurement for over 11 orders of magnitude.

### 3.3 Diffraction and inelastic processes

Fig. 6 shows the typical event topology for non diffractive (Minimum Bias) and diffractive processes together with the associated cross sections, as expected at the LHC. Diffractive scattering processes (Single Diffraction, Double Diffraction, “Double Pomeron Exchange”, and higher order “Multi Pomeron” processes) together with the elastic scattering one, represent about 50% of the total cross section. Nevertheless, many details of these processes with close ties to proton structure and low-energy QCD are still poorly understood. The majority of diffractive events exhibits intact (“leading”) protons in the final state, characterized by their  $t$  and by their fractional momentum loss  $\xi \equiv \Delta p/p$ , most of which (depending on the beam optics) can be detected in the RP detectors. Already at an early stage, TOTEM will be able to measure  $\xi$ -,  $t$ - and mass-distributions in soft Double Pomeron and Single Diffractive events. The integration of TOTEM with the CMS detector will offer the possibility of

more detailed studies of the full structure of diffractive events, with the optimal reconstruction of one or more sizeable rapidity gaps in the particle distributions which can be obtained when the detectors of CMS and TOTEM will be combined for common data taking with an unprecedented rapidity coverage, as detailed in ref <sup>3</sup>). For this purpose the TOTEM triggers, combining information from the inelastic detectors and the silicon detectors in the RPs, are designed to be also incorporated into the general CMS trigger scheme.

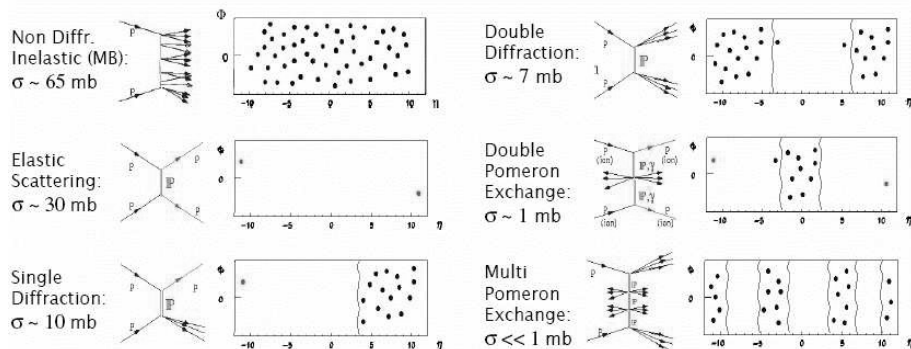


Figure 6: *Typical event topology for non diffractive (Minimum Bias) and diffractive processes in the pseudorapidity-azimuth plane. The associated cross sections, as estimated for the LHC, are also reported.*

TOTEM will also provide a significant contribution to the understanding of very high energy cosmic ray physics as it will give accurate informations on the basic properties of  $pp$  collisions at the maximum accelerator energy. A challenging issue in astrophysics is in fact represented by primary cosmic rays in the PeV ( $10^{15}$  eV) energy range and above. The LHC center of mass energy corresponds to a 100 PeV energy for a fixed target collision in the air. At the same time the LHC will provide a very high event rate relative to the very low rate of cosmic ray particles in this energy domain. Several high energy hadronic interaction models are nowadays available describing the nuclear interaction of primary cosmic ray entering the upper atmosphere and generating air showers. They predict energy flow, multiplicity and other quantities of such showers which characteristics are related to the nature of the primary interaction and to the energy and composition of the incident particle. There are large differences among the predictions of currently available models, with significant inconsistencies in the forward region. Several quantities can be measured by TOTEM

and CMS and compared with model predictions, among which: energy flow, elastic/total cross section, fraction of diffractive events, particle multiplicity. The study of the features of diffractive and inelastic events as measured in TOTEM and CMS may thus be used to validate/tune these generators<sup>3)</sup>.

## 4 Summary and Conclusions

The TOTEM experiment will be ready for data taking since the very beginning of the LHC start. Running under all beam conditions, it will be able to perform an important and exciting physics programme involving total and nuclear elastic scattering  $pp$  cross section measurements as well as diffractive processes studies. Special high  $\beta^*$  runs will be needed in order to perform an optimal measurement of total  $pp$  cross section at the level of  $\sim 1 \div 2$  % (for  $\beta^* = 1540$  m). An early measurement is foreseen with  $\beta^* = 90$  m (more easily achievable) with a relative error at the level of  $\sim 5$  %. The measurement of elastic scattering in the range  $10^{-3} \text{ GeV}^2 < |t| < 10 \text{ GeV}^2$  will allow to distinguish among a wide range of predictions according to current theoretical models. Finally, a common physics programme with CMS on soft and hard diffraction as well as on forward particle production studies will also be pursued.

## 5 Acknowledgements

I'm very grateful to the Conference Organizers, Giorgio Bellettini, Giorgio Chiarelli and Mario Greco for their kind invitation and warm hospitality at this very profitable and pleasant annual appointment for the HEP Community in La Thuile. I would like also to thank my Colleagues of the TOTEM Collaboration for their hard work in the development of the experiment and for precious input to this presentation.

## References

1. TOTEM Technical Design Report, CERN-LHCC-2004-002; addendum CERN-LHCC-2004-020 (2004).
2. CMS Physics Technical Design Report, Volume I: Detector performance and software, CERN-LHCC-2006-001 (2006);
3. The CMS and TOTEM diffractive and forward physics working group, Prospects for Diffractive and Forward Physics at the LHC, CERN-LHCC-2006-039/G-124 (2006).

4. P. Aspell *et al.*, VFAT2 : A front-end system on chip providing fast trigger information, digitized data storage and formatting for the charge sensitive readout of multi-channel silicon and gas particle detectors, Published in \*Prague 2007, Electronics for particle physics\* 63 (2007).
5. E. Noschis *et al.*, Final size planar edgeless silicon detectors for the TOTEM experiment, Nucl. Instr. & Meth. **A563**, 41 (2006).
6. G. Anelli *et al.* (TOTEM Collaboration), The TOTEM Experiment at the LHC, *in preparation*.
7. F. Sauli, GEM: A new concept for electron amplification in gas detectors, Nucl. Instr. & Meth. **A386**, 531 (1997).
8. S. Lami *et al.*, A triple-GEM telescope for the TOTEM experiment, Nucl. Phys. **B172**, 231 (2007).
9. J.R. Cudell *et al.* (COMPETE Collaboration), Benchmarks for the Forward Observables at RHIC, the Tevatron-Run II, and the LHC, Phys. Rev. Lett. **89**, 201801 (2002).
10. M.G. Ryskin *et al.*, Soft diffraction at the LHC: a partonic interpretation, Eur.Phys.J. **C54**, 199 (2008).  
A. Achilli *et al.*, Total cross-section and rapidity gap survival probability at the LHC through an eikonal with soft gluon resummation, Phys.Lett. **B659**, 137 (2008).
11. V. Kandrát *et al.*, To the theory of high-energy elastic nucleon collisions, in Forward Physics and QCD, Proceedings of the 12th International Conference on Elastic and Diffractive Scattering, DESY - Hamburg May 2007, DESY-PROC-2007-02, p.273 (2007).
12. M. M. Islam *et al.*, Near forward  $pp$  elastic scattering at LHC and nucleon structure, Int. J. Mod. Phys. **A21**, 1 (2006).  
C. Bourrely *et al.*, Impact-picture phenomenology for  $\pi^\pm p$ ,  $K^\pm p$  and  $pp$ ,  $\bar{p}p$  elastic scattering at high energies, Eur. Phys. J. **C28**, 97 (2003).  
V. A. Petrov *et al.*, Coulomb interference in high-energy  $pp$  and  $\bar{p}p$  scattering, Eur. Phys. J. **C28**, 525 (2003).  
M. M. Block *et al.*, Photon-proton and photon-photon scattering from nucleon-nucleon forward amplitudes, Phys. Rev. **D60**, 054024 (1999).
13. V. Kandrát *et al.*, Limited validity of West and Yennie interference formula for elastic scattering of hadrons, Phys. Lett. **B 656**, 182 (2007).
14. A. Donnachie, P. V. Landshoff, Elastic scattering at large  $t$ , Z. Phys. **C2**, 55 (1979), Erratum-ibid. **C2**, 372 (1979);  
The interest of large  $-t$  elastic scattering, Phys. Lett. **B387**, 637 (1966).

**PROJECT X AND THE FUTURE FERMILAB PROGRAM**

Boris Kayser

*Fermilab*

Written contribution not received



**PHYSICS WITH HIGH INTENSITY FACILITIES  
(PROJECT X, SLHC)**

Michelangelo Mangano  
*CERN*

Written contribution not received



***SESSION X – PHYSICS AND SOCIETY***

*Grassmann Hans*

Applying Physics Methods to Information Theory

*Buongiorno Jacopo*

New Safer Nuclear Reactors



# APPLYING PHYSICS METHODS TO INFORMATION THEORY

Hans Grassmann  
*University of Udine, Italy*

## Abstract

Currently, information theory is not a part of physics, and makes use of variables, which are not physics variables. We explore the possibility to apply known physics procedures to problems of information theory. We do this by considering whether some well defined mathematical structure can be associated to messages and message processing systems, and by defining variables which can be measured by means of well defined measurement procedures.

## 1 State of the Art

Information theory dates back to Shannon, who created it in order to study problems of signal transmission <sup>1)</sup>. Shannon's major concern was the effect of noise, and for this reason his theory takes a probabilistic character. For instance, the amount of information of a message is defined in the following generally known way: *"If in a set of messages the probabilities of the possible messages are given by  $p_1, p_2, \dots, p_n$ , then the amount of information associated with the first message is  $\log_2(\frac{1}{p_1})$ , that of the second  $\log_2(\frac{1}{p_2})$ , and so forth. The expected value of these amounts of information is called the entropy  $H$ , or the average information of the message set."* <sup>1)</sup>

It is often assumed, that the information "entropy" is identical to the physical entropy variable of thermodynamics. But this is not true. The entropy of physics is a state function, the "entropy" of information theory is not. For instance, a newspaper does not change its amount of information, when put into a refrigerator, while instead its thermodynamic entropy changes.

After Shannon, Chaitin, Kolmogorov and others created the algorithmic information theory, which is primarily concerned with message producing systems <sup>2, 3, 4)</sup> (while Shannon had gone deeper in studying the properties of messages). The logical structure of algorithmic information theory is very similar to Shannon's information theory. In algorithmic information theory the complexity of a program is the minimum length of a program which is capable to produce a certain message. Again, this complexity is not a physics variable, since it is in general not clear what "the shortest program" is supposed to be.

Szilard had attempted to insert the concept of "information" in physics <sup>5)</sup>. Studying the problem of the Maxwell demon, he concluded that storing one bit of information must necessarily dissipate the energy  $1/2kT$  ( $k$  = Boltzmann constant,  $T$  = absolute temperature). Later, Landauer argued that not storing of information dissipates energy, but rather erasing <sup>6)</sup>. Bennett instead concluded that in certain situations (reversible computing) energy dissipation in information processing can be avoided altogether <sup>7)</sup>. This situation with the findings of Szilard, Landauer and Bennett being in part in agreement, in part

---

<sup>1)</sup>Here we quote from Encyclopedia Britannica. For digital messages, and if 1 and 0 have the same probability to occur, the entropy of the message is therefore equal to the length of the message in bits.

not is not satisfying, and it does not yet constitute a conclusive physics theory.

## 2 Purpose of this paper

As far as thermodynamics is concerned, Szilard's arguments are based on a solid mathematical framework (statistics), provided by Boltzmann and others. However, Szilard applied thermodynamic arguments to the new field of "information", where there was no known mathematical structure at all. A possible mathematical structure of messages or message processing system was not known and was not considered. As a consequence concepts like "information" or "erasure" or "storing" were not defined in a general and fundamental way. Terms like "information" or "erasure" were clear in the context of a specific example (like Maxwell Demon or reversible computing etc), but had no general validity. Therefore statements, which were correct in a certain context where not necessarily correct in a different one.

In this paper we shall attempt to better understand the mathematical structure of messages and of message processing systems. This might help to apply Szilard's thermodynamic arguments to problems of information processing, making thereby the physics of information a new field of physics research. Since our contribution to the conference of La Thuile was given in the section *Science and Society* we also want to comment on the implications which the physics of information might have on fields like research on brain mode of operation, philosophy, theology and law, and in general on the position of the human being in this world.

## 3 Mathematical structure of messages and of message processing

We briefly summarize the findings presented in <sup>8)</sup>: "1" and "0" are the elements of the remainder class modulo 2 <sup>9)</sup>, which is a field of dimension 2 commonly referred to as  $F_2$ . Over  $F_2$  one can construct the arithmetic vector space  $F_2^n$ . Therefore digital messages are vectors in a mathematical sense. For instance, (1,0,1,1,0) is a 5-digit digital message, but it is also a element of  $F_2^5$ . It is therefore justified to discuss problems of information processing in terms of algebra. One can, for instance, consider the processing of an input message, a, by an information processing system, T, as a vector transformation, resulting in the output vector b:  $b=T(a)$ .

Considering information processing as an instance of vector operation allows us to connect mathematical concepts to concepts of the physical world by means of postulates. For instance, we can define when two messages have the same meaning: Some contract may have been translated from English into Chinese, and we would like to be sure that the Chinese version “is identical to” or “has the same meaning” as the English original. We can verify this by having the Chinese version translated back to English: if the original and the re-translated text are the same, we know that also the Chinese version is correctly translated.

We can express this now in the more precise mathematical language as follows. We postulate that two messages,  $a$  and  $b$ , have the same meaning, and contain the same information with respect to an information processing system,  $T$ , if  $b=T(a)$  and  $a=T^{-1}(b)$ . In this way also the “information” itself gets defined: An injective System  $T$  will conserve information, or: information is, what is conserved by injective systems. It seems furthermore reasonable to assume that two messages which contain the same information must have the same amount of information. But  $T$  being injective ( $T$  does not delete information) does not necessarily mean that  $a$  and  $b$  must have the same length (in number of bits). Therefore, in our scenario, the length of a message is not a measure of the amount of information of the message, in contrast to classic information theory. In our scenario one might measure the amount of information of a message as the logarithm of the number of possible messages in a vector space, or the number of dimensions of the vector space. For instance, if an information processing system outputs messages of  $n$  bit length, and if there are  $m$  different such messages, the amount of information of each message would be  $\log_2(m)$ , which becomes identical to the Shannon measure only for the case of  $m=2^n$ . One can conclude that considering the vector nature of message allows us to connect the mathematical concepts of information processing to the physics world. This is a significant progress with respect to classic information theory where one cannot compare messages in any way, and where even the concept of “information” is not defined.

A digital message of  $n$  bit length can have  $2^n$  different values. We assume, that  $T$  can process the message regardless of what value it has, that means, that all  $2^n$  possible vectors are possible input messages. Therefore the input vectors form a vector space, we refer to it as  $U$ . We next want to investigate

what properties the output vectors have, assuming certain properties of  $T$ . Throughout this note we always assume  $T$  to be injective.

#### 4 Linearity of information processing systems

If  $T$  is linear, it follows that also the output messages form a vector space,  $V$ , and input and output vector space are isomorphic. It also follows that  $T$  can be represented by a matrix with  $n$  columns, which span a vector space, which is isomorphic to both  $U$  and  $V$ . In different words: the vectors, which form  $T$ , can be injected to both  $U$  and  $V$ . This means that at execution time the information processing system does not input any new information. It rather consists of the information to be processed, already before run time.

Szillards argument (storing information must dissipate energy) can only be applied to the creation of  $T$  itself, since when creating  $T$  (loading of a program, or construction of a hardware device) some information obviously must be imported. Szillards argument does not apply to the operation of  $T$ , since  $T$  does not input new information while operating. One may address at this point Landauers and Bennetts “counter examples” to Szillards findings <sup>6, 7)</sup> in some detail. Here we note simply that those examples were possibly based on the assumption, that when inputting and processing a message an information processing system necessarily inputs information (this assumption is quite natural in conventional information theory). As far as Landauers and Bennets findings on the erasure of information are concerned <sup>6, 7)</sup>, we will later show that messages can be erased without energy dissipation.

Also if  $T$  is not linear there can be no more than  $2^n$  different output values of the  $n$ -digit input message  $a$ . The  $2^n$  different input values can be mapped onto a base with  $2^n$  dimensions, and the same can be done with the output elements. Then  $T$  can be replaced by an operation  $D$  operating between these two bases. Therefore  $D$  can be extended into a linear operation. Said differently:  $T$  always can be executed by means of a look up table with  $2^n$  elements. A lookup table is a special kind of a matrix.

We can conclude with two findings:

1. the “linearity” or “non-linearity” of an instance of physical information processing (we consider  $n$  to be finite) is not a fundamental notion, but rather refers to the technical particularity of the information processing

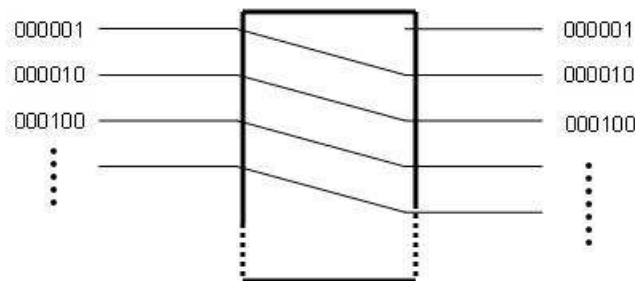


Figure 1: *Device performing a multiplication of a digital input number by 2,  $y=2x$ . The input signal arrives with the signal lines at the left of the device.*

system e.g. the use of digital computers instead of canonical computers.

2. For all information processing systems, also if they are not linear when operating in a digital space it is true: the information processing system must contain the information to be processed already before run time, and input and output messages have the same information.

In our scenario, the processing of a message is just a particular instant of message transmission. There is no explicit need for energy dissipation. And there is no need for a time sequence in information processing, information processing can occur, on the light cone of the message. We want to illustrate these features by a *gedanken experiment* in the following chapter.

## 5 Physical complexity

Figure 1 shows a very simple information processing system. It has a digital number as input and it multiplies this number by 2. This operation occurs without energy dissipation and on the light cone of the message. The processing of the message and the transmission of the message cannot really be

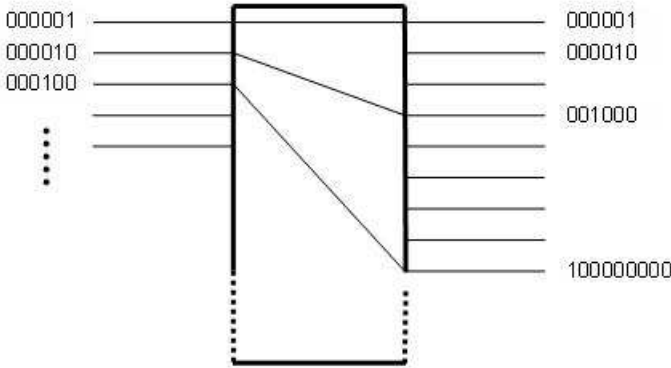


Figure 2: Device performing the operation  $y=x^2$ .

distinguished: the box, which indicates the “information processing system” in figure 1 could as well be omitted. It serves only to guide the eye, but it does not have any relevant function. It is furthermore true, that there is no program operating and therefore one cannot determine the complexity of the program which performs the operation of multiplication. With the same method we can perform any kind of operation if we operate with canonical numbers, instead of digital numbers. An example is shown in figure 2: the box of figure 2 has canonical numbers as input and output and it performs the operation  $y=x^2$ .

Again, one cannot talk about a “program” or its complexity. The information processing boxes of figure 1 or 2 can also erase messages. For example one could connect all input signal lines to always the same output line, for instance one might choose the line representing “0”. Regardless of what the input message is, the device would always produce the same 0 output and it would therefore have erased the message. This again would be done without energy dissipation (in contrast to the findings of Bennett).

The functionality of the computing boxes in figures 1 and 2 can be represented by a lookup table: as the devices in figure 1 and 2, a lookup table can produce for each input number a corresponding output.

In the most general case, in order to process an input number of  $n$  bits, the lookup table would need to have  $2^n$  elements. But for many operations, a system of smaller lookup tables would be sufficient in practice for performing the operation. This is shown in figure 3: the device of figure 3 performs an addition of two numbers of two bits. Each of the boxes indicated with an “+” adds two bits. These “fundamental adders” can be considered lookup table themselves they attribute to each of the  $2^2$  possible combinations of “1” and “0” the corresponding result. In general, if we want to perform the addition of two numbers of  $n$  bits each by a system of lookup tables as in figure 3, we need  $2n$  fundamental adders, each with 4 memory places, for a total of  $8n$  lookup table elements. The complete lookup table would have instead  $2^{2n}$  elements. This suggests to define the complexity of an information processing system as the minimum number of lookup table elements needed for the operation, or as the logarithm thereof. The lookup table elements are physical entities, which can be counted without ambiguity. Therefore this “physical complexity” can be measured (in contrast to the complexity of algorithmic information theory). Once we have decided to use for instance digital numbers, the complexity of an operation is then well defined and quantifiable and it does not depend on the program language.

Still, in lookup table systems like in figure 3 the processing can be performed without the need of organizing the operation in time steps. If we introduce a temporal sequence instead, we then can perform the whole addition with only one fundamental adder. We can do this by using again and again the same one lookup table (for adding two bits), and storing the intermediate results. This presents than what one would refer to as a “program”. The complexity of the program might therefore be measured by the number of repeated uses of a lookup table (or the logarithm thereof).

We have found in this chapter that one can perform mathematical operations like addition or multiplication with a system of lookup tables, which is smaller than the complete lookup table of  $2^n$  elements (for  $n$  bits of input), without making any approximation. In the next chapter we will investigate, whether also an image recognition system can be built with a small size lookup table.

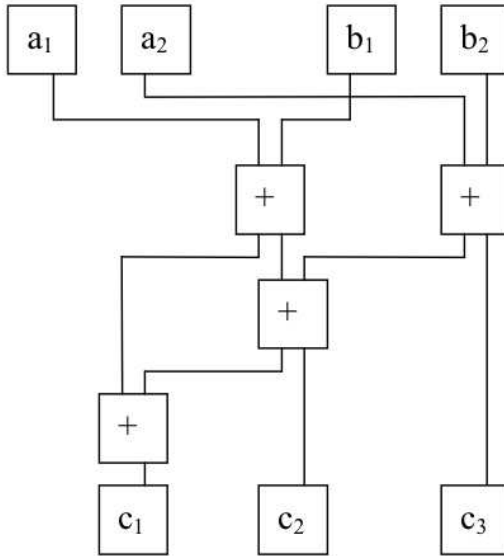


Figure 3: Machine for performing the calculation  $a+b=c$  on two input numbers of two bits each.

### 6 Computing the description of images

Without limiting generality, we assume an image of  $n$  black and white pixels (“1” and “0”). A universal image recognition system would consist of a lookup table of  $2^n$  elements, each element would describe the corresponding image. For instance, the image can be used as a digital address to the lookup table, with the corresponding memory element describing the image. If  $n$  is as large as millions such large lookup tables cannot be built, and the question arises, whether we can replace such large lookup tables with smaller and manageable ones. In order to address this problem, we make use of the tools of Boolean algebra, which has a rich choice of established procedures and definitions.

We define a set of  $m$  objects (anything would do, like apples, oranges, rectangles). They form a  $2^m$  element Boolean algebra (here and in the following we assume that also the position in space is characterizing these objects. For instance a rectangle in one certain position and an otherwise identical rectangle at a different position in space are considered as two different objects. Consider now the images of these objects. In general, the images will not form a  $2^m$  element Boolean algebra, because the objects may overlap, and the image of a

partially occluded object is different from the image of the completely visible object. But this is not a problem of image reconstruction in the very sense rather it is due to the fact that images are two-dimensional, and the physical world has three space dimensions. In a two dimensional physical world overlap would not exist. One might refer to this as a problem of representation, but it is not a problem of message processing.

In a first approach we therefore choose objects which do not overlap, in order to form the set with  $m$  elements (as mentioned before, the position of an object is a property of the object). Then, both the original objects and their images form Boolean Algebras with  $2^m$  elements and are isomorph. Furthermore, if we have associated to each image its correct description by means of a lookup table objects, images and their descriptions would form Boolean Algebras of  $2^m$  elements.

If  $a_i$  is one of the objects, and if  $b_i = D(a_i)$  is the description of the object, it is therefore true that the description of an image showing two objects,  $a_i$  and  $a_j$ , is identical to the list of the two descriptions for each single object:  $D(a_i \vee a_j) = D(a_i) \cup D(a_j) = b_i \cup b_j$ . This is how and why we can dramatically reduce the size of our universal image reconstruction lookup table: instead of describing all possible images of  $m$  objects with a lookup table of  $2^m$  elements, we can describe them equally well with a lookup table of  $m$  elements. Note, that this reduced lookup table is not an approximation. Rather it is analytical precise, like for instance the device in figure 3. In this sense, the fact that images form Boolean Algebras allows us to reconstruct a universal image reconstruction device, which describes images with the same analytical precision with which we can calculate  $a+b=c$ . We are now able to calculate the description of images. The process of "seeing" has become a calculus.

In order to build a real image processing system, we still need to consider two things: our argument does not only apply to sets of apples and oranges, but instead we can use as elements (Boolean atoms) any kind of object, like for instance line segments. The problem then arises of how to combine these segments to build larger objects, like straight lines or curves - and this should not be done by means of geometrical or phenomenological descriptions, but again using the methods of Boolean algebra. This is possible by forming strongly ordered sets. By defining adequate ordering relations, line segments can be ordered into objects. The second problem is how to deal with occluded objects,

which previously have been excluded from the discussion. We can include them by using ideals. An ideal of an image of a rectangle is the set of all images of the rectangle with one or several pixels omitted. Instead of using images of non occluded objects we can use their ideals. (We note that the term “ideal” sounds similar to Platons “ideas” not by accident: an information processing system which disposes of the ideal of a rectangle cannot be distinguished from an observer which knows Platons idea of a rectangle both of them have the same capacity of recognizing incomplete rectangles.)

Along these lines the spin off company Isomorph srl has developed a software package, which allows to recognize complex objects (like human beings) in non controlled environments performing also a three dimensional reconstruction of the scene. The reconstruction program does not make use of motion detection. The software is described in detail in <sup>8)</sup>, Isomorph srl refers to it as “linear computing”. Several demonstration movies can be found on the web site of Isomorph <sup>10)</sup>. Considering that less than two man years of development work have been invested in this software, it is performing in a very satisfying way indicating the practical use of the theoretical scenario presented here. A first industrial application has been highly successful <sup>10)</sup>. Ideally, one would perform linear computing not on a Turing machine, and in particular not on a von Neumann architecture. Rather one would prefer to use a “linear computing machine”. Operating on a digital input of  $n$  bits, an ideal linear computing machine would have  $2^n$  signal lines and  $2^n$  memory elements. Of course, such machines do not exist nowadays. A very interesting development towards such a linear computing machine does exist: IBM has recently presented the CELL processor. Using a system of sub processors, the CELL machine is able to operate on 1024 signal lines concurrently, and each of the sub processors has rather direct access to a dedicated memory space, so that it can very efficiently perform calls to lookup tables. The Isomorph srl software has been installed and executed successfully on this new processor with excellent results: the identification of a human being takes about 0.2 seconds, including three dimensional reconstruction.

## 7 More marginalization of humans?

In the past science has been accused to have marginalized the human being, first by displacing it from the centre of the world onto an arbitrary planet

somewhere in the universe. Then by showing its parenthood to the ape, then by showing that to a large extent humans are controlled by their subconscious, thus reducing the human being to one form of animal<sup>2</sup>. This is not just an academic discussion, rather many people suspect that this marginalization is at least in part responsible for the disastrous crimes which occurred in the 20th century. For this reason many people have a critical and distant relation to modern science. Recently, this development has considerably accelerated and turned into an even heavier underestimate of humanity. It has been claimed that the human brain is nothing but a poorly performing computer, thus moving the human being closer to a machine, which morally speaking is even less than an animal. If we consider what has been discussed in this paper from a purely mechanical point of view, it appears that our discussion may support and accelerate further this marginalization. If we can program “seeing”, “understanding”, “recognizing” into a computer, then this seems to support the view of the human being as a machine. We note instead, that in this paper we have merely tried to create the mathematical foundations on which arguments like the ones of Szilard must be founded in order to arrive at a physics theory of information. This is just the beginning of a discussion on the physical theory of information. As a next step, thermodynamics must be considered, as Szilard had attempted to do. According to the second law of thermodynamics, only processes can occur, which increase the entropy of a closed system (this closed system can for instance be the Universe). Vice versa, processes which increase the entropy of the Universe will spontaneously occur, provided they are allowed by the laws of physics. If Szilard was right, if energy must be dissipated when importing information into an information processing system, then one would deduce, that the “diffusion” of information into the brain would be a spontaneous process. To the best of our knowledge, no experimental research exists as regards to this question, and therefore no experimental evidence. But it is interesting to note, that this question (whether the diffusion of information into the brain is dissipating energy and whether it is therefore spontaneous) should be accessible to the scientific method, it is a question of scientific nature. Further it is interesting to note, that a process of spontaneous diffusion of information into the brain would help to explain cultural evolution. It also would

---

<sup>2</sup>From wikipedia: “The science of evolution is clear ... that humans are animals”

define a direction of evolution. As a consequence one would conclude, that human beings are more highly developed than animals (this conclusion is totally incompatible with present evolution theory) because they represent more information than animals. This would undo the seeming historical marginalization of the human. And it would do this, without contradicting Darwin, Freud or modern evolution biology. It would not be in contradiction, because up to now science was dealing only with the material world, for instance with organic life. And of course, with respect to its organic life, the human being is not different from the other animals.

And even without considering the hypothesis of a spontaneous process of diffusion of information from the outside world into the brain, another conclusion still can be found, again in contrast to the idea, that the human be marginal: if the vector scenario of information is true, then our brain cannot be anything else than an mirror of information found in the outside world. Cultural development would be a development towards a state of isomorphy between our brain and the world. Regardless of what the precise mechanisms are which lead to consciousness we at least could say, whose consciousness our consciuoness would be. If our brain is a mirror of the outside world, our consciousness necessarily would be the consciousness of the world. In this scenario, the Universe would exist also without us, but without us it would not be conscious of itself. In this scenario, we are the consciousness of the Universe. In this sense the old picture of the human as "centre of the world" would be re established and justified.

Much theoretical and experimental work still needs to be done. From a physics point of view this work is worth doing, since the physics of information gives us for the first time the chance of discussing thought itself in terms of physics - how and why we are doing physics becomes a subject of physics. From a more general point of view these studies should be supported, since the physics of information seems to have the potential to undo the seeming marginalization of the human being.

## 8 Acknowledgements

This paper has been made possible by Giorgio Bellettini, and it was financed by Isomorph srl. Many encouraging discussions with Gregory Chaitin have prevented us from abandoning this project.

## References

1. C. E. Shannon: A mathematical theory of communication. Bell System Technical Journal, vol. 27, pp. 379423 and 623656, July and October, 1948.
2. Ray Solomonoff, A Formal Theory of Inductive Inference, Part I", Information and Control, Part I: Vol 7, No. 1, pp. 1-22, March 1964
3. C.S. Wallace, D.L. Dowe, Minimum Message Length and Kolmogorov Complexity, Computer Journal, Vol. 42, No. 4, 1999
4. G.J. Chaitin, Algorithmic information theory, IBM Journal of Research and Development 21 (1977), pp. 350359, 496
5. L. Szilard, ber die Entropieverminderung in einem thermodynamischen System bei Eingriffen intelligenter Wesen, Zeitschrift fr Physik 53, 840-856.
6. R.Landauer, Irreversibility and heat generation in the computing process, IBM Journal of Research and Development, vol. 5, pp. 183-191, 1961
7. C.H.Bennett, Logical reversibility of computation, IBM Journal of Research and Development, vol. 17, pp 525-532 (1973); C.H.Bennett, The thermodynamics of computation a review, Int.J.Theor.Phys. 21, pp 905-940 (1982); C.H.Bennett, Notes on the history of reversible computing, IBM Journal of Research and Development, vol. 32, pp 16-23 (1988)
8. H. Grassmann, On the mathematical structure of messages and message processing systems, Isomorph Letters (A) 1 (2007). <http://letters.isomorph.it>
9. Wu-Ki Tung, Group Theory in Physics, World Scientific Publishing Co., 1999
10. [www.isomorph.it](http://www.isomorph.it)

**NEW SAFER NUCLEAR REACTORS**

Jacopo Buongiorno  
*MIT, Massachusetts, USA*

Written contribution not received



## ***PARTICIPANTS***



---

Adelman Jahred	University of Chicago	USA
Aguilar-Arevalo Alexis	TRIUMF	Canada
Aguilar-Benitez Manuel	CIEMAT-Madrid	Spain
Askev Andrew	Florida State University	USA
Barberio Elisabetta	University of Melbourne	Australia
Baschiera Bruno	Aosta	Italy
Bellettini Giorgio	Università di Pisa/INFN	Italy
Bellomo Massimiliano	INFN-Pavia	Italy
Bernagozzi Andrea	Aosta	Italy
Bertolini Enzo	Aosta	Italy
Blucher Edward	University of Chicago	USA
Bonin Roberto	Aosta	Italy
Bryman Douglas	University of British Columbia	Canada
Buccella Franco	Univerist di Napoli/INFN	Italy
Buongiorno Jacopo	MIT, Massachusetts	USA
Caravaglios Francesco	Università di Milano	Italy
Carbognani Albino	Aosta	Italy
Castaldi Rino	INFN-Pisa	Italy
Castilla-Valdez Heriberto	Cinvestav-Mexico City	Mexico
Cerutti Fabio	INFN-LNF	Switzerland
Cherednikov Igor	Ruhr University	Germany
Chiang Cheng-Chin	Taiwan University	Taiwan
Chiarella Vitaliano	INFN-LNF	Italy
Chiarelli Giorgio	INFN-Pisa	Italy
Colafrancesco Sergio	ASI-ASDC	Italy
Dabagov Sultan	LNF-NFN	Italy
Dar Arnon	Technion	Israel
De Rujula Alvaro	CERN	Switzerland
De Sanctis Luca	Università di Bologna	Italy
Delduca Vittorio	INFN-LNF	Italy
Dell'Agnello Simone	INFN-LNF	Italy

Dokuchaev Vyacheslav	Moscow	Russia
Dolgov Alexander	Ferrara/ITEP Moscow	Italy
Dong Peter	UCLA	USA
Du Shuxian	IHEP–Beijing	China
Ermolaev Boris	Ioffe Institute	Russia
Falk Harris Elisabeth	University of Sussex	UK
Fargion Daniele	Università di Roma 1	Italy
Faucci Giannelli Michele	University of London	UK
Ferrari Ruggero	Università di Milano	Italy
Ferroni Fernando	Università di Roma/INFN	Italy
Fritzsch Harald	University of Munich	Germany
Fucito Francesco	INFN–Roma 2	Italy
Gardi Einan	University of Edinburgh	UK
Garfagnini Alberto	Università di Padova	Italy
Gastaldi Ugo	INFN–LNL	Italy
Gatti Claudio	INFN–LNF	Italy
Gentile Simonetta	Università di Roma	Italy
Gervino Gianpiero	INFN–Torino	Italy
Gorini Benedetto	CERN	Switzerland
Goudzovski Evgueni	INFN–Pisa	Italy
Grassmann Hans	Università di Udine	Italy
Greco Mario	Università di Roma 3/INFN	Italy
Craig Robert	GROUP Fermilab	USA
Ianni Aldo	INFN–LNGS	Italy
Imperial Albino	CORECOM–Aosta	Italy
Jones Matthew	Purdue University	USA
Kajomovitz Enrique	Technion	Israel
Kampert Karl-Heinz	University Wupperta 1	Germany
Kayser Boris	Fermilab	USA
Kazakov Dmitri	JINR/ITEP	Russia
Khoze Valeri	University of Durham	UK

---

Kim Yeongduk	Sejong University	Republic of Korea
Lami Stefano	INFN–Pisa	Italy
Latino Giuseppe	Università di Siena/INFN	Italy
Lavagno Andrea	Politecnico di Torino	Italy
Lehmann Miotto Giovanna	CERN	Switzerland
Leone Sandra	INFN–Pisa	Italy
List Jenny	DESY	Germany
Lubatti Henry	University of Washington	Usa
Lubicz Vittorio	Università di Roma 3	Italy
Lubrano Pasquale	INFN–Perugia	Italy
Magnea Lorenzo	Università di Torino	Italy
Mangano Michelangelo	CERN	Switzerland
Mannocchi Giampaolo	INFN/INAF	Italy
Manoni Elisa	Università di Perugia/INFN	Italy
Marcellini Stefano	INFN–Bologna	Italy
Mariotti Mos	Università di Padova/INFN	Italy
Masiero Antonio	Università di Padova/INFN	Italy
Massó Eduard	Universidad Barcelona	Spain
Mateev Matey	University of Sofia	Bulgaria
Minkowski Peter	University of Bern	Switzerland
Mizuk Roman	ITEP–Moscow	Russia
Moretti Mauro	Università di Ferrara	Italy
Neri Nicola	Università di Pisa/INFN	Italy
Neumeister Norbert	Purdue University	USA
Nikolopoulos Konstantinos	University of Athens	Greece
Novikov Victor	ITEP–Moscow	Russia
Ogburn Walter	Caltech	USA
Pakhlov Pavel	ITEP–Moscow	Russia
Palla Fabrizio	INFN–Pisa	Italy
Papaevangelou Thomas	CEA Saclay	France
Pedlar Todd	Luther College	USA

Penzo Aldo	INFN–Trieste	Italy
Peruzzi Ida	LNF–INFN	Italy
Piccinini Fulvio	INFN–Pavia	Italy
Piccolo Marcello	LNF–INFN	Italy
Playfer Steve	University of Edinburgh	UK
Pleier Marc-Andre	University of Bonn	Germany
Polosa Antonello	INFN–Roma 1	Italy
Pranko Aliaksandr	Fermilab	USA
Rodriguez-Frias Dolores	University of Alcala	Spain
Ronga Frederic	ETH–Zurich	Switzerland
Rozen Yoram	Technion	Israel
Sanders Michiel	LPNHE–Paris	France
Sannino Francesco	University of Denmark	Denmark
Spagnolo Paolo	INFN–Pisa	Italy
Sparvoli Roberta	Università di Roma 2	Italy
Spurio Maurizio	Università di Bologna/INFN	Italy
Stanco Luca	INFN–Padova	Italy
Stdenis Richard	Glasgow University	UK
Tassi Enrico	Università della Calabria/INFN	Italy
Trincherò Gian Carlo	INAF–IFSI Torino	Italy
Truc Fabio	CORECOM	Italy
Turini Nicola	Università di Siena/INFN	Italy
Vannucci Luigi	INFN–LNL	Italy
Verdier Patrice	IPN–Lyon	France
Voena Cecilia	Università di Roma/INFN	Italy
Weber Alfons	University of Oxford	UK
Whiteson Daniel	UC Irvine	USA
Yuan Ye	IHEP–Beijing	China
Zanderighi Giulia	University of Oxford	UK

---

**FRASCATI PHYSICS SERIES VOLUMES****Volume I***Heavy Quarks at Fixed Target*

Eds.: S. Bianco and F.L. Fabbri

Frascati, May 31–June 2, 1993

ISBN—88-86409-00-1

**Volume II – Special Issue***Les Rencontres de Physique de la Vallée d'Aoste –  
Results and Perspectives in Particle Physics*

Ed.: M. Greco

La Thuile, Aosta Valley, March 5–11, 1995

ISBN—88-86409-03-6

**Volume III***Heavy Quarks at Fixed Target*

Ed.: B. Cox

University of Virginia, Charlottesville

October 7–10, 1994, 11

ISBN—88-86409-04-4

**Volume IV***Workshop on Physics and Detectors for DAΦNE*

Eds.: R. Baldini, F. Bossi, G. Capon, G. Pancheri

Frascati, April 4–7, 1995

ISBN—88-86409-05-2

**Volume V – Special Issue***Les Rencontres de Physique de la Vallée d'Aoste –  
Results and Perspectives in Particle Physics*

Ed.: M. Greco

La Thuile, Aosta Valley, March 3–9, 1996

ISBN—88-86409-07-9

**Volume VI***Calorimetry in High Energy Physics*

Eds.: A. Antonelli, S. Bianco, A. Calcaterra, F.L. Fabbri

Frascati, June 8–14, 1996

ISBN—88-86409-10-9

**Volume VII***Heavy Quarks at Fixed Target*

Ed.: L. Köpke

Rhinefels Castle, St. Goar, October 3–6, 1996

ISBN—88-86409-11-7

**Volume VIII***ADONE a milestone on the particle way*

Ed.: V. Valente 1997

ISBN—88-86409-12-5

**Volume IX – Special Issue***Les Rencontres de Physique de la Vallée d'Aoste –**Results and Perspectives in Particle Physics*

Ed.: M. Greco

La Thuile, Aosta Valley, March 2–8, 1997

ISBN—88-86409-13-3

**Volume X***Advanced ICFA Beam Dynamics**Workshop on Beam Dynamics Issue for  $e^+e^-$  Factories*

Eds.: L. Palumbo, G. Vignola

Frascati, October 20–25, 1997

ISBN—88-86409-14-1

**Volume XI***Proceedings of the XVIII International Conference on**Physics in Collision*

Eds.: S. Bianco, A. Calcaterra, P. De Simone, F. L. Fabbri

Frascati, June 17–19, 1998

ISBN—88-86409-15-X

**Volume XII – Special Issue***Les Rencontres de Physique de la Vallée d'Aoste –**Results and Perspectives in Particle Physics*

Ed.: M. Greco

La Thuile, Aosta Valley, March 1–7, 1998

ISBN—88-86409-16-8

**Volume XIII**

*Bruno Touschek and the Birth of the  $e^+e^-$*

Ed.: G. Isidori

Frascati, 16 November, 1998

ISBN—88-86409-17-6

**Volume XIV – Special Issue**

*Les Rencontres de Physique de la Vallée d'Aoste –  
Results and Perspectives in Particle Physics*

Ed.: M. Greco

La Thuile, Aosta Valley, February 28–March 6, 1999

ISBN—88-86409-18-4

**Volume XV**

*Workshop on Hadron Spectroscopy*

Eds.: T. Bressani, A. Feliciello, A. Filippi

Frascati, March 8–2, 1999

ISBN—88-86409-19-2

**Volume XVI**

*Physics and Detectors for DAΦNE*

Eds.: S. Bianco, F. Bossi, G. Capon, F.L. Fabbri,

P. Gianotti, G. Isidori, F. Murtas

Frascati, November 16–19, 1999

ISBN—88-86409-21-4

**Volume XVII – Special Issue**

*Les Rencontres de Physique de la Vallée d'Aoste –  
Results and Perspectives in Particle Physics*

Ed.: M. Greco

La Thuile, Aosta Valley, February 27–March 4, 2000

ISBN—88-86409-23-0

**Volume XVIII**

*LNF Spring School*

Ed.: G. Pancheri

Frascati 15–20 May, 2000

ISBN—88-86409-24-9

**Volume XIX***XX Physics in Collision*

Ed.: G. Barreira

Lisbon June 29–July 1st, 2000

ISBN—88-86409-25-7

**Volume XX***Heavy Quarks at Fixed Target*

Eds.: I. Bediaga, J. Miranda, A. Reis

Rio de Janeiro, Brasil, October 9–12, 2000

ISBN—88-86409-26-5

**Volume XXI***IX International Conference on Calorimetry in**High Energy Physics*

Eds.: B. Aubert, J. Colas, P. Nédélec, L. Poggioli

Annecy Le Vieux Cedex, France, October 9–14, 2000

ISBN—88-86409-27-3

**Volume XXII – Special Issue***Les Rencontres de Physique de la Vallée d’Aoste –  
Results and Perspectives in Particle Physics*

Ed.: M. Greco

La Thuile, Aosta Valley, March 4–10, 2001

ISBN—88-86409-28-1

**Volume XXIII***XXI Physics in Collision*

Ed.: Soo-Bong Kim

Seoul, Korea, June 28–30, 2001

ISBN—88-86409-30-3

**Volume XXIV***International School of Space Science – 2001 Course on:  
Astroparticle and Gamma-ray Physics in Space*

Eds.: A. Morselli, P. Picozza

L’Aquila, Italy, August 30–September 7, 2000

ISBN—88-86409-31-1

**Volume XXV**

*TRDs for the 3rd Millennium Workshop on  
Advanced Transition Radiation Detectors for  
Accelerator and Space Applications*

Eds. N. Giglietto, P. Spinelli

Bari, Italy, September 20–23, 2001

ISBN—88-86409-32-X

**Volume XXVI**

*KAON 2001 International Conference on CP Violation*

Eds.: F. Costantini, G. Isidori, M. Sozzi

Pisa Italy, June 12th 17th, 2001

ISBN—88-86409-33-8

**Volume XXVII – Special Issue**

*Les Rencontres de Physique de la Vallée d’Aoste –  
Results and Perspectives in Particle Physics*

Ed.: M. Greco

La Thuile, Aosta Valley, March 3–9, 2002

ISBN—88-86409-34-6

**Volume XXVIII**

*Heavy Quarks at Leptons 2002*

Eds.: G. Cataldi, F. Grancagnolo, R. Perrino, S. Spagnolo

Vietri sul mare (Italy), May 27th June 1st, 2002

ISBN—88-86409-35-4

**Volume XXIX**

*Workshop on Radiation Dosimetry: Basic Technologies,  
Medical Applications, Environmental Applications*

Ed.: A. Zanini

Rome (Italy), February 56, 2002

ISBN—88-86409-36-2

**Volume XXIX – Suppl.**

*Workshop on Radiation Dosimetry: Basic Technologies,  
Medical Applications, Environmental Applications*

Ed.: A. Zanini

Rome (Italy), February 56, 2002

ISBN—88-86409-36-2

**Volume XXX – Special Issue**

*Les Rencontres de Physique de la Vallée d'Aoste –  
Results and Perspectives in Particle Physics*

Ed.: M. Greco

La Thuile, Aosta Valley, March 9–15, 2003

ISBN—88-86409-39-9

**Volume XXXI**

*Frontier Science 2002 – Charm, Beauty and CP,  
First International Workshop on Frontier Science*

Eds.: L. Benussi, R. de Sangro, F.L. Fabbri, P. Valente

Frascati, October 6–11, 2002

ISBN—88-86409-37-0

**Volume XXXII**

*19th International Conference on x-ray and Inner-Shell Processes*

Eds.: A. Bianconi, A. Marcelli, N.L. Saini

Università di Roma La Sapienza June 24–28, 2002

ISBN—88-86409-39-07

**Volume XXXIII**

*Bruno Touschek Memorial Lectures*

Ed.: M. Greco, G. Pancheri

Frascati, May 11, 1987

ISBN—88-86409-40-0

**Volume XXXIV – Special Issue**

*Les Rencontres de Physique de la Vallée d'Aoste –  
Results and Perspectives in Particle Physics*

Ed.: M. Greco

La Thuile, Aosta Valley, February 29 – March 6, 2004

ISBN—88-86409-42-7

**Volume XXXV**

*Heavy Quarks And Leptons 2004*

Ed.: A. López

San Juan, Puerto Rico, 1–5 June 2004

ISBN—88-86409-43-5

**Volume XXXVI***DAΦNE 2004: Physics At Meson Factories*Eds.: F. Anulli, M. Bertani, G. Capon, C. Curceanu-Petrascu,  
F.L. Fabbri, S. Miscetti

Frascati, June 7–11, 2004

ISBN—88-86409-53-2

**Volume XXXVII***Frontier Science 2004, Physics and Astrophysics in Space*

Eds.: A. Morselli, P. Picozza, M. Ricci

Frascati, 14–19 June, 2004

ISBN—88-86409-52-4

**Volume XXXVIII***II Workshop Italiano sulla Fisica di ATLAS e CMS*

Eds.: Gianpaolo Carlino and Pierluigi Paolucci

Napoli, October 13 – 15, 2004

ISBN—88-86409-44-3

**Volume XXXIX – Special Issue***Les Rencontres de Physique de la Vallée d’Aoste –  
Results and Perspectives in Particle Physics*

Ed.: M. Greco

La Thuile, Aosta Valley, February 27 – March 5, 2005

ISBN—88-86409-45-1

**Volume XL***Frontier Science 2005 – New Frontiers in Subnuclear Physics*

Eds.: A. Pullia, M. Paganoni

Milano, September 12 - 17, 2005

ISBN—88-86409-46-X

**Volume XLI***Discoveries in Flavour Physics at  $e^+e^-$  Colliders*Eds.: L. Benussi, S. Bianco, C. Bloise, R. de Sangro, C. Gatti,  
G. Isidori, M. Martini, F. Mescia, S. Miscetti

Frascati, February 28th - March 3rd, 2006

ISBN—88-86409-51-6

**Volume XLII – Special Issue**

*Les Rencontres de Physique de la Vallée d'Aoste –  
Results and Perspectives in Particle Physics*

Ed.: M. Greco

La Thuile, Aosta Valley, March 5 – March 11, 2006

ISBN—88-86409-47-8

**Volume XLIII – Special Issue**

*Neutral Kaon Interferometry at A Phi-Factory: from Quantum Mechanics to  
Quantum Gravity*

Ed.: A. Di Domenico

Frascati, March 24th 2006

ISBN 978—88-86409-50-8

**Volume XLIV – Special Issue**

*Les Rencontres de Physique de la Vallée d'Aoste –  
Results and Perspectives in Particle Physics*

Ed.: M. Greco

La Thuile, Aosta Valley, February 28, 2 – March 5, 2007

ISBN 978—88-86409-49-4

**Volume XLV *Frontier Science – Science with the New Generation  
High Energy Gamma-ray Experiments***

Eds.: A. Lionetto, A. Morselli

Villa Mondragone, Monteporzio, Italy June 18 -20, 2007

ISBN-978—88-86409-54-0

**Volume XLVI**

*XII International Conference on Hadron Spectroscopy*

Eds.: L. Benussi, M. Bertani, S. Bianco, C. Bloise, R. de Sangro, P. de Simone,  
P. di Nezza, P. Giannotti, S. Giovanella, M.P. Lombardo, S. Pacetti

Laboratori Nazionali di Frascati, October 7-13, 2007

ISBN—978-88-86409-55-1

**FRASCATI PHYSICS SERIES VOLUMES – Italian Collection**

*Collana: Scienza Aperta Vol. I (2006) - Comunicare Fisica 2005*

Atti 1 Convegno "Comunicare Fisica e altre Scienze",

Frascati 24-27 Ottobre 2005

Eds: Franco L. Fabbri, Piero Patteri

ISBN – 88-86-409-48-6













